The standard model for relativistic heavy-ion collisions and electromagnetic tomography

Dissertation

Presented in Partial Fulfillment of the Requirements for the Degree Doctor of Philosophy in the Graduate School of The Ohio State University

By

Chun Shen, B.S.

Graduate Program in Physics

The Ohio State University

2014

Dissertation Committee:

Professor Ulrich Heinz, Advisor

Professor Michael Lisa

Professor Robert Perry

Professor Mohit Randeria

Abstract

This thesis focuses on developing a standard theoretical framework to study the bulk dynamics and electromagnetic probes of ultra-relativistic heavy-ion collisions, which are presently studied experimentally at the Relativistic Heavy-Ion Collider (RHIC) and the Large Hadron Collider (LHC). We developed a modular numerical package with different (exchangeable) modular describing different evolution stages of the expanding fireball created in these collisions. For each stage of the collisions, we will give a detailed description of the theoretical model and its corresponding numerical implementation, supplemented with code checking tests.

With this framework, we then perform a broad range of phenomenological studies of the bulk dynamics of relativistic heavy-ion collisions from RHIC to LHC energies. Our simulations are compared with various soft hadronic observables, in which the transverse momenta of the hadrons are less than 3 GeV/c. (This includes more than 99% of all particles created in the collision.) These comparisons help us to tightly constrain our theoretical modeling of the fireball evolution and to extract information about the transport properties of the quark-gluon plasma (QGP) as well as about the initial state fluctuation spectrum. We also explore the sensitivity of the hadronic observables to a possible temperature dependence of the QGP specific shear viscosity. The collision energy dependences of hadron spectra and elliptic flow coefficients are studied with our model, providing a qualitative baseline for comparison with recent data from the RHIC Beam Energy Scan (BES) program.

Due to the smallness of the electromagnetic coupling compared to the strong interaction, electromagnetic probes in relativistic heavy-ion collisions can provide us with early dynamical evolution information complementary to that obtained from hadronic observables. The emission of direct photons from relativistic heavy-ion collisions is studied. We derive the off-equilibrium corrections to thermal photon emission rates at leading order in $\mathcal{O}(\frac{\pi^{\mu\nu}}{e+\mathcal{P}})$, where $\pi^{\mu\nu}$, e, and $\mathcal{P}$ are the system's shear stress tensor, local energy density, and pressure, respectively. We perform event-by-event simulations for direct as well as hadronic decay photons for relativistic heavy-ion collisions and compare our results with experimental measurements. We map out the space-time structure of thermal photon emission and find that the slope of the measured direct photon spectrum is strongly blue-shifted by the hydrodynamic radial flow. The anisotropic flows of direct photons show a larger sensitivity to the shear pressure tensor of the system than the analogous

hadronic observables. This can be used as a sensitive viscometer for the QGP medium created in relativistic heavy-ion collisions.

To my father

Acknowledgments

First, I would like to sincerely thank my advisor, Professor Ulrich Heinz, for his continuous and patient guidance, encouragements, and supports during my Ph. D period. Working with him is an enjoyable journey. Under his supervision, my hard works always pay off with fruitful insights to the phenomenology and shed lights for future improvements. I have not only learned a great deal of physics from him, but also more importantly the ways of thinking independently, systematically attacking difficult problems, communicating and collaborating with the world experts, and fairly and correctly evaluating colleagues' works. I really appreciate all the opportunities that he has provided me with to broaden my horizon and drive me to grow up fast and healthy as a research scientist in the past five years. I feel so lucky to have him as my Ph. D advisor.

Next, I want to thank all of my collaborators, Zhi Qiu, Huichao Song, Jean-Francois Paquet, Jia Liu, Chris Plumberg, Baoyi Chen, Jiechen Xu, Pasi Huovinen, Steffen Bass, Charles Gale, Abhijit Majumder, Tetsufumi Hirano, Thorsten Renk, and Hannu Holopainen. I especially want to thank Zhi Qiu, who is also one of my best friends. His attitude of being precise and thinking as a mathematician influenced me a lot and helped me to grow up through our collaborations. I also learned a lot computer programming from him. I also thankful for being an active member in the JET Collaboration, from where I got opportunities to know and collaborate with many world experts of our field. I am also grateful for having many enlightening discussions with Mike Lisa, Sangyong Jeon, Bjoern Schenke, Gabriel Denicol, Guy Moore, Yuri Kovchegov, and so on.

My friends have been an anchor of support throughout my years as a graduate student. Yang Yang, my workout buddy, keeps me doing physical exercises regularly which helps me to gain enough strength and energy to face the difficulties in my research and daily life. My roommates, Zhili Yao and Dacong Yan, with whom I share countless enjoyable moments in spare time.

I also thank my undergraduate advisor Professor Lie-Wen Chen, who gave me solid background trainings at the very beginning of my scientific career.

Last but not least, I want to thank my father and grandparents for their continuous cares and supports even though we are apart from the world.

Vita

February 23, 1987	Born - Shanghai, China
September 2005 - June 2009	Bachelor of Science in applied physics, Shanghai Jiao Tong University
September 2009 - June 2013	Research and Teaching Assistant Art and Science College The Ohio State University
June 2013 - May 2014	Presidential Fellowship The Ohio State University
June 2014 - present	Research Assistant Art and Science College The Ohio State University

Publications

Research Publications

U. Heinz, J. Liu and C. Shen, *"Electromagnetic fingerprints of the Little Bang"*, arXiv:1403.8101 [nucl-th]

C. Shen, U. Heinz, J. F. Paquet and C. Gale, *"Thermal photon anisotropic flow serves as a quark-gluon plasma viscometer"*, arXiv:1403.7558 [nucl-th]

C. Shen, U. Heinz, J. F. Paquet and C. Gale, *"Thermal photons as a quark-gluon plasma thermometer reexamined"*, Phys. Rev. C **89**, 044910 (2014)

C. Shen, U. Heinz, J. F. Paquet, I. Kozlov and C. Gale, *"Anisotropic flow of thermal photons as a quark-gluon plasma viscometer"*, arXiv:1308.2111 [nucl-th]

C. J. Plumberg, C. Shen and U. Heinz, *"Hanbury-BrownTwiss interferometry relative to the triangular flow plane in heavy-ion collisions"*, Phys. Rev. C **88**, 044914 (2013) [Erratum-ibid. C **88**, no. 6, 069901 (2013)]

U. Heinz, Z. Qiu and C. Shen, *"Fluctuating flow angles and anisotropic flow measurements"*, Phys. Rev. C **87**, 3, 034913 (2013)

Z. Qiu, C. Shen and U. Heinz, *"Resonance Decay Contributions to Higher-Order Anisotropic Flow Coefficients"*, Phys. Rev. C **86**, 064906 (2012)

C. Shen and U. Heinz, *"Viscous Flow in Heavy-Ion Collisions from RHIC to LHC"*, Nucl. Phys. A **904-905**, 361c (2013)

C. Shen and U. Heinz, *"Collision Energy Dependence of Viscous Hydrodynamic Flow in Relativistic Heavy-Ion Collisions"*, Phys. Rev. C **85**, 054902 (2012)

Z. Qiu, C. Shen and U. Heinz, *"Hydrodynamic elliptic and triangular flow in Pb-Pb collisions at* $\sqrt{s} = 2.76$ *A TeV"*, Phys. Lett. B **707**, 151 (2012)

U. Heinz, C. Shen and H. Song, *"The viscosity of quark-gluon plasma at RHIC and the LHC"*, AIP Conf. Proc. **1441**, 766 (2012)

C. Shen, S. A. Bass, T. Hirano, P. Huovinen, Z. Qiu, H. Song and U. Heinz, *"The QGP shear viscosity: Elusive goal or just around the corner?"*, J. Phys. G **38**, 124045 (2011)

T. Renk, J. Auvinen, K. J. Eskola, U. Heinz, H. Holopainen, R. Paatelainen and C. Shen, *"Systematics of parton-medium interaction from RHIC to LHC"*, J. Phys. G **38**, 124089 (2011)

C. Shen, U. Heinz, P. Huovinen and H. Song, *"Radial and elliptic flow in Pb+Pb collisions at the Large Hadron Collider from viscous hydrodynamic"*, Phys. Rev. C **84**, 044903 (2011)

A. Majumder and C. Shen, *"Suppression of the High* p_T *Charged Hadron* R_{AA} *at the LHC"*, Phys. Rev. Lett. **109**, 202301 (2012)

H. Song, S. A. Bass, U. Heinz, T. Hirano and C. Shen, *"Hadron spectra and elliptic flow for 200 A GeV Au+Au collisions from viscous hydrodynamics coupled to a Boltzmann cascade"* Phys. Rev. C **83**, 054910 (2011) [Erratum-ibid. C **86**, 059903 (2012)]

C. Shen and U. Heinz, *"Hydrodynamic flow in heavy-ion collisions with large hadronic viscosity"* Phys. Rev. C **83**, 044909 (2011)

H. Song, S. A. Bass, U. Heinz, T. Hirano and C. Shen, *"200 A GeV Au+Au collisions serve a nearly perfect quark-gluon liquid"*, Phys. Rev. Lett. **106**, 192301 (2011) [Erratum-ibid. **109**, 139904 (2012)]

C. Shen, U. Heinz, P. Huovinen and H. Song, *"Systematic parameter study of hadron spectra and elliptic flow from viscous hydrodynamic simulations of Au+Au collisions at* $\sqrt{s_{\rm NN}} = 200$ *GeV",* Phys. Rev. C **82**, 054904 (2010)

T. Renk, H. Holopainen, U. Heinz and C. Shen, *"A Systematic comparison of jet quenching in different fluid-dynamical models"* Phys. Rev. C **83**, 014910 (2011)

Fields of Study

Major Field: Physics

Studies in Relativistic heavy-ion collisions: Professor Ulrich Heinz

Table of Contents

List of Tables

List of Figures

Chapter 1: Introduction

The relativistic heavy-ion collision experiments conducted at the Relativistic Heavy-Ion Collider (RHIC) and the Large Hadron Collider (LHC) create fireballs with temperatures that can reach several trillion degrees Kelvin once they reach a state of approximate local thermal equilibrium a short period ($\sim 3 \times 10^{-24} s$) after the collisions. These experiments open a privileged window for studying strongly interacting nuclear matter under extremely hot and dense conditions. These "little bangs" are almost point-like in size ($V \sim 10^{-42} m^3$) and disappears almost instantaneously ($\sim 5 \times 10^{-23} s$). Compared to the big bang of our universe, although they differ dramatically in geometric size and are governed by different fundamental physics (gravity for the big bang, but strong interaction for the little bang), the dynamical evolution of the little bangs share a lot of similarities with the big bang [1].

1.1 The big bang and little bangs

In Fig. 1.1, we sketch the conceptual time-line of the evolution of the big bang and the little bangs. For the little bangs, the fireballs are compressed into a hot and high density matter right after the collision,. This generates huge pressure gradients pointing outward from the fireball center, which leads to a rapid, explosive expansion. Such a strong collective expansion develops a Hubble-like velocity profile which is similar to the expansion of our universe.

The rapid expansion causes both systems to exhibit a hierarchy of sequential decoupling processes that are driven by the competition between the macroscopic expansion rate and the microscopic interaction strength.

In both systems, chemical freeze-out happens before kinetic decouple. From about 10 seconds to 20 minutes after the big bang, the process of big bang nucleosynthesis (BBN) take places, resulting in the formation of most of the He and d nuclei in our universe [2]. As the universe expands and cools during BBN, the relative ratio between the yields of protons and neutrons freezes out at about 3 minutes after the big bang. A similar chemical freeze out process happens during the hadronization stage of the little bang evolution. This happens at around a temperature of $T \sim 165$ MeV ($\sim 2 * 10^{12}$ K), corresponding to a time ~ 10 fm/c (3×10^{-23}s) after the collision.

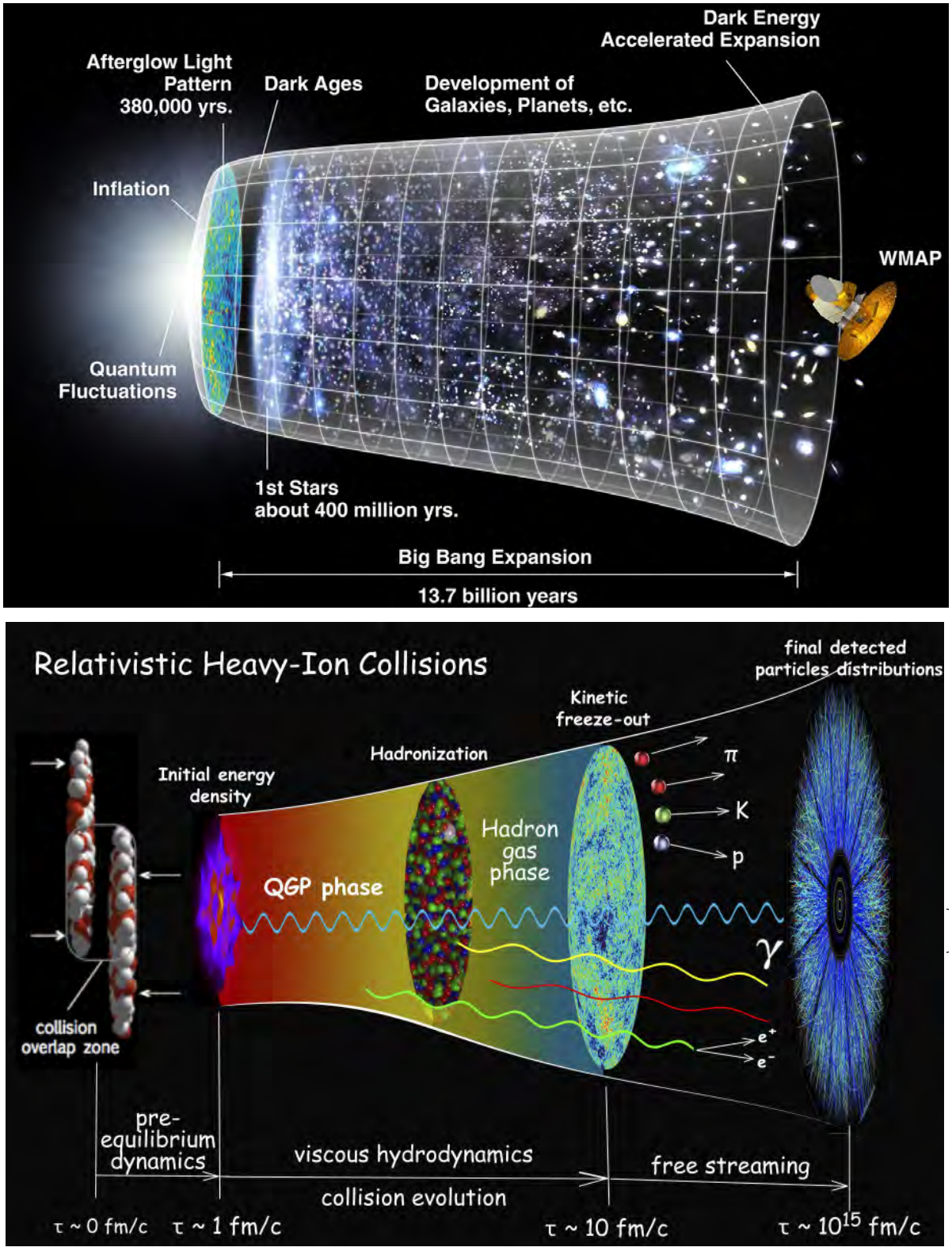

Figure 1.1: Artistic time line of the big bang and the little bangs. The plot for the big bang is taken from `http://en.wikipedia.org/wiki/Big_Bang`.

After the chemical freeze-out, the relative yields of the stable hadrons remain fixed in the little bangs.

Even after their chemical compositions have been fixed, both systems continue to expand in (approximate) thermal equilibrium and undergo a kinetic freeze out at lower density. In the big bang, the universe becomes transparent to light at an age of 380,000 years caused by the recombination of free charges into neutral atom. This freezes out the thermal distribution of the CMB at that moment. By measuring the CMB to good precision, it enables us to reconstruct the dynamical evolution of the early universe. In the little bangs, hadrons stop scattering elastically with each other at around $T = 100 - 120$ MeV ($\sim$ 15 fm/c after the collision) and free-stream to the detectors afterward. There is a huge space-time gap between kinetic freeze-out and the actual measurement of the event (about 15 orders of magnitude difference in time and space). By analyzing the momentum correlations of identical particle pairs (a technique known as particle "femtoscopy"), we can reconstruct quite a bit of the spatial information about the fireball at kinetic freeze out [3].

Due to the short lifetime of the fireball between collision and freeze out, in conjunction with the fast expansion rate, the fireball will never achieve global thermal equilibrium during the heavy-ion collision. So the initial state quantum fluctuations are not completely washed out but rather imprint their trace on the final observables. Similar to the way in which measuring the polarization of the CMB can be traced back to the beginning of inflation in the Big Bang, the measured particle momentum distribution and its anisotropic flow coefficients in relativistic heavy-ion collisions contain valuable information about the initial state fluctuation and the viscous dissipation of the medium.

However, unlike the big bang, the standard model of relativistic heavy-ion collision has not been completely developed yet. The work that will be presented in my thesis are our contributions towards building such a model for the little bangs. With such a model, there is even more to explore in understanding the nuclear matter under extreme conditions.

The nuclei of todays ordinary atoms and the QGP represent two different phases of matter whose constituents interact through the strong interaction. One of the main goal of relativistic heavy-ion collisions is to explore and map out the phase diagram of the nuclear matter as illustrated in Fig. 1.2. In particular, the current RHIC Beam Energy Scan (BES) experiments are now focused on determining the phase boundary between the normal nuclear matter and QGP and search for a possible critical end point of a first order phase transition at large net baryon density to a rapid but smooth cross over at small net baryon density. In order to quantify this phase diagram and turn it into a scientific plot, we need both precision measurements and state-of-the-art theoretical model descriptions of relativistic heavy-ion collisions for a wide range of the collision energies from RHIC to LHC. This is really a big challenge for both theory and experiment, but it drives our field to move forward rapidly.

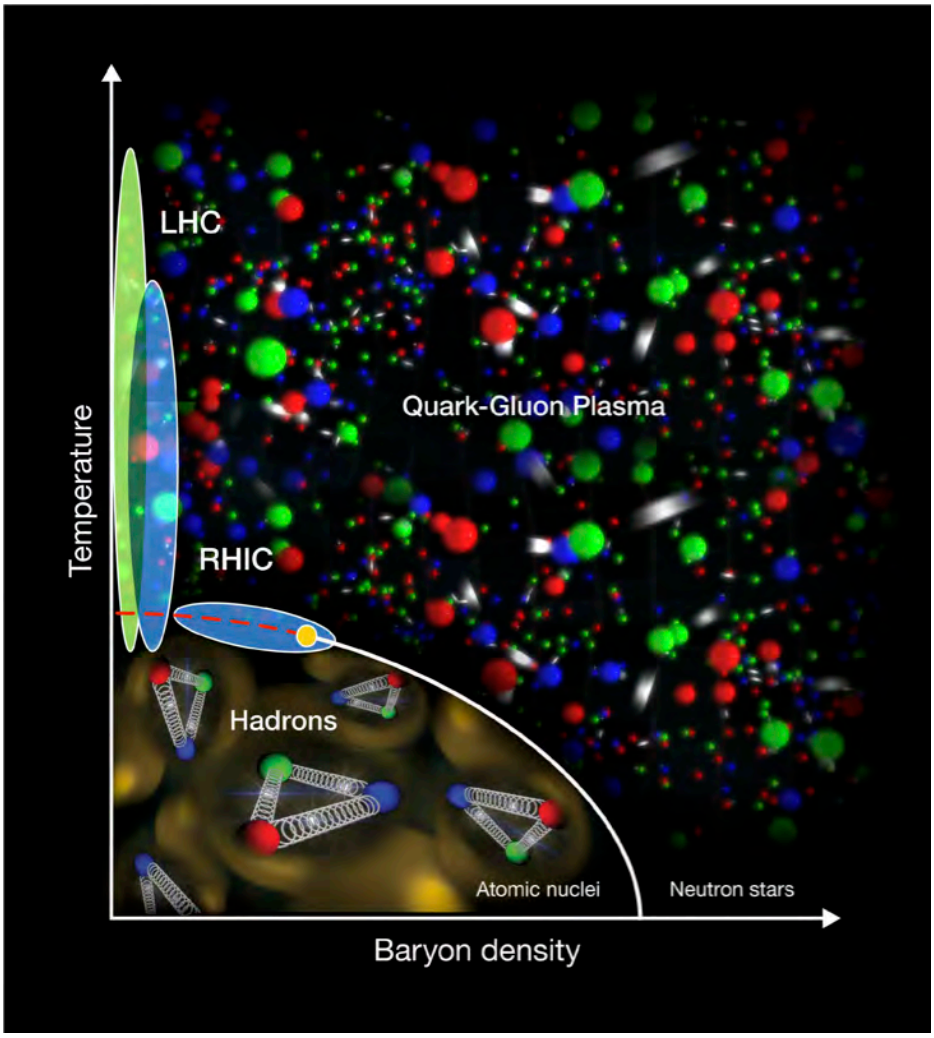

Figure 1.2: Artistic sketch of the QCD phase diagram for nuclear matter. The picture is take from `http://www.bnl.gov/newsroom/news.php?a=11446`

1.2 The standard model of relativistic heavy-ion collisions

The evolution of a relativistic heavy-ion collisions contain multiple stages which are governed by different underlying physics. Right after the collisions, the system is dominated by gluons characterized by an over populated phase-space distribution [4]. The number of gluons is of order $\sim \frac{1}{g^2}$ with $g < 1$ and these gluons carry each a very small fraction of the longitudinal momentum of the incoming nucleus (small-x gluons). During the first 1 fm/c, due to the large occupation number of gluon at leading order in strong coupling g, these saturated small-x gluons will evolve according to the classical Yang-Mills equation of motion. It is believed that the next-to-leading order quantum corrections to the classical field evolution drive the system rapidly towards local isotropy in momentum space [5, 6] and somewhat later to local thermal equilibrium. After $0.3-0.5$ fm/c, the system achieves approximately local momentum isotropy; local thermal equilibrium is reached after a few fm/c. The quarks and gluons that are produced after the collision form a

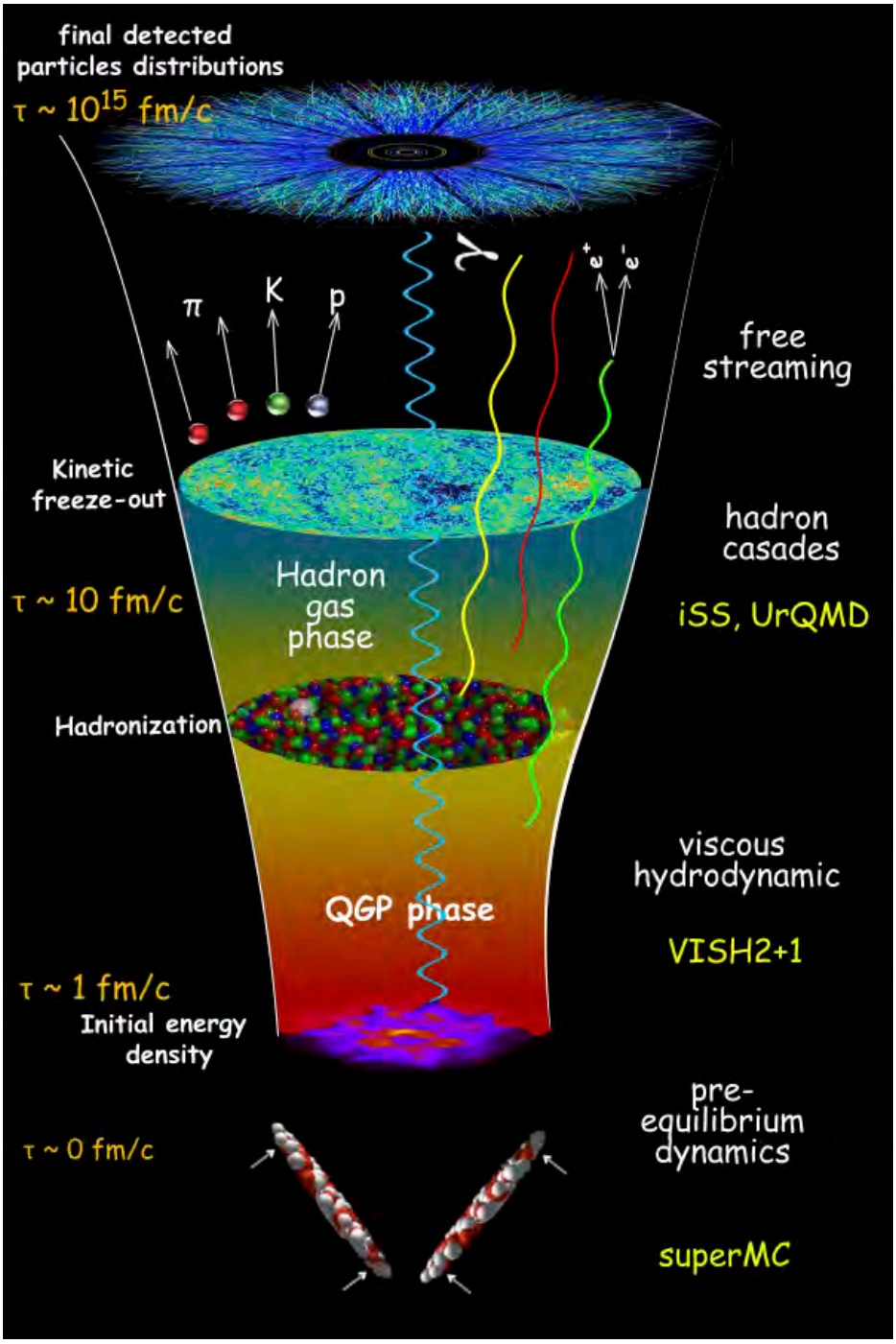

Figure 1.3: Illustration of the evolution of the fireball created in the relativistic heavy-ion collisions together with the theoretical model used in each stage.

strongly coupled plasma (QGP). The dynamics of the QGP can be described by macroscopic viscous hydrodynamics where the viscous corrections account for the remaining deviation from local isotropy and thermal equilibrium. As the system expands and cools, it will smoothly crossover from the QGP phase to a hadron gas phase according to the equation of state (EOS) determined from Lattice QCD calculations. At hadronization, the quark-gluon fluid will convert into hadrons

due to confinement. In the hadronic phase, the hadron cascade model can provide us a detailed microscopic description of the evolution.

As the fireball continues to expand and cool, the collision rates between the hadronic resonances decrease. First, the inelastic collisions between particles cease and the system reaches chemical freeze-out almost directly after hadronization. After this point, only resonance decays and baryon-antibaryon annihilation can change the particle yields. Regeneration of baryon-antibaryon pairs is a rare process that can be neglected. As the system evolves further, the density of the fireball becomes so low that the mean free time of the particles becomes much larger than the Hubble time (i.e. the time over which the inter particle spacing doubles.) [1]. The particles reach kinetic freeze out and subsequently free-stream to the detectors. In Fig. 1.3, we schematically summarize the theoretical models and the corresponding codes that we will use to simulate the different stages of heavy-ion collisions. We will explain them in detail in Chapter 2.

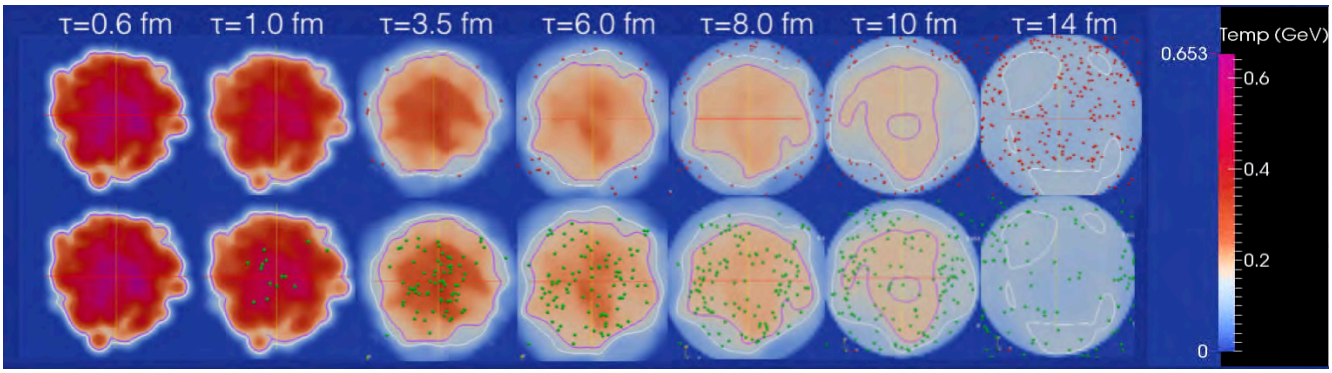

Figure 1.4: The evolution of the fireball in the transverse plane for one collision event with the local temperature color coded. The white contour indicates kinetic freeze-out at $T_{\rm kin} = 120$ MeV, and the purple one represents chemical freeze-out at $T_{\rm chem} = 165$ MeV. Charged hadron emission is illustrated in the upper panels by the red dots; thermal photon emission is plotted in the lower panels indicated by green dots. The number of photons per event has been multiplied by hand by a factor of 10, for better visibility in view of the much small emission rate for photons.

In relativistic heavy-ion collisions, rare electromagnetic observables like photons and dileptons only interact with the medium through the electromagnetic interaction, which is much weaker than the strong interaction. For this reason, their mean free path is much longer than the system size, and hence they suffer negligible final state interactions after they are produced during the fireball evolution. This advantage over strongly interacting probes makes them the cleanest penetrating probe for the heavy-ion collisions. In Fig. 1.4, we illustrate the qualitative difference between the charged hadron and thermal photon production in one typical heavy-ion collision. Hadrons can only break free at the final kinetic freeze-out surface. Their measured momentum distribution carries indirect time integrated evolution information about the fireball. On the other hand, a large fraction of the thermal photons are produced early inside the fireball. Their momentum distribution preserves the dynamical information of the medium directly at their birth points.

Electromagnetic probes can thus provide us with constraints on the early dynamics of the fireball that are complementary to those obtained from the much more abundant hadronic observables. In Chapters 14 to 21, we will discuss in detail the study of these colorless penetrating probes in relativistic heavy-ion collisions.

1.3 The road to precision: extraction of the specific QGP shear viscosity

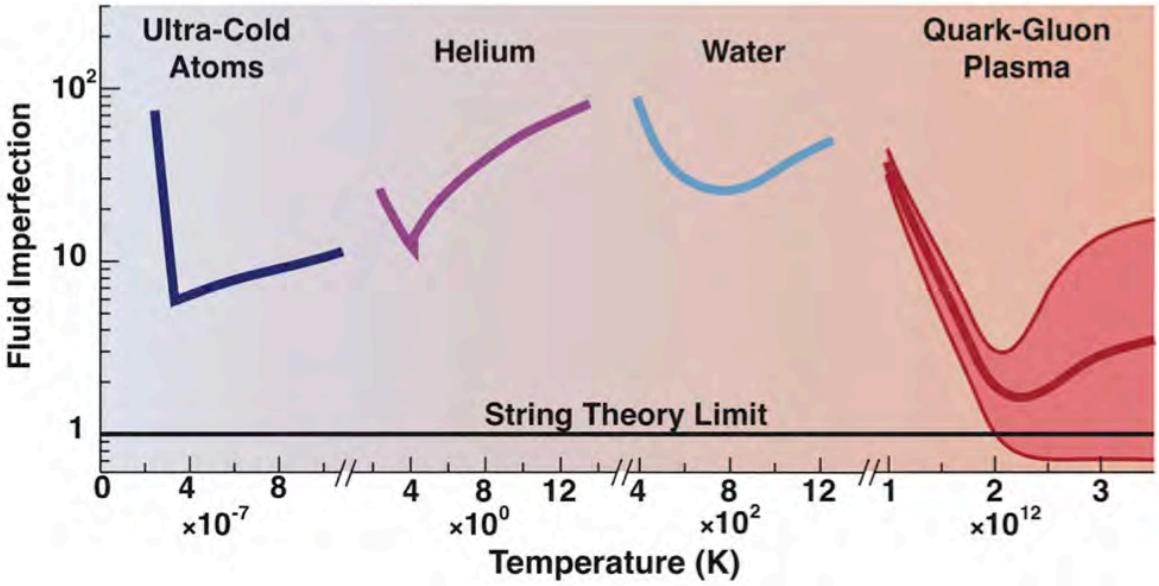

Figure 1.5: The fluid imperfection index $4\pi\frac{k_B}{\hbar}\frac{\eta}{s}$ of various fluids as a function of temperature. Picture taken from Tribble R (chair), Burrows A *et al.* 2013 *Implementing the 2007 Long Range Plan*, Report to the Nuclear Science Advisory Committee, January 31, 2013. Available at `http://science.energy.gov/np/nsac/reports/`.

The anisotropic flow measurements at RHIC and LHC energies reveal that the created QGP is strongly coupled and behaves almost like a "perfect" liquid. The quality of a fluid can be characterized by its shear viscosity to entropy density ratio, η/s. We call this ratio the specific shear viscosity. "Good" fluids are characterized by small η/s, $\eta/s \leq \frac{\hbar}{k_B}$. In Fig. 1.5, we illustrate schematically the specific shear viscosity η/s normalized by $\frac{1}{4\pi}\frac{\hbar}{k_B}$, the minimum bound derived from the limit of infinite strong coupling, for four different types of fluids. As we can see, the QGP at the high temperature end of this Figure has the smallest value of η/s among all other fluids occurring in nature. This finding has raised huge interest since 2000 in both theoretical and experimental work to constrain this transport coefficient of the QGP in relativistic heavy-ion collisions. Due to the short lifetime and explosive nature of the QGP created in such collisions, the uncertainty in the extracted value of η/s and its temperature dependence is still large, as indicated in Fig. 1.5.

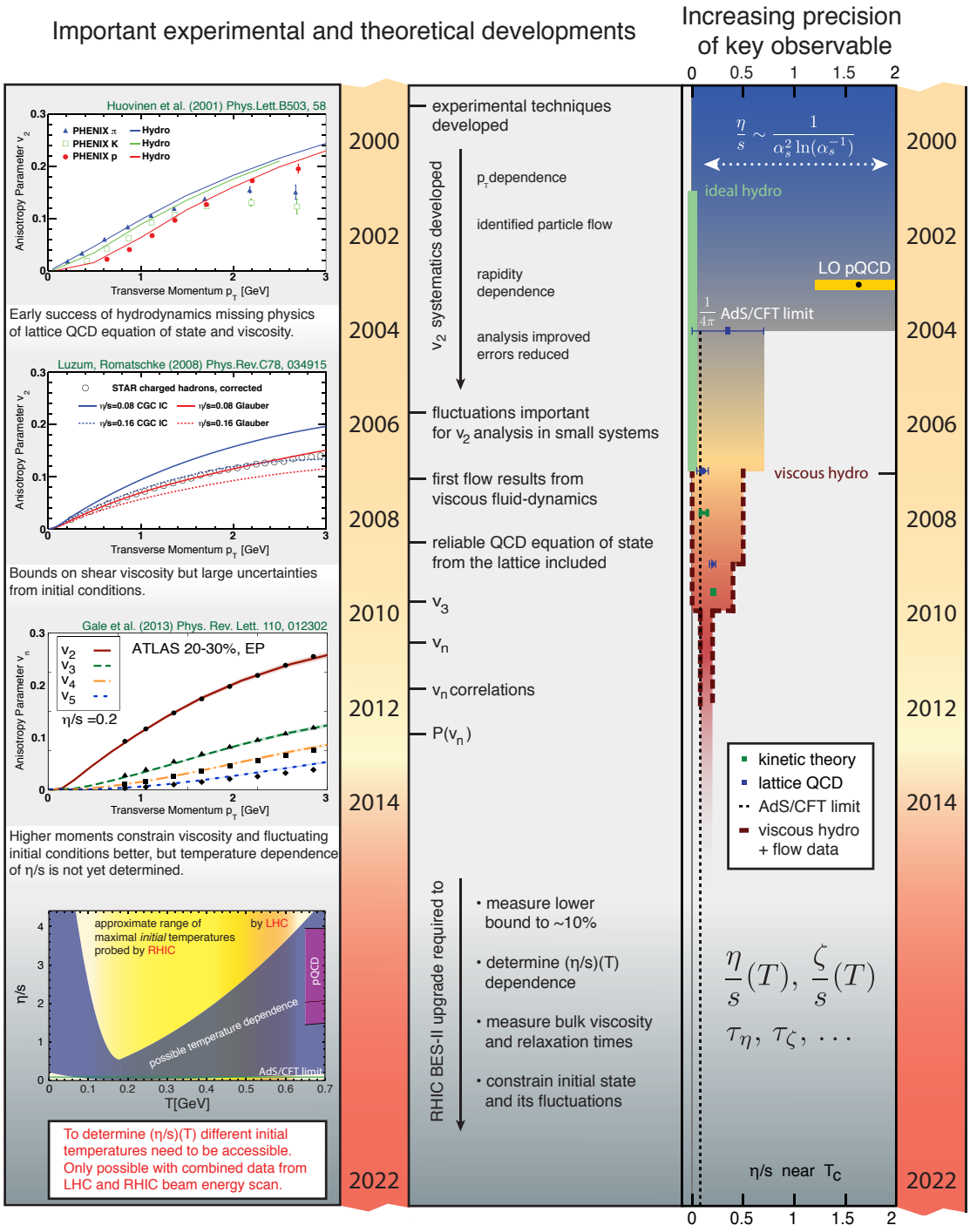

Figure 1.6: Time line of important experimental and theoretical developments leading towards precise extraction of the specific shear viscosity of QGP. Plot taken from the "Hot & Dense QCD White Paper", solicited by the NSAC subcommittee on Nuclear Physics funding in the US. Available at `http://www.bnl.gov/npp/docs/Bass_RHI_WP_final.pdf`.

On the theoretical side, the shear viscosity of QCD matter is challenging to calculate from first principles. The relationship between transport coefficients and correlation functions in a microscopic quantum field theory is provided by Kubo relations. In field theory, the shear viscosity

can be computed using linear response theory from the following retarded correlation function,

$$\begin{aligned}\eta &= \lim_{\omega\to 0}\lim_{k\to 0}\frac{\rho^{xy,xy}(\omega,k)}{2\omega} \\ &= \lim_{\omega\to 0}\lim_{k\to 0}\frac{1}{\omega}\mathrm{Im}\left\{i\int dt\int d^3x e^{i(\omega t-\vec{k}\cdot\vec{x})}\Theta(t)\left\langle\left[T^{xy}(\vec{x},t),T^{xy}(\vec{0},0)\right]\right\rangle\right\},\end{aligned} \tag{1.1}$$

where $\rho^{xy,xy}(\omega,k)$ is called the spectral density. It can be related to the retarded correlation function of the energy momentum tensor in the second line of Eq. (1.1) through the fluctuation-dissipation theorem. At temperatures that are accessible in relativistic heavy-ion collisions at RHIC and LHC energies, the strong coupling constant is not small. The leading order perturbative results may contain large theoretical uncertainty when extrapolated to large values of g_s. On the other hand, since in Eq. (1.1) the shear viscosity depends on the spectral function $\rho^{xy,xy}(\omega,k)$ in the real time formalism, it is very hard to compute this correlation function from Lattice QCD, which is formulated in imaginary time and requires a non-trivial (ill-defined) analytical continuation to real times, using limited information computed at a finite number of lattice points along the imaginary time axis.

An alternative, phenomenological way of extracting the specific shear viscosity of the QGP is to use macroscopic hydrodynamic simulations, and compare them with experimental data. Hydrodynamics is an effective approach which captures the low energy, long wavelength response of the system, whose underlying dynamics is governed by the strong interaction. In this framework, η/s is a free parameter in the model and can be constrained by fitting to the experimental measurements. However, a precise extraction of η/s requires good control of all the other model parameters at the same time and an overall consistent description of a large variety of observables that have been measured in relativistic heavy-ion collisions. Again, this is challenging, but it is the path I will pursue in this thesis.

Fortunately, through efforts in the development of the phenomenological models and improvements in the precision of the anisotropic flows measurements, the extraction of the QGP η/s has become increasingly accurate. Fig. 1.6 summarizes a time line of the developments on both theory and experimental sides in our efforts to constrain η/s of the QGP over the past decade (left and middle columns, respectively). In the right panel, we can see that the uncertainty of the value of the QGP η/s has shrunk dramatically during the time period in which the work summarized in this thesis was performed. The convergence is due to progress on both the theoretical and experimental sides. At the current stage, theoretical models and experiment measurements are both beginning to reach the sensitivity necessary to constrain even the temperature dependence of $(\eta/s)(T)$, as well as that of other transport coefficients, such as the bulk viscosity and various second-order transport coefficients.

With higher statistics accumulated in the experiments, the anisotropic flow of rare probes, like high-p_T charged hadrons ($p_T > 10$ GeV), direct photons, D mesons, J/ψ and etc., are being measured to satisfactory precision. Compared to the bulk soft hadrons, the anisotropies of these rare particles can probe earlier dynamics of the relativistic heavy-ion collisions. In principle, they are more sensitive to the temperature dependence of η/s in the high temperature region. A combined analysis of these rare observables with the anisotropic flow of charged hadrons will help us to further constrain the theoretical model and improve the precision of our extraction of the QGP transport coefficients.

However, in the past 3 years, a surprisingly large direct photon elliptic flow has been reported by the PHENIX collaboration at RHIC and later on by the ALICE collaboration at LHC. All the current theoretical models so far fail to describe the measured direct photon yield as well as its anisotropy. This big challenge has become known in our field as the "direct photon flow puzzle". In the third part of my thesis (Chapters 14 to 21), we will discuss our recent improvements on the theoretical side in the hopes of resolving this puzzle.

1.4 Notation

Throughout this thesis we adopt units in which $\hbar = c = k_{\rm B} = 1$. The metric tensor in Cartesian coordinates is taken to be $g_{\mu\nu} = \mathrm{diag}(+1, -1, -1, -1)$ and in Milne coordinates (τ, x, y, η), $g_{\mu\nu} = \mathrm{diag}(+1, -1, -1, -\tau^2)$, where $\tau = \sqrt{t^2 - z^2}$ and $\eta = \frac{1}{2}\ln\frac{t+z}{t-z}$. The projector onto the space transverse to the fluid velocity u_μ is defined by,

$$\Delta^{\mu\nu} = g^{\mu\nu} - u^\mu u^\nu. \tag{1.2}$$

For any rank-2 tensor, a further double projection operator can be constructed as follows,

$$\Delta^{\mu\nu}_{\alpha\beta} = \frac{1}{2}(\Delta^\mu_\alpha \Delta^\nu_\beta + \Delta^\mu_\beta \Delta^\nu_\alpha) - \frac{1}{3}\Delta^{\mu\nu}\Delta_{\alpha\beta}. \tag{1.3}$$

It picks out the part of the tensor that is orthogonal to u^μ in both indices and traceless.

With $\Delta^{\mu\nu}$, the partial derivative ∂^μ can be decomposed as:

$$\partial^\mu = \nabla^\mu + u^\mu D, \tag{1.4}$$

where $\nabla^\mu = \Delta^{\mu\nu}\partial_\nu$ is the "transverse" component of the partial derivative ∂_μ, and $D = u^\mu\partial_\mu$ is the corresponding "longitudinal" component. In the fluid rest frame, D reduces to the time derivative, and ∇^μ reduces to the spacial gradient. In curvilinear Milne coordinates, the partial derivative ∂_μ in Cartesian coordinates should be replaced by the covariant derivative, d_μ. For any vector, $d_\mu A^\nu = \partial_\mu A^\nu + \Gamma^\nu_{\mu\rho}A^\rho$, where $\Gamma^\nu_{\mu\rho}$ are the Christoffel symbols in the curved space. This

procedure generalizes to tensors of higher rank as found in textbooks on differential geometry. In Milne coordinates, the non-zero components of the Christoffel symbols are

$$\Gamma^{\tau}_{\eta\eta} = \tau,\ \Gamma^{\eta}_{\tau\eta} = \Gamma^{\eta}_{\eta\tau} = \frac{1}{\tau}. \tag{1.5}$$

In the formalism for viscous hydrodynamics, we will have terms which involve derivatives of flow velocity u^{μ}:

$$\begin{aligned} \theta &\equiv \partial \cdot u && \text{scalar expansion rate,} \\ \sigma^{\mu\nu} &\equiv \nabla^{\langle\mu} u^{\nu\rangle} = \tfrac{1}{2}(\nabla^{\mu}u^{\nu} + \nabla^{\nu}u^{\mu}) - \tfrac{1}{3}\nabla^{\mu\nu}\theta && \text{velocity shear tensor} \end{aligned}$$

1.5 Outline

In this thesis, we build up a theoretical framework to model the relativistic heavy-ion collisions from beginning to end. In Chapter 2, we will discuss in detail the theoretical models and their corresponding numerical implementations for each stage of a relativistic heavy-ion collision. A set of benchmark tests of the individual numerical codes are also included in this part of the thesis. In Chapters 3 to 13, we will use this advanced tool to perform phenomenological studies of the relativistic heavy-ion collisions in many different respects. We will discuss the comparisons with the majority of the soft hadronic observables from RHIC to LHC, in which the momenta of the hadrons are less than 3 GeV. These comparisons help us to tightly constrain our theoretical modeling of the fireball evolution and to extract information about the transport properties of the QGP and the initial state fluctuations. Chapters 14 to 21 of the thesis are devoted to the study of the electromagnetic probes, in particular the thermal photon radiation in relativistic heavy-ion collisions. Both theoretical developments in computing photon emission rates from first principles and event-by-event phenomenological studies compared with experimental measurements will be presented. Finally, we will highlight the most important conclusions in Chapter 22.

Chapter 2: The iEBE code Package

This code package was developed together with Zhi Qiu, who shares equal credit for this effort.

2.1 Introduction

Relativistic heavy-ion collisions contain multi-phase dynamics, where each stage is governed by different underlying physics. The iEBE package of dynamical simulation codes contains modules for each of the different stages and interfaces them to form a complete dynamical evolution framework. On the large scale, our package is modulated in terms of the different stages of the heavy-ion collisions. Each component can be easily replaced by users' own codes with minor changes in the input/output(I/O) file formats. In order to utilize some advantages of each computation language for different aspects of the package, our package contains codes in Fortran, C++, python, as well as sqlite database. We have used a git repository for the daily development as well as maintenance. In this chapter, we will start with an introduction of the general structure of our package, followed by a detailed explanation of the underlying physics models that we employ to simulate the different stages of relativistic heavy-ion collisions. For the different components, we also show some code testing benchmark results for reference.

The entire integrated package is open source and can be freely downloaded from the following git repository:

https://github.com/chunshen1987/iEBE.git

2.2 General Simulation Framework

Every relativistic heavy-ion collision is a multi-stage system. In our hybrid package, there is a specific code simulating each stage of the evolution. A python shell script links all the individual programs together to perform large-scale event-by-event simulations of relativistic heavy-ion collisions. The major components include the initial condition generator (superMC), a (2+1)-d viscous hydrodynamic simulator (VISH2+1), a particle sampler (iSS), and a hadron cascade simulator (UrQMD). In the next section, we will discuss in some detail the physics implemented in these codes.

To perform event-by-event simulations on multiple computing cores, for example using N cores on a cluster, we divide the total number of events, $N_{\rm ev}$, into N jobs with $M = N_{\rm ev}/N$ events in each jobs. Then we submit these N jobs in parallel. The M events within each job run sequentially.

2.2.1 Work flow for a single sequential simulation

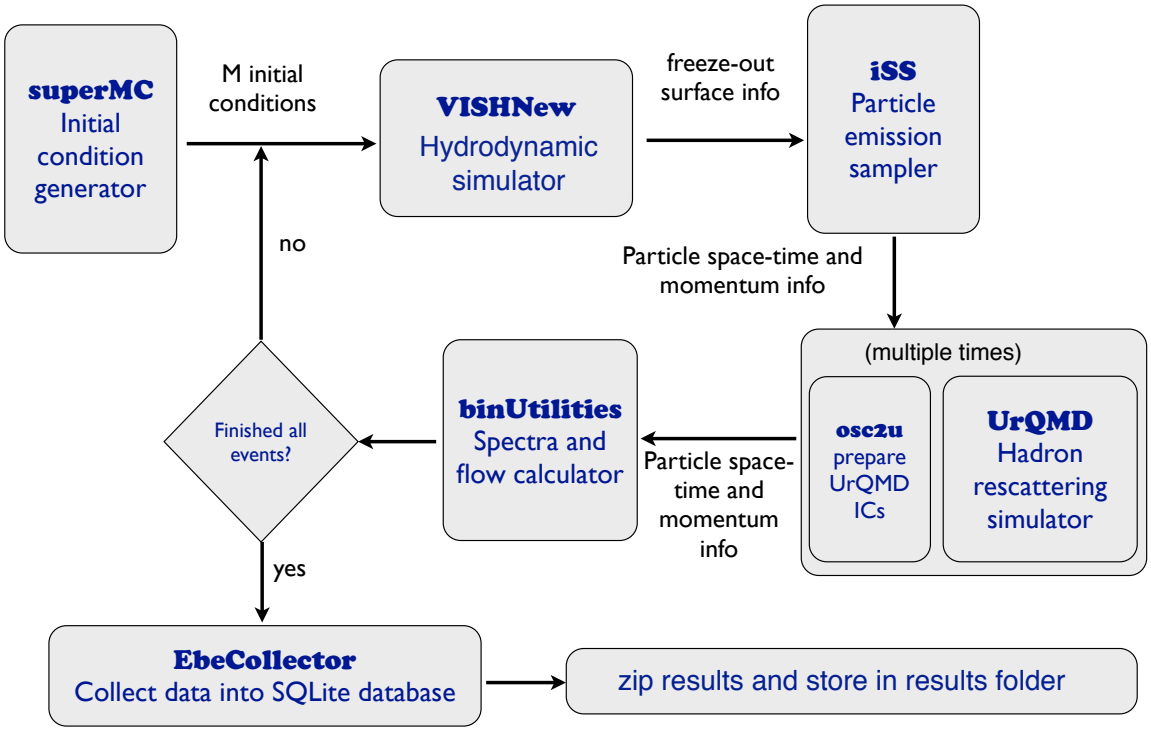

Figure 2.1: The work flow for a single job with M events.

For each job, the work flow is summarized in Fig. 2.1. The job is started by generating M fluctuating initial conditions with the Monte-Carlo generator `superMC`. Then each initial entropy density profile is evolved with the viscous hydrodynamic model, `VISH2+1`. At the end of the hydrodynamic simulation, a switching hypersurface is identified and fluid cells on this switching hyper-surface are converted into individual particles using particle sampler, `iSS`. These particles are fed into `UrQMD`, a hadronic rescattering cascade which follows the particles microscopically until they stop interacting and (if unstable) decay[1]. In the end, we collect the final particle information (momenta and position of their last interaction or decay) from all the M events using

[1]To accumulate statistics, the `UrQMD` casacade is optionally run multiple times (with different sampled particles from `iSS`) for each hydrodynamic siulation.

`binUtilities`, store the final analyzed results in the `SQLite` database using `EbeCollector`, and zip everything.

2.2.2 Large scale event-by-event simulations

For large-scale event-by-event simulations, two additional python scripts are used to generate and submit multiple jobs as illustrated in Fig. 2.2. Users specify the number of jobs and the number of events within each job through `generateJobs.py` which sets up the entire simulation and they use `submitJobs_local.py` or `submitJobs_qsub.py` to submit all the jobs to a local cluster or to a qsub system on the OSC supercomputing center, respectively. Easy adjustments of those latter python scripts can adapt the package to other supercomputing facilities or the Open Science Grid.

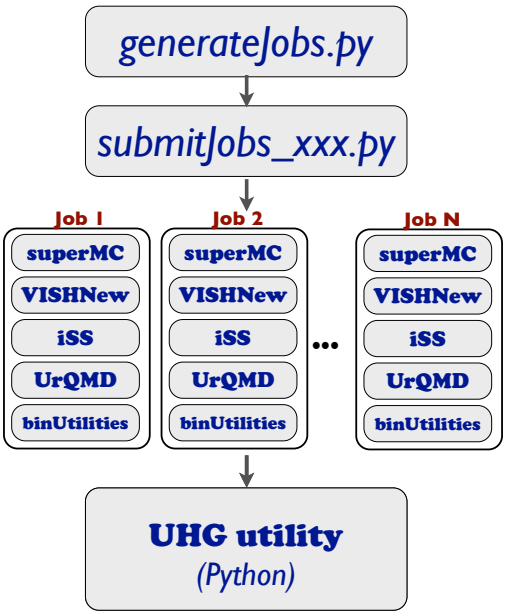

Figure 2.2: Work flow for multiply jobs in the large scale of event-by-event simulations.

After all N jobs are finished, the database files from each job will be combined into one for future physics analysis of the output by users. A user friendly python package tool, `UHG utility`, is provided for querying the database and computing experimental observables and performing various statistical analyses.

2.3 Initial condition generator `SuperMC`

`SuperMC` generates fluctuating initial conditions using the Monte-Carlo Glauber (MC-Glauber) or Monte-Carlo Kharzeev-Levin-Nardi (MCKLN) models. These models can be run in several distinct modes as selected by the users.

2.3.1 Collision geometry

In relativistic heavy-ion collisions, the colliding nuclei are accelerated almost to the speed of light. Due to time dilation, nucleons' intrinsic orbital motion is frozen during the interaction period. Thus we can use a Monte Carlo procedure to sample the position of every nucleon inside the projectile and target nuclei according to their Woods-Saxon distribution.

We take into account the finite size for each individual nucleon. The density distribution of strongly interacting matter for each nucleon is given by

$$\rho_n(\vec{\mathbf{r}}) = \begin{cases} \frac{\theta(r_\perp - r_n)}{\pi r_n^2}\frac{\theta(L-|z|)}{L}, & \text{cylindrical nucleon,} \\ \frac{1}{(2\pi B)^{3/2}} e^{-r^2/(2B)}, & \text{gaussian nucleon.} \end{cases} \tag{2.1}$$

The approximation of a homogeneous cylindrical nucleon density distribution has been popular in the past since it leads to a very simple collision criterium. In this approximation, the transverse radius $r_n = \frac{1}{2}\sqrt{\frac{\sigma_{\rm NN}^{\rm inel}}{\pi}}$, where the factor of 2 accounts for the quantum mechanical nature of the nucleon-nucleon scattering process. Along the z direction, $L = 2r_n$. A more realistic modeling takes a gaussian density distribution for the nucleon with an energy-dependent width $B = B(\sqrt{s_{\rm NN}}) = \frac{\sigma_{\rm NN}^{\rm in}(\sqrt{s_{\rm NN}})}{14.30}$.[7] The corresponding nucleon thickness functions in the transverse plane are,

$$T_n(r_\perp) = \begin{cases} \frac{\theta(r_\perp - r_n)}{\pi r_n^2}, & \text{cylindrical nucleon,} \\ \frac{1}{(2\pi B)} e^{-r^2/(2B)}, & \text{gaussian nucleon.} \end{cases} . \tag{2.2}$$

With the finite size of each nucleon, in order to reproduce the correct Woods-Saxon distribution for the density of the entire nucleus, we need to sample the nucleon positions according to a *modified* Woods-Saxon distribution such that, when folded with the nucleon density distribution, it reproduces the correct experimentally measured Woods-Saxon distribution:

$$\rho_{\rm WS}^{\rm exp.}(\vec{\mathbf{r}}) = \int d^3\mathbf{r}' \tilde{\rho}_{\rm WS}(\vec{\mathbf{r}'})\rho_n(\vec{\mathbf{r}} - \vec{\mathbf{r}'}). \tag{2.3}$$

$$\tilde{\rho}_{\rm WS}(\vec{\mathbf{r}}) = \frac{\rho_0}{1 + \exp\left(\frac{r - R_A\Omega(\theta)}{\xi}\right)}, \tag{2.4}$$

where ρ_0 is the nucleon number density in infinite nuclear matter, R_A is the rms charge radius of nucleus A, and ξ is the surface width parameter. For a deformed nucleus with non-zero quadrupole and hexadecupole ground state deformation $R(\theta) = R_A\Omega(\theta) = R_A(1 + \beta_2 Y_0^2(\theta) + \beta_4 Y_0^4(\theta))$, where

Element	Atomic Mass	ρ_0 (fm^{-3})	R_A (fm)	ξ (fm)	β_2	β_4
Cu	63	0.1686	4.28	0.50	0.162	0.006
Au	197	0.1695	6.42	0.45	-0.130	-0.030
Pb	208	0.1610	6.67	0.44	0	0
U	238	0.1660	6.86	0.44	0.280	0.093

Table 2.1: Parameters for the modified Woods-Saxon density distribution, $\tilde{\rho}_{\rm WS}$, for some heavy nuclei that have been used in relativistic heavy-ion collisions.

$Y_0^2(\theta)$ and $Y_0^4(\theta)$ are the spherical harmonics, describes the angular dependence of the nuclear radius. In Table 2.3.1, we list the parameters used in `superMC` for some typical colliding nuclei.

Note that our parameterization of the nuclear density distribution does not account for the existence of a neutron skin in large nuclei. Inclusion of a neutron skin is left for a future improvement of the `superMC` code.

2.3.2 The MC-Glauber approach

The probability density for an inelastic nucleon-nucleon collision at impact parameter $\vec{\mathbf{b}}$ is

$$P(\vec{\mathbf{b}}) = \begin{cases} \theta(2r_n - b), & \text{cylindrical nucleon,} \\ 1 - \exp(-\sigma_{\rm gg} T_{\rm nn}(b)), & \text{gaussian nucleon.} \end{cases} \tag{2.5}$$

where $\sigma_{\rm gg}$ is the inelastic gluon-gluon cross-section [7] and $T_{\rm nn}$ is the nucleon-nucleon overlap function,

$$T_{\rm nn}(b) = \int d^2\vec{\mathbf{r}}_\perp T_n(\vec{\mathbf{r}}_\perp) T_n(\vec{\mathbf{b}} - \vec{\mathbf{r}}_\perp) = \frac{e^{-b^2/(4B)}}{4\pi B}. \tag{2.6}$$

For unpolarized nucleons the nucleon density is spherically symmetric, so $T_{\rm nn}(b)$ has no directional dependence. A binary collision involving nucleon pair (i, j) will deposit a certain amount of energy in the medium around the collision point $\vec{\mathbf{R}}_{ij,\perp} = \frac{1}{2}(\vec{\mathbf{r}}_{i\perp} + \vec{\mathbf{r}}_{j\perp})$. After thermalization, this energy density is associated with a corresponding amount of entropy density computable from the equation of state. For cylindrical nucleons, we choose a disk-like profile for the deposited energy or entropy density in the transverse plane. For Gaussian nucleons, the deposited energy density is modeled by a gaussian distribution. Thus, the entropy or energy density generated by all the binary collision pairs in the transverse plane is proportional to,

$$BC(\vec{\mathbf{r}}_\perp) = \begin{cases} \sum_{(i,j)\in\text{pairs}} \frac{\theta(r_n - |\vec{\mathbf{r}}_\perp - \vec{\mathbf{R}}_{ij,\perp}|)}{\pi r_n^2}, & \text{cylindrical nucleons,} \\ \sum_{(i,j)\in\text{pairs}} \frac{1}{2\pi B} e^{-|\vec{\mathbf{r}}_\perp - \vec{\mathbf{R}}_{ij,\perp}|^2/(2B)}, & \text{gaussian nucleons.} \end{cases} \tag{2.7}$$

The parameters r_n and B are chosen to be the same as in the definition of the shape of the nucleon, Eq. (2.1).

Every nucleon that participates in an inelastic collision is "wounded" and will "bleed" energy density into the medium. In `superMC`, two distinct ways to distribute the energy deposited by the wounded nucleons are implemented.

The first option is to deposit the energy symmetrically around the center of the wounded nucleon. The total energy or entropy density contributed by all wounded nucleons is then proportional to,

$$WN(\vec{\mathbf{r}}_\perp) = \begin{cases} \sum_{i\in\text{wounded}} \frac{\theta(r_n - |\vec{\mathbf{r}}_\perp - \vec{\mathbf{r}}_{i\perp}|)}{\pi r_n^2}, & \text{cylindrical nucleons,} \\ \sum_{i\in\text{wounded}} \frac{1}{2\pi B} e^{-|\vec{\mathbf{r}}_\perp - \vec{\mathbf{r}}_{i\perp}|^2/(2B)}, & \text{gaussian nucleons.} \end{cases} \tag{2.8}$$

where the index i runs over all wounded nucleons in both nuclei A and B.

In the second approach, the energy bled from each wounded nucleon is distributed evenly over its binary collision partners and deposited symmetrically around their correspond binary collision points. In this case, the total energy or entropy density contributed by all wounded nucleons is proportional to

$$WN(\vec{\mathbf{r}}_\perp) = \begin{cases} \sum_{i\in\text{wounded}} \sum_{j=1}^{N_{b,i}} \frac{1}{N_{b,i}} \frac{\theta(r_n - |\vec{\mathbf{r}}_\perp - \vec{\mathbf{R}}_{ij,\perp}|)}{\pi r_n^2}, & \text{cylindrical nucleon,} \\ \sum_{i\in\text{wounded}} \sum_{j=1}^{N_{b,i}} \frac{1}{N_{b,i}} \frac{1}{2\pi B} e^{-|\vec{\mathbf{r}}_\perp - \vec{\mathbf{R}}_{ij,\perp}|^2/(2B)}, & \text{gaussian nucleon.} \end{cases} \tag{2.9}$$

where $N_{b,i}$ is the number of binary collision partners associated with wounded nucleon i. This way of distributing the energy density is motivated by the idea that the inelastic collisions between nucleons that generate wounded nucleons or binary collision events are fundamentally the same.

The second approach distributes the entropy or energy density of wounded nucleons over a more compact transverse area, which in the end result increases the initial eccentricity of the fireball created in the collision at large impact parameters. In central collisions, the difference in eccentricity between the two energy deposition schemes is negligible.

In the MC-Glauber model, the total energy density produced in the transverse plane after thermalization is taken to be a mixture of the wounded nucleon and binary collision density profiles:

$$\begin{Bmatrix} s_0(\vec{\mathbf{r}}_\perp) \\ e_0(\vec{\mathbf{r}}_\perp) \end{Bmatrix} = \begin{Bmatrix} \kappa_s \\ \kappa_e \end{Bmatrix} \left(\frac{1-\alpha}{2} WN(\vec{\mathbf{r}}_\perp) + \alpha BC(\vec{\mathbf{r}}_\perp) \right), \tag{2.10}$$

Here α is the binary mixing parameter and κ is an overall normalization factor κ is tuned to reproduce to measured final charged multiplicity in the most central collisions, while α is adjusted to reproduce its observed dependence on collision centrality. Due to viscous heating during the hydrodynamic expansion, the normalization κ depends on the specific shear viscosity η/s. The actual parameters we used for the relativistic heavy-ion collisions studied in this thesis are listed in Table 2.2.

Collision system	η/s	α	κ
Au+Au	0.08	0.14	28.656
@200 A GeV	0.10	0.144	27.474
Pb+Pb	0.08	0.118	56.763
@2760 A GeV	0.10	0.128	53.868
	0.16	0.131	48.405

Table 2.2: Parameters used in the MC-Glauber model for different choice of η/s at RHIC and LHC energy.

2.3.3 The MCKLN approach

The MCKLN model [8, 9] is based on a k_T-factorization ansatz [8, 9] in which the produced gluon density distribution can be calculated as

$$\begin{aligned}\frac{dN_g}{dyd^2p_\perp d^2x_\perp} &= \frac{2\pi^3 N_c}{N_c^2-1}\int_0^{p_\perp} d^2k_\perp \frac{\alpha_s(\max\{((\vec{\mathbf{p}}_\perp+\vec{\mathbf{k}}_\perp)/2)^2,((\vec{\mathbf{p}}_\perp-\vec{\mathbf{k}}_\perp)/2)^2\})}{p_\perp^2} \\ &\times \phi_A\left(x_1,\left(\frac{\vec{\mathbf{p}}_\perp+\vec{\mathbf{k}}_\perp}{2}\right)^2;\vec{\mathbf{x}}_\perp+\vec{\mathbf{b}}/2\right) \\ &\times \phi_B\left(x_2,\left(\frac{\vec{\mathbf{p}}_\perp-\vec{\mathbf{k}}_\perp}{2}\right)^2;\vec{\mathbf{x}}_\perp-\vec{\mathbf{b}}/2\right), \end{aligned} \tag{2.11}$$

where α_s is the strong coupling constant and ϕ_A and ϕ_B are the unintegrated gluon distribution functions of the two colliding nucleus. $\vec{\mathbf{p}}_\perp = \frac{\vec{\mathbf{p}}_{1\perp}+\vec{\mathbf{p}}_{2\perp}}{2}$ and $\vec{\mathbf{k}}_\perp = \vec{\mathbf{p}}_{1\perp} - \vec{\mathbf{p}}_{2\perp}$, where $\vec{\mathbf{p}}_{1(2)\perp}$ are the transverse momenta of the fusing gluons from the two nuclei and $x_{1(2)} = \frac{p_\perp}{\sqrt{s_{\rm NN}}}e^{\pm y}$ are their corresponding light-cone momentum fractions. The unintegrated gluon distribution function is parameterized as,

$$\phi(x,k^2;\vec{\mathbf{x}}_\perp) = \kappa\frac{N_c^2-1}{2N_c}\frac{Q_s^2(x,\vec{\mathbf{x}}_\perp)}{2\pi^3\alpha_s(Q_s^2)}\begin{cases}\frac{1}{Q_s^2+\Lambda^2}, & k\le Q_s\\ \frac{1}{k^2+\Lambda^2}, & k>Q_s\end{cases}, \tag{2.12}$$

where $\Lambda = \Lambda_{\rm QCD} = 0.2\,{\rm GeV}$, and $\kappa = 1.8$ is a phenomenological parameter adjusted [10] to fit the measured charged multiplicity at mid rapidity in the most central Au+Au collisions at $\sqrt{s_{\rm NN}} = 200\,{\rm GeV}$ at RHIC. The saturation scale is given by the implicit relation,

$$Q_s^2(x,\vec{\mathbf{x}}_\perp) = \frac{4\pi^2 N_c}{N_c^2-1}\alpha_s(Q_s^2)xG(x,Q_s^2)T_A(\vec{\mathbf{x}}_\perp) \tag{2.13}$$

The running coupling strength is parameterized as,

$$\alpha_s(k^2) = \begin{cases}\frac{4\pi}{\beta_0\ln\left((k^2+\Lambda^2)/\Lambda_{\rm QCD}^2\right)}, & \alpha_s\le 0.5\\ 0.5, & \alpha_s\ge 0.5\end{cases}, \tag{2.14}$$

with $\beta_0 = 11-\frac{2}{3}N_f$. Kharzeev, Levin, and Nardi [9] use the parameterization $xG(x,k^2) = K\ln(\frac{k^2+\Lambda^2}{\Lambda_{\rm QCD}^2}x^{-\lambda}(1-x)^4$ with $\lambda = 0.2$ and $K = 0.7$ adjusted such that the average Q_s^2 in the

transverse plane of a central 200 A GeV Au + Au collision, $\langle Q_s^2(x = 0.01)\rangle \simeq 2.0$ GeV^2.[10] Inserting this into Eq. (2.13) and dropping the $(1-x)^4$ factor since x is small in the kinematic region of interest leads to

$$Q_s^2(x, \vec{\mathbf{x}}_\perp) = 2\text{GeV}^2 \left(\frac{T(\vec{\mathbf{r}}_\perp)}{T_0}\right)\left(\frac{x_0}{x}\right)^\lambda, \tag{2.15}$$

where $T_0 = 1.53$ fm^{-2} and $x_0 = 0.01$ [11].

2.3.4 Collision-by-collision Multiplicity Fluctuation

The entropy (or energy) density dumped into the medium from each binary collision and wounded nucleon can fluctuate. These fluctuations lead to the measured multiplicity fluctuation in pp collisions. We denote such fluctuation as collision-by-collision multiplicity fluctuations.

In 2012, the CMS collaboration measured flow observables in 0-0.2% ultra-central Pb + Pb collisions at the LHC . For these extremely high multiplicity and extremely rare heavy-ion collision events, the event selection is strongly biased towards upward fluctuations in the particles production of the system. Thus, we would expect collision-by-collision multiplicity fluctuations to become important for the event selection in such ultra-central collisions.

In `superMC`, we implement collision-by-collision multiplicity fluctuations in the MC-Glauber model based on the phenomenological KNO scaling observed in pp collisions. In the MC-Glauber model, we regard each binary collision and each wounded nucleon as an independent source of energy with stochastic norm. This can be expressed through the following modification of Eq. (2.7) and (2.8):

$$BC(\vec{\mathbf{r}}_\perp) = \begin{cases} \sum_{(i,j)\in\text{pairs}} \gamma_{i,j} \frac{\theta(r_n - |\vec{\mathbf{r}}_\perp - \vec{\mathbf{R}}_{ij,\perp}|)}{\pi r_n^2}, & \text{cylindrical nucleons,} \\ \sum_{(i,j)\in\text{pairs}} \gamma_{i,j} \frac{1}{2\pi B} e^{-|\vec{\mathbf{r}}_\perp - \vec{\mathbf{R}}_{ij,\perp}|^2/(2B)}, & \text{gaussian nucleon.} \end{cases} \tag{2.16}$$

and

$$WN(\vec{\mathbf{r}}_\perp) = \begin{cases} \sum_{i\in\text{wounded}} \gamma_i \frac{\theta(r_n - |\vec{\mathbf{r}}_\perp - \vec{\mathbf{r}}_{i\perp}|)}{\pi r_n^2}, & \text{cylindrical nucleon,} \\ \sum_{i\in\text{wounded}} \gamma_i \frac{1}{2\pi B} e^{-|\vec{\mathbf{r}}_\perp - \vec{\mathbf{r}}_{i\perp}|^2/(2B)}, & \text{gaussian nucleon.} \end{cases} \tag{2.17}$$

where the multiplicity scaling factors $\gamma_{i,j}$ and γ_i are continuous random variables with unit mean values. In practice, we use the Gamma distribution as the probability distribution for $\gamma_{i,j}$ and γ_i. The Gamma distribution for a random variable X is defined as

$$\text{Gamma}(X) = \frac{1}{\Gamma(k)\theta^k} x^{k-1} e^{-x/\theta}, \tag{2.18}$$

where k and θ are the so-called shape and scale parameters of the Gamma distribution, respectively. The Gamma distribution is positive semi-definite and has the following properties:

(1) If $X_i = \text{Gamma}(k_i, \theta)$, then $\sum_i X_i = \text{Gamma}(\sum_i k_i, \theta)$.

(2) If $X = \text{Gamma}(k, \theta)$, then $cX = \text{Gamma}(k, c\theta)$ for any $c > 0$.

By using these two properties of the Gamma distribution, we can assign two different sets of (k, θ) parameters for γ_i and $\gamma_{i,j}$ in Eqs. (2.16) and Eqs. (2.17), respectively, to ensure that the final total entropy or energy density, which is a weighted sum of all the collisions in the event according to Eq. (2.10) also fluctuates according a Gamma distribution with a desired shape and scale. For $WN(\vec{\mathbf{r}}_\perp)$, we write,

$$\gamma_i = \text{Gamma}\left(k_{WN}, \theta_{WN}\right) \tag{2.19}$$

and for $BC(\vec{\mathbf{r}}_\perp)$

$$\gamma_{i,j} = \text{Gamma}\left(k_{BC}, \theta_{BC}\right). \tag{2.20}$$

Based on Eqs. (2.10), (2.16) and (2.17), we then have

$$s = \kappa \left(\text{Gamma}\left(\sum_{i=1}^{N_{\text{part}}} k_{WN,i}, \frac{1-\alpha}{2}\theta_{WN} \right) + \text{Gamma}\left(\sum_{i=1}^{N_{\text{coll}}} k_{BC,i}, \alpha\theta_{BC} \right) \right). \tag{2.21}$$

By requiring $\frac{1-\alpha}{2}\theta_{WN} = \alpha\theta_{BC} = \theta$, Eq. (2.21) can be further simplified to,

$$\left\{ \begin{array}{c} s \\ e \end{array} \right\} = \left\{ \begin{array}{c} \kappa_s \\ \kappa_e \end{array} \right\} \left(\text{Gamma}\left(N_{\text{part}} k_{WN} + N_{\text{coll}} k_{BC}, \theta\right)\right). \tag{2.22}$$

By further writing $k_{WN} = \frac{1-\alpha}{2}k$ and $k_{BC} = \alpha k$, we finally obtain,

$$\left\{ \begin{array}{c} s \\ e \end{array} \right\} = \left\{ \begin{array}{c} \kappa_s \\ \kappa_e \end{array} \right\} \left(\text{Gamma}\left(\left(\frac{1-\alpha}{2} N_{\text{part}} + \alpha N_{\text{coll}} \right) k, \theta \right) \right), \tag{2.23}$$

which has the mean value $\langle s \rangle = \kappa \left(\frac{1-\alpha}{2} N_{\text{part}} + \alpha N_{\text{coll}} \right) k\theta$. Similar expressions are obtained in case where the energy density is parameterized as in Eq. (2.10). Setting $k\theta = 1$ ensures that with the perviously adjusted normalization κ the event-averaged total entropy continuous to reproduce the value from the conventional MC-Glauber model (and thus the observed final charged multiplicity).

The actual value of θ with $(k = 1/\theta)$ in Eq. (2.23) can be fit to the multiplicity distribution measured in pp collisions, where $N_{\text{part}} = 2$ and $N_{\text{coll}} = 1$. At LHC energies, the multiplicity fluctuations in pp collision have been measured at $\sqrt{s} = 0.9$, 2.36, and 7 TeV [12]. Additionally, the UA5 Collaboration measured pp multiplicity distributions at $\sqrt{s} = 200$ GeV [13]. In Fig. 2.3, we show the results of a χ^2 fit to the experimental data at all these collision energies with $\theta = 0.9175$. According to the KLN scaling hypothesis, $\langle N_{\text{ch}} \rangle P(N_{\text{ch}})$ should be a universal (energy independent) function of the normalized multiplicity $N_{\text{ch}}/\langle N_{\text{ch}} \rangle$. The left panel of Fig. 2.3 shows that at central rapidity $|\eta| < 0.5$, the experimental data show very good KNO scaling for the pp multiplicity distribution at all of these collision energies.

In the right panel of Fig. 2.3, we cross check that our implementation of the MC-Glauber model with multiplicity fluctuations can reproduce the desired normalized multiplicity distribution in the pp collision limit.

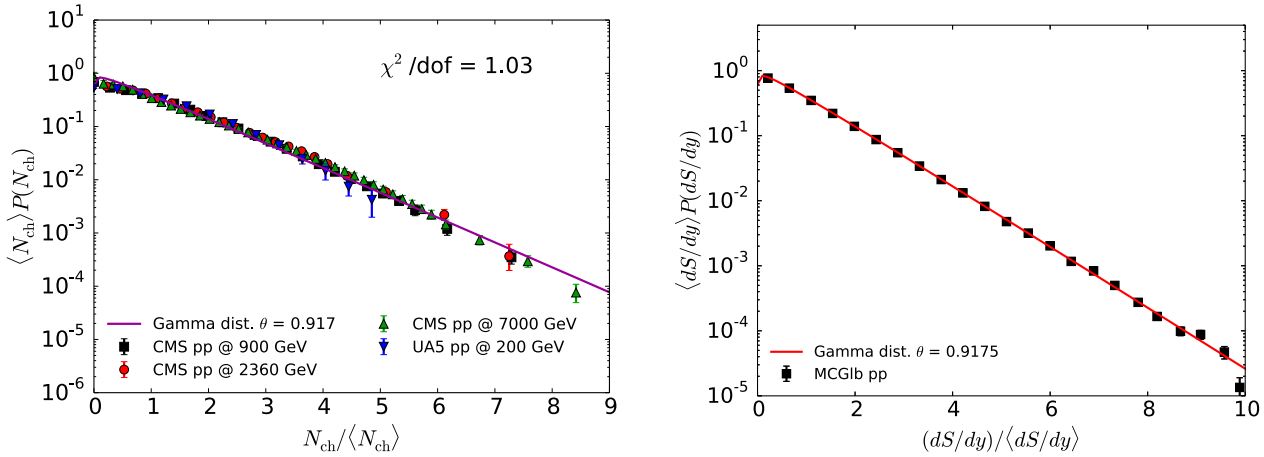

Figure 2.3: Left Panel: KNO scaling of the pp multiplicity distribution in $|\eta| < 0.5$ for $\sqrt{s}$= 200, 900, 2360, and 7000 A GeV. The experimental data are taken from [12, 13]. Right Panel: Numerical cross check that the MC-Glauber code in `superMC` correctly reproduces the Gamma-distributed charged multiplicity distribution measured in pp collisions .

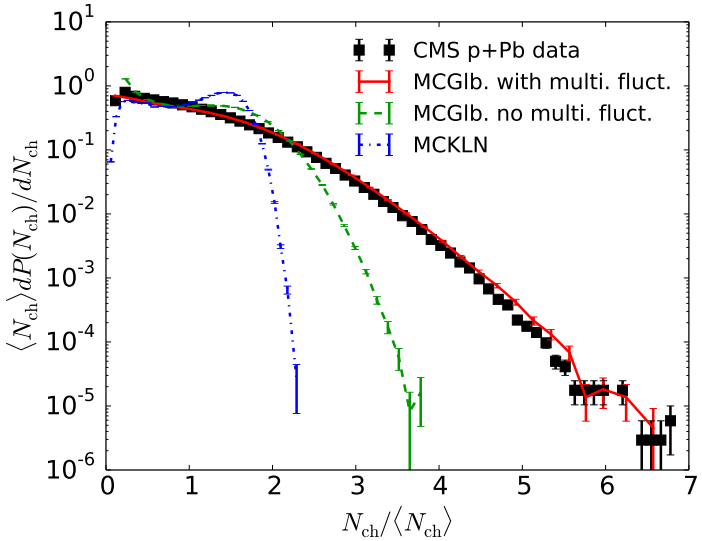

Figure 2.4: Postdiction for the multiplicity distribution in p+Pb collisions at $\sqrt{s_{\rm NN}} = 5.02\,A\,$TeV compared with the CMS measurements [14].

Once the parameters in the Gamma distribution are fixed by the phenomenological KNO scaling, we use this model to make parameter-free postdiction for the multiplicity distribution in p+Pb collisions at $\sqrt{s_{\rm NN}} = 5.02\,$TeV. The comparisons with measurements from the CMS Collaboration are shown in Fig. 2.4. The MC-Glauber model with collision-by-collision multiplicity fluctuation can reproduce the shape of the measured multiplicity distribution very well. While without the multiplicity fluctuation, both the MC-Glauber and the MCKLN models give too less upward fluctuations.

In appendix E, we show that at kinetic freeze out, the Monte-Carlo sampled particle numbers fluctuate from event to event according to a Poisson distribution. By folding the Gamma distribution for the initial entropy density fluctuations with Poisson distribution for the fluctuating final particle yield from a given hydrodynamic event, we find a negative binomial distribution (NBD) for the final multiplicities from many hydrodynamic event, with fluctuating initial conditions.

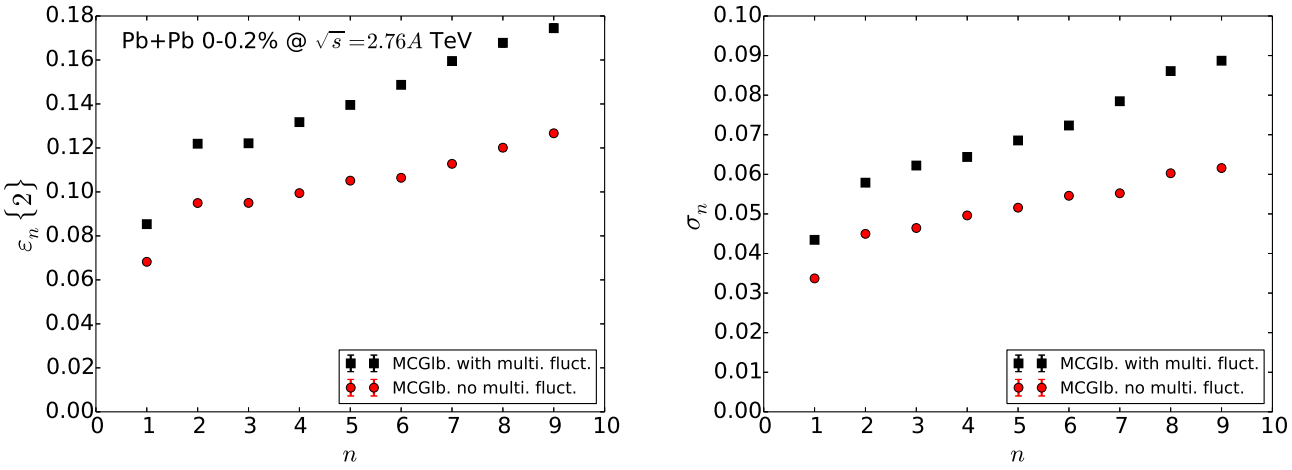

Figure 2.5: Left Panel: Root mean square of the n-th order initial spatial eccentricity as a function of the harmonic order n. Right Panel: The variance of ε_n as a function of n.

In Fig. 2.5, we show a comparison of the initial spatial eccentricity $\varepsilon_n\{2\}$ as a function of the harmonic order n for 0-0.2% ultra-central Pb + Pb collisions at LHC energy. $\varepsilon_n\{2\} = \sqrt{\langle\varepsilon_n^2\rangle}$ is the rms of ε_n, defined in terms of the fluctuating initial energy density profile $e(r_\perp, \phi)$ as

$$\varepsilon_n = \frac{\int d^2\mathbf{r}_\perp r_\perp^n e(r_\perp,\phi) e^{in(\phi-\Phi_n)}}{\int d^2\mathbf{r}_\perp r_\perp^n e(r_\perp,\phi)}, \qquad \text{for} \quad n \leq 2. \tag{2.24}$$

We can clearly see that the collision-by-collision multiplicity fluctuations increase the eccentricity coefficients for all harmonic orders by 20-40%. The increase is larger for higher order n. The multiplicity fluctuations also increase the variance of ε_n similar amount. The existence of such fluctuations therefore changes the mean values and their variances of the initial fluctuation spectrum of the MC-Glauber model dramatically.

In Fig. 2.6, we show ε_2 to ε_5 as functions of the collision centrality. We find that collision-by-collision multiplicity fluctuations are not only important in ultra-central collisions, but that they increase the spatial eccentricities at all collision centralities.

2.3.5 Centrality cut in theoretical calculations

Centrality is a key quantity that links the theoretical calculations with the experimental measurements. It is introduced to characterize the collision geometry in the nucleus-nucleus collisions. Experimentally, the centrality is typically defined by sorting the recorded events according to

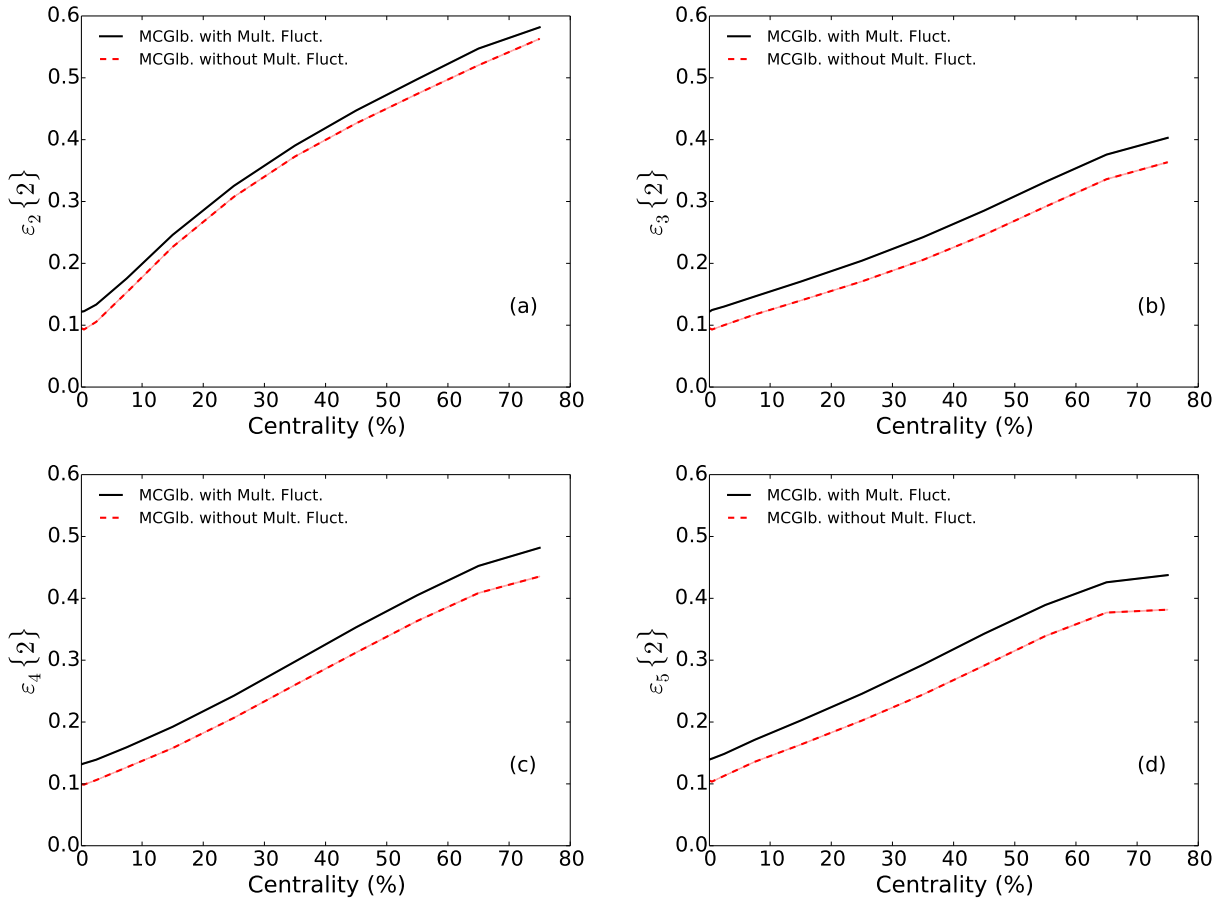

Figure 2.6: Centrality dependence of the root mean square initial spatial eccentricities ε_2, ε_3, ε_4, ε_5.

their measured charged hadron multiplicity at mid-rapidity, $dN^{\rm ch}/d\eta|_{|\eta|<0.5}$. Applying the same procedure theoretically is numerically expensive since, due to viscous heating, the final charged multiplicity can not be determined directly from the initially produced entropy, but requires viscous hydrodynamic evolution, event by event.

However, we can use the following shortcut to save simulation time: we cut centrality on the initially produced total entropy in the transverse plane, $dS/dy|_{y=0}$, assuming that, on average, the final charged multiplicity , $dN^{\rm ch}/d\eta$, is monotonically related with $dS/dy|_{y=0}$. This procedure is illustrated in Fig. 2.7.

After having fixed the normalization constant κ in Eq. (2.10) such that, on average, the measured charged multiplicity in central collisions is correctly reproduced, we first sort the minimum bias events generated by the MC-Glauber model according to the initial entropy dS/dy. Then, we can classify their collision centrality through dividing their relative positions in the sorted array. The events with largest total entropy define the most central collisions where the two nuclei completely overlap each other. The 0-10% centrality bin includes the 10% of all events with the largest initial dS/dy, 90-100% the 10% of all events with the smallest dS/dy values.

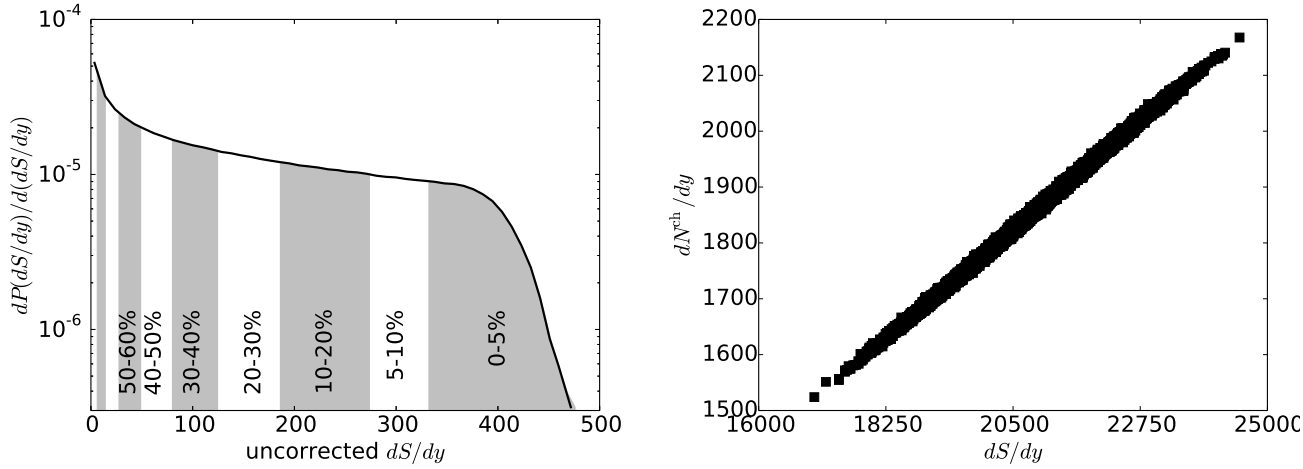

Figure 2.7: Left Panel: Probability distribution of the total entropy density $dS/dy|_{y=0}$ from MC-Glauber model for Pb + Pb at $\sqrt{s} = 2.76A$ TeV. Right Panel: Correlation between initial dS/dy and final measured $dN^{\rm ch}/dy$ at 0-5% most central collisions for MC-Glauber with $\eta/s = 0.08$.

This procedure ignores event-by-event fluctuations in the factional increase of the entropy due to viscous heating during the hydrodynamic evolution. This extra entropy production depends on the actual shape of the initial density profile as well as on the chosen value for the specific shear viscosity, η/s. Event-by-event fluctuation of the viscous entropy production will de-correlate the one-to-one correspondence between the initial total entropy, dS/dy and the final measured charged multiplicity, $dN^{\rm ch}/dy$. However, as shown in the right panel of the Fig. 2.7, this decorrelation is weak: For given dS/dy, the spread in final $dN_{\rm ch}/dy$ is very small. Therefore, our procedure of defining collision centrality by cutting on the initial total dS/dy is a pretty good theoretical approximation to the experimental centrality definition using final charged multiplicities.

2.4 (2+1)-d viscous hydrodynamics `VISH2+1`

2.4.1 Solving the hydrodynamic equations

The module `VISH2+1` is an modified version of `VISH2+1`, (2+1)-d longitudinally boost-invariant viscous hydrodynamic algorithm developed by H. Song. [15] It includes several improvements for efficiency and stability which will be discussed in this section. We solve the following equation of motion for second order viscous hydrodynamics ("Israel-Stewart equations"):

$$d_\mu T^{\mu\nu} = 0,\ T^{\mu\nu} = e u^\mu u^\nu - (p + \Pi)\Delta^{\mu\nu} + \pi^{\mu\nu}. \tag{2.25}$$

The shear stress tensor $\pi^{\mu\nu}$ and bulk pressure Π satisfy the following transport equations,

$$\Delta^{\mu\alpha}\Delta^{\nu\beta} D\pi_{\alpha\beta} = -\frac{1}{\tau_\pi}(\pi^{\mu\nu} - 2\eta\sigma^{\mu\nu}) - \frac{1}{2}\pi^{\mu\nu}\frac{\eta T}{\tau_\pi} d_\lambda\left(\frac{\tau_\pi}{\eta T} u^\lambda\right), \tag{2.26}$$

$$D\Pi = -\frac{1}{\tau_\Pi}(\Pi + \zeta\theta) - \frac{1}{2}\Pi\frac{\zeta T}{\tau_\Pi} d_\lambda\left(\frac{\tau_\Pi}{\zeta T} u^\lambda\right), \tag{2.27}$$

where $D = u^\mu d_\mu$. The hydrodynamic equations need to be solved together with a given equation of state (EOS). `VISH2+1` supports three versions of the lattice-based equation of state, `s95p-v0-PCE`, `s95p-v1`, and `s95p-v1-PCE` [16]. The differences among these three EOS are the different implementations of partial chemical equilibrium in the hadronic phase [16, 17]. In general, Eq. (2.25) must be supplemented by an evolution equation (conservation law) for the baryon current $j^\mu = nu^\mu$. We start with the case $n = 0$.

Without baryon current

The hydrodynamic code evolves the components of energy stress tensor. In order to use the EOS for determining the pressure in the liquid, we first need to solve for the local energy density and velocity of the fluid cell. In the (2+1)-d case, we define a vector $M^\mu = (M^0, M^x, M^y) = (T^{\tau\tau} - \pi^{\tau\tau}, T^{\tau x} - \pi^{\tau x}, T^{\tau y} - \pi^{\tau y})$. Using the decomposition Eq. (2.25) for $T^{\mu\nu}$, we find

$$M^0 = (e + P + \Pi)(u^0)^2 - P - \Pi, \tag{2.28}$$

$$M^1 = (e + P + \Pi)u^0 u^1, \tag{2.29}$$

$$M^2 = (e + P + \Pi)u^0 u^2, \tag{2.30}$$

The local energy density thus satisfies the following equation:

$$e = M^0 - \frac{(M^1)^2 + (M^2)^2}{M^0 + P + \Pi}. \tag{2.31}$$

To solve Eq. (2.31) we define

$$f(e) = (M^0 - e)(M^0 + P + \Pi) - ((M^1)^2 + (M^2)^2). \tag{2.32}$$

We first observe that $f(M^0) = -((M^1)^2 + (M^2)^2) \leq 0$. In order for Eq. (2.31) to have an odd number of positive solutions, we need to require $f(0) \geqslant 0$. With a non-zero bulk viscous pressure, this lead to the condition,

$$f(0) = (M^0)^2 - (M^1)^2 - (M^2)^2 + M^0\Pi \geqslant 0. \tag{2.33}$$

When this requirement is not fulfilled because Π (which is negative) is too large, we regulate Π such that $f(0) = 0$. In this special situation one can further compute

$$\frac{df}{de}(e = 0) = (c_s^2 - 1)M^0 - \Pi. \tag{2.34}$$

If $\frac{df}{de}|_{e=0} \leq 0$, $e = 0$ is the solution. For $\frac{df}{de}|_{e=0} > 0$, there will be a positive energy density solution. Without Π, $\frac{df}{de}|_{e=0}$ is always less than 0 because the square of the speed of sound is always smaller than 1.

Once these two boundary conditions are set up, it is guaranteed that there will be at least one solution of Eq. (2.31) with positive energy density. Newton's root finding method is a very efficient in finding this solution with a minimal number of iteration. To ensure numerical stability and optimal efficiency, we use the fact that to fairly good approximation the pressure is roughly proportional to the energy density. We rewrite Eq. (2.32) as,

$$f(e) = (M^0 - e)\left(M^0 + \frac{P}{e}e + \Pi\right) - ((M^1)^2 + (M^2)^2)$$

and use that $\tilde{c}_s^2 = \frac{P}{e}$ has a very weak dependence on e. This turns the condition $f(e) = 0$ into approximately a quadratic equation with solution

$$e = \frac{-(M^0(1-\tilde{c}_s^2) + \Pi) \pm \sqrt{(M^0(1-\tilde{c}_s^2) + \Pi)^2 + 4\tilde{c}_s^2(M^0(M^0+\Pi) - M)}}{2\tilde{c}_s^2}. \tag{2.35}$$

To identify the correct sign, we note that for $M = 0$ we must recover $e = M^0$. Therefore,

$$e = \frac{-(M^0(1-\tilde{c}_s^2) + \Pi) + \sqrt{(M^0(1-\tilde{c}_s^2) + \Pi)^2 + 4\tilde{c}_s^2(M^0(M^0+\Pi) - M)}}{2\tilde{c}_s^2}. \tag{2.36}$$

This equation is the most efficient satisfying form for applying Newton's method, and it is implemented in `VISH2+1`.

Once Eq. (2.25) has been solved for e, the flow velocity can be calculated from

$$u^0 = \left(\frac{M^0 + P + \Pi}{e + P + \Pi}\right)^{1/2} \tag{2.37}$$

where $P = P(e)$ is obtained from the EOS. Please note that calculating u^0 instead of v is numerically more stable when $v \to 1$. Since $u^0 \geqslant 1$, this requires $M^0 \geqslant e$. So M^0 should be set as an upper limit for e when intreating e using Newton's root finding routine. Similarly,

$$u^i = \frac{M^i}{\sqrt{M^0 + P + \Pi}\sqrt{e + P + \Pi}} \ (i = 1, 2). \tag{2.38}$$

One can check that if e is the exact solution of Eq. (2.31), the flow velocity components Eq. (2.37) and Eq. (2.38) satisfy the normalization constraint

$$(u^0)^2 - (u^1)^2 - (u^2)^2 = 1. \tag{2.39}$$

With baryon density current

The derivations above assumed zero net baryon density where the pressure is only a function of the local energy density. In order to deal with the more general cases of non-zero conserved charge current in the future, we now consider the situation where the baryon current is not zero.

In this case the pressure is a function of both the local energy density and the local net baryon density: $P = P(e, n)$. For the baryon current, we have the additional hydrodynamic equation

$$\partial_\mu j^\mu = 0 \tag{2.40}$$

where (V^μ is the heat flow vector)

$$j^\mu = nu^\mu + V^\mu. \tag{2.41}$$

Now, the problem of implementing the EOS presents itself as follows: knowing $j^0, T^{00}, T^{01}, T^{02}, T^{03}$ and the EOS, we would like to solve for 5 unknowns n, e, u^μ. We have the following 5 equations:

$$M^0 = (e + P + \Pi)(u^0)^2 - P - \Pi, \tag{2.42}$$

$$M^i = (e + P + \Pi)u^0 u^i, \ (i = 1, 2, 3), \tag{2.43}$$

$$j^0 = nu^0 + V^0. \tag{2.44}$$

We can no longer solve for e easily, because the pressure now depends on both e and n. The equations for e and n are coupled with each other. To decouple these two equations, we need to know the actual functional dependence for $P(e, n)$. In such a situation, it is easilier to solve for v or u^0 first. For v, we have solve the following equation:

$$v = \frac{M}{M^0 + P + \Pi} \tag{2.45}$$

where $M = \sqrt{(M^1)^2 + (M^2)^2 + (M^3)^2}$. For the pressure from the EOS, we need to work out

$$e = M^0 - vM \tag{2.46}$$

$$n = (j^0 - V^0)\sqrt{1 - v^2} \tag{2.47}$$

To solve Eq. (2.45) we define

$$f(v) = v(M^0 + P + \Pi) - M. \tag{2.48}$$

We have the boundary conditions

$$f(0) = -M \leqslant 0 \tag{2.49}$$

and

$$f(1) = M^0 + P + \Pi - M. \tag{2.50}$$

Imposing $f(1) \geqslant 0$ will ensure an odd number of solutions. From Eqs. (2.46) and Eq. (2.47) we see that e and n are roughly linear in v, which means that P is also roughly linear in v. So we expect to have only one solution. Please note that since v is bounded between 0 and 1, we need to ensure high precision of the solution, otherwise u^μ will not be accurate, especially when $v \to 1$.

Once v is solved and thus e and n are known from Eqs. (2.46) and (2.47), v_x, v_y, v_z can be solved easily from M^1, M^2, M^3,

$$v^i = \frac{M^i}{M^0 + P(e,n) + \Pi}, \ (i = 1, 2, 3). \tag{2.51}$$

In order to use Newton's method to find the root of the key equation (2.45), we can reorganize it as follows:

$$f(v) = v(M^0 + \tilde{c}_s^2(M^0 - vM) + \Pi) - M. \tag{2.52}$$

Eq. (2.52) can be considered as an approximatly quadratic equation for v. The condition $f(v) = 0$ it has the solutions

$$v = \frac{(M^0(1+\tilde{c}_s^2) + \Pi) \pm \sqrt{(M^0(1+\tilde{c}_s^2) + \Pi)^2 - 4\tilde{c}_s^2 M^2}}{2\tilde{c}_s^2 M}. \tag{2.53}$$

The correct sign is found by checking the limit $M \to 0$, when v approaches to zero. This selects the negative sign in Eq. (2.53), which can thus be rewritten as

$$v = \frac{2M}{(M^0(1+\tilde{c}_s^2) + \Pi) + \sqrt{(M^0(1+\tilde{c}_s^2) + \Pi)^2 - 4\tilde{c}_s^2 M^2}}. \tag{2.54}$$

The advantage of Eq. (2.54) is that the right hand side is only very weakly dependent on v as long as $\tilde{c}_s^2$ is approximately a constant which is true over a very wide range of energy densities for `s95p` EOS. Additionally, it is numerically stable in the limit $M \to 0$. Similarly, we can find a solution for u^0:

$$u^0 = \frac{1}{\sqrt{1-v^2}} = \frac{1}{\sqrt{1 - \left[\frac{2M}{(M^0(1+\tilde{c}_s^2)+\Pi) + \sqrt{(M^0(1+\tilde{c}_s^2)+\Pi)^2 - 4\tilde{c}_s^2 M^2}}\right]^2}}. \tag{2.55}$$

Eqs. (2.54) and (2.55) in principle give consistent solutions for v and u^0. In practice, inevitable numerical errors rends the use of Eq. (2.54) preferable for small velocities $v \to 0$, which Eq. (2.55) should be used for $v \to 1$. Let us see why this is the case:

If we solve u^0 from Eq. (2.55) and write the numerical solution as $\tilde{u}^0 = u^0 + \Delta u$ where u^0 is the exact solution and Δu is the numerical error, the numerical error for v can be estimated as,

$$\Delta v = \frac{dv}{du^0}\Delta u^0 = \frac{\Delta u^0}{(\tilde{u}^0)^2\sqrt{(\tilde{u}^0)^2 - 1}}(1 + O(\Delta u^0)). \tag{2.56}$$

In this situation, Δv becomes small, $\Delta v \ll \Delta u^0$, for large flow velocity, $\tilde{u}^0 \to +\infty$. On the other hand, when $v \to 0$ and $\tilde{u}^0 \to 1$, the numerical error for v is amplified by a factor $\frac{1}{\sqrt{(\tilde{u}^0)^2-1}}$ compared to Δu^0, which is not good. Therefore Eq. (2.55) is numerically stable for $v \to 1$ and unstable for $v \to 0$.

The opposite is true for Eq. (2.54), Writing the numerical solution of Eq. (2.54) as $\tilde{v} = v + \Delta v$, we find,

$$\Delta u = \frac{du^0}{dv}\Delta v = \frac{\tilde{v}}{\left(\sqrt{1-\tilde{v}^2}\right)^3}\Delta v. \tag{2.57}$$

In this case, $\Delta u^0 \ll \Delta v$ for small $\tilde{v} \to 0$, $\Delta u^0 \ll \Delta v$, which is favorable. On the other hand, for large velocity, $\tilde{v} \to 1$, the error in u^0, $\Delta u^0 \sim \frac{1}{\left(\sqrt{1-\tilde{v}^2}\right)^3}\Delta v$, is amplified by a factor $\frac{1}{\left(\sqrt{1-\tilde{v}^2}\right)^3}$ relative to Δv, making u^0 numerically unstable.

In the actual numerical implementation, we solve both Eq. (2.54) and Eq. (2.55), but we then select the preferred solution according to the magnitude of the resulting velocity. The transition point from one choice to the other happens at

$$\frac{\tilde{v}}{\left(\sqrt{1-\tilde{v}^2}\right)^3} = \frac{1}{(\tilde{u}^0)^2\sqrt{(\tilde{u}^0)^2-1}}, \tag{2.58}$$

with the relation $\tilde{u} = \frac{1}{\sqrt{1-\tilde{v}^2}}$.The numerical solution of Eq. (2.58) is $\tilde{v} = 0.563624$ or $\tilde{u}^0 = 1.21061$. For the velocities smaller than this critical value, we use the solution for v from Eq. (2.54) , while for larger velocities, we should select the solution for u^0 from Eq. (2.55) as the more reliable one.

2.4.2 Numerical check for `VISH2+1` using semi-analytic solutions

In [18, 19], the authors derived $SO(3) \otimes SU(1,1) \otimes Z_2$ invariant ("Guber symmetric" solutions of ideal relativistic conformal fluid dynamics which couple boost-invariant longitudinal expansion with azimuthally symmetric transverse expansion. We first use this (1+1)-d solution to check the ideal hydrodynamic mode in `VISH2+1`. We start our ideal hydrodynamic simulation with Gubser's solution for the energy density and flow velocity at $\tau = 1.0$ fm/c and compare results at later proper time with Gubser's analytic solution. Fig. 2.8 shows excellent agreement between our simulations and the analytical solution.

For viscous hydrodynamics, Marrochio et al. [20] have used the same symmetry argument developed by Gubser and constructed a nontrivial semi-analytic solution of the Israel-Stewart equations for (1+1)-d expansion with Gubser symmetry. In order to use this solution as a check of the `VISH2+1` code, we have to change the source term in the transport equation of shear stress tensor as specified in [20],

$$\Delta^{\mu\alpha}\Delta^{\nu\beta}D\pi_{\alpha\beta} = -\frac{1}{\tau_\pi}(\pi^{\mu\nu} - 2\eta\sigma^{\mu\nu}) - \frac{4}{3}\pi^{\mu\nu}\theta. \tag{2.59}$$

The difference between Eqs. (2.26) and (2.59) only appears in third and higher orders in velocity gradients. However, since these gradients are large for the Gubser profile, the difference is noticeable and would be visible even if `VISH2+1` woe a perfect numerical algorithm. We use the same parameters as in [20] (described below) to test our viscous hydrodynamic simulations. We start

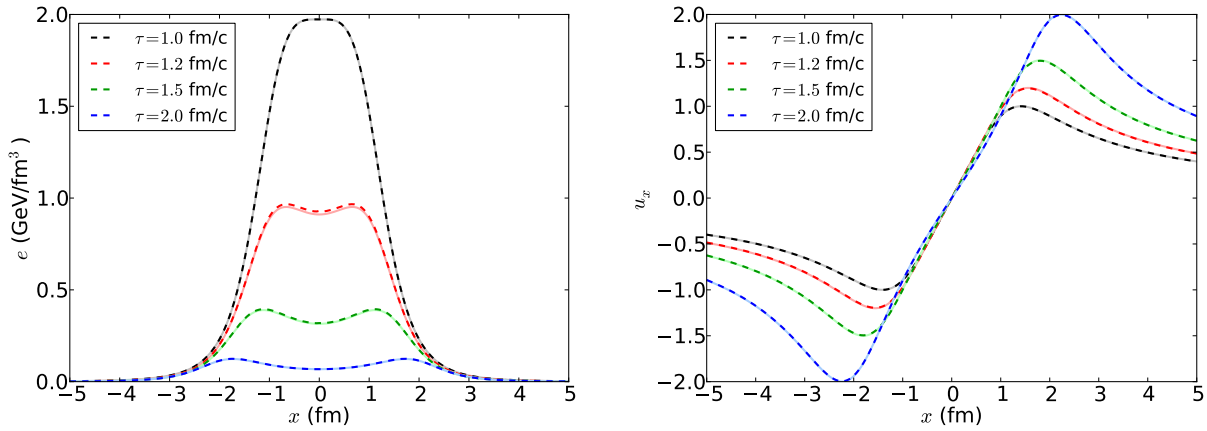

Figure 2.8: Comparison of the numerical solution (dark dashed lines) for (1+1)-d ideal fluid dynamical evolution with Gubser symmetry with Gubser's analytical results (light solid lines).

the simulation at $\tau = 1.0$ fm/c and use the semi-analytical solutions from [20] at $\tau = 1.0$ fm/c as the initial conditions for our simulations. We use an ideal massless gas equation of state $e = 3P$, with

$$e = N_c \times \left(16 + \frac{7}{2} \times 3N_f\right) \times \frac{\pi^2}{90} T^4, \tag{2.60}$$

using $N_c = 3$ for the number of colors and $N_f = 2.5$ for the number of flavors. We set the specific shear viscosity to $\eta/s = 0.2$ and its corresponding relaxation time to $\tau_\pi = 5\eta/(Ts)$.

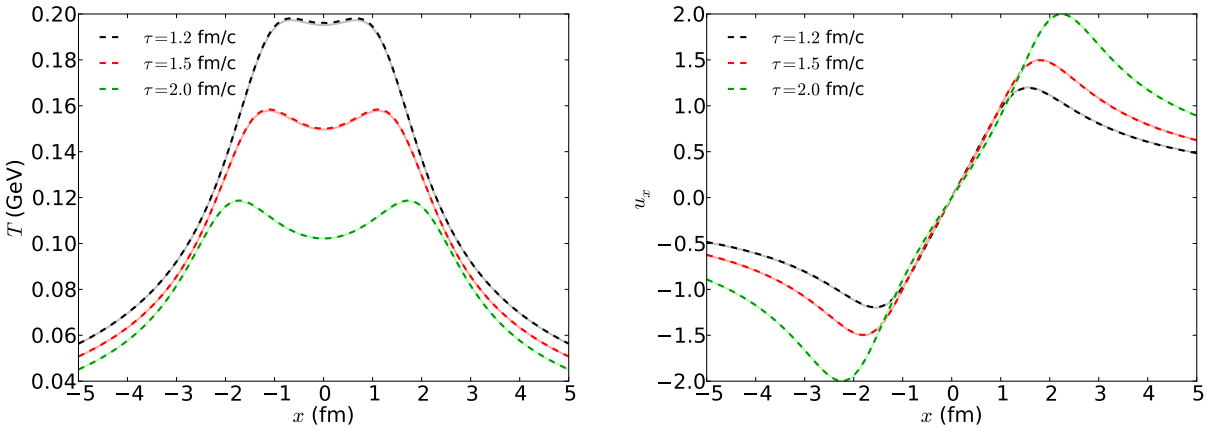

Figure 2.9: Comparison of the temperature and flow velocity evolution from `VISH2+1` (dark dashed) with the semi-analytical solutions from [20] (light solid).

In Figs. 2.9 and 2.10, we compare our numerical calculations with the semi-analytical solutions from [20] for the evolution of the local temperature, flow velocity, and shear stress tensor. For all hydrodynamic quantities we find very good agreement of our `VISH2+1` simulations with the semi-analytical results.

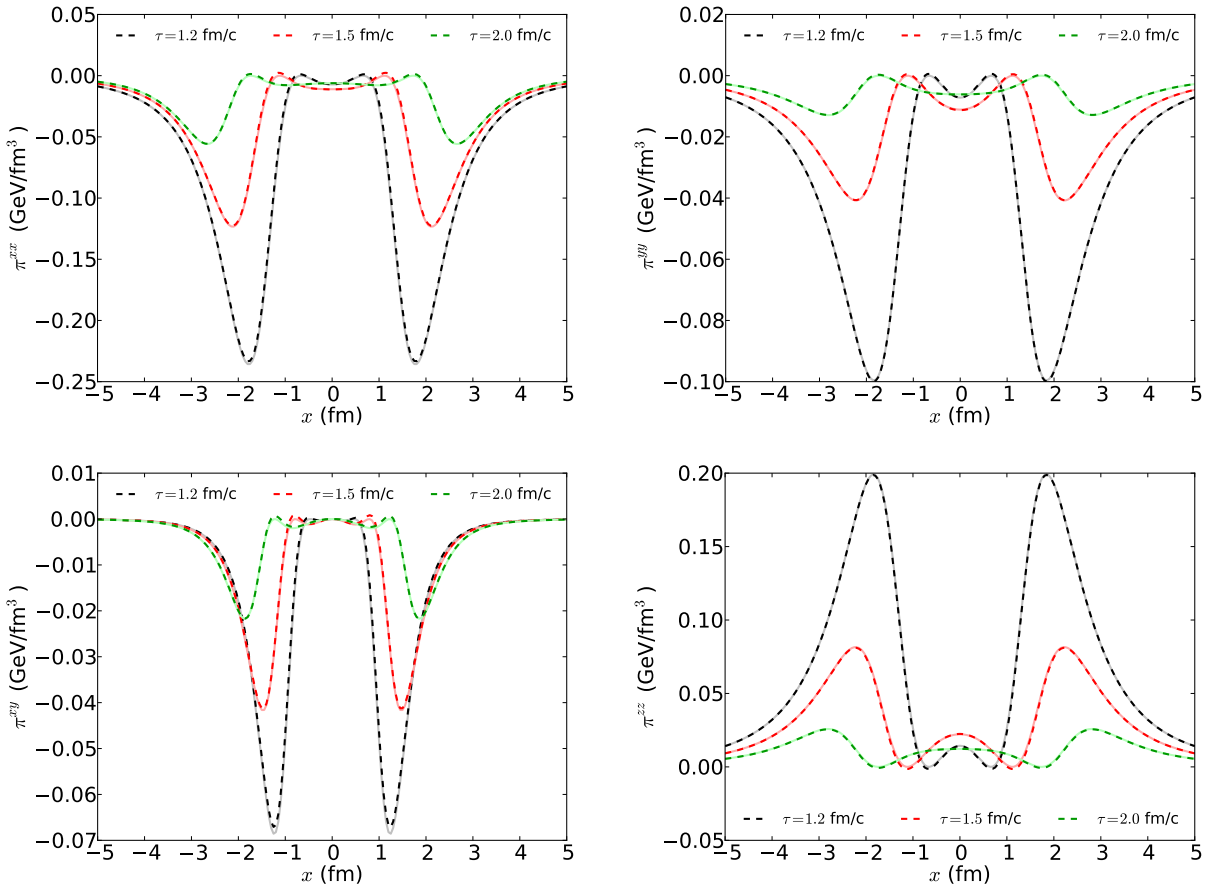

Figure 2.10: The evolution of individual components of the shear stress tensor from `VISH2+1` (dark dashed) compared with the semi-analytical solutions from [20] (light solid).

2.4.3 Stabilizing `VISH2+1` against numerical fluctuation in the viscous shear

`VISH2+1` solves the minimum set of second order viscous hydrodynamic equations. The shear stress tensor is evolved according Eq. (2.26), which only includes spatial gradients up to second order. Such a truncation of the gradient expansion converges and gives good approximations only when higher order gradient terms are negligible. When we perform event-by-event hydrodynamic simulations, the fluctuating initial conditions usually feature large spatial gradients in the transverse plane. Under such conditions, the missing higher order gradient corrections to Eq. (2.26) have the potential to grow large during the hydrodynamic evolution, and not including them in the code may eventually drive the whole numerical simulation into instability. However including all the higher order gradient terms in the transport equation for $\pi^{\mu\nu}$ is not practical. It would require the knowledge of the corresponding higher order transport coefficients, which are poorly constrained both theoretically and experimentally.

Therefore, staying within the framework of second order viscous hydrodynamics, we apply a regulation to the shear stress tensor that aims to suppress numerical instabilities caused by large

spatial gradients. In general, for second order viscous hydrodynamics to be valid, $\pi^{\mu\nu}$ must to satisfy the following criteria:

1. $\pi^{\mu\nu}$ should be smaller than the ideal part of the energy momentum tensor, $T_0^{\mu\nu} = eu^\mu u^\nu - P\Delta^{\mu\nu}$. To implement this we compare the following Lorentz invariant quantities,

$$\mathrm{Tr}(\pi^2) = \pi^{\mu\nu}\pi_{\mu\nu} \text{ and } T_0^{\mu\nu}T_{0\mu\nu} = e^2 + 3P^2.$$

   Consistency for our theoretical framework requires

$$\pi^{\mu\nu}\pi_{\mu\nu} \ll e^2 + 3P^2. \tag{2.61}$$

2. $\pi^{\mu\nu}$ should be traceless:

$$\pi^\mu_{\ \mu} = 0 \tag{2.62}$$

3. $\pi^{\mu\nu}$ should be perpendicular to u^μ:

$$\pi^{\mu\nu}u_\nu = 0 \tag{2.63}$$

`VISH2+1` evolves all seven non-vanishing components of $\pi^{\mu\nu}$, $\pi^{\alpha\beta}$ (where $\alpha, \beta = \tau, x, y$) and $\pi^{\eta\eta}$, independently without enforcing the conditions 2 and 3. Checking the validity of Eqs. (2.62) and (2.63) for the numerically evolved $\pi^{\mu\nu}$ thus accounts to a check of the numerical accuracy of our code. In actual calculations, there are limits to the numerical accuracy of $\pi^{\mu\nu}$ so we choose a small number $\xi_0 \ll 1$ as the "relative numerical zero" and replace conditions 2 and 3 by

$$\pi^\mu_{\ \mu} \leq \xi_0\sqrt{\pi^{\mu\nu}\pi_{\mu\nu}} \text{ and } \pi^{\mu\nu}u_\nu \leq \xi_0\sqrt{\pi^{\mu\nu}\pi_{\mu\nu}}, \forall\mu \tag{2.64}$$

The vector $\pi^{\mu\nu}u_\nu$ should be component-wise zero (in any frame), therefore all its components should be compared to the "relative numerical zero" multiplied by $\sqrt{\pi^{\mu\nu}\pi_{\mu\nu}}$(for dimensional reasons). Here we use the scalar $\sqrt{\pi^{\mu\nu}\pi_{\mu\nu}}$ as a measure for the magnitude of the $\pi^{\mu\nu}$ tensor that sets the scale (via the factor ξ_0) for how close the numerical result is to zero.

In practice, to ensure that Eq. (2.61) is satisfied, we choose a number $\rho_{\max} \ll 1$ and require that[2]:

$$\sqrt{\pi^{\mu\nu}\pi_{\mu\nu}} \leq \rho_{\max}\sqrt{e^2 + 3p^2}. \tag{2.65}$$

In our simulations, we found, that this condition is sometimes violated during the early stage and/or in the dilute regions outside the freeze-out surface (see at Fig. 2.13 for an example). The violation of Eq. (2.61) in these regions do as not have much influence on the dynamical behavior of the QGP in the physical region inside the freeze-out surface; however, if left untreated, such

[2] $\rho_{\max} \ll 1$ corresponds to the required "$\ll$" condition in Eq. (2.64); $\rho_{\max} = \infty$ corresponds to no constraint at all.

violations lead to accumulating numerical errors that eventually cause the evolution code to break down at later times. For these reasons, in the following we develop a systematic treatment that suppresses large viscous terms. This stabilizes the code with negligible effects on the physics and negligible extra numerical cost.

We enforce a continuous systematic regulation on $\pi^{\mu\nu}$ in each time step on the whole lattice by replacing $\pi^{\mu\nu}$ by $\hat{\pi}^{\mu\nu}$:

$$\pi^{\mu\nu} \to \hat{\pi}^{\mu\nu} \equiv \pi^{\mu\nu} \frac{\tanh(\rho)}{\rho}, \tag{2.66}$$

where ρ is the largest quantity at each lattice point among the following:

$$\frac{\sqrt{\pi^{\mu\nu}\pi_{\mu\nu}}}{\rho_{\max}\sqrt{e^2+3p^2}}, \frac{\pi^{\mu}_{\ \mu}}{\xi_0\,\rho_{\max}\sqrt{\pi^{\mu\nu}\pi_{\mu\nu}}}, \text{ or } \frac{\pi^{\mu\nu}u_{\nu}}{\xi_0\rho_{\max}\sqrt{\pi^{\mu\nu}\pi_{\mu\nu}}}, \forall\mu$$

It is easy to check that $\hat{\pi}^{\mu\nu}$ satisfies Eq. (2.65), and that it is close to $\pi^{\mu\nu}$ where no modifications are needed; that is, when the left hand side of the inequality in Eq. (2.65) is small compared to the right hand side, Only at those grid points where $\pi^{\mu\nu}$ violates or is close to violating the inequality (2.65) it will be strongly modified; if this is the case, all components of $\pi^{\mu\nu}$ are suppressed by the same factor.

Because smoother flow velocity profiles give smaller $\pi^{\mu\nu}$, the systematic suppression of $\pi^{\mu\nu}$ can be understood as locally replacing sharp jumps in the flow profile by smoother pieces; the regulation process is therefore an implicit and automatic way of smoothing profiles. This treatment allows us to perform hydrodynamic calculations using very bumpy initial conditions, including those using disk-like nucleons that have density discontinuities. Without this regularization `VISH2+1` breaks down for such initial conditions.We note that typically no regulations are required inside the freeze-out surface at later times; shear viscosity leads to dynamical smoothing of initial fluctuation by dissipation, suppressing sharp velocity gradients and large values of $\pi^{\mu\nu}$ as time proceeds. Regulation remains necessary in the dilute region outside the freeze out surface where e and P (which for massless degree of freedom both fall like T^4) fall faster than $\pi^{\mu\nu}$ (which falls only like T^3).

In our calculations, we take $\xi_0 = 0.1$. If we choose smaller ξ_0 in the simulations, we overkill the physical viscous damping effects. In the following section, we show tests invoking several choices of ξ_0 and their influence on the final observables. During our tests we found that $\rho_{\max}$ is best chosen to be a value between $1-10$. By choosing $\rho_{\max}$ of order unity or larger, we reduce the regulation strength in each step to the point where the code is numerically stable with minimum modification. (Note that this implies that the code may run in a domain where the strong inequality Eq. (2.61) is not satisfied, i.e. second order viscous hydrodynamics may not be strictly valid.)

2.4.4 Hydrodynamic evolution with regulation

In this section, we study the sensitivity of final hadronic observables on the choice of the ξ_0 parameter used in the π regulation routine. For these tests, we choose MC-Glauber initial conditions for Pb + Pb collisions at $\sqrt{s} = 2760$ A GeV at 20-30% centrality, using $\eta/s = 0.20$. We simulate 200 events for every choice of ξ_0.

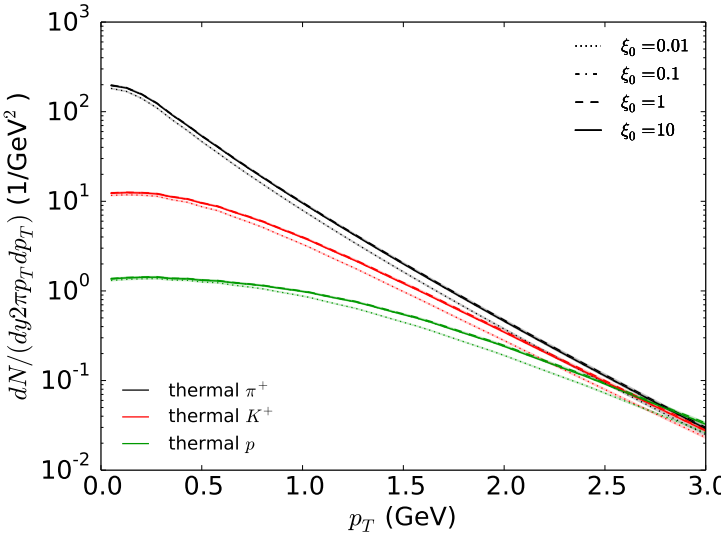

Figure 2.11: Thermal particles' p_T spectra for different choice of ξ_0 used in the regulation trigger routine.

In Fig. 2.11, we show the p_T-spectra for thermal π^+, K^+, and protons, with different values of ξ_0 used in the trigger routine for the $\pi^{\mu\nu}$ regulation. We find that for $0.1 \leq \xi_0 \leq 10$, there is no noticeable difference between different choices of ξ_0 used in the simulations. Only for the very small value $\xi = 0.01$ we see an effect: particle spectra get steeper, and the yield decreases. This means that the system generates less entropy and radial flow during the evolution, which indicates that the shear viscous effects in the simulations are suppressed too strongly by the regulations.

In Fig. 2.12, we show results for the p_T-differential anisotropic flows v_2 to v_5. They show a larger sensitivity to the choice of ξ_0 than the single particle spectra. For $0.1 \leq \xi_0 \leq 10$, the v_n of thermal particles agree reasonably well with each other within the statistical error bands. But for $\xi_0 = 0.01$, the regulation again over-suppresses the viscous effects, which damp the anisotropic flow of the system.

From this parameter study we conclude that the final hadronic observables are not sensitive to the choice of ξ_0 as long as we keep it in the range $0.1 \leq \xi_0 \leq 10$. For ξ_0 larger than 10, the code becomes numerically unstable due to too strong violations of the criteria that ensure validity of the second order viscous hydrodynamic description. For ξ_0 smaller than 0.1, the regulation routine seems to over kill the shear viscous effects in the system. Thereby altering the physics by

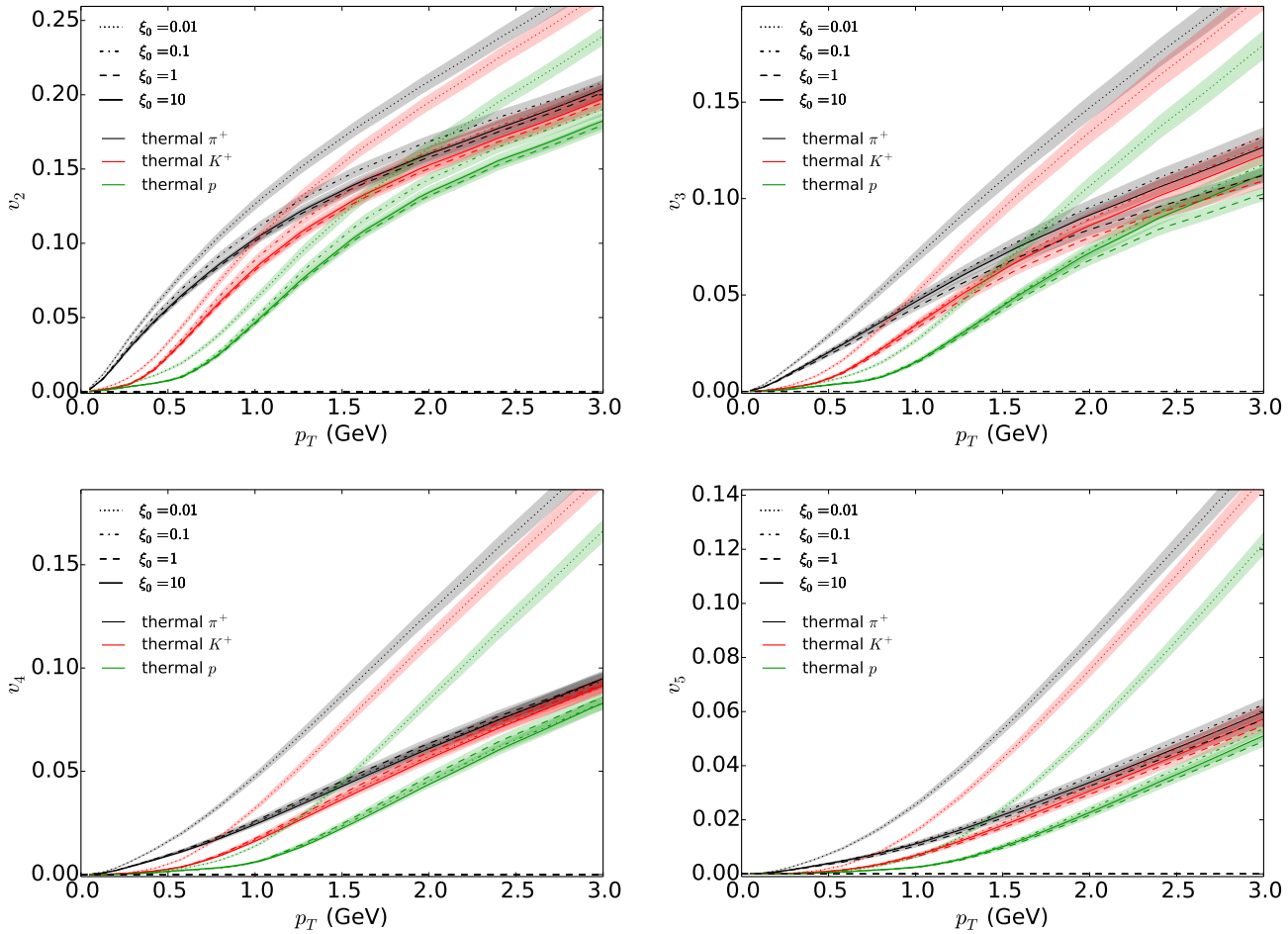

Figure 2.12: Thermal particles' p_T-differential v_n for different choice of ξ_0 used in the regulation trigger routine. Statistical errors are indicate as shaded bands in the plots.

using an effective shear viscosity that is much smaller than the input value. In our application of `VISH2+1`, we therefore always use ξ_0 in the range $0.1 \leq \xi_0 \leq 10$.

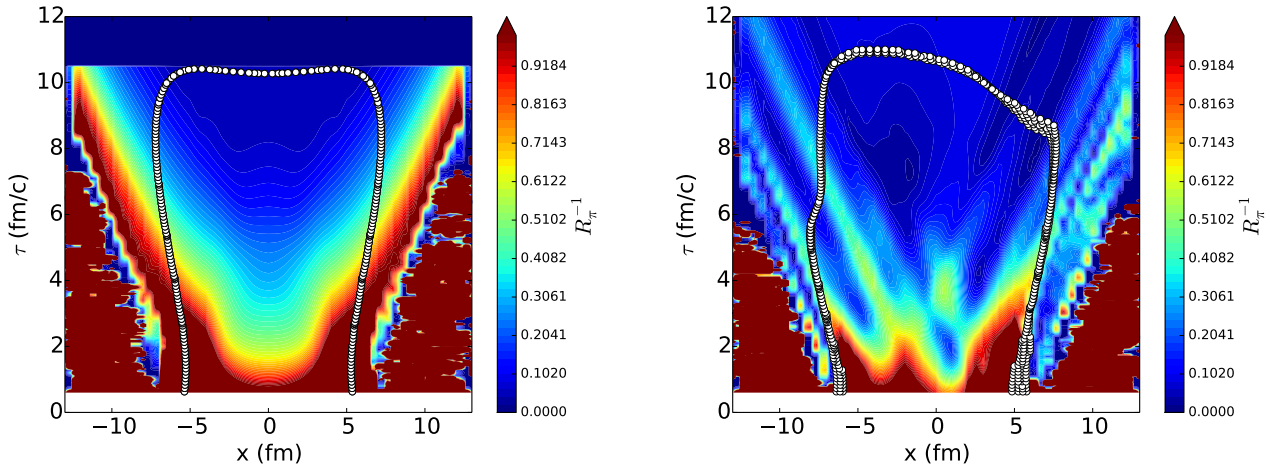

Figure 2.13: Contour plot for the evolution of the inverse Reynolds number in viscous hydrodynamic simulations with $\eta/s = 0.20$ at 20-30% LHC energy. The white points indicate the kinetic freeze surface at $T_{\rm dec} = 120$ MeV.

In order to quantify the quality of reliability of our second order viscous hydrodynamic approach we can monitor the inverse Reynolds number associated with shear stress, defined as,

$$R_\pi^{-1} = \frac{\sqrt{\pi^{\mu\nu}\pi_{\mu\nu}}}{P}, \tag{2.67}$$

where P is the thermal pressure. As long as R_π^{-1} is smaller than 1, the system behaves like a fluid with low viscosity. For $R_\pi^{-1} \gg 1$, the behavior is more dissipative and viscous hydrodynamics is no long a good description. In Fig. 2.13, we show a contour plot of the evolution of the inverse Reynolds number in our hydrodynamic simulation at $y = 0$ in the transverse plane. In the left panel we start with a smooth event-averaged initial condition; in the right panel we show results for a fluctuating initial profile. The white points indicate the position of the kinetic freeze-out surface. We notice that the largest inverse Reynolds numbers are encountered at early times of the hydrodynamic evolution or outside the freeze-out surface for both smooth and fluctuating initial conditions. As time goes on, the magnitude of the shear stress tensor decreases, and the relativistic hydrodynamic modeling becomes more and more reliable. At very early times the use of viscous hydrodynamics becomes questionable, especially for fluctuating initial profiles.

2.5 Cooper-Frye freezeout using `iS` and particle sampler `iSS`

The name "`iS`" stands for "`iSpectra`"; `iS` is a fast Cooper-Frye particle momentum distribution calculator along the conversion surface. Its output is a continuous function, evaluated at discrete momenta provided by the user, for the invariant momentum distributions of the desired hadron species. The code "`iSS`", whose name stands for "`iSpectraSampler`", goes one step further to generate individual particles samples, using the calculated particle momentum distributions as the relative emission probability. `iSS` is an "event generator" which generates a complete collision event of emitted hadrons, similar to the events created in the experiment. Both codes are written keeping the following factors in mind:

- **Readability and extendability.** The most important goal is to create a cleanly written framework that calculates particle momentum distributions and performs sampling, whose components and output can be used easily for further physics analyses and tests of new physical ideas. To achieve this, the entire program is divided into modules according to their functionalities, the structures and the algorithms are documented with comments, and long but informative names are chosen for variables and function names.

- **Efficiency.** Both the `iS` and `iSS` codes are written aiming for intensive event-by-event calculations where every CPU cycle counts. To achieve the necessary degree of efficiency, much effort is put into optimizing the algorithms at different levels of the calculations.

- **Easy maintainability and re-usability.** The framework is divided into different carefully chosen functionality modules, for better interoperability and to maximize re-usability.

2.5.1 Cooper-Frye freeze-out

The particle emission function that implements sudden decoupling from a surface element $d^3\sigma$ located on a freeze-out hyper-surface $\Sigma(x^\mu)$ is given by the Cooper-Frye formula,

$$E\frac{dN}{d^3p}(x^\mu, p^\mu) = \frac{g}{(2\pi)^3}p^\mu d^3\sigma_\mu \left(f_0(x^\mu, p) + \delta f(x^\mu, p^\mu)\right), \tag{2.68}$$

where g is the spin degeneracy, $d^3\sigma_\mu = (\cosh\eta_s, -\partial\tau/\partial x, -\partial\tau/\partial y, -\sinh\eta_s)\tau dx dy d\eta_s$ is the infinitesimal surface element on $\Sigma(x^\mu)$ for systems with longitudinal boost-invariance, and $f_0(x^\mu, p)$ is local thermal equilibrium distribution function. $\delta f(x^\mu, p^\mu)$ represents the deviation from local thermal equilibrium due to viscous effect and takes the following form,

$$\delta f(x^\mu, p^\mu) = f_0(x^\mu, p)(1 \pm f_0(x^\mu, p))\frac{\pi_{\mu\nu}\hat{p}^\mu\hat{p}^\nu}{2(e+P)}\chi\left(\frac{p\cdot u}{T}\right), \tag{2.69}$$

where $\hat{p}^\mu = p^\mu/(p\cdot u)$ and $\chi(p\cdot u/T) = (p\cdot u/T)^\alpha$ with $1 \le \alpha \le 2$. Integrating the emission function over the freeze-out surface we obtain particle momentum distribution

$$\frac{dN}{dyp_T dp_T d\phi_p} = \int_\Sigma \frac{g}{(2\pi)^3}p^\mu d^3\sigma_\mu (f_0(x^\mu, p) + \delta f(x^\mu, p^\mu)). \tag{2.70}$$

The azimuthally averaged p_T-spectrum is given by,

$$\frac{dN}{2\pi dyp_T dp_T} = \int \frac{d\phi_p}{2\pi}\frac{dN}{dyp_T dp_T d\phi} \tag{2.71}$$

while the anisotropic flow coefficients are computed from,

$$V_n \equiv v_n e^{in\Psi_n} = \frac{\int p_T dp_T d\phi_p e^{in\phi_p} dN/(dyp_T dp_T d\phi_p)}{\int p_T dp_T d\phi_p dN/(dyp_T dp_T d\phi_p)}, \tag{2.72}$$

$$V_n(p_T) \equiv v_n(p_T) e^{in\Psi_n} = \frac{\int d\phi_p e^{in\phi_p} dN/(dyp_T dp_T d\phi_p)}{\int d\phi_p dN/(dyp_T dp_T d\phi_p)}. \tag{2.73}$$

To optimize the efficiency of the numerical calculations, gaussian quadrature points are used for the variables p_T, ϕ_p, and η_s. Further optimization for performing the numerical integral in Eq. (2.70) involves adjusting the order of the integration loops, using local variables, pre-tabulating mathematical functions, etc. The resulting code `iS` is ~ 7 times faster compared to its ancestor `AZSpectra` [21].

2.5.2 Methodology for particle sampling

The particle emission function from the Cooper-Frye formula Eq.(2.68) can be regarded as the probability of emitting particle from a given freeze-out fluid cell with specified momentum. The program `iSS` uses this probability to generate sets of momenta and positions for actual particles emitted at the end of the hydrodynamic simulation. This information is then used as input for the following microscopic hadron cascade simulation. In the sampling procedure, we employ two well-known statistical sampling methods, the inverse cumulative distribution function (CDF) method and the direct probability distribution function (PDF) method, the latter is also known as the acceptance and rejection method.

Purely numerical approach

The straightforward (although not necessarily the fastest) approach is to compute all the required quantities numerically.

For a given particle species, the average total number of particles per unit rapidity, dN/dy, is calculated by numerically integrating Eq. (2.68) over all freeze-out fluid cells and all particle transverse momenta $\vec{p}_T$. During the numerical integration, an inverse CDF can be built up with negligible numerical cost for latter efficient sampling. However, in practice, the inverse CDF for a full set of spatial and momentum variables is memory demanding. In order to sample such a multi-dimensional probability distribution function, we divide the random variables into two groups and use efficient specific sampling methods to handle each of them. It is natural to group the spatial information $(\tau, \vec{x}_\perp, \eta_s)$ for the sampled particles into one set of random variables, and their momenta $(p_\perp, \phi_p, y)$ into the other, . Dividing the random variables into two groups allows us to perform the sampling in different order and with different methods.

One way to proceed is to first sample the spatial information, $(\tau, \vec{x}_\perp, \eta_s)$, using the inverse CDF method. Along with calculating the particle yield dN/dy, (see above) we build up the inverse CDF for the particle's spatial variables, $(\tau, \vec{x}_\perp, \eta_s)$, by integrating Eq. (2.68) over the transverse momentum, $(p_\perp, \phi_p)$. For a collision event at top RHIC energy, the typical size of the array to store the inverse CDF is about 30,000 freeze-out fluid cells in the transverse plane times 40 points along the η_s direction. Once we have the particles' spatial information, we can evaluate Eq. (2.68) at any given point $(\tau, \vec{x}_\perp, \eta_s)$ for the particle's probability distribution in momentum space. To sample the particle's transverse momentum (p_T, ϕ_p) from this distribution we use the the direct PDF method. In the end, since we assume longitudinal boost-invariance, the particle's rapidity can be sampled uniformly within given rapidity range. By sampling particles in this order, we optimize the sampling of the particle's spatial coordinates since the inverse CDF method has zero rejection rate. The direct PDF method used in momentum space, on the other hand, allows

us to use continuous random variables for $p_\perp$ and ϕ_p instead of sampling them at some discrete lattice points.

A second way to proceed is to first sample the particle's momentum information with the inverse CDF method. To this end we first build the inverse CDF for the particle's momentum variables, $(p_\perp, \phi_p)$. Using 15 points in $p_\perp$ and 48 points in ϕ_p. Once we have $(p_\perp, \phi_p)$, Eq.(2.68) is used as a probability distribution for the particle's spatial coordinates $(\tau, \vec{x}_\perp, \eta_s)$ which is then sampled with the direct PDF method.

Semi-analytic approach

In a given collision event the number of particles of species a being emitted from a given fluid cell at x^μ can be calculated analytically as follows:

$$\Delta N_a(\tau_f, \vec{x}_\perp, \eta_s) = \frac{g_a}{(2\pi)^3}\Delta^3\sigma_\mu \int \frac{d^3p}{E} p^\mu (f_0(p) + \delta f(p)). \tag{2.74}$$

Here the surface element of the given fluid cell is $\Delta^3\sigma_\mu = \sigma_\mu \Delta^2 x_\perp \tau \Delta\eta_s$ with $\sigma_\mu = (\cosh\eta_s, -\partial\tau/\partial x, -\partial\tau/\partial y, -$ The off-equilibrium correction δf originating from the shear stress tensor does not contribute to the total particle yield, due to the properties that $\pi^{\mu\nu}$ is traceless and orthogonal to the flow velocity.

$$\int \frac{d^3p}{E} p^\mu \delta f(p) = \int \frac{d^3p}{E} p^\mu f_0(p)(1 \pm f_0(p)) \frac{\pi_{\alpha\beta}\hat{p}^\alpha \hat{p}^\beta}{2(e+P)} \chi\left(\frac{p}{T}\right) = A u^\mu, \tag{2.75}$$

where $A = u_\mu \int \frac{d^3p}{E} p^\mu \delta f(p) = \frac{\pi_{\alpha\beta}}{2(e+P)} \int \frac{d^3p}{E} (u\cdot p) \frac{p^\alpha p^\beta}{(u\cdot p)^2} \chi(\frac{p}{T}) f_0(p)(1 \pm f_0(p))$. In the local rest frame of the fluid cell, it is easy to see that the integrand is proportional to $\delta^{\alpha\beta}$, hence

$$A = \int d^3p f_0(p)(1 \pm f_0(p)) \frac{p^2}{3E^2} \frac{\pi^\alpha{}_\alpha}{2(e+P)} \chi\left(\frac{p}{T}\right) = 0. \tag{2.76}$$

Thus the particle yield is totally determined by its equilibrium distribution,

$$\begin{aligned}
\Delta N_a(\tau_f, \vec{x}_\perp, \eta_s) &= \frac{g_a}{(2\pi)^3}\Delta^3\sigma_\mu \int \frac{d^3p}{E} p^\mu f_0(p) \\
&= \frac{g_a}{(2\pi)^3}\Delta^3\sigma_\mu u^\mu \int p^2 dp\, d\phi\, d\cos\theta \frac{1}{e^{\beta(E-\mu_a)} \pm 1} \\
&= \frac{g_a}{2\pi^2}\Delta^3\sigma_\mu u^\mu \frac{m_a^2}{\beta} \sum_{n=1}^{\infty} \frac{(\mp 1)^{n-1}}{n} e^{n\beta\mu_a} K_2(n\beta m_a).
\end{aligned} \tag{2.77}$$

With the assumption of boost invariance, the particle's rapidity y and its space-time rapidity η_s only enters in the combination $y - \eta_s$, and therefore $\frac{dN}{d\eta_s} = \frac{dN}{dy}$. This leads to the following

relation:

$$\begin{aligned}\Delta N_a(\tau_f,\vec{x}_\perp,\eta_s) &= \frac{g_i}{(2\pi)^3}\Delta^3\sigma_\mu\int dy\int d^2p_\perp p^\mu f_0(p)\\ &= \frac{g_i}{(2\pi)^3}\int dy\Delta^2x_\perp\tau\Delta\eta_s\int d^2p_\perp\\ &\quad\times(m_\perp\cosh(y-\eta_s)-\vec{p}_\perp\cdot\vec{\nabla}_\perp\tau)f_0(p)\\ &= \Delta\eta_s\frac{g_a}{(2\pi)^3}\int\tau d\tilde{y}\Delta^2x_\perp\int d^2p_\perp\\ &\quad\times(m_\perp\cosh(\tilde{y})-\vec{p}_\perp\cdot\vec{\nabla}_\perp\tau)f_0(p)\end{aligned} \tag{2.78}$$

This integral is independent of η_s, so

$$\Delta N_a(\tau_f,\vec{x}_\perp,\eta_s)=\Delta\eta_s\frac{\Delta N}{\Delta y}(\tau,\vec{x}_\perp). \tag{2.79}$$

In the numerical sampling procedure, we first consider all freeze-out fluid cells $(\tau,\vec{x}_\perp)$ in the transverse plane and use (2.77) (together with (2.79)) to compute the total particle yield per unit rapidity for particle species a, $\Delta N/\Delta y$, for each cell. (If freeze-out occurs on a surface of constant inverse temperature β and chemical potential μ_a, as will be the assumed in the rest of this thesis, Eq. (2.77) can be written as,

$$\Delta N_a(\tau_f,\vec{x}_\perp,\eta_s)=n_a u_\mu(\tau_f,\vec{x}_\perp,\eta_s)\Delta^3\sigma_\mu(\tau_f,\vec{x}_\perp,\eta_s). \tag{2.80}$$

where $n_a=\frac{g_a}{2\pi^2}\frac{m_a^2}{\beta}\sum_{n=1}^{\infty}e^{n\beta\mu_a}K_2(n\beta m_a)$ is the freeze-out density of particle species a, which is the same for all freeze-out cells. In this case, $\Delta N_a/\Delta y$ depends on the position of the fluid cell only through its freeze-out volume,

$$\Delta V(\tau_f,\vec{x}_\perp,\eta_s)=u^\mu\Delta^3\sigma_\mu(\tau_f,\vec{x}_\perp,\eta_s).) \tag{2.81}$$

The we use $(\Delta N_a/\Delta y)(\tau_f,\vec{x}_\perp)$ to build up an inverse CDF for the spatial variables $(\tau_f,\vec{x}_\perp)$. Their sum over all $(\tau_f,\vec{x}_\perp)$ points gives the total rapidity density $\frac{dN_a}{dy}$ of particle species a in a given collision event. The constructed inverse CDF is then used to sample the positions $(\tau_f,\vec{x}_\perp)$ of the particles of species a. Finally, we use the Cooper-Frye formula Eq. (2.68) at these sampled positions $(\tau_f,\vec{x}_\perp)$ as the relative probability distribution for sampling the particle's momentum $(p_T,\phi_p,y-\eta_s)$ using the direct PDF method:

$$\begin{aligned}P(p_\perp,\phi_p,y-\eta_s;\tau_f,\vec{x}_\perp) &= \frac{g_i}{(2\pi)^3}\Delta^3\sigma_\mu p^\mu(f_0(p)+\delta f(p))\\ &= \frac{g_i}{(2\pi)^3}\tau_f\Delta^2x_\perp\Delta\eta_s(m_\perp\cosh(y-\eta_s)-\vec{p}_\perp\cdot\vec{\nabla}_\perp\tau)\\ &\quad\times(f_0(p)+\delta f(p)).\end{aligned} \tag{2.82}$$

Having obtained $(y-\eta_s)$ by sampling Eq. (2.82), we use boost-invariance and sample y uniformly from a given range specified by the user (e.g., -4 to 4) and then obtain η_s from the previously determined $y-\eta_s$.

Since for every $(\tau, \vec{x}_\perp)$, the probability Eq. (2.82) for $(p_T, \phi_p, y-\eta_s)$ is only sampled once, building an inverse CDF for Eq. (2.82) would be excessively expensive, which is why we choose to use the direct PDF method to sample $(p_\perp, \phi_p, y-\eta_s)$. However, the direct PDF method requires one to estimate the maximum value of the probability distribution function given in Eq. (2.82) which is closely related to the function

$$G(E;A) = \frac{E^A}{e^{\beta(E-\mu)} \pm 1},\ A > 0. \tag{2.83}$$

By setting its derivative to zero, the extrema can be found by solving

$$(1 \mp f_0) = \frac{A}{\beta E} \Longleftrightarrow \begin{cases} xe^x = y;\ x = \beta E - A,\ y = Ae^{\beta\mu - A}, \text{fermions (upper)}, \\ xe^{-x} = y;\ x = A - \beta E,\ y = Ae^{\beta\mu - A}, \text{bosons (lower)}. \end{cases} \tag{2.84}$$

This equation is transcendental and cannot be solved algebraically; however, the solutions to the equations $xe^{\pm x} = y$ in Eq. (2.84) can be pre-calculated and tabulated. For fermions (upper sign), a solution always exists and it is expressed by the Lambert W-function; for bosons (lower sign) the equation has real solutions only when $y < 1/e$, and the it yields two solutions; the physical solution must satisfy $x \in [0, 1]$. In the following, the solution to Eq. (2.84) will be denoted as $E^{\pm}_{\rm max}$ when it exists.

The maximum of $G(E;A)$ with constraint $E \geq m$ will be denoted as $G^{(A)}_{\rm max}$. It depends on several conditions:

1. For fermions (upper sign), $G(E)$ has a single peak at $E^+_{\rm max}$ and the constraint maximum is taken as $G(E^+_{\rm max})$ if $E^+_{\rm max} > m$ and as $G(m)$ otherwise.

2. For bosons (lower sign) with $Ae^{\beta\mu - A} > 1/e$, Eq. (2.84) has no solution and the maximum is takes $G(m)$.

3. For bosons (lower sign) with $Ae^{\beta\mu - A} \leq 1/e$, $G(E)$ has two extrema in (μ, ∞), with the larger one being the maximum and given by $E^-_{\rm max}$. If $E^-_{\rm max} < m$ then the maximum is taken as $G(m)$; otherwise the maximum is taken as the larger one of the two numbers $G(m)$ and $G(E^-_{\rm max})$.

In Eq. (2.82), an upper limit for the factor $p^\mu \Delta^3\sigma_\mu$ can obtained using the Hölder inequality,

$$p^\mu \Delta^3\sigma_\mu = E\Delta^3\sigma_0 + p^i\Delta\sigma_i \leq (p\cdot u)(|\Delta^3\sigma_\mu u^\mu| + \sqrt{|\Delta^3\sigma_\mu \Delta^3\sigma_\nu \Delta^{\mu\nu}|}). \tag{2.85}$$

For the equilibrium contribution, it is clear that the remaining part is to calculate the maximum of the function

$$Ef_0 = \frac{E}{e^{(E-\mu)/T} \pm 1} = G(E;1); \tag{2.86}$$

the solution to this problem is $G^{(1)}_{\rm max}$.

For the off-equilibrium correction, it is convenient to estimate its maximum in the local rest frame of the fluid cell. We can further rotate the shear stress tensor in the transverse plane such that $\pi^{xy} = 0$. In such a coordinate system

$$\begin{aligned} p^\mu p^\nu \pi_{\mu\nu} &= (p^x)^2\pi_{xx} + (p^y)^2\pi_{yy} + (p^z)^2\pi_{zz} \le E(|p^x\pi_{xx}| + |p^y\pi_{yy}| + |p^z\pi_{zz}|) \\ &\le E^2\sqrt{\pi^2_{xx} + \pi^2_{yy} + \pi^2_{zz}} = E^2\sqrt{\pi^{\mu\nu}\pi_{\mu\nu}}. \end{aligned} \tag{2.87}$$

In the last step, we rewrote the expression again in Lorentz invariant form such that it is now valid in any frame. With the form of δf in Eq. (2.69) and assuming $f_0 < 1$,

$$E^{\alpha+1} f_0(1 \mp f_0) \le \lambda E^{\alpha+1} f_0 = \lambda G(E;\alpha+1) \le \lambda G^{(\alpha+1)}_{\rm max}, \tag{2.88}$$

where $\lambda = 1$ for fermions and $\lambda = 2$ for bosons. To summarize, the maximum of the PDF Eq. (2.82) for $(p_\perp, \phi_p, y - \eta_s)$ can be estimated as

$$P \le P_{\rm max} = \frac{g_a}{(2\pi)^3}\tau(|\Delta^3\sigma_\mu u^\mu| + \sqrt{\Delta^3\sigma_\mu\Delta^3\sigma_\nu\Delta^{\mu\nu}})\left(G^{(1)}_{\rm max} + \frac{\sqrt{\pi^{\mu\nu}\pi_{\mu\nu}}}{2(e+P)T^\alpha}\lambda G^{(\alpha+1)}_{\rm max}\right). \tag{2.89}$$

For light mesons, the validity of the assumption $f_0 < 1$ depends on the value of the freeze-out temperature and chemical potential. Especially, kinetic freeze-out at temperature, much below the chemical decoupling temperature can lead to large non-equilibrium chemical potentials than can cause this assumption to break down in some of the fluid cells. We found that $f_0 < 1$ almost all the time, although there were some instances where it was violated. If a more rigorous result is desired, the inequality (2.88) can be replaced by the following one:

$$\begin{aligned} E^{\alpha+1} f_0(1 + f_0) &\le |E^{\alpha+1} f_0| + |E^\gamma f_0||E^{\alpha+1-\gamma} f_0| \\ &\le G^{(\alpha+1)}_{\rm max} + G^{(\gamma)}_{\rm max} G^{(\alpha+1-\gamma)}_{\rm max}, \end{aligned} \tag{2.90}$$

where $0 \le \gamma \le \alpha + 1$.

The negative probability issue

For hyper-surface of constant temperature, the Cooper-Frye formula in Eq. (2.68) is not positive semi-definite. This is because on an isothermal hyper-surface Σ, $d^3\sigma_\mu$ can be a space-like vector. So $p^\mu d^3\sigma_\mu$ can be negative in certain regions. Physically, such regions represent parts of the switching surface through which more particles are flying into the fireball instead of being emitted.

These negative contributions to the Cooper-Frye integral are essential to ensure the conservation of energy across the hyper-surface. However, they become problematic when one wants to use Eq. (2.68) as a probability distribution (which should always be positive). In the practical sampling procedure, we insert a θ-function by hand to enforce positivity of the probability distribution function. Since we group the random variables differently in the different sampling approaches discussed above, insertion of the θ-function will be done slightly differently in each case, with different consequences. In each case, a slight violation of energy-momentum conservation will ensure. Let us therefore explore the implications of the θ-function in some detail, we first sample particle's spatial information using the purely numerical approach, we use a θ-function $\theta(u^\mu d\sigma_\mu)$ to enforce positivity of the $p_\perp$-integrated distribution function. This means that none of our sampled particles will come from the spatial regions where $u^\mu d\sigma_\mu < 0$. In the second step, when sampling the momenta we enforce the positivity of Eq. (2.68) at the already sampled spatial coordinates. In this step, there are two possible quantities that can come negative. First, $p^\mu \sigma_\mu$ may be negative for some values of p^μ. This represents the situation where a net number of particles with momentum p^μ flies into the fireball. Secondly, in the viscous case, when the off-equilibrium correction δf becomes large, it may overwhelm the equilibrium term and turn the entire distribution function to negative. This situation represents a breakdown of the Chapman-Enskog expansion keeping only terms of first order in δf, Eq. (2.68) should not be trusted in such regions of momentum space. With $\eta/s = 0.20$, we find that this problem usually occurs at high $p_T > 2.5\,\mathrm{GeV}$. In the sampling procedure, we enforce both terms to be always positive, by inserting a product of theta functions, $\theta(f_0 + \delta f)\theta(p^\mu d^3\sigma_\mu)$. $\theta(f_0 + \delta f)$ should be always kept in the calculation, even for in the analytic results. The second factor $\theta(p^\mu d\sigma_\mu)$ causes a deviation of the sampled momentum distribution from the analytical result which will be studied below.

If we first sample the particle's momentum information, we enforce positivity of the momentum distribution $dN/(dyp_\perp dp_\perp d\phi_p) \geq 0$. In most cases, the total number of emitted particles with given transverse momentum $\vec{p}_\perp$, integrated over the entire freeze-out surface, is positive. The positivity constraint on $dN/(dyp_T dp_T d\phi_p)$ therefore has almost no effect at all. The set of momentum configurations obtained from this sampling procedure will reproduce momentum distributions and flow coefficients that agree most closely with the analytical Cooper-Frye formalism. In the second step, when we then additionally sample particle's spatial information, we need to enforce positivity of Eq. (2.68) at a given momentum $\vec{p}_\perp$. Regions on the hypersurface where Eq. (2.68) is negative will thus not contribute to particle emission at that $\vec{p}_\perp$. The sampled spatial distribution will therefore show some deviation from the analytic result.

For the semi-analytic approach, the situation is similar to the purely numerical approach when sampling the positions first and the momenta second.

Multiplicity fluctuations at freeze-out

The Cooper-Frye formula only yields the average number of particles emitted from a given hydrodynamic event. Each sampling of the Cooper-Fyre formula will, however, result in a number of emitted particle that fluctuates around that mean value. In principle, these sampling fluctuations are constrained by energy-momentum , baryon number and charge conservation. However, exact implementation of these constraints is non-trivial and will have to be left for future studies.

We use an approximation based on the following procedure: We compute the integer value of the number of particles of species as predicted by Cooper-Frye, sample such particles until that number is exhausted, and then use the non-integers part of the predicted number to uniformly sample for one additional particle. This sampling procedure introduces minimum fluctuations in the total number of particles. In the current version of `iSS`, there are options for users to instead fluctuate the particle number according to Poisson or negative Binomial distributions.

Performance

To demonstrate the performance of the `iSS` algorithm, we use an event-averaged hydrodynamically evolved Pb+Pb profile at 20-30% centrality at LHC energy to obtain a rough estimate for the average running time of our particle sampler. The two sampling approaches have their individual advantages and disadvantages in dealing with different sampling requirements.

100 repeated samplings	purly numerical approach	semi-analytic approach
determining particle yield dN/dy	21.84s for π^+ $\sim \times 100$ for rest of particles	negligible for π^+ 0.01s for all particles
actual sampling	1.25s for π^0 faster for heavier particles	2.65s for π^+ faster for heavier particles
total	2463.75s	15.16s
$50,000$ sampling (π^+ only)	88.73s	1327.99s

Table 2.3: Efficiency comparison between pure numerical and semi-analytic methods. The test case has 32869 conversion surface cells in the transverse plane and $dN/dy|_{\pi^+} \sim 144$. The test is done on a single core personal laptop.

The numerical performance of the code is summarized in Table. 2.3. The tests are done with the Intel C++ compiler with `-O3` optimization. Our code runs about a factor of 6 faster with the Intel compiler compared to the GNU compiler (g++).

The purely numerical approach is most suitable when a large number of repeated samplings of a single hydrodynamical event is desired. This is essential if one wants to study with good statistical precision rare multi-strange hadrons very few of which are emitted in a single event. On the other hand, the semi-analytic approach is extremely fast for small numbers of repeated

samplings. This large gain in the numerical efficiency is due to the fact that it determines the particle yields analytically using, Eq. (2.77). The drawback is that in this approach we need to sample one additional dimension (the rapidity direction) using the direct PDF method, which reduces the total sampling efficiency per simulation cycle.

2.5.3 Code verification

In this section, we show some test results from our particle sampler.

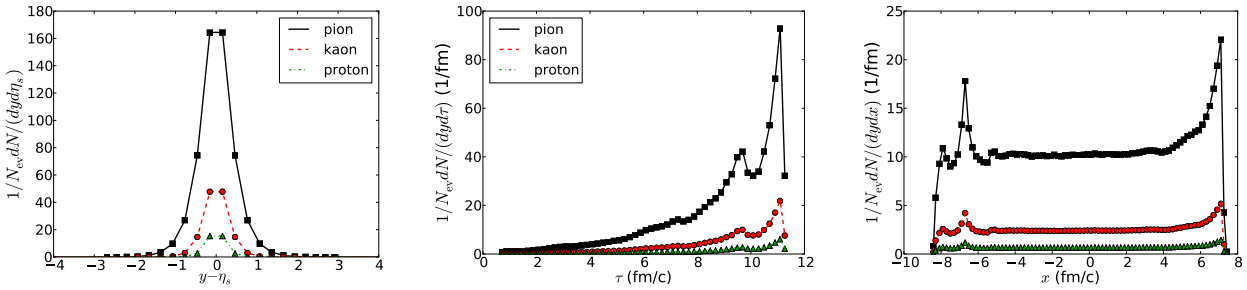

Figure 2.14: For sampling method I in the purely numerical approach, the spatial distributions of the sampled thermal particles (solid dots) are compared to the emission function calculated from the Cooper-Frye Formula (lines). The left panel shows the particle distribution along the η_s direction. The middle panel is the time emission function of the particles and the right panel shows the particle distribution along the x-axis in the transverse plane. All results are from a single hydrodynamic event with bumpy initial conditions.

In Figs. 2.14 and 2.15 we present the spatial and momentum distributions of thermally emitted particles (pions, kaons, and protons) and compare them against the emission function calculated directly from the Cooper-Frye Formula. We perform repeated samplings for a single hydrodynamic simulation with fluctuating initial conditions which emits about 172 positive pions, 40 positive kaons, and 11 protons. per unit rapidity thermally (i.e., not counting particles from resonance decays). To obtain sufficient statistics, we sample 50,000 events for thermal pions, 150,000 events for thermal kaons, and 500,000 events for thermal protons (these numbers account for the relative yields per event of their particle species.) Samples are generated using the purely numerical approach method I, which samples the spatial distributions first and then particle momenta.

We find that the particle samples generated from this method reproduce very accurately the spatial distributions from the Cooper-Frye Formula. The regions where $u_\mu d^3\sigma^\mu < 0$ do not affect the partially integrated emission functions shown in Fig. 2.14. In Fig. 2.15, we compare the particle momentum distributions against the results from the Cooper-Frye formula. We find very good agreements for the particle spectra as well as for the their anisotropy coefficients v_2, v_3, and v_4.

In Figs. 2.16 and 2.17, we show similar comparisons using the semi-analytic approach. Again the spatial distributions in the transverse plane from directly integrating the Cooper-Frye formula

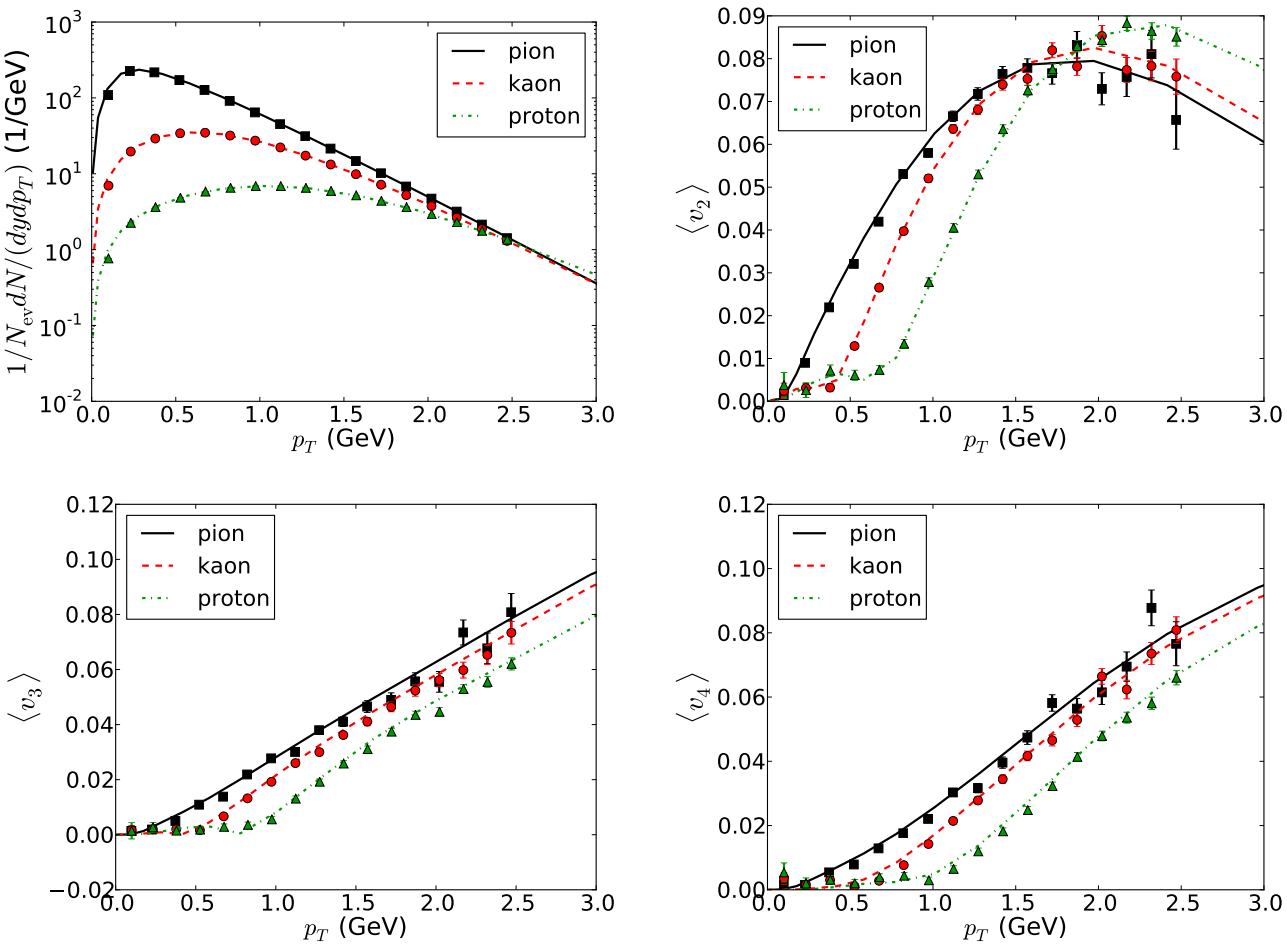

Figure 2.15: Similar to Fig. 2.14, momentum distributions of the sampled particles are compared with results from the Cooper-Frye formula. Particles' p_T-differential spectra, v_2, v_3, and v_4 are presented.

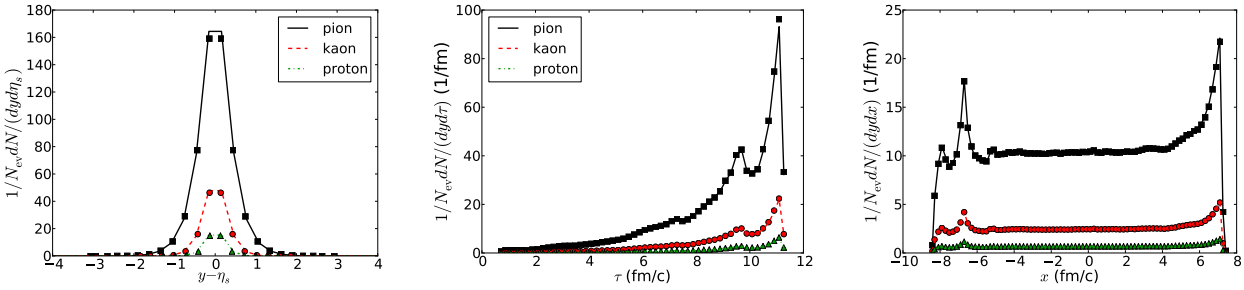

Figure 2.16: Similar to Fig. 2.14, but for sampling method with the semi-analytic approach.

are very well reproduced but some slight differences are seen in the η_s and τ distributions. Fig. 2.17 shows that this method generates some noticeable disagreements in the higher order momentum anisotropies of the particle momentum distribution, caused by the particular way we remove negative contributions in this approach.

Finally, we shown in Figs. 2.18 and 2.19, our results from the sampling method II within the purely numerical approach. In this method, since we first sample the momentum distributions of

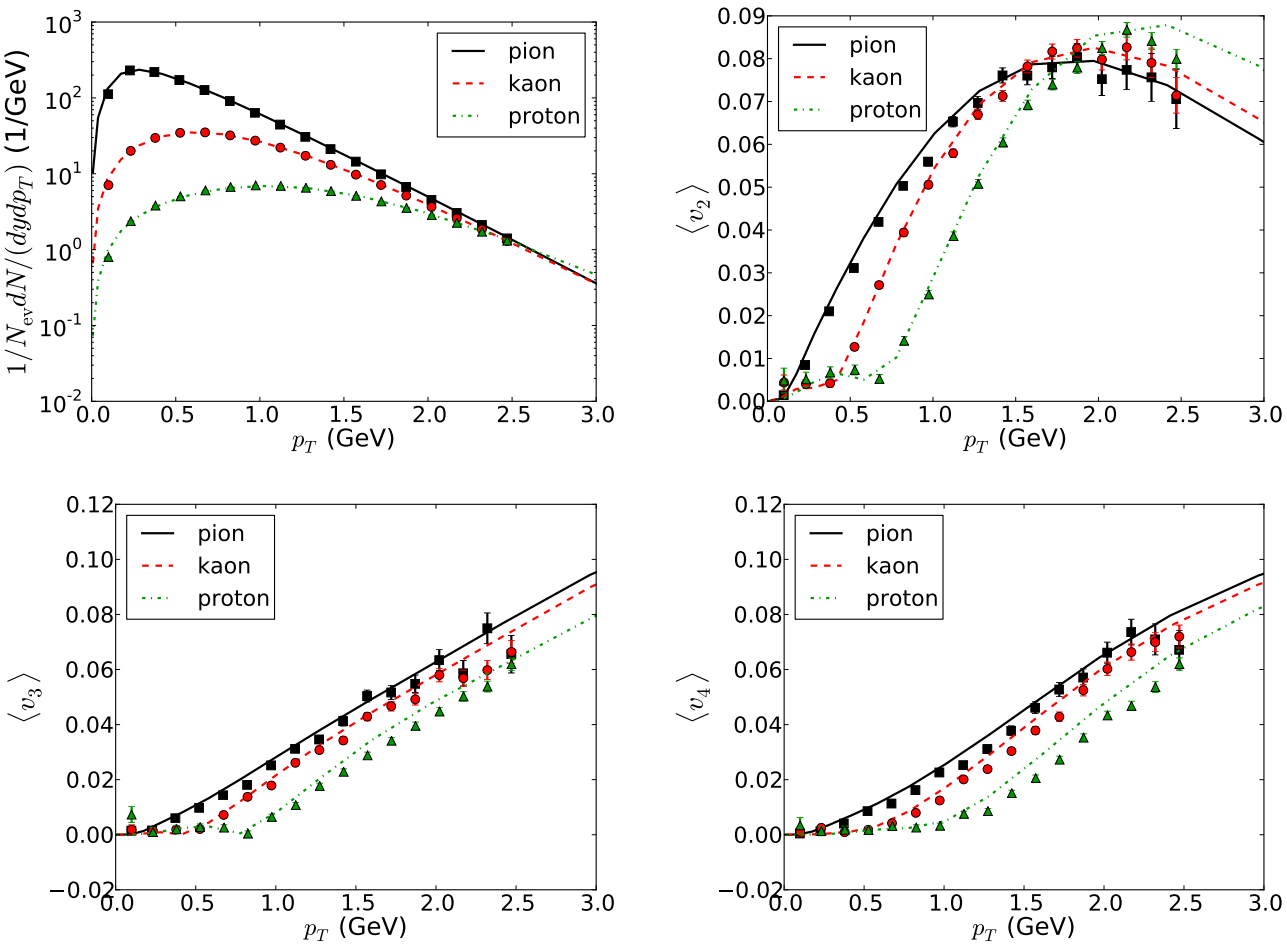

Figure 2.17: Similar to Fig. 2.15, but for sampling with the semi-analytic approach.

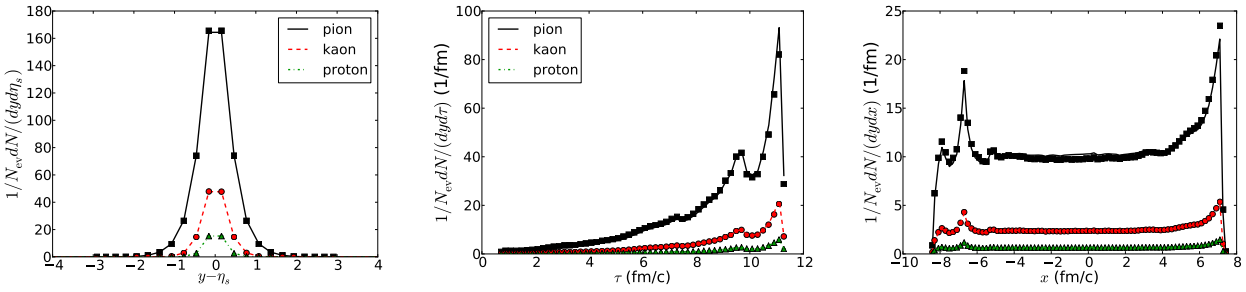

Figure 2.18: Similar to Fig. 2.14, but for sampling method II of the purely numerical approach, which samples particle momenta first.

the particles, the sampled results reproduce the directly calculated particle momentum distributions from the Cooper-Frye formula very well. The spatial distributions of the particles, on the other hand, exhibit some noticeable deviations from the Cooper-Frye results, due to the removal of negative contributions.

Overall, we show that our particle sampler can very well reproduce the desired particle distributions from the Cooper-Frye formula. Due to the negativity issue in the Cooper-Frye integral, the final particle samples deviate from the desired distributions either in momentum or coordinate

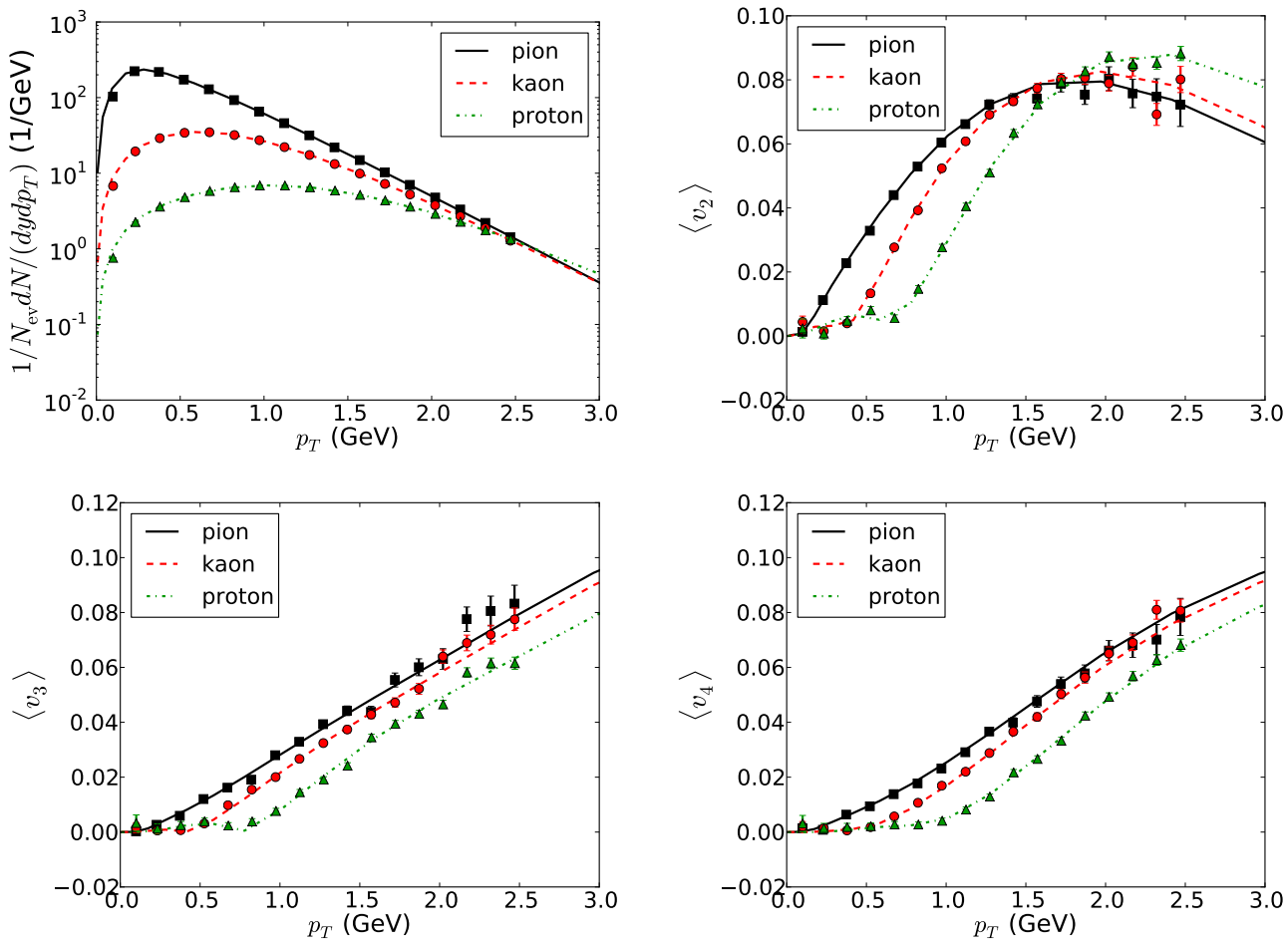

Figure 2.19: Similar to Fig. 2.15, but for sampling method II of the purely numerical approach, which samples particle momenta first.

space, or both. But the deviations are small and quite acceptable for all three sampling methods. For the users who aim at high precision for the anisotropic flow coefficients, we recommend to choose method II from the purely numerical approach. For those who is focus on particle interferometry, where the spatial distributions of the particles maybe more important, method I from the purely numerical approach is preferred.

2.6 Event-by-event flow analysis with finite numbers of particles

Particle event generators (such as `iSS` and `UrQMD`) produce Monte-Carlo samples with a finite number of particles per event. As is true in the actual experiments, this limits the resolution of the flow anisotropy distributions, especially the resolution of the n-th order harmonic flow angle Ψ_n. For each individual event, the true underlying azimuthal particle distribution can be written as

$$E\frac{d^3N}{d^3p} = \frac{1}{2\pi}\frac{d^2N}{dyp_Tdp_T}\left(1+\sum_{n=1}^{\infty}2v_n(p_T,y)\cos[n(\phi-\Psi_n(p_T,y))]\right), \tag{2.91}$$

where v_n is the n-th order anisotropic flow coefficient and Ψ_n is its corresponding flow plane angle. Both depend on the particles' transverse momentum and rapidity. They can be combined into a complex number by writing

$$V_n(p_T, y) = v_n(p_T, y) e^{in\Psi_n(p_T,y)}. \tag{2.92}$$

In the experimental measurement, one can estimate the true $V_n(p_T, y)$ by constructing the event flow vector $Q_n(p_T, y)$ from the finite number of measured particles. The n-th order event flow vector $Q_n(p_T, y)$ is defined as

$$Q_n(p_T, y) = |Q_n(p_T, y)| e^{in\tilde{\Psi}_n(p_T,y)} = \frac{1}{N_{\text{particle}}} \sum_{i=1}^{N_{\text{particle}}} w_i \cos(n\phi_i), \tag{2.93}$$

where the sum goes over all the selected particles. w_i is the weight for each particle which is taken to be 1 or $p_{i,T}$ in most cases, times an acceptance correction. The limited event plane angle $\tilde{\Psi}_n(p_T)$ extracted from the Q vector takes values in the range $\left[0, \frac{2\pi}{n}\right)$. When $N_{\text{particle}} \to \infty$, $Q_n(p_T) \to V_n(p_T)$ for $w_i = 1$. So the true underlying anisotropic flow $V_n(p_T)$ can be regarded as the limit of the measured flow vector as the number of particles per event approaches infinity.

In the `iEBE` package, we provide two python functional classes to filter out particle samples of interests from the event generator outputs and perform a flow analysis on these particles.

2.6.1 Filtering particles

Since the size of the output files from the particle event generator are huge, we develop a two-stage analysis framework to efficiently handle large numbers of Monte-Carlo events, described in Fig. 2.20.

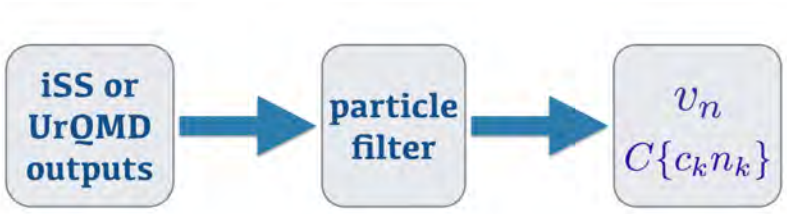

Figure 2.20: Work flow for analyzing the particle event generator outputs.

During the first stage, we first set up a particle filter which only selects only that particle information from the event generator output files in which the users is actually interested. Since the initial condition generator assigns the x-axis in the transverse plane to the direction of the impact parameter, in order to randomize the reaction plane (i.e, to eliminate the trivial correlation between any two Monte-Carlo particle samples from the same hydrodynamic background), we generate a random rotation angle ϕ and apply it to all the selected particles in the event. We also compute and store the n-th order event flow vector $Q_n(p_T, y)$ of the user-selected particles into a

database for the following second stage analysis. In a general flow analysis, we keep the $Q_n(p_T)$ vectors for all charged particles as well as for the stable identified particles with pseudo-rapidity η between -2.5 to 2.5.

In the second stage of the analysis, we perform event averages according to various definitions of the flow correlation functions , thereby obtaining different type of flow coefficients. As we will see in the following sub-sections, all the flow correlation functions can be written as certain combinations of the event flow vectors Q_n. As a result, the computational complexity for any type flow analysis is only $O(N_{\rm ev})$. This greatly improves the numerical efficiency in analyzing the final results, especially for multi-particle correlation functions.

2.6.2 Anisotropic Flow Analysis

Event plane method

The most commonly used flow measurement quantity is the event-plane flow defined as [22]

$$v_n\{\mathrm{EP}\} = \frac{\left\langle Q_n \cdot \frac{Q^\star_{nA}}{|Q_{nA}|} \right\rangle}{\sqrt{\left\langle \frac{Q^\star_{nA}}{|Q_{nA}|} \cdot \frac{Q_{nB}}{|Q_{nB}|} \right\rangle}}, \tag{2.94}$$

where Q_{nA} and Q_{nB} are called sub-event flow vectors, constructed from particles in sub-events. The event plane resolution factor is defined as the variance of the two sub-event plane angles [23],

$$R_n = \sqrt{\left\langle \frac{Q^\star_{nA}}{|Q_{nA}|} \cdot \frac{Q_{nB}}{|Q_{nB}|} \right\rangle}. \tag{2.95}$$

In order to avoid self-correlation in the calculations, we use particles from different pseudo-rapidity regions to define Q_n, Q_{nA}, and Q_{nB}. Particles from mid-rapidity, $\eta \in [-0.5, 0.5]$, are used to construct Q_n, while Q_{nA} is calculated with particles from forward rapidity, $\eta \in (0.5, 2.5]$ and Q_{nB} is calculated with particles from backward rapidity, $\eta \in [-2.5, -0.5)$. For event-plane flows of identified particles, the reference flow vectors Q_{nA} and Q_{nB} are constructed using all charged particles measured in the respective sub-events to gain the largest statistics.

Scalar product method

One disadvantage of the event-plane measurement is that the resolution factor Eq. (2.95) depends on the actual physical properties of the detectors, which are hard to account for in the theory. In order to remove such a bias [22, 24], one can alternatively measure the scalar product anisotropic flow:

$$v_n\{\mathrm{SP}\} = \frac{\langle Q_n \cdot Q^\star_{nA} \rangle}{\sqrt{\langle Q^\star_{nA} \cdot Q_{nB} \rangle}}. \tag{2.96}$$

Note that the usual two particle cumulant method is identical to the scalar product method, $v_n\{2\} = v_n\{\mathrm{SP}\}$ if Q_{nA} and Q_{nB} are the sub-event flow vectors for all charged particles.

Two particle correlations

In both the event-plane and scalar product methods, the reference flow vectors Q_{nA} and Q_{nB} are constructed from all charged particles measured within the given, disjoint pseudo-rapidity ranges. To improve statistics, we can use the same set of particles used to construct Q_n to also calculate the reference flow vector. This is usually referred as the two particle correlation flow, or $v_n[2]$. It is defined as [22],

$$v_n^2[2] = \langle\{e^{in(\phi_i-\phi_j)}\}_{(i,j)}\rangle, \tag{2.97}$$

where $\{\ldots\}_{(i,j)}$ represents averge over all the possible pairs of particle (i,j) (with $i \neq j$) within the selected samples in a single event. Eq. (2.97) can be written in terms of the Q_n flow vector as [25]

$$v_n^2[2] = \left\langle \frac{N|Q_n|^2 - 1}{N-1} \right\rangle, \tag{2.98}$$

where -1 in the numerator subtracts the terms where i and j correpsond to the same particle.

4-particle cumulant method

The 4-particle cumulant flow, $v_n\{4\}$, is constructed from 4-particle correlations by a procedure that suppresses 2-particle non-flow correlations. It is defined as [22]

$$v_n\{4\} = \left[\frac{2\langle\{e^{in\phi_1}\}\{e^{-in\phi_3}\}_{\rm ch}\rangle\langle\{e^{in\phi_2}\}_{\rm ch}\{e^{-in\phi_4}\}_{\rm ch}\rangle - \langle\{e^{in\phi_1}\}\{e^{-in\phi_3}\}_{\rm ch}\{e^{in\phi_2}\}_{\rm ch}\{e^{-in\phi_4}\}_{\rm ch}\rangle}{(2\langle\{e^{in\phi_1}\}_{\rm ch}\{e^{-in\phi_3}\}_{\rm ch}\rangle\langle\{e^{in\phi_2}\}_{\rm ch}\{e^{-in\phi_4}\}_{\rm ch}\rangle - \langle\{e^{in\phi_1}\}\{e^{-in\phi_3}\}_{\rm ch}\{e^{in\phi_2}\}_{\rm ch}\{e^{-in\phi_4}\}_{\rm ch}\rangle)^3}\right]^{1/4},$$

In terms of Q_n vectors,

$$v_n\{4\} = \left[\frac{2\langle Q_n\cdot Q_{nA}^\star\rangle\langle Q_{nA}\cdot Q_{nB}^\star\rangle - \langle Q_n\cdot Q_{nA}^\star Q_{nA}\cdot Q_{nB}^\star\rangle}{(2\langle Q_{nA}\cdot Q_{nB}^\star\rangle^2 - \langle Q_{nA}\cdot Q_{nA}^\star Q_{nA}\cdot Q_{nB}\rangle)^3}\right]^{1/4}, \tag{2.99}$$

Similar to the 2-particle cumulant method, we can also define the anisotropic flow from 4-particle correlations where all 4 particles are taken from the same selected sample in the event. This flow esitmate is denoted [25]

$$v_n^4[4] = 2\langle Q_n\cdot Q_n^\star\rangle^2 - \langle Q_n\cdot Q_n^\star Q_n\cdot Q_n^\star\rangle. \tag{2.100}$$

Please note that self-correlations still need to be subtracted in Eqs. (2.99) and (2.100). The corrected expressions can be found in [26] and are more complicated. In the Appendix A, we derive an induction formula that can help us to subtract the self correlations among any number of Q_n vectors.

2.6.3 Flow plane correlations

One can further construct correlation functions involving more Q_n vectors. The most general correlation function involving all charged hadrons takes the form

$$C\{c_1n_1,\ldots,c_kn_k\} \equiv \langle\{e^{in_1\phi_1}\}^{c_1}\cdots\{e^{in_k\phi_k}\}^{c_k}\rangle, \tag{2.101}$$

where $\langle\cdots\rangle$ runs over all charged hadrons in each event. This correlation function is non-zero when the coefficients $\{c_i\}$ and $\{n_i\}$ satisfies the relation, $c_1n_1 + c_2n_2 + \cdots + c_kn_k = 0$. (Otherwise the correlator averages to zero where summed over many events, due to the random orientation of the reaction plane which drops out from the correlator only if $c_1n_1 + c_2n_2 + \cdots + c_kn_k = 0$.) In experiment, such a correlation function was first introduced to extract the correlation between event planes angles of different harmonic order [27, 28, 29]. In [28] the ATLAS Collaboration studied a slight variation of Eq. (2.101) which, when expressed in Q_n vector, reads,

$$C\{c_1n_1,\ldots,c_kn_k\}\{\mathrm{EP}\} = \frac{\left\langle \frac{Q_{n_1}^{c_1}}{|Q_{n_1}|^{c_1}}\cdots\frac{Q_{n_k}^{c_k}}{|Q_{n_k}|^{c_k}}\right\rangle}{\sqrt{\left\langle \frac{Q_{n_1}^{c_1}}{|Q_{n_1}|^{c_1}}\cdot\left(\frac{Q_{n_1}^{c_1}}{|Q_{n_1}|^{c_1}}\right)^{\star}\right\rangle\cdots\left\langle \frac{Q_{n_k}^{c_k}}{|Q_{n_k}|^{c_k}}\cdot\left(\frac{Q_{n_k}^{c_k}}{|Q_{n_k}|^{c_k}}\right)^{\star}\right\rangle}}, \tag{2.102}$$

with the understanding that for $n_i < 0$, $Q_{n_i} = Q^{\star}_{-n_i}$. Similar to the event-plane flow, such an event-plane correlator suffers from resolution correction issues. One can remove this bias by defining a scalar product correlator [28, 29],

$$C\{c_1n_1,\ldots,c_kn_k\}\{\mathrm{SP}\} = \frac{\langle Q_{n_1}^{c_1}\cdots Q_{n_k}^{c_k}\rangle}{\sqrt{\langle Q_{n_1}^{c_1}\cdot(Q_{n_1}^{c_1})^{\star}\rangle\cdots\langle Q_{n_k}^{c_k}\cdot(Q_{n_k}^{c_k})^{\star}\rangle}}. \tag{2.103}$$

The removal of self-correlations from these expressions is most easily achieved by using disjoint subevents for the Q_n vectors, but less statistic hungry alternatives have been proposed [26].

The flow factorization ratio

The flow factorization ratio is defined as [24, 25],

$$r_n \equiv \frac{V_{n\Delta}(p_1,p_2)}{\sqrt{V_{n\Delta}(p_1,p_1)V_{n\Delta}(p_2,p_2)}}, \tag{2.104}$$

where $V_{n\Delta}(p_1,p_2)$ is the Fourier coefficients of the two particle correlation function,

$$\left\langle E_1E_2\frac{dN}{d^3p_1d^3p_2}\right\rangle = \frac{1}{2\pi}\left\langle\frac{dN}{p_1dp_1d\eta_1p_2dp_2d\eta_2}\right\rangle\left(1+2\sum_{n=1}^{\infty}V_{n\Delta}(p_1,p_2)\cos(n\Delta\phi)\right). \tag{2.105}$$

In a single event, assuming that all particles are emitted independently, $V_{n\Delta}(p_1,p_2)$ factors into a product of $v_n(p_1)$ and $v_n(p_2)$. For a two particle correlation function measured by averaging multiple events, $V_{n\Delta}(p_1,p_2)$ can be calculated from the Q_n vectors as [22]

$$V_{n\Delta}(p_1,p_2) = \langle Q_n(p_1)\cdot Q_n^{\star}(p_2)\rangle. \tag{2.106}$$

Note that for the case $p_1 = p_2$ we need to subtract the self correlations. With Eq. (2.106), the flow factorization ratio can be written as,

$$r_n(p_1, p_2) = \frac{\langle Q_n(p_1) \cdot (Q_n(p_2))^\star \rangle}{\sqrt{\langle Q_n(p_1) \cdot (Q_n(p_1))^\star \rangle \langle Q_n(p_2) \cdot (Q_n(p_2))^\star \rangle}} = C\{n, n\}\{\mathrm{SP}\}(p_1, p_2). \tag{2.107}$$

This ratio can be understood as the correlation between the same-order flow plane angles at different p_T values.

Two-plane correlation (2PC)

The p_T-integrated two-flow-plane correlation can be defined as

$$C\{c_1 n_1, c_2 n_2\}\{\mathrm{SP}\} = \frac{\langle Q_{n_1}^{c_1} \cdot Q_{n_2}^{c_2} \rangle}{\sqrt{\langle Q_{n_1}^{c_1} \cdot (Q_{n_1}^{c_1})^\star \rangle \langle Q_{n_2}^{c_2} \cdot (Q_{n_2}^{c_2})^\star \rangle}}, \tag{2.108}$$

where $c_1 n_1 + c_2 n_2 = 0$. The ATLAS Collaboration [28] constructs the event-plane correlation,

$$\begin{aligned} \text{“}\langle \cos k(\Psi_{n_1} - \Psi_{n_2}) \rangle\text{”} &\equiv \frac{\langle \cos k(\Psi_{n_1}^A - \Psi_{n_2}^B) \rangle + \langle \cos k(\Psi_{n_1}^B - \Psi_{n_2}^A) \rangle}{\mathrm{Res}\{k\Psi_{n_1}^A\}\mathrm{Res}\{k\Psi_{n_2}^B\} + \mathrm{Res}\{k\Psi_{n_1}^B\}\mathrm{Res}\{k\Psi_{n_2}^A\}} \\ &= \frac{\left\langle \left(\frac{Q_{n1}^A}{|Q_{n_1}^A|}\right)^{c_1} \cdot \left(\frac{Q_{n_2}^B}{|Q_{n_2}^B|}\right)^{\star c_2} \right\rangle + \left\langle \left(\frac{Q_{n1}^B}{|Q_{n_1}^B|}\right)^{c_1} \cdot \left(\frac{Q_{n_2}^A}{|Q_{n_2}^A|}\right)^{\star c_2} \right\rangle}{2\sqrt{\left\langle \left(\frac{Q_{n_1}^A}{|Q_{n_1}^A|}\right)^{c_1} \cdot \left(\frac{Q_{n_1}^B}{|Q_{n_1}^B|}\right)^{\star c_1} \right\rangle \left\langle \left(\frac{Q_{n_2}^A}{|Q_{n_2}^A|}\right)^{c_2} \cdot \left(\frac{Q_{n_2}^B}{|Q_{n_2}^B|}\right)^{\star c_2} \right\rangle}}, \end{aligned} \tag{2.109}$$

where $k = |c_1 n_1| = |c_2 n_2|$ and Q_n^A and Q_n^B are the flow vectors from two sub-events. In the implementation, we choose one event containing particles with pseudo-rapidity $\eta > 0.5$ in the forward rapidity and the other event with particles having $\eta < -0.5$ at backward rapidity.

Three-plane correlations (3PC)

The p_T-integrated three-flow-plane correlations are defined as [28]

$$C\{c_1 n_1, c_2 n_2, c_3 n_3\}\{\mathrm{SP}\} = \frac{\langle Q_{n_1}^{c_1} \cdot Q_{n_2}^{c_2} \cdot Q_{n_3}^{c_3} \rangle}{\sqrt{\langle Q_{n_1}^{c_1} \cdot (Q_{n_1}^{c_1})^\star \rangle \langle Q_{n_2}^{c_2} \cdot (Q_{n_2}^{c_2})^\star \rangle \langle Q_{n_3}^{c_3} \cdot (Q_{n_3}^{c_3})^\star \rangle}}, \tag{2.110}$$

where $c_1 n_1 + c_2 n_2 + c_3 n_3 = 0$. The event-plane correlations corresponding to Eq. (2.109) can be defined in a similar fashion. In order to avoid subtracting the self-correlation in the calculation, we usually define the three Q_n vectors in three disjoint rapidity regions. In our implementation, we choose sub-event A to contain particles with $-1.5 \leqslant \eta < -0.5$, sub-event C has particles with $0.5 < \eta \leqslant 1.5$, and sub-event B has particles with pseudo-rapidity, $-2.5 \leqslant \eta < -1.5$ and $1.5 < \eta \leqslant 2.5$.

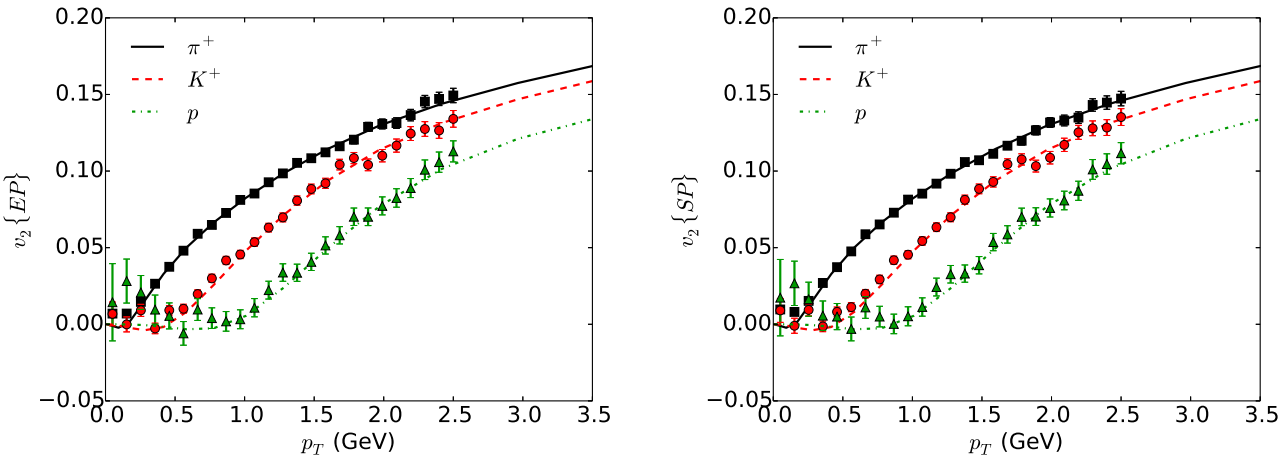

Figure 2.21: Code checking for event plane and scalar product method of elliptic flow coefficients for thermal π^+, K^+ and p. The simulations contains 50,000 repeated samplings of a single hydrodynamic fireball.

2.6.4 Benchmark code checking

In Fig. 2.21, we show a numerical check for the event-plane and scalar-product v_2 from 50,000 events sampled from one underlying hydrodynamic freeze-out hyper-surface. As $N_{\rm ev} \to \infty$, both flow measurements will reproduce the true underlying v_2, which can be calculated from freeze-out hyper-surface using the Cooper-Frye formula. Within the statistical error, the v_2 of thermal π^+, K^+, and protons show in Fig. 2.21 agree quite well with the expected results calculated from the Cooper-Frye formula. The larger statical error bars for thermal protons compared to thermal π^+ are due to the roughly 10 times smaller proton yield in each event. For all three particle species, due to the lack of the statistics at very low p_T, $p_T < 0.2$ GeV, the v_2 results from the event generator deviate from the Cooper-Frye results. For higher order v_n, more events are needed.

2.6.5 Reconstructing HBT correlations from event generators

Particle event generators (`iSS, UrQMD`) assume that every individual particle in the event is emitted independently. The final particle samples are made of classical particles, void of quantum mechanical correction. For pairs of identical pions, wave functions symmetrization effects on their joint emission probability are not included. Similarly, for protons pairs, their joint production probability is not suppressed result from wave function (anti)-symmetrization.

In order to reconstruct the HBT correlations between identical particles, we need both momentum and spatial information of the emitted particles from the event generator.

Once we get a set $\{x_i^\mu, p_i^\mu\}$ of identical particle emission coordinates in phase space, we can reconstruct the HBT correlation between pairs of particles by the following formula [3],

$$C\left(\mathbf{q},\mathbf{K}\right) = 1 + \frac{\left|\int d^4x e^{iq\cdot x} S(x,K)\right|^2}{\left|\int d^4x_a S(x_a,p_a)\right| \left|\int d^4x_b S(x_b,p_b)\right|}, \tag{2.111}$$

where $\mathbf{q} = \mathbf{p}_a - \mathbf{p}_b$ and $\mathbf{K} = \frac{1}{2}(\mathbf{p}_a + \mathbf{p}_b)$ and $S(x, K)$ is the particle emission probability in phase-space. This "emission function" is sampled by the coordinates $\{x_i^\mu, p_i^\mu\}$ from the event generator. In real experiments, due to the limited number of measured particles in each event, we can only measure the event-averaged two-particle correlation function

$$\langle C(\mathbf{q}, \mathbf{K})\rangle = 1 + \frac{\left\langle \int d^4x_a d^4x_b e^{iq\cdot(x_a - x_b)} S(x_a, K) S^*(x_b, K)\right\rangle}{\left\langle \left|\int d^4x_a S(x_a, p_a)\right|\right\rangle \left\langle \left|\int d^4x_b S(x_b, p_b)\right|\right\rangle}. \tag{2.112}$$

Since the particle samples generated from the event generator reflect the underlying particle emission probability distribution $S(x, K)$, we can probe the structure of the particle emission function by averaging over large numbers of events.

Classical interpretation

If we interpret the sample $\{x_i^\mu, p_i^\mu\}$ as the spatial positions and momenta of the emitted particles, we can write the particle emission function as,

$$S(x, p) = \sum_{i=1}^{N} \delta^4(x - x_i)\delta^2(\mathbf{p}_\perp - \mathbf{p}_{\perp,i})\,\delta(y - y_i). \tag{2.113}$$

This emission function has already been normalized,

$$N = \int \frac{d^3p}{E_p} d^4x S(x, p) = \sum_{i=1}^{N} 1 = N.$$

In the numerical implementation, the δ functions need to be replaced by bin functions with a finite width. We can use two types of bin functions:

$$\delta_{\mathbf{p}_i,\mathbf{p}} = \begin{cases} \frac{1}{\pi\varepsilon^2}\frac{1}{\varepsilon_{\Delta y}}, & \text{for } |\mathbf{p}_i - \mathbf{p}| < \varepsilon \quad \text{and} \quad |y_i - y| < \varepsilon_{\Delta y}/2 \\ 0, & \text{otherwise.} \end{cases} \tag{2.114}$$

or

$$\delta_{\mathbf{p}_i,\mathbf{p}} = \frac{1}{\pi^{3/2}\varepsilon^2\varepsilon_{\Delta y}} e^{-(\mathbf{p}_i - \mathbf{p})^2/\varepsilon^2} e^{-(y_i - y)^2/\varepsilon_{\Delta y}^2}. \tag{2.115}$$

Both bin functions are normalized:

$$\int \frac{d^3p}{E_p} \delta_{\mathbf{p}_i,\mathbf{p}} = 1, \tag{2.116}$$

and as $\varepsilon \to 0$ and $\varepsilon_{\Delta y} \to 0$,

$$\delta_{\mathbf{p}_i,\mathbf{p}} \to \delta^2(\mathbf{p}_\perp - \mathbf{p}_{\perp,i})\,\delta(y - y_i). \tag{2.117}$$

In order to construct the HBT correlation function from the particle sample, we can use the bin function to discretize the Eq. (2.112). We first look at the denominator which is constructed by

choosing the two particles from two different events n and m:

$$\begin{aligned}\left\langle E_a\frac{dN}{d^3p_a}E_b\frac{dN}{d^3p_b}\right\rangle_{\rm mix} &= \left\langle\sum_{i=1}^{N_m}\sum_{j=1}^{N_n}\delta_{\mathbf{p}_i,\mathbf{p}_a}\delta_{\mathbf{p}_j,\mathbf{p}_b}\right\rangle_{(m,n)} \\ &= \frac{1}{N_{\rm ev}(N_{\rm ev}-1)}\left[\left(\sum_{m=1}^{N_{\rm ev}}\sum_{i=1}^{N_m}\delta_{\mathbf{p}_i,\mathbf{p}_a}\right)\left(\sum_{n=1}^{N_{\rm ev}}\sum_{i=1}^{N_n}\delta_{\mathbf{p}_i,\mathbf{p}_b}\right)\right. \\ &\quad \left.-\sum_{m=1}^{N_{\rm ev}}\left(\sum_{i=1}^{N_m}\sum_{j=1}^{N_m}\delta_{\mathbf{p}_i,\mathbf{p}_a}\delta_{\mathbf{p}_i,\mathbf{p}_b}\right)\right], \end{aligned} \tag{2.118}$$

where the second term in Eq. (2.118) removes the contribution of the first term from where events are the same.

For numerator, the particle pairs are taken from the same event. The numerator of the second term in Eq. (2.111) can be written as,

$$\begin{aligned}\left\langle E_aE_b\frac{dN}{d^3p_ad^3p_b}\right\rangle &= \frac{1}{N_{\rm ev}}\sum_{m=1}^{N_{\rm ev}}\sum_{i=1}^{N_m}\sum_{j\neq i}\delta_{\mathbf{p}_i,\mathbf{K}}\delta_{\mathbf{p}_j,\mathbf{K}}e^{iq\cdot(x_i-x_j)} \\ &= \frac{1}{N_{\rm ev}}\sum_{m=1}^{N_{\rm ev}}\left(\left|\sum_{i=1}^{N_m}\delta_{\mathbf{p}_i,\mathbf{K}}e^{iq\cdot x_i}\right|^2-\sum_{i=1}^{N_m}\left(\delta_{\mathbf{p}_i,\mathbf{K}}\right)^2\right), \end{aligned} \tag{2.119}$$

where the last term subtracts the self-correlation between a particle and itself. The two-particle correlation function Eq. (2.111) can thus be written as

$$\begin{aligned}\langle C(\mathbf{q},\mathbf{K})\rangle = 1 + \\ +\frac{(N_{\rm ev}-1)\sum_{m=1}^{N_{\rm ev}}\left(\left|\sum_{i=1}^{N_m}\delta_{\mathbf{p}_i,\mathbf{K}}e^{iq\cdot x_i}\right|^2-\sum_{i=1}^{N_m}\left(\delta_{\mathbf{p}_i,\mathbf{K}}\right)^2\right)}{\left[\left(\sum_{m=1}^{N_{\rm ev}}\sum_{i=1}^{N_m}\delta_{\mathbf{p}_i,\mathbf{p}_a}\right)\left(\sum_{n=1}^{N_{\rm ev}}\sum_{i=1}^{N_n}\delta_{\mathbf{p}_i,\mathbf{p}_b}\right)-\sum_{m=1}^{N_{\rm ev}}\left(\sum_{i=1}^{N_m}\delta_{\mathbf{p}_i,\mathbf{p}_a}\sum_{j=1}^{N_m}\delta_{\mathbf{p}_i,\mathbf{p}_b}\right)\right]}. \end{aligned} \tag{2.120}$$

If we use the smoothness approximation in the denominator $\delta_{\mathbf{p}_i,\mathbf{p}_a}\delta_{\mathbf{p}_i,\mathbf{p}_b}\simeq\left(\delta_{\mathbf{p}_i,\mathbf{K}}\right)^2$, we obtain

$$\langle C(\mathbf{q},\mathbf{K})\rangle = 1+\frac{\frac{1}{N_{\rm ev}}\sum_{m=1}^{N_{\rm ev}}\left(\left|\sum_{i=1}^{N_m}\delta_{\mathbf{p}_i,\mathbf{K}}e^{iq\cdot x_i}\right|^2-\sum_{i=1}^{N_m}\left(\delta_{\mathbf{p}_i,\mathbf{K}}\right)^2\right)}{\frac{1}{N_{\rm ev}(N_{\rm ev}-1)}\left[\left(\sum_{m=1}^{N_{\rm ev}}\sum_{i=1}^{N_m}\delta_{\mathbf{p}_i,\mathbf{K}}\right)^2-\sum_{m=1}^{N_{\rm ev}}\left(\sum_{i=1}^{N_m}\delta_{\mathbf{p}_i,\mathbf{K}}\right)^2\right]}. \tag{2.121}$$

2.7 Interface for Thermal Photon Emission

In the `iEBE` package, we provide a separate branch to allow users to perform calculations for electromagnetic probes from relativistic heavy-ion collisions. In Fig. 2.22, we illustrate the work flow of such integrated calculations.

In order to compute thermal photon emission from an evolving viscous hydrodynamic medium, we need to output the evolution history of the local temperature, flow velocity and shear stress

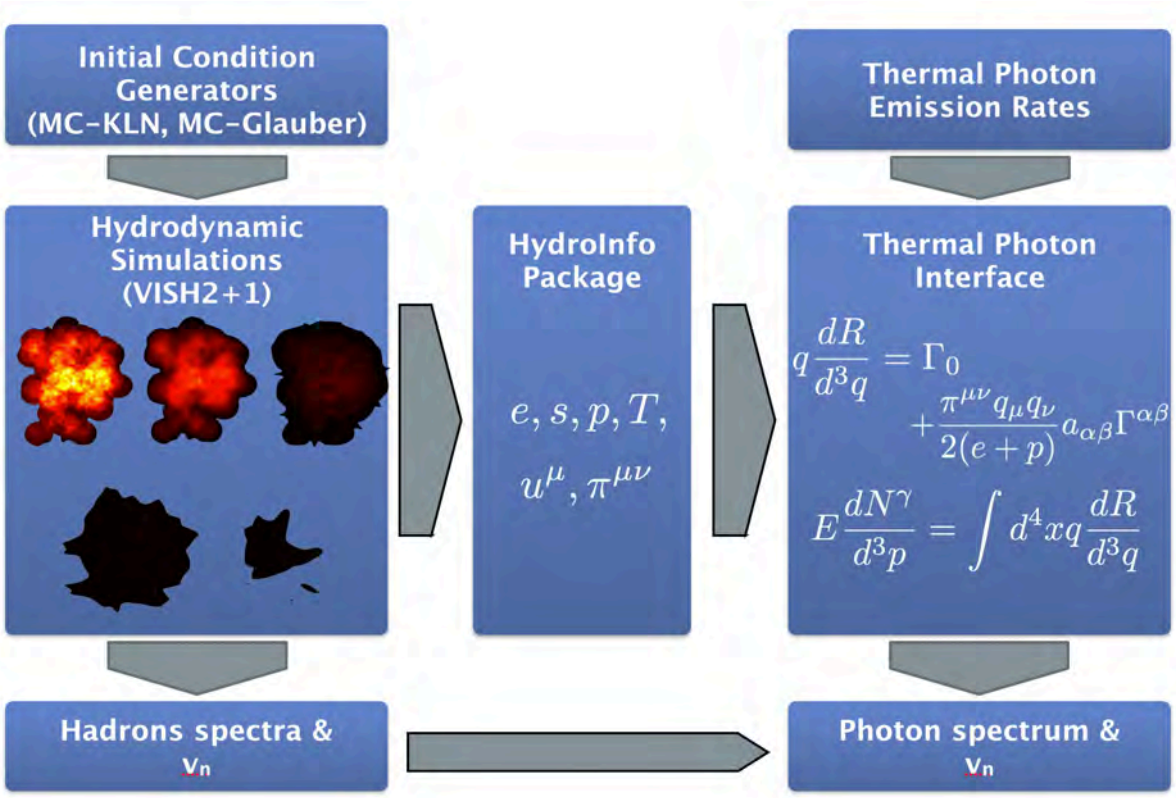

Figure 2.22: Work flow for event-by-event hydrodynamic simulation with photon emission.

tensor and fold them with thermal photon emission rates to compute electromagnetic observables. Since the hydrodynamic evolution information is very demanding in terms of storage space, we output it in `HDF5` binary format to minimize the storage requirement and increase the I/O efficiency. `HDF5` format (Hierarchical Data Format) is a data model, library, and file format for storing and managing data. It supports an unlimited variety of datatypes, and is designed for flexible and efficient I/O and for high volume and complex data. The `HDF5` library also provides multi-language support, which enables us to build our interface in both `Fortran` and `C++` for future support.

The momentum spectrum of thermal photons emitted from the expanding fireball can be written as

$$E\frac{dN^\gamma}{d^3p} = \int d^4x \left(\Gamma_0 + \frac{\pi^{\mu\nu}}{2(e+P)}\Gamma_{\mu\nu}\right), \tag{2.122}$$

where the integral goes over the space-time volume occupied by the radiating hot medium, Γ_0 is the thermal equilibrium emission rate, and the second term $\sim \pi_{\mu\nu}$ describes the shear viscous correction to the thermal emission rate. We can decompose $\Gamma_{\mu\nu}$ in a complete tensor basis and use the properties of the shear stress tensor, $\pi^{\mu\nu} = \Delta^{\mu\nu}_{\alpha\beta}\pi^{\alpha\beta}$, to write Eq. (2.122) in the form

$$E\frac{dN^\gamma}{d^3p} = \int d^4x \left(\Gamma_0(u\cdot q, T) + \frac{\pi^{\mu\nu}\hat{q}_\mu\hat{q}_\nu}{2(e+P)}a_{\alpha\beta}\Gamma^{\alpha\beta}(u\cdot q, T)\right), \tag{2.123}$$

where $\hat{q}^\mu = q^\mu/(u\cdot q)$, $a_{\alpha\beta}$ is a projection operator:

$$a_{\alpha\beta} = \frac{3}{2(u\cdot q)^2}q_\alpha q_\beta + u_\alpha u_\beta + g_{\alpha\beta} - \frac{3}{2(u\cdot q)}(q_\alpha u_\beta + q_\beta u_\alpha). \tag{2.124}$$

The use of tensor decomposition in Eq. (2.123) is particularly efficient numerically, because the anisotropic correction factors into a product of Lorentz scalars of which the first, $\pi^{\mu\nu}\hat{q}_\mu\hat{q}_\nu$, is most easily evaluated in the laboratory frame (where we know $\pi^{\mu\nu}$ from the solution of the hydrodynamic equations) while the second, $\Gamma_1 \equiv a_{\alpha\beta}\Gamma^{\alpha\beta}$, is best worked out in the local rest frame of the fluid cell (where $u \cdot q$ reduces to the local rest frame energy of the photon). This helps to avoid performing extensive Lorentz boosts and 3-D rotations of $\pi^{\mu\nu}$ for each fluid cell when coupled to hydrodynamic simulations. Besides speeding-up the calculation, it allows us to tabulate the viscous corrections into one convenient table that can easily be used for phenomenological studies.

Please note that the work flow in Fig. 2.22 is generic for the calculation of all rare probes coupled to the evolving bulk medium that probe its temperature and flow velocity, such as jet energy loss and heavy quark diffusion.

2.8 Pre-equilibrium dynamics

Up to now, the `iEBE` code misses a module to describe the pre-equilibrium evolution of the energy momentum tensor before the onset of viscous hydrodynamics. Such a module, together with a Landau matching algorithm that matches the pre-equilibrium $T^{\mu\nu}$ to the viscous hydrodynamic form Eq. (2.25), at the hydrodynamic starting time, is presently being developed by Jia Liu.

Chapter 3: Phenomenological Studies of hadronic observables: introduction and overview

Heavy-ion collisions at the Relativistic Heavy-Ion Collider (RHIC) and the Large Hadron Collider (LHC) offer a privileged window to study the physics of the quark-gluon plasma (QGP) under extremely hot and dense conditions. Measurements of large anisotropic flow of hadrons serve as a hallmark that the QGP generated in the collisions is strongly coupled and reaches near local thermal equilibrium. Transport coefficients such as the shear viscosity represent the fundamental properties of this QCD matter created in the relativistic heavy-ion collisions. Recently, interest in the theoretical and phenomenological determination of the QGP transport parameters, in particular its specific shear viscosity η/s, has soared. Over the past decade, relativistic hydrodynamics has established itself as an indispensable component in modeling the collective dynamics of the quark-gluon plasma (QGP) produced in relativistic heavy ion collisions [30, 31, 32, 33, 34, 35, 36, 37, 38, 39, 40, 41, 42, 43, 44, 45, 46, 47, 48, 49, 50]. In this part of my thesis, we will apply relativistic viscous hydrodynamics to perform phenomenological studies of a variety of different aspects of relativistic heavy-ion collisions.

In Chapter 4, we will start our journey by exploring the sensitivity of the final experimental observables to the input parameters in hydrodynamic simulations. We then proceed to perform a global fit to the measured single particle spectra and their elliptic flows at top RHIC energy and use it as a starting point to extrapolate to higher LHC energies. This well-constrained prediction for the LHC flow measurements will be discussed in detail in Chapter 5.

The extraction of the specific shear viscosity of the QGP from phenomenological studies has received a lot of attention and recent effort [51, 33, 35, 36, 37, 40, 52, 41, 42, 43, 44, 45, 46, 47, 17]. Based on both pure hydrodynamic simulations and more advanced modeling using a hydrodynamic + cascade hybrid approach, it has been established that now the remaining largest uncertainty lie in the initial conditions [40]. An estimated $\mathcal{O}(20\%)$ uncertainty in the initial ellipticity of the energy density profiles was found to translate into a $\mathcal{O}(100\%)$ uncertainty in the extracted value of the η/s of the QGP. In Chapter 6 we will discuss that with the discovery and meanwhile precise measurement of higher order anisotropic harmonic flow coefficients, especially the triangular flow v_3, a combined analysis of measured v_2 and v_3 data can help us disentangle

the initial state fluctuations from the medium transport properties. In a following event-by-event viscous hydrodynamic study at LHC energy in Chapter 7, where higher order anisotropic flow coefficients, $v_n(n > 3)$, will be compared with experimental data, we will further demonstrate the discriminating power provided by a complete measurement of all flow harmonics.

In general, the specific shear viscosity is expected to change with temperature [53, 54]. In Chapter 8, we will further explore the sensitivity of the flow observables to the temperature dependence of $(\eta/s)(T)$.

One of the major goals of heavy-ion collision experiments at RHIC is to explore the QCD phase diagram. For this purpose, in the last few years the Beam Energy Scan (BES) program has been carried out at RHIC. By combining the measurements from RHIC to LHC energies, we will focus on studying the collision energy dependence of the flow observables in Chapter 9. Due to the current limitations in our model, we ignore the effects from the dynamical evolution of the non-zero net baryon density that characterizes the lower-energy collisions, and from corrections arising from the voilation of boost-invariance for the longitudinal expansion in our simulations. These effects are expected to become more and more important for quantitative comparisons with experimental measurements at lower collision energies at RHIC. Nonetheless our study can be regarded as the first step towards a more precise phenomenological studies of the RHIC BES program. The qualitative behavior of our results yields a number of key theoretical insights for understanding the phenomena that manifest themselves in the low energy runs at RHIC.

Chapters 10 and 11 are devoted to studying flow fluctuations in heavy-ion collisions. From event-by-event hydrodynamic simulations we know that both the magnitude and direction ("flow plane angle") of the anisotropic flow fluctuate as functions p_T and η and from event to event. Such fluctuations manifest themselves in flow correlation measurements. In Chapter 10, we will show that our event-by-event viscous hydrodynamic simulations successfully describe (and in a few cases even predicted) these flow correlations measured in the experiments. Finally, in Chapter 11 we study the anisotropic flows in ultra-central Pb+Pb collisions at the LHC, where the initial state fluctuations entirely dominate the final v_n spectrum.

We will wrap up this phenomenological part of my thesis by discussing a collection of small but interesting projects that I finished while following my main research stream.

Chapter 4: Systematic parameter study of hadron spectra and elliptic flow from viscous hydrodynamic simulations

4.1 Chapter introduction

The specific shear viscosity of the QGP can be extracted as a model fitting parameter in the comparisons between the measured hadron spectra and their azimuthal anisotropies and viscous hydrodynamical simulations of the collision dynamics. However, in practice, a reliable extraction procedure requires highly constrained simulations of all dynamical stages of the collision from the initial non-equilibrium phase, which describes the initial geometry and early evolution towards local thermalization, to the viscous hydrodynamic expansion of the QGP fireball and to the final off-equilibrium hadronic rescattering stage after its hadronization [55, 56].

This chapter is a contribution to help prepare the path for such a phenomenological extraction of $(\eta/s)_{\rm QGP}$. We would like to first build intuition for systematic trends and parameter dependences that will be useful in forthcoming more ambitious fit attempts. This work reported here is based on Ref. [17].

4.2 Setups: Hydrodynamic parameters, initial and final conditions

To initialize the hydrodynamic evolution, we must specify the following parameters,

- The starting time τ_0 at which the system is sufficiently close to the local thermal equilibrium. We here consider τ_0 as a tunable parameter and vary it between 0.2 and 0.8 fm/c in order to study how it affects the final hadron spectra and elliptic flow.

- Initial energy density profile

  For the initial energy density profile we study both Glauber [57, 30, 58, 38] and color glass condensate motivated (CGC-fKLN) initializations [59, 60, 61, 62]. In contrast to later chapters, we here use the optical limit. We do not account for event-by-event fluctuations [11, 63, 45, 64, 65].

- Initial flow velocity and viscous stress tensor $\pi^{\mu\nu}$

  The shear viscous pressure tensor $\pi^{\mu\nu}$ is initialized with its Navier-Stokes profile $\pi^{\mu\nu} = 2\eta\sigma_0^{\mu\nu}$ where $\sigma_0^{\mu\nu}$ is the velocity shear tensor at time τ_0, calculated from the initial Bjorken velocity profile, $u^\mu = (u^\tau, u^x, u^y, u^\eta) = (1, 0, 0, 0)$. Since η/s is taken constant here, $\pi^{\mu\nu} \sim s$ follows the initial entropy density profile in the transverse plane. A more systematic study of the initial transverse flow velocity and the $\pi^{\mu\nu}$ tensor requires a model description of the pre-equilibrium stage. We leave this for a future study.

- The equation of state (EOS)

  The equation of state of the QGP is a key property that we would like to study in relativistic heavy-ion collisions. It also serves as an essential ingredient when we solve the hydrodynamic equations. We will explore the dynamical consequences of three different types of EOS in our study. The details for them will be explained in the next section.

- The specific shear viscosity η/s

  At the top RHIC energy, the initial peak temperature of the fireball reaches around 350-400 MeV. Within the temperature range explored in heavy-ion collisions, the temperature dependence of η/s is expected to be weak. So for the following exploratory study we use of a constant ratio η/s, tuned from 0.08 to 0.24 which, as we will see, covers the physical range allowed by the experimental data, in order to study the effects of shear viscosity on the hadron spectra and elliptic flow. We will perform a systematic study of the effects from a temperature dependence of $(\eta/s)(T)$ in Chapter 8.

- The kinetic decoupling temperature $T_{\rm dec}$

  At the end of the hydrodynamic evolution, we use the Cooper-Frye formula (see Eq. (4.1) below) to convert the energy contained in each fluid cell into individual particles. This procedure is implemented on a constant temperature hyper-surface. In our pure hydrodynamic simulation framework, we let the converted particles stream freely to the detectors without any further interactions [3]. We call the temperature on the conversion surface the kinetic decoupling temperature, $T_{\rm dec}$. We will tune $T_{\rm dec}$ between 100 and 160 MeV and study how it affects the hadron spectra and elliptic flow.

Figure 4.1 shows a comparison of typical initial energy density profiles generated from the Glauber and CGC initializations. In the Glauber model we assume a mixture of 85% wounded

[3] A more realistic approach would be to feed these particles into a microscopic hadronic cascade model to further propagate them according to the relativistic Boltzmann equation, untill all collisions have stopped.

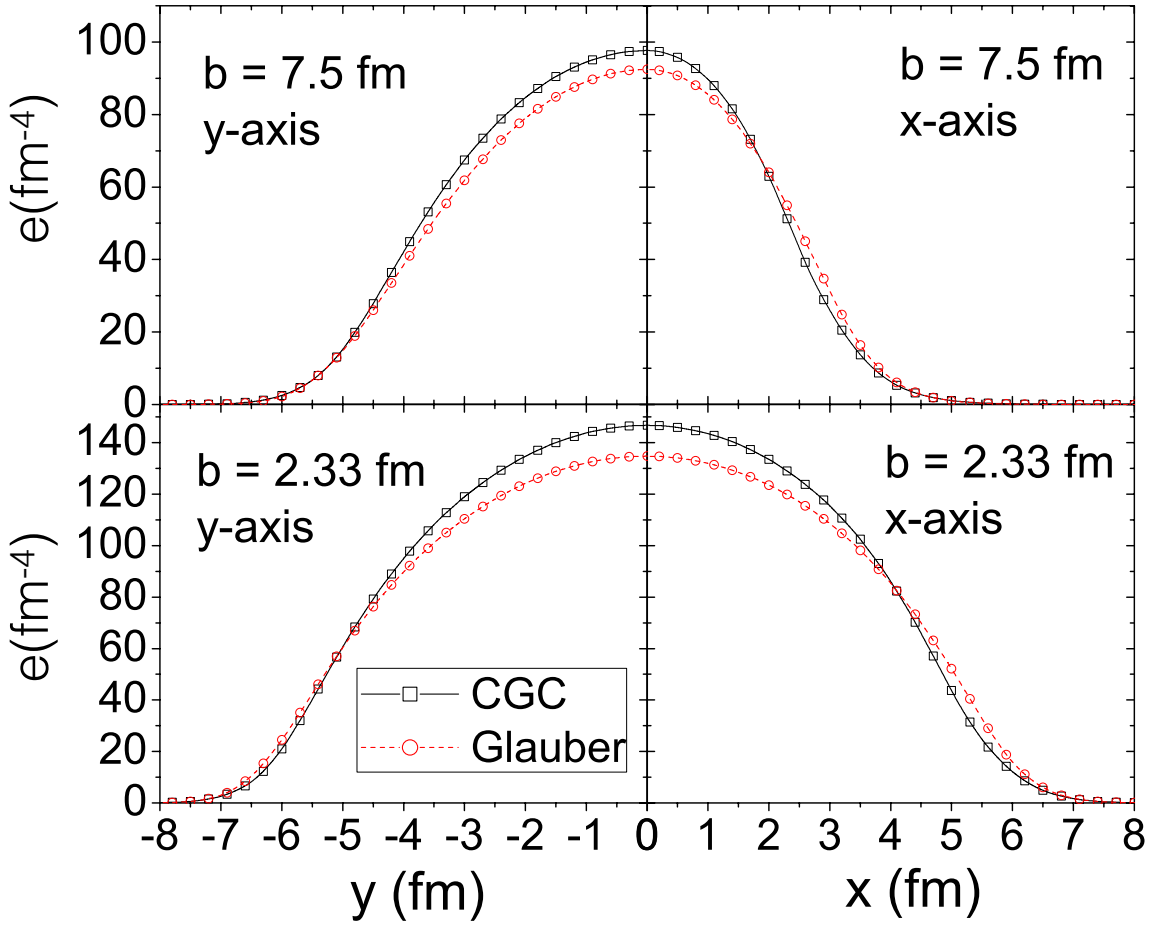

Figure 4.1: A comparison of initial energy density profiles at $\tau_0 = 0.4\,\mathrm{fm}/c$ for "central" ($b = 2.33\,\mathrm{fm}$, bottom) and "semi-peripheral" ($b = 7.5\,\mathrm{fm}$, top) Au+Au collisions from the Glauber and CGC-fKLN models. Shown are cuts along the x-axis (right panels) and y-axis (left panels). The two profiles are normalized to the same total entropy at $b = 2.33\,\mathrm{fm}$, using the EoS `s95p-v0-PCE` to convert energy to entropy density.

nucleon and 15% binary collision contributions to the entropy production [34]. For the CGC model we assume that the entropy density is proportional to the produced gluon density distribution, computed with the publicly available fKLN code [66]. In central Au+Au collisions, both profiles are normalized to the same total entropy (adjusted to reproduce the total final charged hadron multiplicity dN_{ch}/dy in these collisions) and converted to energy density using the equation of state `s95p-v0-PCE` [16]. With this normalization, both initializations correctly describe the centrality dependence of dN_{ch}/dy for *ideal* fluid dynamics.

With non-zero specific shear viscosity, viscous heating produces additional entropy, resulting in larger final multiplicities which we must correct for by renormalizing the initial entropy density profile in such a way that the final multiplicity is held fixed. This renormalization is performed in 0-5% most central Au+Au collisions. We keep the normalization factor fixed for the other non-central collisions. Since the viscous effects depend on the system size [67], the fractional increase

of the final entropy over its initial value is expected to be larger in peripheral than in central Au+Au collisions. We have checked that the centrality dependence of viscous entropy production is sufficiently weak so that it does not strongly modify the centrality dependence of $dN_{\rm ch}/dy$.

Figure 4.1 shows that the energy density profile from the CGC initialization has a steeper surface gradient than the Glauber profile. This leads to larger radial acceleration (i.e. radial flow develops more quickly) and is also in part responsible for the larger spatial eccentricity of the CGC profiles at nonzero impact parameters when compared to the Glauber eccentricities [34, 68].

Final state hadron spectra are calculated from the hydrodynamic output via the Cooper-Frye procedure [69],

$$E\frac{d^3N_i}{d^3p} = \frac{g_i}{(2\pi)^3}\int_\Sigma p\cdot d^3\sigma(x)\, f_i(x,p), \tag{4.1}$$

where Σ is the isothermal freeze-out surface with normal vector $d^3\sigma_\mu(x)$. After computing the spectra of all 319 hadronic resonances included in EoS `s95p-v0-PCE` from Eq. (4.1), we use the resonance decay program [70, 71] from the `AZHYDRO` package[4] to let the unstable resonances decay. The pion and proton spectra shown in this work include all strong decay products from strong decays.

4.3 Equation of State

Hydrodynamic equations have to be solved together with the equation of state $\mathcal{P}(e, n_B)$ (EoS) of the medium. To study how the EoS affects the hadron spectra and elliptic flow, we employ three different EOS for our hydrodynamic simulations.

- `SM-EOS Q` [38] : It implements a (slightly smoothed) first order phase transition between an ideal massless parton gas and a hadron resonance gas (HRG). It assumes the system to be in chemical equilibrium all the way down to kinetic freeze-out at temperature $T_{\rm dec}$.

- `EOS L` [67] : It is a rough attempt to match lattice QCD (LQCD) data [72] above $T_{\rm c}$ to the HRG in a smooth crossover transition. It assumes chemical equilibrium for the system at all temperatures.

- `s95p-v0-PCE` [16] : It interpolates between the HRG at low temperature and the lattice EoS at high temperatures, but the matching procedure is more sophisticated than the one used to construct `EOS L`, and the lattice EoS is based on the results by the hotQCD collaboration [73, 74]. Furthermore, below $T_{\rm chem} = 165\,{\rm MeV}$ temperature, the EoS is that of a *chemically frozen* HRG. We have considered as stable particles those with half-life larger than 40 fm/c. The matching procedure using a chemically equilibrated HRG is explained in detail in [16].

[4] `AZHYDRO` is available at the URL: `http://www.physics.ohio-state.edu/~froderma/`.

The procedure for the chemically frozen HRG is identical since the chemical freeze-out temperature is below the temperature where the interpolated EoS deviates from the HRG EoS. In the hadron resonance gas part, we included all resonances listed in the summary of the 2004 edition of the Review of Particle Physics [75] up to 2 GeV mass.

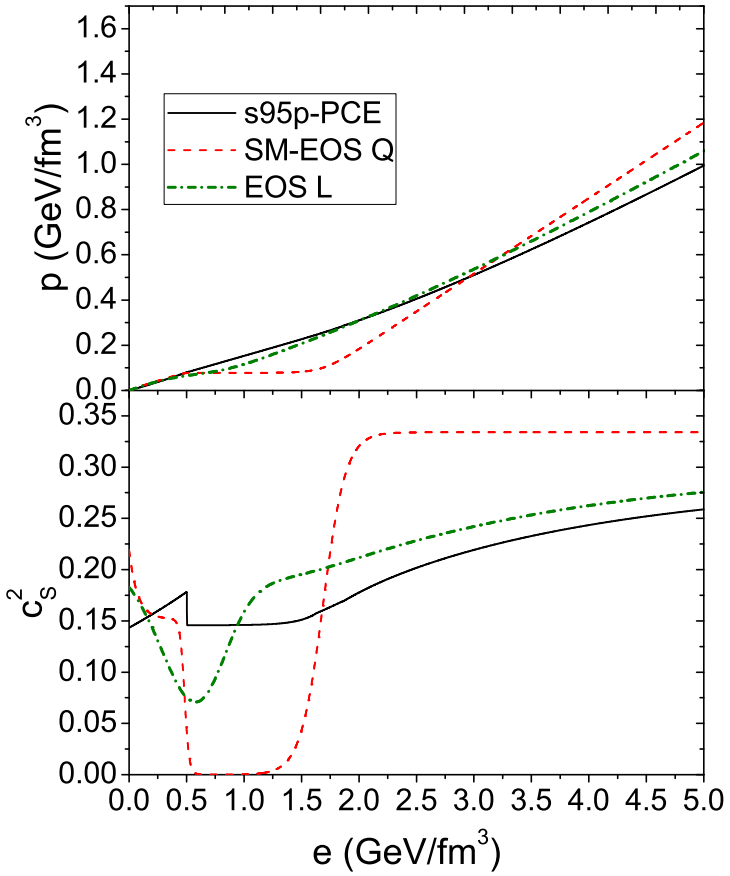

Figure 4.2: The three equations of state `s95p-v0-PCE`, `SM-EOS Q`, and `EOS L` used in this paper. The lower panel shows the squared speed of sound $c_s^2 = \frac{\partial p}{\partial e}$ as a function of energy density e whereas $p(e)$ is shown in the upper panel.

The partial chemical equilibrium in `s95p-v0-PCE` is built using the standard procedure in the literature: Below $T_{\rm chem}$ the ratios of stable hadron yields are fixed to their chemical equilibrium values at $T_{\rm chem}$ by finite non-equilibrium chemical potentials $\mu_i(T)$ [76, 77, 78, 79, 80]. It is worth noting that the ratios of individual particle densities are not conserved. What is conserved are the ratios of the *total densities* of stable particles, $\bar{n}_i$, where total density means the sum of the actual density of species i and the additional density of the same species that would arise if all unstable resonances in the system were allowed to immediately and irreversibly decay. The rapid processes that form and decay resonances through strong interactions are still in equilibrium, and thus the resonance populations are in equilibrium with the populations of their daughter particles (see [76, 77] for a detailed discussion). We describe the numerical implementation of partial chemical equilibrium in the EOS in Appendix D.

In practice the chemically frozen EoS is evaluated assuming that the evolution is isentropic and the ratios $\bar{n}_i/s$ stay constant. Strictly speaking this is not the case in viscous hydrodynamics since dissipation causes an increase in entropy. However, the viscous entropy production in the region where $T < T_{\rm chem} = 165\,{\rm MeV}$ was checked and found to be small ($\sim 4\%$ of the total entropy production for $\eta/s = 0.16$ in Au + Au collisions at 20-30% centrality). So our EoS is a good approximation of the physical EoS.

We compare the three equations of state in Fig. 4.2. The upper panel shows the pressure and the lower panel the squared speed of sound as a function of the local energy density e. The discontinuity in $c_s^2(e)$ at $e \sim 0.5\,{\rm GeV/fm^3}$ for `s95p-v0-PCE` is due to a sudden breaking of chemical equilibrium at $T_{\rm chem} = 165\,{\rm MeV}$. We have checked that it has negligible consequences for the expansion dynamics. Fig. 4.2 shows that in the QGP phase `s95p-v0-PCE` is much softer than `SM-EOS Q`. It approaches the Stefan Boltzmann limit more slowly than `EOS L` in the high temperature limit. But `s95p-v0-PCE` is much harder in the phase transition region around $T_{\rm c}$ and below, which will cause the fireball to expand and cool rapidly through the phase transition [81]. The EOS `s95p-v0-PCE` has a rapid crossover transition between quarks and hadrons according to lattice QCD calculation. Contrary to `SM-EOS Q` and `EOS L`, there is no well-defined "softest point" [82] which would cause the fireball to spend an extended time period in the critical region.

4.4 Spectra and elliptic flow

In this section, we study the dependence of the transverse momentum spectra in central $200\,A\,{\rm GeV}$ Au+Au collisions (0-5% centrality, $b = 2.33\,{\rm fm}$) and the elliptic flow $v_2(p_T)$ in semi-peripheral collisions (20-30% centrality, $b = 7.5\,{\rm fm}$) for pions, protons and (for v_2) all charged hadrons, on the EoS and various input parameters discussed in Secs. 4.2 and 4.3. We have also checked that everything we find below for central collision spectra also applies, at the same level of precision, to the azimuthally averaged spectra in semi-peripheral collisions.

We use the PHENIX results [83, 84] as guidance for only a qualitative comparison. A serious dynamical model fit to the RHIC data will be presented in Chapter 5.

In the following we show hadron spectra and elliptic flow up to transverse momenta of $3\,{\rm GeV}/c$ only for illustrative purposes, which does not necessarily imply that hydrodynamics can provide a valid description up to such large p_T. We will focus on the comparison with the experimental data below $p_T < 1.5$ GeV for pions and $p_T < 2.5$ for protons [85]. Specifically for pions, since the hard (pQCD) physics becomes dominant at high $p_T > 2.5$ GeV (experimental spectra transit from a exponential to a power-law shape), we will discard the discrepancy in the spectra above $p_T \sim 1.5\,{\rm GeV}$.

4.4.1 η/s-dependence at fixed $\tau_0 = 0.4\,\mathrm{fm}/c$ and $T_{\mathrm{dec}} = 140\,\mathrm{MeV}$

Transverse momentum spectra of pions and protons with different η/s used in the hydrodynamic simulations are are shown in Fig. 4.3 (and in the upper left panel of Fig. 4.4) for the most central Au+Au collisions. We find that larger η/s-values result in flatter spectra; the effect is particularly strong for protons at low p_T. This is because larger shear viscosity helps the system to develop more radial transverse flow from the positive shear viscous contribution to the effective transverse pressure gradients at early times [86, 87, 88].

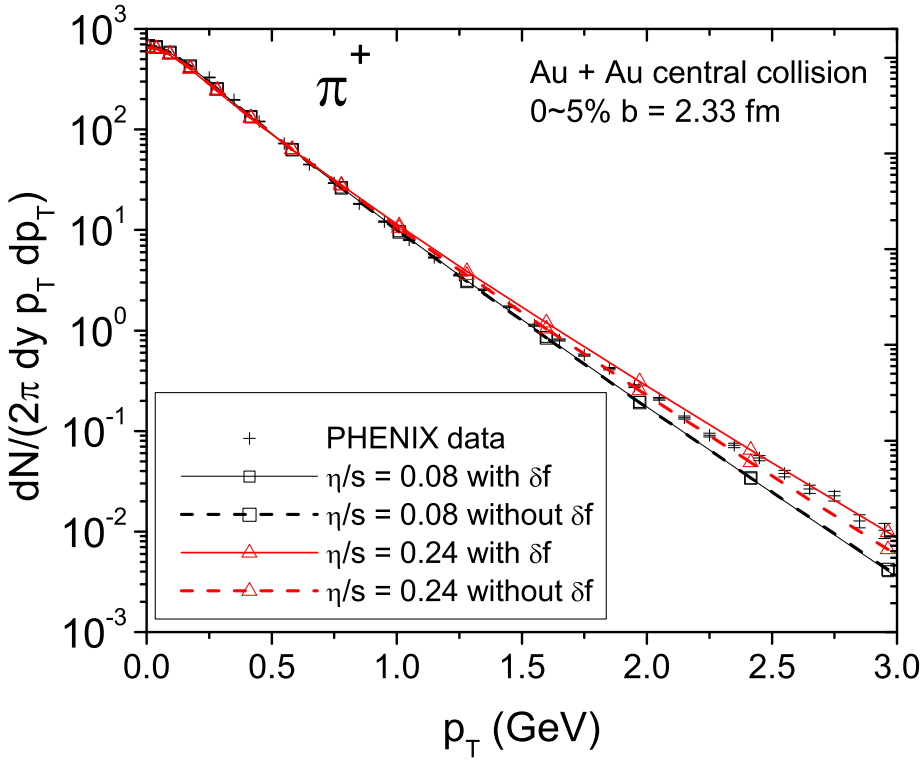

Figure 4.3: Pion spectra for 200 A GeV Au+Au collisions at 0-5% centrality from `VISH2+1`, compared with PHENIX data [84]. Results for two different constant values of η/s (0.08 and 0.24) are shown; strong resonance decays are included. Solid and dashed lines show the spectra calculated from the full distribution function $f = f_{\mathrm{eq}} + \delta f$ ("with δf") and from the equilibrium part only ("without δf"). The hydrodynamic evolution starts at $\tau_0 = 0.4\,\mathrm{fm}/c$ with an initial CGC energy density profile and ends at $T_{\mathrm{dec}} = 140\,\mathrm{MeV}$. The EoS is `s95p-v0-PCE`.

Figure 4.3 shows a detailed study of how the shear viscosity affects the hadron spectra. Using large $\eta/s = 0.16$ or 0.24 with `s95p-v0-PCE`, we find that the viscous correction due to the non-equilibrium deviation δf of the distribution function on the freeze-out surface further hardens the particle spectra at $p_T \gtrsim 1\,\mathrm{GeV}/c$[5]. The sign of the δf contribution is sensitive to the EOS and the value of η/s used for the hydrodynamic evolution. `s95p-v0-PCE` gives the same sign

[5] As we have shown in Chapter 2.5, the Landau matching conditions require the δf correction to integrate to zero when summing over all momenta, so a positive δf contribution at high p_T implies a negative δf contribution at low and/or intermediate p_T.

for δf as found in [89] (for a different EoS) but opposite to what had been found earlier with VISH2+1 for smaller values of η/s using SM-EOS Q (i.e. for a first order phase transition) [38]. (For $\eta/s = 0.08$ Fig. 4.3 shows a *negative* δf correction for pions at large p_T, of *same* sign but much smaller magnitude than found earlier [38] with Glauber initial conditions and SM-EOS Q). Our finding confirms the fragility of the sign of δf that was already discussed in [38][6].

The total shear viscous correction to hadron spectra comes from the time-integrated effects of the shear viscous pressure on the radial flow and the "instantaneous" effect of the viscous correction δf to the distribution function on the freeze-out surface.

For $\eta/s = 0.08$ we see in Fig. 4.3 that with s95p-v0-PCE the δf correction to the pion spectrum is almost negligible, but the upper left panel in Fig. 4.4 shows that the pion and proton spectra are still flatter than for the ideal fluid, reflecting the larger radial flow caused by the shear viscous increase of the transverse pressure gradients [38]. Thus both the effect of viscosity on radial flow *and* δf contribute to the flattening of the hadron spectra.

With s95p-v0-PCE, pion and proton spectra in Fig. 4.4 prefer a relatively large shear viscosity, $\eta/s = 0.16 \sim 0.24$ when compared with the PHENIX measurements.

Now, we proceed to discuss the elliptic flow. For the charged hadron v_2 in the lower left panel of Fig. 4.4, a larger shear viscosity leads to a smaller elliptic flow. The shear viscosity acts to reduce the differences between the fluid velocity components along different directions, hence it suppresses the development of the momentum anisotropy during the hydrodynamic evolution. In the right panels in Fig. 4.4, we further study this suppression in detail by performing additional calculations of the elliptic flow keeping only the equilibrium distribution function in the Cooper-Fyre formula (dotted lines in Fig. 4.4). The comparison between the full results (dashed and dash-dotted lines) and the results without δf helps us to disentangle the suppression from the viscous reduction of the time-integrated buildup of anisotropic collective flow and the additional viscous suppression of v_2 caused by the δf correction.

We find that both suppression effects increase monotonically with shear viscosity. Each effect contributes about 50% to the suppression seen in the final results. (This is not the case for thermal photon elliptic flow as will be shown in Chapter 19.)

Compared to the measured charged hadron elliptic flow, we find that the data favor a small $\eta/s = 0.08 - 0.16$ in our calculations. This is in contrast to the preferred large $\eta/s = 0.16 - 0.24$

[6]For EOS L and SM-EOS Q and $\eta/s > 0.08$, we find a negative sign of the δf contribution to both pion and proton spectra at high p_T, while the corresponding contribution is positive in the case of s95p-v0-PCE. The negative sign appears to be correlated with the use of an EoS with a "softest point". From ideal fluid dynamic simulations with such first-order or almost-first-order phase transitions we know that the rapid change of c_s^2 in the transition region generates strong structures in the radial velocity profile in fireball regions that are close to the critical temperature [30], and that these structures partially survive until the matter has reached decoupling. We suspect that velocity gradients associated with these structures play an important role in generating for EOS L and SM-EOS Q a negative δf contribution to the spectra at high p_T.

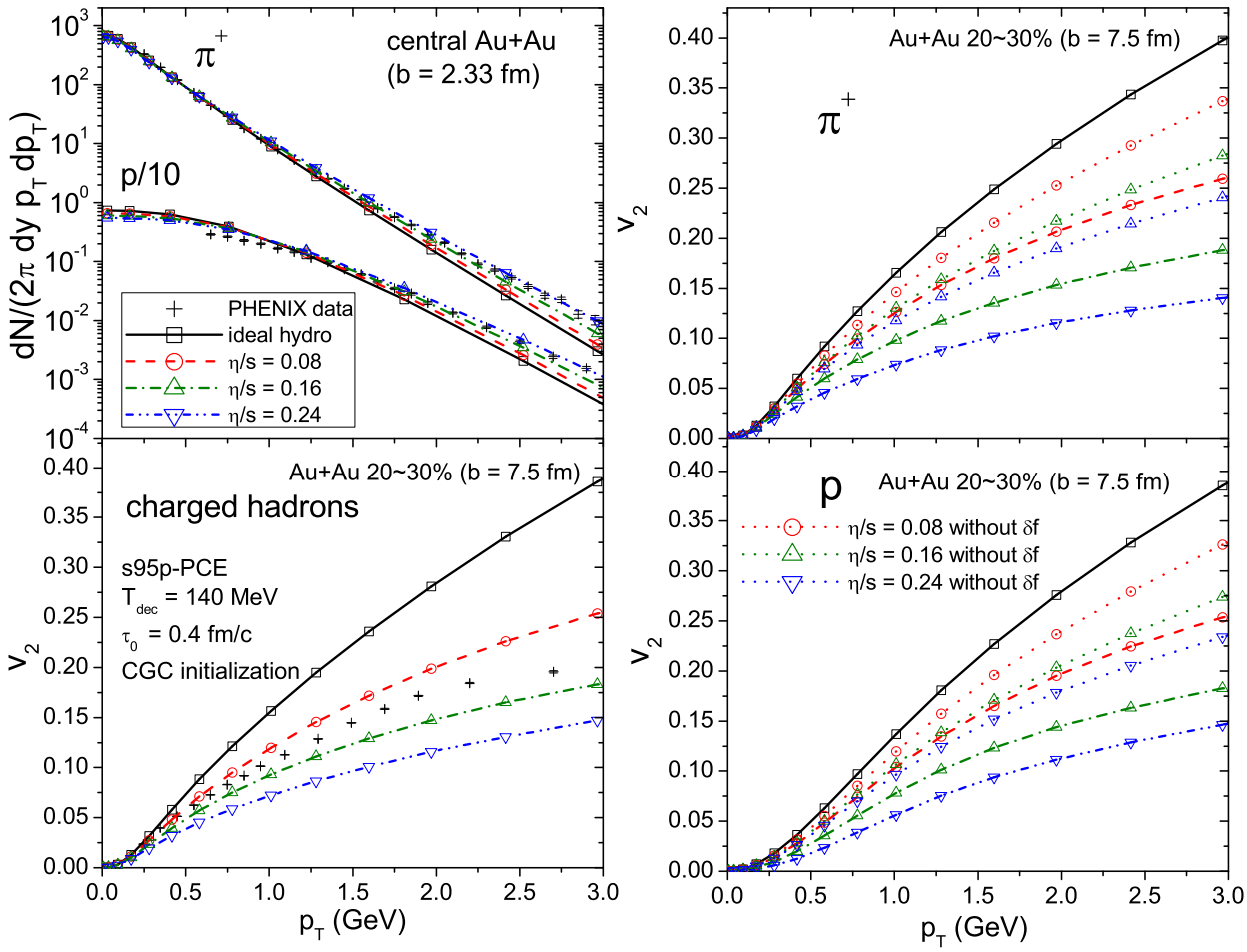

Figure 4.4: *Upper left panel:* Transverse momentum spectra $dN/(2\pi\, dy p_T\, dp_T)$ (GeV^{-2}) for positive charged pions and protons in the 0-5% most central Au+Au collisions ($b = 2.33$ fm), compared with experimental data from the PHENIX Collaboration [84]. *Lower left panel:* Differential elliptic flow $v_2(p_T)$ for charged hadrons from Au+Au collisions at 20-30% centrality ($b = 7.5$ fm), compared with PHENIX data [83]. *Right panels:* $v_2(p_T)$ for pions (top) and protons (bottom). Results of elliptic flow computed with only equilibrium part of the distribution function are indicated as the dotted lines for comparisons. All strong resonance decays are included; charged hadrons comprise $\pi^{\pm}$, $K^{\pm}$, p, $\overline{p}$, $\Sigma^{\pm}$, $\overline{\Sigma}^{\mp}$, Ξ^{-}, $\overline{\Xi}^{+}$, Ω^{-}, and $\overline{\Omega}^{+}$. The EoS, initial and final conditions are the same as in Fig. 4.3.

from the measured slope of the p_T spectra. However, please note that our calculations are based on using the initial conditions from the optical models which do not include initial state fluctuation effects. As will be shown in the later chapters, fluctuation effects largely remove this tension between particle p_T spectra and v_2.

4.4.2 $T_{\rm dec}$-dependence at fixed $\tau_0 = 0.4\,\mathbf{fm}/c$ and $\eta/s = 0.16$

In Fig. 4.5 we explore the sensitivity of spectra and elliptic flow on the value of the decoupling temperature $T_{\rm dec}$, holding all other parameters fixed. We choose $\tau_0 = 0.4$ fm/c, $\eta/s = 0.16$, and EOS `s95p-v0-PCE` for the calculations.

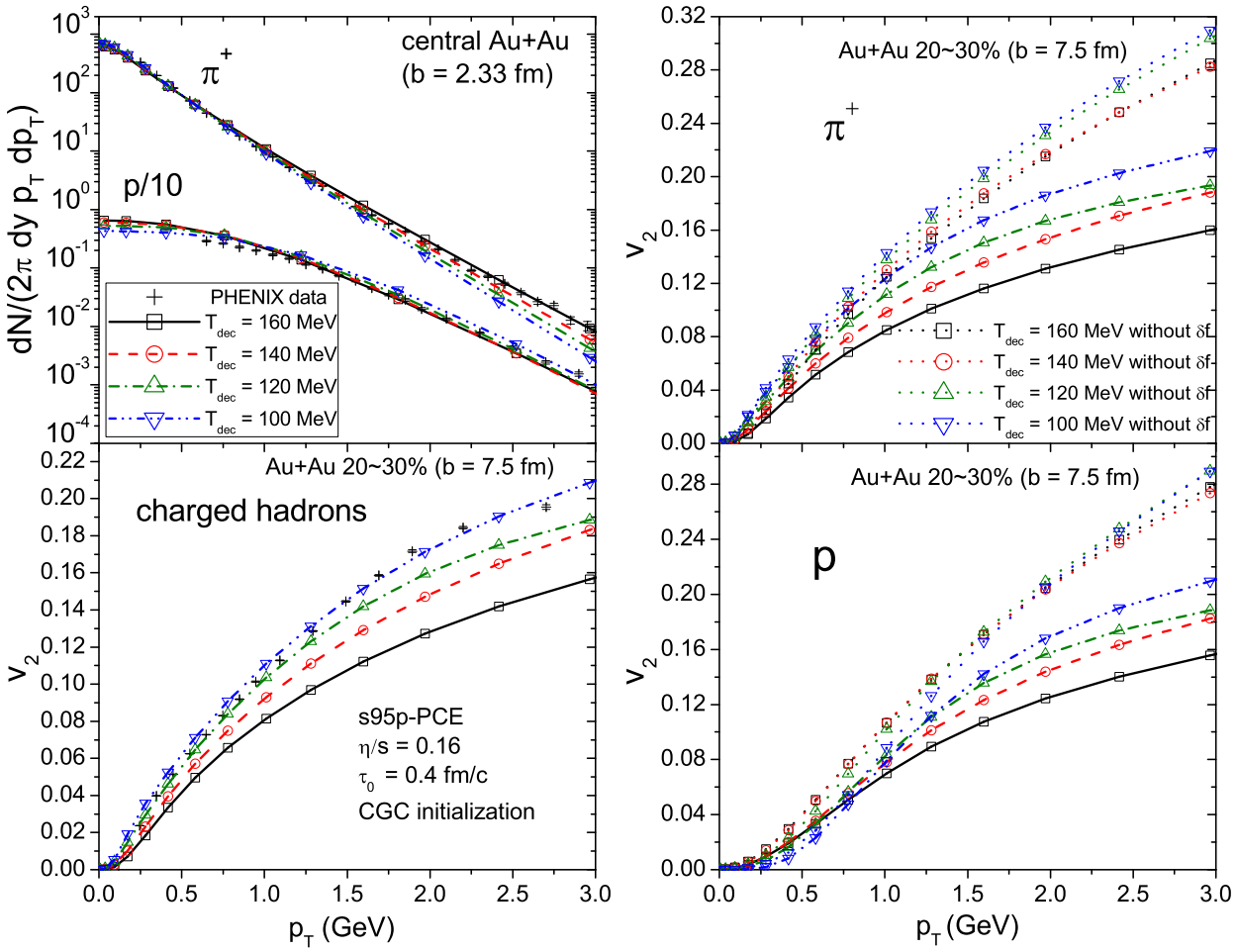

Figure 4.5: Similar to Fig. 4.4, but for fixed $\eta/s = 0.16$ and varying decoupling temperature $T_{\rm dec}$ ranging from 100 to 160 MeV as indicated.

In the top left panel, we find that the pion and proton spectra react differently to the freeze-out temperature. The pion spectra become *steeper* as $T_{\rm dec}$ is lowered (this agrees with [90]). This is because pions can be considered as almost massless on the scale of measured transverse momenta ($\langle p_T \rangle \sim 0.6$ GeV). The inverse slope of their p_T-spectrum receives relativistic blueshift effect from hydrodynamic radial flow. It can be estimated as $T_{\rm slope} = T_{\rm dec}\sqrt{\frac{1+\langle v_\perp \rangle}{1-\langle v_\perp \rangle}}$ where $\langle v_\perp \rangle$ is the average radial flow at $T_{\rm dec}$ [91, 92]. As the $T_{\rm dec}$ decreases, the cooling effect overwhelms the flattening effects resulting from the associated increase of $\langle v_\perp \rangle$, causing a net softening of the pion spectra for lower freeze-out temperatures. On the other hand, a lower freeze-out temperature leads to a flatter proton spectra. This is because the heavier protons receive a larger push to higher p_T from radial flow than the lighter pions, which is well known from [91, 92]. In contrast to pions, the relatively large rest mass of proton can not be neglected anymore. Thus, its spectrum is dominated by the growing radial flow over the temperature cooling. The additional radial flow built up during the extra time the fireball needs to cool down to lower $T_{\rm dec}$ makes the proton spectra flatter.

From the lower left panel of Fig. 4.5 one sees that lower decoupling temperatures lead to larger elliptic flow $v_2(p_T)$ for charged hadrons. To fully understand this systematics it is worth comparing charged hadrons to the p_T-spectra and $v_2(p_T)$ of pions (upper left and right panels, respectively) which dominate the charged hadron yield. The observed tendency reflects a combination of three effects:

(i) Since the p_T-spectrum of pions (which dominate the charged hadrons) gets steeper, even the same hydrodynamic momentum anisotropy would lead to a larger slope of $v_2(p_T)$, to compensate for the lower yield at high p_T.

(ii) Since the fireball hasn't lost all of its eccentricity by the time the QGP converts to hadrons [38], additional momentum anisotropy is generated during the hadronic stage. Lower decoupling temperatures give the system time to develop more momentum anisotropy, leading to a larger v_2. If the p_T-spectrum stays unchanged or gets steeper (as is the case for pions in Fig. 4.5), a larger v_2 must lead to a larger $v_2(p_T)$. The combination of effects (i) and (ii) is seen in the dotted lines in the upper right panel, which reflect the hydrodynamic flow anisotropy at decoupling, undistorted by viscous corrections δf to the local equilibrium distributions at freeze-out. The effect (ii) decreases with increasing η/s in the hadronic phase (not shown here), so the combined effect may be weaker than seen in Fig. 4.5 if viscous hydrodynamics is replaced by a microscopic hadron cascade such as UrQMD in the hadronic phase.

(iii) The (negative) viscous corrections from δf to v_2 are smaller at lower temperatures, due to the general decrease of the viscous pressure components [38]. This contributes the largest fraction of the observed increase of $v_2(p_T)$ with decreasing $T_{\rm dec}$, especially at large p_T.

Combining the information from the two left panels in Fig. 4.5 we conclude that both the proton spectra in central collisions and charged hadron $v_2(p_T)$ in peripheral collisions favor decoupling temperatures near the lower end of the window studied here (i.e. $T_{\rm dec} = 100\,{\rm MeV}$ works better than $T_{\rm dec} = 140\,{\rm MeV}$). The pion spectra are affected by variations of $T_{\rm dec}$ mostly at $p_T \sim 1 - 1.5\,{\rm GeV}/c$ where they fall increasingly below the experimental data as we lower $T_{\rm dec}$. However, this is also the region where the hydrodynamic description of the pion spectra is known to begin to break down [85], due to the gradual transition from soft to hard physics which causes the pion spectrum to change from an exponential to a power-law shape. Focusing therefore on the region $p_T < 1.5\,(2.5)\,{\rm GeV}/c$ for pions (protons), we conclude that a purely hydrodynamic description of the experimental data favors freeze-out temperatures near 100 MeV.

The right panels of Fig. 4.5 show how $T_{\rm dec}$ affects the elliptic flow of different identified hadrons. Charged hadrons mostly reflect the behavior of the dominating pions whose $v_2(p_T)$ increases with decreasing freeze-out temperature. But protons behave differently: At low $p_T < 1\,{\rm GeV}$, their elliptic flow decreases with decreasing decoupling temperature, while at high p_T it increases with decreasing $T_{\rm dec}$. The latter feature reflects the increasing hydrodynamic momentum anisotropy

and decreasing magnitude of the δf correction, just like it is reflected in the pion and charged hadron v_2. The decrease of proton v_2 at low p_T, on the other hand, is a consequence of having larger radial flow at lower $T_{\rm dec}$ which pushes the protons to larger p_T. So, rather than thinking of this effect as a decrease of proton v_2 at fixed p_T, we should think of it as shifting the elliptic flow to larger p_T.

4.4.3 τ_0-dependence at fixed $\eta/s = 0.16$ and $T_{\rm dec} = 140\,\mathrm{MeV}$

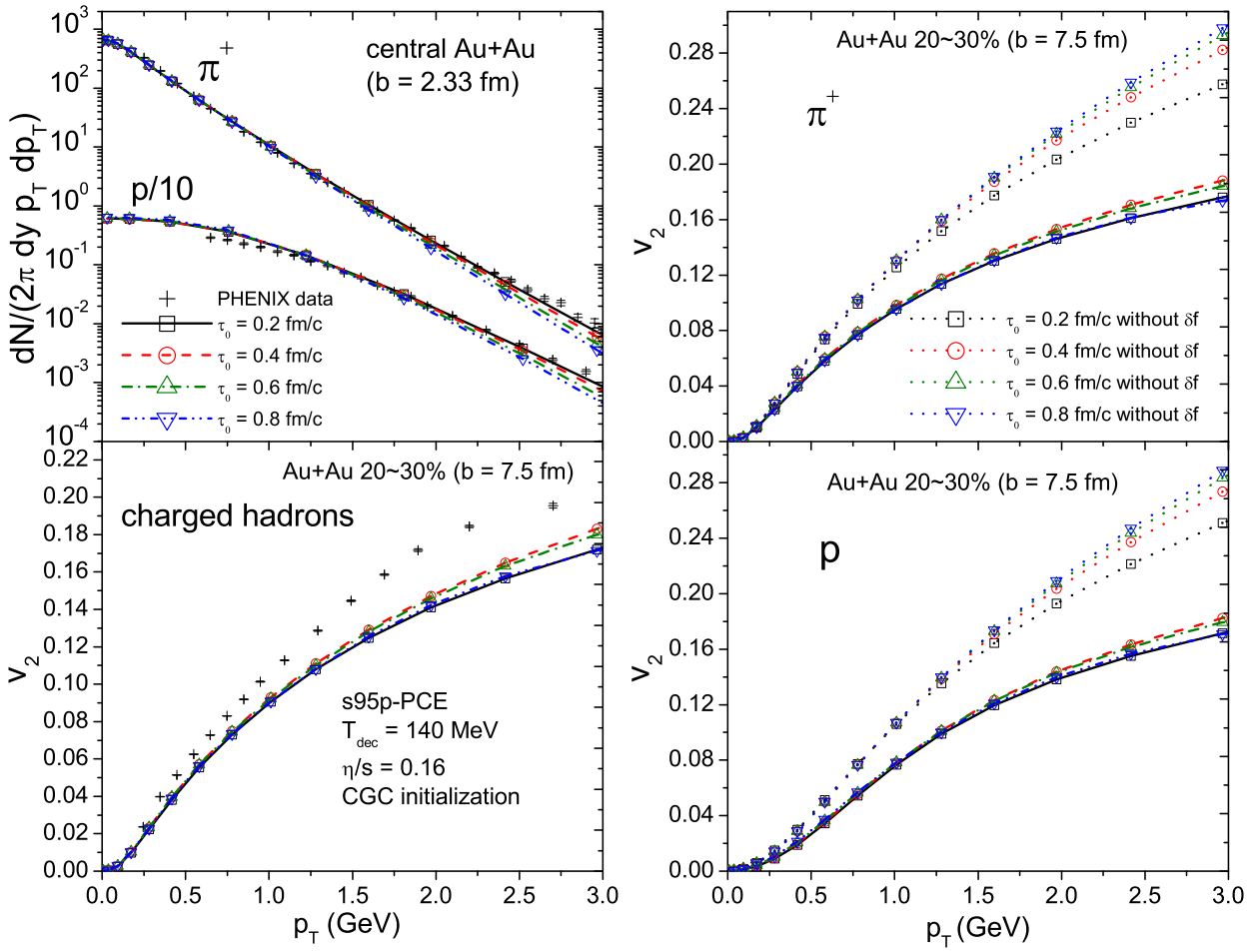

Figure 4.6: Similar to Fig. 4.4, but for fixed $\eta/s = 0.16$ and varying starting time τ_0 for the hydrodynamic evolution, ranging from 0.2 to 0.8 fm/c as indicated.

The upper left panel of Fig. 4.6 shows that the pion and proton spectra react similarly to a change of the starting time τ_0 of the hydrodynamic evolution. Since both pion and proton spectra get flatter with a smaller τ_0, we conclude that the system develops more radial flow if we start the hydrodynamic evolution earlier. An earlier starting time allows the fireball the generate radial flow earlier, but it also cools down the fireball faster. The net effect is still a slight increase of the average radial flow at freeze-out.

For soft momenta $p_T < 1.5\,\mathrm{GeV}/c$, the effect of τ_0 on $v_2(p_T)$ is negligible. This is true even for protons, showing that the increase of radial flow with decreasing τ_0 is a small effect and not enough to visibly push the proton v_2 to larger p_T. At higher p_T, the dependence of the charged hadron, pion and proton v_2 on τ_0 is non-monotonic. The right panels of Fig. 4.6 show that this non-monotonic behaviour is the result of two counteracting tendencies which both depend on τ_0 monotonically: (i) The elliptic flow computed from the local equilibrium part f_{eq} of the distribution function at freeze-out increases monotonically with increasing τ_0, reflecting the longer total fireball lifetime (and thus the longer time available to build up momentum anisotropy) when the hydrodynamic evolution starts later. (ii) The v_2-suppression resulting from the viscous correction δf at freeze-out also increases monotonically with increasing τ_0. We don't have a complete understanding of why starting (and thus also ending) the hydrodynamics later leads to a larger δf on the decoupling surface; we suspect that since the hydrodynamical flow would eventually settle into a three-dimensional spherically symmetric Hubble flow with no shear stress, starting earlier leads to a stronger transverse flow, and thus to a flow profile which is closer to a spherically symmetric flow at the time of decoupling.

4.4.4 EoS dependence at fixed $\tau_0 = 0.4\,\mathbf{fm}/c$, $\eta/s = 0.16$, and $T_{\mathrm{dec}} = 140\,\mathbf{MeV}$

In Fig. 4.7 we study the sensitivity of hadron spectra and elliptic flow on the equation of state, holding all other hydrodynamic parameters fixed (except for the normalization of the initial energy density profile which is again adjusted to ensure constant final multiplicity in central Au+Au collisions).

We first note a lower proton yield from the hydrodynamic runs with `EOS L` and `SM-EOS Q` compared to the case using `s95p-v0-PCE`. This is because with the chemical equilibrium EOS (`EOS L` and `SM-EOS Q`), we allow protons to annihilate with anti-protons all the way down to kinetic freeze-out, whereas such annihilation processes are forbidden in the partial chemical equilibrium `s95p-v0-PCE` below $T_{\mathrm{chem}} = 165$ MeV. To explore how this affects the hydrodynamic flow, we should concentrate on the *shape* (i.e. inverse slopes) of the pion and proton spectra. `EOS L` produces the flattest spectra, followed by `SM-EOS Q`, whereas the spectra from `s95p-v0-PCE` are steepest. This is because for fixed freeze-out temperature, we find `s95p-v0-PCE` produces the weakest radial flow averaged over the freeze-out surface, `EOS L` generates the strongest flow, with `SM-EOS Q` falling in between.[7] The reasons for `s95p-v0-PCE` generating less radial flow than the other two equations of state are an interplay between a few subtle effects. The key difference lies in the partial chemical equilibrium that, at a fixed freeze-out temperature, causes the

[7] We have checked that the viscous δf correction do not change the hierarchy of the slope of particle p_T spectra.

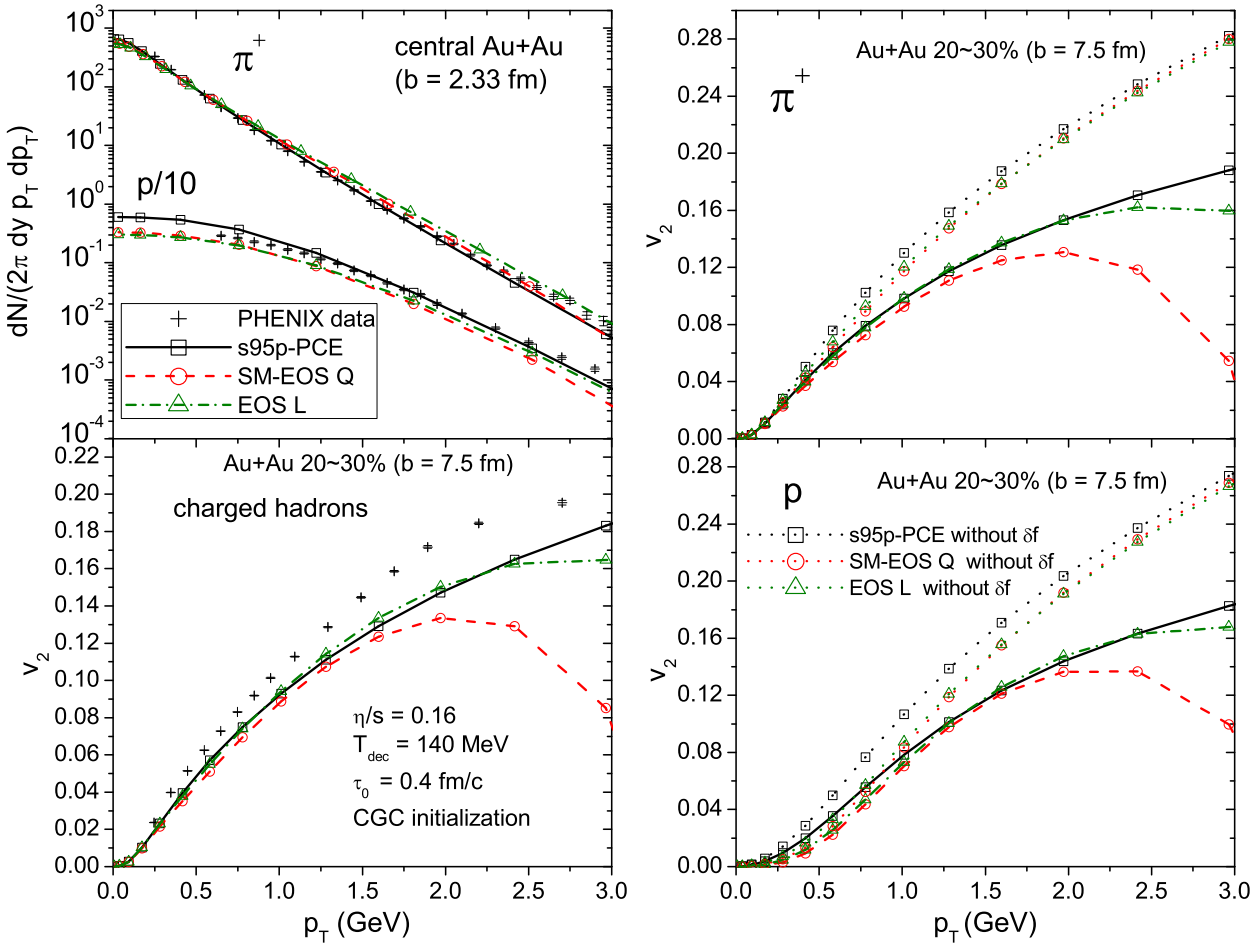

Figure 4.7: Similar to Fig. 4.4, but for fixed $\eta/s = 0.16$ and different equations of state (`SM-EOS Q`, `EOS L`, and `s95p-v0-PCE`) as indicated. Since `SM-EOS Q` and `EOS L` have different chemical composition than `s95p-v0-PCE` at $T_{\rm dec} = 140\,$MeV, they yield fewer protons than `s95p-v0-PCE` when normalized to the same pion yield.

chemically frozen HRG embodied in `s95p-v0-PCE` to have a considerably larger energy density ($e_{\rm dec} = 0.301\,{\rm GeV/fm}^3$ at $T_{\rm dec} = 140\,$MeV) than the chemically equilibrated HRG used in `EOS L` and `SM-EOS Q` (which has $e_{\rm dec} = 0.143\,{\rm GeV/fm}^3$ at the same temperature) [77]. This is due to the larger-than-equilibrium abundances of of baryon-antibaryon pairs and mesons that are prohibited from annihilating as the system cools below $T_{\rm chem}$. So the fireball has less lifetime when evolved with `s95p-v0-PCE`, and its space-time volume is also smaller compared to the other two cases. The differences in speed of sound during the evolution largely cancel out (see Ref. [16]).

The charged hadron, pion and proton elliptic flows $v_2(p_T)$ exhibit quite large sensitivity to the EoS, especially at high p_T. Most of this sensitivity comes in through the δf correction at freeze-out which is particularly large for `SM-EOS Q`. The reason for this is that the first-order phase transition leads to large velocity gradients at the QGP-to-mixed-phase and mixed-phase-to-HRG interfaces [30] which are largely but not completely washed out by viscous effects [38] and leave traces on

the decoupling surface. δf effects are weaker with the smoother `EOS L` than with `SM-EOS Q` even though `EOS L` generates on average more radial flow.

To discuss the contribution from collective flow anisotropies to pion and proton $v_2(p_T)$ we focus on the dotted lines in the right panels of Fig. 4.7. We see that, while `s95p-v0-PCE` creates less radial flow, it generates a larger flow *anisotropy* (we checked this by direct computation), resulting in larger $v_2(p_T)$ for *both* pions and protons than with the other two equations of state. For `EOS Q` it was found in [78, 77, 80] that if the kinetic freeze-out temperature $T_{\rm dec}$ is adjusted to reproduce the p_T-spectra, the correct implementation of chemical freeze-out at $T_{\rm chem}$ in the HRG phase increases the mass-splitting between $v_2(p_T)$ of pions and protons at low p_T. On the other hand, if the freeze-out temperature is kept constant, the mass-splitting at low p_T decreases [77]. Since we have kept the freeze-out temperature fixed in our calculations, we see a similar phenomenon here: The elliptic flow mass splitting between pions and protons is weaker for the chemically frozen `s95p-v0-PCE` than for the chemically equilibrated `EOS L` and `SM-EOS Q`. This is a consequence of the weaker radial flow generated by `s95p-v0-PCE`.

4.4.5 Dependence on the shape of the initial energy density profile (CGC vs. Glauber)

We close with a discussion of the influence of the shape of the initial energy density profile on the hadron spectra and elliptic flow, using the Glauber and CGC-fKLN models as examples. Their energy density profiles are shown in Fig. 4.1.

The energy density gradient is slightly larger in the CGC profile compared to the Glauber one. The spatial gradient of the pressure (or energy density) controls the acceleration of the fluid flow velocity as shown in the ideal hydrodynamic equation

$$\dot{u}_\nu = \frac{\nabla_\nu P}{e+P} \simeq \frac{c_s^2}{1+c_s^2}\frac{\nabla_\nu e}{e}, \tag{4.2}$$

where we approximate $P = c_s^2 e$ with $c_s^2 = \frac{dP}{de}$. So the CGC energy density profile leads to a larger radial acceleration compared to the Glauber one. Indeed, the upper left panel of Fig. 4.8 exhibits slightly flatter pion and proton spectra for CGC-initialized simulations than for Glauber initial conditions.

In Fig. 4.8, we find that the CGC-initialized runs give larger elliptic flow coefficients for charged hadrons, pions and protons than for the Glauber initial conditions. This is due to the larger initial eccentricity of the CGC density profiles [34, 61, 36, 68] which drives the system to develop a larger momentum anisotropy. The influence on the p_T-dependence of the proton v_2 due to the slightly stronger radial flow from the CGC initialization is negligible compared to the effects coming from the larger initial eccentricity. The δf suppression of v_2 is similar for CGC and Glauber initial conditions.

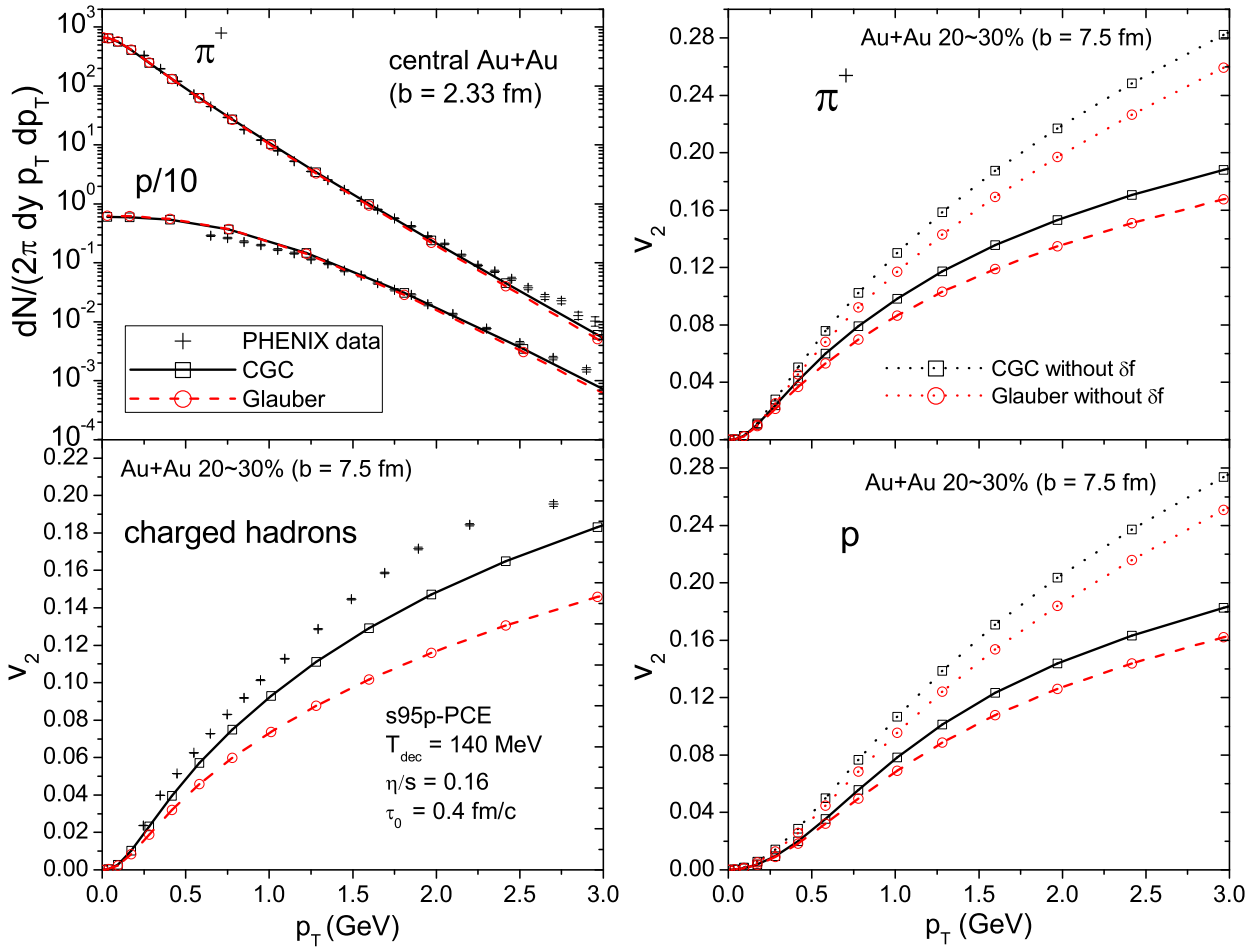

Figure 4.8: Similar to Fig. 4.4, but for fixed $\eta/s = 0.16$ and different initial energy density profiles (Glauber vs. CGC) as indicated. The elliptic flow from an initial CGC density profile is larger than for the Glauber initialization, due its larger initial eccentricity.

4.5 Chapter conclusion

In this chapter, we have performed a systematic study of the dependence of the pion and proton transverse momentum spectra and their p_T-dependent elliptic flow on the thermalization time τ_0, initial energy density profile, equation of state, freeze-out temperature and specific shear viscosity in (2+1)-dimensional viscous hydrodynamic simulations. We find that the shear viscosity helps the system to develop more radial flow but suppresses the momentum anisotropy. The final observed particle spectra and v_2 are affected from the viscous modification of the hydrodynamic evolution as well as the off-equilibrium δf correction on the Cooper-Frye freeze-out surface. Both contributions are important and increase with η/s. The kinetic freeze-out temperature $T_{\rm dec}$ affects pion spectra differently than proton spectra. A lower $T_{\rm dec}$ gives the system more time to develop hydrodynamic radial and elliptic flow. The system's momentum anisotropy is monotonically related to the charged hadron p_T-integrated elliptic flow coefficient. The particle p_T-differential elliptic flow coefficient is a result of the interplay between hydrodynamic radial and integrated elliptic flow.

We saw very little sensitivity to the choice of the termalization time τ_0, but for larger values of τ_0 we did not allow for the development of pre-equilibrium flow and the pre-equilibrium evolution of the shear stress tensor, that would be expected in a more realistic description. A more detailed study on the pre-equilibrium stage evolution is needed in the future, especially if the beginning of the hydrodynamic stage were delayed by slow thermalization to times $\tau_0 > 1$ fm/c.

Chapter 5: Radial and elliptic flow in Pb+Pb collisions at the Large Hadron Collider from viscous hydrodynamics

5.1 Chapter introduction

In this chapter, we will perform a global fit of the particle spectra and elliptic flow coefficients at top RHIC energy based on our systematic study of hydrodynamic simulations in Chapter 4. Then we will consider this as our starting point for an extrapolation to Pb + Pb collisions at $\sqrt{s} = 2.76$ and 5.5 A TeV. We would like to explore to what extent the present and future LHC elliptic flow data can tell us novel facts about the transport behavior of hot QCD matter at temperatures that exceed those accessible at RHIC but are within reach at the LHC. This work reported here is based on Ref. [48].

5.2 Hydrodynamic fit of RHIC Au+Au data

We employ (2+1)-d viscous hydrodynamics [39] with the lattice QCD based equation of state `s95p-v0-PCE` [16, 17], which accounts for chemical freeze-out before thermal decoupling at $T_{\rm chem} = 165\,\mathrm{MeV}$, to simulate the expansion of the collision fireball. Different from Chapter 4, we use the initial energy density profiles generated from the Monte-Carlo KLN (MCKLN) model. We first generate 10,000 fluctuating initial energy density profiles from MCKLN model, recenter and rotate them such that the main axis of each event's elliptic deformation lines up with each other. Then we compute the event average of these profiles to get a smooth initial energy density profile. Due to event-by-event fluctuations, this smooth density profiles has non-zero eccentricity even for fully central ($b = 0$) collisions. We choose the value of $\eta/s = 0.20$ (corresponding to MC-KLN initial conditions) for the effective specific shear viscosity of the strongly interacting fluid. Using the insights obtained from the systematic parameter study presented in Chapter 4 [17], we initialize the hydrodynamic expansion at time $\tau_0 = 0.6\,\mathrm{fm}/c$ and decouple at $T_{\rm dec} = 120\,\mathrm{MeV}$ at both RHIC and LHC energies. For Au+Au collisions at RHIC energies these parameters allow for a good global description of the hadron p_T-spectra and differential elliptic flow. Lacking strong theoretical or phenomenological guidance how to adjust their values for Pb+Pb collisions at the

LHC, we here decided to keep them unchanged. (We emphasize that this study was done before the LHC data become available.) We initialize the shear stress tensor by its Navier-Stokes value $\pi^{\mu\nu} = 2\eta\sigma^{\mu\nu}$ and assume zero initial flow, $(u^\tau, u^x, u^y, u^\eta) = (1, 0, 0, 0)$.

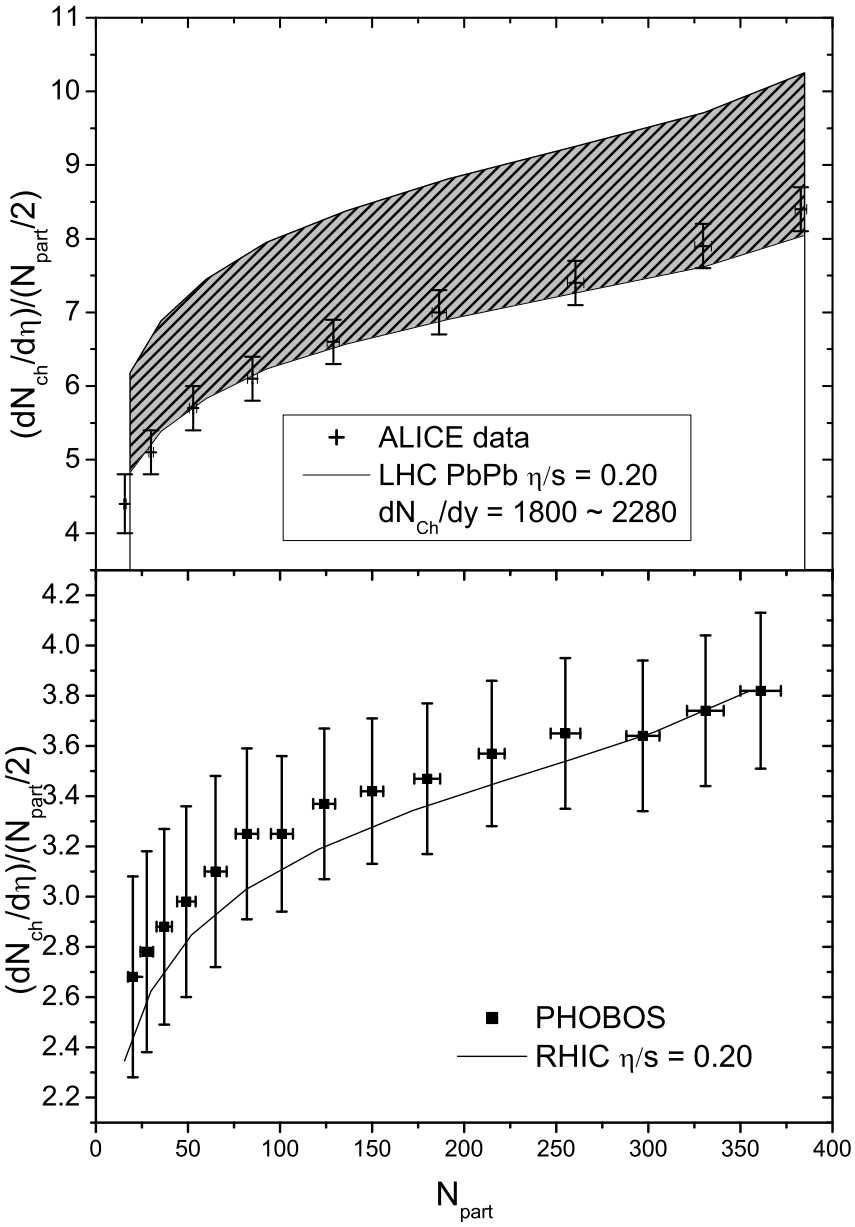

Figure 5.1: Centrality dependence of the charged hadron multiplicity per unit pseudo-rapidity, $dN^{\rm ch}/d\eta/(N_{\rm part}/2)$ as a function of $N_{\rm part}$, in 200 A GeV Au+Au collisions at RHIC (bottom panel) and in $(2.76 - 5.5)$ A TeV Pb+Pb collisions at the LHC (top panel). Experimental data are from the PHOBOS Collaboration [93] for Au+Au collisions at $\sqrt{s} = 200\,A\,$GeV, and from the ALICE Collaboration [94] for Pb+Pb collisions at $\sqrt{s} = 2.76\,A\,$TeV. The lines are from the MC-KLN model (see text). For Au+Au at RHIC the MC-KLN model was normalized to the measured multiplicity in the 0-5% centrality bin; at the LHC, the lines bounding the shaded region were normalized to $dN^{\rm ch}/d\eta = 1548$ and 1972 (or $\frac{dN}{dy} = 1800$ and 2280) at 0-5% centrality, respectively.

Due to the viscous entropy production during the hydrodynamic evolution, we perform an iterative renormalization of the initial entropy density profile until the measured charged hadron multiplicity in the 0−5% most central 200 A GeV Au+Au collisions at RHIC is reproduced. In the lower panel of Fig. 5.1, we show our results of the centrality dependence of the charged multiplicity compared with the PHOBOS measurements [93] at RHIC energy. The centrality dependence of $dN_{\rm ch}/d\eta$ is controlled by the initial condition model. Our calculations contain extra viscous entropy production which is relatively larger in peripheral than in central collisions [39]. But we find that its effect is (at least at RHIC energies) sufficiently weak and does not destroy the agreement of the model with experimental observations that was observed earlier in ideal fluid dynamical studies.

The reason for us to choose the MCKLN model over the MC-Glauber model for the initial conditions of our hydrodynamic simulations is that the MCKLN model can describe the centrality dependence of charged hadron production without additional parameters, which help us to eliminate one of the model parameter uncertainties when we extrapolate our calculations to LHC energies. (In the MC-Glabuer model we would also need to guess the hard/soft ratio at LHC energies.) It was recently shown [95] that this centrality dependence is robust against running coupling corrections [96, 97, 98] in the Balitsky-Kovchegov evolution (on which the KLN model is based) which were found to hardly affect its shape. They do, however, modify the collision energy dependence of particle production, with the LHC Pb+Pb data being better described if running coupling corrections are included [94]. Our version of the MC-KLN model does not include running coupling corrections,[8] and we must normalize the initial entropy density profile for Pb+Pb collisions at the LHC separately from Au+Au collisions at RHIC. Without such an independent renormalization, we overpredict the measured charged multiplicity from central 2.76 A TeV Pb+Pb collisions [99, 94] by about 10%.

At LHC energy, after renormalization we obtain the solid lines bounding the shaded region in the upper panel of Fig. 5.1, with the lower (upper) bound corresponding to Pb+Pb collisions at 2.76 (5.5) A GeV, respectively. The data in that panel are from the ALICE Collaboration for Pb+Pb at 2.76 A GeV [99, 94]. (For 5.5 A GeV Pb+Pb collisions we assumed $\frac{dN}{dy} = 2280$ (corresponding to $dN^{\rm ch}/d\eta = 1972$), based on an extrapolation of Fig. 3 in Ref. [99].) We can see that the centrality dependence of charged hadrons in our calculations is slightly flatter than the experimental data. Part of the reason is due to the viscous entropy production, which is relatively stronger in the peripheral collisions. But overall, the MCKLN model, even without running coupling corrections, does a good job in describing the measured centrality dependence of charged hadron production in Pb+Pb collisions at the LHC. This gives hope that the successful description of the centrality dependence of hadron spectra and elliptic flow at RHIC energies

[8] The `rcBK` code in [95] includes running coupling corrections but it has not been renormalized to take into account viscous entropy production at RHIC energies.

(see below and Ref. [40]) translates into a reliable prediction of the corresponding centrality dependences in Pb+Pb collisions at the LHC.

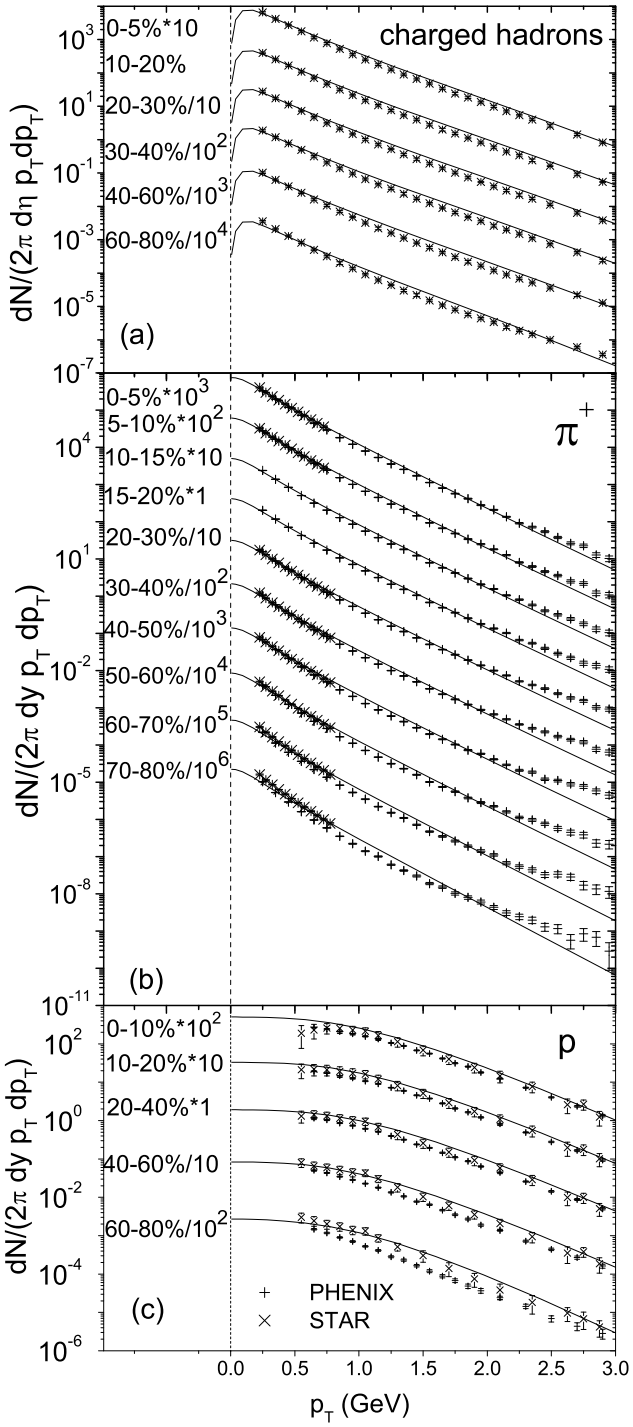

Figure 5.2: p_T-spectra of all charged hadrons (a), positive pions (b) and protons (c) for 200 A GeV Au+Au collisions of different centralities as indicated. The symbols show data from the STAR ([100, 101, 102], $\times$) and PHENIX ([103, 84], +) experiments. The lines are results from the viscous hydrodynamic model for constant $\eta/s = 0.20$ and MC-KLN initial conditions. Particle spectra are in unit of GeV^{-2}.

Figures 5.2 and 5.3 shows our global fits of the measured particle spectra and their elliptic flow coefficients at top RHIC energy, which establish our baseline for the extrapolation to LHC energies. The used parameter set τ_0, η/s, $T_{\rm chem}$, and $T_{\rm dec}$ is described above. Please note that compared to the global fit with more advanced hydro + hadron cascade hybrid approach, the starting time of our pure hydrodynamic simulation ($\tau_0 = 0.6\,{\rm fm}/c$) is 45% smaller than the value of $1.05\,{\rm fm}/c$ used for $\eta/s = 0.2$ in the hybrid simulations in [40]. We think the earlier evolution of hydrodynamic transverse flow arising from this smaller τ_0 value compensates for the lack of a highly dissipative hadronic phase in the purely hydrodynamic approach. Hadronic dissipation leads to a significant broadening in particular of the proton p_T-spectra during the hadronic stage which (given the constraints from the elliptic flow data which prohibit us from simply lowering $T_{\rm dec}$) viscous hydrodynamics with temperature-independent $\eta/s = 0.2$ cannot replicate.

The fit to the hadron spectra measured in $200\,A\,{\rm GeV}$ Au+Au collisions at RHIC is shown in Fig. 5.2 for all the centrality bins from central to peripheral. On the logarithmic scale, our calculations give a fairly good description of particle spectra in the central collision, but are too flat in the peripheral cases. Fig. 5.2a shows the mid-rapidity transverse momentum spectra per unit pseudo-rapidity for unidentified charged hadrons from the STAR [100] and PHENIX [103] experiments compared with the hydrodynamical model. Figs. 5.2b,c show a similar comparison for the p_T-spectra per unit rapidity of identified pions and protons from STAR [101, 102] and PHENIX [84]. In the experimental spectra, protons from weak decays were removed; STAR quotes a large systematic error associated with this feeddown correction, and within that large error band the two data sets agree with each other, even if the central values of the STAR proton data appear to be up to 50% higher than PHENIX data. Our results agree well with the STAR protons for $p_T > 0.6\,{\rm GeV}/c$ but overpredict the PHENIX protons by up to a factor 2. (We now know [104] that baryon-antibaryon annihilation below T_c, which can be accounted for, in a hydrodynamic + cascade hybrid approach, decreases the normalization of the proton spectra by 35-40%, which would lead to better agreement with the PHENIX than with STAR proton spectra.)

Figure 5.3 shows the charged hadron p_T-differential elliptic flow comparison between our calculation and the STAR $v_2\{4\}(p_T)$ data [105], for four centrality classes ranging from semi-central to mid-peripheral collisions (10−50% centrality). Our viscous hydrodynamics gives an excellent description of the STAR $v_2\{4\}$ data, even up to $3\,{\rm GeV}/c$ in transverse momentum.

In Chapter 4 [17], we noted a potential tension in fitting the proton p_T-spectra and the charged hadron differential elliptic $v_2^{\rm ch}\{2\}(p_T)$ simultaneously using `s95p-v0-PCE` within a purely viscous hydrodynamic approach. But in Figs. 5.2 and 5.3, we see that this tension is largely resolved when using the $v_2\{4\}(p_T)$ data (Fig. 5.3) instead of $v_2\{2\}(p_T)$ (see Fig. 5.8 further below). Strictly speaking, the $v_2\{2\}$ data (also known as the rms elliptic flow coefficient) receives positive contribution

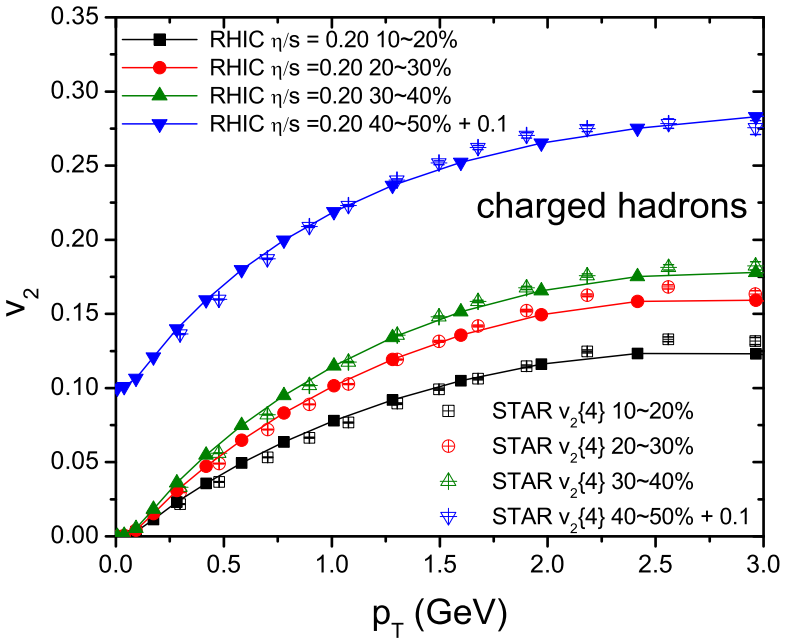

Figure 5.3: Differential elliptic flow $v_2(p_T)$ for charged hadrons from 200 A GeV Au+Au collisions of different centralities as indicated. Open symbols are experimental data from the STAR experiment for $v_2\{4\}(p_T)$ [105], lines with filled symbols of the same shape are the corresponding hydrodynamic fits with the same model as in Fig. 5.1. For the 40−50% centrality bin data and theory are vertically offset by 0.1 for better visibility.

from the event-by-event fluctuation. So our current calculations should lie in between the $v_2\{2\}$ and $v_2\{4\}$ measurements. The tension we saw in Chapter 4 is somewhat exaggerated.

Overall, the viscous fluid dynamic description of the hadron spectra and charged hadron elliptic flow $v_2(p_T)$ shown here is of similar quality as the hybrid model description with presented in [40]. We will now use them to generate a broad range of predictions for soft hadron production in Pb+Pb collisions at the LHC.

5.3 Predictions and follow-up comparisons for Pb+Pb collisions at the LHC

Based on the global fit to the RHIC data, we now keep τ_0, $T_{\rm chem}$, $T_{\rm dec}$ and η/s fixed and extrapolate to LHC energies. Our goal here is to use the comparison between our LHC prediction with later on measured experimental data to search for indications from experiment that would motivate changing these parameters. The first results for p_T-spectra [106] as well as both the p_T-differential and p_T-integrated elliptic flow of charged hadrons [52] were published and will be compared with the theoretical predictions below. Further experimental measurements on identified hadrons spectra and elliptic flow were reported in [107, 108] and will be compared with our predictions [49] too.

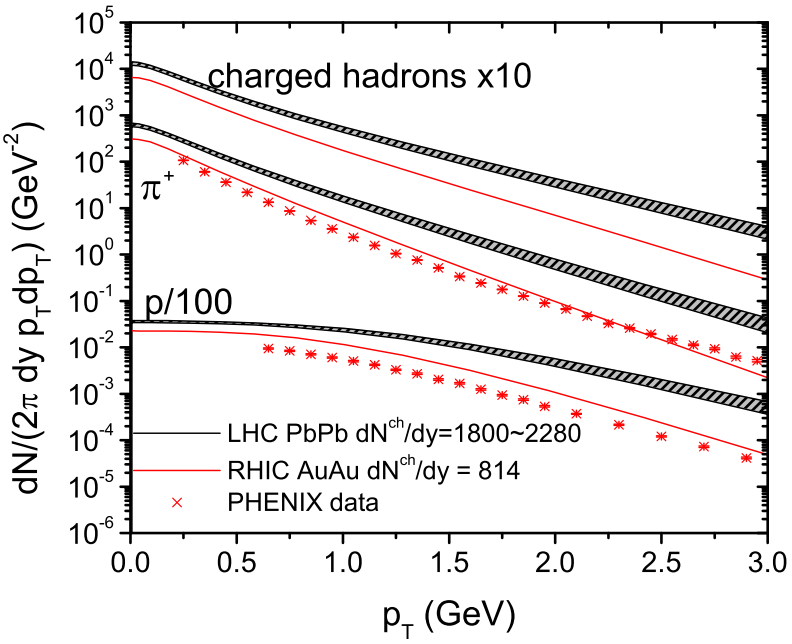

Figure 5.4: p_T-spectra of all charged hadrons, positive pions, and protons for minimum bias 200 A GeV Au+Au (thin red lines and data points) and (2.76−5.5) A TeV Pb+Pb collisions (black lines with shaded area). The RHIC data are from the PHENIX experiment [84]. The shaded bands for the LHC predictions are limited at the bottom (top) by lines for $\sqrt{s} = 2.76$ (5.5) A TeV, corresponding to $\frac{dN}{dy} = 1800$ (2280) ($dN_{\rm ch}/d\eta = 1548$ (1972)). The calculations assume the same constant $\eta/s = 0.2$ at all shown collision energies.

In Fig. 5.4 we show the transverse momentum spectra for all charged hadrons, as well as for identified pions and protons, for minimum bias collisions of Au+Au at RHIC and Pb+Pb at the LHC.[9] Identified particle spectra at the top RHIC energy are compare with the PHENIX measurements [84]. We indicate our prediction at $\sqrt{s} = 2.76$ and 5.5 A TeV as the upper and lower bounds of the shaded areas. We find that the particle spectra at LHC energies are flatter than at the top RHIC energy, reflecting stronger radial flow. This is due to a longer fireball lifetime at LHC energies (about 19% and 24% longer than Au+Au at RHIC, respectively, for 0-5% most central collisions at 2.76 and 5.5 A TeV collision energies). The average radial flow velocity increases in central collisions (0−5% centrality) by 5 and 7%, respectively, and in peripheral collisions (70−80% centrality) by 9 and 11%.

Figure 5.5 shows the integrated charged hadron elliptic flow v_2 as a function of collision centrality for Au+Au collisions at RHIC and Pb+Pb collisions at the LHC. Our results at RHIC energy (lower red line) agrees nicely with $v_2\{\rm EP\}$ except for the most peripheral collisions[10]. Since we do

[9]To simulate minimum bias collisions, we compute the spectra for the centrality classes shown in Figs. 5.2(b) and 5.6 and average them. Any additional observables, such as the minimum bias elliptic flow in Fig. 5.8 below, are calculated from these minimum bias spectra.

[10]In very peripheral collisions, v_2 is not saturated due to the short fireball lifetime. In addition, the viscous effects are stronger in the small fireballs created in peripheral collisions. The experimental $v_2\{2\}$ and $v_2\{\rm EP\}$ measurements are, however, contaminated by non-flow effects, in particular in very peripheral collisions.

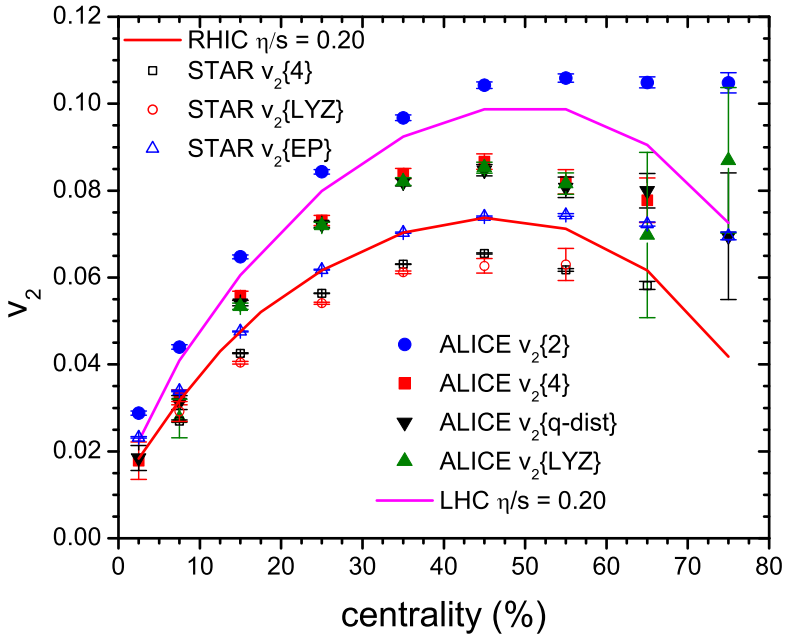

Figure 5.5: p_T-integrated elliptic flow of charged hadrons for 200 A GeV Au+Au collisions at RHIC (open symbols are STAR data [105], the lower red line is the result from viscous hydrodynamics) and for 2.76 A TeV Pb+Pb collisions at the LHC (filled symbols are ALICE data [52], the upper magenta line shows the viscous hydrodynamic prediction). In both experiment and theory the differential elliptic flow $v_2(p_T)$ (see Figs. 5.3 and 5.7) was integrated over the range $0.15\,\mathrm{GeV}/c < p_T < 2\,\mathrm{GeV}/c$ for Au+Au at RHIC and over $p_T > 0.2\,\mathrm{GeV}/c$ for Pb+Pb at the LHC.

not include event-by-event fluctuations, our v_2 overestimates the STAR $v_2\{4\}$ data by about 11% in mid-central collisions.

At first sight, since we have an excellent description of the differential elliptic flow $v_2\{4\}(p_T)$ shown in Fig. 5.3, the overprediction of the p_T-integrated $v_2\{4\}$ at RHIC is because our charged hadron p_T-spectra shown in Fig. 5.2 are somewhat harder than measured, thereby giving too much weight in the p_T-integral to the range $0.75 < p_T < 2\,\mathrm{GeV}/c$ where $v_2\{4\}(p_T)$ is large.[11]

At LHC energy ($\sqrt{s} = 2.76\,A\,\mathrm{TeV}$) our integrated v_2 lies between the $v_2\{2\}$ and $v_2\{4\}$ values measured by the ALICE Collaboration [52]. Again, we overpredict the p_T-integrated $v_2\{4\}$ by about 10−15%. We note that from RHIC to LHC the hydrodynamically computed integrated v_2 in mid-central to mid-peripheral collisions increases by about 30%, in agreement with the experimental observations. This is due to reduced viscous suppression effects in the larger and denser fireballs created at the LHC and a longer fireball lifetime which allows the momentum flow anisotropy to approach saturation more closely than at lower energies [21, 110]. In very peripheral collisions, even at LHC energies such a saturation of v_2 does not happen; this is the reason why

[11] The agreement with the $v_2\{\mathrm{EP}\}$ data is fortuitous and should, in fact, not happen since the measured $v_2\{\mathrm{EP}\}$ includes a positive contribution from event-by-event v_2 fluctuations [109] while our hydrodynamic calculation yields the average elliptic flow $\langle v_2 \rangle$ which is smaller.

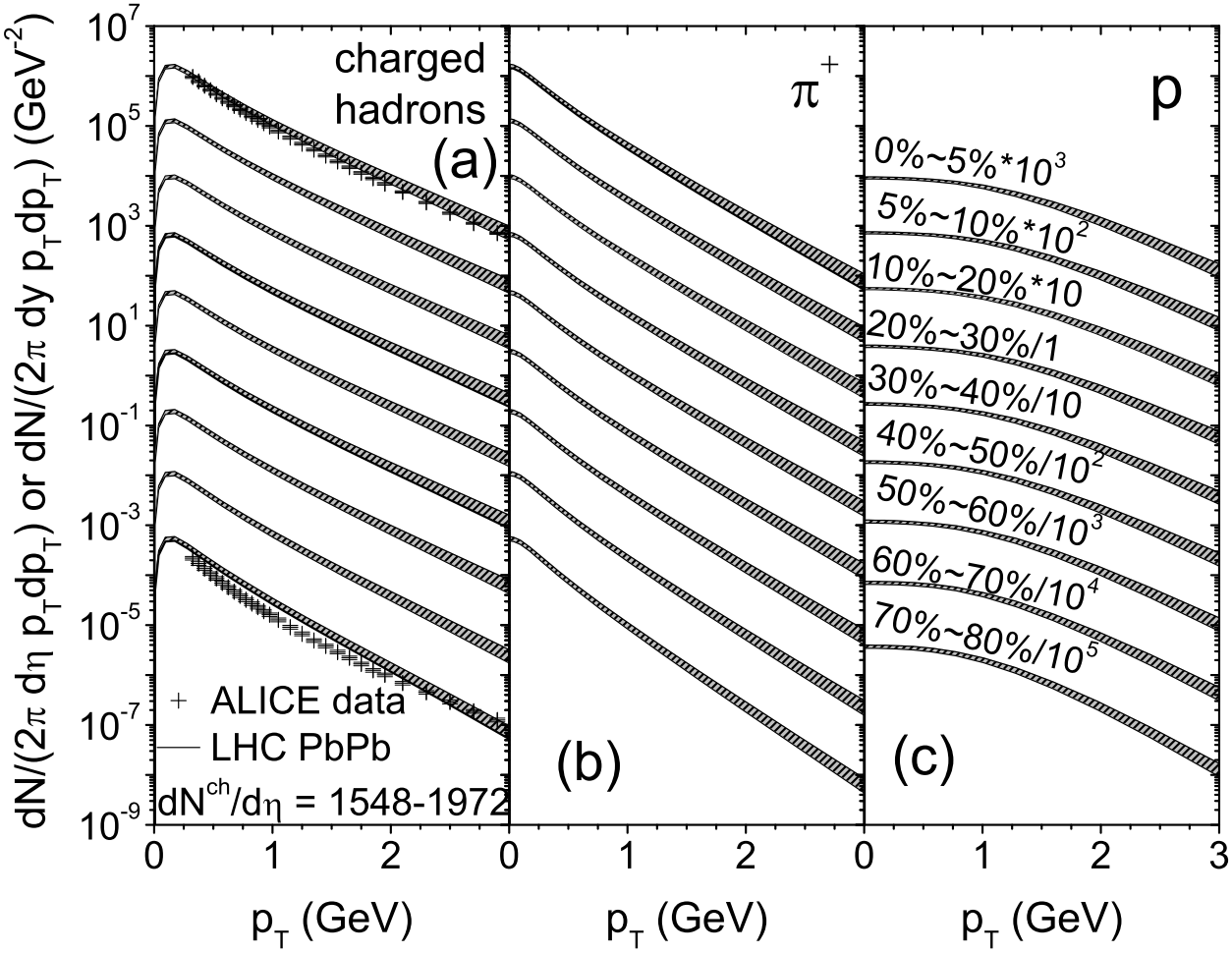

Figure 5.6: p_T-spectra per unit pseudorapidity for charged hadrons (a) and per unit rapidity for pions (b) and protons (c) for Pb+Pb collisions at the LHC. The lower and upper end of the shaded bands represent viscous hydrodynamic predictions for $\sqrt{s} = 2.76$ and $5.5\,A$ TeV (corresponding to $dN_{\rm ch}/d\eta = 1548$ and 1972, or $\frac{dN}{dy} = 1800$ and 2280), respectively. Experimental data in panel (a) are from the ALICE experiment [106]. A full comparisons with the ALICE measured identified particle spectra will be shown in Fig. 5.10.

in Fig. 5.5 the integrated v_2 is seen to decrease at large collision centralities, both at RHIC and LHC.

In Fig. 5.6 we present hadron transverse momentum spectra for Pb+Pb collisions at LHC energies, from central to peripheral centralities. In panel (a) we compare the hydrodynamic predictions with first data from the ALICE experiment [106]. Overall, we get a similar quality agreement with the experimental data as we had at the top RHIC energy (see Fig. 5.2). The shape of our charged hadron spectra at 2.76 A TeV agrees with the ALICE measurements quite well up to $p_T = 3$ GeV in the most central collisions, but is too flat in the very peripheral collisions.

We proceed to compare the differential $v_2^{\rm ch}(p_T)$ for charged hadrons with the ALICE $v_2\{4\}$ data [52] in Figure 5.7. For the 40-50% centrality, measurement of $v_2\{2\}$ is also available for comparison. Our predictions agree nicely with the data at low $p_T < 1\,{\rm GeV}/c$, but overshoot the experimental

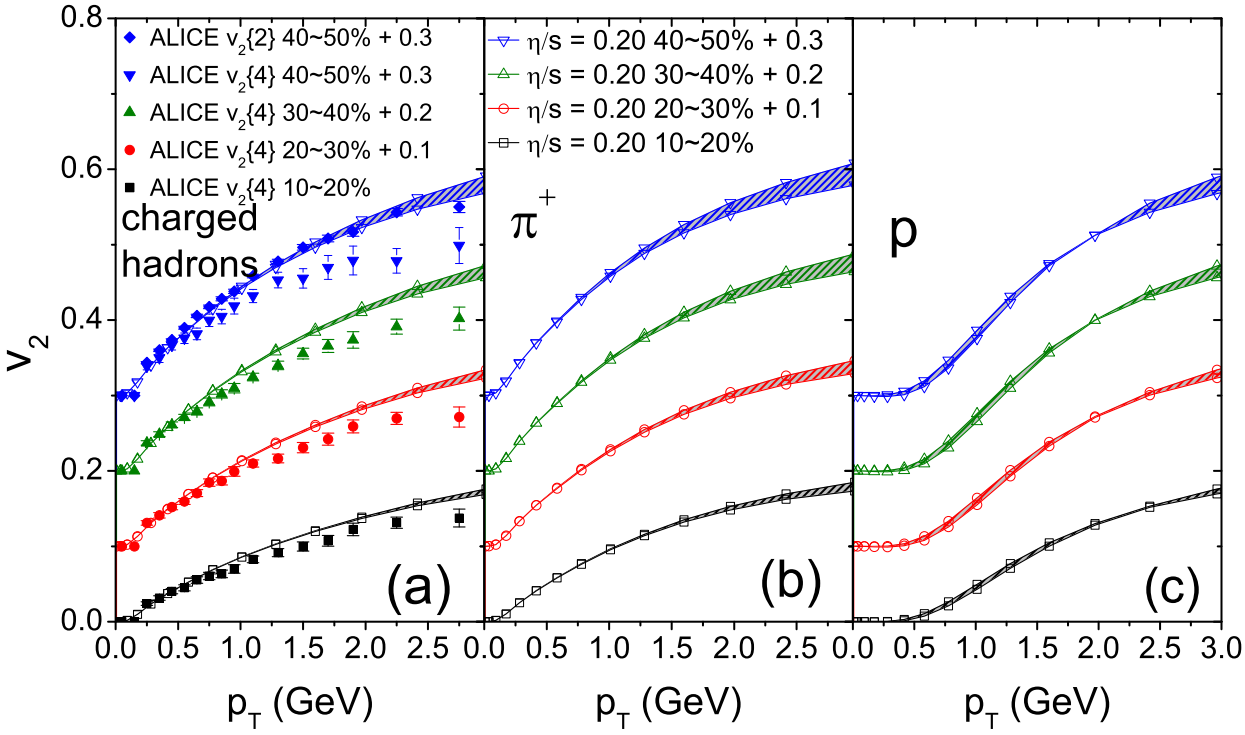

Figure 5.7: Differential elliptic flow $v_2(p_T)$ for charged hadrons (a) and identified pions (b) and protons (c), for Pb+Pb collisions of 4 different centralities at the LHC. Experimental data for charged hadron $v_2(p_T)$, denoted by solid symbols, are from the ALICE experiment [52]; they should be compared with theoretical lines carrying open symbols of the same shape and color. The shaded bands show the variation of the hydrodynamic predictions with collision energy between $\sqrt{s} = 2.76$ and 5.5 TeV (corresponding to $\frac{dN}{dy} = 1800$ and 2280, respectively). The lines corresponding to the lower collision energy ($\sqrt{s} = 2.76$ TeV) define the lower end of the shaded regions at $p_T = 3\,\mathrm{GeV}/c$.

values by 10−20% at larger p_T, especially in the more peripheral bins. In the 40−50% centrality bin, the theoretical prediction happens to agree nicely with $v_2\{2\}(p_T)$ even though the latter should be shifted upward by flow fluctuations that are not included in the theoretical calculation. Panels (b) and (c) of Fig. 5.7 give predictions for the differential $v_2(p_T)$ of identified pions and protons.

Please note the low-p_T elliptic flow of protons is pushed to larger p_T by the hydrodynamic radial flow. As the collision energy increases from $\sqrt{s} = 2.76$ and $5.5\,A\,\mathrm{TeV}$, we see that this "radial push" of the proton v_2 also increases. So for higher $\sqrt{s}$ the rise of $v_2(p_T)$ is shifted to larger transverse momenta, while at fixed $p_T < 1.5\,\mathrm{GeV}/c$ the proton elliptic flow *decreases* with increasing collision energy. This happens only for heavy hadrons but not for the much lighter pions (see panel (b)).

To further emphasize this, we directly compare identified particle differential elliptic flows at RHIC and LHC energies in Figs. 5.8 and 5.9. Fig. 5.8 shows the results for minimum bias collisions. Our RHIC results are compared with data from STAR [111]. The elliptic flow of charged hadrons

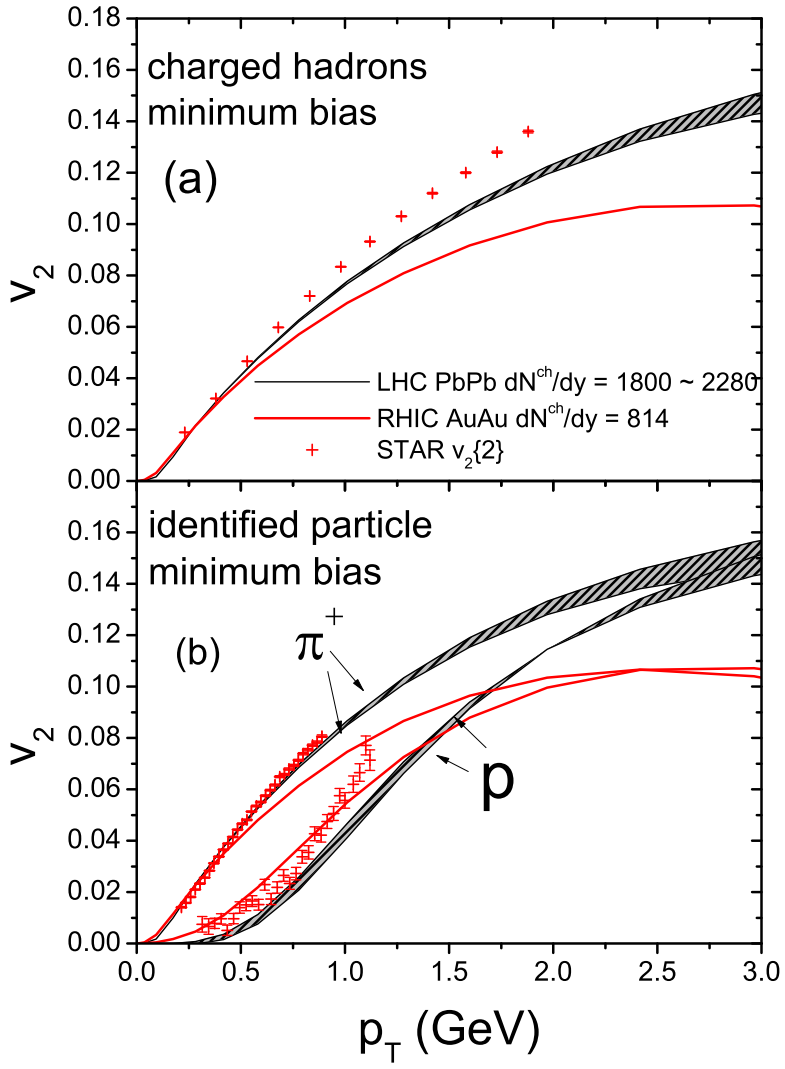

Figure 5.8: Differential elliptic flow $v_2(p_T)$ for all charged hadrons (a) and identified pions and protons (b), for minimum bias 200 A GeV Au+Au collisions at RHIC and (2.76−5.5) A TeV Pb+Pb collisions at the LHC. Experimental data for $v_2\{2\}$ from Au+Au collisions at RHIC are from the STAR experiment [111]. Solid lines are viscous hydrodynamic results for 200 A GeV Au+Au collisions with the same hydrodynamic parameters as in Figs. 5.1-5.4; note their disagreement with the $v_2\{2\}$ data shown here (in contrast to their excellent agreement with $v_2\{4\}$ data shown in Fig. 5.3). The shaded bands are LHC predictions and show the variation of the theoretical expectations for Pb+Pb collisions at collision energies ranging from $\sqrt{s} = 2.76$ to 5.5 A TeV (corresponding to $\frac{dN}{dy} = 1800$ and 2280, respectively). As in Fig. 5.7, the lines defining the lower end of the shaded region at $p_T = 3\,\mathrm{GeV}/c$ correspond to the lower LHC energy $\sqrt{s} = 2.76\,A$ TeV.

(which are strongly pion dominated) and charged pions increases from RHIC to LHC energy at all p_T, which is opposite for proton v_2 at $p_T < 1.2$ GeV. The shift of proton v_2 to high p_T increases with hydrodynamic radial flow. In Fig. 5.9, we show how this shift depends on hadron species. In both semi-central (10−20%) and peripheral (40−50%) collisions, the heavier the hadron the stronger the push of v_2 it receives towards higher p_T. At sufficiently large p_T, $v_2(p_T)$ is larger at the LHC than at RHIC for all particle species, but at low p_T this holds only for pions whereas all

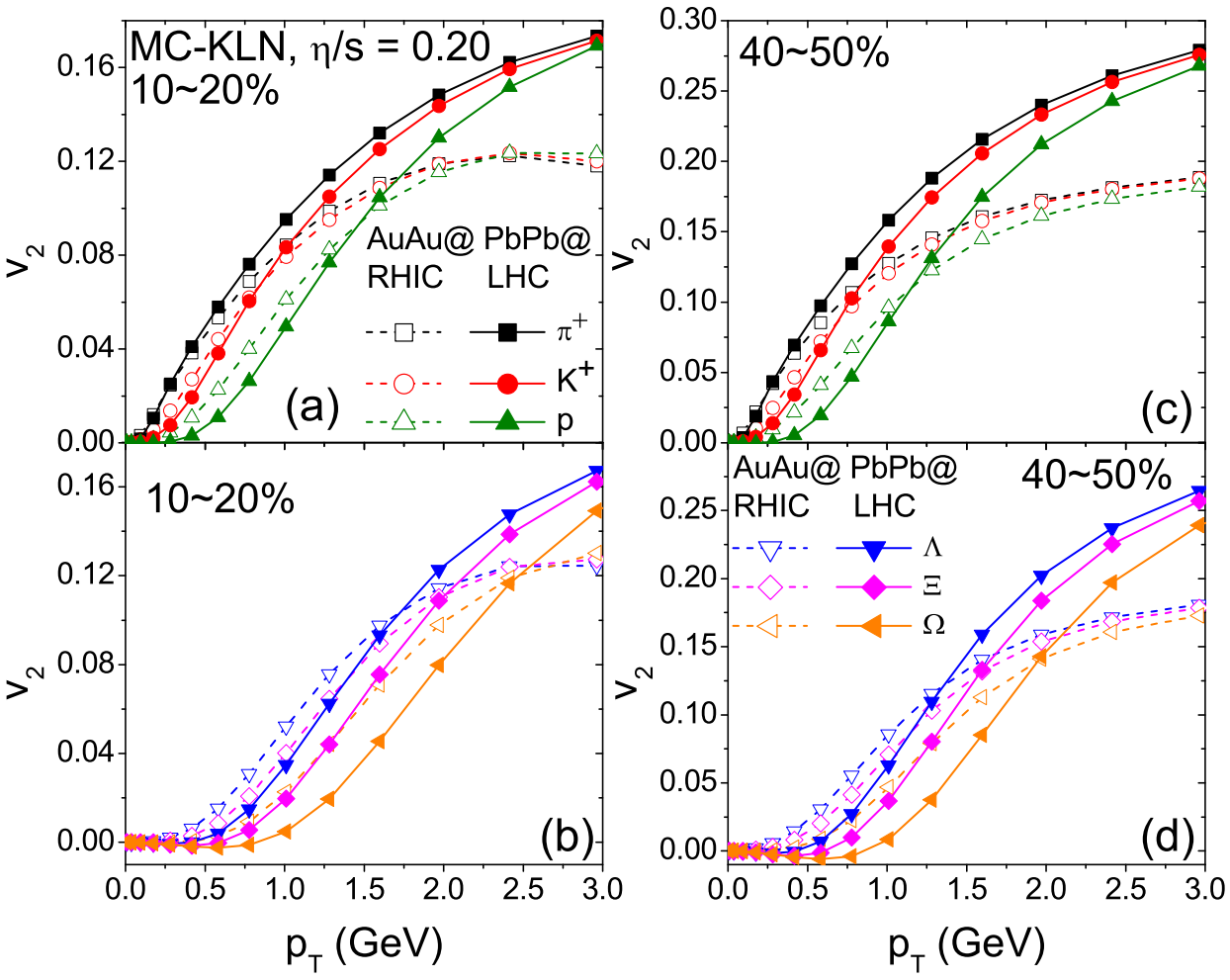

Figure 5.9: Comparison of the differential elliptic flow $v_2(p_T)$ for 200 A GeV Au+Au collisions at RHIC (dashed lines) and 2.76 A TeV Pb+Pb collisions at the LHC (solid lines), at 10%−20% (a,b) and 40%−50% (c,d) centrality, for a variety of different hadron species. Note the slightly negative elliptic flow for the heavy Ω hyperons at low p_T.

heavier hadrons show a decrease of $v_2(p_T)$ from RHIC to LHC at fixed p_T. As the hadron rest mass grows, the crossing point where the decrease of v_2 at fixed p_T with rising collision energy turns into an increase shifts to larger p_T values.

In view of Fig. 5.9, the experimental observation [52] that for charged hadrons $v_2^{\rm ch}(p_T)$ hardly changes at all from RHIC to LHC appears accidental:[12] The increase of $v_2(p_T)$ at fixed p_T for pions is balanced by a corresponding decrease for all heavier hadrons leaving, as it happens, no visible net effect once all charged hadrons are lumped together.

In Figs. 5.10 and 5.11, we show comparisons of our hydrodynamic predictions of identified particle p_T-spectra and differential v_2 with the ALICE measurements from central to peripheral

[12]Contrary to the claim made in [42], the observation that the ratio between $v_2^{\rm ch}(p_T)$ measured at LHC and at RHIC is approximately independent of p_T cannot be directly used to conclude that $(\eta/s)_{\rm QGP}$ does not change from RHIC to LHC. If that argument were correct, this ratio should be independent of p_T not only for the sum of all charged hadrons, but also for each identified hadron species separately. Our hydrodynamic calculations show that the latter does not hold even if η/s remains unchanged from RHIC to LHC.

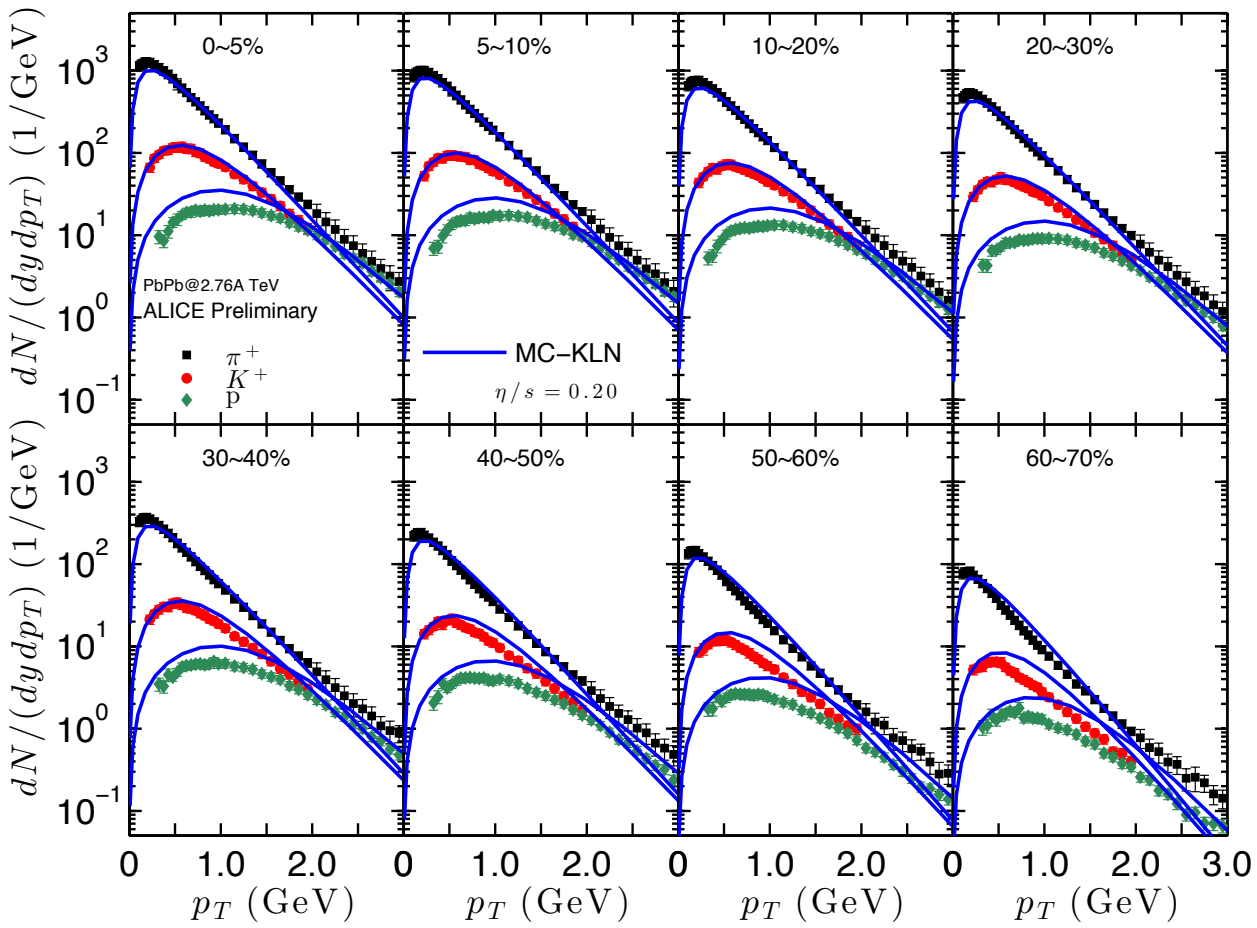

Figure 5.10: Our prediction of the identified particle (π^+, K^+, and proton) spectra are compared with the ALICE measurements [107] from central to peripheral Pb+Pb collisions at $\sqrt{s} = 2.76$ A TeV.

collisions at LHC. We first notice that our proton yield is about a factor of 2 larger than the ALICE data. This is similar to the case at top RHIC energy, where we overestimate the proton yield measured by PHENIX by about a factor of 2. Our predictions for positive pion and kaon spectra agree well with the ALICE measurements at $p_T \lesssim 1.5$ GeV from central collisions to 40-50% in centrality, but become too flat in the more peripheral centrality bins. However, the centrality dependence of the slope of the proton spectra is not well predicted by our pure hydrodynamic simulations. The slopes of the proton spectra are too steep in the central collisions and become comparable with the data in 40-50% centrality and then turn to be too flat in the more peripheral cases.

In Fig. 5.11, we compared our predictions of the differential elliptic flow with the ALICE measurements. We find that our calculations using the MCKLN initial conditions with $\eta/s = 0.20$ successfully predict the charged pion and kaon p_T differential flow coefficients from central up to 50-60% in centrality. However, our pure hydrodynamic simulations fail to correctly reproduce the centrality dependence of the proton elliptic flow $v_2(p_T)$. Especially in central collisions, $v_2^p(p_T)$ is

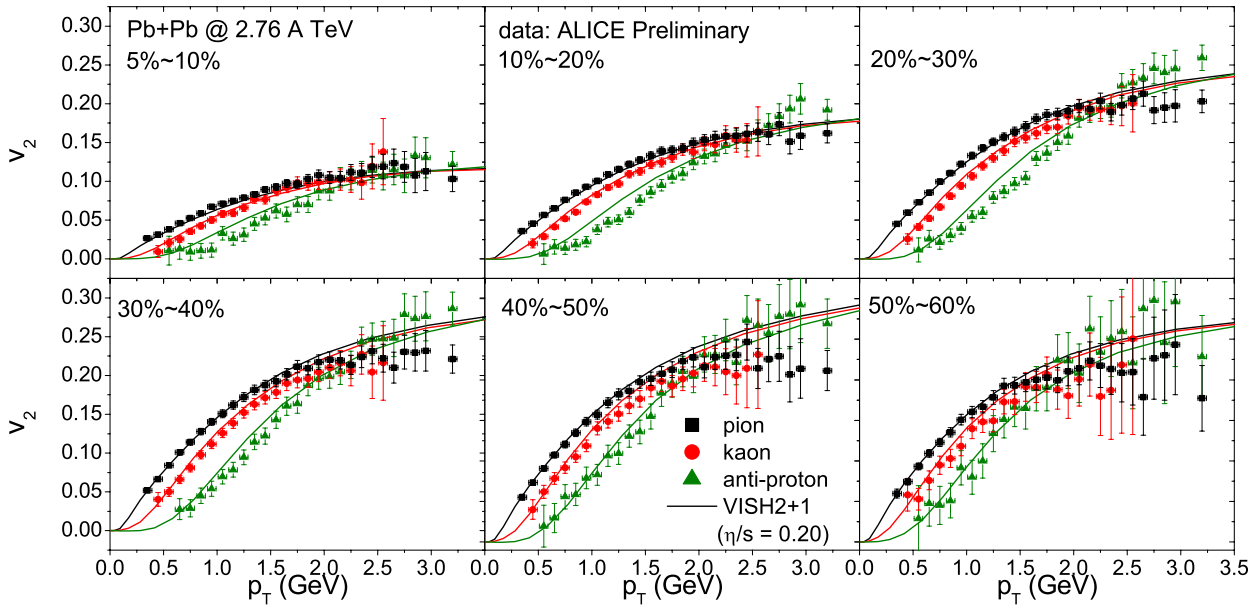

Figure 5.11: Our prediction fo the identified particle (π^+, K^+, and proton) differential v_2 are compared with the ALICE measurements [108] from central to peripheral Pb+Pb collisions at $\sqrt{s} = 2.76$ A TeV.

overpredicted at small p_T (i.e. our model does not generate strong enough radial flow to push the elliptic flow to higher p_T). The lack of hydrodynamic radial flow already seen in the shape of proton spectra in Fig. 5.10 thus also reflects itself in the proton p_T differential elliptic flow. This problem disappears in the more peripheral bins, indicating an incorrect centrality dependence of the balance between radial and elliptic flow in our simulations. The main result that our pure hydrodynamic simulations fail to predict proton spectra and v_2 is because viscous hydrodynamics can not capture the detailed microscopic dynamics in the (highly viscous) hadronic phase. A later more robust viscous hydrodynamics + hadronic cascade hybrid approach has cured this problem and provides a consistent centrality dependence of proton elliptic flow from central to peripheral centrality [49].

5.4 Chapter conclusion

Based on a successful global fit of soft hadron production data in 200 A GeV Au+Au collisions at RHIC within the pure viscous hydrodynamic framework, we generated hydrodynamic predictions for the p_T-spectra and differential elliptic flow of charged hadrons and identified particles for Pb+Pb collisions at the LHC. Our extrapolation from RHIC to LHC energies was based on the assumption that the QGP shear viscosity η/s does not change with increasing fireball temperature and stays fixed at the value $\eta/s = 0.2$ extracted from the RHIC data, assuming the MCKLN initial conditions. The starting time τ_0 for the hydrodynamic evolution and the freeze-out temperature $T_{\rm dec}$ were held fixed, too. We find that such an extrapolation gives a good description of the

centrality dependence of charged hadron production and the charged hadron p_T-spectra in central Pb-Pb collisions, but overpredicts the slope of the p_T-differential elliptic flow and the value of its p_T-integrated value by about $10-15\%$ in mid-central to mid-peripheral collisions. In the most peripheral collisions, the predicted charged hadron p_T-spectra are too flat, and the integrated elliptic flow is too small compared to the experimental data. For identified particle observables, our calculations successfully predicted charged pions and kaons spectra and p_T differential elliptic flow, but gave a slightly inconsistent centrality dependence of proton v_2.

Chapter 6: Extraction of η/s at RHIC and LHC

6.1 Chapter introduction

A major road block in extracting η/s of the QGP is insufficient knowledge of the initial shape of the thermalized fireball created in these collisions, whose initial ellipticity is uncertain by about 20% [34, 61, 11, 68, 112]. This induces an $\mathcal{O}(100\%)$ uncertainty in the value of $(\eta/s)_{\rm QGP}$ extracted from elliptic flow [36, 40].

Due to similar fluctuation mechanisms, the MC-KLN and MC-Glauber models generate similar third-order eccentricities ε_3 whereas the ellipticity ε_2, which is mostly controlled by collision geometry, folded with the (different) average density profiles from the two models, is about 20% larger in the MC-KLN model. Event-by-event ideal [112] and viscous hydrodynamic simulations with both realistically fluctuating and deformed smooth Gaussian initial conditions [113] (with simultaneously non-zero ε_2 and ε_3 eccentricities) have shown that the hydrodynamic conversion efficiencies for translating initial spatial eccentricities into final flow anisotropies [114, 115, 116], although different for v_2/ε_2 and v_3/ε_3, are very similar in the MC-KLN and MC-Glauber models. The similarities in ε_3 and differences in ε_2 between these two models should thus straightforwardly reflect themselves in analogous differences in v_2 and v_3 [117, 113], allowing for an experimental distinction between the models. The work reported in this chapter is based on Ref. [118].

In this chapter, we present a combined analysis of the elliptic and triangular flow coefficients v_2 and v_3 which could disentangle the initial state fluctuations from the hydrodynamic medium response. Such an analysis yields a more precise value for the QGP shear viscosity and thereby reduces (or could even eliminate) the model uncertainty in the initial deformation of the QGP fireball and its event-by-event fluctuations.

6.2 Transverse momentum spectra

Figure 6.1(b) shows the charged hadron p_T-spectra for 2.76 A TeV Pb-Pb collisions at different centralities, for both MC-Glauber ($\eta/s = 0.08$) and MC-KLN ($\eta/s = 0.2$) initial conditions. For the most central ($0-5\%$) collisions the spectra from both models agree well with published ALICE

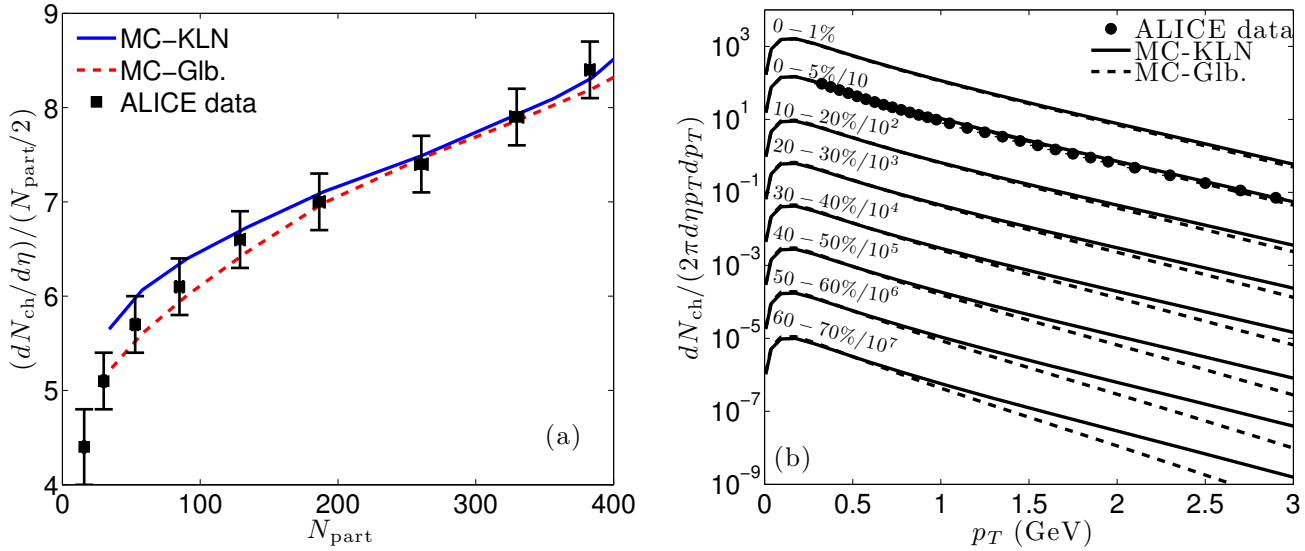

Figure 6.1: (a) Centrality dependence of charged particle multiplicity density as a function of $N_{\rm part}$ from the MC-Glauber (dashed) and MC-KLN (solid) models, compared with ALICE measurements [94] for 2.76 A TeV Pb-Pb collisions. (b) Charged particle p_T-spectra from the MC-Glauber and MC-KLN models for different centralities. The most central (0−5%) results are compared with ALICE data [106].

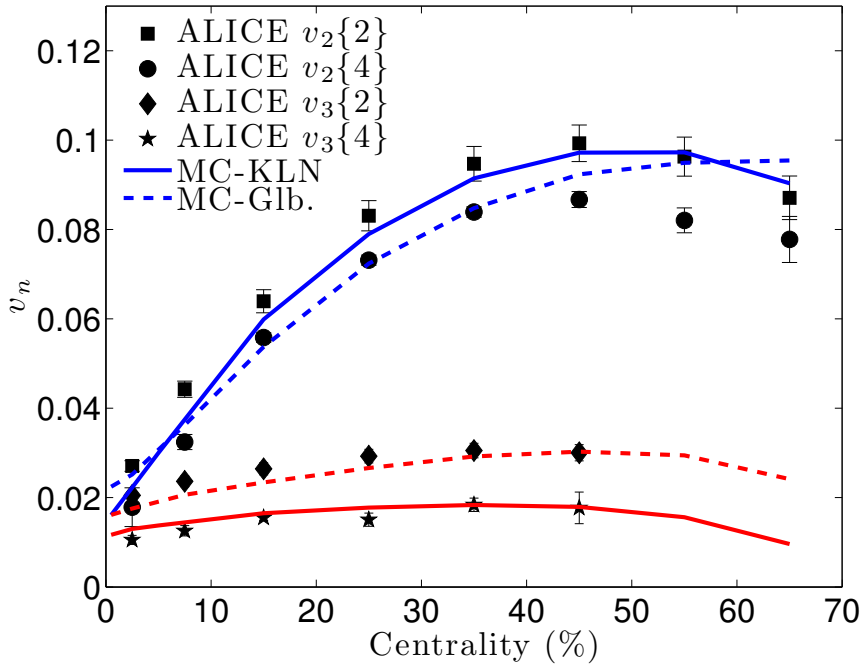

Figure 6.2: v_2 and v_3 vs. centrality, compared with ALICE $v_2\{2\}$, $v_2\{4\}$, $v_3\{2\}$, and $v_3\{4\}$ data for 2.76 A TeV Pb+Pb [119].

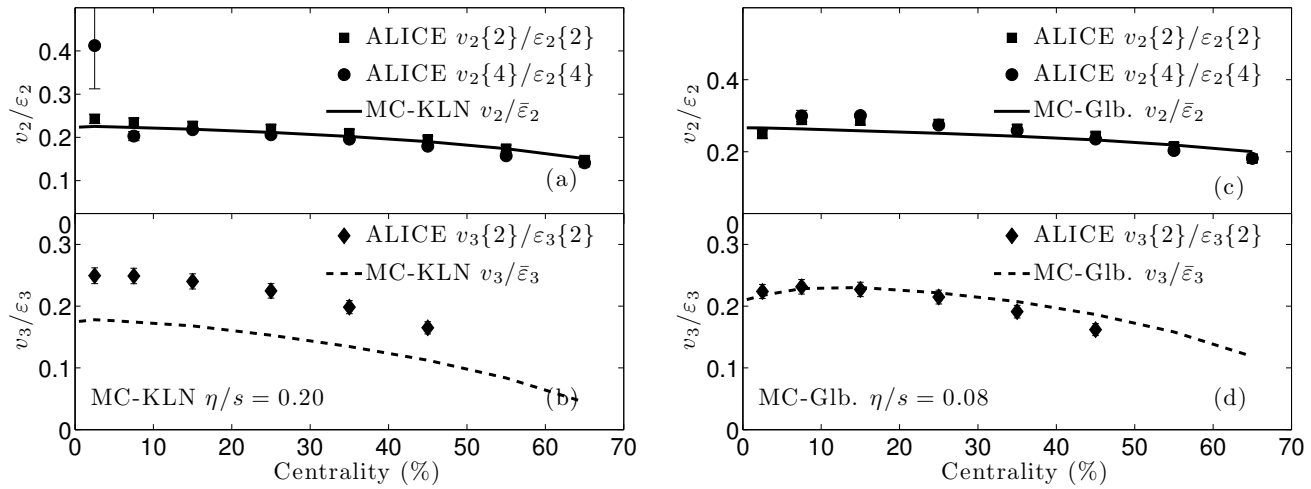

Figure 6.3: Eccentricity-scaled, p_T-integrated $v_{2,3}$ for the hydrodynamically evolved MC-KLN (a,b) and MC-Glauber (c,d) models, compared with ALICE $v_{2,3}$ data for 2.76 A TeV Pb-Pb collisions [119] scaled by their corresponding eccentricities (see text).

data. In more peripheral collisions the MC-KLN spectra are harder than those from MC-Glauber initial conditions. This is a consequence of larger radial flow caused by larger transverse viscous pressure gradients in the MC-KLN case where the fluid is taken to have 2.5 times larger shear viscosity than for the MC-Glauber simulations, in order to obtain the same elliptic flow [36, 40]. In peripheral collisions these viscous effects are stronger than in more central collisions where the fireball is larger [67]. As shown in [120, 112], event-by-event evolution of fluctuating initial conditions generates, for small values of η/s, flatter hadron spectra than single-shot hydrodynamics, especially in peripheral collisions, due to stronger radial flow driven by hot spots in the fluctuating initial states. Proper event-by-event evolution of the latter is therefore expected to reduce the difference between the MC-Glauber and MC-KLN curves in Fig. 6.1(b) since this effect is relatively strong for $\eta/s = 0.08$ (MC-Glauber) [112] but almost absent for $\eta/s = 0.2$ (MC-KLN) [113].

6.3 p_T integrated elliptic and triangular flow

In Figure 6.2 we compare our p_T-integrated v_2 and v_3 as functions of centrality with ALICE $v_2\{2\}$, $v_2\{4\}$, $v_3\{2\}$, and $v_3\{4\}$ data, extracted from 2- and 4-particle correlations [119]. To compute $v_2(v_3)$, we sample for each centrality calss 10,000 events, recenter their entropy density distributions and align their elliptic (triangular) deformation axes and then average these entropy distributions. These elliptically (triangularly) deformed almost smooth average initial entropy density profiles are then evolved hydrodynamically. For both models, the computed $v_{2,3}$ values from the averaged smooth initial conditions lie between the experimental $v_{2,3}\{2\}$ and $v_{2,3}\{4\}$ values. This is consistent with the theoretical expectation [121, 122] that $v_n\{2\}$ ($v_n\{4\}$) is shifted up (down) relative to the average flow by event-by-event flow fluctuations and was also found

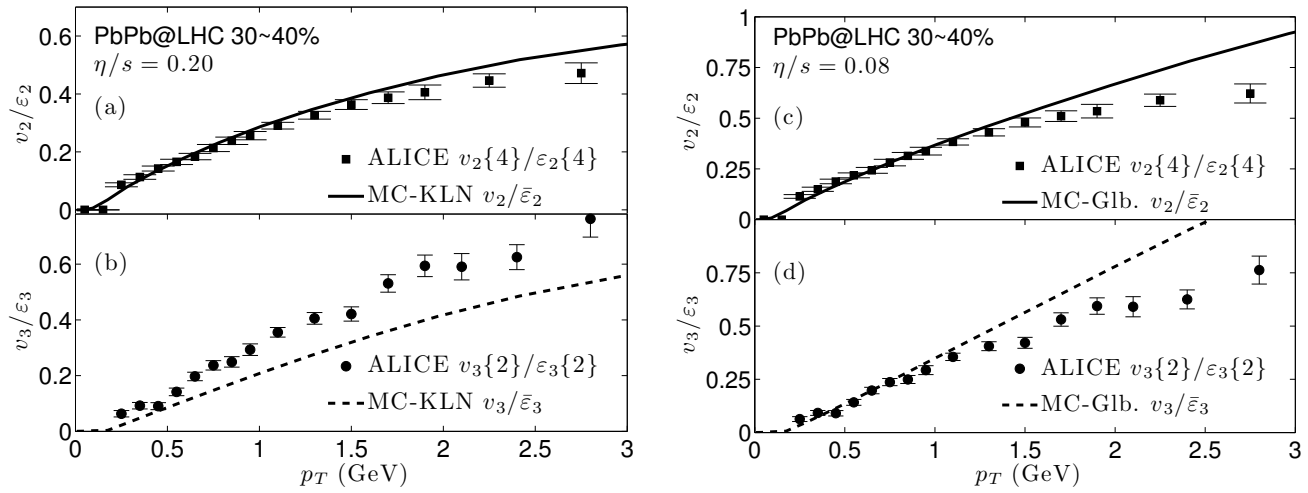

Figure 6.4: Eccentricity-scaled, p_T-differential elliptic and triangular flow for 2.76 A TeV Pb-Pb collisions from viscous hydrodynamics with MC-KLN (a,b) and MC-Glauber (c,d) initial conditions. The ALICE data [119] are scaled according to their corresponding eccentricities, see text.

elsewhere [40, 46, 41]. Upon closer inspection, however, and recalling that ideal single-shot hydrodynamics with smooth initial condition was shown [112] to generate v_2 similar to $v_2\{2\}$ from the corresponding event-by-event evolution, it seems that the MC-KLN is favored since it produces v_2 results closer to the $v_2\{2\}$ data. Unfortunately, a similar argument using v_3 can be held against the MC-KLN model. To eliminate the interpretation difficulties associated with a comparison of average flows from single-shot evolution of averaged initial conditions with data affected irreducibly by naturally existing event-by-event fluctuations, we proceed to a comparison of eccentricity-scaled flow coefficients.

Assuming linear response of $v_{2,3}$ to their respective eccentricities $\varepsilon_{2,3}$ (which was found to hold with reasonable accuracy for v_2 and v_3 but not for higher order anisotropic flows [112]), we follow [123] and scale the flow $v_{2,3}$ from single-shot hydrodynamics by the eccentricity $\bar{\varepsilon}_{2,3}$ of the ensemble-averaged smooth initial energy density, while scaling the experimental $v_{2,3}\{2\}$ and $v_{2,3}\{4\}$ data by the corresponding fluctuating eccentricity measures $\epsilon_{2,3}\{2\}$ and $\epsilon_{2,3}\{4\}$, respectively, calculated from the corresponding models. In [113] we justify this procedure for $v_{2,3}\{2\}$ and $v_2\{4\}$ and also show that it fails for $v_3\{4\}/\epsilon_3\{4\}$ since this ratio is found to differ strongly from $v_3/\bar{\varepsilon}_3$.

The eccentricity-scaled elliptic and triangular flow coefficients for the MC-KLN and MC-Glauber models are shown in Figs. 6.3(a,b) and 6.3(c,d), respectively, and compared with the corresponding data from ALICE. The first thing to note is the impressively accurate agreement between the experimentally measured $v_2\{2\}/\epsilon_2\{2\}$ and $v_2\{4\}/\epsilon_2\{4\}$, showing that for elliptic flow the idea of scaling "each flow with its own eccentricity" [123] works very well. The same is not true for $v_3\{2\}/\epsilon_3\{2\}$ and $v_3\{4\}/\epsilon_3\{4\}$ for which the experimental measurements do not at all agree (not shown), nor are they expected to [113]. Secondly, both $v_2\{2\}/\epsilon_2\{2\}$ and $v_2\{4\}/\epsilon_2\{4\}$ measured by ALICE agree well with the viscous hydrodynamic calculations, for both the MC-Glauber and

MC-KLN models, confirming that for each model the correct value of η/s has been used as far as elliptic flow is concerned.

The bottom panels in Fig. 6.3 show the triangular flow v_3. Clearly, with the viscosities needed to reproduce v_2, the MC-KLN model badly disagrees with the experimental v_3 data. The measured triangular flow is too big to accommodate a specific shear viscosity as large as 0.2. Within the present approach, the only possibility to avoid this conclusion is that somehow the MC-Glauber and MC-KLN models both underpredict the initial third-order eccentricity ε_3 by about 50%. With MC-Glauber initial conditions and $\eta/s = 0.08$, on the other hand, the ALICE data agree well with viscous hydrodynamics, even if the measured centrality dependence of $v_3\{2\}/\epsilon_3\{2\}$ is slightly steeper than the calculated one.

Summarizing Fig. 6.3, the ALICE data for the p_T-integrated elliptic and triangular data taken together strongly favor MC-Glauber initial conditions and, by implication, a small value of $\eta/s \simeq 0.08$ for the specific QGP shear viscosity.

6.4 p_T-differential elliptic and triangular flow.

We now cross-check, at one collision centrality (30−40%) where $v_3(p_T)$ data are available [119], the p_T-differential anisotropic flows. The corresponding comparison between data and theory is shown in Fig. 6.4; as in Fig. 6.3 we compare the eccentricity-scaled flows, plotting $v_{2,3}/\bar{\varepsilon}_{2,3}$ for the models and $v_2\{4\}/\epsilon_2\{4\}$ ($v_3\{2\}/\epsilon_3\{2\}$) for the elliptic (triangular) flow data. As seen in the upper panels, both initial state models describe the measured elliptic flow well up to $p_T \sim 1{-}1.5\,\mathrm{GeV}/c$; at larger p_T, they overpredict $v_2(p_T)$ for charged particles – a problem noticed before [47, 48] and possibly related to an imperfect model description of the measured final chemical composition [49]. The disagreement at larger p_T is worse for MC-Glauber initial conditions; this is likely related to our earlier observation in Fig. 6.1(b) that our MC-Glauber p_T-spectra are steeper than the MC-KLN ones in peripheral collisions – an artifact of our single-shot approach and possibly remedied by a proper event-by-event hydrodynamical simulation.

Figure 6.4(b) shows again the disagreement between theory and experiment for triangular flow when we use MC-KLN initial conditions: the model strongly underpredicts the data at all p_T, i.e. it gives the wrong slope for $v_3(p_T)$. With MC-Glauber initial conditions and correspondingly lower shear viscosity $\eta/s = 0.08$ (Fig. 6.4(d)), the measured $v_3(p_T)$ is well described up to $p_T \sim 1\,\mathrm{GeV}/c$ but overpredicted at larger p_T. Again, the latter can be at least partially attributed to the fact that the MC-Glauber p_T-spectrum from our single-shot hydrodynamic approach is too steep at this collision centrality, which can in future studies be corrected by performing the hydrodynamic evolution properly event by event.

6.5 Chapter summary

Using a well-calibrated single-shot viscous hydrodynamic approach without hadronic cascade afterburner but properly implementing hadronic chemical freeze-out at $T_{\rm chem} \approx 165\,{\rm MeV}$ and including a full set of resonance decays, we have shown that a combined analysis of the ALICE data for elliptic and triangular flow from $2.76\,A\,{\rm TeV}$ Pb-Pb collisions leads to a strong preference for initial conditions from the Monte-Carlo Glauber model, combined with a low value for the QGP shear viscosity $\eta/s \simeq 0.08$, and disfavors the considerably larger viscosities of $\eta/s \sim 0.2$ that are required to reproduce the measured elliptic flow when assuming the more eccentric Monte-Carlo KLN initial profiles. Final confirmation of these conclusions will require a proper event-by-event evolution of the fluctuating initial density profiles and coupling viscous hydrodynamics to a microscopic description of the dilute late hadronic stage where viscous hydrodynamics breaks down [124], and a similar analysis of recently published PHENIX data at lower RHIC energies [125]. Given the large magnitude of the underprediction v_3 in the MC-KLN model observed here we expressed in [118], however, doubt that such more sophisticated approaches will be able to reverse the conclusions drawn here. In the meantime we learnt, however, that subnucleonic color density fluctuations as well as the inclusion of pp multiplicity fluctuations indeed have the potential to drastically alter the initial ϵ_n spectrum, and that neither the MC-Glauber nor the MCKLN model in the form presented here are able to describe simultaneously with a single common η/s value, all measured v_n coefficients (see Chapter 7).

Chapter 7: Event-by-event simulations for LHC energies

In this chapter, we perform realistic event-by-event hydrodynamic simulations for Pb+Pb collisions at $\sqrt{s} = 2.76\ A$ TeV at LHC, using the same hydrodynamic parameter set which was tuned to the experimental data in the last two Chapters. The results for the mean charged hadron elliptic and triangular flows are very close to our results using event-averaged smooth initial conditions shown in the last Chapter. However, the event-by-event calculations allow us to make an apple-to-apple comparison with the measured $v_{2,3}\{\mathrm{SP}\}$ as well as higher order anisotropic flow coefficients, all of which are crucially affected by event-by-event flow fluctuations. The work presented in this chapter has not yet been published.

7.1 Charged hadron anisotropic flow coefficients

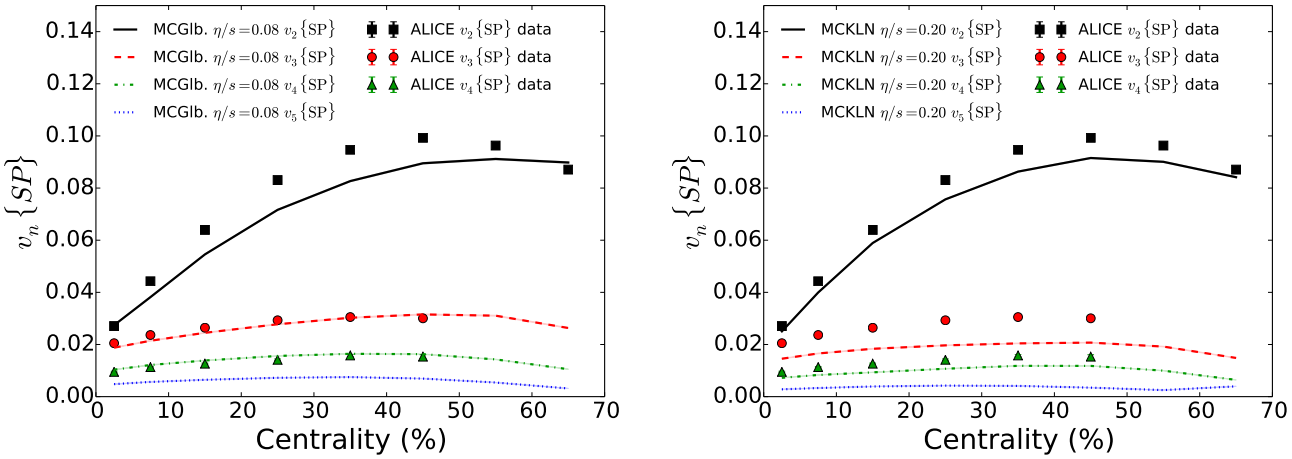

Figure 7.1: Centrality dependence of charged hadron anisotropic p_T-integrated flow coefficients, $v_n\{\mathrm{SP}\}$ (n =2-5) compared with the ALICE measurements in Pb+Pb collisions at $\sqrt{s_{\mathrm{NN}}}$ = 2760 A GeV. p_T is integrated from 0.2 to 3.5 GeV in our calculations. Calculations from the MC-Glauber initial conditions using $\eta/s = 0.08$ are shown in the left panel. The right panel shows the results using MCKLN model with $\eta/s = 0.20$.

We first show the charged hadron p_T-integrated $v_n\{\mathrm{SP}\}$ as a function of centrality in Fig. 7.1. With event-by-event calculations, both our MC-Glauber amd MCKLN runs underestimate the data by about 5-10%. The MCKLN runs shows a better centrality dependence than runs

with MC-Glauber initial conditions. However, the MC-Glauber model with $\eta/s = 0.08$ correctly reproduce the measured $v_{3,4}\{\mathrm{SP}\}$ data from central to peripheral collisions, while the MCKLN initial conditions underestimate $v_3\{\mathrm{SP}\}$ by almost 50% due to the 2.5 times larger η/s used for the QGP in the hydrodynamic simulations. In short, in a combined comparisons of $v_{2,3,4}\{\mathrm{SP}\}$ the ALICE measurements, the experimental data favor the MC-Glauber initial conditions with QGP η/s close to $\frac{1}{4\pi}$.

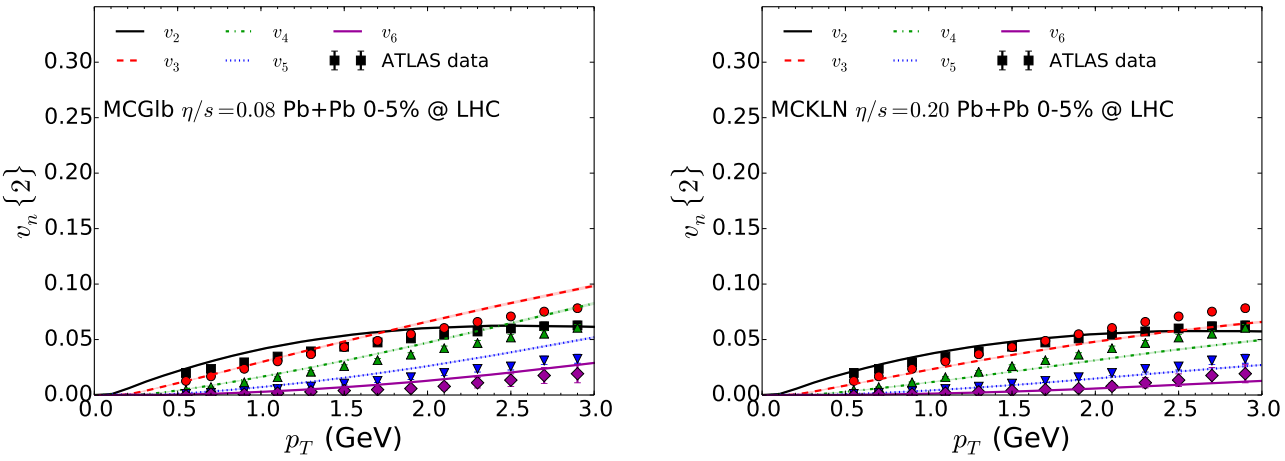

Figure 7.2: Comparisons of charged hadron anisotropic flow coefficients, $v_n\{2\}$ (n =2-6), with ATLAS measurements at 0-5% most central Pb+Pb collisions at $\sqrt{s_{\mathrm{NN}}} = 2760$ A GeV. Calculations from the MC-Glauber initial conditions using $\eta/s = 0.08$ are shown in the left panel. The right panel shows the results using MCKLN model with $\eta/s = 0.20$.

In Figs. 7.2 to 7.7, we show comparisons of the charged hadron p_T-differential anisotropic flow $v_2\{2\}$ to $v_6\{2\}$ with the ATLAS measurements from the 0-5% most central collisions all the way to semi-peripheral collisions at 40-50% centrality. Both the MC-Glauber and MCKLN models with their corresponding choices of η/s give good descriptions of the elliptic flow data at the LHC. Since in Fig. 7.1 both models underestimate the p_T-integrated $v_n\{\mathrm{SP}\}$, we think the good agreement with $v_2\{2\}(p_T)$ is due to the fact that the computed charged hadron spectra are somewhat steeper than the measured data (see comparisons of identified particle spectra below). The MCKLN model does a better job than the MC-Glauber model in the region $2 < p_T < 3$ GeV. This is mostly because the larger specific shear viscosity in the MCKLN runs helps the system to develop more radial flow, which results in flatter charged hadron spectra compared with the MC-Glauber model. Once the specific shear viscosity is fixed by the measured elliptic flow data, higher order anisotropic flows are parameter-free predictions from event-by-event viscous hydrodynamic simulations. The relative size of the higher order v_n compared to v_2 is now determined by the fluctuation spectrum from the initial condition model. We find that the MC-Glauber model overpredicts the higher order $v_n\{2\}(p_T)$, while the MCKLN model, on the other hand, underestimates the data. Since we only consider the nucleon position fluctuations in the current implementation of the MC-Glauber

and the MCKLN models, both of them do not contain the correct initial fluctuation spectrum which controls the relative size between the initial eccentricities of different harmonic orders, which translate themselves to final flow anisotropies through hydrodynamic evolution.

In short, the experimentally measured anisotropic flow coefficients place powerful constraints on the extraction the specific shear viscosity of the QGP medium and initial fluctuation spectrum. The MC-Glauber and MCKLN models, in their standard form, do need appear to give the correct initial fluctuation spectrum. As shown in [126], in order to describe the all the measured v_n coefficients simultaneously, one needs to take into account sub-nucleonic quantum fluctuations in the initial state, like IP-Glasma model.

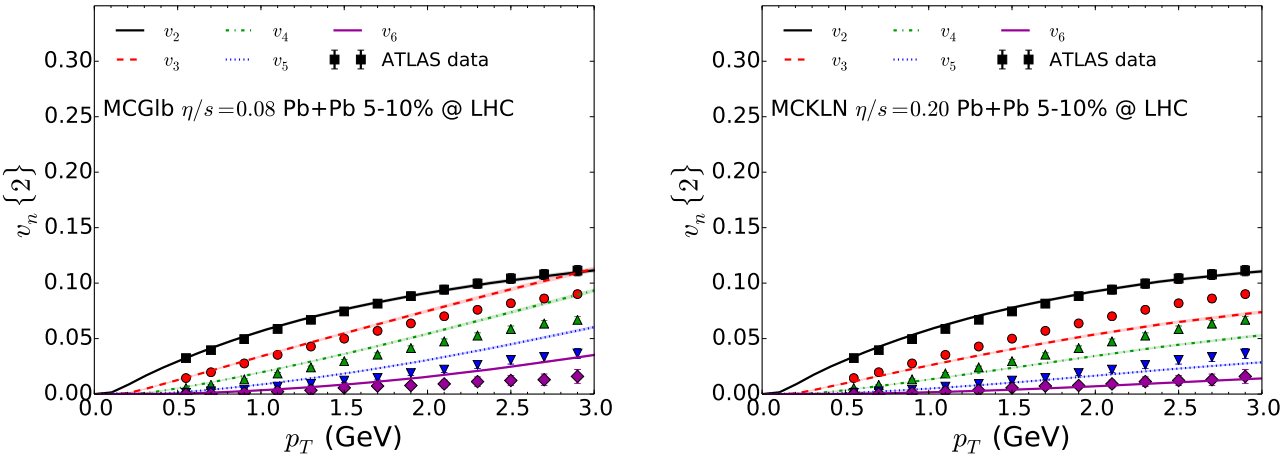

Figure 7.3: Similar to Fig. 7.2, but for 5-10% centrality bin.

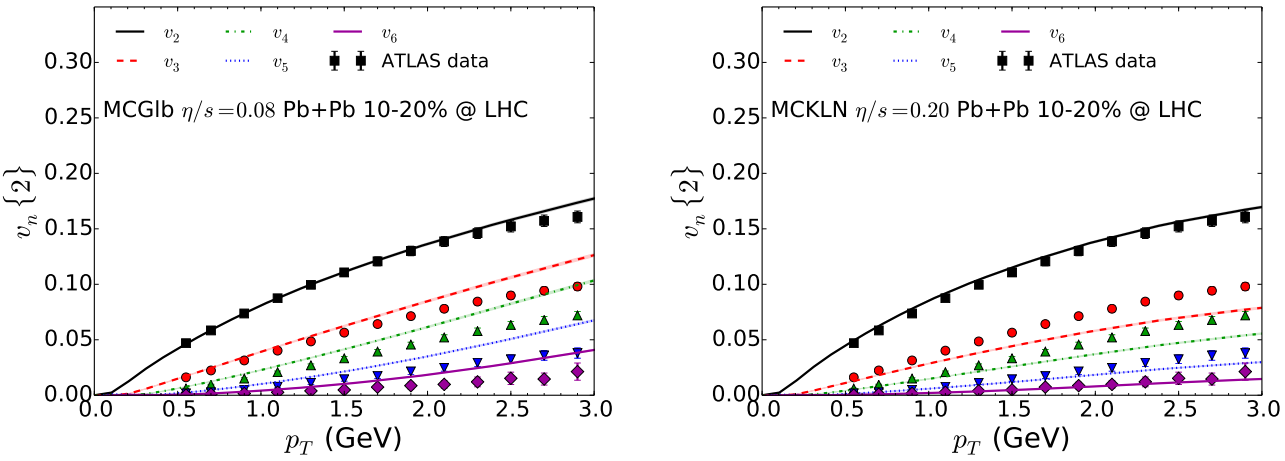

Figure 7.4: Similar to Fig. 7.2, but for 10-20% centrality bin.

7.2 Identified particle spectra and their elliptic flow coefficients

We complete this first event-by-event study of higher order charged hadron v_n with a discussion of the concomitant p_T-spectra and elliptic flows of identified hadron species. Figs. 7.8 to 7.13,

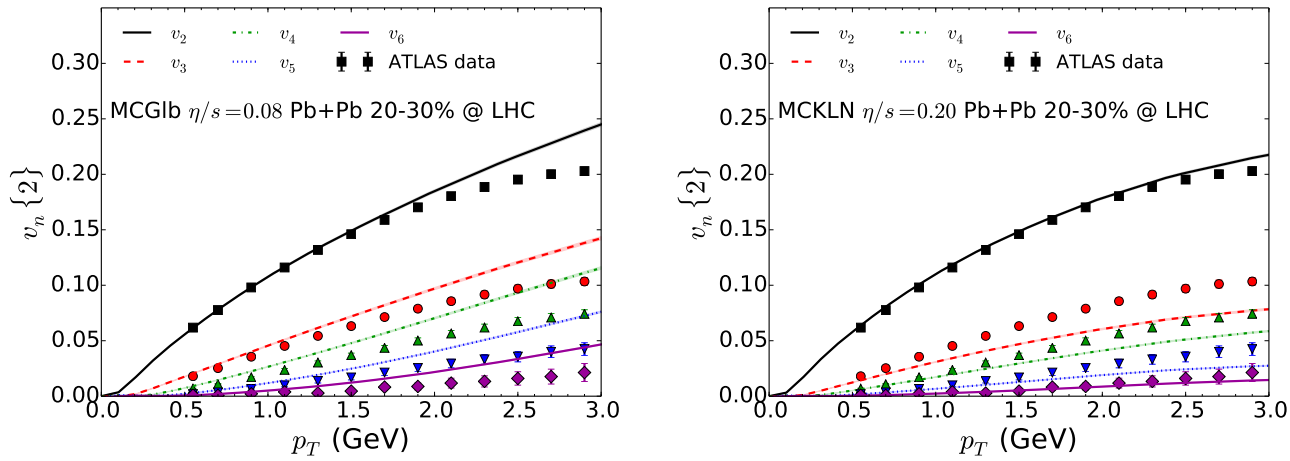

Figure 7.5: Similar to Fig. 7.2, but for 20-30% centrality bin.

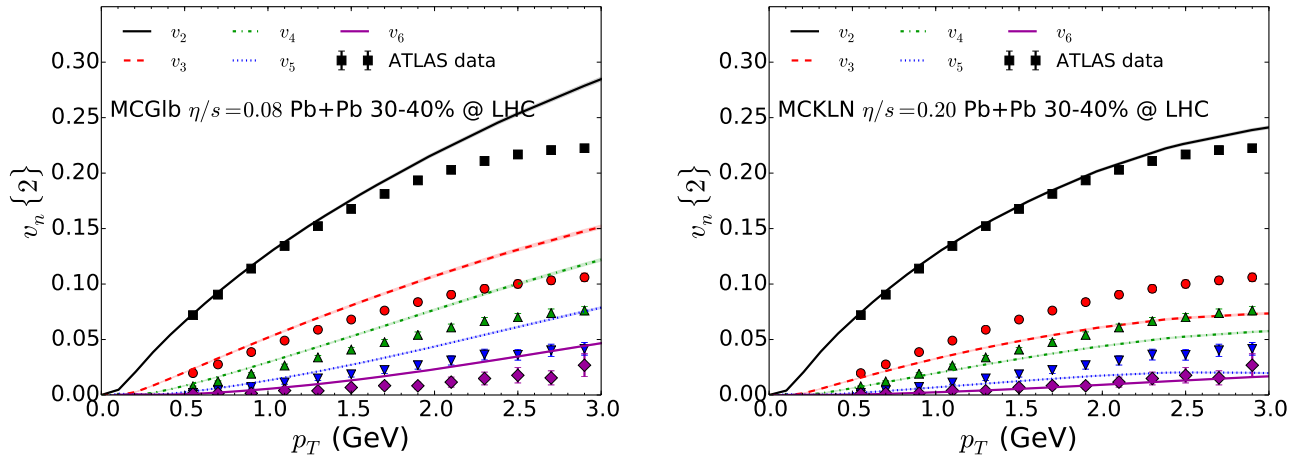

Figure 7.6: Similar to Fig. 7.2, but for 30-40% centrality bin.

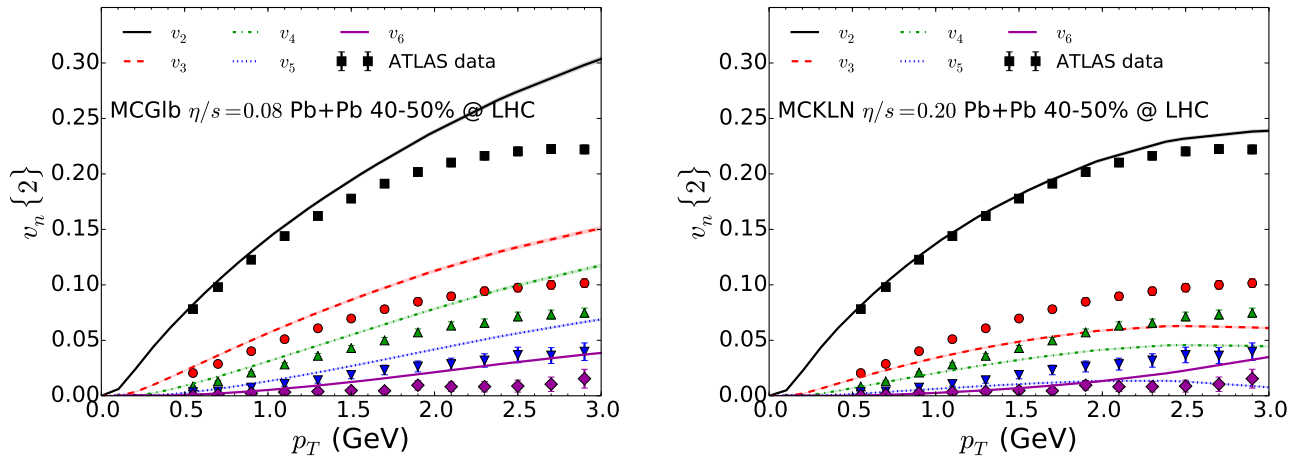

Figure 7.7: Similar to Fig. 7.2, but for 40-50% centrality bin.

we study the particle species dependence in comparison with experimental data from different centrality bins. We find that the particle spectra from our hydrodynamic calculations are generally too steep compared with the experimental data. The larger specific shear viscosity in the MCKLN

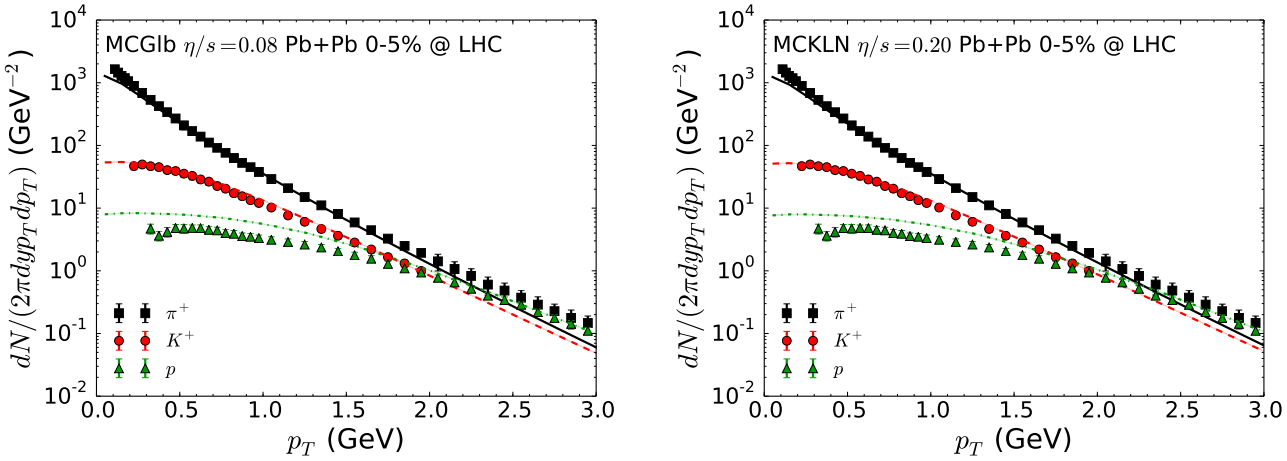

Figure 7.8: Comparisons of identified pions, kaons, and protons spectra with ALICE measurements at 0-5% most central Pb+Pb collisions at $\sqrt{s_{\rm NN}} = 2760\,{\rm A\,GeV}$. Results from MCGlb initial conditions with $\eta/s = 0.08$ are shown in the left panel. Calculations with MCKLN model and $\eta/s = 0.20$ are shown in the right panel.

runs helps the system to develop more radial flow, which gives somewhat flatter spectra than the MC-Glauber ones, but not enough. The lack of radial flow also shows up in the proton $v_2\{2\}$, where the mass splitting in the experimental data is larger than in the calculations for central collisions. We find that the more advanced hybrid calculations [124], which describe the hadronic phase with a microscopic cascade model, help the system to develop more radial flow in the hadronic phase and thereby improve the description of the measured data, especially for central collisions [49].

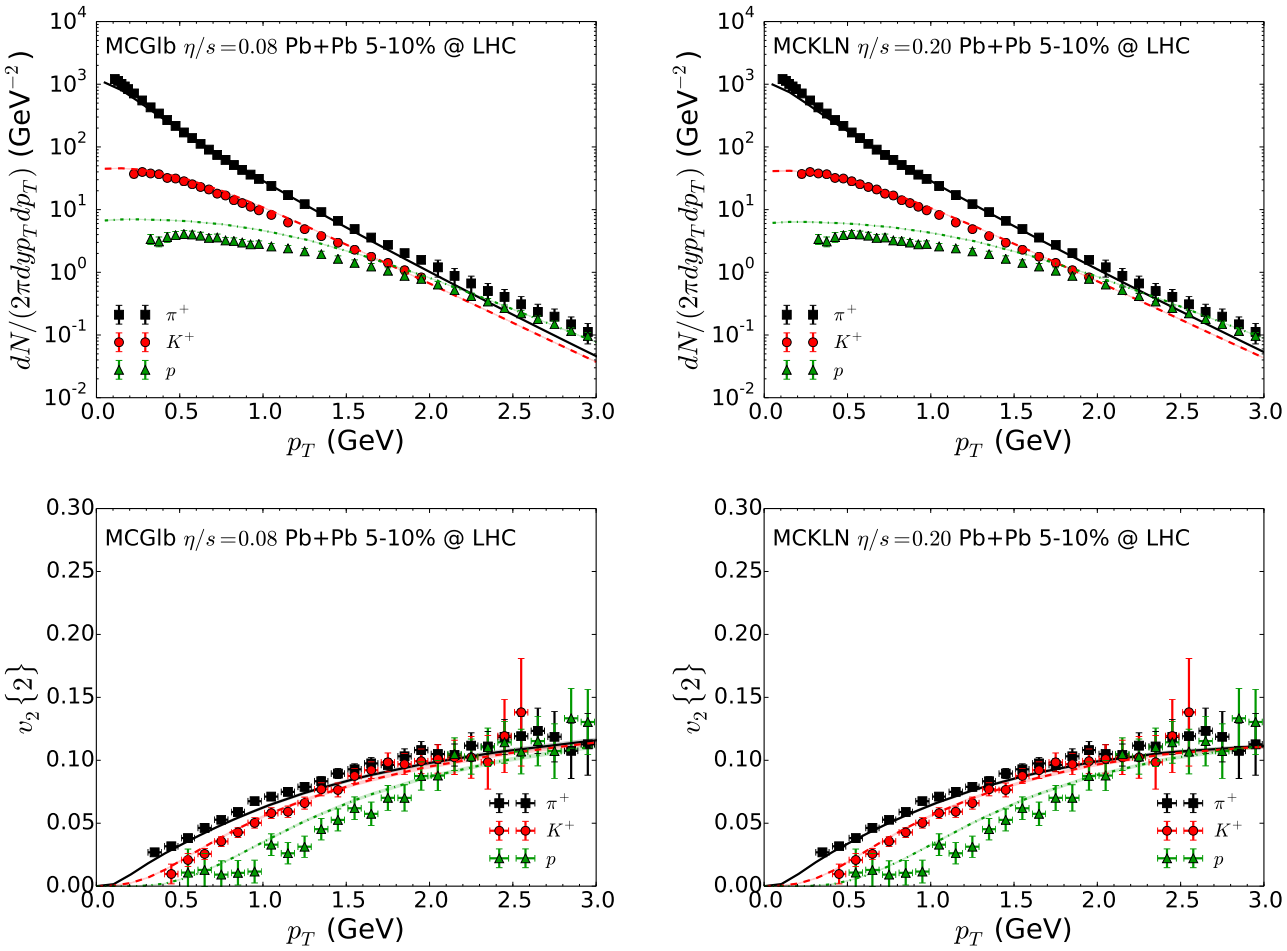

Figure 7.9: Upper panels: Similar to Fig. 7.8, but for 5-10% centrality bin. Lower panels: Comparisons of identified particle v_2 with ALICE measurements at 5-10% most central Pb+Pb collisions at $\sqrt{s_{\rm NN}} = 2760\,{\rm A\,GeV}$. Results from MCGlb initial conditions with $\eta/s = 0.08$ are shown in the left panel. Calculations with MCKLN model and $\eta/s = 0.20$ are shown in the right panel.

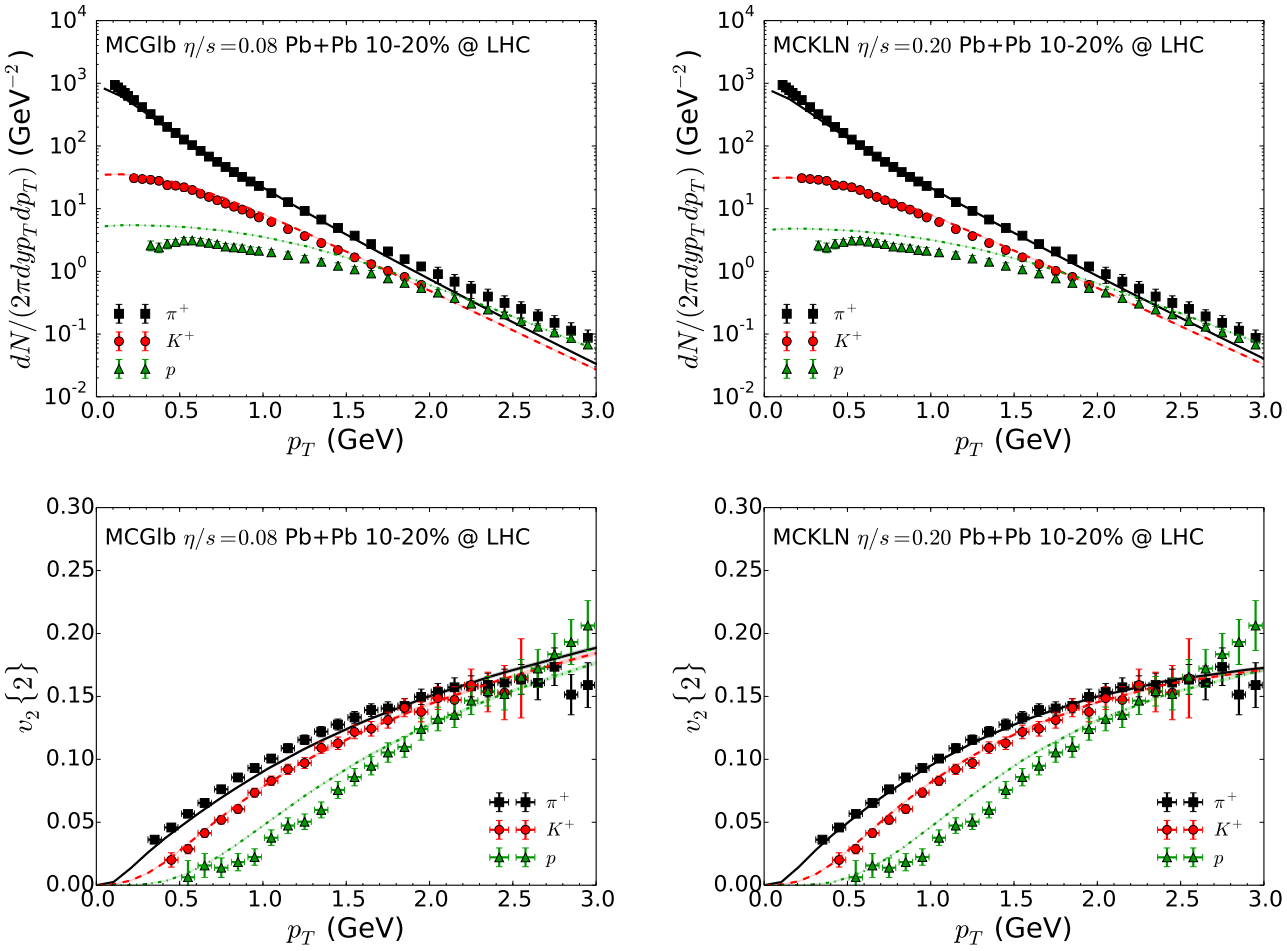

Figure 7.10: Similar to Fig. 7.9, but for 10-20% centrality bin.

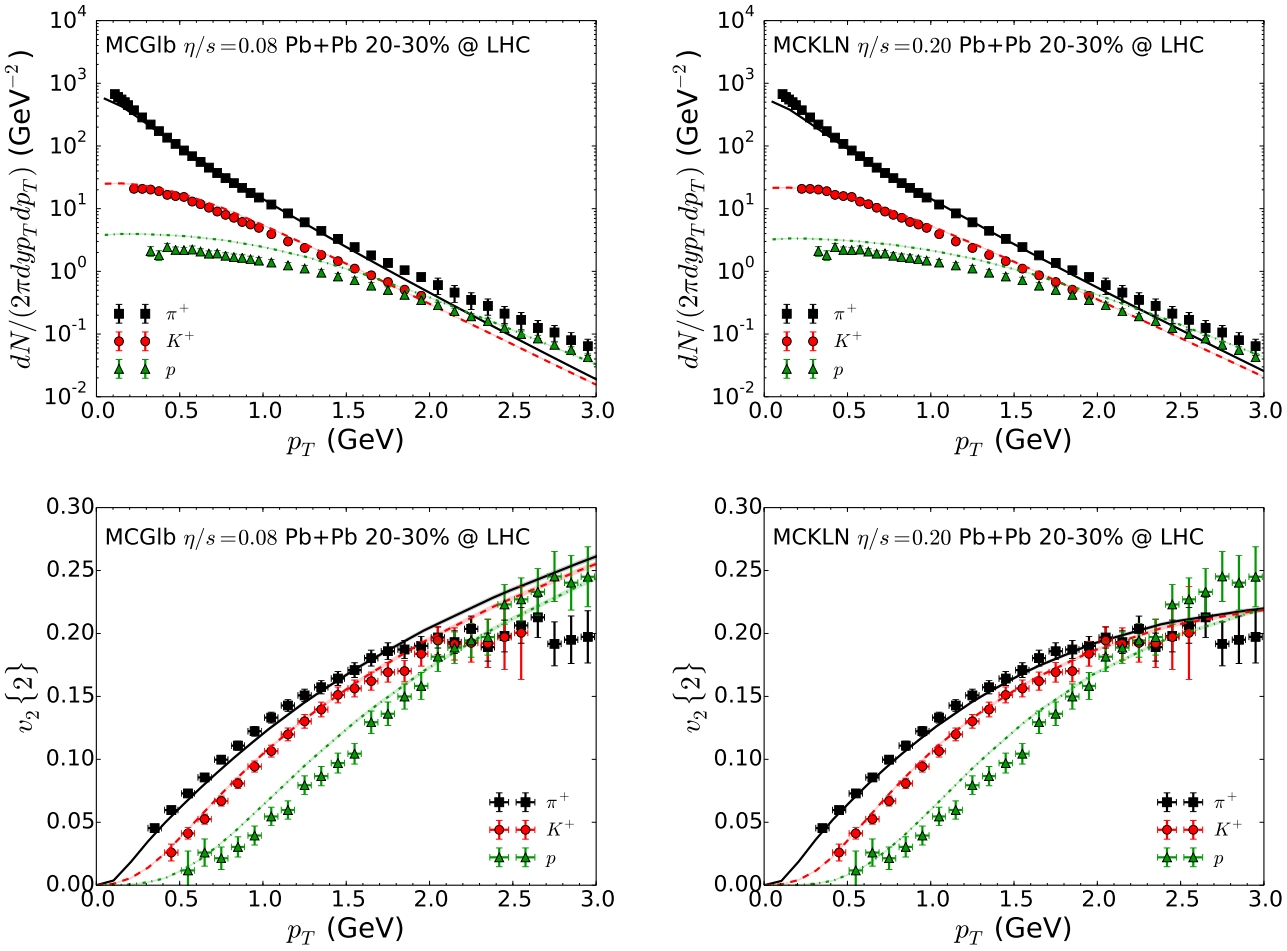

Figure 7.11: Similar to Fig. 7.9, but for 20-30% centrality bin.

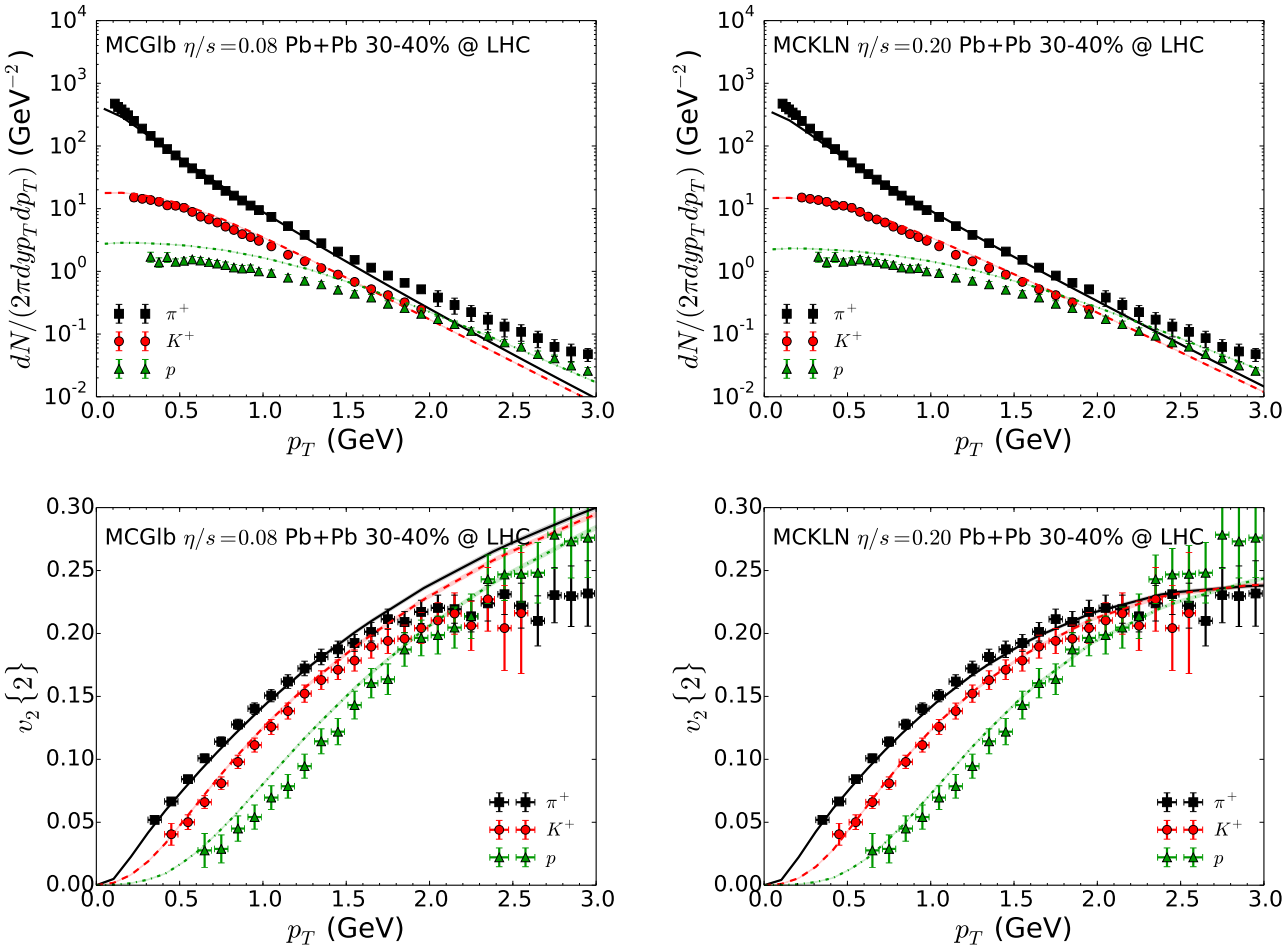

Figure 7.12: Similar to Fig. 7.9, but for 30-40% centrality bin.

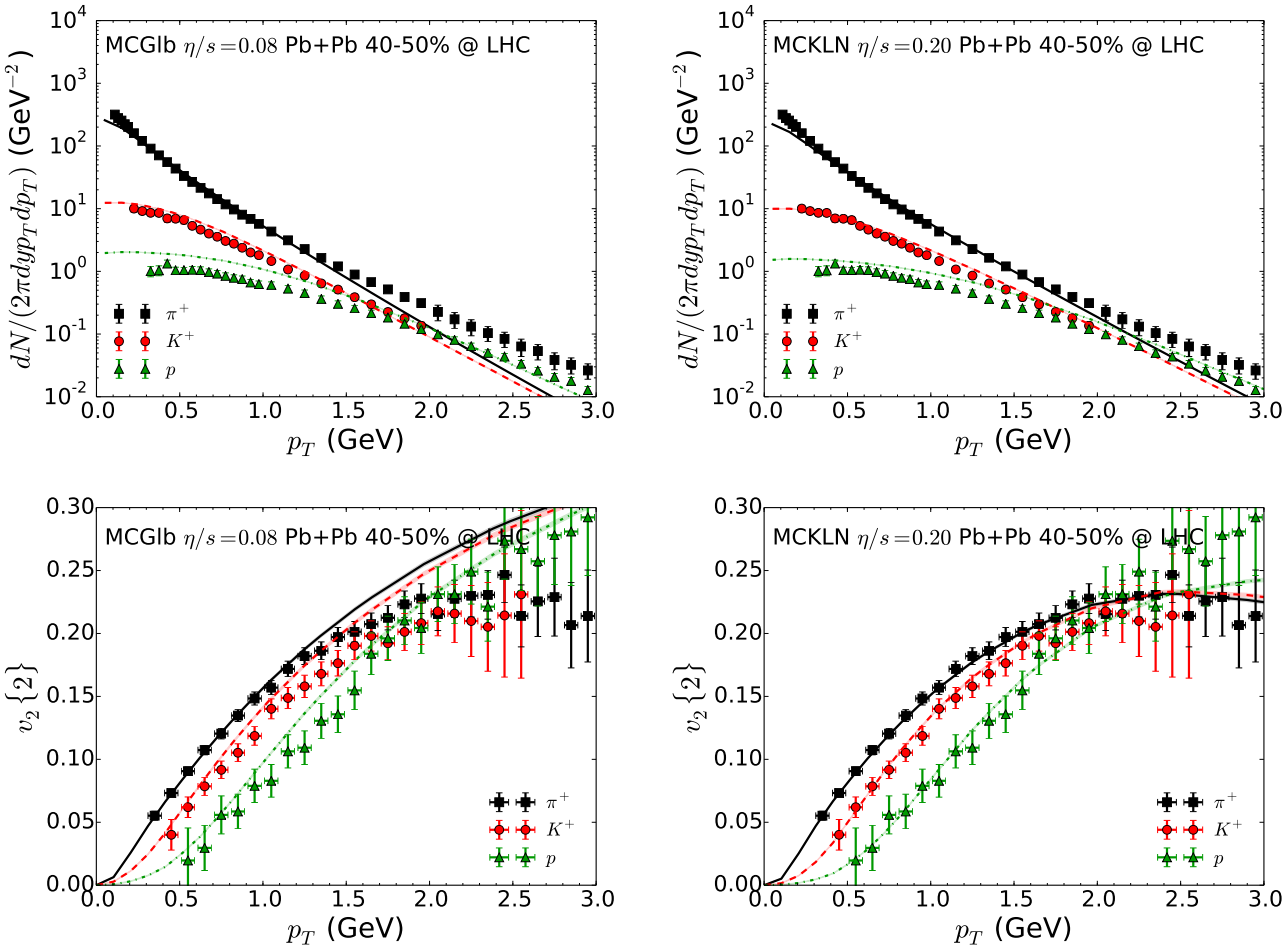

Figure 7.13: Similar to Fig. 7.9, but for 40-50% centrality bin.

Chapter 8: Temperature dependent $(\eta/s)(T)$

8.1 Chapter introduction

In this chapter, we explore the effects of considering temperature dependent specific shear viscosity $(\eta/s)(T)$ on the final measured hadronic observables. This chapter is based on work reported in [127, 48].

At temperatures well above the transition region, one would expect the QGP to approaches weakly coupled limit, leading to an increase of η/s as the temperature increases. As we increase the collision energy from RHIC to LHC, the created fireballs probe the QGP at a higher temperature. We would like to study to what extent a larger value of η/s during the early high temperature stage will manifest itself in the bulk flow observables at LHC energies. This question was first addressed by H. Niemi et al. [128] and Schenke et al. [126].

On the other hand, the specific shear viscosity is also expected to again increase in the hadronic phase as the temperature drops below the quark-hadron transition temperature. The mean free path of the constituent hadrons increases as the system becomes more dilute. In order to deal with the large viscosity in the late stage of the evolution, advanced hybrid models which switch from a the macroscopic hydrodynamic modeling of the QGP fireball dynamics to a microscopic Boltzmann description of the hadronic phase have been developed over the last years. However, microscopic simulations of the late hadronic stage are numerically very expensive. A possible effective macroscopic description with viscous fluid dynamics and an $(\eta/s)(T)$ that increases with decreasing T would therefore be much preferred if valid. Here we will explore the temperature dependence of $(\eta/s)(T)$ as well as of the shear relaxation time $\tau_\pi(T)$ within a pure hydrodynamic framework below the transition temperature region and study systematically the consequences of increasing shear viscosity and shear pressure relaxation time in the late hadronic stage on the transverse momentum spectra and elliptic flow of soft ($p_T < 2\,\mathrm{GeV}/c$) hadrons produced in Au+Au collisions at RHIC.

This chapter is organized as follows: In Sec. 8.2 we briefly review the viscous hydrodynamic model and discuss the specific ingredients used in the present study. The effects of a large hadronic

specific shear viscosity $(\eta/s)_{\rm HG}$ on the fireball evolution are discussed in Sec. 8.3. In Sec. 8.4 we discuss the dependence of the transverse momentum spectra and elliptic flow of emitted hadrons in Au+Au collisions on $(\eta/s)_{\rm HG}$, the decoupling temperature $T_{\rm dec}$, and the collision centrality. Section 8.5 is dedicated to a detailed discussion of the viscous corrections to the freeze-out phase-space distribution and their effects on spectra and elliptic flow. All results up to this point assume a constant factor $\kappa = 3$ in the relation $\tau_\pi T = \kappa \frac{\eta}{s}$ between the specific shear viscosity η/s and the microscopic relaxation time τ_π; in Sec. 8.6 we explore the consequences of making $\kappa(T)$ temperature dependent and letting it grow during the quark-hadron phase transition. In Sec. 8.7, we discuss the effect of $(\eta/s)(T)$ at high temperatures that we may access at higher LHC collision energies. A final discussion in Sec. 8.8 concludes this chapter.

8.2 Viscous hydrodynamics: specific ingredients for the present study

The key ingredients whose influence on the generation of radial and elliptic flow we want to study here are the temperature dependence of the specific shear viscosity η/s and of the proportionality constant between η/s and the temperature-scaled microscopic relaxation time $\tau_\pi T$, $\kappa = \frac{\tau_\pi T}{\eta/s}$. Specifically, we will explore scenarios where $\eta/s = 0.16$ is a constant in the QGP phase but increases by variable amounts during the transition from QGP to hadrons, using the following parametrization for its temperature dependence:

$$\frac{\eta}{s}(T) = \frac{(\eta/s)_{\rm QGP} + (\eta/s)_{\rm HG}}{2} + \frac{(\eta/s)_{\rm QGP} - (\eta/s)_{\rm HG}}{2} \tanh\left(40\frac{T-T_c}{T_c}\right). \tag{8.1}$$

Here $T_c = 170\,\text{MeV}$, and $(\eta/s)_{\rm QGP} = 0.16$ and $(\eta/s)_{\rm HG}$ are (different) constants for the QGP and HG (hadron gas) phases. We will explore the range $0.16 \leq (\eta/s)_{\rm HG} \leq 0.48$, as illustrated in Figure 8.1. In the next three sections κ will be held constant at $\kappa = 3$;[13] consequences of a temperature dependent $\kappa(T) = (e+p)/p$ will be explored in Sec. 8.6.

8.3 Hydrodynamic evolution

In order to study how the fireball evolves with a temperature dependent $(\eta/s)(T)$ that increases in the HG phase, we graph the time evolution for the average transverse flow velocity $\langle\langle v_\perp \rangle\rangle$ (the average over the transverse plane being defined with the lab-frame energy density $\gamma_\perp e$ as weight), the spatial eccentricity $\epsilon_x = \frac{\langle y^2 - x^2\rangle}{\langle y^2 + x^2\rangle}$ of the lab-frame energy density distribution, the *flow* momentum anisotropy $\epsilon_p = \frac{\langle T_0^{xx} - T_0^{yy}\rangle}{\langle T_0^{xx} + T_0^{yy}\rangle}$ (where $\langle \dots \rangle$ denotes simple integration over the transverse plane and $T_0^{\mu\nu}$ is the ideal fluid part of the energy-momentum tensor, without viscous pressure

[13] The specific values $(\eta/s)_{\rm QGP} = 0.16$ and $\kappa = 3$ chosen here agree with those used by us in the earlier studies [17, 40] while the recent work [128] assumes $\kappa = 5$.

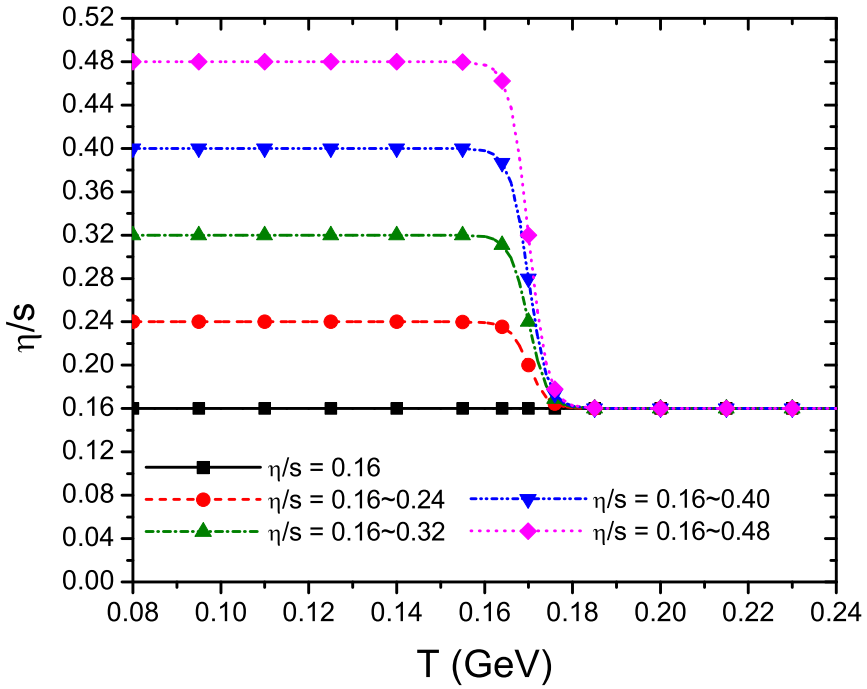

Figure 8.1: Five choices for the temperature dependent $(\eta/s)(T)$ studied in this work. The constant values at low T are multiples of $0.08 \approx \frac{1}{4\pi}$.

contributions), and the *total* momentum anisotropy $\epsilon_p' = \frac{\langle T^{xx} - T^{yy} \rangle}{\langle T^{xx} + T^{yy} \rangle}$ for different choices of the temperature dependence of η/s.

Since shear viscosity leads to viscous heating which generates entropy, holding the finally observed hadron multiplicity fixed requires that an increase in $(\eta/s)(T)$ must be accompanied by a decrease of the initial entropy of the fireball. We implement this by a decrease of the normalization of the initial entropy density distribution, keeping its shape fixed. Whereas for fixed initial conditions an overall increase of η/s leads to stronger radial acceleration due to a positive contribution from the viscous pressure tensor $\pi^{\mu\nu}$ to the transverse pressure gradients [51, 87, 129, 39, 38], this effect is largely compensated [130, 17, 128] after rescaling the initial entropy density to ensure fixed final multiplicity. For our temperature-dependent η/s this compensation no longer works in the same way: after rescaling the initial entropy density profile, to compensate for increased viscous heating in the hadronic phase, the QGP core shrinks and the HG corona grows in size. Since the viscous pressure is relatively larger in the hadronic phase than in the QGP, the *effective* transverse pressure gradient is *reduced* when increasing η/s only in the hadronic phase, leading to weaker radial acceleration. This can be seen in Fig. 8.1a, where we see a reduction oof the growth rate of the average radial flow velocity $\langle\langle v_\perp \rangle\rangle$ with increasing values of $(\eta/s)_{\rm HG}$, holding $(\eta/s)_{\rm QGP} = 0.16$ fixed.

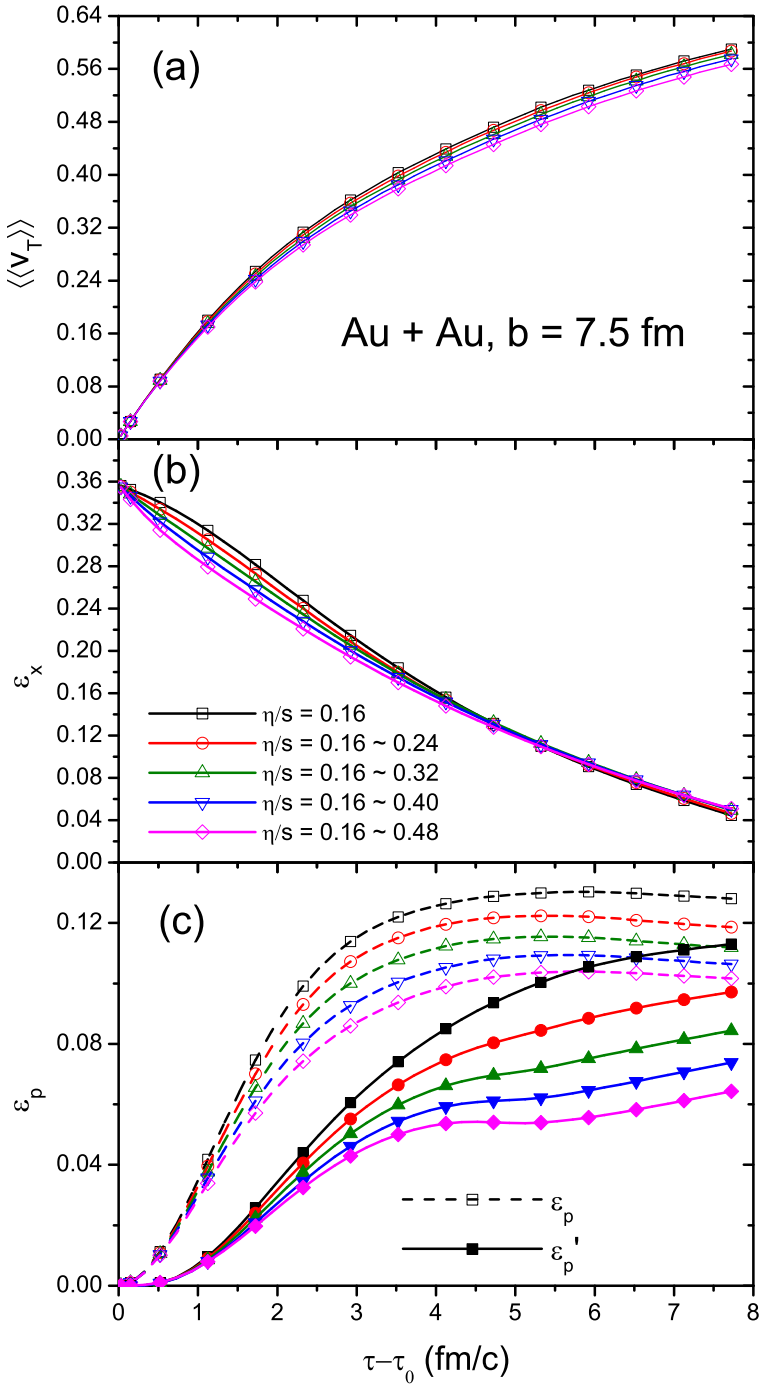

Figure 8.2: The average radial flow $\langle v_\perp \rangle$, spatial eccentricity ϵ_x, and the flow and total momentum anisotropies ϵ_p and ϵ_p' for Au+Au collisions at $b = 7.5\,\mathrm{fm}$ as functions of hydrodynamic evolution time $\tau - \tau_0$, for $\tau_0 = 0.4\,\mathrm{fm}/c$ and kinetic freeze-out temperature $T_{\mathrm{dec}} = 120\,\mathrm{MeV}$. Lines with different symbols correspond to different temperature dependences of η/s as shown in Fig. 8.1.

The larger shear viscosity in the hadronic corona leads to a more rapid initial decay[14] of the spatial fireball eccentricity ϵ_x (see Fig. 8.2b) and a slower growth rate and lower asymptotic value

[14]We note that ϵ is defined by integrating at fixed time τ over the entire transverse plane, including both thermalized and already decoupled matter. It is possible that the strong initial decay of ϵ seen in Fig. 8.2b arises mostly from contributions in that part of the hadronic corona that has already decoupled.

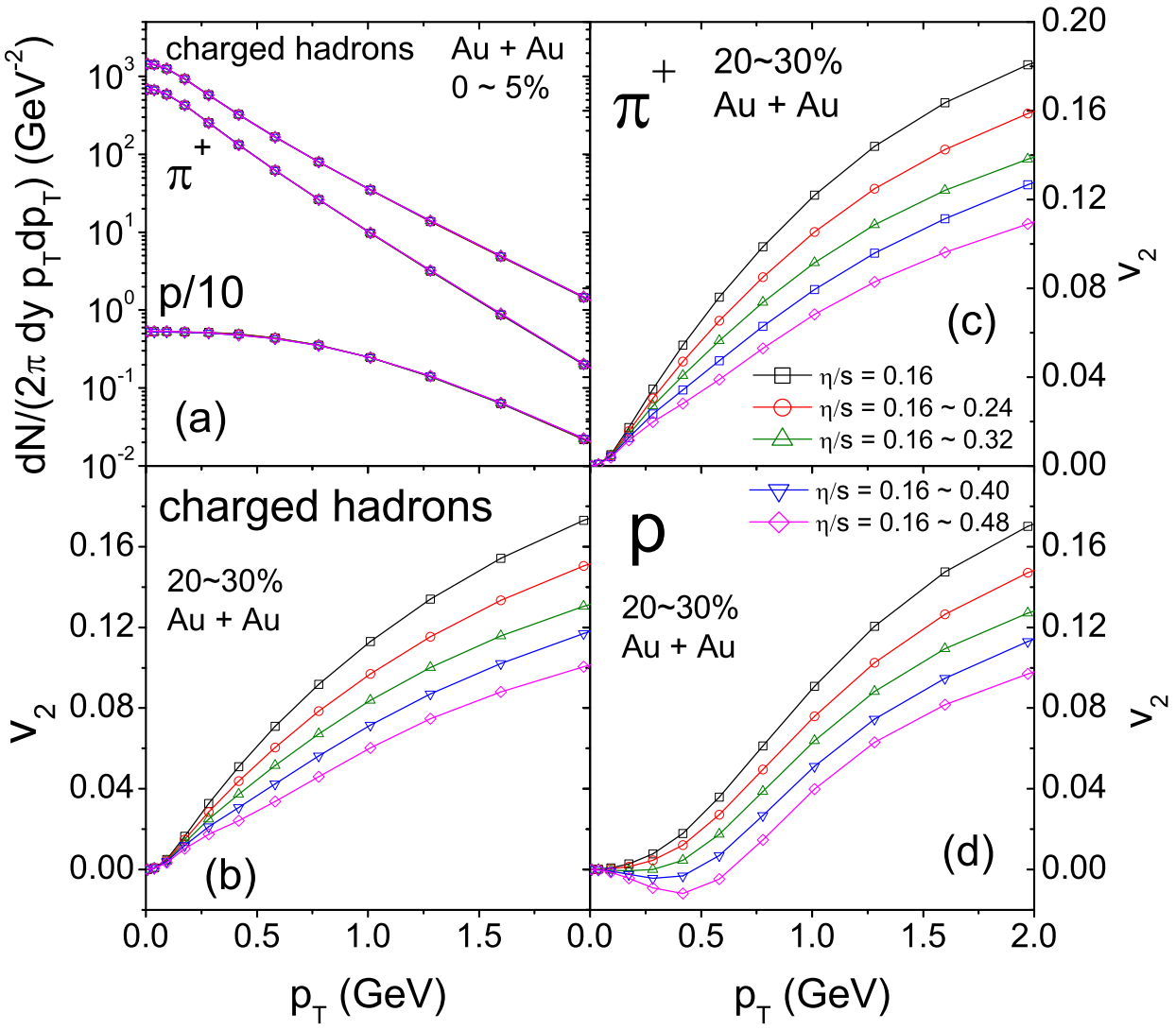

Figure 8.3: (a): Transverse momentum spectra for charged hadrons, pions, and protons from `VISH2+1` for the 5% most central Au+Au collisions ($b = 2.33\,\mathrm{fm}$). (b-c): Differential elliptic flow $v_2(p_T)$ for charged hadrons (b), pions (c) and protons (d) from Au+Au collisions at 20-30% centrality ($b = 7.49\,\mathrm{fm}$). Lines with different symbols correspond to different values of $(\eta/s)_{\mathrm{HG}}$ as shown in Fig. 8.1; $T_{\mathrm{dec}} = 120\,\mathrm{MeV}$. Decay products from all strong resonance decays are included. Charged hadrons include π^+, K^+, p, $\Sigma^{\pm}$, Ξ^-, Ω^-, and their antiparticles.

of the flow momentum anisotropy ϵ_p (Fig. 8.2c, open symbols). The spatial eccentricity curves in Fig. 8.2b all cross around $\tau - \tau_0 = 4.5\,\mathrm{fm}/c$, indicating the transition from stronger decay of ϵ_x at early times to weaker decay at late times for larger values of $(\eta/s)_{\mathrm{HG}}$. This is a consequence of the reduced flow anisotropy ϵ_p shown in Fig. 8.2c.

The lines with filled symbols in Figure 8.2c show that the effects of increased hadronic viscosity on the asymptotic values of the total momentum anisotropy ϵ_p' are much stronger than on the flow anisotropy ϵ_p: while the latter decreases by about 25% from $(\eta/s)_{\mathrm{HG}} = 0.16$ to $(\eta/s)_{\mathrm{HG}} = 0.48$, the corresponding decrease for ϵ_p' is almost twice as large. Also, most of the effect on ϵ_p' happens at late times $\tau - \tau_0 > 4.5\,\mathrm{fm}/c$ when most of the matter has converted into hadron gas. This reflects

the growth of the Navier-Stokes value $\pi^{\mu\nu}_{\rm NS} = 2\eta\sigma^{\mu\nu}$ of the viscous pressure contribution to $T^{\mu\nu}$ in the hadronic phase where $\eta_{\rm HG}$ increases. In contrast to ϵ_p, the total momentum anisotropy ϵ'_p does not saturate at late times after the spatial eccentricity (which drives the flow anisotropy) has essentially decayed to zero; its continued increase is due to the continuing decrease of the magnitude of the $\pi^{\mu\nu}$ components whose contribution to ϵ'_p is negative [38].

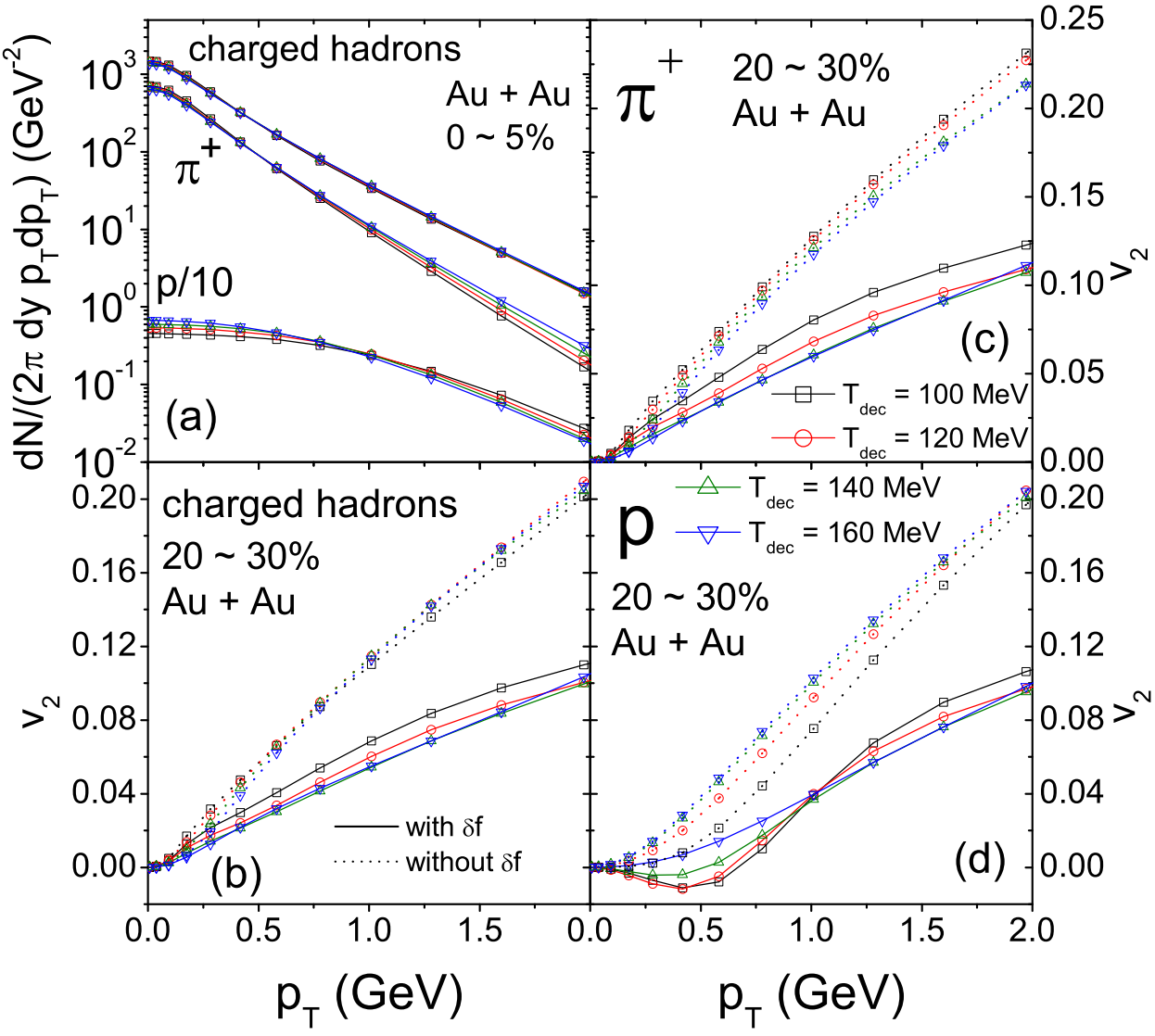

Figure 8.4: Similar to Fig. 8.3, for fixed $(\eta/s)_{\rm HG} = 0.48$ and different decoupling temperatures $T_{\rm dec}$ ranging from 160 to 100 MeV. In panels (b)-(d), dotted lines show $v_2(p_T)$ calculated without the δf correction whereas the solid lines show the full calculations.

The large difference between the late-time values of ϵ_p and ϵ'_p for high values of $\eta_{\rm HG}$ shows that, for strong hadronic viscosity, the viscous corrections to the local thermal equilibrium distribution on the kinetic decoupling surface at $T_{\rm dec}$ are big. We will explore this in more detail in Sec. 8.5.

8.4 Spectra and elliptic flow

8.4.1 Central and semi-peripheral Au+Au collisions

Figure 8.3 shows the transverse momentum spectra for charged hadrons, pions and protons from central Au+Au collisions (0−5% centrality) and their elliptic flows $v_2(p_T)$ for semiperipheral Au+Au collisions (20−30% centrality) for different choices of the hadronic shear viscosity $(\eta/s)_{\rm HG}$. The p_T-spectra in Fig. 8.3a are seen to be completely insensitive to the value of $(\eta/s)_{\rm HG}$. From the reduction of the radial flow seen in Fig. 8.2a one would have expected steeper spectra for larger $(\eta/s)_{\rm HG}$ since $T_{\rm dec} = 120\,{\rm MeV}$ is held fixed; clearly, for $p_T < 2\,{\rm GeV}/c$, the viscous correction δf to the local equilibrium distribution at freeze-out (which will be analyzed in greater depth in Sec. 8.5) happens to almost exactly compensate for the loss of radial flow, over the entire range of $(\eta/s)_{\rm HG}$ values studied here.

This is not true for the elliptic flow which is strongly reduced when the hadronic viscosity is increased (Figs. 8.3b-d). For protons a striking effect is seen for $(\eta/s)_{\rm HG} > 0.32$: The proton elliptic flow turns *negative* (i.e. protons show stronger flow perpendicular than parallel to the reaction plane) for low p_T. This effect is caused entirely by the δf correction. δf grows not only with p_T, as is well known, but also with the mass of the hadron. For massive hadrons, the shear viscous δf correction can be a strong effect even at $p_T = 0$. In Fig. 8.3 negative $v_2(p_T)$ caused by δf at low p_T is not visible for pions, but for protons and would be much stronger for Ω hyperons or J/ψ mesons if they also followed viscous hydrodynamical evolution down to $T_{\rm dec} = 120\,{\rm MeV}$.

The effect of the δf correction is studied in Fig. 8.4, for various choices of the decoupling temperature $T_{\rm dec}$. We hold the hadronic shear viscosity fixed at $(\eta/s)_{\rm HG} = 0.48$, the largest value studied here. The effect of variations in $T_{\rm dec}$ on the spectra in Fig. 8.4a is similar to what we observed in [17]: lower decoupling temperatures cause flatter proton spectra due to larger radial flow, steeper pion spectra due to the cooling effect which dominates for light particles, and almost no change in the charged hadron spectra whose mix of light and heavy particles effectively balances the counteracting cooling and radial flow effects.

In Figs. 8.4b-d we plot the differential elliptic flow for charged hadrons, pions and protons. The dotted lines show a calculation that ignores the viscous δf correction at freeze-out and thus only includes the $T_{\rm dec}$-dependence of the pure flow effects. We see that lower $T_{\rm dec}$ values suppress $v_2(p_T)$ for protons but increase it for pions at low p_T. This is really a consequence of the accompanying change of the p_T-spectra: Due to the large hadronic viscosity, very little additional flow momentum anisotropy is generated at temperatures below T_c. However, due to cooling, the pion spectra get steeper with decreasing $T_{\rm dec}$, moving more of their momentum anisotropy to low transverse momenta which leads to the increase of pion $v_2(p_T)$ at low p_T. Conversely, the proton spectra get flatter, in spite of cooling, due to additional radial flow developing between T_c and

$T_{\rm dec}$; consequently, their total momentum anisotropy gets shifted on average to larger transverse momenta, causing a reduction of proton $v_2(p_T)$ at low p_T (accompanied by an increase at high $p_T < 2\,{\rm GeV}/c$, beyond the range shown here). Both the flattening of the proton spectra and the shifting of their elliptic flow to larger p_T are stronger for the case of large hadronic shear viscosity ($(\eta/s)_{\rm HG} = 0.48$) studied here than for the case of temperature-independent $\eta/s = 0.16$ studied in [17]: The large hadronic viscosity generates stronger additional radial flow but less additional momentum anisotropy in the hadronic stage than does constant $\eta/s = 0.16$. Note that, without δf, proton $v_2(p_T)$ never turns negative, even for the largest hadronic shear viscosity studied in this work.

The solid lines in Figs. 8.4b-d show the full calculation of $v_2(p_T)$ including the δf correction. We see larger δf effects for protons than pions, due to their larger rest mass [38]. The full calculations feature a non-monotonic variation of pion and charged hadron $v_2(p_T)$ with decoupling temperature $T_{\rm dec}$: The suppression from δf is smaller for $T_{\rm dec} = 160$ MeV than for $T_{\rm dec} = 140\,{\rm MeV}$. The like explanation is that $T_{\rm dec} = 160\,{\rm MeV}$ is so close to the inflection point T_c of the shear viscosity $(\eta/s)(T)$ that, due to the finite relaxation time $\tau_\pi \sim 2\,{\rm fm}/c$ at this temperature, the viscous pressure tensor has not yet had time to fully evolve to its (larger) hadronic Navier-Stokes value whereas at $T_{\rm dec}$ complete relaxation has been achieved. At sufficiently low $T_{\rm dec}$, δf decreases with decreasing the decoupling temperature, since now η/s has reached its new, higher hadronic level and $\pi^{\mu\nu}$ becomes smaller simply due to hydrodynamic expansion [38].

8.4.2 Minimum bias collisions

In Figure 8.5 we show p_T spectra and differential elliptic flow for charged hadrons, pions and protons from minimum bias Au+Au collisions with $T_{\rm dec} = 120\,{\rm MeV}$. For these we summed our calculated results over all collision centralities $\leq 80\%$. The dependence on collision centrality is discussed in the next section.

Similar to what we saw in Fig. 8.3a for central Au+Au collisions, the spectra shown in Fig. 8.5a exhibit almost no sensitivity at all to variations of the specific shear viscosity $(\eta/s)_{\rm HG}$ in the hadron gas stage. We did observe some flattening of the charged hadron spectrum in the most peripheral (70−80%) centrality bin studied, where the viscous effects are strongest and the δf correction is largest. Due to its low weight in the average, this weak effect is not visible in the minimum bias result.

In Figures 8.5b and c, the minimum bias differential $v_2(p_T)$ of all charged hadrons, pions and protons are shown for different $(\eta/s)_{\rm HG}$. We see that the features observed in Fig. 8.3 for the specific 20−30% centrality bin carry over, qualitatively unchanged, to event samples without centrality selection: a significant increase of η/s in the hadron gas phase has a strong suppression

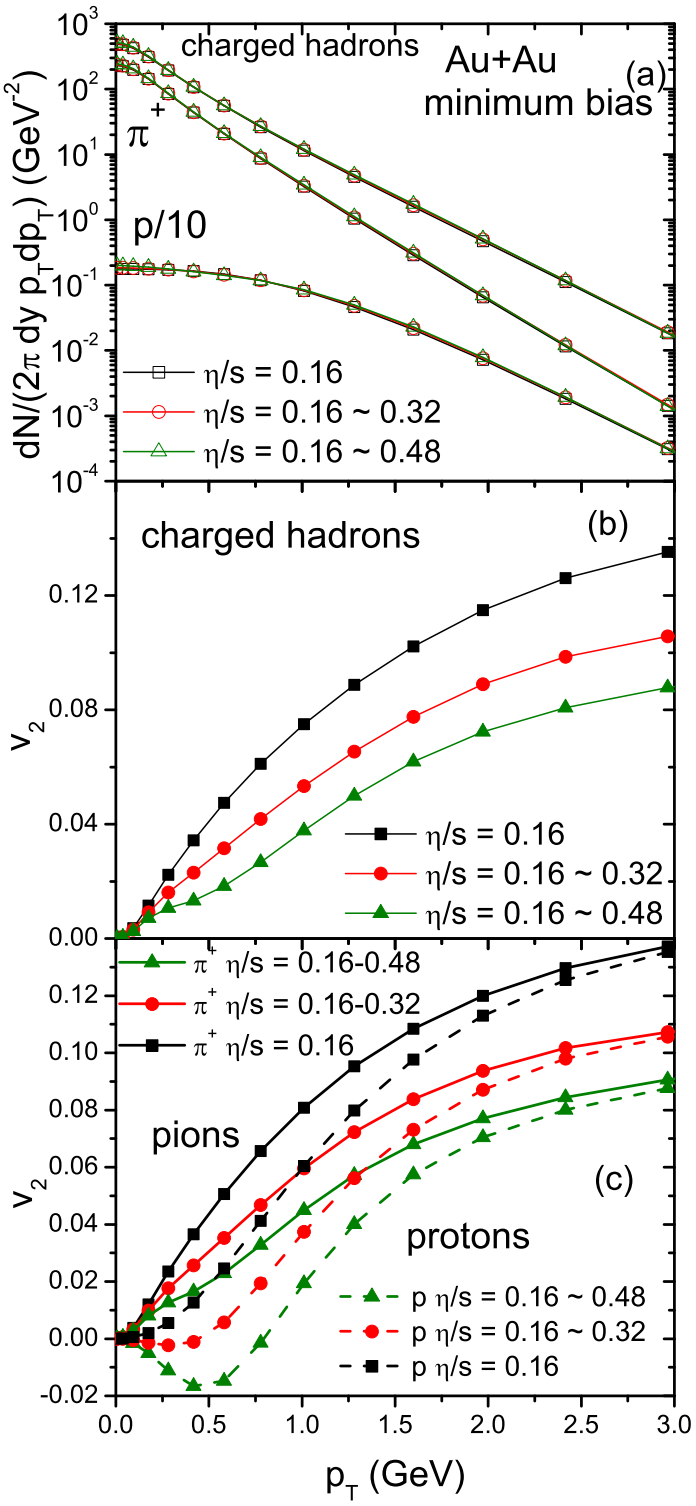

Figure 8.5: Transverse momentum spectra (a) and differential elliptic flow $v_2(p_T)$ for charged hadrons (b) and pions and protons (c) from minimum bias Au+Au collisions at RHIC, for various $(\eta/s)(T)$ as indicated (*c. f.* Fig. 8.1).

effect on $v_2(p_T)$. However, as shown in Sec. 8.4.1, the suppression arises mostly from the δf correction at kinetic freeze-out, with a much smaller contribution accounting for the lack of growth of the total momentum anisotropy in the hadronic phase when $(\eta/s)_{\rm HG}$ becomes large. Hence, the

strong suppression of differential elliptic flow by large hadronic shear viscosity shown here depends critically on the validity of viscous hydrodynamics as the correct framework for evolving δf all the way down to $T_{\rm dec} = 120\,{\rm MeV}$. This is assumed here, but not supported by the analysis presented in [124].

8.4.3 Centrality dependence of elliptic flow

The centrality dependence of the eccentricity-scaled elliptic flow v_2/ϵ is shown in Fig. 8.6 where we graph this quantity as a function of the final charged multiplicity density $(1/S)dN^{\rm ch}/dy$. for

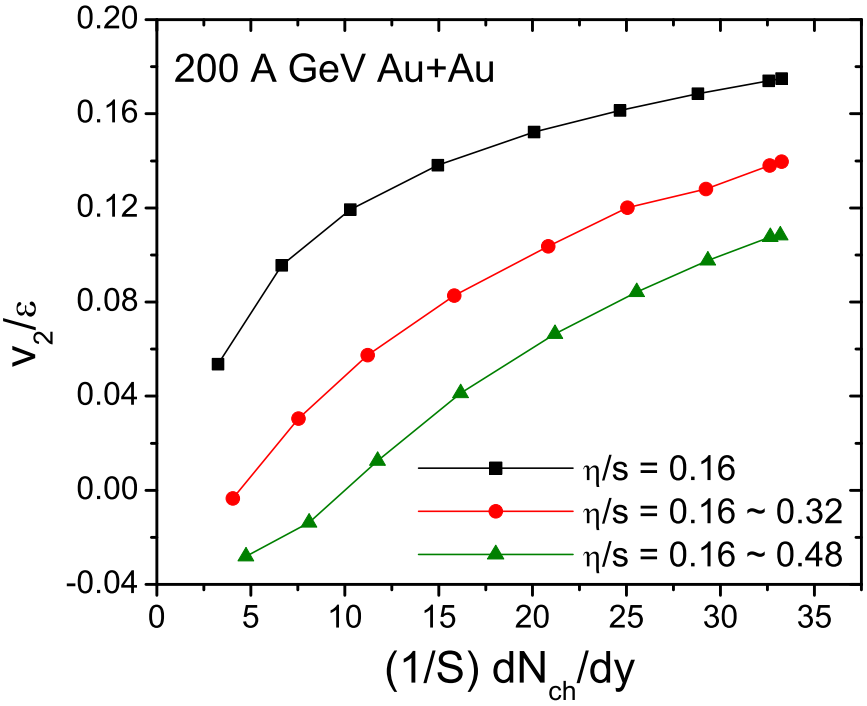

Figure 8.6: Eccentricity-scaled charged hadron elliptic flow v_2/ϵ as a function of the multiplicity density $(1/S)(dN^{\rm ch}/dy)$, for different values of $(\eta/s)_{HG}$. The overlap area $S = \pi\sqrt{\langle x^2\rangle\langle y^2\rangle}$ is calculated from the same initial profiles as the spatial eccentricity ϵ.

different values of $(\eta/s)_{\rm HG}$. (We obtain v_2 by integrating $v_2(p_T)$ over all p_T, without regard to possible p_T cuts imposed by experimental constraints.) Strong suppression of v_2/ϵ by hadronic viscosity is observed even in the most central collisions, but the effect is stronger in peripheral collisions. An increase of $(\eta/s)_{\rm HG}$ thus not only decreases v_2/ϵ, but also changes the slope of its centrality dependence. We note in passing that in recent studies with the hydro+cascade hybrid code `VISHNU` [40] this slope was fixed and controlled by the effective dissipation encoded in the hadron cascade, and that in [124] an (unsuccessful) attempt was made to extract the temperature-dependence of $(\eta/s)_{\rm HG}$ (here assumed to be T-independent) by matching the magnitude and slope of the corresponding v_2/ϵ vs. $(1/S)dN^{\rm ch}/dy$ curves from `VISH2+1` to those from `VISHNU`. We also observe that for the largest value of $(\eta/s)_{\rm HG}$ studied here, $(\eta/s)_{\rm HG} = 0.48$, the total charged

hadron elliptic flow turns negative in the most peripheral (70−80%) centrality bin. We found that this is caused by negative *pion* $v_2(p_T)$ around $p_T = 0.5\,\mathrm{GeV}/c$ (i.e. close to their average p_T), caused by large δf corrections at freeze-out.[15]

8.5 δf contributions

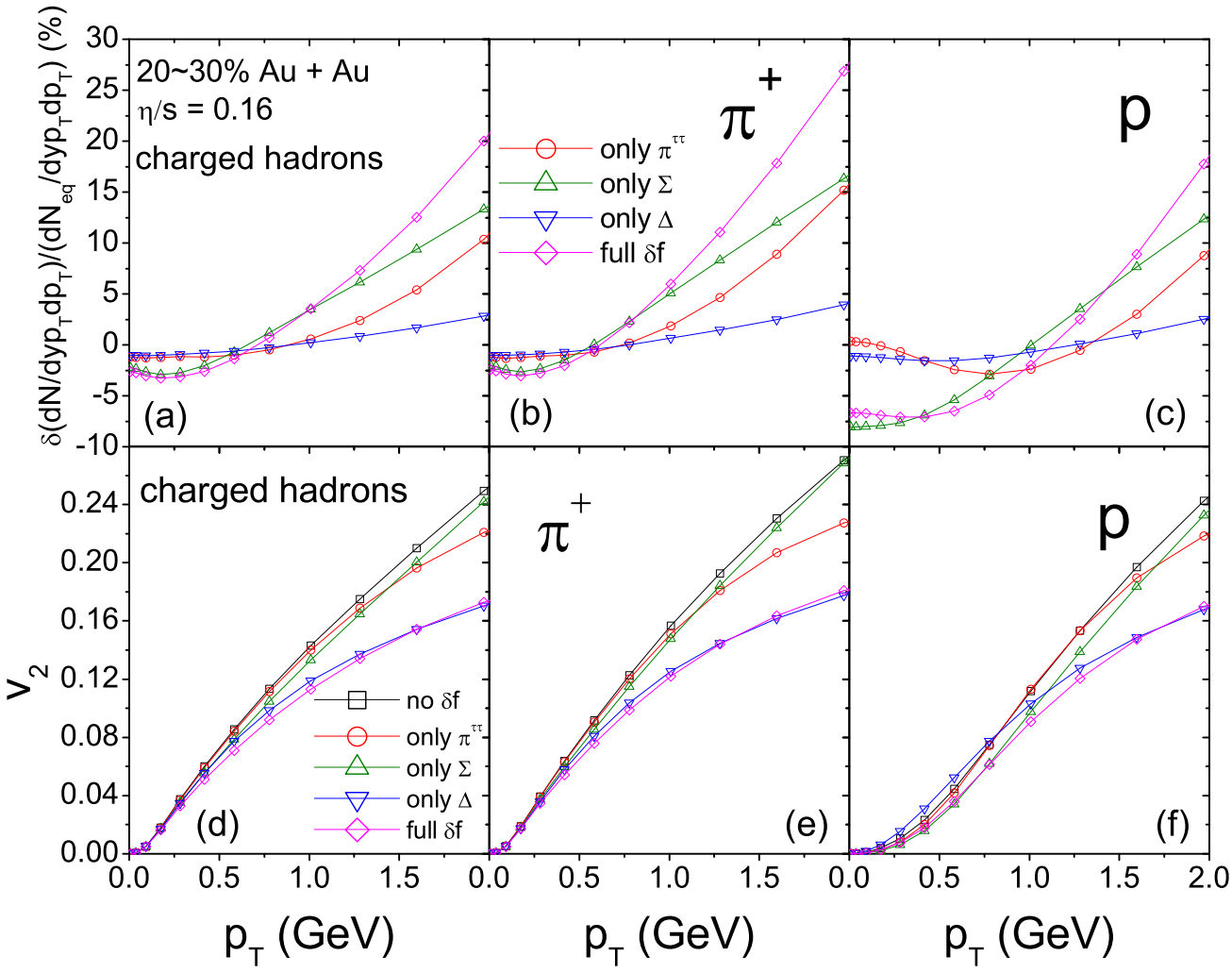

Figure 8.7: The δf correction for constant $\eta/s = 0.16$ to the p_T-spectra for charged hadrons (a), pions (b) and protons (c) at 0−5% centrality, and to their differential elliptic flow (d-f) at 20−30% centrality. Lines with different symbols denote individual contributions as described in the text.

[15]For 70−80% centrality and $(\eta/s)_{\mathrm{HG}} = 0.32$−$0.48$, we found for that for pions $v_2(p_T)$ first rises at very low p_T, then turns negative for $0.25 < p_T < 0.75\,\mathrm{GeV}/c$ before turning positive again and continuing to grow approximately linearly with p_T. This is different from protons whose $v_2(p_T)$ turns negative right away at small p_T, again with a minimum around $0.5\,\mathrm{GeV}/c$. All these effects are caused by large δf effects; in this centrality bin we do not trust viscous hydrodynamic predictions to be very robust.

Due to non-zero viscous pressure components $\pi^{\mu\nu}$, the distribution function $f_i(x,p)$ for hadron species i must deviate on the freeze-out surface from local equilibrium:

$$f_i(x,p) = f_{\mathrm{eq},i}(x,p) + \delta f_i(x,p). \tag{8.2}$$

We use [51]

$$\delta f_i = f_{\mathrm{eq},i} \cdot \frac{1}{2}\frac{p^\mu p^\nu}{T^2}\frac{\pi_{\mu\nu}}{e+p}, \tag{8.3}$$

noting that also other forms have been suggested in the literature [131, 132]. The numerator can be written as

$$\begin{aligned} & p^\mu p^\nu \pi_{\mu\nu}(x) = \\ & \pi^{\tau\tau}(x)\left[m_T^2\big(2\cosh^2(y-\eta)-1\big) + \frac{p_T^2}{v_\perp^2}\frac{\sin(2\phi_p)}{\sin(2\phi_v)} - 2\frac{p_T}{v_\perp}m_T\cosh(y-\eta)\frac{\sin(\phi_p+\phi_v)}{\sin(2\phi_v)}\right] \\ + \;& \Sigma(x)\left[-m_T^2\sinh^2(y-\eta) + \frac{p_T^2}{2}\Big(1-\frac{\sin(2\phi_p)}{\sin(2\phi_v)}\Big) + p_T m_T\cosh(y-\eta)v_\perp\frac{\sin(\phi_p-\phi_v)}{\tan(2\phi_v)}\right] \\ + \;& \Delta(x)\left[p_T m_T\cosh(y-\eta)v_\perp\frac{\sin(\phi_p-\phi_v)}{\sin(2\phi_v)} - \frac{p_T^2}{2}\frac{\sin(2(\phi_p-\phi_v))}{\sin(2\phi_v)}\right] \end{aligned} \tag{8.4}$$

where $\Sigma = \pi^{xx}+\pi^{yy}$, $\Delta = \pi^{xx}-\pi^{yy}$. Because of boost-invariance, tracelessness and orthogonality to u^μ, only three components of $\pi^{\mu\nu}$ are independent; we take them as Σ, Δ, and $\pi^{\tau\tau}$. $m_T = \sqrt{m^2+p_T^2}$ is the transverse mass of the particles, ϕ_p is the azimuthal angle of $\boldsymbol{p}_T$, and $\phi_v(x)$ is the azimuthal angle of the fluid velocity $\boldsymbol{v}$ at point x.

We now discuss the individual contributions from Eq. (8.4) to the p_T-spectra and elliptic flow, for the cases of constant $\eta/s = 0.16$ (Figure 8.7) and temperature-dependent $(\eta/s)(T)$ (Figure 8.8). In panels (a-c) we show the fractional contribution $\delta N/N_{\mathrm{eq}}$ from δf to the Cooper-Frye spectra of charged hadrons (a), pions (b) and protons (c). At low p_T, the contributions proportional to $\pi^{\tau\tau}$ and Δ (first and last terms on the r.h.s. of Eq. (8.4)) are small and overshadowed by the contribution from the average transverse viscous pressure Σ. The first (negative) term $\sim -m_T^2$ in the expression multiplying Σ dominates at low p_T. It obviously grows with rest mass, leading to large negative $\delta N/N_{\mathrm{eq}}$ corrections at low p_T for heavy hadrons such as Ω and J/ψ. For protons the effect remains below 10% in central Au+Au collisions, i.e. δf corrections are small and the calculation is reliable. At larger p_T, all three contributions in Eq. (8.4) turn positive and $\delta N/N_{\mathrm{eq}}$ switches sign (around $0.5\,\mathrm{GeV}/c$ for pions and around $1\,\mathrm{GeV}/c$ for protons). Again, the term $\sim\Sigma$ first dominates, but since it grows only linearly at large p_T it is eventually (at $p_T \sim 2\,\mathrm{GeV}/c$) overtaken by the term $\sim\pi^{\tau\tau}$. For constant $\eta/s = 0.16$, $|\delta N/N_{\mathrm{eq}}|$ remains below 25% up to $p_T = 2\,\mathrm{GeV}/c$ for all three spectra shown,[16] and the calculation is therefore reliable. For large

[16]The δf effects on charged hadron spectra can be qualitatively understood from those on pion and proton spectra by noting that at low p_T charged hadrons are dominated by pions whereas at larger p_T heavier hadrons become increasingly more important.

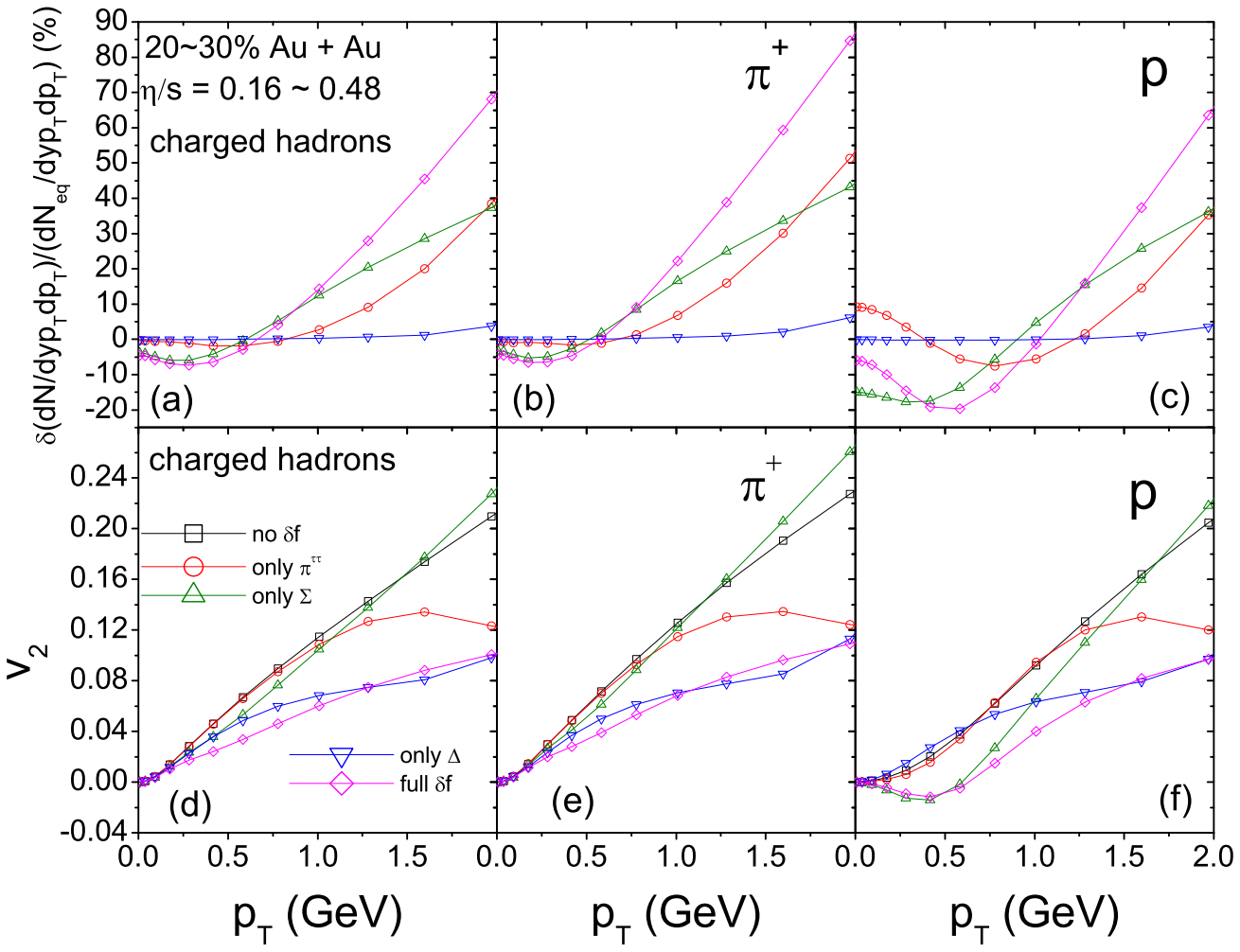

Figure 8.8: Similar to Fig. 8.7, but for temperature dependent $(\eta/s)(T)$, Eq. (8.1), with $(\eta/s)_{\rm HG} = 0.48$.

hadronic viscosity $(\eta/s)_{\rm HG} = 0.48$ (Fig. 8.8) the δf corrections to the p_T-spectra are larger, in particular the term $\sim \pi^{\tau\tau}$, and $|\delta N/N_{\rm eq}|$ reaches 70−80% at $p_T = 2\,{\rm GeV}/c$, indicating the imminent breakdown of the viscous hydrodynamic expansion $|\delta f| \ll f_{\rm eq}$.

In the lower panels of Figs. 8.7 and 8.8 we show the δf contributions to the differential $v_2(p_T)$ for charged hadrons (d), pions (e), and protons (f), again separated into their individual contributions according to Eq. (8.3). We see that for low p_T all three terms in Eq. (8.4) contribute to the suppression of elliptic flow, but that in this case at high p_T the term proportional to the viscous pressure *anisotropy* $\Delta = \pi^{xx} - \pi^{yy}$ plays the dominant role, overshadowing the terms $\sim \Sigma$ and (except for the largest hadronic viscosities) also $\sim \pi^{\tau\tau}$. The latter grows quadratically with p_T and eventually wins over the term $\sim \Sigma$; for large hadronic viscosity (Fig. 8.8) it even exceeds the anisotropy term $\sim \Delta$ at sufficiently large p_T. The term proportional to the average transverse viscous pressure Σ individually generates a positive elliptic flow correction at large p_T (i.e. at $p_T \sim 2\,{\rm GeV}/c$ for constant $\eta/s = 0.16$ and at $p_T \sim (1{-}1.5)\,{\rm GeV}/c$ for T-dependent $(\eta/s)(T)$ with $(\eta/s)_{\rm HG} = 0.48$). Similarly the anisotropy term $\sim \Delta$ by itself increases proton elliptic flow at low p_T

if the hadronic viscosity is large enough (Fig. 8.8f). In the sum, however, these positive individual corrections are always overwhelmed by the remaining two negative corrections, leading to an overall suppression of $v_2(p_T)$ at all p_T in all cases. Interestingly, the negative proton elliptic flow at low p_T and large $(\eta/s)_{\rm HG}$ values noted earlier (Figs. 8.3-8.5) is not caused by the viscous pressure anisotropy Δ, but by the average transverse viscous pressure Σ (green triangles in Fig. 8.8f). This phenomenon is driven by the effect of Σ on the proton spectra (Figs. 8.7c and 8.8c): Σ suppresses the spectra at low p_T, leading (in extreme situations) to the formation of a shoulder in the proton spectra which is known [32] to cause negative v_2.

8.6 Large hadronic relaxation times

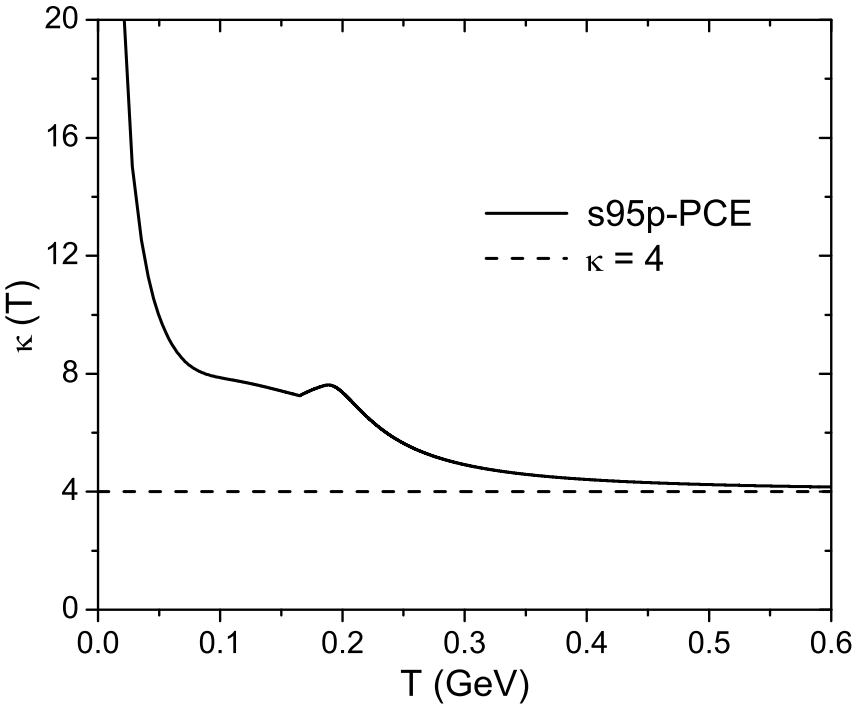

Figure 8.9: The temperature dependent $\kappa(T)$ from Eq. (8.5) for EOS `s95p-PCE` (solid), compared with the massless limit $\kappa = 4$ (dashed).

Motivated by the study of the `VISHNU` model in [124] we explore in this section the consequences of very large relaxation times τ_π in the hadronic phase. Specifically, we assume a relation proposed in [133],

$$\kappa(T) = \frac{e+p}{p}(T), \tag{8.5}$$

which can be easily worked out for our EOS `s95p-PCE` and is shown in Fig. 8.9. In the massless limit (i.e. at large T where the EOS approaches $e = 3p$), this expression approaches the value $\kappa = 4$. To explore effects specifically related to the T-dependence of κ, we compare in this section results from Eq. (8.5) with those for constant $\kappa = 4$ (and not $\kappa = 3$ as in the preceding sections).

The QGP viscosity is kept at $(\eta/s)_{\rm QGP} = 0.16$ throughout, but we toggle $(\eta/s)_{\rm HG}$ in Eq. (8.1) between the two values 0.16 and 0.48 (see Fig. 8.1).

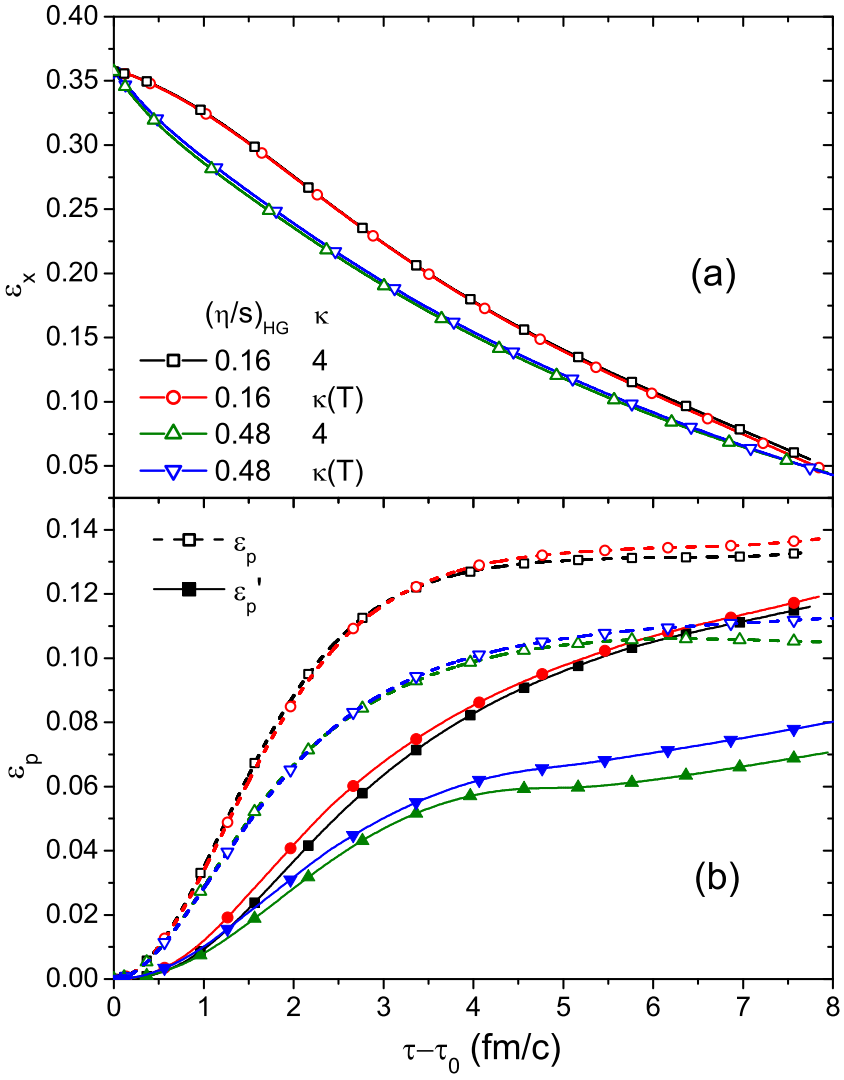

Figure 8.10: Same as Fig. 8.2b,c, but for $\kappa(T)$ from Eq. (8.5) and constant $\kappa = 4$ instead of $\kappa = 3$. For the QGP $(\eta/s)_{\rm QGP} = 0.16$ is used throughout whereas $(\eta/s)_{\rm HG}$ is varied between 0.16 and 0.48 as indicated in the legend.

Figure 8.10 shows a similar analysis as Fig. 8.2, but now comparing constant with T-dependent κ values. From Fig. 8.10a we conclude that the temperature dependence of κ has no visible influence on the evolution of the spatial eccentricity ϵ_x, irrespective of whether the specific shear viscosity η/s grows in the hadronic phase or not. On the other hand we see in Fig. 8.10b that a $\kappa(T)$ that grows around and below T_c as shown in Fig. 8.9 reduces significantly the viscous suppression of the total momentum anisotropy ϵ_p' that is otherwise caused by a large hadronic shear viscosity.[17] Analyzing panel (b) of Fig. 8.10 in more detail, we observe that during the early

[17]Please note that the extremely rapid rise of $\kappa(T)$ below $T \sim 50\,$MeV seen in Fig. 8.9 is irrelevant in this context because the fireball matter decouples already at $T_{\rm dec} = 120\,$MeV.

stage of the evolution larger hadronic relaxation times have little effect on the flow momentum anisotropy ϵ_p, consistent with the almost unchanged decay rate of the spatial eccentricity seen in panel (a) that drives the anisotropic flow. At late times, however, the larger $\kappa(T)$ is seen to have a small positive effect on the generation of anisotropic collective flow. Increasing the response time τ_π with which the viscous pressure tensor $\pi^{\mu\nu}$ can react to changes in the velocity shear tensor apparantly allows the collective flow anisotropy to grow more easily, with less viscous damping, than if $\pi^{\mu\nu}$ is allowed to relax to its Navier-Stokes value $\pi^{\mu\nu}_{\rm NS} = 2\eta\sigma^{\mu\nu}$ more quickly. This is a cumulative effect that becomes visible most clearly at late times when most of the fireball matter is affected by the larger $\kappa(T)$ values at lower temperatures.

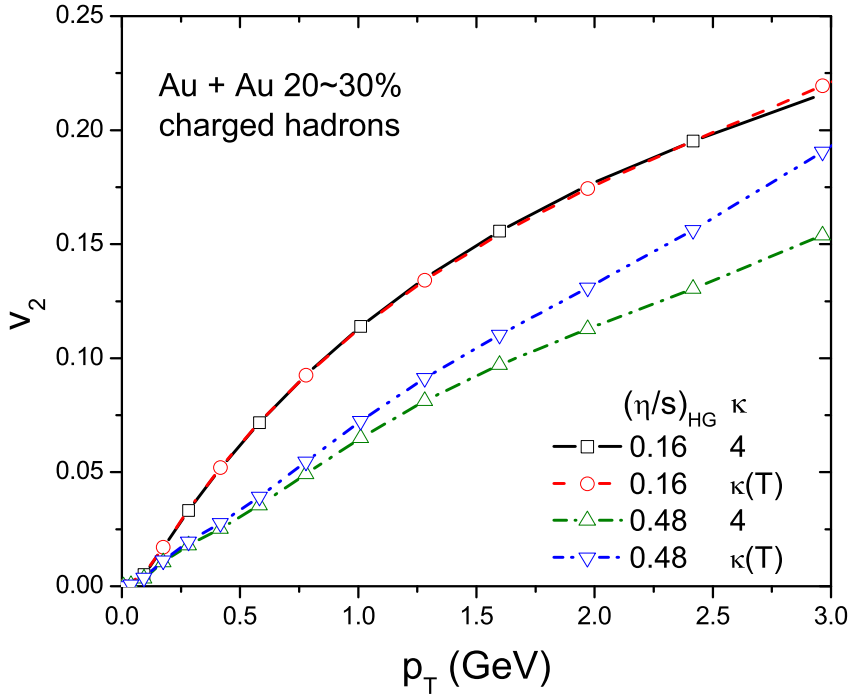

Figure 8.11: Differential elliptic flow $v_2(p_T)$ for charged hadrons, using a temperature dependent $\kappa(T)$. Same parameters as in Fig. 8.10.

The total momentum anisotropy ϵ_p', on the other hand, is more strongly affected by a low-temperature growth of $\kappa(T)$ (solid lines in Fig 8.10b). ϵ_p' is suppressed relative to the flow anisotropy ϵ_p by the non-equilibrium corrections $\sim\pi^{\mu\nu}$ in the energy-momentum tensor. When the relaxation time $\tau_\pi T$ is allowed to grow large in the hadronic phase, this suppression is found to be reduced, and the reduction is relatively larger for large values of $(\eta/s)_{\rm HG}$ (corresponding to a larger Navier-Stokes value $\pi^{\mu\nu}_{\rm NS}$) than for smaller $(\eta/s)_{\rm HG}$. We also note that this suppression of the $\pi^{\mu\nu}$-contribution to ϵ_p' is visible already at early times when the larger $\kappa(T)$ values affect only the fireball corona. In fact, for constant $\eta/s = 0.16$ (solid squares and circles) the low-temperature growth of $\kappa(T)$ leads to a bigger increase of ϵ_p' over ϵ_p at early than at late times; this is due to the larger longitudinal expansion rates at early times which lead to larger Navier-Stokes values

for $\Delta = \pi^{xx} - \pi^{yy}$ everywhere, thus causing greater sensitivity to increased $\kappa(T)$ values in the fireball corona. In the case of T-dependent η/s (solid upright and inverted triangles) the effects from a delayed response τ_π are larger at late times; in this situation, the Navier-Stokes values for $\Delta = \pi^{xx} - \pi^{yy}$ grow in the hadronic phase due the sudden increase of η/s below T_c, clearly reflected by a "kink" in the growth of ϵ_p' around $\tau - \tau_0 = 4\,\mathrm{fm}/c$ (see upright green solid triangles in Fig 8.10b). This kink is largely washed out by a simultaneous rise of $\kappa(T)$ (inverted blue solid triangles in Fig 8.10b).

The behavior of the total momentum anisotropy ϵ_p' is directly reflected in the charged hadron elliptic flow, shown in Fig. 8.11. We point especially to the reduction of the (negative) $\pi^{\mu\nu}$ contributions to ϵ_p' in the case of T-dependent $(\eta/s)(T)$, which manifests itself through reduced δf corrections to $v_2(p_T)$ which again are most pronounced at large p_T (green triangles and blue inverted triangles in Fig. 8.11). For constant η/s, on the other hand, the larger hadronic relaxation time has little effect on the differential $v_2(p_T)$, consistent with the very small effect on the total momentum anisotropy ϵ_p' at late times seen in Fig. 8.10b.

8.7 Temperature dependent $(\eta/s)(T)$ in the QGP phase

Now, we would like to change gear and explore the temperature dependence of $(\eta/s)(T)$ in the high temperature QGP phase. From the study in Chapter 5, we found that we over-predict of $v_2\{4\}(p_T)$ in Pb+Pb collisions at the LHC seen in Fig. 5.7a, together with the excellent description of the same quantity in Au+Au collisions at RHIC seen in Fig. 5.3, thus suggests that the fireball liquid formed in LHC collisions might be slightly more viscous (i.e. possess larger average η/s) than at RHIC energies [128, 47]. In this section we present some results using a temperature dependent specific shear viscosity, $(\frac{\eta}{s})(T)$, that were motivated by such considerations.

Figure 8.12 illustrates the following three trial functions explored in this section:

$$\left(\frac{\eta}{s}\right)_1 = 0.2 + 0.3\,\frac{T - T_{\mathrm{chem}}}{T_{\mathrm{chem}}}, \tag{8.6}$$

$$\left(\frac{\eta}{s}\right)_2 = 0.2 + 0.4\,\frac{(T - T_{\mathrm{chem}})^2}{T_{\mathrm{chem}}^2}, \tag{8.7}$$

$$\left(\frac{\eta}{s}\right)_3 = 0.2 + 0.3\,\sqrt{\frac{T - T_{\mathrm{chem}}}{T_{\mathrm{chem}}}}. \tag{8.8}$$

Here $T_{\mathrm{chem}} = 165\,\mathrm{MeV}$ is the chemical decoupling temperature and stands for the "transition temperature" at which the hadronization of quarks and gluons is complete.

As pointed out in [128], the spectra and elliptic flow in Au+Au collisions at RHIC energies are most sensitive to the average value of η/s in the temperature region below 220-230 MeV. We have checked that altering η/s at higher temperatures as shown in Fig. 8.12 has little influence on the results at RHIC energies shown in Sec. 5.2.

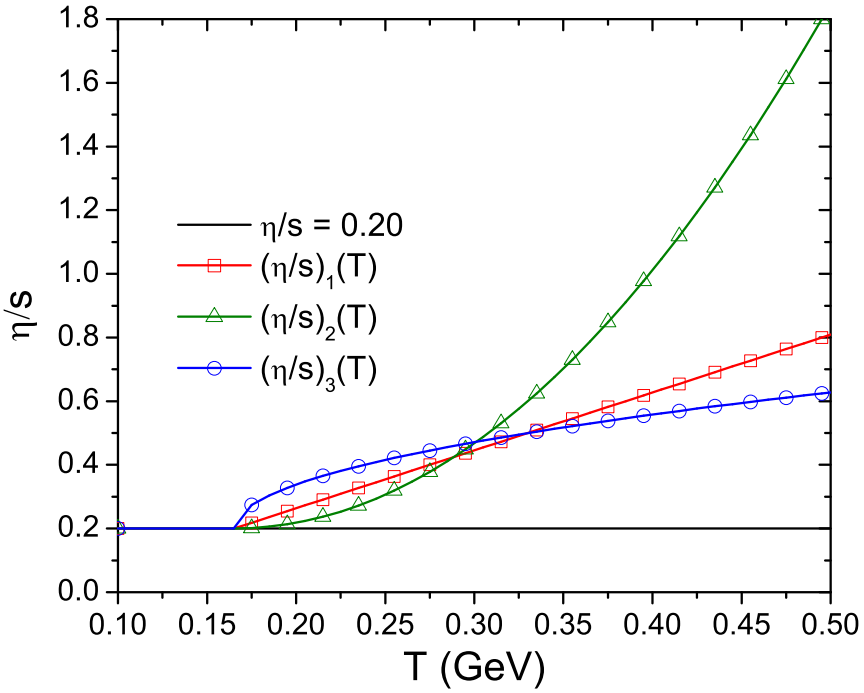

Figure 8.12: Three temperature dependent parametrizations $(\eta/s)(T)$ studied in this section. In all cases, $\eta/s = 0.2$ for $T < T_{\rm chem} = 165\,{\rm MeV}$.

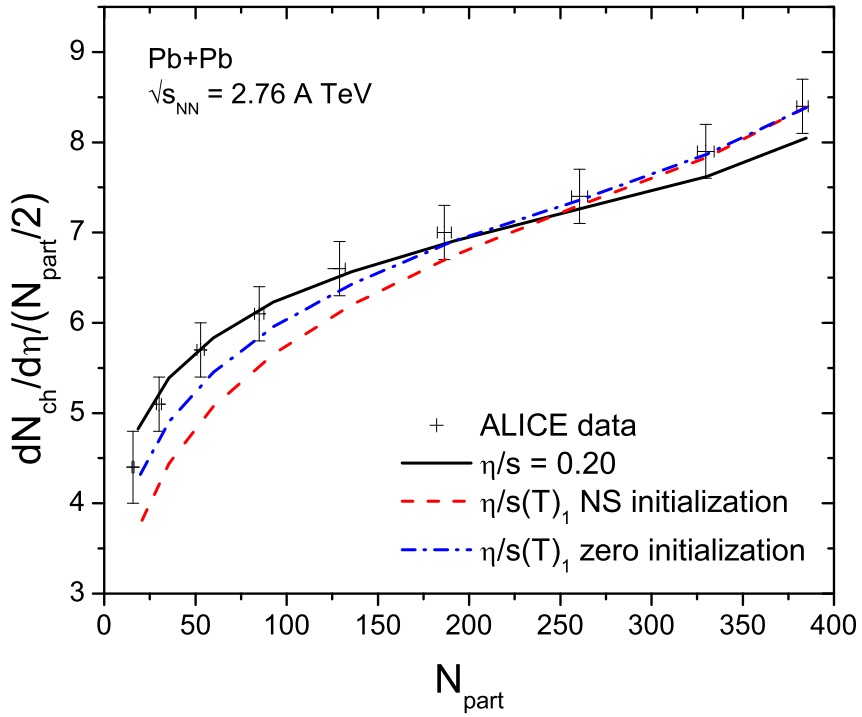

Figure 8.13: Final charged multiplicity per wounded nucleon pair as a function of number of participant nucleons in Pb+Pb collisions at $\sqrt{s} = 2.76\,A\,{\rm TeV}$, for different functional forms of $(\eta/s)(T)$ and initial conditions for the shear stress tensor $\pi^{\mu\nu}$ (see text).

Figure 8.13 illustrates the influence of a linear temperature dependence of η/s as in Eq. (8.6) on the centrality dependence of charged hadron production. The solid black line is the same as shown in the upper part of Fig. 8.12 where it forms the lower bound of the shaded region; it corresponds

to constant $\eta/s = 0.2$ and Navier-Stokes initial conditions for the shear stress tensor, $\pi^{\mu\nu} = 2\eta\sigma^{\mu\nu}$ at $\tau_0 = 0.6\,\mathrm{fm}/c$. The dashed and dash-dotted lines in Fig. 5.1 use $(\eta/s)_1(T)$ with either Navier-Stokes (dashed) or zero (dash-dotted) initial conditions for $\pi^{\mu\nu}$. These last two lines were normalized to the ALICE point for the 0−5% most central Pb+Pb collisions ($dN^{\mathrm{ch}}/d\eta = 1584\pm80$ [99]), whereas the black line was normalized to our best guess before the ALICE data became available ($dN^{\mathrm{ch}}/dy = 1800$, corresponding to $dN^{\mathrm{ch}}/d\eta = 1548$). The centrality dependence is then controlled by the predictions from the MC-KLN model, modified by viscous entropy production during the hydrodynamic evolution.

We see that even a relatively modest temperature dependent increase of η/s in the QGP phase leads to a significantly stronger non-linearity in the dependence of charged particle production on the number of wounded nucleons. The reason is that an increase of η/s with temperature leads to more viscous heating in central collisions (which probe higher initial temperatures and such larger effective shear viscosities) than in peripheral ones (whose initial temperatures are lower). Since the entropy production rate is given by

$$\partial_\mu S^\mu = \frac{\pi^{\mu\nu}\pi_{\mu\nu}}{2\eta T}, \tag{8.9}$$

this effect is stronger for Navier-Stokes initial conditions (where $\pi^{\mu\nu}$ is proportional to the velocity shear tensor $\sigma^{\mu\nu}$ which at early times diverges like $1/\tau$) than for zero initial shear stress (where $\pi^{\mu\nu}$ starts from zero and approaches its Navier-Stokes value $2\eta\sigma^{\mu\nu}$ only after several relaxation times τ_π when, due to its $1/\tau$ decay, it has already decreased to much smaller values).[18]

If one were to postulate the validity of the MC-KLN model as the correct description of the initial particle production, the ALICE data shown in Fig. 8.13 would exclude a temperature dependence of η/s as given in Eqs. (8.6) and (8.7) for Naver-Stokes initial conditions. While we are not prepared to make such a statement on the basis of Fig. 8.13 alone, we believe that it is important to point out this relatively strong sensitivity of the centrality dependence of $dN^{\mathrm{ch}}/d\eta$ to the transport properties of the expanding fireball medium and to emphasize the constraints it thus places on possible models for the QGP shear viscosity.

We now turn to the discussion of the influence of a possible temperature dependence of η/s on the charged hadron p_T-spectra and elliptic flow. Figure 8.14 shows LHC predictions for 2.76 A TeV Pb+Pb collisions of 20−30% centrality. To ensure comparability of the different cases studied in this figure we simply normalized the initial entropy density profile such that we always obtain $dN^{\mathrm{ch}}/dy = 770$, i.e. the same value that we had obtained before for constant $\eta/s = 0.2$ at this centrality. We first note that for constant $\eta/s = 0.2$, we don't observe any significant difference

[18]For reference we list the fractions of the finally measured entropy in the most central and most peripheral centrality bins shown in Fig. 8.13 that are generated by viscous heating during the hydrodynamic expansion: Constant $\eta/s = 0.2$: $\Delta S/S_{\mathrm{final}} = 26\%$ (0−5%) and 33% (70−80%); $(\eta/s)_1(T)$ with $\pi_0^{\mu\nu} = 0$: $\Delta S/S_{\mathrm{final}} = 25\%$ (0−5%) and 15% (70−80%); $(\eta/s)_1(T)$ with $\pi_0^{\mu\nu} = 2\eta\sigma^{\mu\nu}$: $\Delta S/S_{\mathrm{final}} = 60\%$ (0−5%) and 49% (70−80%).

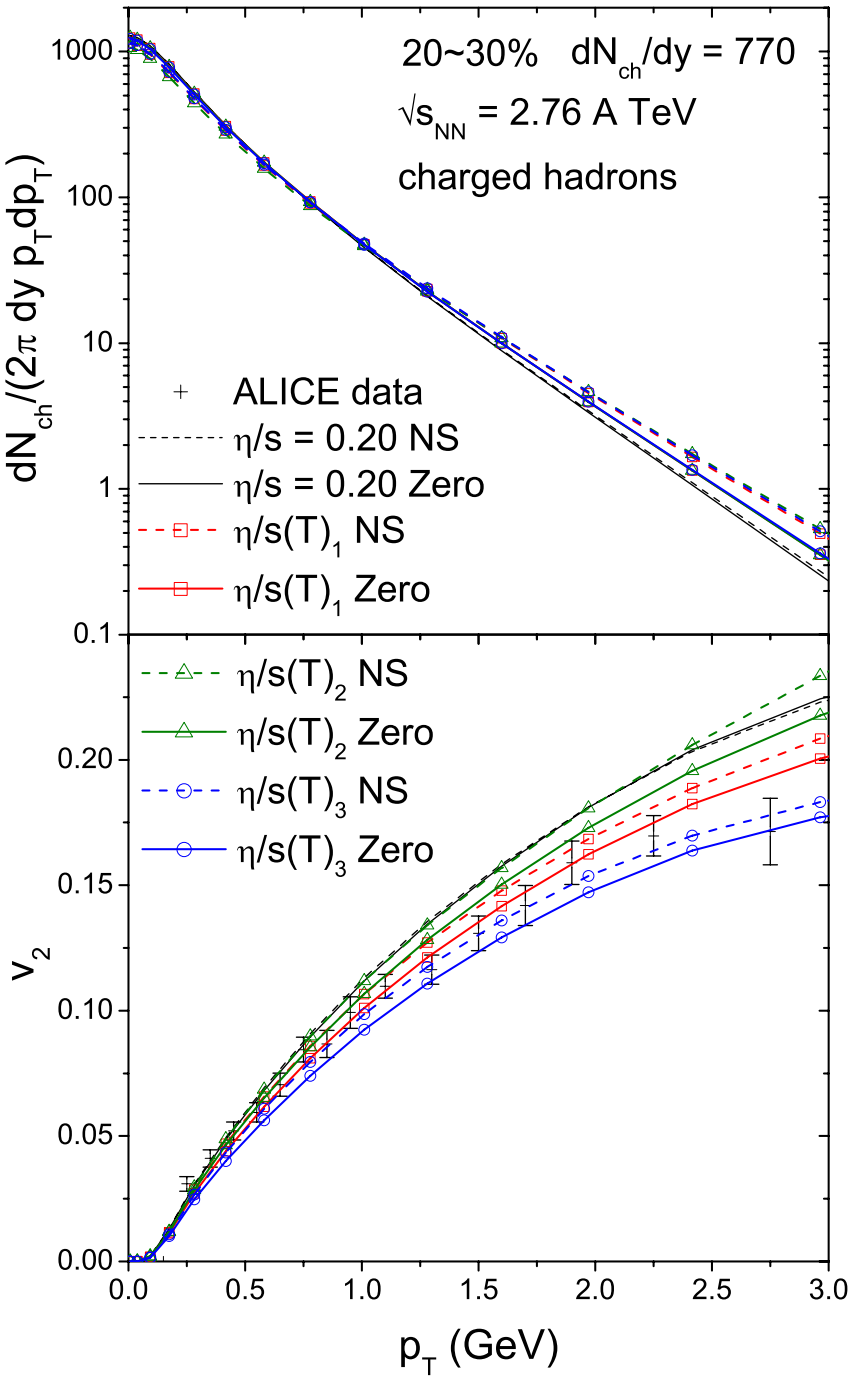

Figure 8.14: Charged hadron transverse momentum spectra (top) and differential elliptic flow (bottom) for 2.76 A TeV Pb+Pb collisions at 20−30% centrality, for different models for the temperature dependence of η/s and different initial conditions for $\pi^{\mu\nu}$ (Navier-Stokes ("NS") or 0 ("Zero")). The ALICE data in the bottom panel are from Ref. [52].

in the charged hadron spectra and elliptic flow between zero and Navier-Stokes initialization for $\pi^{\mu\nu}$. Turning to the temperature-dependent parametrizations $(\eta/s)_i(T)$, we note that for zero initialization of $\pi^{\mu\nu}$ (solid lines) our results agree with those reported in [128]: An increase of η/s at higher QGP temperatures leads to somewhat harder charged hadron p_T-spectra (i.e. somewhat stronger radial flow, caused by the larger tranverse effective pressure gradients at early times)

η/s model	$\pi_0^{\mu\nu}$	$s_0\,(\mathrm{fm}^{-3})$	$T_0\,(\mathrm{MeV})$
$\eta/s = 0.2$	0	191.6	427.9
	NS	172.4	413.9
$(\eta/s)_1(T)$	0	179.6	419.2
	NS	119.3	368.7
$(\eta/s)_2(T)$	0	179.6	419.2
	NS	115.6	365.1
$(\eta/s)_3(T)$	0	175.2	416.0
	NS	116.6	366.1

Table 8.1: Initial central entropy densities s_0 and temperatures T_0 for the viscous hydrodynamic simulations of 20−30% centrality Pb+Pb collisions at the LHC ($\sqrt{s} = 2.76\,A\,\mathrm{TeV}$) shown in Fig. 8.14. The different models for the T-dependence of η/s are defined in Eqs. (8.6)–(8.8). "0" stands for $\pi_0^{\mu\nu} = 0$ at τ_0, "NS" stands for Navier-Stokes initialization of the shear stress tensor, $\pi_0^{\mu\nu} = 2\eta\sigma^{\mu\nu}$ at τ_0.

and a suppression of the differential elliptic flow (due to an increase of the time-averaged effective shear viscosity of the fluid). It is interesting to observe the hierarchy of the curves in Fig. 8.14 corresponding to the three parametrizations (8.6)–(8.8): For the p_T-spectra, all three T-dependent viscosities lead to almost identical hardening effects on the spectral slope, while for the differential elliptic flow $v_2^{\mathrm{ch}}(p_T)$ the curves are ordered not according to the η/s-values at the initial central fireball temperature (see Table 8.1), but according to their hierarchy in the $165 < T < 280\,\mathrm{MeV}$ range. In fact, the observed magnitudes of the viscous v_2 suppression for the three $(\eta/s)(T)$ functions suggest that, at this beam energy and collision centrality, the buildup of elliptic flow is dominated by the QGP transport properties at $200 < T < 250\,\mathrm{MeV}$. (At RHIC energies, the transport properties for $T \sim 200{-}220\,\mathrm{MeV}$ dominate the generation of v_2 [128].)

For Navier-Stokes initial conditions (dashed lines in Fig. 8.14), the increase in radial flow caused by an increase of η/s at high temperature is stronger and the viscous v_2 suppression is weaker than for zero initial $\pi^{\mu\nu}$. This is caused by the much larger initial shear stress tensor components in the NS case, compared to the case of $\pi_0^{\mu\nu} = 0$ where $\pi^{\mu\nu}$ approaches its (by that time already much smaller) Navier-Stokes limit only after several relaxation times τ_π [39]. The increase of η/s with temperature generates a steeper initial transverse effective pressure gradient (since $\pi^{\mu\nu}$ grows faster than the entropy density s when η/s increases with temperature), and this generates stronger radial flow. It also causes a larger spatial eccentricity of the initial effective pressure profile which (when compared to the case of $\pi_0^{\mu\nu} = 0$) generates stronger elliptic flow. In fact, we found that for earlier starting times τ_0 (where the Navier-Stokes values for $\pi^{\mu\nu}$ are even larger), the quadratic parametrization $(\eta/s)_2(T)$ with NS initial conditions can lead to *more* elliptic flow than a constant $\eta/s = 0.2$, in spite of the larger mean viscosity of the fluid.

We conclude from this exercise that a firm determination whether or not the ALICE data point towards a temperature-dependent growth of η/s with increasing T, as expected from perturbative

QCD [54] and (perhaps) from lattice QCD [134], is not possible without a better understanding of the initial conditions for the energy momentum tensor (in particular the shear stress components) at the beginning of the hydrodynamic evolution. Whereas generically larger viscosities cause a suppression of the elliptic flow, temperature-dependent viscosities can influence the initial effective pressure profile and its eccentricity in a way that counteracts this tendency and, for some models such as Navier-Stokes initial conditions, can even overcompensate it.

8.8 Discussion and conclusions

Figure 8.11 has important implications: Comparing the blue line with inverted triangles to the case of constant κ and η/s (black squares), we conclude that the suppression of $v_2(p_T)$ reflected in the blue line could have arisen in two different ways: (i) by a large increase of η/s in the hadronic phase, accompanied by a similarly large increase of κ, as shown here, or (ii) by a much less pronounced increase of the hadronic shear viscosity, compensated by a correspondingly reduced increase of the hadronic relaxation time. In other words, the hadronic shear viscosities and relaxation times extracted from a given charged hadron $v_2(p_T)$ are strongly correlated and impossible to determine independently from a single elliptic flow measurement. Whether and how the systematic exploration of differential elliptic flow for different particle species and different collision systems at different centralities can help to resolve this ambiguity remains to be seen.

The study presented here shows that any discussion of large dissipative effects in the hadronic phase of heavy-ion collisions, reflected by specific shear viscosities and (scaled) microscopic relaxation times that grow as the system cools below the critical quark-hadron transition temperature, is really a discussion of δf, i.e. of the deviation of the freeze-out distribution function from its local equilibrium form and its reflection in the final hadron spectra and anisotropies. As the system cools and approaches kinetic freeze-out, dissipative effects become stronger and stronger, bringing the framework of viscous hydrodynamics closer and closer to breakdown. In this sense, our results have to be taken as qualitative insights but should not be confused with quantitative predictions. Their main value, as we see it, is that they shed light on and help to classify and qualitatively understand the late-stage dissipative effects on hadron spectra and their elliptic flow as seen in a realistic microscopic approach (as embodied, for example, by `VISHNU`). The results presented here do provide support to the conclusion of Ref. [124] that an effective viscous hydrodynamic description of the hadronic stage in heavy-ion collisions, if valid at all, likely requires both large shear viscosity *and* long relaxation times below T_c.

Our study of possible temperature dependent variations of η/s in the high temperature region explored for at the LHC remained unconclusive but pointed to a clear need for better theoretical control over the initial conditions for the hydrodynamic energy-momentum tensor, in particular

its shear stress components. The development of detailed dynamical models for the pre-thermal evolution of the collision fireball and their matching to the viscous hydrodynamic stage is a matter of priority for continued progress towards quantifying the transport properties of the quark-gluon plasma at different temperatures and densities.

Chapter 9: Collision energy dependence

9.1 Chapter introduction

The recent Beam Energy Scan (BES) program [135, 136, 137, 138, 139, 140] at RHIC is motivated by searching for the phase boundary between normal nuclear matter and sQGP as well as for the theoretically predicted QCD critical point [141, 142, 143, 144]. The BES program at RHIC together with Pb+Pb collisions at the Large Hadron Collider (LHC) provide us with a unique opportunity to study systematically the collision energy dependence of relativistic heavy-ion collision observables. In the mid-rapidity region, the dependence of elliptic flow on transverse momentum and collision energy are crucial for our understanding of the properties of sQGP.

In [145] the collision energy dependence of particle transverse momentum spectra and elliptic flow coefficients were studied using (2+1)-d ideal hydrodynamics with longitudinal boost invariance and a bag-model equation of state. In this chapter (taken from Ref. [50]), we revisit this problem using more realistic (2+1)-d viscous hydrodynamics coupled with a modern lattice QCD based equation of state [17, 16].

Our work has some limitations which must be kept in mind before comparing them with experimental data. As the collision energy decreases, the Bjorken assumption of longitudinal boost invariance will gradually break down [146]. Furthermore, since the fireball will spend less time in the QGP phase, the hadronic phase becomes more important and occupies a larger part in its dynamical history. Curing these two major shortcomings will require (3+1)-d viscous hydrodynamic simulations [45, 147] coupled with a microscopic hadronic afterburner [148, 40, 124]. Here we are not aiming at extracting precise information of QGP transport properties from a comparison with experimental data. Its main purpose is to expose systematic quantitative trends in observables as a function of collision energy in the relativistic heavy-ion collisions.

In the next section, we will describe the setup of our model and discuss our parametrization of the initial conditions as a function of $\sqrt{s}$. In Sec. 9.3, we will present trends for the transverse momentum spectra and differential elliptic flow for charged hadrons as $\sqrt{s}$ increases from 7.7 A GeV to 2760 A GeV. Identified particle spectra and their elliptic flow v_2 will be discussed in Sec. 9.4.

In Sec. 9.5, we generalize the definition of the spatial eccentricity to an isothermal hyper-surface. Based on this generalized formulation, we perform a shape analysis on the final kinetic freeze-out surface and study the dependence of the final eccentricity on $\sqrt{s}$. Sec. 9.6 is devoted to some concluding remarks.

9.2 Evolution of charged hadron multiplicity and total elliptic flow

To limit the numerical effort, we do not perform an event-by-event study here but use smooth event averaged initial entropy density profiles from the MC-Glauber and MCKLN models and perform only a single hydrodynamic evolution for each class of collisions. In the MC-Glauber runs we take for the specific shear viscosity the value $\eta/s = 0.08$. The wounded nucleon (WN) to binary collision (BC) mixing ratio α is adjusted to reproduce the measured centrality dependence of the final charged hadron multiplicity density $dN_{\rm ch}/d\eta$. For Pb+Pb collisions at $\sqrt{s} = 2760\,A\,\mathrm{GeV}$ we use $\alpha = 0.118$ as determined in [118]. For Au+Au collisions at RHIC energies, we fit to the RHIC data at $\sqrt{s} = 200\,A\,\mathrm{GeV}$ [102, 93, 149, 150, 151] obtaining $\alpha = 0.14$. For RHIC collisions at lower $\sqrt{s}$ we keep the mixing ratio fixed[19] at $x = 0.14$, tuning only the normalization factor κ to reproduce the charge multiplicity in the 0-5% most central collisions. For $\sqrt{s} = 63\,A\,\mathrm{GeV}$, the desired charged multiplicity is taken from experiment [102]. For $\sqrt{s} < 63\,A\,\mathrm{GeV}$, we presently lack experimental information and therefore use the empirical formula [145]

$$\frac{dN_{\rm ch}}{d\eta} = 312.5 \log_{10}\sqrt{s_{\rm NN}} - 64.8. \tag{9.1}$$

The actually employed final charged multiplicities are listed in Table 9.1.

$\sqrt{s}$ (A GeV)	T_0 (MeV)	$\tau_{\rm f}-\tau_0$ (fm/c)	$dN_{\rm ch}/d\eta$
AuAu@ 7.7	269.2/233.7	9.3/9.1	212.3/212.1
AuAu@ 11.5	287.5/252.0	10.0/9.8	266.7/266.4
AuAu@ 17.7	304.8/269.8	10.5/10.3	325.3/324.9
AuAu@ 19.6	308.7/274.3	10.6/10.4	339.2/338.8
AuAu@ 27	320.1/286.4	10.9/10.7	382.9/382.1
AuAu@ 39	332.2/298.9	11.2/11.0	432.7/432.3
AuAu@ 63	341.1/306.4	11.4/11.2	472.0/472.9
AuAu@ 200	378.6/347.0	12.2/12.1	661.9/690.0
PbPb@ 2760	485.2/443.9	14.2/14.2	1575.7/1597.2

Table 9.1: The initial temperature at the center of the fireball, fireball lifetime and final charged hadron multiplicity of 0-5% most central collisions are listed. The results on the left are from MC-Glauber initial conditions with $\eta/s = 0.08$, the right are for MCKLN with $\eta/s = 0.2$.

[19]The main reason of keeping the mixing ratio fixed is because the measured centrality dependence of charged multiplicity for the lower energy runs had, at the time of this study, not yet been published. We do not expect qualitative changes to the conclusions drawn in this paper once our assumed values will be replaced by actual measurements.

The MCKLN calculations are done using a Monte-Carlo sample of initial profiles with identical properties as those used in [48]. These initial MCKLN profiles were evolved hydrodynamically with a larger viscosity $\eta/s = 0.2$ to compensate for the larger initial eccentricities. For Au+Au at $200\,A\,\mathrm{GeV}$ and Pb+Pb at $2760\,A\,\mathrm{GeV}$ the normalization constant for the initial entropy density was determined by an overall fit to the centrality dependence of $\frac{dN_{\mathrm{ch}}}{d\eta}$. These best fits result in slightly different $\frac{dN_{\mathrm{ch}}}{d\eta}$ values for the 0-5% most central collisions than obtained for the corresponding MC-Glauber cases (see Table 9.1). At lower energies, the normalization factor was again fixed to reproduce the desired charged hadron multiplicity density $dN_{\mathrm{ch}}/d\eta$ for the 0-5% most central collisions for all $\sqrt{s}$ (see Table 9.1).

We point out that we keep the value of the specific shear viscosity η/s unchanged as we go to lower collision energies. As the highly viscous hadronic phase becomes more and more important at lower collision energies, viscous hydrodynamic simulations with temperature independent η/s will eventually break down. Worse, larger η/s values in the hadronic phase jeopardize the validity of the viscous hydrodynamic approach altogether [127]. In this study, we are not trying to extract the temperature dependence of η/s from a serious comparison with experimental data; our goal is to present a systematic study of the $\sqrt{s}$ dependence of hydrodynamic variables. For this reason, we run viscous hydro all the way down to $\sqrt{s} = 7.7\,A\,\mathrm{GeV}$ with constant η/s; compared to [145], our simulations are more realistic by including viscous effects in the hydrodynamic evolution and using a better EOS.[20] Also, we here study two different initialization models and include (at least on average) the effects of event-by-event fluctuations whereas in [145] an optical Glauber model was used for initialization which gives too small eccentricities in the most central collisions. We will see that the different $\sqrt{s}$ dependence from the two initialization models will help us to further distinguish between the two initialization models.

In Table 9.1 we have summarized the global variables for our hydrodynamic simulations. At higher collision energies the evolution starts with a higher peak initial temperature, thus probing the nuclear matter at higher temperature and resulting in a longer lifetime of the fireball. At LHC energy we find a peak temperature that is about twice as large as that reached at the lowest collision energies at RHIC, and the lifetime is about 5 fm/c longer. MC-Glauber initial conditions have about 30 MeV higher peak temperatures than MCKLN ones. This is mostly due to the fact

[20] It should be noted that our EOS assumes zero net baryon density – an assumption that is untenable in the lower half of the collision energy range explored here. To include effects from non-zero baryon density would require an upgrade of `VISH2+1` to solve additionally for the space-time evolution of the conserved baryon current. This is important for the correct prediction of the final baryon and meson abundances at lower $\sqrt{s}$ which our present code can not achieve. However, what matters for the evolution of radial and elliptic flow is the stiffness of the EOS, embodied by the pressure (whose gradients supply the hydrodynamic acceleration) and its relation to the energy density (inertia) of the fluid, $p(e, n)$. Since, for not too large baryon densities n, this relation depends on n only very weakly [30], the use of a baryon-free EOS is expected to work well for the systematic flow study presented here.

that the specific shear viscosity in the MCKLN runs is about 2.5 times larger than for MC-Glauber runs, causing stronger viscous heating and larger entropy production during the hydrodynamic evolution. The same final multiplicity $\frac{dN_{\rm ch}}{d\eta}$ can thus be reached starting from less initial entropy. A larger specific shear viscosity also helps the system to develop more radial flow in the transverse plane, by speeding up the equalization between transverse and longitudinal velocity gradients (the latter are initially very large). This larger transverse expansion rate compensates for the viscous heating effects on the lifetime, resulting in a slightly shorter lifetime for the MCKLN runs.

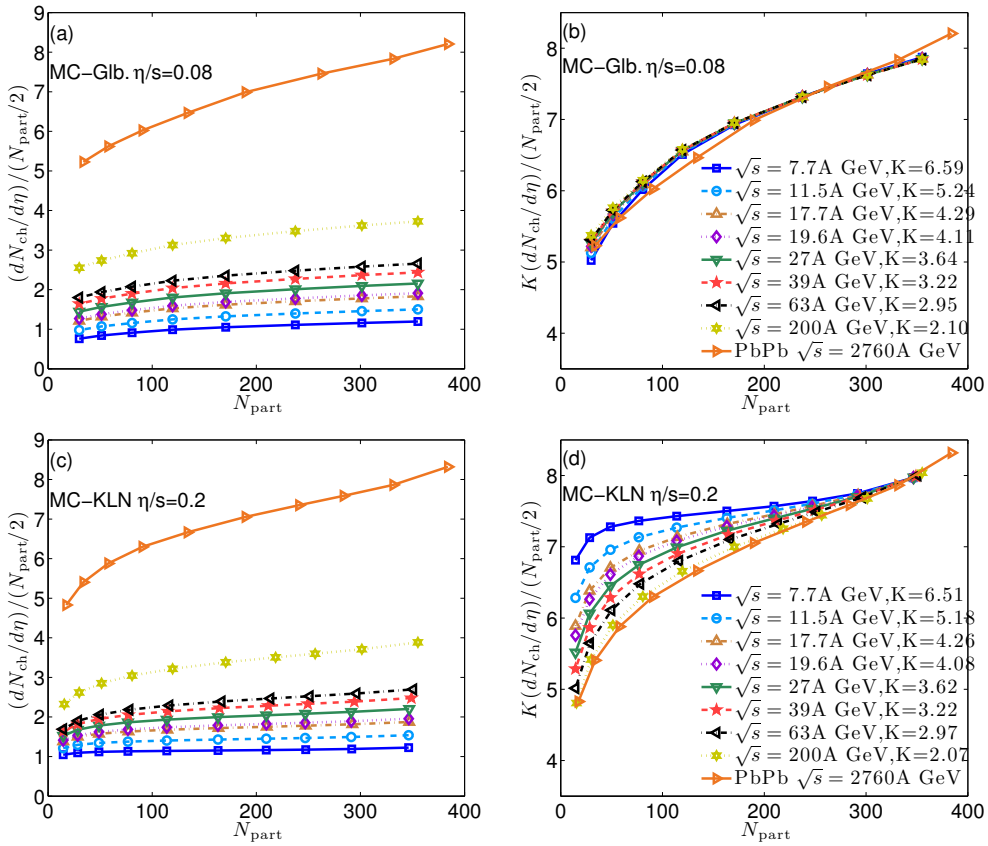

Figure 9.1: **(a):** Centrality dependence of final charged hadron multiplicity per participant nucleon pair as a function of $N_{\rm part}$ for MC-Glauber initial conditions, with collision energies varying from $\sqrt{s}=7.7A\,$GeV to $\sqrt{s}=2760A\,$GeV. **(b):** Centrality dependence of $\frac{dN_{\rm ch}}{d\eta}$ from the lower energy runs in (a) scaled up to the LHC results, for shape comparison. **(c, d):** Same as (a, b) but for MCKLN initial conditions.

In Figs. 9.1(a,c) we show the centrality dependence of the charged hadron multiplicity for both MC-Glauber and MCKLN models with collision energies from $\sqrt{s}$ = 7.7 to 2760 $A\,$GeV. The reader should note that all results in Fig. 9.1 account for viscous entropy production during the hydrodynamic evolution. We checked that at LHC and top RHIC energies (top two curves in Figs. 1(a,c)) our results for both initialization models agree well with the experimental data [102, 93, 149, 150, 151, 99, 94]. Our lower collision energy predictions can in the future be checked against data collected in the RHIC BES program.

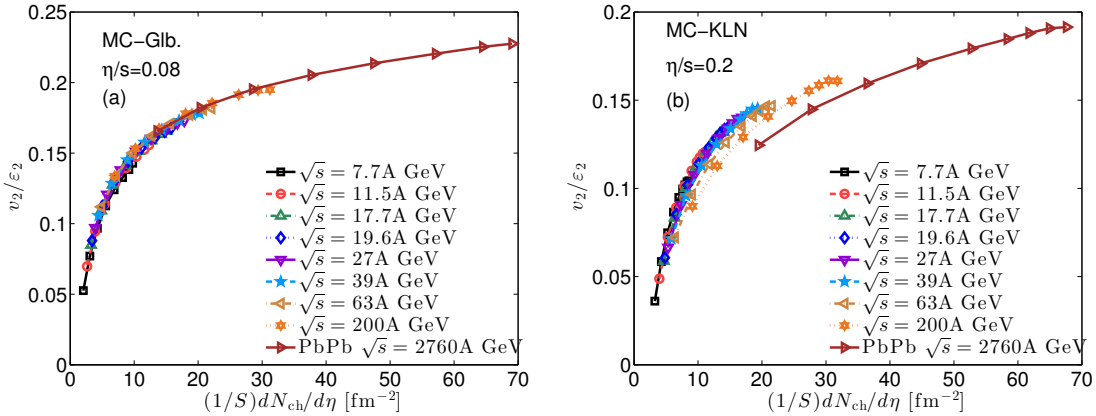

Figure 9.2: Eccentricity-scaled p_T-integrated v_2 plotted as a function of the charged hadron multiplicity density for different collision energies, for MC-Glauber initial conditions with $\eta/s = 0.08$ (a) and MCKLN profiles with $\eta/s = 0.2$ (b), respectively.

In order to study how the centrality dependence changes with $\sqrt{s}$, we scale in Figs. 9.1b,d the lower collision energy results by constant factors to align them with the LHC curve in central (0-10%) collisions. For the MC-Glauber model we find good $\sqrt{s}$-scaling: the curves almost fall on top of each other. For the low energy runs at RHIC this is, of course, sensitive to the fact that we keep the mixing ratio between the wounded nucleons and binary collisions fixed, and it also reflects the fact that viscous entropy production is small and has little effect on the centrality dependence. On the other hand, for the MCKLN model the slope of the centrality dependence gets flatter as the collision energy decreases. Only the top RHIC and LHC energy curves approximately fall on top of each other; at lower energy this $\sqrt{s}$-scaling is broken. We found that this tendency originates in the nature of the MCKLN model itself: Even though viscous entropy production is larger (due to the larger η/s used in the MCKLN runs), its centrality dependence has only a minor effect on the centrality dependence of $\frac{dN_{\rm ch}}{d\eta}$ and cannot explain the different shapes of the curves in Figs. 9.1b,d. Our MCKLN calculations thus predict a violation of the $\sqrt{s}$-scaling of the centrality dependence of $\frac{dN_{\rm ch}}{d\eta}$ at lower collision energies that is not seen with the MC-Glauber initial conditions. This may help to discriminate experimentally between these models.

A "universal" scaling behavior of the eccentricity-scaled elliptic flow as a function of charged hadron multiplicity density ("multiplicity scaling") [152] was studied within viscous hydrodynamics in [67] and was later used to extract the specific shear viscosity from $\sqrt{s} = 200\,A\,$GeV Au+Au collisions at RHIC [40]. The authors of [44] and [48] found that this "universal" scaling breaks down as $\sqrt{s}$ increases but disagreed on the sign of the scaling breaking effects. In Fig. 9.2 we explore the breaking of "multiplicity scaling" over a wider range of $\sqrt{s}$, for both of the initialization models. For MC-Glauber initial conditions (Fig. 9.2a) eccentricity-scaled elliptic flow shows surprisingly good universality of the "multiplicity scaling" curve as the collision energy varies from 7.7 to 2760 $A\,$GeV: The curves at different $\sqrt{s}$ fall almost perfectly on top of each other. For MCKLN

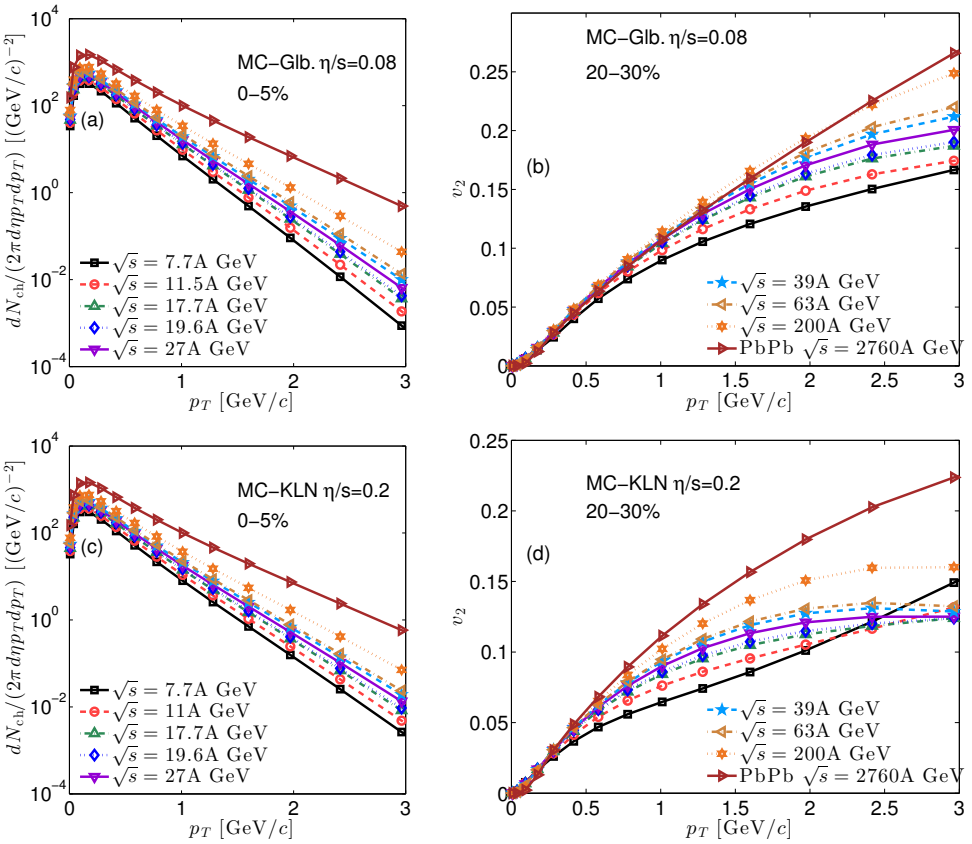

Figure 9.3: (a,c): Transverse momentum spectra of all charged hadrons from central (0-5% centrality) Au+Au and Pb+Pb collisions at 0-5% centrality for different collision energies. (b,d): the corresponding differential elliptic flow at 20-30% centrality.

(Fig. 9.2b), on the other hand, the "universal scaling" breaks in the same direction as previously shown in [48]: lower collision energies result in larger v_2/ϵ_2 values at the same charged hadron multiplicity density. We found that the main reason for the different collision energy dependence between the MC-Glauber and MCKLN models lies in the different centrality dependences of the initial overlap area in the two models. The initial overlap area is calculated as $S = \pi\sqrt{\langle x^2\rangle\langle y^2\rangle}$, where $\langle x^2\rangle = \frac{\int d^2\boldsymbol{r}\gamma e(\boldsymbol{r})x^2}{\int d^2\boldsymbol{r}\gamma e(\boldsymbol{r})}$ is evaluated with the initial energy density as weight function.[21] As the collisions become more peripheral, the overlap area in the MCKLN model decreases more rapidly than in the MC-Glauber model. In Pb+Pb collisions at $\sqrt{s} = 2760\,A\,\mathrm{GeV}$, the overlap area S for MCKLN decreases from $23.6\,\mathrm{fm}^2$ in the 0-5% most central collisions to $4.7\,\mathrm{fm}^2$ in the 60-70% centrality class; for MC-Glauber, S decreases instead from $22.8\,\mathrm{fm}^2$ to $6.5\,\mathrm{fm}^2$. This slightly faster drop of the overlap area in the MCKLN model shifts the "universal" scaling curves in Fig. 9.2 to the right and shrinks the covered range in $(1/S)dN_{\mathrm{ch}}/d\eta$. We further checked that the centrality dependence of the overlap area changes little as $\sqrt{s}$ varies from 7.7 to 2760 A GeV. The different $\sqrt{s}$-dependences of v_2/ϵ_2 as function of $dN_{\mathrm{ch}}/d\eta$ in Figs. 9.2a and 9.2b thus reflect primarily the

[21]The initial entropy density can also be used as weight. In [48] we showed that the scaling breaking behavior is independent of the choice of weight function.

fact that the shape of the initial profiles evolves differently with centrality in the two initialization models. Fig. 9.2 can thus be used to check experimentally the consistency of the centrality dependence of the source size and shape in the initialization models.

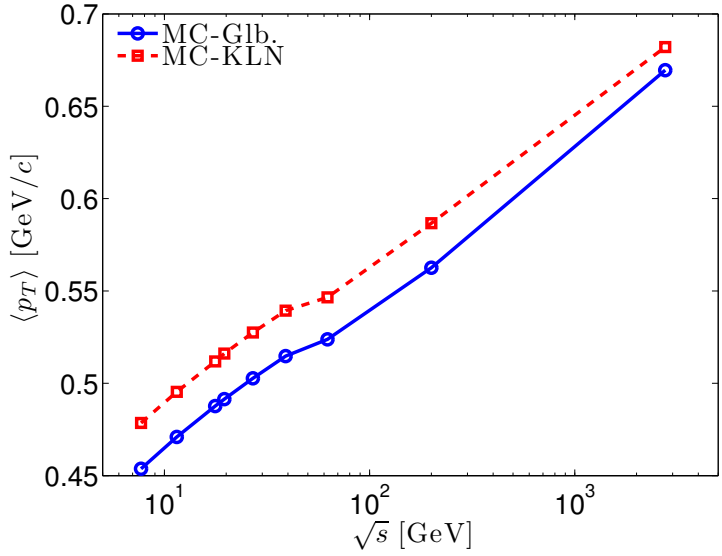

Figure 9.4: Evolution with $\sqrt{s}$ of the average transverse momentum of charged hadrons from central (0-5% centrality) Au+Au and Pb+Pb collisions, for MC-Glauber and MCKLN initial conditions.

9.3 Charged particle p_T-spectra and differential elliptic flow

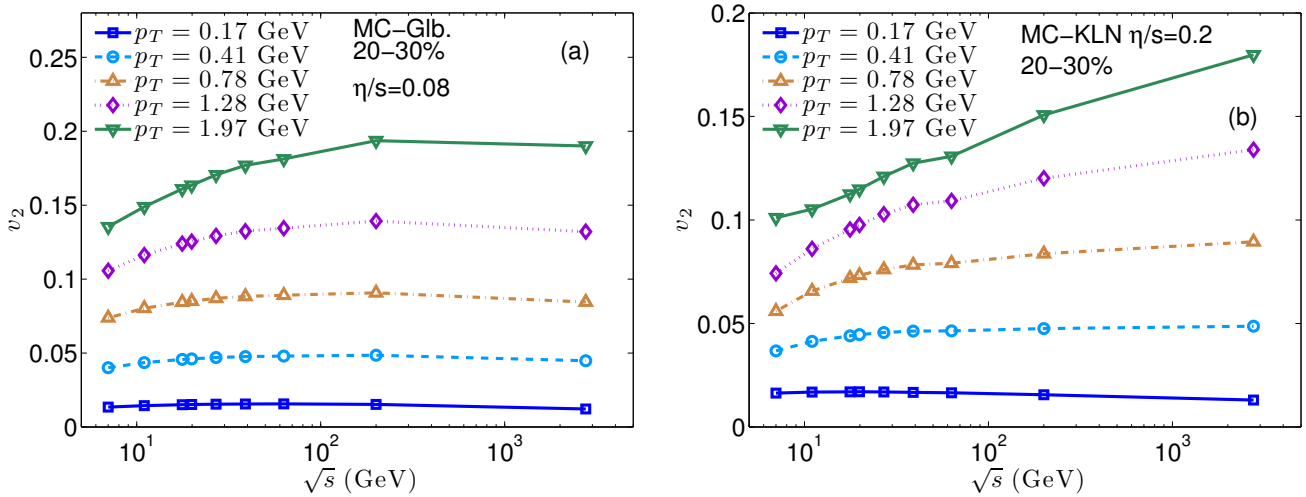

Figure 9.5: Evolution with $\sqrt{s}$ of the differential charged hadron elliptic flow $v_2^{\rm ch}(p_T, \sqrt{s})$ at 5 fixed p_T values.

Figures 9.3a,c show the p_T-spectra of all charged hadrons in the 0-5% most central collisions. For both the MC-Glauber and MCKLN models the slopes of the p_T-spectra get flatter as $\sqrt{s}$ increases: At higher collision energy the fireball lifetime is longer, which allows the system to develop

more radial flow. The additional radial flow pushes more particles into the high-p_T region, thus flattening the spectra. From $\sqrt{s} = 7.7$ to 2760 A GeV, the mean p_T, $\langle p_T \rangle = \int dp_T p_T \frac{dN}{d\eta dp_T} / \int dp_T \frac{dN}{d\eta dp_T}$, increases by 43% (from 0.48 to 0.68 GeV/c) for the MCKLN model and by 140% (from 0.29 to 0.63 GeV/c) for the MC-Glauber model (see Fig. 9.4).

The differential charged hadron elliptic flow is shown in Figs.9.3b,d, for 20-30% centrality. With MC-Glauber initial conditions the differential elliptic flow for $p_T < 2$ GeV remains almost unchanged for $\sqrt{s} \geq 39\,A$ GeV. Below 39 A GeV the slope of $v_2(p_T)$ begins to decrease. This tendency is indeed observed in the RHIC BES experiments [138, 137, 140]. We emphasize that our EOS s95p-PCE has no pronounced soft point in the phase transition region. This means that the often highlighted "saturation" of $v_2(p_T)$ above $\sqrt{s} = 39A$ GeV can not be associated with a softest point in the transition region. It is rather caused by a subtle cancellation of opposite $\sqrt{s}$-dependences of the differential $v_s(p_T)$ from light and heavy particles (see Fig. 9.8 below).

For the MCKLN model, the slope of the differential $v_2(p_T)$ decreases monotonically and continuously with decreasing collision energy. For a temperature-independent specific shear viscosity, $\eta/s = 0.2$, the collision energy dependence of the differential elliptic flow observed here is somewhat inconsistent with the experimental observation of a $v_2^{\rm ch}(p_T)$ that does not change between $\sqrt{s} = 39$ and 2760A GeV. Within the MCKLN framework, this might be taken as an indication for a possible temperature dependence of η/s [128, 127, 48]. Additional studies are, however, necessary to fully address this issue [49]. For $\sqrt{s} = 7.7$ and 11.5 A GeV, the differential v_2 is seen to increase more quickly above $p_T > 2.5$ GeV. We find this to be caused by large δf corrections (i.e. non-equilibrium corrections arising from non-zero shear stresses at freeze out [48]). The larger δf corrections at lower collision energies indicate a narrowing of the temporal interval during which viscous hydrodynamics is a valid description. At lower p_T ($p_T < 2$ GeV), our results show monotonic $\sqrt{s}$ dependence.

To further illustrate this point we plot in Fig. 9.5 the $\sqrt{s}$-dependence of $v_2^{\rm ch}(p_T)$ at 5 fixed p_T points. In this representation one sees that for the MC-Glauber model $v_2^{\rm ch}$ at any fixed p_T-value features as a function of $\sqrt{s}$ a very broad maximum somewhere around top RHIC energy (200 A GeV); for low $p_T < 0.5$ GeV/c, this maximum occurs at lower $\sqrt{s}$. A similar behavior was seen in [145] for ideal hydrodynamics with a bag-model equation of state which features a strong minimum ("softest point") in the speed of sound at the phase transition temperature. We see that the existence of this maximum does not depend on the appearance of a softest point in the EOS. Compared to the earlier ideal fluid calculations, the position where $v_2^{\rm ch}$ at fixed p_T assumes its largest value has been shifted to larger $\sqrt{s}$ values by viscous effects. This shift is seen to be even stronger in the MCKLN case (Fig. 9.5b) where the fluid is much more viscous. For shear viscosities as large as those needed to describe the $v_2^{\rm ch}$ measured in 200 A GeV Au+Au

collisions with MCKLN initial conditions ($\eta/s \simeq 2.5/(4\pi)$) [37, 40], $v_2^{\rm ch}(p_T, \sqrt{s})$ at fixed p_T has not yet reached its maximum value even at top LHC energies (except for very small $p_T < 200\,{\rm MeV}/c$).

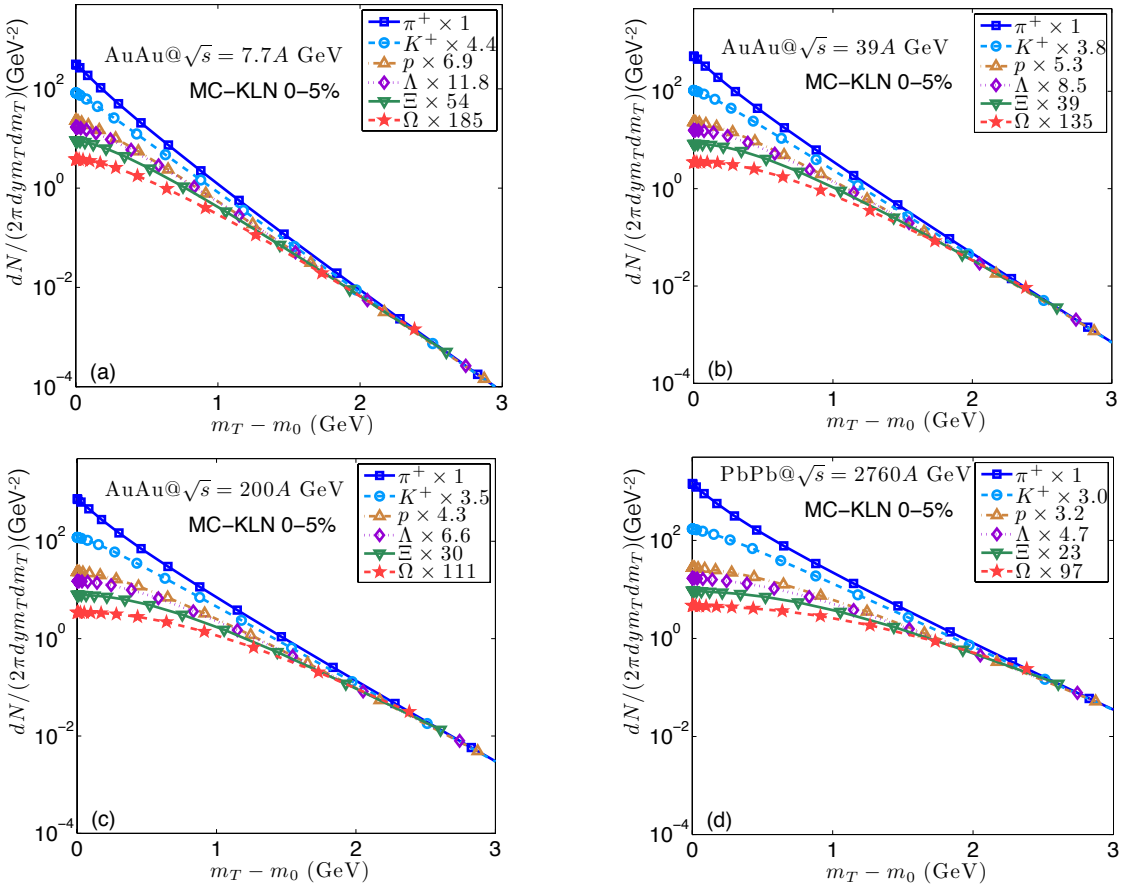

Figure 9.6: Identified particle spectra as a function of $m_T - m_0$ for the MCKLN model in the 0-5% most central collisions, at $\sqrt{s} = 7.7,\ 39,\ 200$, and 2760 A GeV. The spectra for MC-Glauber initial conditions look qualitatively similar.

At the lower end of the $\sqrt{s}$-range studied in Fig. 9.5, the increase with collision energy of $v_2(p_T, \sqrt{s})$ at fixed p_T is a consequence of increasing fireball lifetimes which allow the initial spatial eccentricity of the fireball to convert more fully into anisotropic hydrodynamic flow. At higher collision energies eventually the point is reached where this momentum anisotropy is fully saturated before the system falls apart; longer fireball lifetimes will then no longer lead to more anisotropic flow, only to more radial flow. Stronger radial flow, however, pushes the momentum anisotropy out to larger p_T, by generating flatter p_T distributions. As a result, elliptic flow at fixed p_T begins to decrease. In practice, this radial flow driven decrease of $v_2(p_T)$ at fixed p_T sets in even before the p_T-integrated total charged hadron elliptic flow $v_2^{\rm ch}$ has reached saturation [153], and it accelerates thereafter.

9.4 p_T-spectra and elliptic flow of identified hadrons

We now proceed to study how hydrodynamical flow affects identified particles.

It is well known that thermal spectra from a static fireball exhibit m_T-scaling, $dN_i/(2\pi dy m_T dm_T) \sim \sqrt{m_T} e^{-m_T/T}$ [154], and that radial flow breaks this scaling. In order to isolate the radial flow effects we therefore plot in Fig. 9.6 the m_T-spectra of identified particles as a function of $m_T - m_0$, for four selected $\sqrt{s}$ values. Except for minor effects from the viscous δf corrections, resonance feed-down and Bose statistics for pions, in the absence of flow the slopes of the m_T-spectra would be the same for all hadron species. To show the flow-induced slope difference, we scaled in Figs. 9.6 the heavy particle spectra by constant factors to the same value at $m_T - m_0 = 3\,\mathrm{GeV}$. At large $m_T - m_0$ rest mass effects become negligible, and all hadrons have approximately the same inverse slope $T_{\rm eff} = T_{\rm dec}\sqrt{(1+\langle v_\perp\rangle)/(1-\langle v_\perp\rangle)}$ [154]. In Fig. 9.6 we find that for low $\sqrt{s}$ values m_T-scaling is significantly broken only at $m_T - m_0 < 2\,\mathrm{GeV}$, while at LHC energy the flow-induced breaking of m_T-scaling extends to 3 GeV of transverse kinetic energy. At low $m_T - m_0$ the spectra are split by hadron mass effects, and this splitting increases with $\sqrt{s}$ due to the increasing radial flow which pushes heavier particles to larger p_T. At the highest collision energy $\sqrt{s} = 2760\,A\,\mathrm{GeV}$ we observe a particularly strong concavity of the pion spectra at low $m_T - m_0$, due to Bose statistics. For other mesons, their heavy rest masses suppress Bose effects.

The flow-induced breaking of m_T-scaling is seen even more clearly when one plots heavy-to-light particle ratios (such as p/π^+, Λ/K^+) as a function of transverse kinetic energy. For a static thermalized fireball, these ratios should be independent of $m_T - m_0$, up to small quantum statistical corrections arising from the pion spectra at small $m_T - m_0$. Fig. 9.7 shows that for an expanding fireball these ratios increase with increasing transverse kinetic energy, at a rate that itself increases with $\sqrt{s}$, reflecting the larger radial flow at higher collision energies. A little more careful inspection and thought reveal that, in fact, stronger radial flow *increases* the p/π^+ and Λ/K^+ ratios at large $m_T - m_0$ while *decreasing* them at small $m_T - m_0$. This is so because in our simulations the p_T-integrated particle ratios are the same at all collision energies, as we assumed zero baryon chemical potential and the same chemical and kinetic freeze-out temperatures at all $\sqrt{s}$. In addition, radial flow flattens the m_T-dependence of these ratios at low $m_T - m_0$, due to the "flow shoulder" developing in the heavy-particle m_T-spectra at low transverse kinetic energy when radial flow gets strong. This shoulder is weaker for protons than for Λ's, but in the p/π^+ ratio the more prominent Bose effect in the pion spectra at high collision energies additionally helps to flatten out the p/π^+ ratio at small $m_T - m_0$. Overall, Fig. 9.7 shows that these features are all very similar for MC-Glauber and MCKLN initial conditions.

In Fig. 9.8 we show the differential elliptic flow of π^+ and p for $\sqrt{s} = 7.7$ to $2760\,A\,\mathrm{GeV}$. For pions, the differential v_2 varies with $\sqrt{s}$ very similarly to the total charged hadron elliptic flow

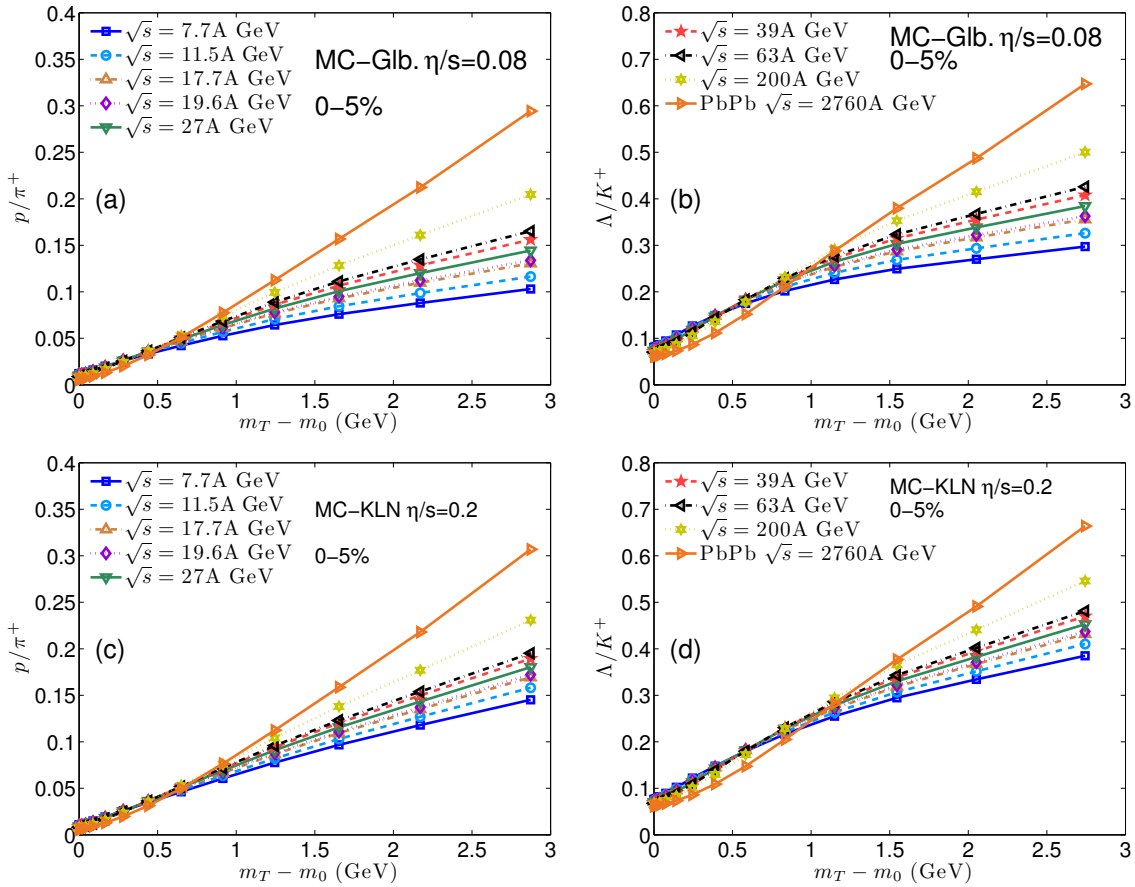

Figure 9.7: The p/π^+ (a,c) and Λ/K^+ (b,d) ratios as functions of $m_T - m_0$, for MC-Glauber (a,b) and MCKLN (c,d) initial conditions at 0-5% most central collisions, from $\sqrt{s} = 7.7$ to 2760 A GeV. Please note the dramatic increase of radial flow effects on these ratios between RHIC and LHC energies.

shown in Figs. 9.3b,d. For protons the strong radial flow "blueshifts" the entire elliptic flow to higher p_T. So for higher collision energies, the values of v_2 are smaller in the low p_T-region and larger in the high-p_T region. We find that below 200 A GeV the proton $v_2(p_T)$ at low p_T is almost independent of $\sqrt{s}$. At LHC energy, on the other hand, the blueshift is really dramatic, reflecting the much stronger radial flow at this high collision energy. The total charged hadron elliptic flow is the combination of contributions from light pions and less abundant heavy particles. Since with increasing collision energy the elliptic flow of heavy particles decreases at low p_T, they effectively cancel the weak increase of the light pion v_2. This results in the apparent saturation of charged hadron differential elliptic flow over a wide p_T range from $\sqrt{s} = 39$-2760 A GeV that was seen in Fig. 9.3b for MC-Glauber model. For the MCKLN model, this cancellation is less efficient because the increase with $\sqrt{s}$ of the pion v_2 is stronger (see Fig. 9.8c,d). Therefore, for the MCKLN model the total charged hadron elliptic flow keeps increasing as the collision energy increases.

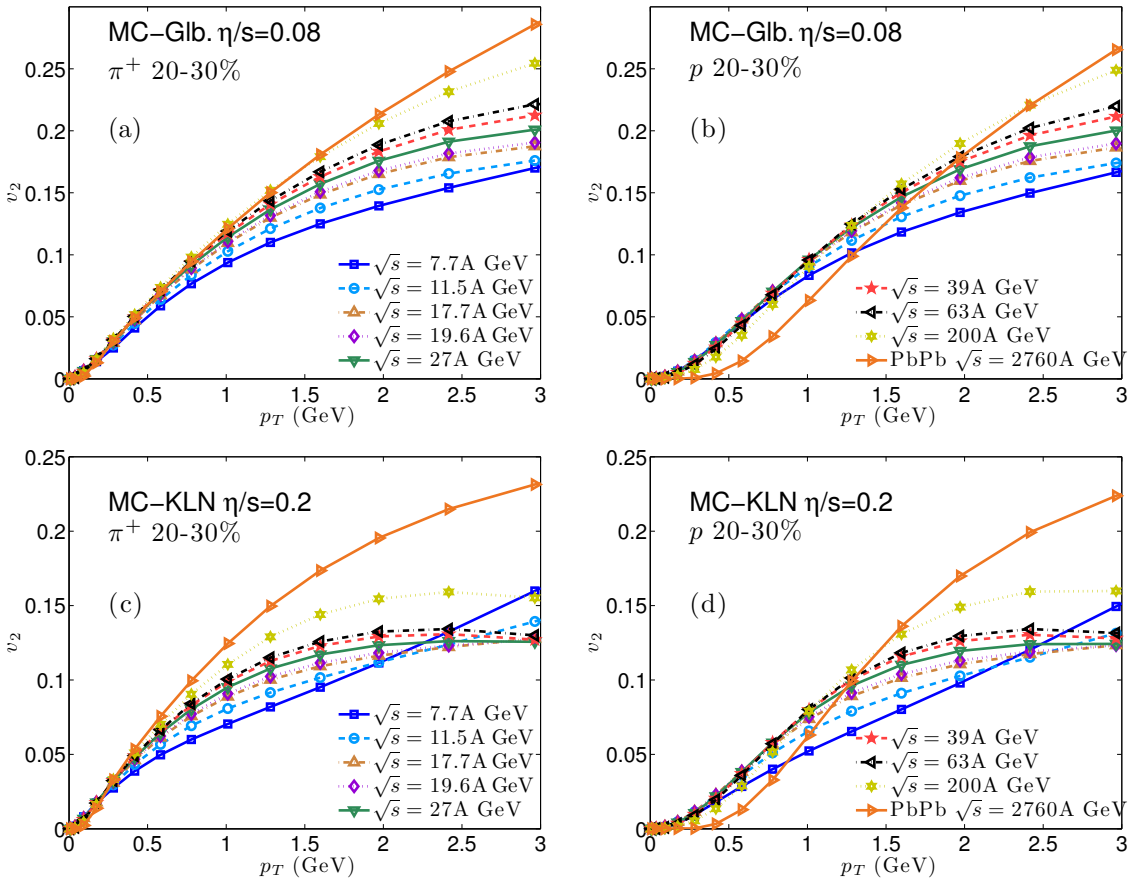

Figure 9.8: Differential elliptic flow of π^+ (a,c) and p (b,d) at 20-30% centrality, for MC-Glauber (a,b) and MCKLN (c,d) profiles.

9.5 Spatial eccentricity at freeze-out

We conclude this paper by presenting a novel shape analysis of the evolving fireball. Theoretically, the spatial eccentricity ϵ_x is conventionally defined at fixed proper time τ by

$$\epsilon_x(\tau) = \frac{\int dx\, dy\, (y^2 - x^2)\gamma e(x,y;\tau)}{\int dx\, dy\, (y^2 + x^2)\gamma e(x,y;\tau)}. \tag{9.2}$$

The weight function $\gamma e(x,y;\tau)$ is the energy density in the laboratory frame.[22]

Since the measured hadrons are only emitted from the final kinetic freeze-out surface, experimentalists can only infer the shape of that surface, by exploiting two-particle momentum correlations among the emitted particles and their dependence on the azimuthal angle around the beam axis [155, 156]. For comparison with such experimentally determined final source eccentricities [157, 158, 159, 160], a more meaningful theoretical quantity would be the spatial eccentricity

[22]The entropy density $s(x,y;\tau)$ can also be used as weight function for calculating the eccentricity. The authors of [112] concluded from a study of fluctuating initial conditions that these two definitions yield initial spatial eccentricities that are linearly related to each other although the actual values are slightly different.

of the final freeze-out surface Σ,

$$\epsilon_x(\Sigma) = \frac{\int_\Sigma u^\mu d^3\sigma_\mu \, (y^2 - x^2)}{\int_\Sigma u^\mu d^3\sigma_\mu \, (y^2 + x^2)}, \tag{9.3}$$

instead of a constant proper time surface. In Eq. (9.3) u^μ is the flow velocity on the surface Σ, and we used the fact that for our EOS an isothermal freeze-out surface is also a surface of constant local energy or entropy density, and that therefore the weight functions $e(x, y, \tau)$ or $s(x, y, \tau)$ cancel between numerator and denominator.[23] Thus the spatial eccentricity (9.3) defined on an isothermal surface is independent of whether we weight ϵ_x with energy or entropy density.

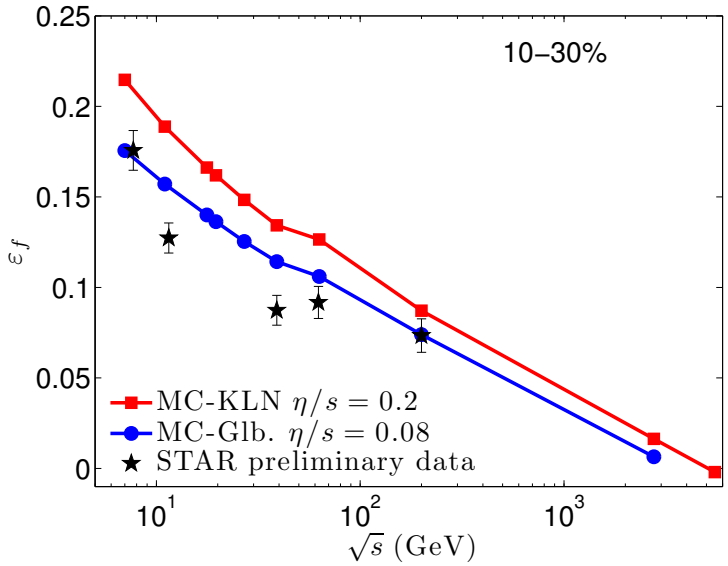

Figure 9.9: $\sqrt{s}$-dependence of the final spatial eccentricity ε_f of the isothermal kinetic freeze-out surface at $T_\mathrm{dec} = 120\,\mathrm{MeV}$, for 10-30% centrality. The initial eccentricity is 0.26 for the MC-Glauber model and 0.32 for the MCKLN model. The experimental points indicate preliminary data [161] from an azimuthal HBT analysis by the STAR Collaboration.

In Fig. 9.9, we show the final eccentricity calculated along the kinetic freeze-out surface, $T_\mathrm{dec} = 120\,\mathrm{MeV}$, as a function of collision energy. For both MC-Glauber and MCKLN models, as the collision energy increases, the final spatial eccentricity ε_f decreases monotonically. This is because at higher collision energy the system lives longer, giving the fireball more time to decompress and (due to anisotropic flow) become less deformed. For sufficiently large initial energy density, the fireball has actually enough time to become elongated along the reaction plane, instead of its original elongation perpendicular to it [162, 163]. In Fig. 9.9 we compare our results with recent (preliminary) STAR data from an azimuthal HBT analysis [161]. MC-Glauber runs with $\eta/s = 0.08$ quantitatively reproduce the data at $\sqrt{s} = 200A\,\mathrm{GeV}$ while underpredicting the final eccentricity by ∼10% at lower energies. MCKLN initial conditions with $\eta/s = 0.2$ result in 15-20% larger final

[23] If we do not cancel the weight function and replace Σ by a constant proper time surface, the definition (9.3) reduces to Eq. (9.2) for longitudinally boost-invariant systems.

eccentricities than both the MC-Glauber runs and the STAR data, due to the ∼20% larger initial eccentricities of the MCKLN profiles. In Table 9.1 we see that, at the same $\sqrt{s}$, the fireball lifetimes with MCKLN and MC-Glauber initial conditions are very similar. In spite of the faster evolution of radial flow for the MCKLN initial conditions, the larger initial eccentricity in the MCKLN model is preserved all the way to the end of the hydrodynamic evolution. Extending our calculations to LHC energy we predict that $\varepsilon_{\rm f}$ will approach zero around $\sqrt{s} = 2.76\text{-}5.5\,A\,\text{TeV}$. Again, this is a result of the longer fireball lifetime at LHC energies. For even larger $\sqrt{s}$, $\varepsilon_{\rm f}$ will turn negative, in qualitative agreement with previous calculations in [162, 163] using ideal fluid dynamics and a less realistic EOS. Contrary to our present work, the authors of [162, 163] calculated the azimuthal HBT radii from the Cooper-Frye output of their hydrodynamic simulations. In future work we will calibrate our definition (9.3) for $\varepsilon_{\rm f}$ against the final eccentricity value extracted from azimuthal oscillations of HBT radii. Here we only note that an azimuthal HBT analysis at LHC energy will help to further test predictions from the viscous hydrodynamic model.

The careful reader may have noticed that there is a small kink at $\sqrt{s} = 63\,A\,\text{GeV}$ in the slopes of the solid and dashed lines in Fig. 9.9 and earlier in Figs. 9.4 and 9.5. Unfortunately, this is not a phase transition signature but rather an artifact from our normalization of the initial energy density profile to experimentally measured final charged multiplicity data for $\sqrt{s} \geq 63\,A\,\text{GeV}$ and to the empirical formula Eq. (9.1) for $\sqrt{s} \leq 39\,A\,\text{GeV}$. At $\sqrt{s} = 63\,A\,\text{GeV}$ the experimentally measured $dN_{\rm ch}/d\eta$ is $\sim 5\%$ smaller than the value obtained from Eq. (9.1). If we use Eq. (9.1) instead of the measured value to normalize our initial energy density profiles at $\sqrt{s} = 63\,A\,\text{GeV}$, the fireball lifetime increases slightly, decreasing the final eccentricity by a few precent and removing the kink in the theoretical curves. The origin of an apparently similar kink in the STAR data which happens to occur (we believe: accidentally) also around $\sqrt{s} = 63A\,\text{GeV}$ deserves further study.

9.6 Chapter summary

In this chapter, we have studied systematically the evolution of hydrodynamic observables with collision energy in the range $7.7 \leq \sqrt{s} \leq 2760\,A\,\text{GeV}$. Over this range of energies, the initial peak temperature almost doubles and the fireball lifetime increases by about 60%. We find that for temperature independent specific shear viscosity the MC-Glauber model shows almost perfect "multiplicity-scaling" of the eccentricity-scaled charged hadron elliptic flow. For the MCKLN model this scaling is broken: as $\sqrt{s}$ increases, the $v_2^{\rm ch}/\varepsilon_2$ vs. $(1/S)(dN_{\rm ch}/dy)$ curves shift to the right (Fig. 9.2b). We found that this breaking of multiplicity scaling in the MCKLN model originates from a steeper centrality dependence of the nuclear overlap area.

For both initialization models, higher collision energies generate stronger radial flow which results in flatter hadron spectra and a corresponding increase of the mean p_T of charged hadrons. For the MC-Glauber model we observed an approximate "saturation" of the charged hadron differential elliptic flow at fixed p_T in the region $\sqrt{s} \geq 39\,A\,\mathrm{GeV}$, similar to what is observed experimentally. We believe, however, that the word "saturation" describes the observations incorrectly and that what is seen is better described as a very broad maximum (as a function of $\sqrt{s}$) of the differential elliptic flow at fixed p_T, caused by the interplay of (i) growing total momentum anisotropy (which increases v_2) and increasing radial flow (which decreases v_2 at fixed p_T by shifting it to larger p_T), and (ii) increasing $v_2(p_T)$ for pions and decreasing $v_2(p_T)$ for kaons, protons and other heavy hadrons between RHIC and LHC energies. The mechanism (i) causes maxima of $v_2(p_T)$ at fixed p_T for all hadron species, but located at lower $\sqrt{s}$ values for heavier than for lighter hadrons (due to the mass-dependence of radial flow effects on the p_T-spectra). The mechanism (ii) ensures that the maximum for all charged hadrons is broader in $\sqrt{s}$ than for each hadron species individually and thus manifests itself as a broad plateau that (for $\eta/s = 0.08$) happens to span the collision energy range from upper RHIC to LHC energies. The position in $\sqrt{s}$ of the maximum of $v_2(p_T)$ at fixed p_T for each hadron species depends on the viscosity of the fluid (which controls the interplay in the development of radial and elliptic flow during the fireball expansion) and increases with η/s. For MCKLN initial conditions, which require $\sim$2.5 times larger η/s for a successful description of elliptic flow data at RHIC and LHC, $v_2^{\mathrm{ch}}(p_T)$ at fixed p_T has not yet reached its maximal value even at LHC energies.

Finally, we have proposed an improved measure for the final fireball eccentricity at kinetic freeze-out and studied its evolution with collision energy. It is found to decrease monotonically with increasing collision energy, at a rate that is roughly consistent with recent experimental measurements. Its absolute value agrees with the data better for the MC-Glauber than for the MCKLN model – the $\sim$20% larger initial eccentricities of the MCKLN profiles yield final freeze-out eccentricities that again appear to be $\sim$20% larger than those from MC-Glauber initial profiles, and lie significantly above the measured values. Neither model describes the available data perfectly; in view of the limitations of the purely hydrodynamic approach employed here (*cf.* our discussion in the Introduction) this is not too surprising. The model predicts, however, robustly that at top RHIC energies the final freeze-out source is still out-of-plane elongated (as experimentally observed), but that at LHC energies the final eccentricity should approach zero. Measurements that test this prediction should soon become available.

Chapter 10: Flow fluctuations in heavy-ion collision

10.1 Chapter introduction

Due to quantum fluctuations of the distribution of strongly interacting matters inside the colliding nuclei, the produced energy density profile in every relativistic heavy-ion collision event is highly inhomogeneous in the transverse plane. Event-by-event fluctuations in the initial state density distribution will translate to fluctuations in the flow profile after the hydrodynamic evolution, which is imprinted on the momentum distributions of the finally emitted particles. Thus, the measured anisotropic flow coefficients of hadrons, v_n and their associated flow angles Ψ_n fluctuate from collision to collision [164].

For each collision event the momentum distribution of finally emitted particles can be characterized by a set of harmonic flow coefficients v_n and flow angles Ψ_n through the complex quantities

$$V_n = v_n e^{in\Psi_n} := \frac{\int p_T dp_T d\phi\, e^{in\phi}\, \frac{dN}{dy p_T dp_T d\phi}}{\int p_T dp_T d\phi\, \frac{dN}{dy p_T dp_T d\phi}} \equiv \{e^{in\phi}\}, \tag{10.1}$$

$$V_n(p_T) = v_n(p_T) e^{in\Psi_n(p_T)} := \frac{\int d\phi\, e^{in\phi}\, \frac{dN}{dy p_T dp_T d\phi}}{\int d\phi\, \frac{dN}{dy p_T dp_T d\phi}} \equiv \{e^{in\phi}\}_{p_T}. \tag{10.2}$$

Here ϕ is the azimuthal angle around the beam direction of the particle's transverse momentum $\boldsymbol{p}_{\mathrm{T}}$, and the curly brackets denote the average over particles from a single collision.[24] Eq. (10.1) defines the flow coefficients and associated flow angles for the entire event, whereas Eq. (10.2) is the analogous definition for the subset of particles in the event with a given magnitude of the transverse momentum p_T. We suppress the dependence of both types of flow coefficients on the rapidity y. By definition, both v_n and $v_n(p_T)$ are positive definite. Hydrodynamic simulations show that in general the flow angles Ψ_n depend on p_T, and that, as a function of p_T, $\Psi_n(p_T)$ wanders around the "average angle" Ψ_n that characterizes the integrated flow v_n of the entire event. Some theoretical and experimental definitions of v_2 have yielded values that turn negative over certain p_T ranges; we will see that this is due to defining the flows of each event relative to a

[24] The average can include all charged particles or only particles of a specific identified species; we will not clutter our notation to account for these different possibilities.

fixed azimuthal angle (for example, relative to the direction of the impact parameter of the collision in theoretical calculations, or relative to the "integrated" elliptic flow angle Ψ_2 in experiment), and that the same thing can happen for higher order harmonic flow coefficients when defining them relative to a fixed (i.e. p_T-independent) flow angle Ψ_n. The subject of this chapter is to elucidate the origins of such differences between different anisotropic flow measures and, in particular, the manifestation of event-by-event fluctuations of the p_T-dependent flow coefficients $v_n(p_T)$ and flow angles $\Psi_n(p_T)$ in different experimental flow measures. Except for Figs 10.2 to 10.9 and their discussion, which are new, the bulk of this chapter was previously published in Ref. [25].

10.2 Differential flows from the event-plane method and from two-particle correlations

The key experimental difficulty is that, due to the finite number of particles emitted in a each collision, the left hand sides of Eqs. (10.1) and (10.2) cannot be determined accurately for a single event. The V_n are characterized by probability distributions that depend on the studied class of events (system size, collision energy and centrality) from which each collision takes a sample. Experimental flow measurements rely on a number of different methods that amount to taking different moments of that probability distribution, by averaging over large numbers of events. Understanding the nature of these moments and reconstructing them from theoretical event-by-event dynamical simulations are essential steps in a meaningful comparison between theory and experiment.

In this chapter we leave the fluctuations arising from finite sampling statistics to a future work but rather focus on the hydrodynamical consequences of unavoidable event-by-event fluctuations in the initial state.

The most extensively used experimental methods for measuring anisotropic flows are the event-plane and two-particle correlation methods [165]. We begin with a discussion of the latter. Two-particle azimuthal correlations receive contributions from the anisotropic collective flow as well as from non-flow correlations; the latter can be minimized by appropriate experimental cuts and corrected for [165, 109]. Again, we are not interested in non-flow correlations and will here simply ignore their existence, assuming that they have been corrected for in the experimental analysis.

Two-particle correlation measures of anisotropic flow are based on correlators of the type

$$\langle\{e^{in(\phi_1-\phi_2)}\}\rangle \tag{10.3}$$

where ϕ_1 and ϕ_2 are the azimuthal angles around the beam direction of two particles with transverse momenta $\boldsymbol{p}_{\mathrm{T}1}$ and $\boldsymbol{p}_{\mathrm{T}2}$, and $\langle\ldots\rangle$ denotes the average over $N_{\mathrm{ev}} \gg 1$ events from a set of given

characteristics (e.g. of collisions in a certain centrality bin),

$$\langle O \rangle = \langle \{\mathcal{O}\} \rangle := \frac{1}{N_{\rm ev}} \sum_{i=1}^{N_{\rm ev}} \{\mathcal{O}\}_i, \tag{10.4}$$

whereas $\{\dots\}_i$ is the average of the observable $\mathcal{O}$ over all (or a specified subset of all) particle pairs in the event i:

$$\{e^{in(\phi_1-\phi_2)}\}_i = \frac{1}{N^{(i)}_{\rm pairs}} \sum_{\rm pairs \in i} e^{in(\phi_1-\phi_2)} \ . \tag{10.5}$$

Different chosen subsets for the event-wise average $\{\dots\}_i$ define different correlation measures for the anisotropic flow coefficients as we will explain below. We note that throughout this paper we will always correlate pairs of particles of the same kind (e.g. protons with protons or charged hadrons with charged hadrons, but not protons with charged hadrons), unless specifically stated otherwise. We will also assume that they have the same rapidity y; generalization to particles with different rapidities is straightforward, following the procedure discussed below when we go from particles with the same to particles with different p_T.

The magnitudes $v_n(p_T)$ of the anisotropic flow coefficients defined in Eq. (10.2) fluctuate from event to event according to some probability distribution $P(v_n(p_T))$. Let us denote the rms mean of this distribution by $v_n[2](p_T) := \sqrt{\langle v_n^2(p_T) \rangle}$, and similarly the rms mean for the integrated flow v_n by $v_n[2] := \sqrt{\langle v_n^2 \rangle}$. These rms means can be obtained from two-particle correlators of the type (10.3) as follows:

$$\begin{aligned} v_n^2[2](p_T) &= \langle \{e^{in(\phi_1-\phi_2)}\}_{p_T} \rangle = \langle \{e^{in\phi_1}\}_{p_T} \{e^{-in\phi_2}\}_{p_T} \rangle, \\ v_n^2[2] &= \langle \{e^{in(\phi_1-\phi_2)}\} \rangle = \langle \{e^{in\phi_1}\} \{e^{-in\phi_2}\} \rangle. \end{aligned} \tag{10.6}$$

Note that for the differential flow in the first line of equation (10.6), both particles are taken from the same p_T bin, and that the event-wise pair averages $\{e^{in(\phi_1-\phi_2)}\}$ factorize in each event due to our assumptions (absence of non-flow two-particle correlations, independent hydrodynamic emission of particles 1 and 2). Due to $1 \leftrightarrow 2$ symmetry under particle exchange, the exponential can be replaced by the cosine, and we get

$$\begin{aligned} v_n^2[2](p_T) &= \left\langle \frac{\int d\Delta\phi \, \cos(n\Delta\phi) \, \frac{dN_{\rm pairs}}{dy_1 dy_2 p_{\rm T1} dp_{\rm T1} p_{\rm T2} dp_{\rm T2} d\Delta\phi}\Big|_{p_{\rm T1}=p_{\rm T2}}}{\int d\Delta\phi \, \frac{dN_{\rm pairs}}{dy_1 dy_2 p_{\rm T1} dp_{\rm T1} p_{\rm T2} dp_{\rm T2} d\Delta\phi}\Big|_{p_{\rm T1}=p_{\rm T2}}} \right\rangle, \\ v_n^2[2] &= \left\langle \frac{\int d\Delta\phi \, \cos(n\Delta\phi) \, \frac{dN_{\rm pairs}}{dy_1 dy_2 d\Delta\phi}}{\int d\Delta\phi \frac{dN_{\rm pairs}}{dy_1 dy_2 d\Delta\phi}} \right\rangle, \end{aligned} \tag{10.7}$$

where $\Delta\phi = \phi_1 - \phi_2$ and the pair distribution has already been integrated over the average angle $\tilde{\phi} \equiv (\phi_1 + \phi_2)/2$.

Note that in Eqs. (10.7) the single-event averages are normalized by the number of pairs in the event, before averaging over events. This is important: Since the pair multiplicity fluctuates from event to event and within a multiplicity bin, and multiplicity anti-correlates with impact parameter with which the magnitudes of some of the anisotropic flow coefficients are geometrically correlated, this event-wise normalization avoids biasing the measured flow coefficients towards their values in events with larger than average multiplicity.

Our definition of the integrated flow $v_n[2]$ agrees with the standard definition for the "two-particle cumulant" flow $v_n\{2\}$ [166, 167, 168], but the same is not true for the differential flow $v_n[2](p_T)$ which differs from $v_n\{2\}(p_T)$. The experimental definition of $v_n\{2\}(p_T)$ is [166, 167, 168]

$$v_n\{2\}(p_T) = \langle\{e^{in\phi_1}\}_{p_{T1}}\{e^{-in\phi_2}\}\rangle / v_n\{2\} = \Big\langle v_n(p_T) v_n \cos[n(\Psi_n(p_T) - \Psi_n)]\Big\rangle / v_n[2] \; . \qquad (10.8)$$

Here only the first of the two particles within an event is taken from the desired p_T bin and particle species; it is correlated with *all* other particles detected in the event, with obvious statistical advantages compared with $v_n[2](p_T)$ which requires both particles to be of the same kind and from the same p_T bin. The normalization factor is the total rms flow of all charged hadrons. The last expression shows that $v_n\{2\}(p_T)$ reduces to $v_n[2](p_T) = \sqrt{\langle v_n^2(p_T)\rangle}$ if and only if the flow angle Ψ_n does not depend on p_T, the event-by-event fluctuations of $v_n(p_T)$ affect only its normalization but not the shape of its p_T dependence, and the v_n fluctuations of the particle species of interest are proportional to those of all hadrons. All of these assumptions are violated in hydrodynamic simulations of bumpy expanding fireballs. The difference between $v_n\{2\}(p_T)$ and $v_n[2](p_T)$ is thus sensitive to event-by-event fluctuations of the p_T-dependent difference $\Psi_n(p_T) - \Psi_n$ between the flow angle of particles with momentum p_T and the average event flow angle,[25] in addition to the (largely independent) fluctuations in the magnitudes of v_n and $v_n(p_T)$.

[25] More precisely, $v_n\{2\}(p_T)$ depends on the difference between $\Psi_n(p_T)$ *of the particles of interest* and the average flow angle Ψ_n *of all detected particles*. We checked numerically that the average hydrodynamic flow angles Ψ_n for identified pions and protons agree with great precision with the average flow angles for all particles in the event: Computing the ensemble average of $\langle\cos[n(\Psi_n^\pi - \Psi_n^p)]\rangle$ for all harmonics n and all collision centralities, we found deviations of less than 1–2% in all cases except for some of the high-order harmonics with $n > 6$ whose calculation is plagued by numerical errors at low $p_T \lesssim 0.2\,\mathrm{GeV}$ arising from the finite grid spacing of our square numerical grid used in solving the hydrodynamic equations.

Another approach to isolating effects arising from the p_T-dependence of the flow angles is a comparison of the p_T-dependent rms flow $v_n[2](p_T)$ with the so-called event-plane flow[26,27]

$$\begin{aligned} v_n\{\mathrm{EP}\}(p_T) &:= \left\langle \frac{\int d\phi\, \cos[n(\phi - \Psi_n)]\, \frac{dN}{dy p_T dp_T d\phi}}{\int d\phi\, \frac{dN}{dy p_T dp_T d\phi}} \right\rangle \\ &= \Re\Big\langle \{e^{in\phi}\}_{p_T} e^{-in\Psi_n} \Big\rangle = \Re\Big\langle v_n(p_T) e^{in(\Psi_n(p_T) - \Psi_n)} \Big\rangle \\ &= \Big\langle v_n(p_T) \cos[n(\Psi_n(p_T) - \Psi_n)] \Big\rangle. \end{aligned} \tag{10.9}$$

The equality in the second line arises from Eq. (10.2). Here for each event the "average flow angle" Ψ_n is first obtained by computing the $\boldsymbol{Q}_n$ vector [23]

$$\boldsymbol{Q}_n = Q_n e^{in\Psi_n} := \frac{1}{N} \sum_{k=1}^{N} \omega_k\, e^{in\phi_k} \tag{10.10}$$

(where N is the number of detected particles in the event) and determining its phase. In principle, different choices for the weights ω_k can be considered [165], but for consistency with Eq. (10.9) one must choose $\omega_k = 1$. The "average angle" Ψ_n for the event extracted from $\boldsymbol{Q}_n$ in general depends on the types of particles included in the sum in Eq. (10.10).

The last line in Eq. (10.9) makes it clear that the differential event-plane flows $v_n\{\mathrm{EP}\}(p_T)$ are sensitive to the event-by-event fluctuations of the p_T-dependent flow angles $\Psi_n(p_T)$ around the "average flow" angle Ψ_n. Just like the finite number statistical fluctuations[28] of the flow angle reconstructed from $\boldsymbol{Q}_n$ around the "true" flow angle of the event, these fluctuations smear out the azimuthal oscillations of the transverse momentum spectra and thus reduce the oscillation amplitudes $v_n\{\mathrm{EP}\}(p_T)$. In contrast to the former, they arise from fluctuations in the initial state and thus cannot be eliminated by improving or accounting for the resolution of the measurement of the final state. They carry valuable physical information about the initial state and the dynamics of its evolution into the final state.

[26] One can replace the cosine function in this definition by the exponential, omitting taking the real part in the second line, since the flow-angle fluctuations are symmetrically distributed such that the imaginary part vanishes after taking the event average (this has been verified numerically).

[27] Note that we define the n^{th}-order event-plane flow relative to the n^{th}-order flow plane Ψ_n, and not relative to the elliptic flow plane Ψ_2 as sometimes done.

[28] Due to the finite number of particles detected in each event, the accuracy of determining Ψ_n is limited by finite number statistics, and an accurate experimental estimation of the event-plane flow $v_n\{\mathrm{EP}\}$ requires an "event-plane resolution correction" [165]. As shown in [164, 109] (see also the discussion in [24]), which moment of the underlying v_n distribution is actually measured by the total event-plane flow $v_n\{\mathrm{EP}\}$ depends on this event-plane resolution: for perfect resolution $v_n\{\mathrm{EP}\}$ approaches the average flow $\langle v_n \rangle$ whereas in the case of poor resolution it is closer to the rms flow $v_n[2] = v_n\{2\}$ [164, 109]. The mathematical analysis in [109] applies only to the integrated flow which allowed to ignore the p_T-dependence of v_n fluctuations as well as initial-state related, p_T-dependent fluctuations of the flow angles that are not caused by finite multiplicity in the final state. In view of the latter, event-plane resolution effects on differential flow measurements and their correction require a new analysis.

We can remove the sensitivity of the measured quantity to the p_T-dependent fluctuations of the flow angle by first computing *for each event* the magnitude $v_n(p_T)$ of $\{e^{in\phi}\}_{p_T} = V_n(p_T)$, before summing over events:

$$\begin{aligned}\langle v_n(p_T)\rangle &= \left\langle \left| \{e^{in\phi}\}_{p_T} e^{-in\Psi_n} \right| \right\rangle = \left\langle \left| \{e^{in\phi}\}_{p_T} \right| \right\rangle \\ &= \left\langle \sqrt{\{\cos(n\phi)\}^2_{p_T} + \{\sin(n\phi)\}^2_{p_T}} \right\rangle . \end{aligned} \tag{10.11}$$

Since the quantity inside the event average does not depend on the average flow angle Ψ_n, this observable is not subject to an event-plane resolution correction. However, due to finite multiplicity in the final state, the right hand side will still in general be positive and non-zero experimentally even if there is no underlying anisotropic flow in the event. Again, how to properly account for such finite sampling statistical effects requires additional analysis.

By comparing $\langle v_n(p_T)\rangle$ (10.11) with $v_n[2](p_T)$ (10.6,10.7), $v_n\{2\}(p_T)$ (10.8), and $v_n\{\mathrm{EP}\}(p_T)$ (10.9), we can experimentally assess and separate the relative importance of event-by-event fluctuations in the magnitudes and directions of the anisotropic flows as functions of p_T.

Let us now proceed to two-particle correlations between particles of different (but specified) momenta. Since in the first line of Eq. (10.7) both particles are taken from the same bin in p_T, the flow angle $\Psi_n(p_T)$ drops out from the expression. This is not true for azimuthal correlations between two particles with different p_T [24]. In this case one finds [24, 169]

$$\begin{aligned}&\tilde{V}_{n\Delta}(p_{\mathrm{T}1}, p_{\mathrm{T}2}) := \left\langle \{e^{in(\phi_1-\phi_2)}\}_{p_{\mathrm{T}1}p_{\mathrm{T}2}} \right\rangle \\ &= \left\langle \{e^{in\phi_1}\}_{p_{\mathrm{T}1}} \{e^{-in\phi_2}\}_{p_{\mathrm{T}2}} \right\rangle = \langle V_n(p_{\mathrm{T}1}) V_n^*(p_{\mathrm{T}2})\rangle \\ &= \left\langle v_n(p_{\mathrm{T}1}) v_n(p_{\mathrm{T}2}) e^{in(\Psi_n(p_{\mathrm{T}1})-\Psi_n(p_{\mathrm{T}2}))} \right\rangle \\ &= \Big\langle v_n(p_{\mathrm{T}1}) v_n(p_{\mathrm{T}2}) \cos[n(\Psi_n(p_{\mathrm{T}1})-\Psi_n(p_{\mathrm{T}2}))] \Big\rangle . \end{aligned} \tag{10.12}$$

Due to parity symmetry, $\tilde{V}_{n\Delta}(p_{\mathrm{T}1}, p_{\mathrm{T}2})$ is real: while the quantity inside the event average $\langle \dots \rangle$ is in general complex for each individual event, its imaginary part averages to zero when summed over many events.

To properly account for multiplicity fluctuations, in Eq. (10.12) the averages $\{\dots\}_{p_{\mathrm{T}i}}$ within an event are once again normalized by the total number of particles included in the average, similar to Eq. (10.7). For this reason, $\tilde{V}_{n\Delta}(p_{\mathrm{T}1}, p_{\mathrm{T}2}) = \langle\{\cos(n\Delta\phi)\}_{p_{\mathrm{T}1},p_{\mathrm{T}2}}\rangle$ defined in Eq. (10.12) is not identical with the experimental quantity $V_{n\Delta}(p_{\mathrm{T}1}, p_{\mathrm{T}2})$ which is obtained from a Fourier decomposition with respect to the difference angle $\Delta\phi$ of the two-particle distribution obtained by summing over many events, without normalizing the contribution from each event by the corresponding event multiplicity [170, 171, 172, 169, 173]. For a meaningful comparison between theory and experiment, one should either normalize on the experimental side the contribution from each event to the two-particle distribution by the number of pairs in the event, or weight the theoretical

prediction for $v_n(p_{T1})v_n(p_{T2})e^{in(\Psi_n(p_{T1})-\Psi_n(p_{T2}))}$ for each event i with a factor $N^{(i)}_{\rm pairs}/\langle N_{\rm pairs}\rangle$ before summing over events. We prefer the first option since it avoids the geometric bias arising from the correlation between collision geometry and particle multiplicity.

10.3 The effect of flow fluctuations on differential v_n measures

In this section we compare the differential flows $v_n(p_T)$ extracted from the 20,000 viscous hydrodynamic simulations per centrality bin of 2.76 A TeV Pb+Pb collisions at the LHC (10,000 each with MC-Glauber and MC-KLN initial density profiles) that were generated in Ref. [174]. We use the Cooper-Frye prescription to compute from the hydrodynamic output on the freeze-out surface the single-particle distributions $dN/(dyp_Tdp_Td\phi)$ as continuous functions of p_T and ϕ (i.e. we do not sample the distribution to generate a finite number of particles per event, but pretend that the spectrum is sampled infinitely finely – this avoids the need to correct for effects arising from finite number statistics, such as imperfect event-plane resolution). All resonance decays are included in the final stable hadron spectra. The MC-Glauber (MC-KLN) initial conditions were hydrodynamically evolved with specific shear viscosity $\eta/s = 0.08$ (0.2).

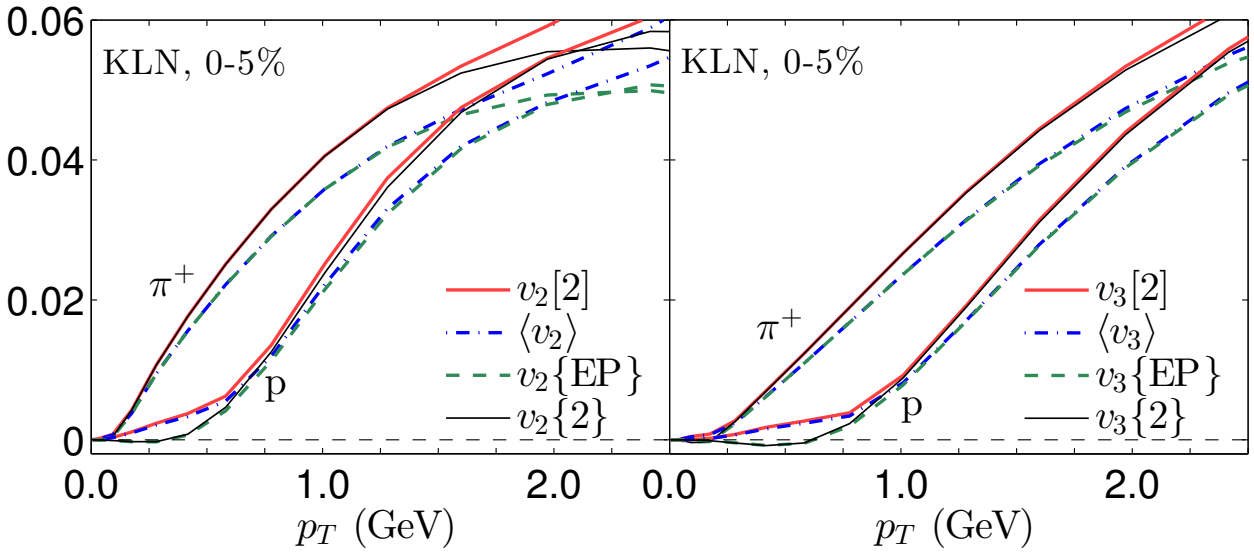

Figure 10.1: Comparison between the different definitions of the differential flows $v_n[2](p_T)$ (10.6,10.7), $v_n\{2\}(p_T)$ (10.8), $v_n\{\mathrm{EP}\}(p_T)$ (10.9), and $\langle v_n(p_T)\rangle$ (10.11), for pions and protons from central (0−5% centrality) Pb+Pb collisions at $\sqrt{s} = 2.76\,A$ TeV, computed with the viscous hydrodynamic code `VISH2+1`. See text for discussion.

We first present results for pions and protons, representing light and heavy particle species. Qualitatively, although not quantitatively, the same generic features are observed with MC-KLN and MC-Glauber model initial density profiles, and we show examples of the MCKLN initial conditions. Figures 10.1 shows elliptic and triangular flows in its left and right panels, for

central Pb+Pb collisions. The reader should compare the curves for $v_{2,3}[2]$ and $\langle v_{2,3}\rangle$, which are not affected by flow angle fluctuations (*c.f.* Eqs. (10.6) and (10.11)), with those for $v_{2,3}\{2\}$ and $v_{2,3}\{\mathrm{EP}\}$, which *are* affected by the p_T-dependence of the flow angles Ψ_n and their event-by-event fluctuations (*c.f.* Eqs. (10.8) and (10.9)): For protons with transverse momenta below about 1 GeV, flow angle fluctuations are seen to cause a significant suppression of the latter (in some cases even leading to negative elliptic flow values).[29] For the much lighter pions flow angle fluctuation effects are almost invisible at low p_T.[30]

Event-by-event fluctuations of the *magnitudes* of $v_{2,3}$ are accessible by comparing $\langle v_{2,3}\rangle$ with $v_{2,3}[2] = \langle v_{2,3}^2\rangle^{1/2}$. For central (0−5% centrality) collisions, where anisotropic flows are caused exclusively by fluctuations, with negligible geometric bias from a non-zero average deformation of the nuclear overlap region, we find for both pions and protons a constant (i.e. p_T-independent) value of $2/\sqrt{\pi} \approx 1.13$. This is expected [122, 22]: If the flow angle Ψ_n is randomly distributed relative to the reaction plane, the components of $V_n(p_T)$ along and perpendicular to the reaction plane are approximately Gaussian distributed around zero, and the magnitude $v_n(p_T)$ of the complex flow coefficient is Bessel-Gaussian distributed with $\sqrt{\langle v_n^2(p_T)\rangle} = \frac{2}{\sqrt{\pi}}\langle v_n(p_T)\rangle$ (see Eqs. (4) and (5) in Ref. [122]). Interestingly, for central collisions we find approximately the same constant value $2/\sqrt{\pi}$ for the ratio $v_{2,3}\{2\}(p_T)/v_{2,3}\{\mathrm{EP}\}(p_T)$ (except near the p_T values where either the numerator or denominator passes through zero). Looking at the definitions Eq. (10.8) and Eq. (10.9), this suggests an approximate factorization of the p_T-dependent flow angle fluctuations (which enter through the factor $\cos[n(\Psi_n(p_T)-\Psi_n)]$ that cancels between numerator and denominator if it fluctuates independently) from the fluctuations of the magnitude $v_n(p_T)$, as well as an approximate p_T-independence of the $v_{2,3}$ fluctuations.

In Fig. 10.1, the $v_n\{\mathrm{EP}\}$ is calculated with infinite resolution, $R_n \to 1$. However, in the real experimental measurements, due to only finite emitted particles in each final state, the resolution of $v_n\{\mathrm{EP}\}$ is not perfect, especially for p_T-differential $v_n\{\mathrm{EP}\}$. In the low resolution limit, $R_n \to \kappa v_n$, so $v_n\{\mathrm{EP}\} \to v_n\{2\}$. So the measured $v_n\{\mathrm{EP}\}$ usually lies in between $v_n\{2\}$ and $\langle v_n\rangle$ and its exact position depends on the collision centrality, system size, physical condition of the detector, and so on. Hence it is hard to extract the flow fluctuation information through the comparisons between the well measured $v_n\{\mathrm{EP}\}$ and $v_n\{2\}$ in the literature.

[29] Note that the factor $\cos[n(\Psi_n(p_T)-\Psi_n)]$ in Eqs. (10.8) and (10.9) is maximal if $\Psi_n(p_T)$ is always aligned with Ψ_n. The suppression of, say, $v_n\{\mathrm{EP}\}(p_T)$ relative to $\langle v_n\rangle(p_T)$ does therefore not indicate a definite momentum tilt of the emitting source at a given p_T relative to the average Ψ_n, but simply reflects a nonzero difference $\Psi_n(p_T)-\Psi_n$ that fluctuates from event to event, suppressing the value of $\cos[n(\Psi_n(p_T)-\Psi_n)]$ for either sign of the difference.

[30] The curves shown in Figs. 10.2, 10.3 include the decay products from unstable hadronic resonances. We have observed that for protons the flow angle fluctuation induced difference at low p_T between ($v_{2,3}[2]$, $\langle v_{2,3}\rangle$) on the one hand and ($v_{2,3}\{2\}$, $v_{2,3}\{\mathrm{EP}\}$) on the other hand doubles if only directly emitted ("thermal") particles are included in the analysis. Resonance decays thus dilute the sensitivity of the proposed observables to flow angle fluctuations by about 50%.

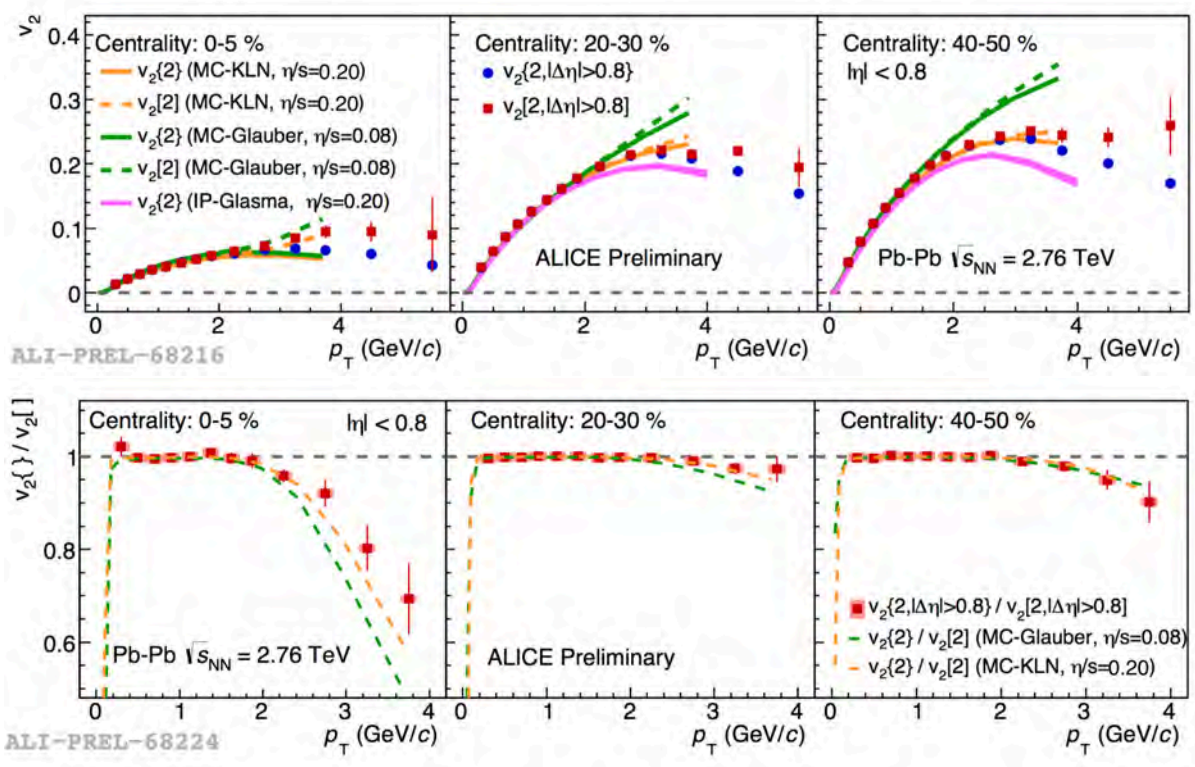

Figure 10.2: Upper panels: Charged hadrons $v_2\{2\}(p_T)$ and $v_2[2](p_T)$ measurements by the ALICE collaboration (preliminary results presented by You Zhou in Quark Matter 2014) are compared with viscous hydrodynamic predictions at 0-5%, 20-30%, and 40-50% centrality bins in Pb + Pb collisions at 2.76 A TeV. Lower panels: The ratio $v_2\{2\}/v_2[2]$ of charged hadrons as a function of p_T for the corresponding three centrality bins compared with hydrodynamic predictions.

In order to probe the fluctuations in the flow plane angle at different p_T, recent measurements of $v_n[2](p_T)$ for charged hadrons have been made by the ALICE collaboration at LHC. In the upper panels of Fig. 10.2 and Fig. 10.3, we show the measured charge particle $v_n[2](p_T)$ and $v_n\{2\}(p_T)$ compared with predictions from event-by-event viscous hydrodynamics. For the elliptic flow data shown in Fig. 10.2, we find that MCKLN initial conditions with $\eta/s = 0.20$ can describe the data fairly well up to 3.5 GeV. The theory calculations correctly predict qualitatively (even quantitatively for MCKLN with $\eta/s = 0.20$) the measured difference between $v_2[2]$ and $v_2\{2\}$. For v_3 and v_4 in Fig. 10.3, the IP-Glasma model with $\eta/s = 0.20$ gives better description of the data. Our results from the MCGlb (MCKLN) model overestimate (underestimate) the data. Neither of these two models appears to produce the correct initial fluctuation spectra. In the lower panels of Fig. 10.2, the ratio $v_2\{2\}/v_2[2]$ is plotted to further show the difference between the two flow measurements. Based on Eq. (10.6) and Eq. (10.8), we have

$$\frac{v_n\{2\}}{v_n[2]} = \frac{\langle v_n(p_T) v_n \cos(n(\Psi_n(p_T) - \Psi_n))\rangle}{\sqrt{\langle v_n^2(p_T)\rangle}\sqrt{\langle v_n^2\rangle}}. \tag{10.13}$$

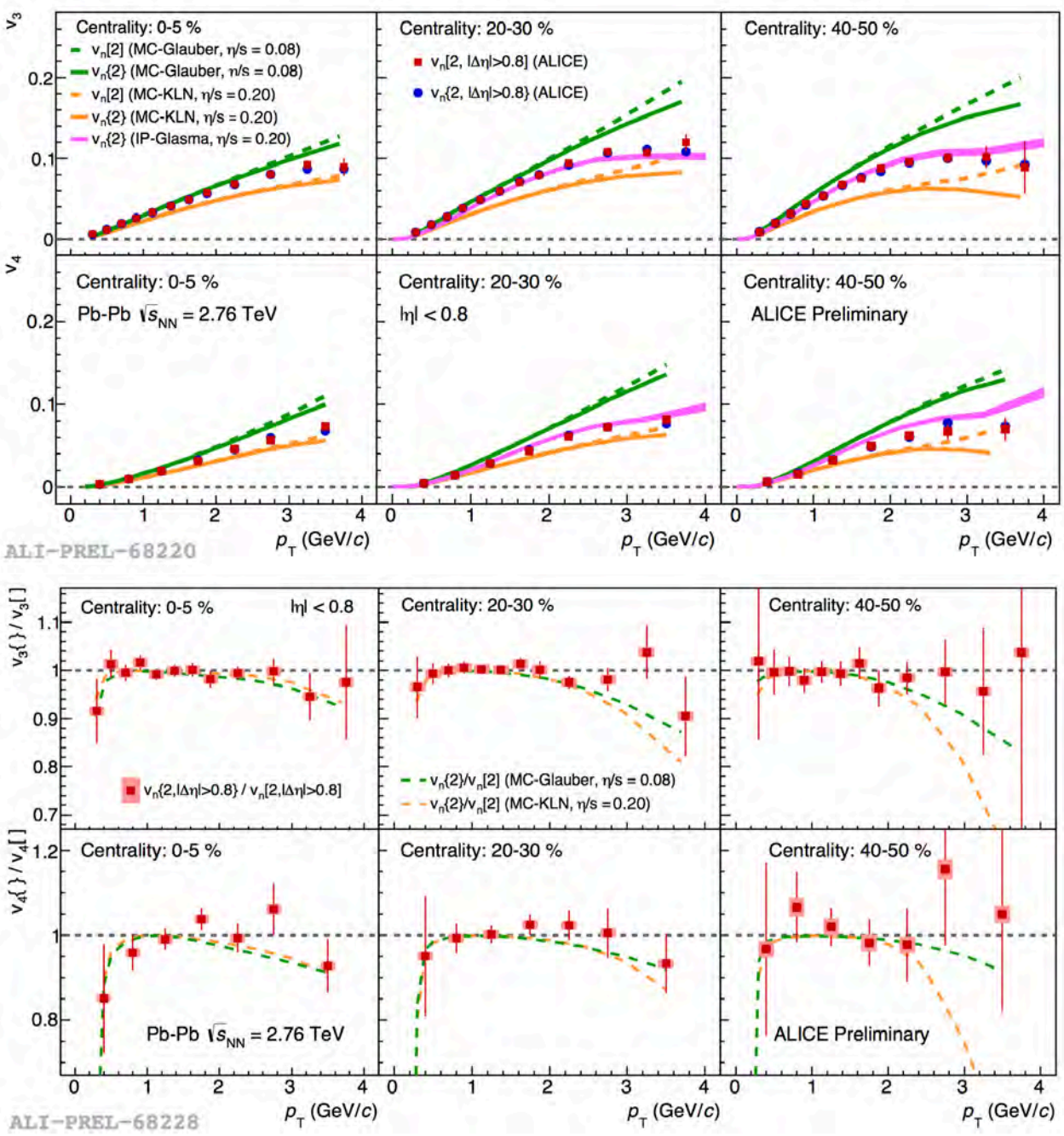

Figure 10.3: Similar plots as Fig. 10.2, but for v_3 and v_4 of charged hadrons.

The ratio has an upper bound at 1. Any fluctuations in $\Psi_n(p_T)$ deviating away from Ψ_n or in the magnitude of v_n will make this ratio smaller than 1. For charged hadrons, we find that the ratio $v_2\{2\}/v_2[2]$ deviates from 1 at high p_T. This deviation is the largest in central collisions. Our hydrodynamic simulations successfully predict the centrality dependence of this ratio. This is because in the non-central collisions the flow plane angle is dominated by the geometric deformation, which reduces the fluctuations of $\Psi_n(p_T)$ away from Ψ_n. In the bottom two panels of Fig. 10.3, we find that the ratio for higher order flow is consistent with 1 within error bar through

the whole p_T range. The deviation from 1 for $v_{3,4}\{2\}/v_{3,4}[2]$ is much smaller than for $v_2\{2\}/v_2[2]$. For MC-Glauber initial conditions and $\eta/s = 0.08$, our hydrodynamic predictions agree with the experimental measurements within the experimental uncertainty bands. Except for the 40-50% centrality bin, our calculations with MCKLN initial conditions with $\eta/s = 0.20$ disagree with the measured values at high p_T. We suspect this is due to large viscous δf corrections in the Cooper-Frye freeze-out procedure. In Fig. 10.3, we notice that $v_{3,4}\{2\}/v_{3,4}[2]$ is smaller than 1 at the lowest p_T point in 0-5% central collisions. Although this point carries relatively large error bar, this qualitative feature was predicted by hydrodynamics. Recalling Fig. 10.1, where we find a larger difference between $v_n\{2\}$ and $v_n[2]$ for identified protons in a wider p_T range at low p_T, we are interested to see possible future measurements of $v_n[2]$ for identified particles.

Based on Figs. 10.2 and 10.3, we can see that through a systematic comparisons between $v_2\{2\}$ and $v_2[2]$ measurements and theoretical calculations from viscous hydrodynamic simulations it is possible to extract new information about the $v_n(p_T)$ and $\Psi_n(p_T)$ fluctuations. They can provide us with new constraints on the spectrum of initial state fluctuations as well as for the extraction of the specific shear viscosity.

10.4 Non-factorization of flow-induced two-particle correlations

The breaking of factorization of flow-induced two-particle correlations by flow fluctuations was first emphasized by Gardim *et al.* [24]. Their study was based on simulations using ideal fluid dynamics, which are here repeated with viscous fluid dynamics. A comparison of Figs. 10.4, 10.5, 10.6 below with the plots shown in Ref. [24] shows that viscous effects reduce the amount by which event-by-event fluctuations break factorization. We will study these flow factorization effects more systematically over the whole range of centralities and explore the relative role played in this context by fluctuations in the magnitudes and angles of the flows.

To this end we define the following two ratios, both symmetric in $p_{\rm T1}$ and $p_{\rm T2}$:

$$\begin{aligned} r_n(p_{\rm T1}, p_{\rm T2}) &= \frac{\tilde{V}_{n\Delta}(p_{\rm T1}, p_{\rm T2})}{\sqrt{\tilde{V}_{n\Delta}(p_{\rm T1}, p_{\rm T1})\tilde{V}_{n\Delta}(p_{\rm T2}, p_{\rm T2})}} \\ &= \frac{\langle V_n(p_{\rm T1})V_n^*(p_{\rm T2})\rangle}{\sqrt{\langle|V_n(p_{\rm T1})|^2\rangle\langle|V_n(p_{\rm T2})|^2\rangle}} \\ &= \frac{\langle v_n(p_{\rm T1})v_n(p_{\rm T2})\cos[n(\Psi_n(p_{\rm T1})-\Psi_n(p_{\rm T2}))]\rangle}{\sqrt{\langle v_n^2(p_{\rm T1})\rangle\langle v_n^2(p_{\rm T2})\rangle}}; \end{aligned} \tag{10.14}$$

$$\tilde{r}_n(p_{\rm T1}, p_{\rm T2}) = \frac{\langle v_n(p_{\rm T1})v_n(p_{\rm T2})\cos[n(\Psi_n(p_{\rm T1})-\Psi_n(p_{\rm T2}))]\rangle}{\langle v_n(p_{\rm T1})v_n(p_{\rm T2})\rangle}. \tag{10.15}$$

The ratio r_n, first introduced and studied with ideal fluid dynamics in [24], is sensitive to fluctuations of both the magnitudes $v_n(p_T)$ and angles $\Psi_n(p_T)$ of the complex anisotropic flow coefficients

$V_n(p_T)$ defined in Eq. 10.2). The second ratio $\tilde{r}_n$, on the other hand, differs from unity only on account of flow angle fluctuations, $r_n \leq \tilde{r}_n$. By comparing the two ratios with each other and with experimental data we can isolate the role played by flow angle fluctuations in the breaking of factorization of the event-averaged two-particle cross section. In the absence of non-flow correlations both ratios are always ≤ 1.

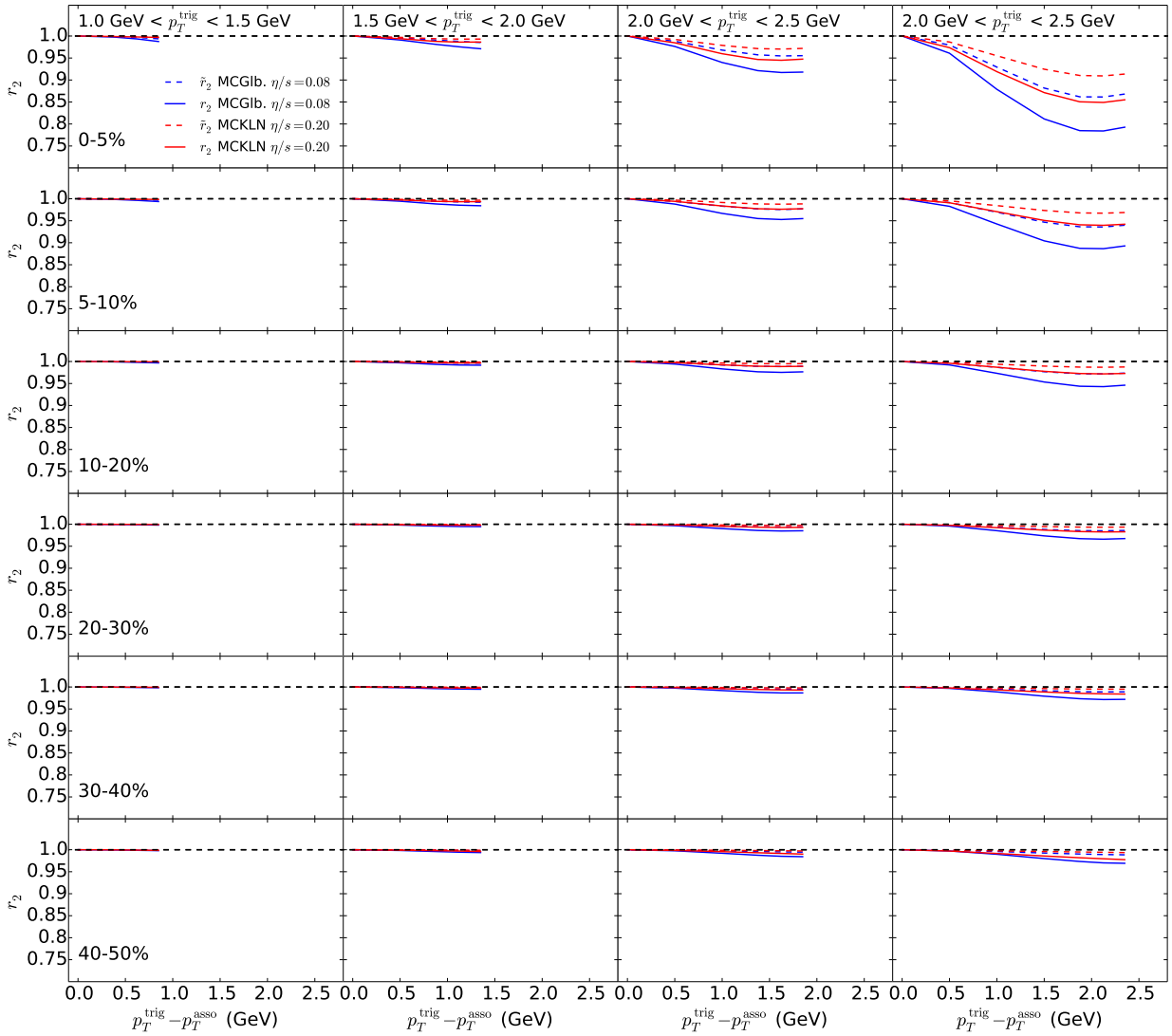

Figure 10.4: The ratios $r_2(p_{\mathrm{T}}^{\mathrm{trig}}, p_{\mathrm{T}}^{\mathrm{asso}})$ (solid lines) and $\tilde{r}_2(p_{\mathrm{T}}^{\mathrm{trig}}, p_{\mathrm{T}}^{\mathrm{asso}})$ (dashed lines), defined in Eqs. (10.14) and (10.15), as functions of $p_{\mathrm{T}}^{\mathrm{trig}} - p_{\mathrm{T}}^{\mathrm{asso}}$ for different $p_{\mathrm{T}}^{\mathrm{trig}}$ ranges, as indicated. From top to bottom, r_2 and $\tilde{r}_2$ results are shown in different centrality bins.

Figures 10.4, 10.5, and 10.6 show these ratios for all charged hadrons as functions of $p_{\mathrm{T}}^{\mathrm{trig}} - p_{\mathrm{T}}^{\mathrm{asso}}$ for fixed ranges of $p_{\mathrm{T}}^{\mathrm{trig}}$, indicated in different columns.[31]

[31]The p_{T} ranges are adjusted to the CMS measurement for direct comparison and the ratios were computed by first averaging the numerator and denominator over the given p_{T} range.

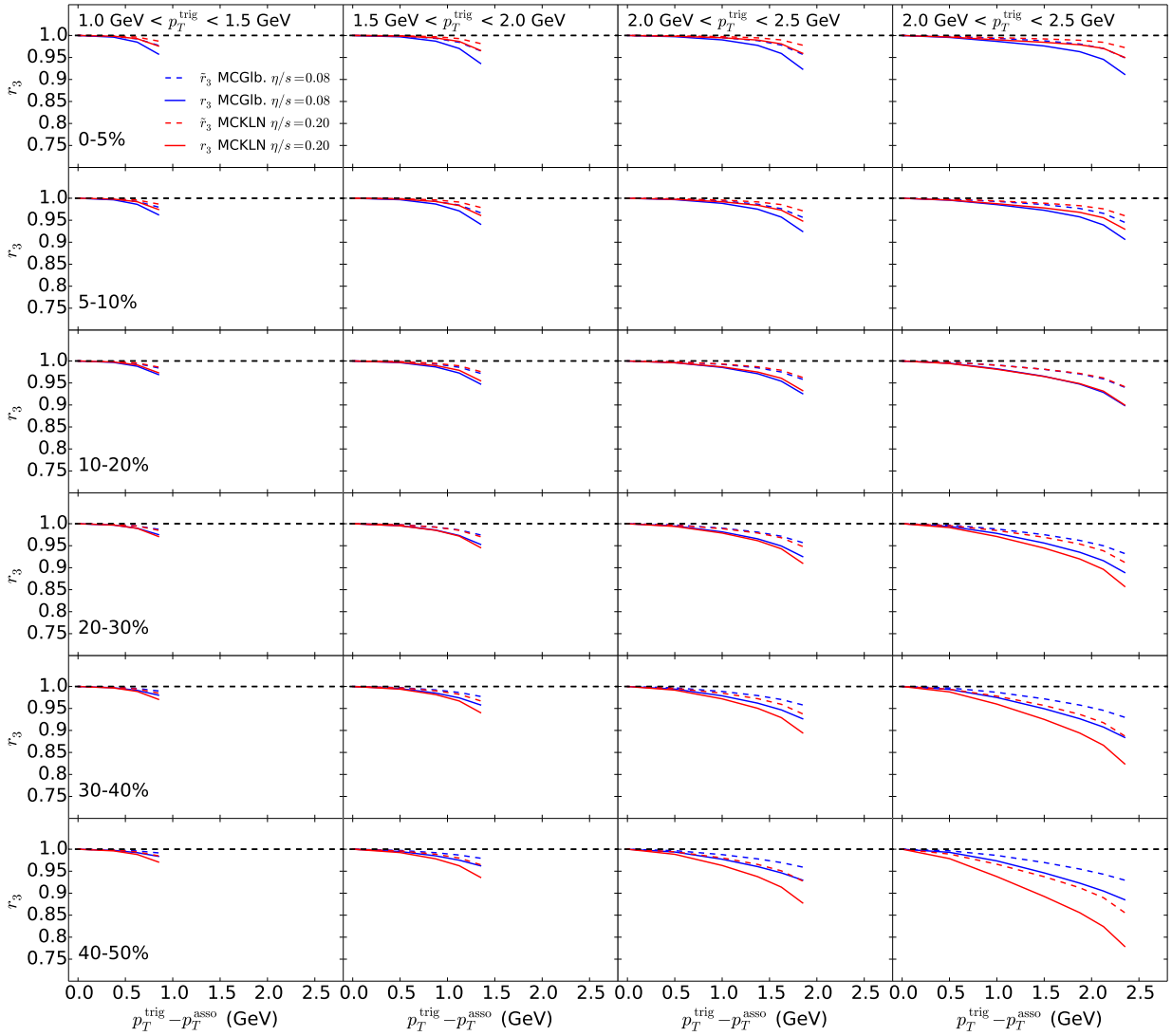

Figure 10.5: Similar to Fig. 10.4, but for r_3 and $\tilde{r}_3$.

The comparison of r_n (solid lines) with $\tilde{r}_n$ (dashed lines) shows that a significant fraction ($\sim$50% or more) of the effects that cause the breaking of factorization arises from flow angle fluctuations. This seems to hold at all the transverse momenta shown in the figures.

A comparison from the top to bottom rows of panels in Fig. 10.4(Fig. 10.6) shows that factorization-breaking effects in $r_2(r_4)$ are stronger in central collisions compared to in peripheral ones. It is because the the magnitudes of $v_{2,4}$ and the flow angles $\Psi_{2,4}$ are mostly controlled by the collision geometry in the peripheral collisions. The centrality dependence of r_2 in MCGlb is slightly stronger than MCKLN model. For r_4, MCKLN initial conditions show big factorization-breaking effects in the largest p_T bin. The story is not completely the same for r_3 in Fig. 10.5, where the size of the factorization-breaking effect shows much less centrality dependence than for r_2. This is mainly due to the fact that the triangular flow is fluctuation driven at all centralities.

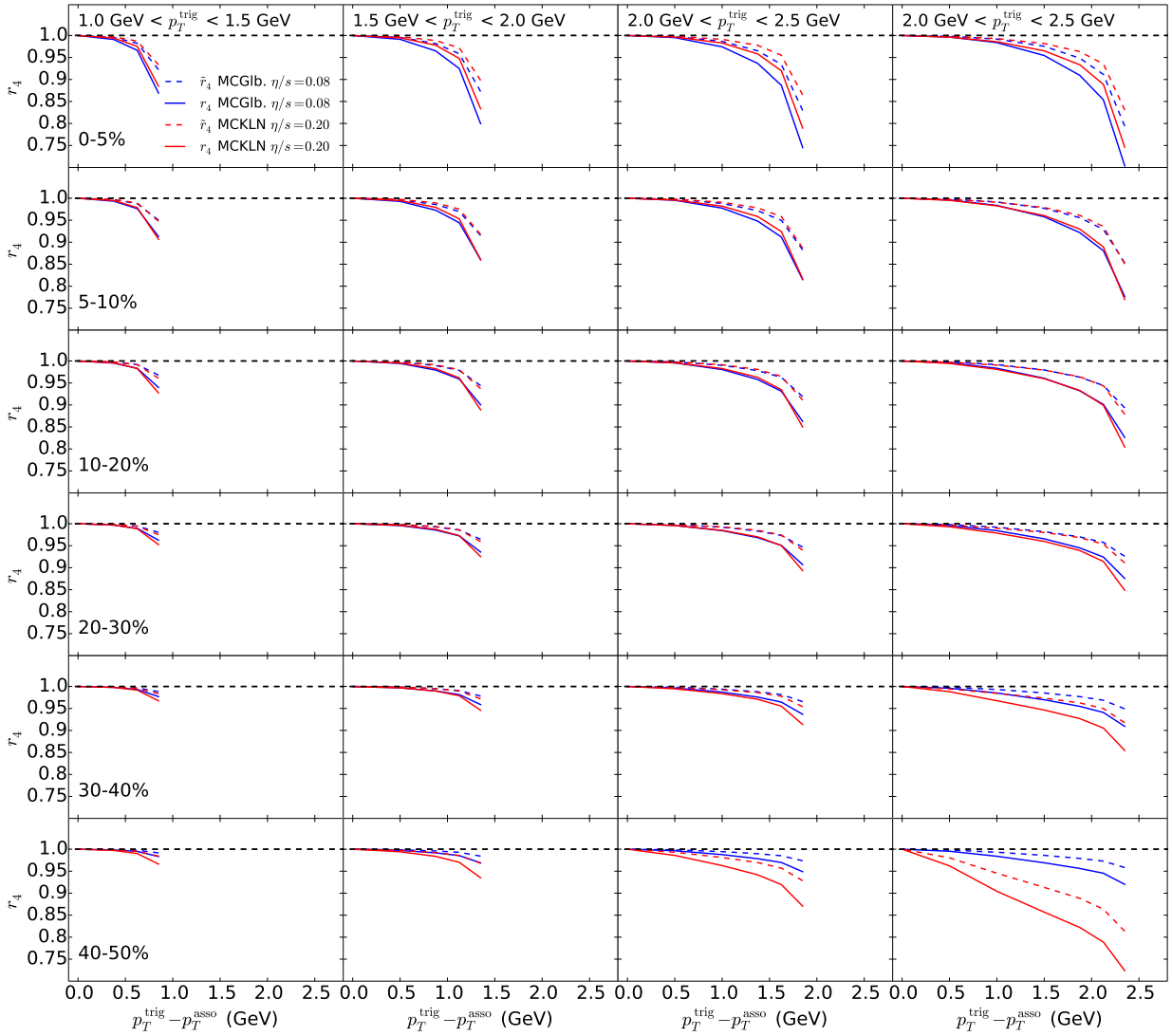

Figure 10.6: Similar to Fig. 10.4, but for r_4 and $\tilde{r}_4$.

To explore the effects of shear viscosity of the expanding fluid on the breaking of factorization, we compare the red and blue curves in each panel. Obviously, the MCKLN model produces a different initial fluctuation spectrum than the MC-Glauber model, so not all of the differences between the red and blue cures can be attributed to the larger viscosity used in the MCKLN runs. However, in conjunction with the ideal fluid results reported in [24], the comparison of these two figures strengthens the conclusion that increased shear viscosity tends to weaken the fluctuation effects that cause the event-averaged two-particle cross section to no longer factorize.

Finally, in Figs. 10.7, 10.8, and 10.9, we show the comparisons of our event-by-event hydrodynamic predictions of the $r_{2,3,4}$ ratios against the CMS measurements [175]. The results from event-by-event hydrodynamic simulations successfully predict the qualitative features (even quantitatively for the MCKLN initial conditions with $\eta/s = 0.20$) in the experimental data.

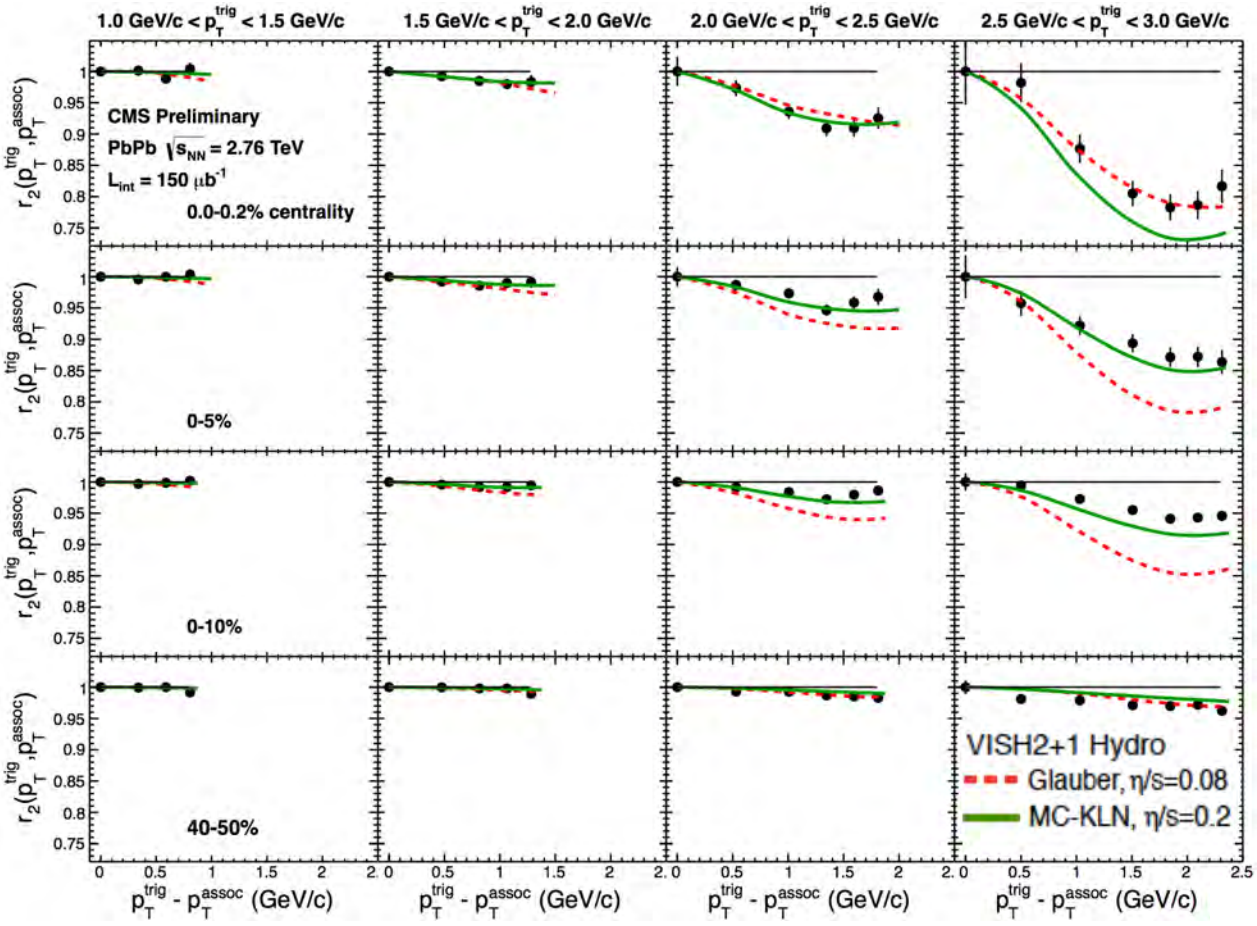

Figure 10.7: Hydrodynamic predictions of the flow factorization ratios r_2 for Pb+Pb collisions at the LHC are compared with the CMS measurements. From top to bottom panels, comparisons are shown from central to semi-peripheral centrality bins. Figure is taken from Wei Li's plenary talk at Hard Probes 2013 and the data are published in [175].

10.5 Chapter summary

All experimental precision measures of anisotropic flow in relativistic heavy-ion collisions are based on observables that average over many collision events. It has been known for a while that both the magnitudes v_n and flow angles Ψ_n of the complex anisotropic flow coefficients V_n fluctuate from event to event, but only very recently it became clear that not only the v_n, but also their associated angles Ψ_n depend on p_T, and that the difference $\Psi_n(p_T)-\Psi_n$ between the p_T-dependent and p_T-averaged flow angles also fluctuates from event to event. In the present study we have pointed out that these flow angle fluctuations leave measurable traces in experimental observables from which the ensemble-averaged p_T-dependent anisotropic flows are extracted. We have introduced several new flow measures and shown how their comparison with each other and

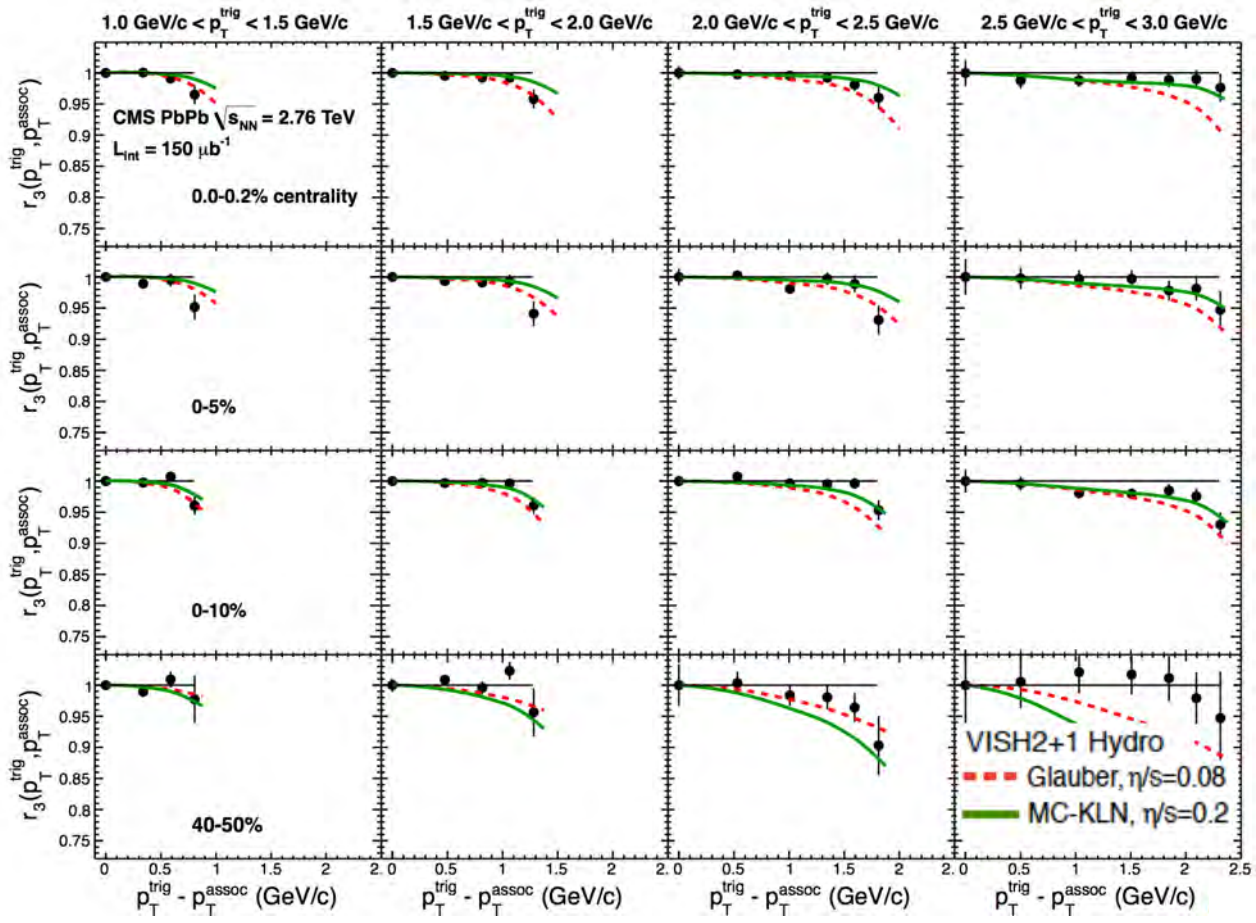

Figure 10.8: Similar to Fig. 10.7, but for r_3. Figure is taken from Wei Li's plenary talk at Hard Probes 2013 and the data are published in [175].

with flow measures that are already in wide use allows to separately assess the importance of event-by-event fluctuations of the magnitudes and angles of $V_n = v_n e^{in\Psi_n}$ on experimentally determined flow coefficients.

Viscous hydrodynamic simulations show that flow angle fluctuations affect the p_T-dependent flow coefficients of heavy hadrons (such as protons) more visibly than those of light hadrons (pions). In near-central collisions, where anisotropic flow is dominated by initial density fluctuations rather than overlap geometry, the effects from flow angle fluctuations appear to be strongest for particles with transverse momenta $p_T \lesssim m$. A precise measurement and comparison of $\langle v_n(p_T)\rangle$ (Eq. (10.11)), $v_n\{\mathrm{EP}\}(p_T)$ (Eq. (10.9)), $v_n[2](p_T)$ (Eqs. (10.6,10.7)), and $v_n\{2\}(p_T)$ (Eq. (10.8) for identified pions, kaons and protons with transverse momenta $p_T < 2\,\mathrm{GeV}$ should be performed to confirm the hydrodynamically predicted effects from flow angle fluctuations. The theoretical interpretation of these measurements requires a reanalysis of finite sampling statistical effects on the p_T-*dependent differential* flows, stemming from the finite multiplicity of particles of interest in a single event, which we did not consider here. The proposed comparison holds the promise

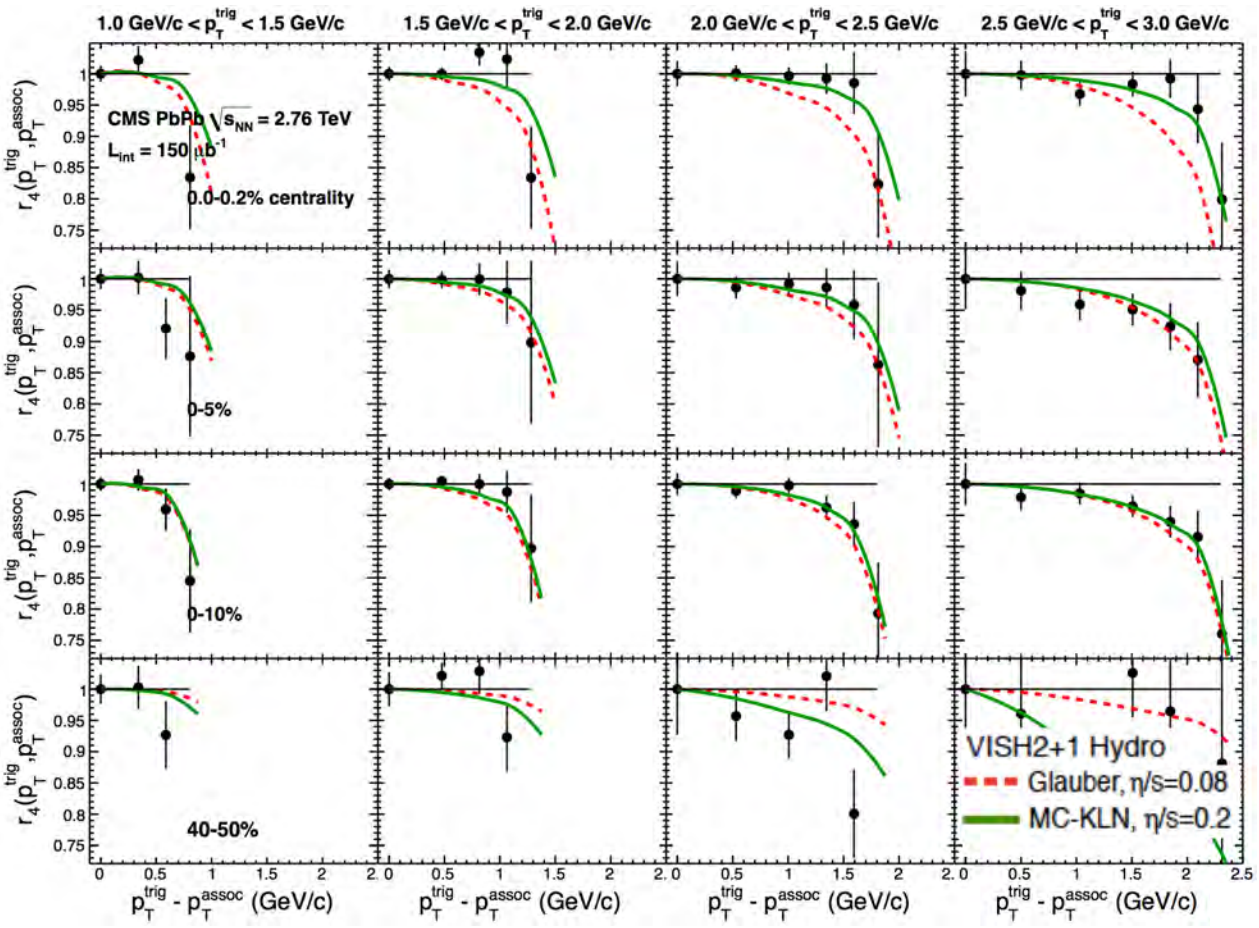

Figure 10.9: Similar to Fig. 10.7, but for r_4. Figure is taken from Wei Li's plenary talk at Hard Probes 2013 and the data are published in [175].

of yielding valuable experimental information to help constrain the distribution of initial density fluctuations in relativistic heavy ion collisions and may prove crucial for a precision determination of the QGP shear viscosity.

We also showed that flow angle fluctuations are responsible for more than half of the hydrodynamically predicted factorization breaking effects studied in Ref. [24] and in Sec. 10.4 above, and that these effects are directly sensitive to the shear viscosity of the expanding fluid, decreasing with increasing viscosity. By combining the study of various types of differential anisotropic flow measures with an investigation of the flow-induced breaking of the factorization of two-particle observables into products of single-particle observables one can hope to independently constrain the fluid's transport coefficients and the initial-state fluctuation spectrum.

Chapter 11: Ultra-central Pb+Pb collisions at the LHC

11.1 Chapter introduction

In the effort to extract the specific shear viscosity phenomenologically, the currently biggest road block lies in the large uncertainty of the initial conditions for the hydrodynamic simulations [40]. The authors of [176] proposed to extract the specific QGP shear viscosity in ultra-central collisions, where anisotropies from the geometric overlap of the colliding nuclei are minimized. Furthermore, since the initial eccentricities $\{\varepsilon_n\}$ are roughly equal in size for all n in ultra-central collisions, the non-linear mode-coupling effects [112, 177] for higher order v_n are also expected to be suppressed [176]. Thus, the measured anisotropic flow coefficients can maximally expose the intrinsic nucleon and sub-nucleon fluctuations at the beginning of the heavy-ion collisions. The spectrum of final flow v_n as a function of their harmonic order n in these ultra-central collisions has discriminating power to constrain the initial conditions as well as the extraction of the specific shear viscosity of the QGP medium. Because of these advantages, the CMS collaboration at LHC has measured the anisotropic flow coefficients of charged hadrons in 0-0.2% ultra-central Pb+Pb collisions at $\sqrt{s} = 2.76\,A\,\mathrm{TeV}$ [175].

In this chapter, we will simulate these ultra-central collisions using event-by-event viscous hydrodynamics and conduct apple-to-apple comparisons with the experimental observables.

11.2 Event selection and initial state fluctuations in ultra-central collisions

Experimentally, in ultra-central collision events are defined as those with the highest measured final charged multiplicities. However, in theoretical calculations, using final charged multiplicities to determine the event centrality is numerically very expensive. Especially for 0-0.2% ultra-central collisions, the remaining 99.8% of the simulated events are wasted. So we would like to determine (at least estimate) the event centrality of each initial profile before evolving them through viscous hydrodynamics.

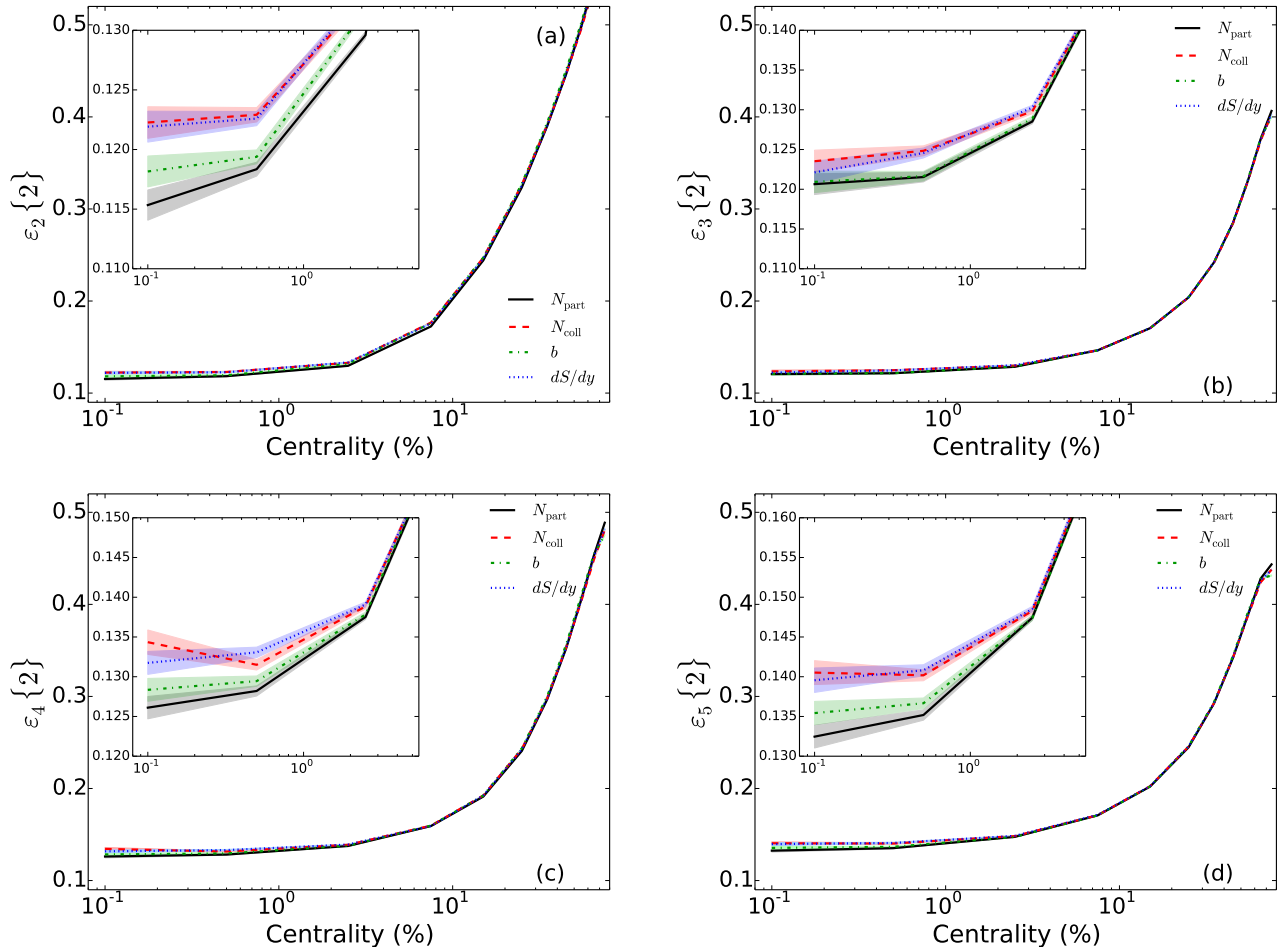

Figure 11.1: The root mean square (rms) initial eccentricity $\epsilon_n\{2\}$ for $n = 2 - 5$ as a function of centrality. The event centrality is determined using the number of participant nucleons $N_{\rm part}$ (solid black), or the number of binary collisions $N_{\rm coll}$ (red dashed), or impact parameter b (green dotted), or initial total entropy dS/dy (dotted blue). Results are generated using 1 million events from the MC-Glauber model for Pb + Pb collisions at $\sqrt{s} = 2.76A$ TeV, with binary collision to wounded nucleon ratio $\alpha = 0.118$.

In Fig. 11.1, we try 4 popular choices of the collision parameters ($N_{\rm part}$, $N_{\rm coll}$, b, dS/dy) to categorize the event centrality of each initial density profile generated from the MC-Glauber model. We check how the initial fluctuation spectrum $\{\varepsilon_n\{2\}\}$ varies as we change the method for cutting on centrality. Fig. 11.1 shows that $\{\varepsilon_n\{2\}\}$ is insensitive to the method used for cutting on centrality for centralities larger than 10%. Differences become noticeable when we select events within the top 1%. $\{\varepsilon_n\{2\}\}$ can differ by up to $\sim 10\%$ if one cuts the centrality using initial total entropy compared to using the number of participant nucleons. In Chapter 2.3.5, we argued that the initial total entropy shows a good correlation with the final charged multiplicity. In the following study in this chapter, we will use the total entropy of the initial profile to select events belonging to the 0-0.2% centrality class of ultra-central collisions. We employ both MCGlb and MCKLN initial conditions and evolve them using viscous hydrodynamics with three different

specific shear viscosities, $\eta/s = 0.08, 0.12, 0.20$. We generate 200 events for each set of runs, which is sufficient for a statistical analysis of anisotropic flows.

In order to capture the bias in ultra-central collisions towards events whose entropy production fluctuates upward from the mean, we implement pp multiplicity fluctuations in the MC-Glauber model, using a method that is motivated by the phenomenologically observed KNO scaling of multiplicities in pp collisions. The detailed implementation is described in Chapter 2.3.4. The shape fluctuations of the initial conditions can be characterized by a series of harmonic eccentricity coefficients. For ($n \geq 2$), the n-th order eccentricity of the initial condition is defined as the modulus of the complex quantity

$$\varepsilon_n e^{in\Phi_n} = \frac{\int d^2r r^n e(r,\phi) e^{in\phi}}{\int d^2r r^n e(r,\phi)}, \tag{11.1}$$

where $e(r,\phi)$ is the transverse energy density profile and the phase Φ_n of the complex quantity (11.1) defines the n-th order participant plane angle. For $n = 1$,

$$\varepsilon_1 e^{i\Phi_1} = \frac{\int d^2r r^3 e(r,\phi) e^{i\phi}}{\int d^2r r^3 e(r,\phi)}. \tag{11.2}$$

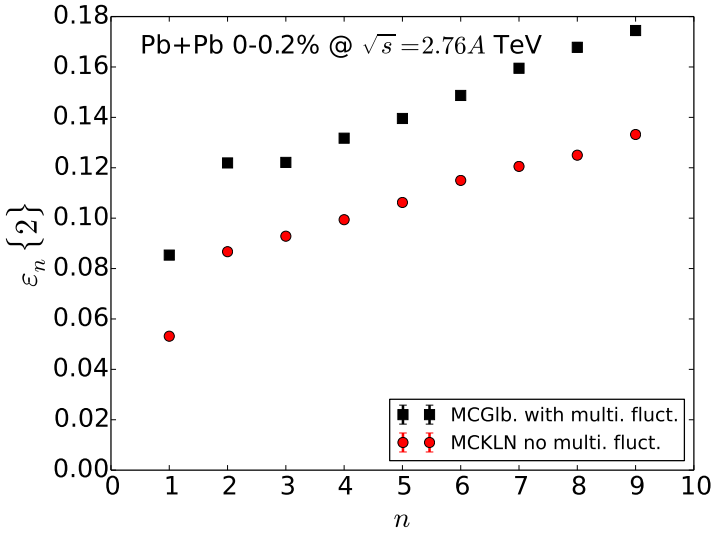

Figure 11.2: The rms initial eccentricity $\varepsilon_n\{2\}$ as a function of harmonic order n from MC-Glauber and MCKLN models in 0-0.2% ultra-central Pb+Pb collisions at 2.76 A TeV.

In Fig. 11.2 we plot the initial fluctuation power spectrum $\varepsilon_n\{2\}$ for the MC-Glauber and MCKLN models in the ultra-central collisions at LHC. In these ultra-central collisions, fluctuations dominate over geometric overlap effects in $\varepsilon_n\{2\}$. With the r^n weighting factor in Eq. (11.1), the absolute values of all orders of $\varepsilon_n\{2\}$ (except for $\varepsilon_1\{2\}$) are comparable with each other, for both initial condition models. The $\varepsilon_n\{2\}$ from the MCKLN model is about 30% smaller compared to the MC-Glauber model, mostly due to the implementation of pp multiplicity fluctuations in the former that are not included in the latter. (see comparisons in Fig. 2.5).

11.3 Particle spectra and their flow anisotropies in ultra-central Pb+Pb collisions

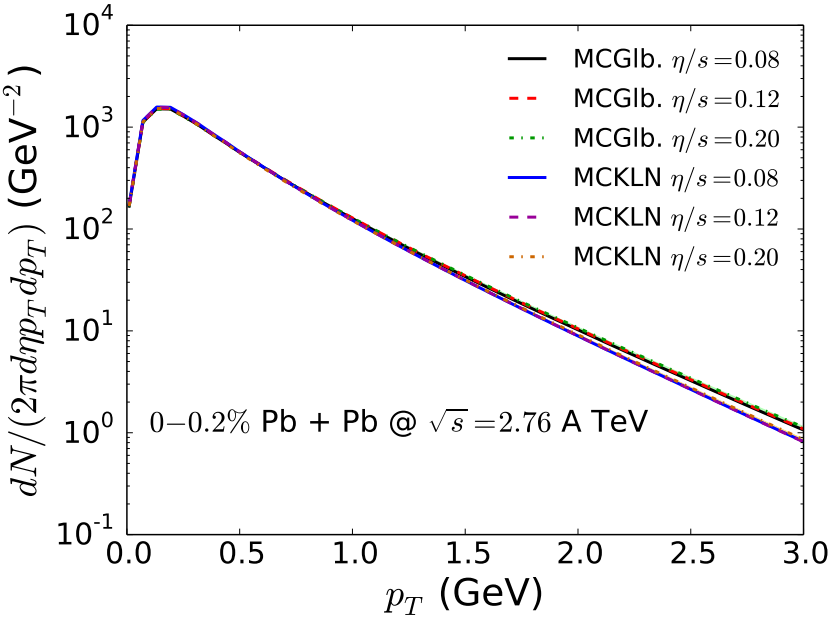

Figure 11.3: Charged hadron p_T-spectra from the MCGlb and MCKLN models for different specific shear viscosities as indicated in the legend, for Pb+Pb collisions at $\sqrt{s} = 2.76\,A\,\text{TeV}$ 0-0.2% centrality.

Model	$dN/d\eta\|_{\|\eta\|<0.5}$	$\langle p_T \rangle$ (GeV)
MCGlb. $\eta/s = 0.08$	1822.36 ± 2.75	0.721 ± 0.001
MCGlb. $\eta/s = 0.12$	1846.9 ± 2.65	0.723 ± 0.001
MCGlb. $\eta/s = 0.20$	1837.85 ± 3.02	0.729 ± 0.001
MCKLN $\eta/s = 0.08$	1806.7 ± 1.12	0.695 ± 0.001
MCKLN $\eta/s = 0.12$	1802.35 ± 1.13	0.696 ± 0.001
MCKLN $\eta/s = 0.20$	1774.9 ± 0.98	0.703 ± 0.001

Table 11.1: The total yield of charged hadrons and their mean p_T in 0-0.2% in Pb+Pb collisions at LHC. In each set of runs, we fixed the overall normalization factor to the experimental measured charged hadron multiplicity at 0-5% centrality.

In Fig. 11.3, we show the transverse momentum spectra of charged hadrons from the MC-Glauber and the MCKLN models evolved with different η/s in the hydrodynamic simulations. In ultra-central collisions, we find that the shear viscosity has only minor effects on the slope of the hadron spectra. The MC-Glauber initial conditions, which include multiplicity fluctuations in pp collisions, result in slightly flatter particle spectra compared to the MCKLN model. In Table 11.1, we summarize the total yield of charged hadrons and their mean p_T in the 0-0.2% ultra-central Pb+Pb collisions at LHC. A larger η/s results in only a slightly larger mean p_T for the charged

hadrons. This means that the amount of radial flow generated in the system is very similar in all these runs.

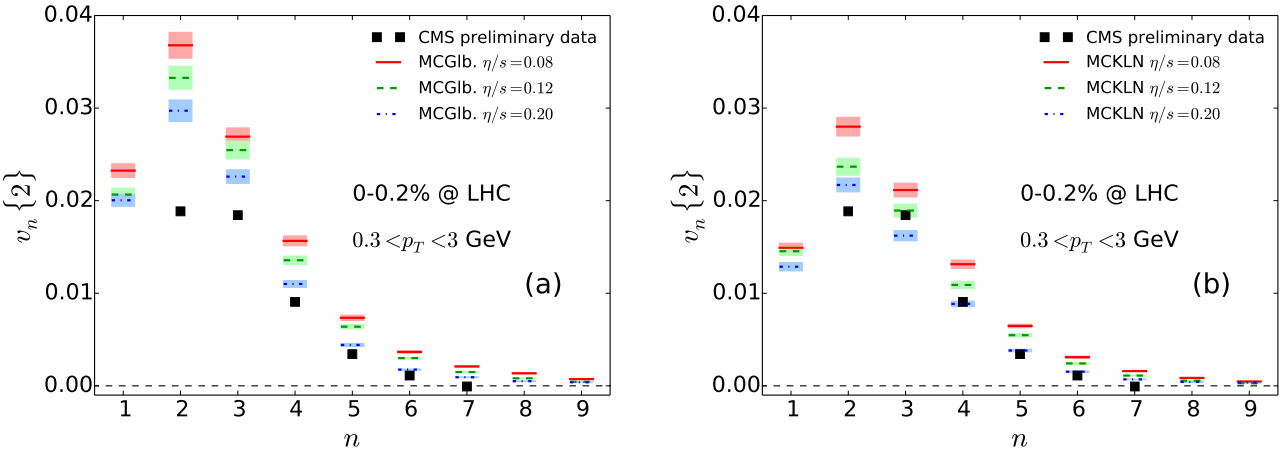

Figure 11.4: p_T-integrated $v_n\{2\}$ of charged hadrons in 0-0.2% centrality from the MC-Glauber (left panel) and the MCKLN (right panel) models compared to the CMS preliminary measurements (data extracted from [175]). $v_n\{2\}$ is integrated from 0.3 to 3 GeV as measured in the CMS experiments.

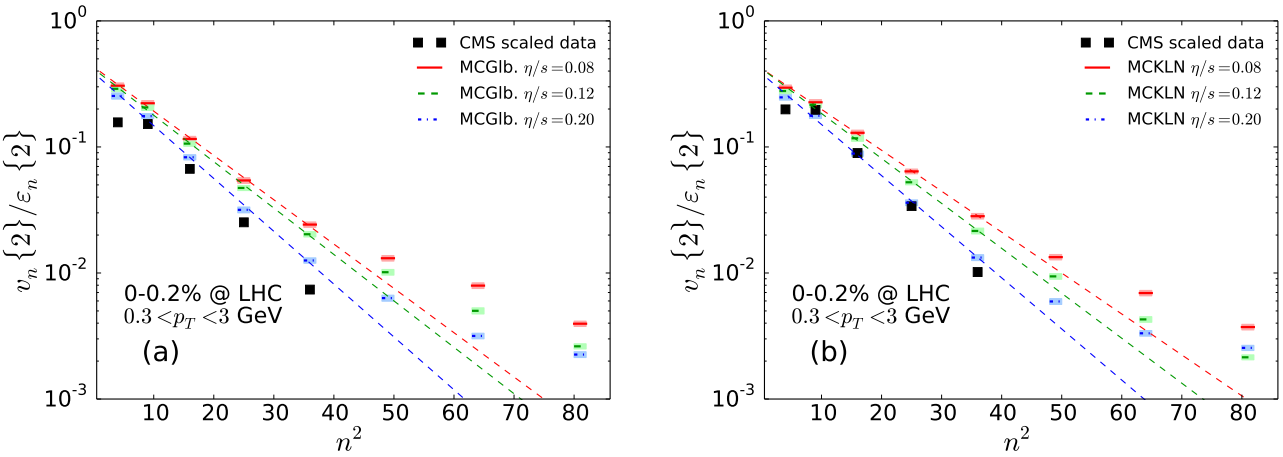

Figure 11.5: The hydrodynamic conversion efficiency coefficients $v_n\{2\}/\varepsilon_n\{2\}$ are plotted a function of n^2 from the MC-Glauber (left panel) and the MCKLN (right panel) models. Linear fits performed for $n = 2-6$ are indicated as the dashed lines. We also scale the CMS flow data by the $\varepsilon_n\{2\}$ from two initial condition models. (The CMS v_n data are extracted from [175]). $v_n\{2\}$ is integrated from 0.3 to 3 GeV as measured in the CMS experiments.

In Fig. 11.4, we show the charged particle p_T-integrated $v_n\{2\}$ as a function of its harmonic order n for both the MC-Glauber and the MCKLN models for 0-0.2% ultra-central Pb+Pb collisions at LHC. Since the initial eccentricity $\varepsilon_n\{2\} \sim 0.09-0.12$ for MCKLN and $\varepsilon_n\{2\} \sim 0.13-17$ for MC-Glauber model, non-linear mode couplings involving the product of multiple ε_n are suppressed in the higher order ($n > 3$) anisotropic flow coefficients v_n. We expect a dominantly linear response between the initial $\varepsilon_n\{2\}$ and the final $v_n\{2\}$. The conversion efficiency $v_n\{2\}/\varepsilon_n\{2\}$ is controlled

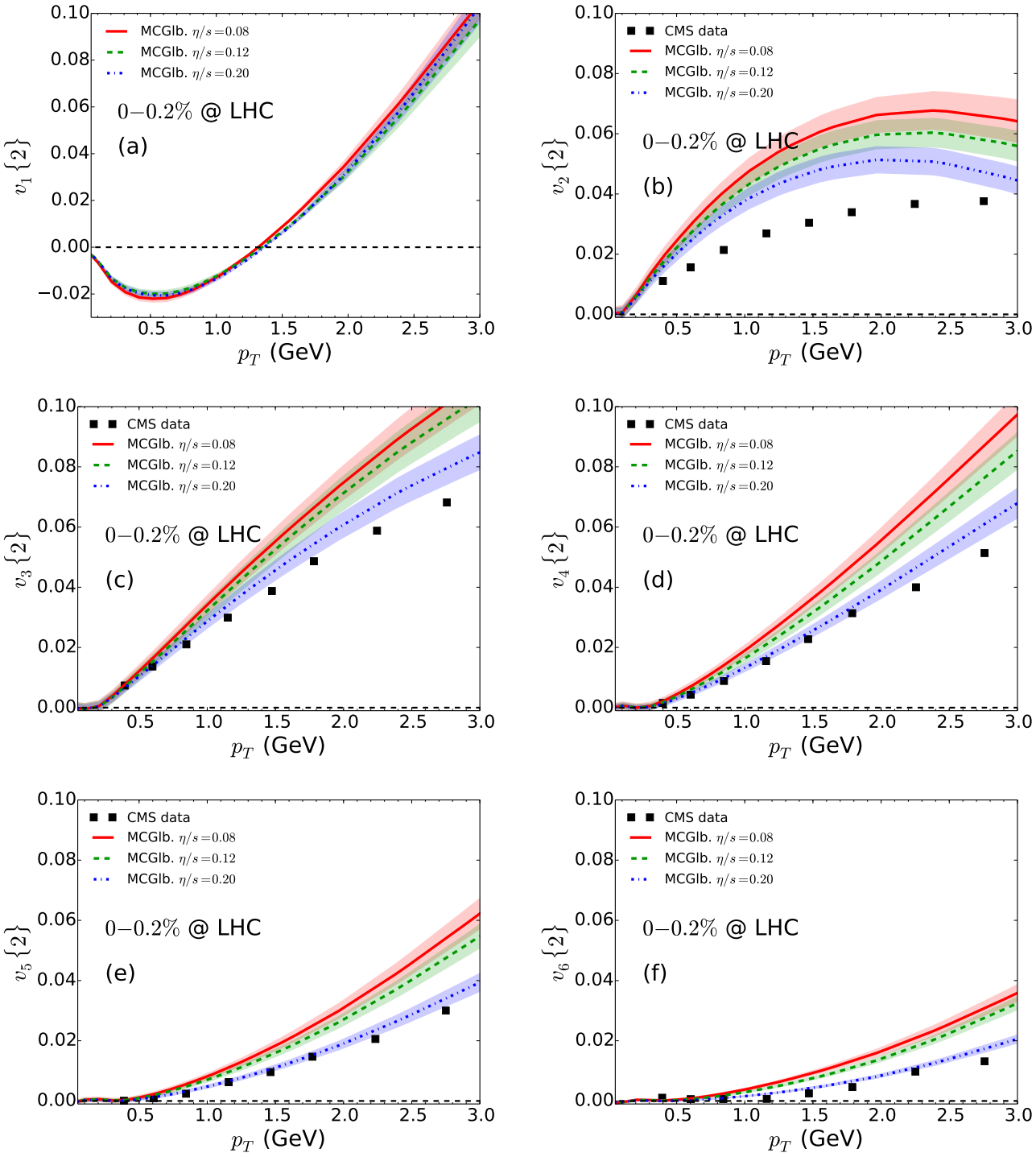

Figure 11.6: MC-Glauber model calculations of the p_T-differential 2-particle cumulant $v_n\{2\}$ ($n \in [1,6]$) of charged hadrons compared to CMS preliminary measurements in 0-0.2% centrality Pb+Pb collisions at $\sqrt{s} = 2.76$ A TeV (data extracted from [175]).

by the specific shear viscosity of the medium. Whereas all simulations capture the general trend of increasingly strong suppression of v_n for higher harmonics n, which is caused by the non-zero shear viscosity of the medium, both initial condition models fail to quantitatively reproduce the measured $v_n\{2\}$ spectrum ($v_n\{2\}$ as a function of n). This statement is valid for all the η/s values

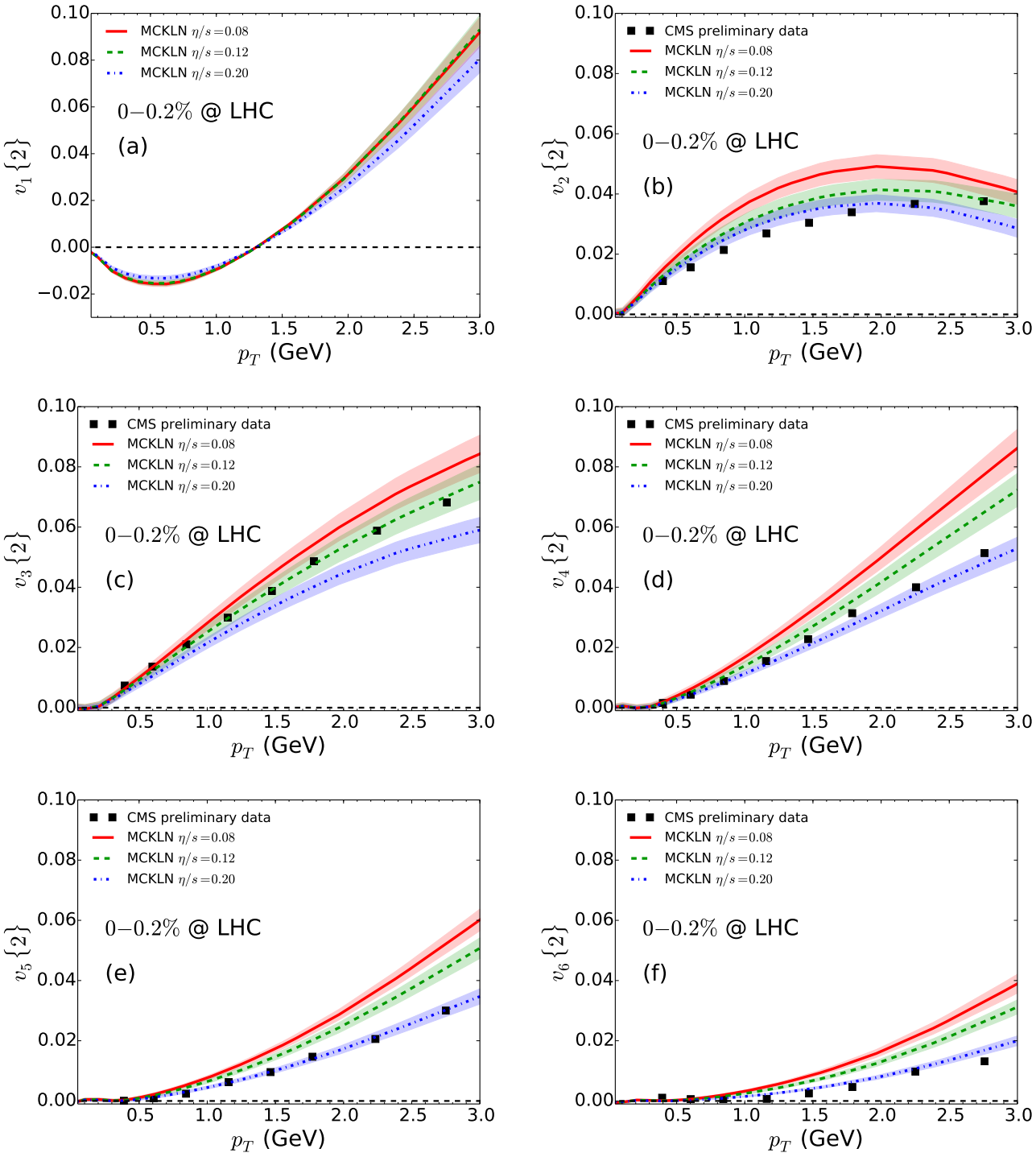

Figure 11.7: Similar to Fig. 11.6, but for MCKLN initial conditions.

explored in the simulations. In the CMS data, the magnitude of $v_2\{2\}$ is very close to $v_3\{2\}$, which can not be reproduced using either MCGlb. or MCKLN initial models. In hydrodynamic simulations, the conversion efficiency from initial $\varepsilon_n\{2\}$ to final $v_n\{2\}$ decreases with increasing order n, $\propto e^{-\frac{\eta}{s}n^2}$ [178]. In Fig. 11.5 we find $\log(v_n\{2\}/\varepsilon_n\{2\})$ shows very good linear dependence on n^2 up to $n = 6$ in the ultra-central Pb+Pb collisions. The slope of the correspond linear fit

increases with η/s used in the simulations. Starting with an initial fluctuation spectrum featuring $\varepsilon_2\{2\} \sim \varepsilon_3\{2\}$, as shown in Fig. 11.2, the final $v_2\{2\}$ will always be about 30% larger than $v_3\{2\}$ in hydrodynamic calculations with reasonable η/s values. Any theoretical calculation using such initial conditions will overestimate the measured v_2/v_3 ratio (at least as long as only shear viscous effect are included). Within the current hydrodynamic framework, to reproduce a v_n hierarchy similar to the one observed by CMS, we need an initial condition model that provides a triangular deformation $\varepsilon_3\{2\}$ that is significantly larger than $\varepsilon_2\{2\}$ in these ultra-central collisions. Both MCGlb. and MCKLN models fail to give such a feature.

Comparing the absolute magnitude of $v_n\{2\}$, we find that the CMS preliminary data prefer a relatively large specific shear viscosity, for both MCGlb (η/s 0.3) and MCKLN (η/s 0.2) initial conditions.

Since the anisotropic flow coefficients are dominated by the initial state fluctuation in the ultra-central collisions, the fluctuations of the flow angles at different p_T are important, especially for v_2 (see Fig. 10.4 in Chapter 10) and will affect p_T-differential $v_n\{2\}$ measurements. In order to have an apple-to-apple comparison to the CMS measurements, we calculate the p_T-differential 2-particle cumulant flow of charged hadrons defined as

$$v_n\{2\}(p_T) = \langle v_n(p_T) v_n^{\rm ref} \cos[n(\Psi_n(p_T) - \Psi_n^{\rm ref})]\rangle_{\rm ev} / \sqrt{\langle (v_n^{\rm ref})^2\rangle} \tag{11.3}$$

where the $v_n^{\rm ref}\{2\}$ and $\Psi_n^{\rm ref}$ are the p_T integrated flow for reference particles and its flow angle, respectively. We choose all charged particles with transverse momentum between 1 and 3 GeV as the reference particles, the same as in the CMS analysis, which optimize sensitivity for higher order v_n in the measurements.

In Figs. 11.6 and 11.7 we show the p_T-differential flow $v_n\{2\}(p_T)$ at 0-0.2% centrality from the MC-Glauber. and MCKLN models, compared with the CMS data. We find that the direct flow $v_1\{2\}$ is insensitive to the η/s value used in the simulations. It flips from negative to positive at $p_T \sim 1.2\,\text{GeV}$ due to global momentum conservation. Comparing $v_2\{2\}$ to $v_6\{2\}$ against the CMS preliminary data, our results using MC-Glauber model with $\eta/s = 0.20$ give a fairly good description of $v_n\{2\}(p_T)$ except for the differential elliptic flow $v_2\{2\}(p_T)$ which is overestimated by the calculation. MCKLN initial conditions with $\eta/s = 0.20$ can describe $v_2\{2\}(p_T)$ better but underestimate $v_3\{2\}(p_T)$. Although neither model describes all the data equally well, the overall picture seems to favor a somewhat larger QGP shear viscosity $(\eta/s)_{\rm QGP} \sim 0.20$ in the hydrodynamic simulations.

11.4 Flow factorization

In Figs. 11.8,11.9 and 11.10, we calculate the flow factorization ratios $r_{2,3,4}$ in 0-0.2% centrality bin. We find that the ratio r_2 shows a large factorization breaking behavior at large $p_T^{\rm trig} - p_T^{\rm asso}$.

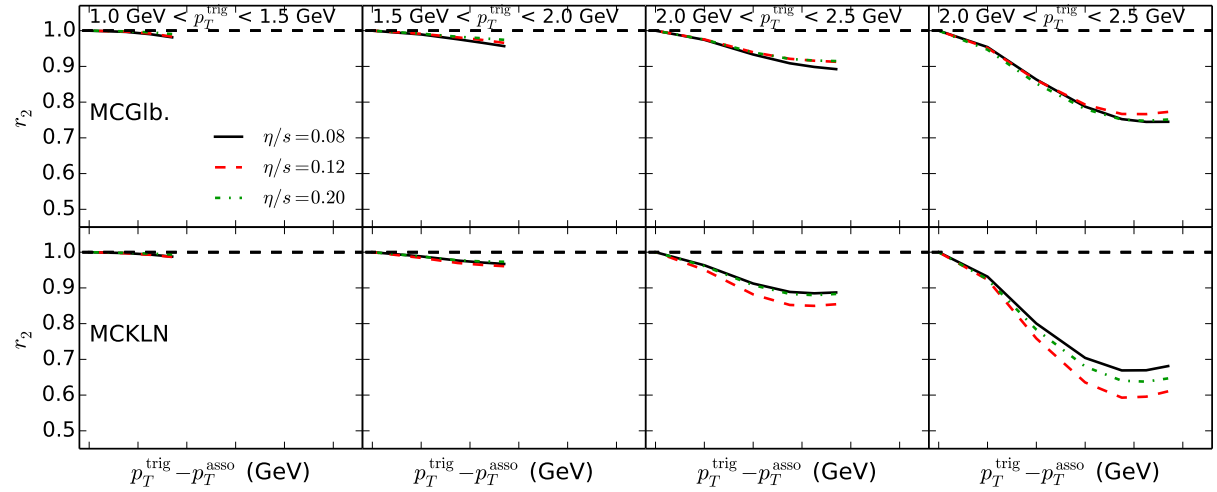

Figure 11.8: Flow factorization ratio $r_2(p_T^{\rm trig}, p_T^{\rm asso})$ from MCGlb (upper panels) and MCKLN (lower panels) model calculations in 0-0.2% ultra-central Pb + Pb collisions at $\sqrt{s} = 2.76\,A$ TeV, for three different η/s values as in the legend.

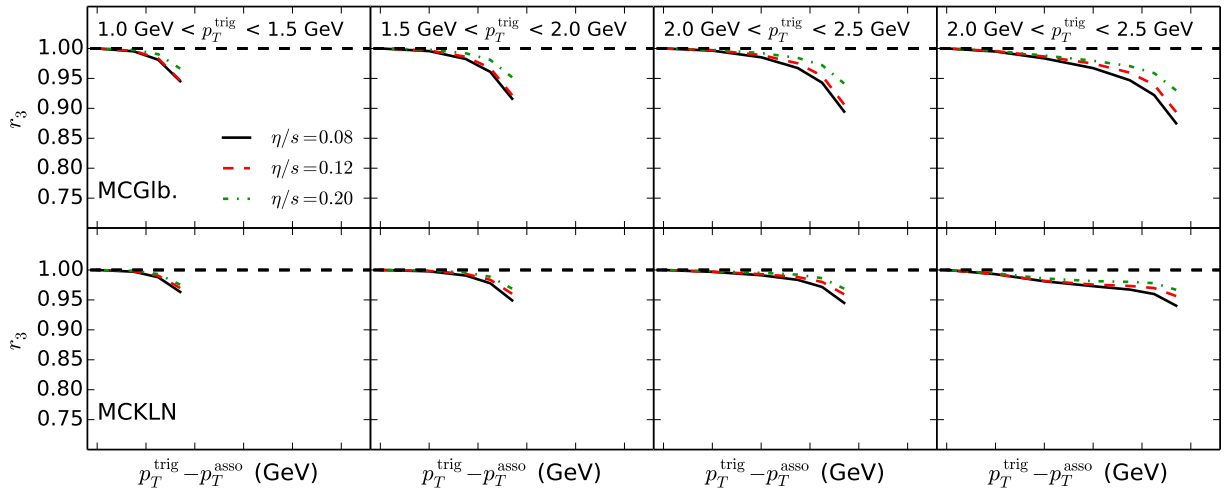

Figure 11.9: Similar to Fig. 11.8, but for the ratio r_3.

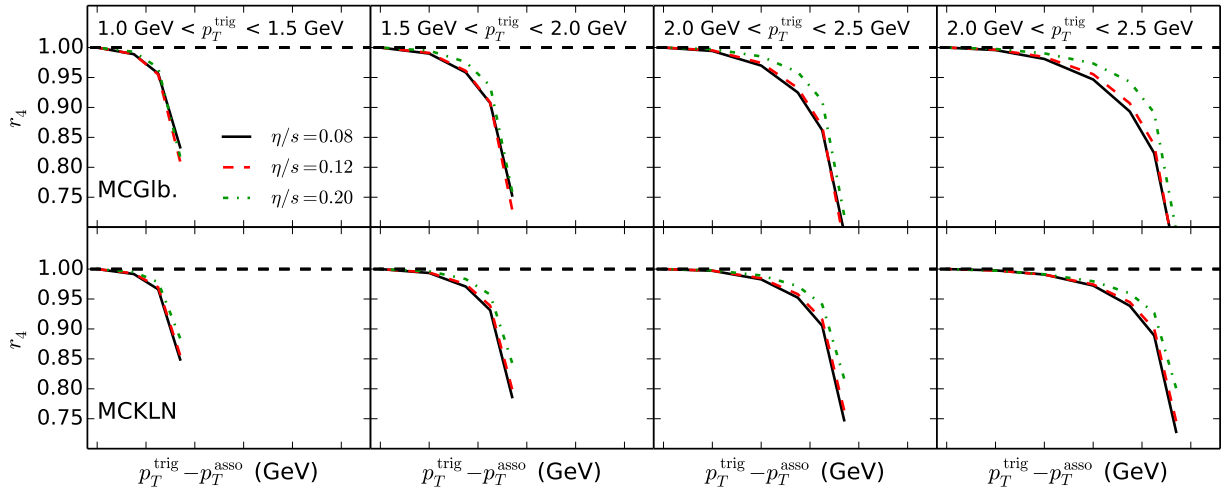

Figure 11.10: Similar to Fig. 11.8, but for the ratio r_4.

We have checked that about half of the contribution comes from the flow angle fluctuations. We find that η/s affects r_2 non-monotonically. This may indicate a non-trivial interplay between initial state fluctuations and the viscous damping during the evolution. Comparing the upper panels with the lower ones in Fig. 11.8, we find that, irrespective of the choice of η/s, the ratio r_2 deviates from 1 more strongly when we use MCKLN initial conditions than for MC-Glauber profiles. This implies that the r_n ratio is more sensitive to the initial state fluctuations than to the specific shear viscosity of the medium.

Fig. 11.9, the breaking of flow factorization is significantly smaller for r_3 than for r_2. The MCKLN model gives a smaller effect than MC-Glauber. For the ratios r_3 and r_4, a larger shear viscosity monotonically reduces the the strength of the breaking behavior of flow factorization.

11.5 Chapter conclusion

In this chapter, we presented anisotropic flow studies for 0-0.2% ultra-central Pb+Pb collisions at the LHC using the MC-Glauber and the MCKLN initial condition models with $\eta/s = 0.08, 0.12,$ and 0.20. In the MC-Glauber model, we implement multiplicity fluctuations in the initial state, which boost the initial eccentricities $\varepsilon_n\{2\}$ by 20-40%. A comparison with CMS preliminary data, reveals that both MCGlb. and MCKLN models fail to reproduce the p_T-integrated v_n hierarchy, especially the $v_2\{2\}/v_3\{2\}$ ratio. Further comparisons with the p_T-differential v_n tend to favor a large value of $\eta/s \sim 0.2$ for the medium.

We found a large breaking of flow factorization for the elliptic flow coefficient in ultra-central collisions. Both the fluctuations of the flow magnitude and of the flow angle are important. Simulations show that the ratio r_2 behaves non-monotonically as η/s increases, which needs further investigation. For the ratios r_3 and r_4 measuring the breaking of flow factorization for triangular and quadrangular flow, we found a monotonic decrease of the factorization breaking effects with increasing η/s.

Chapter 12: Viscous hydrodynamic scaling in p+Pb vs. Pb+Pb collisions

In this chapter, we discuss the scaling properties of the hydrodynamic equations. This work is based on unpublished notes from 2011 by Zhi Qiu and Ulrich Heinz. We find that for fixed final charged multiplicity, a small system will show the same viscous effects as a large system. This scaling property from viscous hydrodynamics has intriguing consequences for recent observations of flow like features in high multiplicity p+Pb collision.

We introduce two scales to characterize our system at the initial starting time of the hydrodynamic simulations. One is the system size, $R_{\rm sys}$ and the other is an energy scale E_0, which we both allow to vary independently, but which are related to each other by the condition $dN/dy =$ constant. We fix that the shape of the initial profiles, i.e. assume the same $\{\varepsilon_n\}$ distribution, when we vary $R_{\rm sys}$. At high energies where the initial state is dominated by gluons which show universal scaling properties controlled by a (spatially averaged) saturation momentum. E_0 can be identified with this momentum scale. [179]

12.1 Scaling in ideal hydrodynamics

Ideal hydrodynamics solves the following equations:

$$De = -(e+P)\theta, \tag{12.1}$$

$$Du^\mu = \frac{\nabla^\mu P}{e+P}, \tag{12.2}$$

where $D = u^\mu\partial_\mu$ and $\nabla^\mu = \Delta^{\mu\nu}\partial_\nu$ are the temporal and spatial derivatives in the comoving frame. The expansion rate of the system is $\theta = \partial_\mu u^\mu$. Using $R_{\rm sys}$ and E_0, we can define the following unitless variables,

$$\tilde{\tau} = \frac{\tau}{R_{\rm sys}}, \tilde{x} = \frac{x}{R_{\rm sys}}, \tilde{y} = \frac{y}{R_{\rm sys}}, \tilde{\eta}_s = \eta_s, \tag{12.3}$$

$$\tilde{e} = \frac{R_{\rm sys}^3}{E_0}e, \tilde{P} = \frac{R_{\rm sys}^3}{E_0}P, \tilde{u}^\mu = u^\mu. \tag{12.4}$$

According to Eq. (12.3) the derivatives scale as,

$$\tilde{D} = R_{\rm sys}D, \tilde{\nabla}^\mu = R_{\rm sys}\nabla^\mu, \tilde{\theta} = R_{\rm sys}\theta. \tag{12.5}$$

Then the ideal hydrodynamic equations can be rewritten with these unitless quantities as follows:

$$\tilde{D}\tilde{e} = -(\tilde{e}+\tilde{P})\tilde{\theta} \tag{12.6}$$

$$\tilde{D}\tilde{u}^{\mu} = \frac{\tilde{\nabla}^{\mu}\tilde{P}}{\tilde{e}+\tilde{P}} \tag{12.7}$$

With these scaled parameters, the ideal hydrodynamic equations and their solutions are independent of the system size $R_{\rm sys}$ and E_0 but only depend on the shape of the (unitless) initial energy density profile $\tilde{e}(\tilde{x}^{\mu})$, provided the pressure and energy density are linearly related.

12.2 Scaling in viscous hydrodynamics

Second order Israel-Stewart theory solves the following equations:

$$De = -(e+P+\Pi)\theta + \pi^{\mu\nu}\sigma_{\mu\nu}, \tag{12.8}$$

$$(e+P+\Pi)Du^{\mu} = \nabla^{\mu}(P+\Pi) - \Delta^{\mu\nu}\nabla^{\sigma}\pi_{\nu\sigma} + \pi^{\mu\nu}Du_{\nu}, \tag{12.9}$$

$$D\pi^{\mu\nu} = -\frac{1}{\tau_{\pi}}(\pi^{\mu\nu}-2\eta\sigma^{\mu\nu}) - u^{\mu}\pi^{\nu\rho}Du_{\rho} - \frac{1}{2}\pi^{\mu\nu}\frac{\eta T}{\tau_{\pi}}\partial_{\rho}\left(\frac{\tau_{\pi}}{\eta T}u^{\rho}\right) - \pi_{\rho}^{(\mu}\omega^{\nu)\rho}, \tag{12.10}$$

$$D\Pi = -\frac{1}{\tau_{\Pi}}(\Pi+\zeta\theta) - \frac{1}{2}\Pi\frac{\zeta T}{\tau_{\Pi}}\partial_{\mu}\left(\frac{\tau_{\Pi}u^{\mu}}{2\zeta T}\right), \tag{12.11}$$

where $\pi^{\mu\nu}$ and Π are the shear and bulk pressures and $\sigma^{\mu\nu}$ is the velocity shear tensor. $\omega^{\mu\nu}$ is the vorticity tensor.

Generalizing the scaling of variables introduced in ideal hydrodynamics, we can define additional scaled variables for the viscous quantities:

$$\tilde{\pi}^{\mu\nu} = \frac{R_{\rm sys}^3}{E_0}\pi^{\mu\nu}, \tilde{\Pi} = \frac{R_{\rm sys}^3}{E_0}\Pi, \tilde{\sigma}^{\mu\nu} = R_{\rm sys}\sigma^{\mu\nu}, \tilde{\omega}^{\mu\nu} = R_{\rm sys}\omega^{\mu\nu}. \tag{12.12}$$

In order to fully scale out the $R_{\rm sys}$ and E_0 dependence in the Eq. (12.10) and Eq. (12.11), we have to additionally scale the shear and bulk viscosity and their corresponding relaxation times as follows,

$$\tilde{\eta} = \eta\frac{R_{\rm sys}^2}{E_0}, \tilde{\zeta} = \zeta\frac{R_{\rm sys}^2}{E_0}, \tilde{\tau}_{\pi} = \frac{\tau_{\pi}}{R_{\rm sys}}, \tilde{\tau}_{\Pi} = \frac{\tau_{\Pi}}{R_{\rm sys}}. \tag{12.13}$$

According to the first law of thermal dynamics, $sT = e+P$ (in the absence of a chemical potential). We scale the entropy density and temperature as,

$$\tilde{s} = s\frac{R_{\rm sys}^{9/4}}{E_0^{3/4}}, \tilde{T} = T\frac{R_{\rm sys}^{3/4}}{E_0^{1/4}}. \tag{12.14}$$

Then we have,

$$\frac{\tilde{\eta}}{\tilde{s}} = \frac{\eta}{s}\frac{1}{R_{\rm sys}^{1/4}E_0^{1/4}}, \frac{\tilde{\zeta}}{\tilde{s}} = \frac{\zeta}{s}\frac{1}{R_{\rm sys}^{1/4}E_0^{1/4}}. \tag{12.15}$$

If we compare two systems with different sizes with fixed E_0, we have

$$\frac{(\eta/s)_{\rm small}}{(\eta/s)_{\rm large}} = \left(\frac{(R_{\rm sys})_{\rm large}}{(R_{\rm sys})_{\rm small}}\right)^{1/4}, \tag{12.16}$$

which means that the small system has stronger viscous effects compared to a large system with the same value of η/s.

The relaxation time are usually chosen to be $\tau_\pi \propto \frac{\eta}{sT}$ and $\tau_\Pi \propto \frac{\zeta}{sT}$, which is self-consistent with Eq. (12.13).

In Eq. (12.14), we divided the power dependence of $R_{\rm sys}$ and E_0 equally to s and T. We can perform a more general analysis,

$$\tilde{s} = sR_{\rm sys}^{3-\alpha}E_0^{-\alpha}, \tilde{T} = TR_{\rm sys}^{\alpha}E_0^{\alpha-1}. \tag{12.17}$$

Eq. (12.14) would be the case when $\alpha = 3/4$. Then,

$$\frac{\tilde{\eta}}{\tilde{s}} = \frac{\eta}{s}\left(\frac{1}{R_{\rm sys}E_0}\right)^{1-\alpha}, \frac{\tilde{\zeta}}{\tilde{s}} = \frac{\zeta}{s}\left(\frac{1}{R_{\rm sys}E_0}\right)^{1-\alpha} \tag{12.18}$$

and

$$\frac{(\eta/s)_{\rm small}}{(\eta/s)_{\rm large}} = \left(\frac{(R_{\rm sys})_{\rm large}}{(R_{\rm sys})_{\rm small}}\right)^{1-\alpha}. \tag{12.19}$$

Note that, the combination $\frac{\eta\theta}{sT}$ is a size and energy rescaling invariant measure of the fluidity of the matter.

12.3 Scaling in Cooper-Frye Freeze-out

The final observed particle spectra and their anisotropies can be calculated using the Cooper-Frye Freeze-out procedure,

$$\begin{aligned}\frac{dN}{dyp_Tdp_Td\phi} &= \int_\Sigma \tau dxdyd\eta_s\left(m_T\cosh(y-\eta_s) - \mathbf{p}_T\cdot\nabla_T\tau_f - \frac{m_T}{\tau_f}\sinh(y-\eta_s)\frac{\partial\tau_f}{\partial\eta_s}\right)\\ &\quad\times(f_0(p)+\delta f(p)),\end{aligned} \tag{12.20}$$

where Σ is the kinetic freeze-out surface taken here as an isothermal surface. The particle distribution function can be written as $f_0(p) = \frac{1}{e^{(E-\mu)/T}\pm1}$ with the deviation $\delta f(p) = f_0(p)(1\pm f_0(p))\frac{p^\mu p^\nu\pi_{\mu\nu}}{2T^2(e+P)}$.

If we now scale the particle's 4-momentum and chemical potential according to temperature,

$$\tilde{p}^\mu = p^\mu\frac{R_{\rm sys}^{3/4}}{E_0^{1/4}}, \tilde{\mu} = \mu\frac{R_{\rm sys}^{3/4}}{E_0^{1/4}}, \tag{12.21}$$

we can write Eq. (12.20) as,

$$\begin{aligned}\frac{dN}{d\tilde{y}\tilde{p}_T d\tilde{p}_T d\phi} &= E_0^{3/4} R_{\rm sys}^{3/4} \int_{\tilde{\Sigma}} \tilde{\tau} d\tilde{x} d\tilde{y} d\tilde{\eta}_s \\ &\times \left(\tilde{m}_T \cosh(\tilde{y} - \widetilde{\eta_s}) - \tilde{\mathbf{p}}_T \cdot \tilde{\nabla}_T \tilde{\tau}_f - \frac{\widetilde{m_T}}{\widetilde{\tau_f}} \sinh(\tilde{y} - \widetilde{\eta_s}) \frac{\partial \widetilde{\tau_f}}{\partial \widetilde{\eta_s}} \right) \\ &\times (f_0(\tilde{p}) + \delta f(\tilde{p})) \end{aligned} \tag{12.22}$$

Eq. (12.22) has a lot of interesting consequences. First of all, if we integrate over p_T and ϕ in Eq. (12.20) we obtain,

$$\begin{aligned} N &= \frac{g}{(2\pi)^3} \int_\Sigma d^3\sigma_\mu \int \frac{d^3p}{E} p^\mu (f_0(p) + \delta f(p)) \\ &= \frac{g}{(2\pi)^3} \int_\Sigma d^3\sigma_\mu u^\mu \frac{m^2}{\beta} \sum_{n=1}^{\infty} \frac{(\mp)^{n-1}}{n} e^{n\beta\mu} K_2(n\beta m). \\ &= \frac{g}{(2\pi)^3} E_0^{3/4} R_{\rm sys}^{3/4} \int_{\tilde{\Sigma}} d^3\tilde{\sigma}_\mu \tilde{u}^\mu \frac{\tilde{m}^2}{\tilde{\beta}} \sum_{n=1}^{\infty} \frac{(\mp)^{n-1}}{n} e^{n\tilde{\beta}\tilde{\mu}} K_2(n\tilde{\beta}\tilde{m}). \end{aligned}$$

where $-(+)$ is for fermions (bosons). So

$$\frac{dN}{dy} \propto E_0^{3/4} R_{\rm sys}^{3/4}, \tag{12.23}$$

that is, the total charged hadron multiplicity scales with the 3/4 power of the product of the system size with the initial energy scale. With the more general power dependence Eq. (12.17), $\frac{dN}{dy} \propto (E_0 R_{\rm sys})^{3-3\alpha}$. More interestingly, combing with Eq. (12.18), we have,

$$\frac{(\eta/s)_{\rm small}}{(\eta/s)_{\rm large}} = \left(\frac{(dN^{\rm ch}/dy)_{\rm large}}{(dN^{\rm ch}/dy)_{\rm small}} \right)^{1/3}, \tag{12.24}$$

which states that the shear viscous effects are the SAME for two systems of different size if the final charged multiplicities are the same. So if we compare high multiplicity p+Pb collisions to non-central Pb+Pb at the same multiplicity, the shear viscous effects will be the same, regardless of the fact that the system size in p+Pb is much smaller than in the Pb+Pb collisions.

Eq. (12.22) also states that the p_T integrated anisotropic flows, v_n, will be the same for the small and large system as long as the shape of the initial energy density profile, characterized by $\{\varepsilon_n\}$, are the same. In the actual experiments, integrated v_n are usually reported with a p_T cut. In this case comparisons between large and small systems should be made for v_n integrated over the same range of $\tilde{p}_T = \frac{p_T}{E_0} \sim \frac{p_T}{Q_s}$ (for fixed $\frac{dN}{dy}$). Current experiments turn out to support this statement for v_3 (see Fig. 3 in [179]).

We can compute the mean $\tilde{p}_T$ from Eq. (12.22),

$$\langle \tilde{p}_T \rangle = \langle p_T \rangle \frac{R_{\rm sys}^{3/4}}{E_0^{1/4}}. \tag{12.25}$$

So,

$$\frac{\langle p_T\rangle_{\rm small}}{\langle p_T\rangle_{\rm large}} = \left(\frac{(R_{\rm sys})_{\rm large}}{(R_{\rm sys})_{\rm small}}\right)^{3/4} \left(\frac{(E_0)_{\rm small}}{(E_0)_{\rm large}}\right)^{1/4}. \tag{12.26}$$

And more generally,

$$\frac{\langle p_T\rangle_{\rm small}}{\langle p_T\rangle_{\rm large}} = \left(\frac{(R_{\rm sys})_{\rm large}}{(R_{\rm sys})_{\rm small}}\right)^{\alpha} \left(\frac{(E_0)_{\rm small}}{(E_0)_{\rm large}}\right)^{\alpha-1}. \tag{12.27}$$

If we compare two systems with the same $dN^{\rm ch}/dy$, then $R_{\rm sys}E_0$ is fixed,

$$\frac{\langle p_T\rangle_{\rm small}}{\langle p_T\rangle_{\rm large}} = \frac{(R_{\rm sys})_{\rm large}}{(R_{\rm sys})_{\rm small}}. \tag{12.28}$$

Please note that this ratio does not depend on the particle species. So Eq. (12.28) indicates that the ratio of the mean p_T between p-Pb and Pb-Pb should be the same for all hadron species.

For the differential $v_n(p_T)$, we know from Eq. (12.22) that $v_n(\tilde{p}_T)$ are the same between the two systems. So if we scale $v_n(p_T)$ by its corresponding $\langle p_T\rangle$, the system size and initial energy scale dependence will be gone. So we find that $v_n(p_T/\langle p_T\rangle)$ should be the same for small and large systems, independent of multiplicity. This is also supported by the experimental data (see Fig. 5 in [179]).

One drawback of this Cooper-Frye analysis is that it introduces multiple mass scales for the different particle species, breaking the simple conformal symmetry logic. One alternative way to get around this is to instead calculate the total entropy crossing through the freeze-out surface instead. The total entropy can be calculated as follows:

$$\begin{aligned}
\frac{dS}{dy} &= \frac{d}{dy}\int_\Sigma d^3\sigma_\mu s^\mu \\
&= \frac{d}{dy}\int_\Sigma d^3\sigma_\mu u^\mu s \\
&= (RE_0)^{3/4}\frac{d}{dy}\int_{\tilde{\Sigma}} d^3\tilde{\sigma}_\mu \tilde{u}^\mu \tilde{s},
\end{aligned} \tag{12.29}$$

Since y is scale invariant, for a conversion surface at $\tilde{T}$, the total entropy per unit rapidity is also proportional to $(R_{\rm sys}E_0)^{3/4}$. Converting both the small and large system at the same $\tilde{T}$ yields,

$$\frac{T_{\rm small}}{T_{\rm large}} = \left(\frac{(R_{\rm sys})_{\rm large}}{(R_{\rm sys})_{\rm small}}\right)^{3/4} \left(\frac{E_{0\rm large}}{E_{0\rm small}}\right)^{1/4} = \left(\frac{(R_{\rm sys})_{\rm large}}{(R_{\rm sys})_{\rm small}}\right)^{1/2}.$$

This is because that the expansion rate θ is larger in a small system which cause the kinetic freeze-out to take place at a higher temperature.

Chapter 13: Viscous hydrodynamics in 2 and 3 spatial dimensions – a comparison

At top RHIC and LHC energies, (2+1) dimensional viscous hydrodynamic simulations with assumed longitudinal boost invariance have achieved great successes in describing experimental measurements near mid-rapidity in relativistic heavy ion collisions.

In this chapter, we perform a direct comparison between our (2+1)-d and a (3+1)-d viscous hydrodynamic simulations from [45] (`MUSIC`) to check quantitatively how good the assumption of longitudinal boost invariance is near mid-rapidity at RHIC and LHC energies. This so far unpublished work was performed in collaboration with Bjoern Schenke and Ulrich Heinz.

13.1 Hydrodynamic Evolution

We use event averaged initial conditions in the transverse plane generated from the MCKLN model. Along the longitudinal direction, the MCKLN model provides a non-boost-invariant initial entropy distribution according to the color glass condensate (CGC) picture. In Fig. 13.1, the

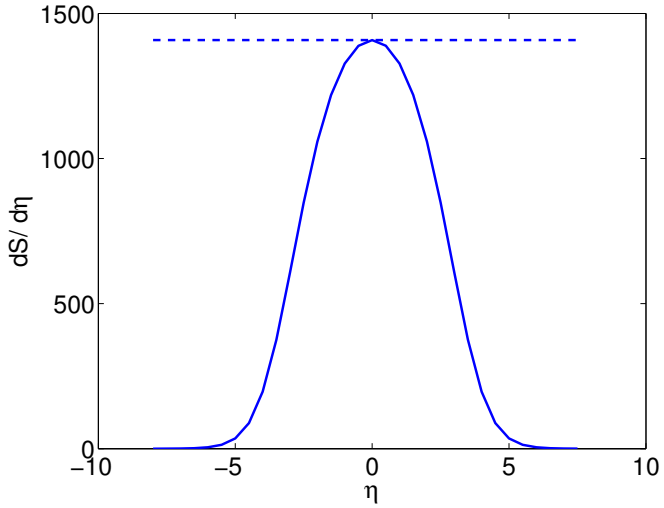

Figure 13.1: Space-time rapidity dependence of the initial total entropy from MCKLN model at $\sqrt{s_{\rm NN}} = 200\,\mathrm{GeV}$ at RHIC.

corresponding entropy density per unit space-time rapidity is shown and compare to the boost-invariant case indicated as the dashed line. In order to study the net effects from the non-boost-invariant initial conditions, we fix all other hydrodynamical parameters to be identical in the simulations. We compare our results for the $0-5\%$ most central AuAu collisions at $\sqrt{s_{\rm NN}} = 200\,{\rm GeV}$.

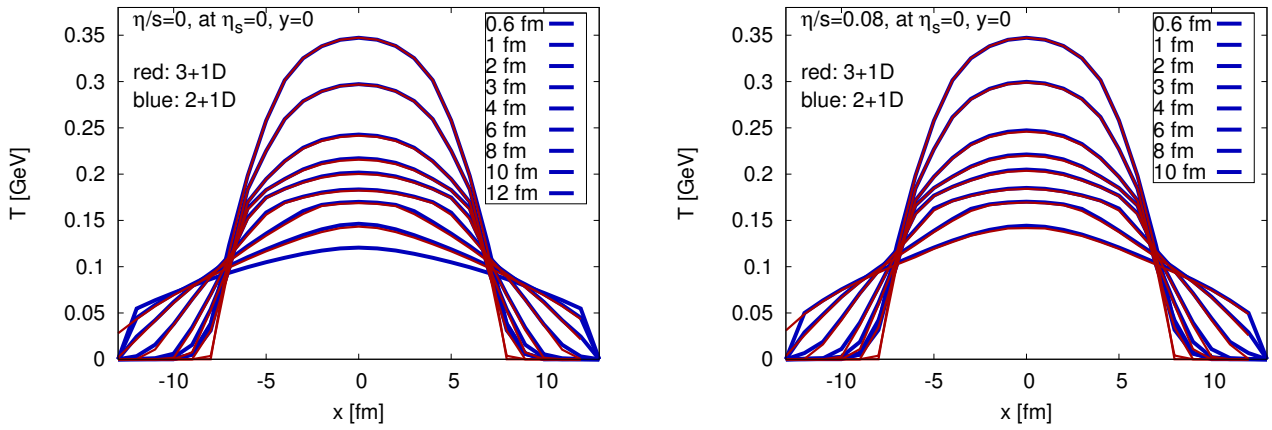

Figure 13.2: Left panel: Temperature profile along x axis in the transverse plane at $\eta_s = 0$ from ideal hydrodynamics. Right panel: Same quantities but from viscous hydrodynamic simulation with $\eta/s = 0.08$. Blue lines are calculated from `VISH2+1` and red curves are (3+1)-d hydrodynamic results from `MUSIC` [45].

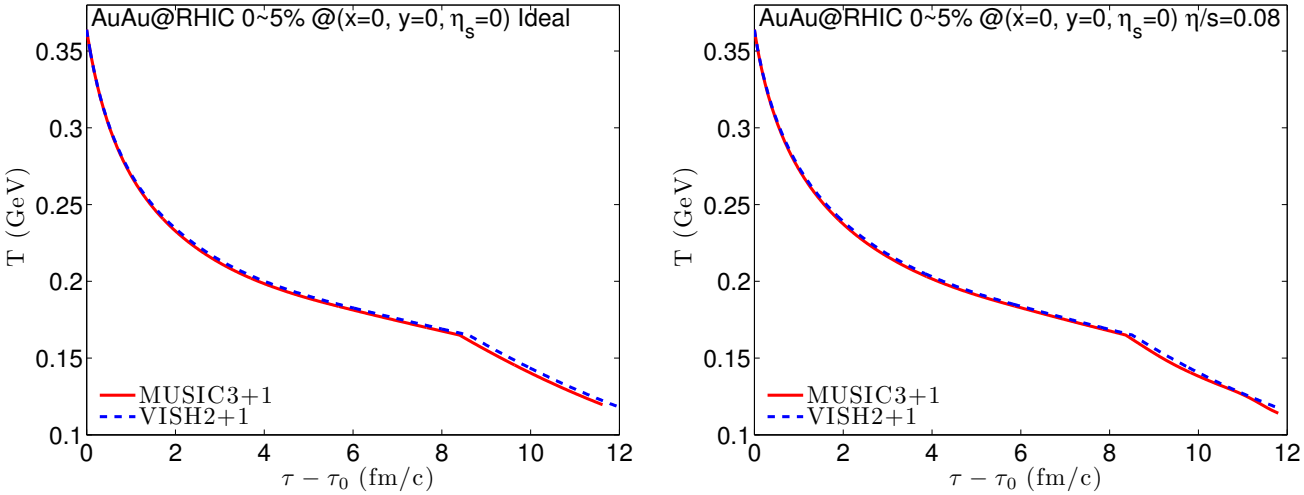

Figure 13.3: Temperature evolution at the center of the fireball at mid-rapidity. Left panel for the ideal case and right panel for viscous calculations with $\eta/s = 0.08$.

We first compare the temperature evolutions at mid-rapidity in Fig. 13.2. Overall, (2+1)-d and (3+1)-d hydrodynamics are found to give very close temperature evolution histories at $\eta_s = 0$. For both ideal and viscous runs, the results from (3+1)-d hydrodynamic simulations show a slightly faster cooling rate than the (2+1)-d evolution, which can be understood in terms of a more rapid longitudinal expansion in the (3+1)-d case driven by the extra longitudinal pressure gradients.

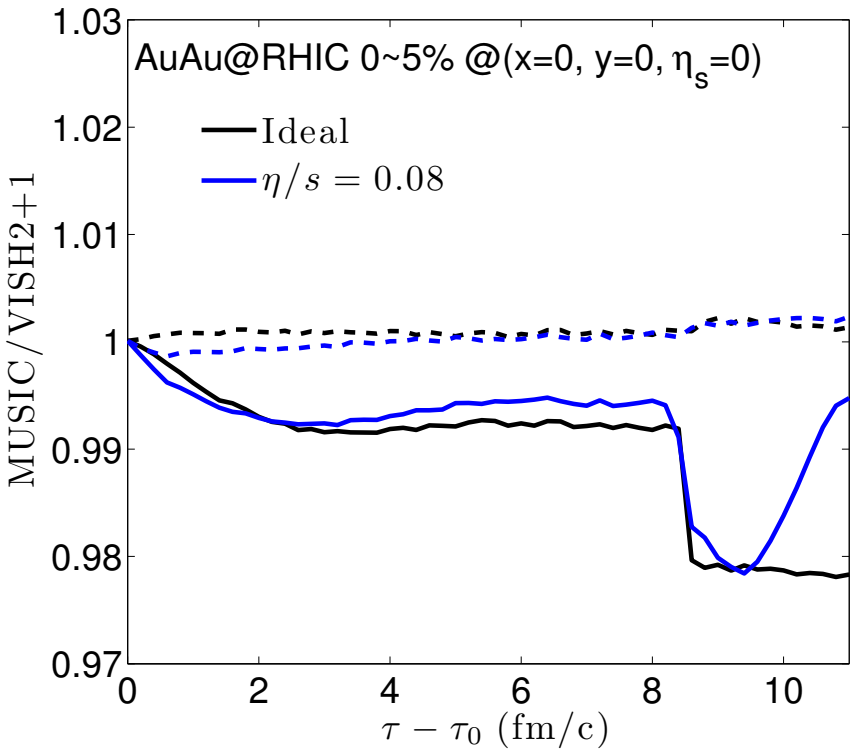

Figure 13.4: The ratio of the temperature evolution at the center of the fireball at mid-rapidity between (2+1)-d and (3+1)-d hydrodynamic simulations. Dashed lines represents the ratio between `VISH2+1` and `MUSIC` with identical boost-invariant initial conditions for numerical code checking purpose.

In Fig. 13.3, we further focus on the temperature evolution at the center of the fireball. The corresponding ratio between (2+1)-d and (3+1)-d results is shown in Fig. 13.4. The dashed lines in Fig. 13.4 are the ratio between `MUSIC` with boost invariant initial conditions and `VISH2+1`. They are used for code checking. The differences are within 0.2% for both the ideal and viscous case, which means that the two hydrodynamic codes work consistently for identical initial conditions. The solid lines represents the ratio between `MUSIC` with non-boost invariant initial conditions and `VISH2+1`. We find the temperature drops about 1% more quickly in the non-boost invariant case. The faster cooling rate at $\tau - \tau_0 \sim 8$ fm/c is an artifact generated by the implementation of partially chemical equilibrium in the equation of state: due to the slightly faster cooling in the (3+1)-d simulations, the breaking of chemical equilibrium (and the concomitant transition to a stage of faster cooling) occurs earlier in `MUSIC`, resulting in the additional drop in the temperature ratio shown in Fig. 13.4 around $\tau - \tau_0 \sim 9$ fm/c. For the viscous case, we observe small wiggles in the temperature evolution in the (3+1)-d run. We found that they are caused by large viscous corrections originating from the bumpy profiles caused by discretization errors at large rapidity; and therefore unphysical.

13.2 Thermal particle spectra and elliptic flow

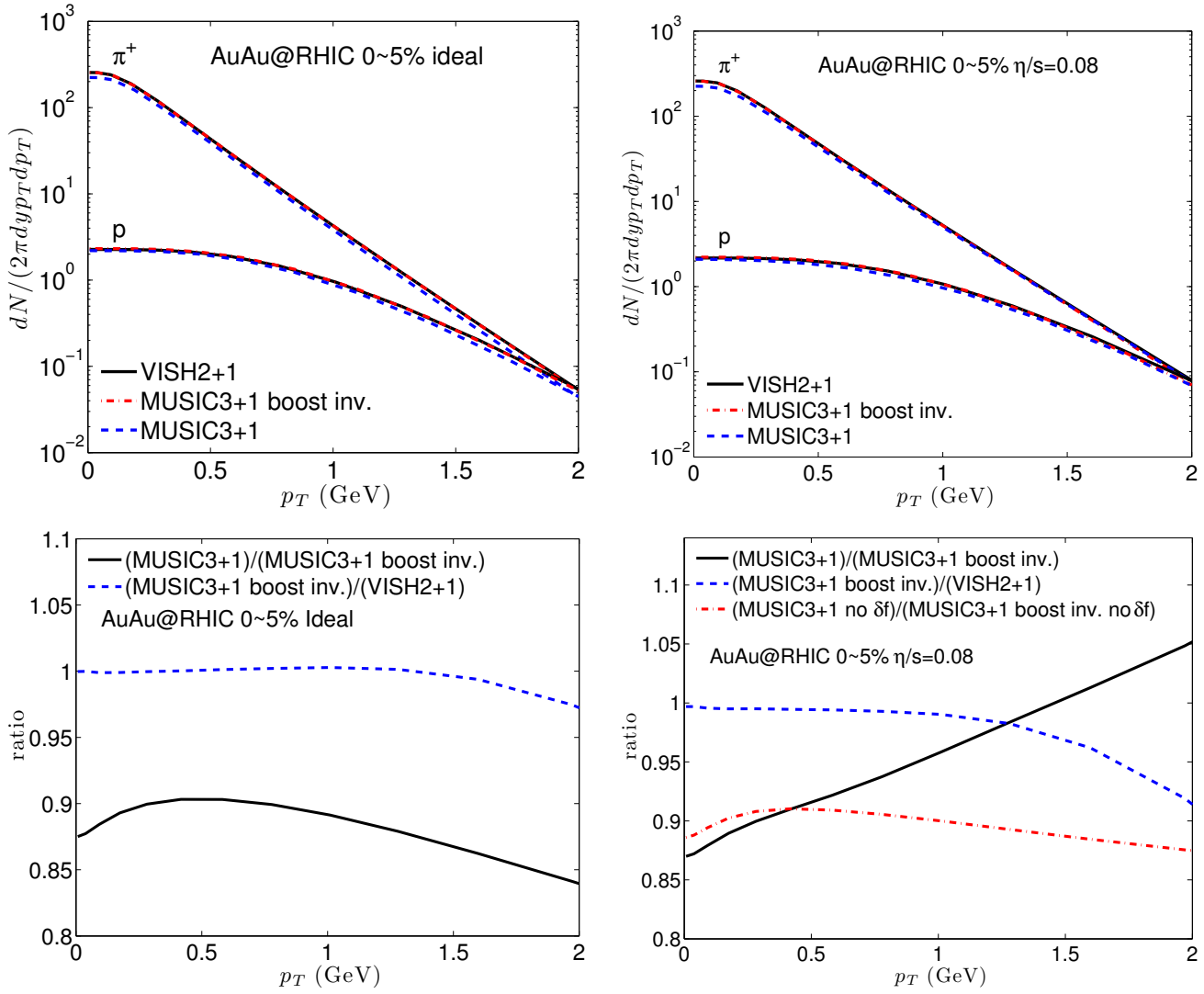

Figure 13.5: Upper panels: p_T-spectra of thermal pions and protons at 0-5% most central collision at top RHIC energy. Lower panels: The relative ratio of the thermal pion spectra between (3+1)-d hydrodynamic simulation and (2+1)-d calculations. The left(right) panels show results form ideal(viscous, $\eta/s = 0.08$) hydrodynamic simulations.

In Fig. 13.5, we compare the p_T-spectra for thermal pions and protons from (3+1)-d and (2+1)-d hydrodynamic simulations for both the ideal and viscous cases. On the logarithmic scale, this difference is negligible. In order to compare them quantitatively, we show their ratio for thermal poins in the lower panels of Fig. 13.5. For the purpose of code checking , we also plot as a blue dashed line the ratio between the spectra from the two hydrodynamic codes obtained for identical boost invariant initial conditions. In the ideal case, `MUSIC` and `VISH2+1` agree with each other quite well up to 2 GeV, while differences up to $\mathcal{O}(10\%)$ are visible for the viscous run. We found that this difference arises from the use of a too coarse lattice spacing in eta direction ($\Delta\eta = 0.5$)

for the (3+1)-d runs. In order to estimate the physical difference caused by non-boost-invariant initial profiles, we divide the non-boost invariant `MUSIC` results by the boost-invariant results from the same code, using the same lattice spacing in η_s direction. This ratio is shown in Fig. 13.5 as the solid black curves. We find that the non-boost-invariant runs result in about 15% smaller particle yield, due to the leakage of entropy from mid-rapidity to forward rapidity. For the viscous case, we find that the non-boost invariant case results in flatter spectra than for boost-invarant initial conditions, whereas for ideal hydrodynamics the breaking of boost-invariance makes the pion spectra steeper. This is due to the large δf corrections in the non-boost-invariant case: the red dashed curve, which represents the ratio between the spectra without δf corrections, shows a similar shape as for ideal hydrodynamics. Obviously, the δf correction here exhibits a large sensitivity to the breaking of longitudinal boost-invariance.

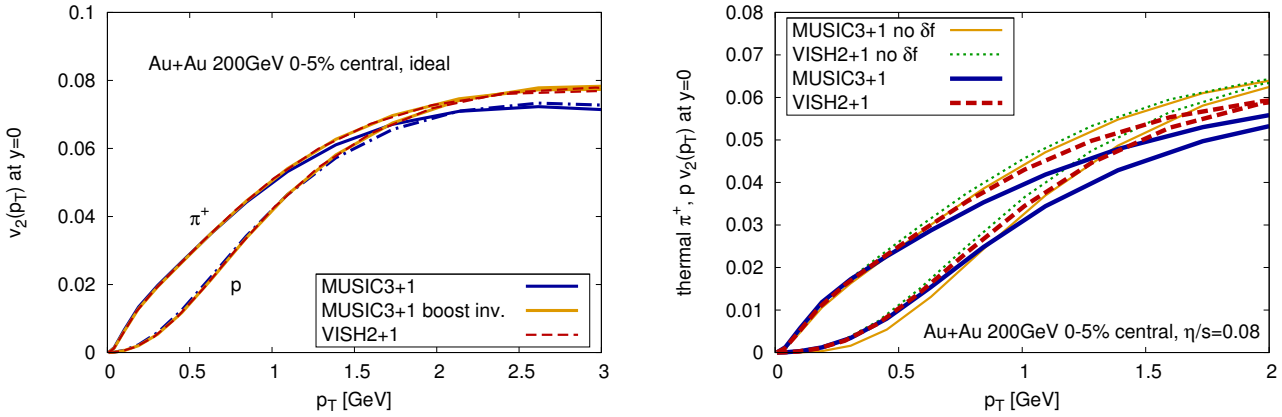

Figure 13.6: p_T differential elliptic flow coefficient for thermal pions and protons at 0-5% most central collisions at top RHIC energy. Left panel is the results from ideal hydrodynamic calculation and right panel is for the viscous case with $\eta/s = 0.08$.

In Fig. 13.6, we proceed to study the p_T differential elliptic flow. Using the same boost-invariant initial conditions in both codes, we find that `VISH2+1` and `MUSIC` agree within 1%, for both ideal and viscous cases. To further quantify effects from the violation of boost invariance in the initial conditions, we observe that for MCKLN intial conditions ideal hydrodynamics produces about 5% less v_2 at high p_T in the (3+1)-d case compared to `VISH2+1`. For the viscous case, the δf corrections are again larger in the non-boost-invariant (3+1)-d case, enlarging the difference between (3+1)-d `MUSIC` and `VISH2+1` to about 8%.

13.3 Chapter conclusion

In summary, by comparing boost invariant results from `VISH2+1` and `MUSIC`, we find numerical differences that are at least an order of magnitude smaller than the physical effects on the two hydrodynamic evolutions generated by initial conditions that violate longitudinal boost invariance.

This holds for both p_T-spectra and elliptic flow. This means that numerical errors in the two numerical codes are under good control. By comparing results fro non-boost-invariant initial conditions, we find that the hydrodynamic evolution and the p_T spectra near mid rapidity show good boost invariant behavior for ideal hydrodynamics, but less so for the for viscous case, where the δf corrections exhibit some worrisome non-boost-invariant corrections for v_2. A more detailed analysis is needed to clarify whether this effect is caused by numerical inaccuracies or of physical origin.

Chapter 14: Electromagnetic probes in heavy-ion collisions: Introduction and general framework

Electromagnetic probes such as photons and dileptons are considered to be clean and penetrating probes in relativistic heavy-ion collisions. Since they can only interact with the underlying medium through electromagnetic interaction, they suffer negligible final state interactions after they are born and fly almost freely to the detectors, preserving the valuable dynamical information at their birth points. This wonderful advantage over the much more abundant hadronic observables has generated great interest in calculating and measuring electromagnetic probes in heavy-ion collisions.

Experiments measure the inclusive photons from relativistic heavy-ion collisions. The inclusive photons are categorized into direct and decay photons. The decay photons are defined as the photons generated from electromagnetic decays of hadrons. The main source of decay photons are π^0 and η decays. All other photons are called direct photons. At low transverse momenta, $p_T < 4$ GeV, the decay photons dominate the measured inclusive photon signals. The yield ratio between direct and decay photons is about 1/9 at RHIC and 1/5 at LHC energies. This small ratio poses a big challenge to the experimentalist: measuring the direct photon signal at low transverse momenta with decent precision is very hard.

Simulating direct photon emission from relativistic heavy-ion collisions is realistically not an easy job either. State-of-the-art calculations of direct photon signals include several ingredients. At the initial nuclear impact, prompt photons generated from hard pQCD scatterings and photons from jet fragmentation are emitted. Before the system reaches approximate local thermal equilibrium, secondary scatterings between partons produce so-called pre-equilibrium photons. Once the medium thermalizes sufficiently to be described hydrodynamically, thermal electromagnetic radiations will shine through the QGP, the quark-hadron transition region, and the hot dense hadronic phase. When an energetic jet passes through the hot medium, photons may also be produced by jet-medium interactions. Last but not least, at a very late stage of the evolution, photons will be produced from the dilute hadronic gas phase where the medium is falling out of equilibrium. Currently, contributions from pre-equilibrium photons and jet-plasma conversion photons have been estimated but are not fully integrated even in advanced dynamical evolution

models. In general, thermal radiation from the fireball evolution dominates the direct photon signals at low transverse momenta, $p_T < 4$ GeV, while the hard prompt photon component takes over at high p_T.

In this part of my thesis, we will focus on the direct photon observables at low p_T. We calculate the thermal component of the direct photon observables by employing a macroscopic evolution of the medium using viscous hydrodynamics and coupling it with photon emission rates computed from thermal field theory. The thermal photon momentum distribution can be calculated as,

$$E\frac{dN^\gamma}{d^3p} = \int d^4x \left(E\frac{dR^\gamma}{d^3p}(p \cdot u(x)/T(x), \{\mu_i(x)\}, \pi^{\mu\nu}(x)p_\mu p_\nu\}) \right). \tag{14.1}$$

The space-time volume is controlled by event-by-event viscous hydrodynamic evolution. Information on the local temperature, flow velocity, and shear stress tensor is needed for the photon emission rates that control the local photon production from a given hydrodynamic fluid cell. In order to calculate the photon momentum distribution correctly, we need to have good theoretical control of both the underlying medium evolution and the thermal photon emission rates.

We use our (2+1)-d viscous hydrodynamic model to simulate the fireball evolution. The local temperature, fluid velocity, and shear stress tensor are evolved according to second order Israel-Stewart hydrodynamic equations. Event-by-event hydrodynamic simulations takes into account initial state fluctuations by propagating each bumpy initial energy density profile (generated from either the MC-Glauber or the MCKLN model) separately. We use `s95p-v0-PCE` for the EOS. It controls not only the conversion between the local energy density and pressure, which affects the local expansion rate, but also the partial chemical freeze out, which ensures the correct chemical abundances for the finally measured hadrons yields. These are important for a calculation of the background of photons from hadron decays. Below chemical freeze-out at $T_{\rm chem} = 165$ MeV for `s95p-v0-PCE`, the non-zero non-equilibrium chemical potentials boost the local real photon emission rates by the corresponding fugacity factors. Since our hydrodynamic modeling builds in a sudden kinetic freeze-out at a given temperature, $T_{\rm kin} = 120$ MeV, it can not fully capture the out-of-equilibrium dynamics in the dilute hadronic phase. A more robust approach would be to switch hydrodynamics to a microscopic hadronic cascade model where hadron freeze-out happens gradually. In current implementations, we only take into account the photon contributions from electromagnetic decay channels of short lived hadronic resonances whose lifetime is on the order of a few fm/c, after the hydrodynamic kinetic freeze-out. Photons from electromagnetic decays of long-lived hadrons are experimentally subtracted from the inclusive photons when determining the direct photon signal, and therefore do not need to be computed.

For the photon emission rates, the general calculation framework in real-time thermal field theory is based on the in-medium correlator of the electromagnetic current, J_μ:

$$E\frac{dR^\gamma}{d^3p} = \frac{i}{2(2\pi)^3}\Pi^{12,\mu}_{\mu}(p). \tag{14.2}$$

Here $\Pi^{12,\mu}_{\mu}(p)$ is the (12)-component of the photon polarization tensor,

$$\Pi^{12}_{\mu\nu}(p) = i\int d^4x e^{-ip\cdot x}\langle j^1_\mu(x) j^2_\nu(0)\rangle, \tag{14.3}$$

where 1 and 2 label the corresponding branch of the closed time-path contour [180] on which the current operator is located, and $\langle \dots \rangle$ represents an ensemble average over the density matrix of the system. An alternative method is to use relativistic kinetic theory, where photon rates are expressed through matrix elements for specific photon producing reactions,multiplied by phase-space density factors describing the distribution of particles in the medium. In the QGP phase, the emission rate was calculated to complete leading order in $O(\alpha_{\rm em}\alpha_s)$ at thermal equilibrium in [181]; this rate is known as the AMY rate. In the hadronic gas phase, photon production rates have been derived using Massive Yang-Mills effective theory. Mesonic reactions including the strange sector are taken into account in the calculations. The equilibrium hadron gas rate was originally derived in [182].

For the prompt photons, we use NLO pQCD prompt photon rates with nuclear parton distribution functions that are corrected for isospin and shadowing effects, folded with a smooth event-averaged binary collision profiles. (we presently lack the technology for computing prompt photons for fluctuating bumpy initial density profiles.) The pQCD rate is extrapolated to low transverse momentum using a fit of the form $A/(1+p_T/p_0)^n$ that was checked to describe well the available low-p_T p-p data at RHIC. Here we give the corresponding parametrization at the top RHIC and LHC energies:

For Pb+Pb collisions at $\sqrt{s} = 2.76\,A\,\text{TeV}$:

$$\frac{dN^\gamma_{\rm prompt}}{2\pi dy p_T dp_T} = 12.8\frac{1.21}{(1+p_T/0.692)^{-5.5}} \qquad \text{for 0-40\% centrality.} \tag{14.4}$$

For Au+Au collisions at $\sqrt{s} = 200\,A\,\text{GeV}$,

$$\frac{dN^\gamma_{\rm prompt}}{2\pi dy p_T dp_T} = 18.65\frac{4.86}{(1+p_T/0.517)^{6.42}} \qquad \text{for 0-20\% centrality,} \tag{14.5}$$

$$\frac{dN^\gamma_{\rm prompt}}{2\pi dy p_T dp_T} = 7.16\frac{4.86}{(1+p_T/0.517)^{6.42}} \qquad \text{for 20-40\% centrality.} \tag{14.6}$$

From Chapter 15 to Chapter 17, we will discuss how to derive photon emission rates and their corresponding viscous corrections in the QGP and hadron gas (HG) phases. We also will discuss about how to smoothly switch the QGP and HG rates in the quark-hadron transition region. From Chapter 18 to Chapter 21, we proceed to perform a phenomenological study of direct photon spectra and their anisotropic flow coefficients.

Chapter 15: Thermal photon emission rates: QGP rates

15.1 Chapter introduction

Viscous hydrodynamics provides a successful macroscopic description of the dynamical evolution of the QGP created in the heavy-ion collisions [183, 184]. The non-vanishing viscosity leads to deviations in particle momentum distributions from local thermal equilibrium as the medium expands anisotropically. As a result, the momentum distributions of partons become anisotropic in the local fluid rest frame and fall off faster along the directions in which the fireball expands more rapidly. Existing known thermal photon emission rates at leading order (LO) [185] and next-to-leading order (NLO) [186] from the QGP were derived assuming a static, homogeneous, weakly coupled ($g_s \ll 1$), and fully thermalized medium. In order to study the thermal radiation from an evolving QGP fireball in relativistic heavy-ion collisions, we must derive the viscous corrections to the QGP photon emission rates. We will do so at leading order of $\pi^{\mu\nu}$ in this Chapter.

Several previous attempts to calculate the off-equilibrium corrections to the QGP photon emission rates have been published [187, 188, 189]. However, all these works considered only the anisotropy in the local momentum distribution functions for the incoming and outgoing particles. However, for scattering processes in a QCD medium, the dynamical Debye screening is essential to regulate the infrared logarithmic divergence associated with the long range nature of the massless quark and gluon exchange. In an anisotropic medium, the viscous corrections to this medium effect can lead to important modifications to the collision matrix element, causing additional anisotropies in the photon emission rate. This problem was first tackled in [190, 191, 192] for simple parametrizations of the local momentum anisotropy. We extend this previous works to a more general ansatz for the local momentum anisotropy, namely,

$$f(K) \equiv f_0(k) + \delta f(k) = f_0(k) \left[1 + \big(1 \pm f_0(k)\big) \frac{\pi^{\mu\nu} \hat{k}_\mu \hat{k}_\nu}{2(e+\mathcal{P})} \chi(k/T) \right]. \tag{15.1}$$

Here e, $\mathcal{P}$, T, and $\pi^{\mu\nu}$ are local energy density, pressure, temperature, and shear stress tensor of the expanding medium. We define $\hat{k}^\mu = K^\mu/(K \cdot u)$ as a light-like unit vector pointing in the direction of the parton momentum, and the scalar function $\chi(k/T) = (k/T)^\lambda$ with $1 \leq \lambda \leq 2$

controls the energy dependence of the off-equilibrium correction. The form (15.1) for the deviation δf from local equilibrium can be derived from Grad's 14 moment expansion [193]. Eq. (15.1) is general enough to describe the momentum distribution of massless particles in a weakly coupled plasma as long as its $\pi^{\mu\nu}$ is not too large [194].

We restrict our derivation of the photon emission rates from a static, infinite medium (with the given values for T, $\pi^{\mu\nu}$ etc). In order to apply the derived rates to an evolving fireball in the relativistic heavy-ion collision, we assume that the spatial and temporal variations of the medium are small at the microscopic scale of the photon formation time.

In this chapter, we will compute the leading order corrections in the shear stress $\pi^{\mu\nu}$ for $2 \to 2$ scattering processes. The calculation and inclusion of viscous corrections for the family of soft $2 \to n$ diagrams that are required for a complete leading order (in g_s) calculation of the photon emission rate that is complete to leading order in g_s [185] is left for future work.

We will derive the viscous corrections to the QGP photon emission rate in Sec. 15.2 from both the diagrammatic (in Sec. 15.2.2) and kinetic approaches (in Sec. 15.2.3). Numerical results for the equilibrium rates and the viscous corrections are presented in Sec. 15.3 for both weak and moderately (realistically) strong coupling g_s. In the diagrammatic calculations, we explore the sensitivity on the cut-off, which splits the kinematic regions between soft and hard exchanged momentum. Comparing the two approaches quantitatively, we use the difference between the corresponding equilibrium rates and viscous correction coefficients as a measure to gauge the theoretical uncertainty of our leading-order result. Conclusions and final comments are offered in Sec. 15.4.

15.2 Photon emission rates

15.2.1 General formalism

To calculate real photon production from a momentum anisotropic medium, we adopt the real-time or Closed Time Path (CTP) formalism [195] where the rate of photon emission can be expressed as [190, 180]

$$k\frac{dR}{d^3k} = \frac{i}{2(2\pi)^3}\Pi^{\mu}_{12\,\mu}(K). \tag{15.2}$$

Based on the finite temperature cutting rules, such a diagrammatic approach is equivalent [196, 197, 198] to a description in terms of relativistic kinetic theory as a process with m incoming

particles and n outgoing particles plus a photon,

$$\begin{aligned} k\frac{dR}{d^3k} &= N\int \frac{d^3p_1}{2E_1(2\pi)^3}\cdots\frac{d^3p_m}{2E_m(2\pi)^3}\cdots\frac{d^3p_{m+n}}{2E_{m+n}(2\pi)^3}(2\pi)^4 \\ &\quad\times\delta^{(4)}\left(\sum_{i=1}^{m}P_i^\mu-\sum_{j=m+1}^{m+n}P_j^\mu-K^\mu\right)|\mathcal{M}|^2 \\ &\quad\times f(P_1)\cdots f(P_m)(1\pm f(P_{m+1}))\cdots(1\pm f(P_{m+n})), \end{aligned} \tag{15.3}$$

where $f(P)$ are Bose (Fermi) distribution functions for bosons (fermions), and N is an overall degeneracy factor that depends on the specific production channel.

Assuming the medium is near thermal equilibrium, $\delta f \ll f_0$, with our choice of ansatz for particle distribution in Eq. (15.1), the photon emission rates can be expanded around equilibrium as,

$$k\frac{dR}{d^3k} = \Gamma_0 + \frac{\pi^{\mu\nu}}{2(e+P)}\Gamma_{\mu\nu} + \mathcal{O}\left(\left(\frac{\pi^{\mu\nu}}{2(e+P)}\right)^2\right), \tag{15.4}$$

where Γ_0 stands for the thermal equilibrium emission rate while $\Gamma_{\mu\nu}$ is the rate coefficient of the first order viscous correction.

$\Gamma_{\mu\nu}$ can be decomposed into an orthogonal tensor basis that is constructed from the photon momentum K_μ, the flow velocity u^μ and the metric tensor $g^{\mu\nu}$. Since $\pi^{\mu\nu}$ is symmetric, traceless, and orthogonal to the flow velocity, the only term surviving in this expansion after contraction with $\pi^{\mu\nu}$ is $\propto \hat{k}_\mu\hat{k}_\nu$:

$$\pi^{\mu\nu}\Gamma_{\mu\nu} = \pi^{\mu\nu}\Delta^{\alpha\beta}_{\mu\nu}\Gamma_{\alpha\beta} = \Gamma_1\pi^{\mu\nu}\hat{k}_\mu\hat{k}_\nu. \tag{15.5}$$

The scalar coefficient Γ_1 can be obtained from $\Gamma^{\mu\nu}$ by contracting with

$$a_{\mu\nu} = \frac{1}{2}\Delta_{\mu\alpha}\Delta_{\nu\beta}\left(g^{\alpha\beta}+3\hat{k}^\alpha\hat{k}^\beta\right). \tag{15.6}$$

This leads to

$$k\frac{dR}{d^3k} = T^2\left(\tilde{\Gamma}_0(k,T) + \frac{\pi^{\mu\nu}\hat{k}_\mu\hat{k}_\nu}{2(e+\mathcal{P})}\tilde{\Gamma}_1(k,T)\right), \tag{15.7}$$

with $\tilde{\Gamma}_0 = \Gamma_0/T^2$ and $\tilde{\Gamma}_1 \equiv a_{\alpha\beta}\Gamma^{\alpha\beta}/T^2$. Both $\tilde{\Gamma}_0$ and $\tilde{\Gamma}_1$ are unitless functions of k/T, where k is the local rest frame energy of the produced photon.

It is worth mentioning that the general structure of Eq. (15.7) does not depend on the details of the collision kernel when evaluating $\Gamma^{\alpha\beta}$. It is valid not only in the QGP phase, at arbitrary order in g_s, but also in the hadronic phase, where one can compute the hadronic photon-producing reaction cross sections using some effective field theory [182].

The use of the above tensor decomposition is particularly efficient numerically, because the anisotropic correction in Eq. (15.7) is a product of two Lorentz invariant quantities each of which is most easily calculated in a different frame: the laboratory frame for $\pi^{\mu\nu}\hat{k}_\mu\hat{k}_\nu$, the local rest

frame of the fluid cell for $a_{\alpha\beta}\Gamma^{\alpha\beta}$. This helps to avoid performing extensive Lorentz boosts and 3-D rotations for each fluid cell when coupling the rate to hydrodynamic simulations. Besides speeding-up the calculation, it allows us to tabulate the effect of viscous corrections in terms of the photon energy and local temperature, which can easily be used in phenomenological studies.

15.2.2 Diagrammatic approach

Calculating the photon production rate in the diagrammatic approach (as in Eq. 15.2) involves evaluating the off-diagonal photon self-energy $\Pi^{\mu}_{12\,\mu}(K)$. The calculation is divided into two disjoint kinematic phase-space regions, referred to as the soft and the hard parts. Both are evaluated in this section, starting with the soft part.

The soft part is affected by an infrared singularity associated with distant collisions whose regulation requires the evaluation of $\Pi^{\mu}_{12\,\mu}(K)$ in the HTL formalism. In equilibrium, the use of the Kubo-Martin-Schwinger (KMS) relation simplifies this task significantly (For the fermion propagator this relation leads to [195, 199, 200] $S_{12}(Q) = -e^{-Q^0/T}S_{21}(Q)$.) In what follows we show that a similar approach can be used even if the emitting medium has a momentum anisotropy.

KMS-like relation for the fermionic self-energy with anisotropic momentum distributions

Here, we prove that for the one-loop dressed quark propagator, a similar relation between $S_{12}(Q)$ and $S_{21}(Q)$ as the one derived from the KMS relation in thermal equilibrium still holds at leading order g_s, for an arbitrary particle distribution function that has reflection symmetry in momentum space. We follow the strategy of [191]: we calculate the one-loop off-diagonal quark self-energies $\Sigma^{12}(P)$ and $\Sigma^{21}(P)$ and check that the relation $\Sigma^{12}(P) = -\Sigma^{21}(P)$ holds in the hard loop approximation $K^0, |\boldsymbol{K}| \sim T \gg P^0 \sim \mathcal{O}(g_s T)$(see Fig. 15.1). (Note that in this approximation, $e^{-p^0/T} \sim 1$.)

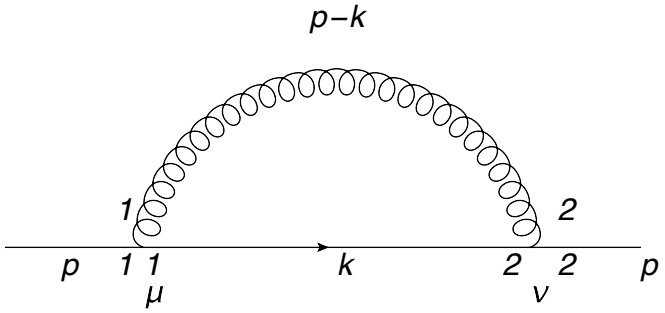

Figure 15.1: Off-diagonal component $\Sigma^{12}(P)$ of the one-loop quark self energy.

We can write $\Sigma^{12}(P)$ as

$$-i\Sigma^{12}(P) = \int \frac{d^4K}{(2\pi)^4}(t^a t^a)(ig\gamma^{\mu})iS_{12}(K)(-ig\gamma^{\nu})(-ig_{\mu\nu}\Delta_{12}(P-K)). \tag{15.8}$$

In the color space,

$$t^a t^a = C_F \mathbb{I}. \tag{15.9}$$

So,

$$\Sigma^{12}(P) = -2ig^2 C_F \int \frac{d^4K}{(2\pi)^4} S_{12}(K)\Delta_{12}(P-K), \tag{15.10}$$

where $S(K)$ and $\Delta(K)$ are the free fermion and scalar propagators [201],

$$S(K) = \not{K}\left[\begin{pmatrix} \frac{1}{K^2+i\epsilon} & 0 \\ 0 & \frac{-1}{K^2-i\epsilon} \end{pmatrix} + 2\pi i\delta(K^2)\begin{pmatrix} f_F(K) & -\theta(-k^0)+f_F(K) \\ -\theta(k^0)+f_F(K) & f_F(K) \end{pmatrix}\right], \tag{15.11}$$

$$\Delta(K) = \left[\begin{pmatrix} \frac{1}{K^2+i\epsilon} & 0 \\ 0 & \frac{-1}{K^2-i\epsilon} \end{pmatrix} - 2\pi i\delta(K^2)\begin{pmatrix} f_B(K) & \theta(-k^0)+f_B(K) \\ \theta(k^0)+f_B(K) & f_B(K) \end{pmatrix}\right]. \tag{15.12}$$

Inserting the propagators into Eq. (15.10) we find

$$\begin{aligned} \Sigma^{\mu}_{12}(P) &= -2ig_s^2 C_F \int \frac{d^4K}{(2\pi)^4} K^\mu 2\pi i\delta(K^2)[-\theta(-K^0)+f_F(K)] \\ &\quad \times(-2\pi i)\delta((P-K)^2)[\theta(-(P^0-K^0))+f_B(P-K)] \\ &\approx -2ig_s^2 C_F \int \frac{d^4K}{(2\pi)^2} K^\mu \delta(K^2)[-\theta(-K^0)+f_F(K)] \\ &\quad \times\delta(2P\cdot K)[\theta(K^0)+f_B(K)]. \end{aligned} \tag{15.13}$$

In the last step, we assumed $P \sim O(g_s T)$ and $K \sim O(T)$. Similarly, we can compute $\Sigma^{21}(P)$ and get,

$$\begin{aligned} \Sigma^{\mu}_{21}(P) &= -2ig_s^2 C_F \int \frac{d^4K}{(2\pi)^4} K^\mu 2\pi i\delta(K^2)[-\theta(K^0)+f_F(K)] \\ &\quad \times(-2\pi i)\delta((P-K)^2)[\theta(P^0-K^0)+f_B(P-K)] \\ &\approx -2ig_s^2 C_F \int \frac{d^4K}{(2\pi)^2} K^\mu \delta(K^2)[-\theta(K^0)+f_F(K)] \\ &\quad \times\delta(2P\cdot K)[\theta(K^0)+f_B(K)]. \end{aligned} \tag{15.14}$$

We assumed $g \ll 1$. Now, we let $K^\mu \to -K^\mu$ and assume that the particle distribution functions are invariant under such a change of variable, $f_{F(B)}(K) = f_{F(B)}(-K)$, we can get,

$$\begin{aligned} \Sigma^{\mu}_{12}(P) &= 2ig_s^2 C_F \int \frac{d^4K}{(2\pi)^2} K^\mu \delta(K^2)[-\theta(K^0)+f_F(K)]\delta(2P\cdot K)[\theta(-K^0)+f_B(K)] \\ &= -\Sigma^{\mu}_{21}(P). \end{aligned} \tag{15.15}$$

With Eq. (15.15) we have

$$\Sigma_{12}(Q) = \frac{\Sigma_{12}(Q)-\Sigma_{21}(Q)}{2} = \frac{\Sigma_{\rm Adv}(Q)-\Sigma_{\rm Ret}(Q)}{2} = -i{\rm Im}\Sigma_{\rm Ret}(Q). \tag{15.16}$$

With this KMS-like relation, we can further show that the fluctuation dissipation theorem [195, 200] still holds in the HTL regime. In order to see this, we start with the Dyson equation: the self-energy resummed propagator in the real-time formalism can be written as

$$G = G_0 + G_0 \Sigma G, \tag{15.17}$$

where both the propagators and self-energy are 2×2 matrices. The (12)-component of the resumed propagator can be written as [200, 202],

$$\begin{aligned} G_{12}(P) &= G_R(P)\Sigma_{12}(P)G_A(P) \\ &= (-2i)\frac{\Sigma_{12}(P)}{\Sigma_{21}(P) - \Sigma_{12}(P)}\mathrm{Im}\, G_R(P). \end{aligned} \tag{15.18}$$

In thermal equilibrium, Eq. (15.18) can be simplified to,

$$G_{12}(P) = \frac{2i}{e^{P^0/T}+1}\mathrm{Im}\, G_R(P). \tag{15.19}$$

This is (a variant of) the fluctuation-dissipation theorem. For our case, with the KMS-like relation (15.15) we see that in the hard loop limit $P^0 \ll T$ it reduces to the simple form

$$G_{12}(P) = i\mathrm{Im}\, G_R(P). \tag{15.20}$$

The KMS-like relation in Eq. (15.15) will also help one to prove the generalization to anisotropic situations of the application of the sum rule techniques developed in [186].

Retarded quark self-energy near thermal equilibrium

In the hard loop approximation the retarded quark self-energy can be calculated as follows [203]:

$$\Sigma_{\mathrm{Ret}}(P) = \frac{C_F}{4}g^2 \int \frac{d^3k}{(2\pi)^3}\frac{f(K)}{|\vec{k}|}\frac{K\cdot\gamma}{K\cdot P + i\epsilon} \equiv \gamma_\mu \Sigma^\mu_{\mathrm{Ret}}(P). \tag{15.21}$$

Here γ^μ are the Dirac matrices and f is the following combination of fermionic and bosonic distribution functions:

$$f(K) = 2(f_F(K) + \bar{f}_F(K)) + 4f_B(K). \tag{15.22}$$

In chemical equilibrium at zero net baryon density, $f_F(K) = \bar{f}_F(K)$. Hence,

$$\Sigma_{\mathrm{Ret}}(P) = C_F g^2 \int \frac{kdk}{2\pi^2}\frac{d\Omega_k}{4\pi}(f_F(K) + f_B(K))\frac{\hat{k}\cdot\gamma}{\hat{k}\cdot P + i\epsilon}, \tag{15.23}$$

where $\hat{k}^\mu = K^\mu/k$. The corresponding expressions in the momentum isotropic case are available in [204]. To perform the calculation in the present case we insert the anisotropic distribution

function Eq. (15.3) into Eq. (15.23):

$$\begin{aligned}\Sigma^{\mu}_{\rm Ret}(p^0,p) &= \frac{C_F g^2}{2\pi^2}\int kdk(f_{F0}(k)+f_{B0}(k))\int\frac{d\Omega_k}{4\pi}\frac{\hat{k}^\mu}{\hat{k}\cdot P+i\epsilon}\\ &+ \frac{C_F g^2}{2\pi^2}\frac{\pi_{\alpha\beta}}{2(e+\mathcal{P})}\int kdk\left[f_{F0}(k)(1-f_{F0}(k))+f_{B0}(k)(1+f_{B0}(k))\right]\chi\Big(\frac{k}{T}\Big)\\ &\times \int\frac{d\Omega_k}{4\pi}\frac{\hat{k}^\alpha\hat{k}^\beta\hat{k}^\mu}{\hat{k}\cdot P+i\epsilon}.\end{aligned}\tag{15.24}$$

Note that the additional term is linear in $\pi_{\alpha\beta}$. We write

$$\Sigma^{\mu}_{\rm Ret}(Q)=\Sigma^{\mu}_0(Q)+\frac{\pi_{\alpha\beta}}{2(e+\mathcal{P})}\Sigma^{\alpha\beta\mu}_1(Q)\tag{15.25}$$

with

$$\begin{aligned}\Sigma^{\alpha\beta\mu}_1 &\equiv \frac{C_F g^2}{2\pi^2}\int kdk\left[f_{F0}(k)(1-f_{F0}(k))+f_{B0}(k)(1+f_{B0}(k))\right]\chi\Big(\frac{k}{T}\Big)\\ &\times \int\frac{d\Omega_k}{4\pi}\frac{\hat{k}^\alpha\hat{k}^\beta\hat{k}^\mu}{\hat{k}\cdot P+i\epsilon}.\end{aligned}\tag{15.26}$$

For a given choice of $\chi\left(\frac{k}{T}\right)$, the k integral can be evaluated and yields a pure number that we denote as $C_{\rm neq}$:

$$\Sigma^{\alpha\beta\mu}_1(P)=\frac{C_F g^2T^2}{2\pi^2}C_{\rm neq}\int\frac{d\Omega_k}{4\pi}\frac{\hat{k}^\alpha\hat{k}^\beta\hat{k}^\mu}{\hat{k}\cdot P+i\epsilon}.\tag{15.27}$$

Using tensor decomposition and the tracelessness and transversality of $\pi_{\alpha\beta}$ again, we write

$$\pi_{\alpha\beta}\Sigma^{\alpha\beta\mu}_1(P)=\pi_{\alpha\beta}\left[A_1(P)\hat{p}^\alpha\hat{p}^\beta\hat{p}^\mu+B_1(P)\hat{p}^\alpha\hat{p}^\beta u^\mu+C_1(P)(\hat{p}^\alpha g^{\beta\mu}+\hat{p}^\beta g^{\alpha\mu})\right],\tag{15.28}$$

where $\hat{p}^\mu=P^\mu/p$ with $p=|\boldsymbol{P}|$. The coefficients A_1, B_1, and C_1 can be calculated to be

$$\begin{aligned}A_1(p^0,p) &= m_\infty^2\frac{2C_{\rm neq}}{\pi^2}\frac{1}{2p^3}\left[(5(p^0)^2-3p^2)Q_0\left(\frac{p^0}{p}\right)-5(p^0)^2+\frac{4}{3}p^2\right]\\ B_1(p^0,p) &= m_\infty^2\frac{2C_{\rm neq}}{\pi^2}\frac{1}{2p^4}\left[\left(-5(p^0)^3+6p^0p^2-\frac{p}{p^0}p^3\right)Q_0\left(\frac{p^0}{p}\right)+5(p^0)^3-\frac{13}{3}p^0p^2\right]\\ C_1(p^0,p) &= m_\infty^2\frac{2C_{\rm neq}}{\pi^2}\frac{1}{2p^3}\left[\left((p^0)^2-p^2\right)Q_0\left(\frac{p^0}{p}\right)-(p^0)^2+\frac{2}{3}p^2\right],\end{aligned}\tag{15.29}$$

where $m_\infty^2=C_F g_s^2T^2/4$ is the leading order asymptotic thermal quark mass, and $Q_0(z)=\frac{1}{2}\ln(\frac{1+z}{1-z})$ is the Legendre function of the second kind.

We have now derived all the essential ingredients for the calculation of the photon emission rate (15.2).

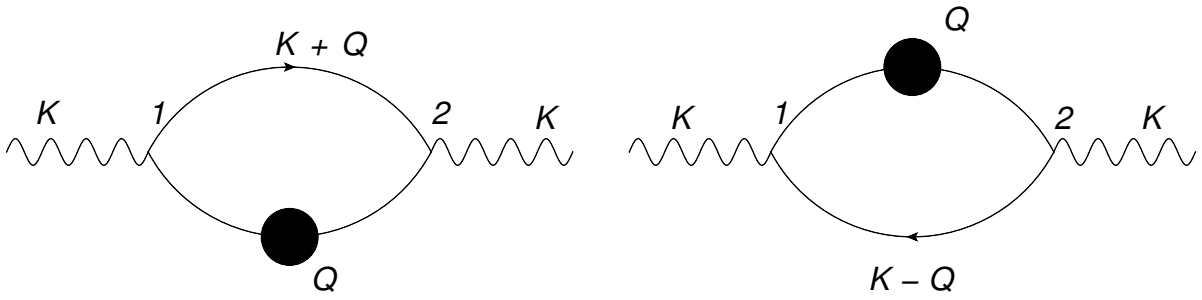

Figure 15.2: (12)-component of one-loop photon self-energy with one HTL-resummed quark propagator

Soft contribution

The proof of the KMS relation with anisotropic distribution functions Eq. (15.15) greatly simplifies the following calculations. We can now calculate the soft part of the photon emission rates using Eq.(15.2). The Feynman diagrams for a one-loop photon self-energy are shown in Fig.15.2.

At leading order in g_s, only one of the two quark propagators in the loop requires hard loop resummation, indicated by the blob [205, 206, 207, 208]. We can write down the photon self-energy according to the Feynman rules:

$$\begin{aligned} i\Pi^{\mu}_{12\mu}(K) &= e^2\Big(\sum_s q_s^2\Big)N_C\int\frac{d^4Q}{(2\pi)^4}\mathrm{Tr}\Big[\gamma^\mu i\tilde{S}^\star_{21}(Q)\gamma_\mu iS_{12}(Q+K) \\ &\qquad +\gamma^\mu iS_{21}(Q-K)\gamma_\mu i\tilde{S}^\star_{12}(Q)\Big]. \end{aligned} \tag{15.30}$$

Here $S_{12}(Q+K)$ and $S_{21}(Q-K)$ are free quark propagators as in Eq. (15.11) and $\tilde{S}^\star_{12}(Q)|_{HL}$ and $\tilde{S}^\star_{21}(Q)|_{HL}$ are hard-loop resummed propagators [206, 204, 200, 202]:

$$\tilde{S}^\star_{12(21)}(Q) = \tilde{S}^\star_{\mathrm{Ret}}(Q)\Sigma_{12(21)}(Q)\tilde{S}^\star_{\mathrm{Adv}}(Q). \tag{15.31}$$

Using this together with the relations derived in Sec. 15.2.2 in the hard loop approximation,

$$\Sigma_{12}(Q) = -\Sigma_{21}(Q) = -i\mathrm{Im}\,\Sigma_R(Q). \tag{15.32}$$

we can rewrite Eq. (15.30) as

$$i\Pi^{\mu}_{12\mu}(K) = -e^2\Big(\sum_s q_s^2\Big)N_C\frac{8}{k}f_F(K)\int^{q_{\mathrm{cut}}}\frac{d^3q}{(2\pi)^3}\,\mathrm{Im}\left(K_\nu\tilde{S}^{\star\nu}_{\mathrm{Ret}}(Q)\right). \tag{15.33}$$

We used the kinematic assumptions $Q\sim O(g_sT)$, $K\sim O(T)$ and $g_s\ll 1$, relevant in the hard loop approximation. We introduced the cut-off q_{cut} on the magnitude of the quark momentum. It is assumed that $g_sT\ll q_{\mathrm{cut}}\ll T$. The cut-off q_{cut} is the parameter that divides the phase-space in two. The contribution from above the cut-off is calculated in the following section.

Inserting Eqs. (15.1) and (15.25) into Eq. (15.33) and linearizing in $\pi_{\alpha\beta}/2(e+\mathcal{P})$ we obtain

$$\begin{aligned} i\Pi^{\mu}_{12\mu}(K) &= -e^2\Big(\sum_s q_s^2\Big)N_C\frac{8}{k}f_{F0}(K)\int^{q_{\rm cut}}\frac{d^3q}{(2\pi)^3}\bigg[\mathrm{Im}\Big\{\frac{K\cdot Q_0}{Q_0\cdot Q_0}\Big\} \\ &\quad +\frac{\pi_{\alpha\beta}}{2(e+P)}\bigg(\mathrm{Im}\Big\{-\frac{K_\mu\Sigma_1^{\alpha\beta\mu}}{Q_0\cdot Q_0}\Big\}+\mathrm{Im}\Big\{\frac{K\cdot Q_0}{Q_0\cdot Q_0}\frac{2Q_{0\mu}\Sigma_1^{\alpha\beta\mu}}{Q_0\cdot Q_0}\Big\} \\ &\quad +\hat{k}^\alpha\hat{k}^\beta(1-f_{F0}(K))\chi\Big(\frac{k}{T}\Big)\mathrm{Im}\Big\{\frac{K\cdot Q_0}{Q_0\cdot Q_0}\Big\}\bigg)\bigg], \end{aligned} \tag{15.34}$$

where we used the shorthand $Q_0 = Q - \Sigma_0(Q)$. The equilibrium part of the emission rate thus reads

$$\Gamma_0(K) = -\frac{e^2}{2(2\pi)^3}\Big(\sum_s q_s^2\Big)N_C\frac{8f_{F0}(K)}{k}\int^{q_{\rm cut}}\frac{d^3q}{(2\pi)^3}\mathrm{Im}\left\{\frac{K\cdot Q_0}{Q_0\cdot Q_0}\right\} \tag{15.35}$$

while the viscous correction coefficient is given by

$$\begin{aligned} \Gamma^{\alpha\beta}(K) &= -\frac{e^2}{2(2\pi)^3}\Big(\sum_s q_s^2\Big)N_C\frac{8}{k}f_{F0}(K) \\ &\quad\times\int^{q_{\rm cut}}\frac{d^3q}{(2\pi)^3}\bigg[\hat{k}^\alpha\hat{k}^\beta(1-f_{F0}(K))\chi\Big(\frac{k}{T}\Big)\mathrm{Im}\Big\{\frac{K\cdot Q_0}{Q_0\cdot Q_0}\Big\} \\ &\quad -\mathrm{Im}\Big\{\frac{K_\mu\Sigma_1^{\alpha\beta\mu}}{Q_0\cdot Q_0}\Big\}+\mathrm{Im}\Big\{\frac{K\cdot Q_0}{Q_0\cdot Q_0}\frac{2Q_{0\mu}\Sigma_1^{\alpha\beta\mu}}{Q_0\cdot Q_0}\Big\}\bigg]. \end{aligned} \tag{15.36}$$

In Eqs. (15.35) and (15.36), our final results only depend on the retarded quark self-energy $\Sigma_{\rm Ret}$.

Hard contribution

When the internal quark momentum is larger than the cut-off momentum $q_{\rm cut}$, which satisfies $g_sT \ll q_{\rm cut} \ll T$, we can neglect the medium corrections to the internal quark propagator [198]. In this kinematic region, the photon emission rates from $2\to 2$ scattering processes can be easily calculated from relativistic kinetic theory, resulting in the following expression [207]:

$$k\frac{dR}{d^3k} = \sum_{\rm channels}\int_{p,p',k'}\frac{1}{2(2\pi)^3}(2\pi)^4\delta^{(4)}(P+P'-K-K')|\mathcal{M}|^2f(P)f(P')(1\pm f(K')). \tag{15.37}$$

Here $\int_p$ is a shorthand notation for $\frac{1}{(2\pi)^3}\int\frac{d^3p}{2p}$ (all incoming and outgoing particles are on-shell and massless). Note that this expression is identical to what one obtains in the kinetic approach discussed in the following subsection [196]. This is a consequence of the finite temperature Cutcosky rules for computing the imaginary part of the loop diagrams in Fig. 15.2 (without the HTL insertion on the internal quark lines.)

In Fig. 15.3, we show the Feynman diagrams for the scattering amplitudes of the two contributing processes, Compton scattering, $q+g\to q+\gamma$, $\bar{q}+g\to\bar{q}+\gamma$, and quark-antiquark annihilation

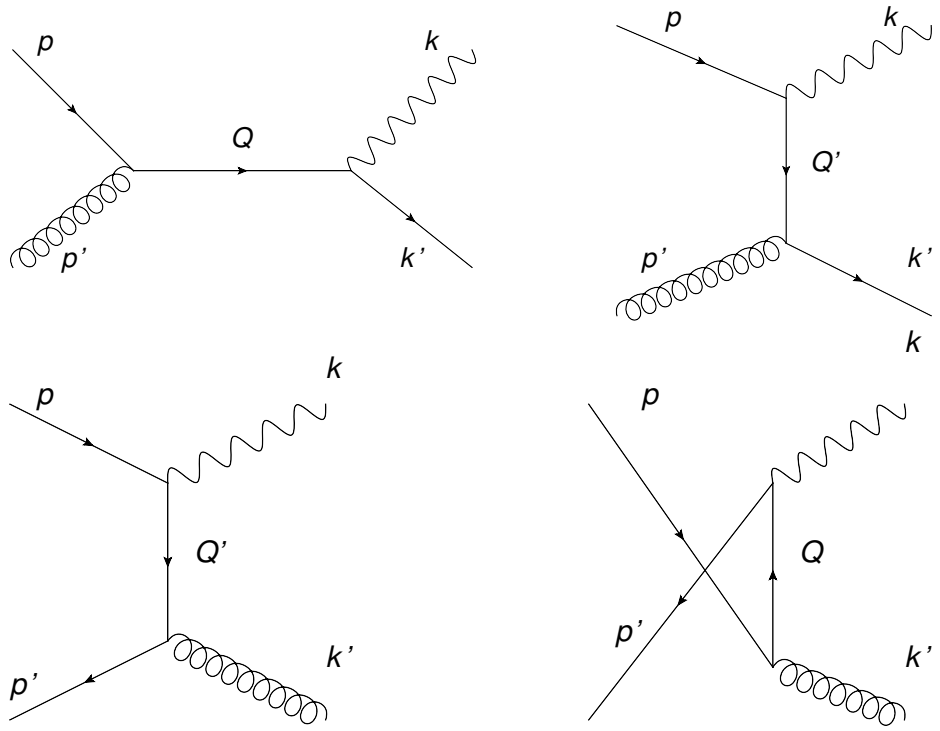

Figure 15.3: Compton scattering and pair annihilation. Compton scattering can involve gluons scattering off quarks (shown) or antiquarks (not shown).

$q+\bar{q} \to \gamma+g$. For Compton scattering $|\mathcal{M}|^2 \propto -\frac{s}{t} - \frac{t}{s}$, which for pair annihilation $|\mathcal{M}|^2 \propto \frac{u}{t}$. We follow the treatment of the phase space integrals from [185] treating the t-channel terms together and the s-channel one separately. For the t-channel parts, we make a change of variable $Q = P-K$ so that the cut-off momentum in the exchange quark phase space can be explicitly implemented. There is no cut on the phase space for the s-channel case.

Here we first treat the t-channel terms. We define $\boldsymbol{q} = \boldsymbol{p}-\boldsymbol{k}$ and $\omega = p-k$ (where $p = |\boldsymbol{p}|$ etc.) such that an infrared cut-off can be placed on the exchanged momentum q. In order to use the maximum symmetry in the pahse-space integrals, we first consider the momentum-integrated photon emission rate for a single scattering channel:

$$R = \int_{p,p',k,k'} (2\pi)^4 \delta^{(4)}(P+P'-K-K') |\mathcal{M}|^2 f(P) f(P') (1 \pm f(K')). \tag{15.38}$$

The integrals are most easily evaluated in the local fluid rest frame, using a coordinate system with its z axis aligned with the photon momentum $\boldsymbol{k}$ and the $x-z$ plane spanned by $\boldsymbol{k}$ and $\boldsymbol{q}$. In this frame, the integrand in Eq. (15.38) is determined by the momentum magnitudes p, p', and k and three angles, θ_{kq}, $\theta_{p'q}$, and $\phi_{p'}$. The remaining angular integrals give trivial factors. We use $\delta^{(3)}(\boldsymbol{p}+\boldsymbol{p'}-\boldsymbol{k}-\boldsymbol{k'})$ to perform the integration over $\boldsymbol{k'}$:

$$\begin{aligned} R &= \int p'^2 dp' q^2 dq\, k^2 dk\, d\cos\theta_{kp}\, d\cos\theta_{p'q}\, d\phi_{p'} \frac{2(2\pi)^2}{(2\pi)^8 2^4 p p' k k'} \delta(p+p'-k-k'). \\ &\quad \times |\mathcal{M}|^2 f(p) f(p') \big(1 \pm f(p+p'-k)\big). \end{aligned} \tag{15.39}$$

The remaining δ-function is split in two by introducing a dummy integration:

$$\delta(p{+}p'{-}k{-}k') = \int_{-\infty}^{+\infty} d\omega\, \delta(\omega{+}k{-}p)\, \delta(\omega{+}p'{-}k'), \tag{15.40}$$

with each factor rewritten to perform one of the polar angle integrations:

$$\delta(\omega{+}k{-}p') = \frac{p}{qk}\,\delta\left(\cos\theta_{qk} - \frac{\omega^2{-}q^2{+}2\omega k}{2qk}\right)\theta(\omega{+}k), \tag{15.41}$$

$$\delta(\omega{+}p'{-}k') = \frac{k'}{qp'}\,\delta\left(\cos\theta_{p'q} - \frac{\omega^2{-}q^2{+}2\omega p'}{2p'q}\right)\theta(\omega{+}p'). \tag{15.42}$$

Doing so yields

$$R = \int dq\, dp'\, dk\, d\omega\, d\phi_{p'}\, \frac{1}{8(2\pi)^6}|\mathcal{M}|^2 f(\omega{+}k) f(p')\big(1{\pm}f(\omega{+}p')\big)\theta(\omega{+}k)\theta(\omega{+}p'). \tag{15.43}$$

Now we can return to the differential photon emission rate for the selected channel:

$$k\frac{dR}{d^3k} = \frac{1}{16(2\pi)^7 k}\int dq\, dp'\, d\omega d\phi_{p'}|\mathcal{M}|^2 f(\omega{+}k) f(p')\big(1{\pm}f(\omega{+}p')\big)\theta(\omega{+}k)\theta(\omega{+}p'). \tag{15.44}$$

The Mandelstam variables in the matrix elements are expressed in terms of these integration variables as

$$t = \omega^2 - q^2, \qquad s = -t - u, \tag{15.45}$$

$$u = -2p'k(1 - \cos\theta_{kq}\cos\theta_{p'q} + \sin\theta_{kq}\sin\theta_{p'q}\cos\phi_{p'}), \tag{15.46}$$

with $\cos\theta_{kq}$ and $\cos\theta_{p'q}$ given by the poles of the δ-functions in Eqs. (15.41) and (15.42).

With our anisotropic distribution function (Eq. (15.1)), the integral over $\phi_{p'}$ can be done analytically. Splitting $f = f_0{+}\delta f$ and ignoring all δf terms we obtain the equilibrium rate Γ_0 in Eq. (15.7) which, after adding all three t-channel contributions, summing over quark species s and over quark- and antiquark contributions to the Compton channel, reads

$$\begin{aligned}\Gamma_0 \;=\; & \frac{\mathcal{N}}{16(2\pi)^6 k}\int_{q_{\rm cut}}^{+\infty} dq \int_{\max\{q-2k,-q\}}^{q} d\omega \int_{(q-\omega)/2}^{+\infty} dp' \\ & \times\Big[\Big(1 - \frac{2p'k}{\omega^2{-}q^2}(1-\cos\theta_{kq}\cos\theta_{p'q})\Big) f_{F0}(\omega{+}k) f_{B0}(p')\big(1{-}f_{F0}(p'{+}\omega)\big) \\ & \quad -\frac{2p'k}{\omega^2{-}q^2}(1-\cos\theta_{kq}\cos\theta_{p'q}) f_{F0}(\omega{+}k) f_{F0}(p')\big(1{+}f_{B0}(p'{+}\omega)\big)\Big],\end{aligned} \tag{15.47}$$

where we implemented the infrared cutoff $q_{\rm cut}$ in the q integral, and where

$$\mathcal{N} = 16 N_C C_F e^2 g_s^2 \sum_s q_s^2 \;= 2^8\pi N_C \alpha_{\rm em}\frac{m_\infty^2}{T^2}\sum_s q_s^2. \tag{15.48}$$

In (15.47) the first term in the square brackets accounts for Compton scattering, the second for $q\bar{q}$ annihilation.

Now we add all contributions linear in δf, write the result as in Eq. (15.4) and read off the coefficient $\Gamma^{\mu\nu}$. Contracting with $a_{\mu\nu}$ to obtain the viscous correction coefficient $\Gamma_1 = a_{\mu\nu}\Gamma^{\mu\nu}$ in Eq. (15.7) we get from the $-\frac{s}{t}$ part of $|\mathcal{M}|^2$ the Compton scattering contribution,

$$
\begin{aligned}
\Gamma_1^{(-s/t)} &= \frac{\mathcal{N}}{16(2\pi)^6 k}\int_{q_{\rm cut}}^{+\infty} dq \int_{\max\{q-2k,-q\}}^{q} d\omega \int_{(q-\omega)/2}^{+\infty} dp' \\
&\times\ f_{F0}(\omega{+}k)\, f_{B0}(p')\,\big(1{-}f_{F0}(p'{+}\omega)\big) \\
&\times\ \Big\{\Big(1-\frac{2p'k}{\omega^2{-}q^2}(1-\cos\theta_{kq}\cos\theta_{p'q})\Big) \\
&\quad\times\Big[\big(1{-}f_{F0}(\omega{+}k)\big)\chi\Big(\frac{\omega{+}k}{T}\Big)\Big(-\frac{1}{2}+\frac{3}{2}\Big(\frac{q\cos\theta_{kq}{+}k}{\omega{+}k}\Big)^2\Big) \\
&\qquad -f_{F0}(p'{+}\omega)\chi\Big(\frac{p'{+}\omega}{T}\Big)\Big(-\frac{1}{2}+\frac{3}{2}\frac{1}{(p'{+}\omega)^2}\big((p'\cos\theta_{p'q}+q)^2\cos^2\theta_{kq} \\
&\qquad\qquad +\tfrac{1}{2}p'^2\sin^2\theta_{kq}\sin^2\theta_{p'q}\big)\Big) \\
&\qquad +\big(1{+}f_{B0}(p')\big)\chi\Big(\frac{p'}{T}\Big) \\
&\qquad\times\Big(-\frac{1}{2}+\frac{3}{2}\big(\cos^2\theta_{kq}\cos^2\theta_{p'q}+\tfrac{1}{2}\sin^2\theta_{kq}\sin^2\theta_{p'q}\big)\Big)\Big] \\
&\quad +\frac{2p'k}{\omega^2{-}q^2}\sin\theta_{kq}\sin\theta_{p'q} \\
&\quad\times\Big[\big(1{+}f_{B0}(p')\big)\chi\Big(\frac{p'}{T}\Big)\frac{3}{2}\cos\theta_{kq}\cos\theta_{p'q}\sin\theta_{kq}\sin\theta_{p'q} \\
&\quad -f_{F0}(p'{+}\omega)\chi\Big(\frac{p'{+}\omega}{T}\Big)\frac{3}{2}\frac{1}{(p'{+}\omega)^2} \\
&\quad\times\big(p'\sin\theta_{kq}\sin\theta_{p'q}\cos\theta_{kq}(p'\cos\theta_{p'q}{+}q)\big)\Big]\Big\}, \qquad (15.49)
\end{aligned}
$$

while the $\frac{u}{t}$ part gives the contribution from $q\bar{q}$ annihilation:

$$\begin{aligned}
\Gamma_1^{(u/t)} &= \frac{\mathcal{N}}{16(2\pi)^6 k}\int_{q_{\rm cut}}^{+\infty} dq \int_{\max\{q-2k,-q\}}^{q} d\omega \int_{(q-\omega)/2}^{+\infty} dp' \\
&\times\ f_{F0}(\omega{+}k)\, f_{F0}(p')\,\big(1{+}f_{B0}(p'{+}\omega)\big) \\
&\times\ \Big(-\frac{2p'k}{\omega^2{-}q^2}\Big)\Big\{(1-\cos\theta_{kq}\cos\theta_{p'q}) \\
&\times\ \Big[\big(1{-}f_{F0}(\omega{+}k)\big)\chi\Big(\frac{\omega{+}k}{T}\Big)\Big(-\frac{1}{2}+\frac{3}{2}\Big(\frac{q\cos\theta_{kq}{+}k}{\omega{+}k}\Big)^2\Big) \\
&\quad +\big(1{-}f_{F0}(p')\big)\chi\Big(\frac{p'}{T}\Big)\Big(-\frac{1}{2}+\frac{3}{2}\big(\cos^2\theta_{kq}\cos^2\theta_{p'q}+\tfrac{1}{2}\sin^2\theta_{kq}\sin^2\theta_{p'q}\big)\Big) \\
&\quad +f_{B0}(p'{+}\omega)\chi\Big(\frac{p'{+}\omega}{T}\Big)\Big(-\frac{1}{2}+\frac{3}{2}\frac{1}{(p'{+}\omega)^2}\big((p'\cos\theta_{p'q}+q)^2\cos^2\theta_{kq} \\
&\qquad\qquad +\tfrac{1}{2}p'^2\sin^2\theta_{kq}\sin^2\theta_{p'q}\big)\Big)\Big] \\
&+\ \sin\theta_{kq}\sin\theta_{p'q} \\
&\times\ \Big[\big(1{-}f_{F0}(p')\big)\chi\Big(\frac{p'}{T}\Big)\frac{3}{2}\cos\theta_{kq}\cos\theta_{p'q}\sin\theta_{kq}\sin\theta_{p'q} \\
&+\ f_{B0}(p'{+}\omega)\chi\Big(\frac{p'{+}\omega}{T}\Big)\frac{3}{2}\frac{1}{(p'{+}\omega)^2}\big(p'\sin\theta_{kq}\sin\theta_{p'q}\cos\theta_{kq}(p'\cos\theta_{p'q}{+}q)\big)\Big]\Big\}.
\end{aligned} \tag{15.50}$$

For the s-channel diagrams we define $\boldsymbol{q}=\boldsymbol{p}+\boldsymbol{p'}$ and $\omega=p+p'$ and follow the same procedure:

$$\begin{aligned}
\Gamma_0 &= \frac{\mathcal{N}}{16(2\pi)^6 k}\int_{k}^{+\infty} d\omega \int_{|2k-\omega|}^{\omega} dq \int_{(\omega-q)/2}^{(\omega+q)/2} dp' \\
&\quad\times \frac{2p'k}{\omega^2{-}q^2}\,(1{-}\cos\theta_{kq}\cos\theta_{p'q})\, f_{B0}(\omega{-}p')\, f_{F0}(p')\,\big(1{-}f_{F0}(\omega{-}k)\big),
\end{aligned} \tag{15.51}$$

where now $\cos\theta_{kq} = \frac{q^2-\omega^2+2\omega k}{2qk}$ and $\cos\theta_{p'q} = \frac{q^2-\omega^2+2\omega p'}{2qp'}$. The s-channel contribution to the viscous correction coefficient is

$$
\begin{aligned}
\Gamma_1 \;=\; & \frac{\mathcal{N}}{16(2\pi)^6 k}\int_k^{+\infty} d\omega \int_{|2k-\omega|}^{\omega} dq \int_{(\omega-q)/2}^{(\omega+q)/2} dp'\, f_{B0}(\omega-p')\, f_{F0}(p')\big(1+f_{F0}(\omega-k)\big) \\
& \times \frac{2p'k}{\omega^2-q^2}\Big\{(1-\cos\theta_{kq}\cos\theta_{p'q}) \\
& \times \Big[\big(1-f_{F0}(p')\big)\chi\Big(\frac{p'}{T}\Big)\Big(-\frac{1}{2}+\frac{3}{2}\big(\cos^2\theta_{kq}\cos^2\theta_{p'q}+\tfrac{1}{2}\sin^2\theta_{kq}\sin^2\theta_{p'q}\big)\Big) \\
& \quad -f_{F0}(\omega-k)\chi\Big(\frac{\omega-k}{T}\Big)\Big(-\frac{1}{2}+\frac{3}{2}\Big(\frac{q\cos\theta_{kq}-k}{\omega-k}\Big)^2\Big) \\
& \quad +\big(1+f_{B0}(\omega-p')\big)\chi\Big(\frac{\omega-p'}{T}\Big) \\
& \quad \times\Big(-\frac{1}{2}+\frac{3}{2}\frac{(q-p'\cos\theta_{p'q})^2\cos^2\theta_{kq}+\frac{1}{2}p'^2\sin^2\theta_{kq}\sin^2\theta_{p'q}}{(\omega-p')^2}\Big)\Big] \\
& + \sin\theta_{kq}\sin\theta_{p'q} \\
& \times \Big[-\big(1-f_{F0}(p')\big)\,\chi\Big(\frac{p'}{T}\Big)\,\frac{3}{2}\cos\theta_{kq}\cos\theta_{p'q}\sin\theta_{kq}\sin\theta_{p'q} \\
& \quad +\big(1+f_{B0}(\omega-p')\big)\,\chi\Big(\frac{\omega-p'}{T}\Big)\,\frac{3}{2}\frac{p'\sin\theta_{kq}\sin\theta_{p'q}\cos\theta_{kq}(q-p'\cos\theta_{p'q})}{(\omega-p')^2}\Big]\Big\}. \qquad (15.52)
\end{aligned}
$$

The remaining three integrals are straightforward to evaluate numerically, using e.g. Gaussian quadrature.

One should note that strictly speaking this calculation is only valid for internal quark momenta $q \sim \mathcal{O}(T) \gg g_s T$ [206, 207, 208] whereas the soft part (15.35,15.36) is valid only for $q \sim \mathcal{O}(g_s T) \ll T$. In Sec. 15.3.1 we will explore to what extent there exists a "window of insensitivity" $g_s T \ll q_{\rm cut} \ll T$ where both approximations are simultaneously valid and can be matched to each other without strong dependence on the cutoff $q_{\rm cut}$.

15.2.3 Kinetic approach

Alternatively, photon emission rates at leading-log order can also be calculated through the kinetic approach, which in the equilibrated case has been shown to be equivalent to the diagrammatic approach, up to higher order corrections in g_s [207, 208, 198, 209]. For Compton scattering and pair annihilation, logarithmic infrared divergences will be generated in t and u channels if one uses free fermion propagators for the internal exchanged quark. This infrared sensitivity is cut off by using the retarded hard loop resummed self-energy $\Sigma(Q)$ in the internal quark propagator, where calculating $|\mathcal{M}|^2$ in Eq. (15.3)

Here we will include the quark self-energy only in the internal quark propagators in t and u channels but not in the s channel neither any of the quark propagators. This is because in the s-channel, if the HTL self-energies were included in the internal quark line, the time-like virtual quark

could go on-shell and become a long-lived quasi-particle excitation in the medium [209]. This is, however, kinematically allowed even with massless external particles, and in inclusion of the HTL self-energy with s-channel quark propagator would double-count these "$2 \to 1$ joining processes", which should be treated explicitly, including Landau-Pomeranchuk-Migdal (LPM) interference effects. To avoid this double-counting problem, it is easiest to simply use bare quark propagators in this channel which is infrared finite and does not require any HTL regulation.

We note that in the u and t channels HTL resummation is required for consistency *at leading order* in the soft exchange region but not for hard scatterings where it contributes only at *next-to-leading order* in g_s. As mentioned earlier, using the HTL resummed propagators everywhere is not a consistent approximation scheme, but the inconsistencies are restricted to subleading order in g_s. In the diagrammatic approach described in the preceding subsection, we used free internal quark propagators for hard collisions, consistently matched to matrix elements using resummed internal propagators in the soft region. In the kinetic approach described in the present section, we use HTL resummed matrix elements for the entire kinematic range in order to avoid introducing artificial momentum cut-off. The difference amounts to different prescriptions for a partial resummmation of higher order terms that are subleading in g_s. For sufficiently small g_s, both approaches are expected to yield identical results; for moderate values of g_s, the differences between the approaches can be taken as a (rough) indicator for the theoretical uncertainties associated with the leading logarithmic approximation on which our analysis is based.

According to the labeling in Fig. 15.3, the matrix element for Compton scattering in the QGP can be written as

$$\begin{aligned}
\sum_{\text{spins}}\sum_{\text{colors}} |M_{\text{Comp}}|^2_{\text{eq}} &= e^2 g^2 (t^a t^a) \\
&\times \left\{ \frac{16}{|Q\cdot Q|^2}\Big(2\text{Re}\big[(K'\cdot Q)(P\cdot Q^*)\big] - (K'\cdot P)(Q\cdot Q^*)\Big)\right. \\
&- 64(K'\cdot P)\text{Re}\Big[\frac{Q\cdot Q'^*}{(Q\cdot Q)(Q'^*\cdot Q'^*)}\Big] \\
&+ \left. \frac{16}{|Q'\cdot Q'|^2}\Big(2\text{Re}\big[(K'\cdot Q')(P\cdot Q'^*)\big] - (K'\cdot P)(Q'\cdot Q'^*)\Big)\right\},
\end{aligned} \tag{15.53}$$

where $Q^\mu = P^\mu + P'^\mu$ and $Q'^\mu = P^\mu - K^\mu - \Sigma^\mu_R(P-K)$. And the pair annihilation channel gives,

$$\begin{aligned}\sum_{\text{spins colors}}\sum |M_{\text{pair}}|^2_{\text{eq}} &= e^2 g^2 (t^a t^a) \\ &\times \left\{ \frac{16}{|Q'\cdot Q'|^2}\Big(2\text{Re}\big[(P'\cdot Q')(P\cdot Q'^*)\big] - (P'\cdot P)(Q'\cdot Q'^*)\Big)\right. \\ &- 64(P'\cdot P)\text{Re}\Big[\frac{\tilde{Q}\cdot Q'^*}{(\tilde{Q}\cdot\tilde{Q})(Q'^*\cdot Q'^*)}\Big] \\ &+ \left.\frac{16}{|\tilde{Q}\cdot\tilde{Q}|^2}\Big(2\text{Re}\big[(P'\cdot\tilde{Q})(P\cdot\tilde{Q}^*)\big] - (P'\cdot P)(\tilde{Q}\cdot\tilde{Q}^*)\Big)\right\},\end{aligned} \tag{15.54}$$

where $Q'^\mu = P^\mu - K^\mu - \Sigma^\mu_{\text{Ret}}(P-K)$ and $\tilde{Q}^\mu = P^\mu - K'^\mu - \Sigma^\mu_{\text{Ret}}(P-K')$. The matrix elements for both channels involve the retarded quark self-energy Σ^μ_{Ret} calculated in Eqs. (15.24)-(15.29).

15.3 Results and discussion

In this section, we compare the photon emission rates calculated with the diagrammatic and the kinetic approaches. We use $\chi\left(\frac{p}{T}\right) = (p/T)^2$ for the momentum dependence of δf in Eq. (15.1). The λ dependence of is studied at the end of this section. For completeness we also compare our rates with two other approaches currently on the market: the $2 \leftrightarrow 2$ part of the ideal rate from AMY [185], and the viscous calculation by Dusling using the forward-scattering dominance approximation (FSDA) [188].

The calculation from AMY is formally equivalent to the diagrammatic approach described in the previous section, but as will be seen in the next section, our treatment of the cut-off dependence of the calculation makes our results differ from theirs when g_s is not small. The use of FSDA allows one to simplify enormously the photon rate calculation with respect to the full approach presented here [32]

To simplify the comparison of rates, it is convenient to plot the dimensionless equilibrium rates and viscous correction coefficients $\tilde{\Gamma}_0$ and $\tilde{\Gamma}_1$ in Eq. (15.7) as functions of k/T for selected values of the parameters g_s. The diagrammatic approach has an extra dependence originating from the cut-off introduced to divide the soft and hard phase space. We begin this section by looking at this dependence.

[32]Dusling used a slightly different ansatz for the momentum anisotropy but his formula

$$k\frac{dR}{d^3k} = \frac{e^2 g_s^2\left(\sum_s q_s^2\right)}{\pi(2\pi)^3} f(K)\, T^2 \ln\left[\frac{3.7388\, k}{g_s^2 T}\right] \tag{15.55}$$

can be straightforwardly to adapted to our case by replacing his ansatz in [188] for $f(K)$ by our Eq. (15.1). The results of doing so are labelled as "Dusling" in the figures below.

15.3.1 Cut-off dependence in the diagrammatic approach

Recall that the cut-off introduced in the diagrammatic approach is artificial: the soft scattering region below the cut-off where HTL self-energy is essential to regulate the infrared logarithmic divergence should match smoothly to the hard scattering sector, where the medium correction to the matrix elements are negligible. The value of the cut-off is formally to be chosen so that $g_s T \ll q_{\rm cut} \ll T$. Physically, the final photon emission rates should be completely insensitive to this artificial cut-off. In practice this means that there should be a range of values for $q_{\rm cut}$ between $g_s T$ and T for which the rate is largely insensitive to $q_{\rm cut}$. On the other hand it also means that the cut-off independence should quickly go away when the $g_s T$ scale overlaps with the T scale. Both of these effects are discussed in this section.

Two different values of g_s are used in this section. The first one, $g_s = 0.01$, is chosen to be well in the $g_s \ll 1$ regime. The second value chosen is $g_s = 2$ ($\alpha_s \sim 0.3$), which is about the value relevant for phenomenological studies related to current heavy ion collision experiments.

In Fig. 15.4, we show the scaled photon emission rates $\tilde{\Gamma}_0$ and the viscous correction coefficient $\tilde{\Gamma}_1$ from the diagrammatic approach at $k/T = 10$ as a function of the temperature-scaled cut-off momentum $q_{\rm cut}/T$. Remember that tensor decomposition allowed us to extract the $\pi^{\mu\nu}$ dependence from the viscous rate correction, and that what is plotted here is the coefficient of this tensor decomposition, which only depends on k/T, g_s and the cut-off. We see that at $g_s = 0.01$ (Fig. 15.4(a) and (b)), there is an extended large plateau in the cut-off dependence for both the equilibrium rate and the viscous correction. The plateau extends roughly between g_s and 1, with a minimum, indicated by a vertical line, around $\sqrt{g_s}$. This means that in the small g_s limit, we have a wide window for choosing cut-off momentum, $q_{\rm cut}/T$, such that both the equilibrium rate and the viscous correction are basically insensitive to the cut-off.

Increasing the value of g_s shrinks the width of the plateau. At $g_s = 2$, which is shown on Fig. 15.4(c) and (d), the plateau becomes a local minimum; only a very small region of weak cut-off dependence is left. The same behavior is seen in both equilibrium and viscous cases. This behavior is not surprising considering that for $g_s > 1$, the $O(g_s T)$ energy scale overlaps with the $O(T)$ scale. This means that there is no room to introduce a separation energy scale to treat hard and soft parts differently. It is worth noting, however, that the local minimum for both equilibrium and viscous rates still occurs at $q_{\rm cut}/T \sim O(\sqrt{g_s})$.

This prescription agrees with the one adopted in [192] but not with the approach taken by AMY in [185]. AMY start from the observation that for sufficiently small coupling the $q_{\rm cut}/T$ dependences of the soft and hard contributions to the thermal photon rate must cancel exactly, and that in the asymptotic regions ($q_{\rm cut}/T \gg 1$ for the soft contribution, $q_{\rm cut}/T \ll 1$ for the hard one) the cutoff dependences of both contributions are linear in $\ln(q_{\rm cut}/T)$ (with opposite slopes).

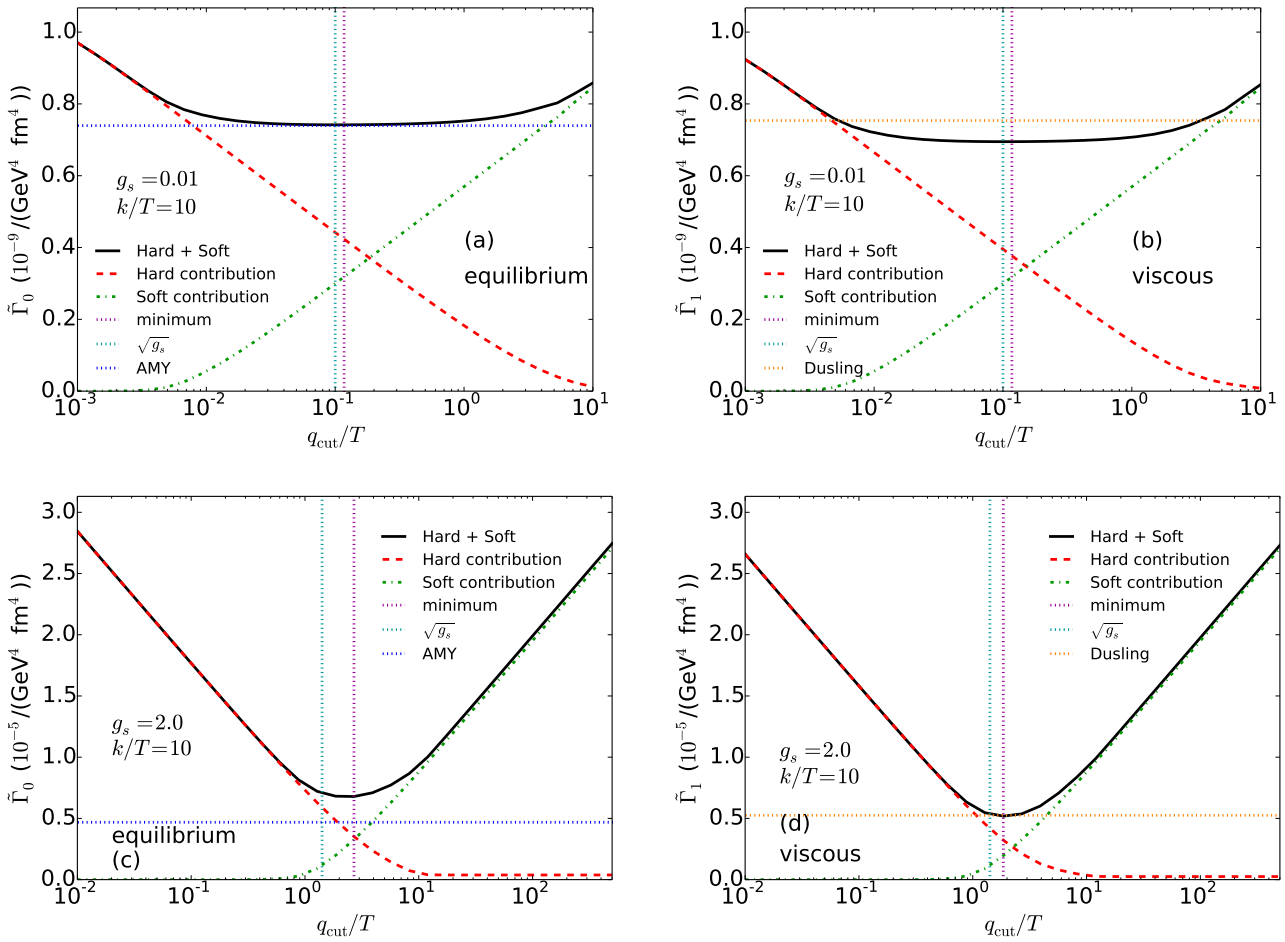

Figure 15.4: (Color online) Cutoff dependence of the normalized equilibrium rate $\tilde{\Gamma}_0$ (a,c) and viscous correction coefficient $\tilde{\Gamma}_1$ (b,d) from the diagrammatic approach at $k/T = 10$, for two values of the strong coupling constant, $g_s = 0.01$ (a,b) and $g_s = 2.0$ (c,d). Horizontal dotted lines indicate the value from the AMY parametrization [185] in (a,c) and from Dusling's FSDA [188] in (b,d). Vertical dotted lines indicate the positions of the minima of the numerical curves and of $q_{\rm cut}/T = \sqrt{g_s}$, respectively. See text for discussion.

They then eliminate the $\ln(q_{\rm cut}/T)$ dependence of the total rate by adding these two asymptotic logarithmic terms; this leads to the horizontal dotted lines in Figs. 15.4a,c and 15.5a,c. Figs. 15.4c and 15.5c show, however, that for $g_s = 2$ the cutoff dependences of the hard and soft contributions to the rate are no longer linear in $\ln(q_{\rm cut}/T)$ in the region $q_{\rm cut}/T \sim 1$ where the soft and hard contributions should be matched. For moderately strong coupling, evaluating both contributions numerically and adding them as we do here therefore gives a larger result than the one obtained by AMY. These observations hold for both low ($k/T = 1$, Fig. 15.5) and high ($k/T = 10$, Fig. 15.4) photon energies.

Dusling [188] applies a similar prescription to $\tilde{\Gamma}_1$ as AMY do for $\tilde{\Gamma}_0$: He obtains a $q_{\rm cut}$-independent result by exactly canceling the leading logarithmic $q_{\rm cut}/T$-dependences of the soft and hard contributions to $\tilde{\Gamma}_1$ in their respective asymptotic regions (as defined above). However,

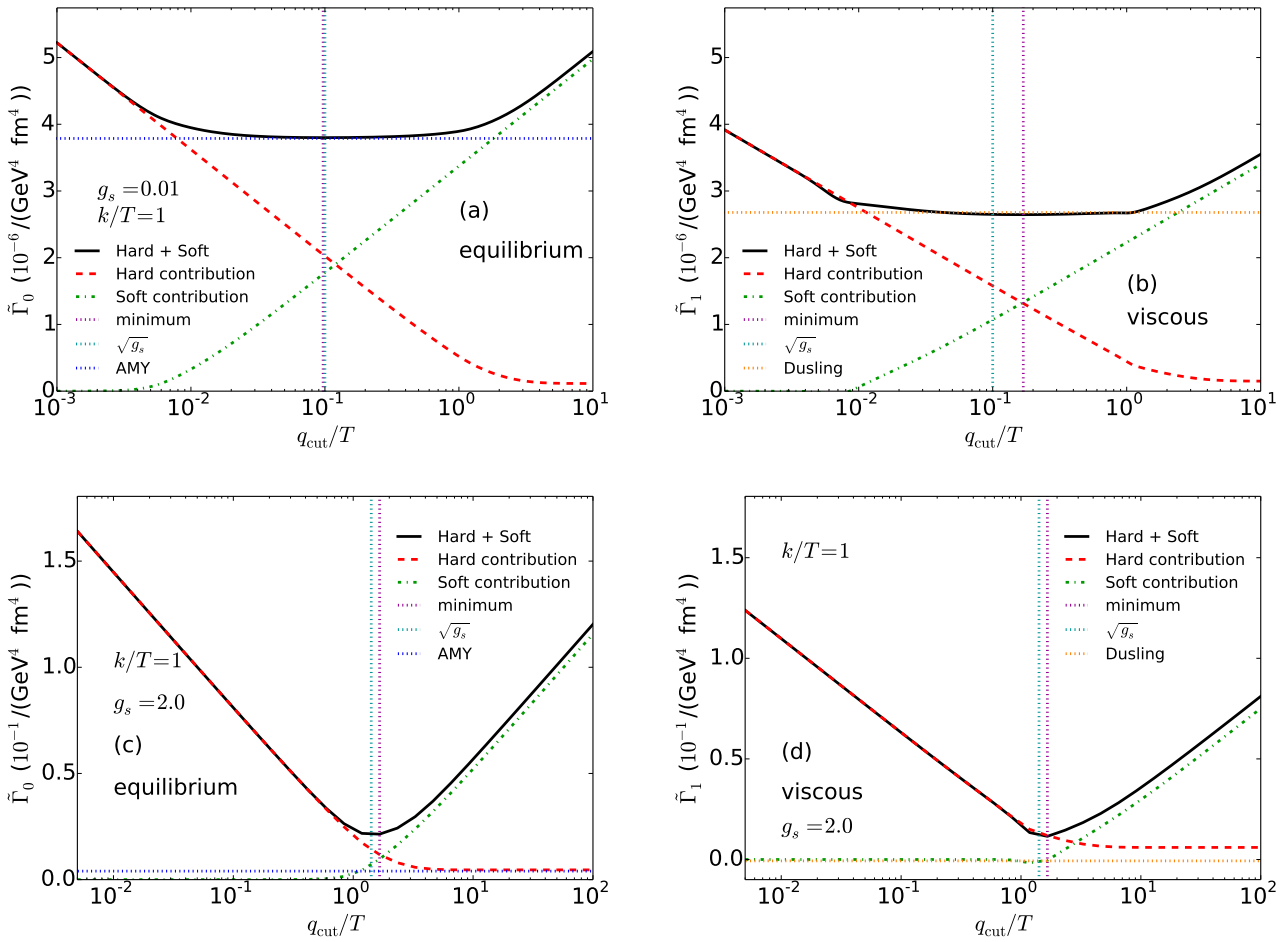

Figure 15.5: (Color online) Same as Fig.15.4, but for softer photons at $k/T = 1$.

an additional difference of his work to ours is his use of the FSDA. Fig. 15.4b shows that, even for weak coupling $g_s \ll 1$ where our calculations show a wide window of insensitivity of $\tilde{\Gamma}_1$ to $q_{\rm cut}/T$, this approximation leads to somewhat larger $\tilde{\Gamma}_1$ values than our estimate. At stronger coupling ($g_s = 2$, Fig. 15.4d), this FDSA effect accidentally cancels against the approximation of replacing the correct numerical cutoff dependence by its asymptotic form. At smaller photon energy $k/T = 1$ this cancellation no longer happens at $g_s = 2$ (Fig. 15.5d), instead it has moved to $g_s \simeq 0.01$ (Fig. 15.5b).

15.3.2 Rate comparison

We now compare our results from diagrammatic approach with kinetic approach, along with forward scattering dominant approximation (FSDA) calculations and AMY's results when relevant. For the diagrammatic approach we use $q_{\rm cut} = \sqrt{g_s}T$ for the momentum cut-off, since this value is generally close to the region of minimum cut-off dependence.

We show both the scaled equilibrium rate $\tilde{\Gamma}_0$ (Fig. 15.6) and the viscous correction $\tilde{\Gamma}_1$ (Fig. 15.7), for two values of the coupling constant, $g_s = 0.1$ and $g_s = 2$. For $g_s = 0.1$ in Fig. 15.6(a), we find

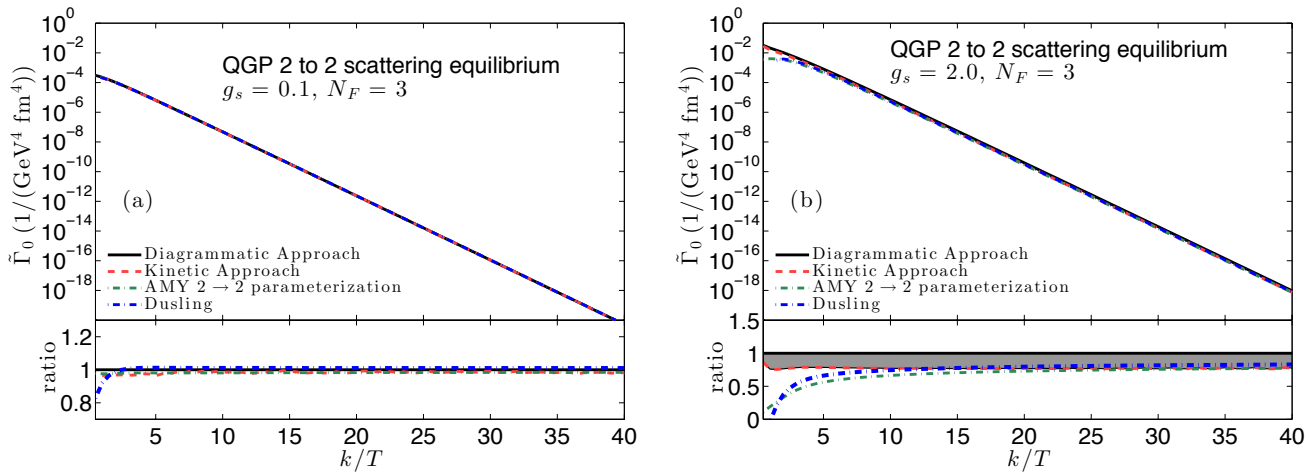

Figure 15.6: (Color online) The temperature-scaled equilibrium photon emission rate $\tilde{\Gamma}_0$ as a function of k/T for relatively weak ($g_s = 0.1$, (a)) and moderately strong coupling ($g_s = 2$, (b)). Results are shown for the diagrammatic approach, the kinetic approach, AMY's parametrization [185], and for the forward scattering dominance approximation (FSDA) [188] as labelled. In the lower panels we show the ratio between these rates and the one from the diagrammatic approach are shown on a linear scale.

the equilibrium photon emission rates calculated from all four approaches agree very well with each other. The difference between our results and AMY is within 2%. The result from FSDA only deviates from the others when $k/T < 1$.

In Fig. 15.6(b), we plot the equilibrium rates for $g_s = 2.0$. All four approaches produce similar k/T dependence for $k/T > 5$. The relative ratios show that the equilibrium rates from kinetic approach is systematically $\sim 25\%$ smaller compared to the results from diagrammatic approach over the whole k/T range from 0.5 to 40. This difference is not surprising considering that the kinetic and diagrammatic approaches have only been shown to be equivalent up to $O(g_s)$ corrections. Recall that the difference between AMY and our diagrammatic approach is due to the different treatment to the cut-off dependence. In the asymptotic limit of k/T, AMY's and FSDA results agree with our calculations from kinetic approach within few percent. Both AMY and FSDA results start to deviate from kinetic approach for $k/T < 10$, where the higher order corrections become important. Result with FSDA works very well for large k/T, but becomes unreliable and turns to negative for $k/T < 1$.

We now turn to the viscous correction, $\tilde{\Gamma}_1$. In Fig. 15.7a, at small coupling limit, $g_s = 0.1$, results from diagrammatic approach agrees well with kinetic approach when $k/T > 5$. The difference is within 2%. The results begin to deviate from each other significantly for $k/T < 2$. Results with FSDA again reproduces the correct k/T dependence for the viscous correction, but overestimates the absolute value by $\sim 10\%$ compared to the other two approaches. We checked that such difference is coming from the forward scattering dominance approximation and does not vanish in the asymptotic small coupling limit.

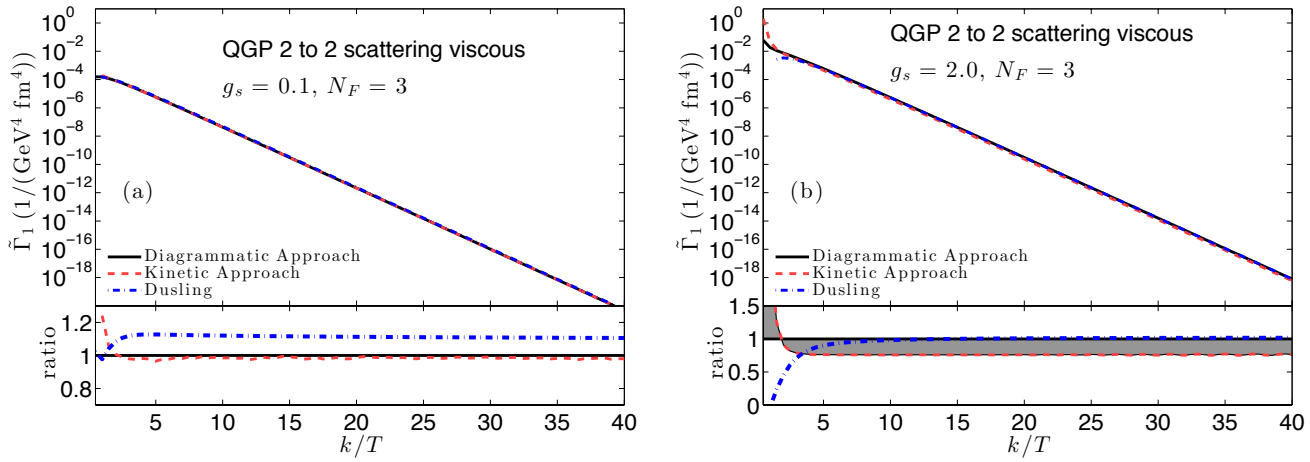

Figure 15.7: (Color online) Similar to Fig. 15.6 but for the viscous correction coefficient $\tilde{\Gamma}_1$.

In Fig. 15.7b, at $g_s = 2.0$, the situation is similar to the equilibrium one. Viscous corrections from our diagrammatic approach is systematically about 25% larger than kinetic approach. For $k/T < 1$, the results begin to deviate significantly from each other. Results from FSDA gives about 25% larger viscous corrections compared to kinetic approach. The good agreement with diagrammatic approach is merely a coincident at $g_s = 2.0$.

The difference between the kinetic and diagrammatic approach can be considered as a lower bound on the theoretical uncertainty in our rates. Since the results from the diagrammatic approach additionally depend on the choice of the cut-off. A more conserved estimation of the uncertainty should also include the variation by changing the cut-off around the minimum.

15.3.3 Photon energy dependence of the ratio $\tilde{\Gamma}_1/\tilde{\Gamma}_0$

All results presented up to this point assumed that the function $\chi\left(\frac{p}{T}\right)$ appearing in Eq.(15.3) had a quadratic form ($\chi\left(\frac{p}{T}\right) = (p/T)^2$). However the actual power dependence in $\chi\left(\frac{p}{T}\right)$ is determined by the underlying kinetic theory. Depending on the energy dependence of the collision kernels, the p/T-dependence of $\chi\left(\frac{p}{T}\right)$ is expected to be between linear and quadratic [132].

In Fig. 15.8, we compare the viscous correction factors $\tilde{\Gamma}_1(k/T)$ with $\chi\left(\frac{p}{T}\right) = p/T$ and $\chi\left(\frac{p}{T}\right) = (p/T)^2$. In the right panel, we find that although the viscous correction to the photon emission rate is a result of integrating the distribution functions of the reacting particles over their phase spaces, the ratio of viscous correction to equilibrium rates exhibits very good power law dependence to k/T. Performing a linear fit of the results for $k/T > 5$, we find that the power dependence is very close to λ for both $\lambda = 1$ and $\lambda = 2$, as shown in the right panel of Fig. 15.8.

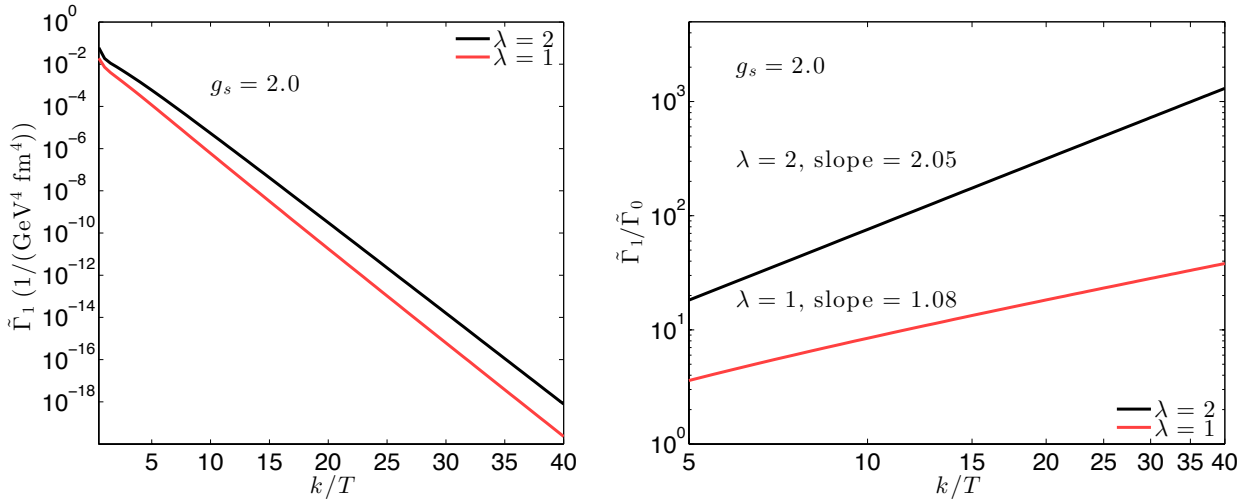

Figure 15.8: (Color online) The viscous correction coefficient $\tilde{\Gamma}_1$ (a) and its ratio $\tilde{\Gamma}_1/\tilde{\Gamma}_0$ to the thermal equilibrium emission rate (b) as functions of k/T at $g_s = 2.0$ for two values λ, $\lambda = 1$ and 2 (see text for details). The slope parameters in panel (b) were obtained by a linear fit of the log-log plot for $k/T > 5$.

15.4 Chapter conclusions

In this chapter, we calculated the photon production rates from $2 \leftrightarrow 2$ scattering processes in a nearly thermalized quark-gluon plasma with underlying particle momentum distribution functions as in Eq. (15.1). Numerical calculations of the rates from the diagrammatic and kinetic approaches were compared in the weak coupling and realistic moderate coupling limit. A KMS-like relation has been proved in the hard loop limit not only with our assumption of the particle momentum distribution function in Eq. (15.1), but also for any local momentum distribution that is mirror symmetric under momentum reflection in the local rest frame. This relation simplifies the viscous rate calculation considerably.

We compared our equilibrium rates and viscous corrections from both approaches with well-known parametrization from AMY [185] as well as the results using the forward scattering dominance approximation introduced in [188]. In the diagrammatic approach, we investigated the cut-off dependence for both equilibrium rates and viscous corrections in the small $g_s = 0.01$ limit as well as for $g_s = 2.0$, representing the realistic situation in relativistic heavy-ion collisions. For small coupling we found a plateau of approximate cut-off independence for matching the soft and hard contributions for both equilibrium rates and their viscous corrections. For strong coupling, this plateau disappears, and the rates have to be matched at the point of minimal cut-off sensitivity near $q_{\rm cut}/T \sim \sqrt{g_s}$. Finally, we found that the momentum dependence in the rate of the viscous correction to the equilibrium rate is very close to the momentum dependence in the off-equilibrium particle distribution for quarks and gluons.

We finally remark that the current calculations only considered $2 \leftrightarrow 2$ scattering processes. In order to obtain a complete leading order $\mathcal{O}(e^2 g_s^2)$ photon emission rate and its corresponding viscous correction, we must additionally calculate the Bremsstrahlung processes induced by soft collinear collisions, modified by the LPM effect [185].

Chapter 16: Thermal photon emission rates: HG photon rates

16.1 Massive Yang-Mills theory

In the hadronic phase, we consider photon production through mesonic interactions. Photon production through reaction with baryons are not included in this effective theory yet. Since the interactions between mesons have non-perturbative nature, we need to use effective theory instead of solving QCD from first principles. The effective Lagrangian with mesonic degrees of freedom in the hadronic phase should preserve the intrinsic symmetry of the underlying QCD theory. The chiral symmetry is not exactly preserved due to the small mass of light quarks in the QCD Lagrangian. But since our relevant energy scale is on the order of 100 MeV, we can expect the chiral currents to be approximately conserved [210, 211].

In order to consider the interactions between different species of mesons, including the strange sector, we assume a global chirally $SU(3)_L \times SU(3)_R$ symmetry. Similar to the non-linear sigma model, we have

$$U_3 = U = \exp\left[\frac{2i}{F_\pi}\sum_a \frac{\lambda_a \psi_a}{\sqrt{2}}\right] = \exp\left[\frac{2i}{F_\pi}\psi\right], \tag{16.1}$$

where ψ_a are real fields, $F_\pi = \sqrt{2} f_\pi$, $f_\pi = 93$ MeV is the π decay constant and $\lambda_a (a = 1, \ldots, 8)$ are the Gell-Mann matrices. ψ is the pseudo-scalar octet,

$$\psi = \begin{pmatrix} \frac{\pi^0}{\sqrt{2}} + \frac{\eta_8}{\sqrt{6}} & \pi^+ & K^+ \\ \pi^- & -\frac{\pi^0}{\sqrt{2}} + \frac{\eta_8}{\sqrt{6}} & K^0 \\ K^- & \bar{K}^0 & -\frac{2\eta_8}{\sqrt{6}} \end{pmatrix}, \tag{16.2}$$

Similarly, we can include the vector and axial vector octets for vector and axial vector mesons into the effective theory, respectively. The vector meson octet can be written as,

$$V = \lambda_a V_a = \begin{pmatrix} \frac{\rho^0}{\sqrt{2}} + \frac{\omega_8}{\sqrt{6}} & \rho^+ & K^{*+} \\ \rho^- & -\frac{\rho^0}{\sqrt{2}} + \frac{\omega_8}{\sqrt{6}} & K^{*0} \\ K^{*-} & \bar{K}^{*0} & -\frac{2\omega_8}{\sqrt{6}} \end{pmatrix}. \tag{16.3}$$

For axial vector mesons, we will only consider the a_1 meson, which occupies at the same place as the π in the pseudo-scalar octet. The vector and axial vector mesons are regarded as massive

gauge fields in our theory and are coupled to the light pseudo-scalar mesons through the covariant derivative,

$$D_\mu U = \partial_\mu U - ig_0 A^L_\mu U + ig_0 U A^R_\mu, \tag{16.4}$$

where,

$$A^L_\mu = \frac{1}{2}(V_\mu + A_\mu) \text{ and } A^R_\mu = \frac{1}{2}(V_\mu - A_\mu). \tag{16.5}$$

The complete Massive Yang-Mills Lagrangian [212] can be written as

$$\begin{aligned}\mathcal{L} &= \frac{1}{8}F_\pi^2 \mathrm{Tr}\{D_\mu U D^\mu U^\dagger\} + \frac{1}{8}F_\pi^2 \mathrm{Tr}\{M(U + U^\dagger - 2)\} \\ &\quad -\frac{1}{2}\mathrm{Tr}\{F^L_{\mu\nu}F^{L\mu\nu} + F^R_{\mu\nu}F^{R\mu\nu}\} + m_0^2 \mathrm{Tr}\{A^L_\mu A^{L\mu} + A^R_\mu A^{R\mu}\} \\ &\quad +\gamma \mathrm{Tr}\{F^L_{\mu\nu} U F^{R\mu\nu} U^\dagger\} - i\xi \mathrm{Tr}\{D_\mu U D_\nu U^\dagger F^{L\mu\nu} + D_\mu U^\dagger D_\nu U F^{R\mu\nu}\},\end{aligned} \tag{16.6}$$

where

$$F^{L,R}_{\mu\nu} = \partial_\mu A^{L,R}_\nu - \partial_\nu A^{L,R}_\mu - ig_0[A^{L,R}_\mu, A^{L,R}_\nu], \tag{16.7}$$

$$M = \frac{2}{3}\left[m_K^2 + \frac{1}{2}m_\pi^2\right] - \frac{2}{\sqrt{3}}(m_K^2 - m_\pi^2)\lambda_8. \tag{16.8}$$

The second line of Eq. (16.6) represents the kinetic and mass terms of the massive gauge fields. m_0, g_0, γ, and ξ are the parameters of the theory. The third line is added for phenomenological considerations [213]. The electromagnetic interaction is introduced by requiring an additional symmetry under local $U(1)$ transformations [214, 213]:

$$\delta U = i\epsilon[Q, U], \tag{16.9}$$

$$\delta A^{\mathrm{L,R}}_\mu = i\epsilon[Q, A^{\mathrm{L,R}}_\mu] + \frac{1}{g_0}Q\partial_\mu\epsilon, \tag{16.10}$$

where $\epsilon(x)$ is the infinitesimal $U(1)$ transformation parameter and

$$Q = \frac{\lambda_3}{2} + \frac{\lambda_8}{\sqrt{12}} = \begin{pmatrix} \frac{2}{3} & & \\ & -\frac{1}{3} & \\ & & -\frac{1}{3} \end{pmatrix}, \tag{16.11}$$

is the quark charge matrix. The Lagrangian (16.6) is invariant under $U(1)$ transformation except for the mass term of the vector and axial vector fields,

$$\delta\mathcal{L} = m_0^2 \frac{2}{g_0}\partial_\mu\epsilon \mathrm{Tr}\{Q(A^{\mathrm{L},\mu} + A^{\mathrm{R},\mu})\}. \tag{16.12}$$

In order to ensure the Lagrangian is invariant under $U(1)$, we need to add three additional terms [214, 213]

$$\mathcal{L}_1 + \mathcal{L}_2 + \mathcal{L}_3 = \frac{-2em_0^2}{g_0}\mathrm{Tr}\{Q(A^L_\mu + A^R_\mu)\}B^\mu - \frac{1}{4}(\partial_\mu B_\nu - \partial_\nu B_\mu)^2 + \frac{2e^2m_0^2}{g_0^2}B_\mu B^\mu \mathrm{Tr}\{Q^2\}, \tag{16.13}$$

Here B^μ stands for as the electromagnetic field. It transforms as

$$\delta B_\mu = \frac{1}{e}\partial_\mu \epsilon. \tag{16.14}$$

The variation of B_μ in $\delta\mathcal{L}_1$ cancels $\delta\mathcal{L}$ in Eq. (16.12). The variations of A^L_μ and A^R_μ in $\delta\mathcal{L}_1$ are canceled by $\delta\mathcal{L}_3$. In the end, the total Lagrangian $\mathcal{L}+\mathcal{L}_1+\mathcal{L}_2+\mathcal{L}_3$ is invariant under $U(1)$ transformation [214, 213].

However, if we expand $\mathcal{L}$ in Eq. (16.6) in terms of pseudo-scalar, vector and axial vector fields, we will get an unphysical mixing term, $\propto \partial_\mu \psi A^\mu$ from $\mathrm{Tr}\{D_\mu U D^\mu U^\dagger\}$. In order to get rid of this mixing term, we need to perform the following transformation, with γ being the coupling constant in front of the first term in the third line of Eq. (16.6):

$$V_\mu \to \frac{\tilde{V}_\mu}{\sqrt{1-\gamma}}, \tag{16.15}$$

$$A_\mu \to \frac{\tilde{A}_\mu}{\sqrt{1+\gamma}} + \frac{g_0 \tilde{F}_\pi}{2m_0^2}\left(\partial_\mu \tilde{\psi} - \frac{i\tilde{g}}{2}[\tilde{V}_\mu, \tilde{\psi}]\right), \tag{16.16}$$

$$\psi \to \frac{\tilde{\psi}}{Z}, \tag{16.17}$$

$$\tilde{g} = \frac{g_0}{\sqrt{1-\gamma}}, \tag{16.18}$$

$$Z = \sqrt{1-\frac{\tilde{g}^2\tilde{F}_\pi^2}{4m_V^2}}, \tilde{F}_\pi = \frac{F_\pi}{Z} = 135\mathrm{MeV}, \tag{16.19}$$

$$m_V = \frac{m_0}{\sqrt{1-\gamma}}, m_A = \frac{m_0}{Z\sqrt{1+\gamma}}. \tag{16.20}$$

We denote the $\tilde{\psi}, \tilde{V}_\mu$, and $\tilde{A}_\mu$ as the physical fields and m_V and m_A are the physical vector and axial vector meson masses, respectively. With this transformation, we find that $\mathcal{L}_1$ can be rewritten as,

$$\mathcal{L}_1 = -\frac{2em_V^2}{\tilde{g}} B_\mu \left[\frac{\rho_0^\mu}{\sqrt{2}} + \frac{\omega_8^\mu}{\sqrt{6}}\right] = -B_\mu(C_\rho m_\rho^2 \rho_0^\mu + C_\omega m_\omega^2 \omega^\mu + C_\phi m_\phi^2 \phi^\mu), \tag{16.21}$$

which has the same form as in the Vector Meson Dominance (VMD) Model [215]. In principle, the coefficients C_ρ, C_ω, and C_ϕ are determined by m_V and $\tilde{g}$. But we will take them as free parameters in the model and fit them to experimental measurements.

To compute the photon production from $2 \to 2$ scattering processes, we need to expand the Lagrangian $\mathcal{L}$ to get the interaction vertices:

$$\mathcal{L}_{VA\psi} = \frac{i\eta_2\tilde{g}}{2}\mathrm{Tr}\{(\partial_\mu \tilde{A}_\nu - \partial_\nu \tilde{A}_\mu)[\partial^\mu \tilde{V}^\nu, \tilde{\psi}]\} + \frac{i\eta_1\tilde{g}}{2}\mathrm{Tr}\{(\partial_\mu \tilde{V}_\nu - \partial_\nu \tilde{V}_\mu)[\tilde{A}^\mu, \partial^\nu \tilde{\psi}]\}, \tag{16.22}$$

$$\mathcal{L}_{V\psi\psi} = \frac{i\tilde{g}}{2}\mathrm{Tr}\{\tilde{V}_\mu[\partial^\mu \tilde{\psi}, \tilde{\psi}]\} + \frac{i\tilde{g}\delta}{2m_V^2}\mathrm{Tr}\{(\partial_\mu \tilde{V}_\nu - \partial_\nu \tilde{V}_\mu)\partial^\mu \tilde{\psi}\partial^\nu \tilde{\psi}\}, \tag{16.23}$$

$$\mathcal{L}_{VVV} = \frac{i\tilde{g}}{2}\mathrm{Tr}\{(\partial_\mu \widetilde{V}_\nu - \partial_\nu \tilde{V}_\mu)\tilde{V}^\mu \tilde{V}^\nu\}, \tag{16.24}$$

$$\begin{aligned}\mathcal{L}_{VV\psi\psi} &= -\frac{\tilde{g}^2}{8}\mathrm{Tr}\{[\tilde{V}_\mu, \tilde{\psi}]^2\} + \frac{\tilde{g}^2\delta}{4m_V^2}\mathrm{Tr}\{[\tilde{V}_\mu, \tilde{V}_\nu]\partial^\mu\tilde{\psi}\partial^\nu\tilde{\psi}\} \\ &+\frac{\tilde{g}^2\delta}{4m_V^2}\mathrm{Tr}\{(\partial_\mu\tilde{V}_\nu - \partial_\nu\tilde{V}_\mu)([\tilde{V}^\mu, \tilde{\psi}]\partial^\nu\tilde{\psi} + \partial^\mu\tilde{\psi}[\tilde{V}^\nu, \tilde{\psi}])\} \\ &+\frac{\tilde{g}^2 C_4}{2}\mathrm{Tr}\{(\partial_\mu\tilde{V}_\nu - \partial_\nu\tilde{V}_\mu)\tilde{\psi}(\partial^\mu\tilde{V}^\nu - \partial^\nu\tilde{V}^\mu)\tilde{\psi} - (\partial_\mu\tilde{V}_\nu - \partial_\nu\tilde{V}_\mu)^2\tilde{\psi}^2\},\end{aligned} \tag{16.25}$$

where

$$\eta_1 = \frac{\tilde{g}\tilde{F}_\pi}{2m_V^2}\sqrt{\frac{1-\gamma}{1+\gamma}} + \frac{4\xi Z^2}{\tilde{F}_\pi\sqrt{1+\gamma}}, \tag{16.26}$$

$$\eta_2 = \frac{\tilde{g}\tilde{F}_\pi}{2m_V^2}\sqrt{\frac{1-\gamma}{1+\gamma}} - \frac{4\gamma}{\tilde{F}_\pi\tilde{g}\sqrt{1+\gamma}}, \tag{16.27}$$

$$\delta = 1 - Z^2 - \frac{2Z^4\xi\tilde{g}}{(1-Z^2)\sqrt{1-\gamma}}, \tag{16.28}$$

$$C_4 = \frac{\tilde{g}^2\tilde{F}_\pi^2}{16m_V^4}\left(\frac{1+\gamma}{1-\gamma}\right) - \frac{\gamma}{m_V^2(1-\gamma)} + \frac{2\gamma}{\tilde{g}^2\tilde{F}_\pi^2(1-\gamma)}. \tag{16.29}$$

Using the properties of the Gell-Mann matrices, we can evaluate the commutator and trace in Eqs. (16.22) to (16.25). For the $V\psi\psi$ vertex, we obtain,

$$\mathcal{L}_{V\psi\psi} = -\frac{\tilde{g}}{\sqrt{2}}\left((1-\delta)f^{abc} + i\frac{\delta}{2}d^{abc}\right)\tilde{V}_\mu^a\partial^\mu\tilde{\psi}^b\tilde{\psi}^c, \tag{16.30}$$

where f^{abc} and d^{abc} are the antisymmetric and symmetric structure constants of the $SU(3)$ group. Next, we use Eqs. (16.2) and (16.3) to express the $\tilde{\psi}^a$ and $\tilde{V}^a$ fields in terms of the physical particle fields. For the $\pi^{\pm,0}$ and $\rho^{\pm,0}$, one finds, interactions,

$$\mathcal{L}_{\rho^0,\pi^\pm,\pi^\mp} = -\frac{i\tilde{g}}{\sqrt{2}}\left(1 - \frac{\delta}{2}\right)\rho_\mu^0(\pi^+\partial^\mu\pi^- - \pi^-\partial^\mu\pi^+), \tag{16.31}$$

$$\mathcal{L}_{\rho^+,\pi^-,\pi^0} = -\frac{i\tilde{g}}{\sqrt{2}}\left(1 - \frac{\delta}{2}\right)\rho_\mu^+(\pi^-\partial^\mu\pi^0 - \pi^0\partial^\mu\pi^-), \tag{16.32}$$

$$\mathcal{L}_{\rho^-,\pi^+,\pi^0} = -\frac{i\tilde{g}}{\sqrt{2}}\left(1 - \frac{\delta}{2}\right)\rho_\mu^-(\pi^0\partial^\mu\pi^0 - \pi^+\partial^\mu\pi^0). \tag{16.33}$$

Similarly, we can also get the interaction vertices for $K^\pm$, K^0, $\bar{K}^0$, and $\rho^{\pm,0}$ mesons from $\mathcal{L}_{V\psi\psi}$ in Eq. (16.30).

The interactions between pseudo-scalar, vector, and axial vector mesons in Eq. (16.22) can be simplified as

$$\mathcal{L}_{VA\psi} = -\frac{\eta_2\tilde{g}}{\sqrt{2}}f^{abc}(\partial_\mu\tilde{A}_\nu^a - \partial_\nu\tilde{A}_\mu^a)(\partial^\mu\tilde{V}^{b\nu})\tilde{\psi}^c + \frac{\eta_1\tilde{g}}{\sqrt{2}}f^{abc}\tilde{A}^{a\mu}(\partial_\mu\tilde{V}_\nu^b - \partial_\nu\tilde{V}_\mu^b)(\partial^\nu\tilde{\psi}^c). \tag{16.34}$$

So the interactions between $\pi^{\pm,0}$, $\rho^{\pm,0}$, and $a_1^{\pm,0}$ can be derived as

$$\mathcal{L}_{\rho^0,a_1^+,\pi^-} = -\frac{i\eta_2\tilde{g}}{\sqrt{2}}[(\partial_\mu a_{1\nu}^+ - \partial_\nu a_{1\mu}^+)(\partial^\mu \rho^{0\nu})\pi^-] + \frac{i\eta_1\tilde{g}}{\sqrt{2}} a_1^{+\mu}(\partial_\mu \rho_\nu^0 - \partial_\nu \rho_\mu^0)(\partial^\nu \pi^-), \tag{16.35}$$

$$\mathcal{L}_{\rho^0,a_1^-,\pi^+} = +\frac{i\eta_2\tilde{g}}{\sqrt{2}}[(\partial_\mu a_{1\nu}^- - \partial_\nu a_{1\mu}^-)(\partial^\mu \rho^{0\nu})\pi^+] - \frac{i\eta_1\tilde{g}}{\sqrt{2}} a_1^{-\mu}(\partial_\mu \rho_\nu^0 - \partial_\nu \rho_\mu^0)(\partial^\nu \pi^+), \tag{16.36}$$

$$\mathcal{L}_{\rho^+,a_1^-,\pi^0} = -\frac{i\eta_2\tilde{g}}{\sqrt{2}}[(\partial_\mu a_{1\nu}^+ - \partial_\nu a_{1\mu}^+)(\partial^\mu \rho^{+\nu})\pi^0] + \frac{i\eta_1\tilde{g}}{\sqrt{2}} a_1^{+\mu}(\partial_\mu \rho_\nu^- - \partial_\nu \rho_\mu^-)(\partial^\nu \pi^0), \tag{16.37}$$

$$\mathcal{L}_{\rho^-,a_1^+,\pi^0} = +\frac{i\eta_2\tilde{g}}{\sqrt{2}}[(\partial_\mu a_{1\nu}^+ - \partial_\nu a_{1\mu}^+)(\partial^\mu \rho^{-\nu})\pi^0] - \frac{i\eta_1\tilde{g}}{\sqrt{2}} a_1^{+\mu}(\partial_\mu \rho_\nu^- - \partial_\nu \rho_\mu^-)(\partial^\nu \pi^0). \tag{16.38}$$

The interactions between three vector mesons in Eq. (16.24) can be rewritten as

$$\mathcal{L}_{VVV} = \frac{i\tilde{g}}{2\sqrt{2}}(d^{abc} + if^{abc})(\partial_\mu \tilde{V}_\nu^a - \partial_\nu \tilde{V}_\mu^a)\tilde{V}^{b\mu}\tilde{V}^{c\nu}. \tag{16.39}$$

This helps us to get for the ρ^+, ρ^-, and ρ^0 interactions,

$$\mathcal{L}_{\rho^+\rho^-\rho^0} = \frac{i\tilde{g}}{\sqrt{2}}[(\partial_\mu \rho_\nu^+ - \partial_\nu \rho_\mu^+)\rho^{-\mu}\rho^{0\nu} - (\partial_\mu \rho_\nu^- - \partial_\nu \rho_\mu^-)\rho^{+\mu}\rho^{0\nu} + (\partial_\mu \rho_\nu^0 - \partial_\nu \rho_\mu^0)\rho^{+\mu}\rho^{-\nu}]. \tag{16.40}$$

Once we have the interaction vertices, we can derive the corresponding Feymann rules for the interaction vertices.

In the Massive Yang-Mills theory, we have 5 unknown parameters in the theory, m_0, ξ, γ, $\tilde{g}$, and C_ρ, [33] which need to be fixed in terms of the experimentally measured vector and axial vector meson masses and their decay widths, $(m_\rho, \Gamma_{\rho\to\pi\pi})$ and $(m_{a_1}, \Gamma_{a_1\to\pi\rho})$. For ρ^0 we have

$$m_\rho = \frac{m_0}{\sqrt{1-\gamma}}, \tag{16.41}$$

$$\Gamma_{\rho\to\pi\pi} = \frac{\tilde{g}^2\left(1-\frac{\delta}{2}\right)^2}{12\pi m_\rho^2}\left(\left(\frac{m_\rho}{2}\right)^2 - m_\pi^2\right)^{3/2}. \tag{16.42}$$

For the a_1 axial vector meson, one finds,

$$m_{a_1} = \frac{m_0}{Z\sqrt{1+\gamma}}, \tag{16.43}$$

$$\Gamma_{a_1\to\pi\rho} = \frac{1}{12\pi m_{a_1}^2}|q_\pi^a|\left[2g_{a_1\rho\pi}^2 + \left(g_{a_1\rho\pi}\left(\frac{E_\rho}{m_\rho}\right) + \frac{m_{a_1}}{m_\rho}|q_\pi^a|^2 h_{a_1\rho\pi}\right)^2\right], \tag{16.44}$$

where $g_{a_1\rho\pi} = \frac{\tilde{g}}{\sqrt{2}}[(\eta_2-\eta_1)E_\rho m_{a_1} + \eta_1 m_\rho^2]$, $h_{a_1\rho\pi} = \frac{\tilde{g}}{\sqrt{2}}(\eta_1-\eta_2)$, $E_\rho = \frac{m_{a_1}^2+m_\rho^2-m_\pi^2}{2m_{a_1}}$, and $|q_\pi^a| = \sqrt{\left(\frac{m_{a_1}^2+m_\rho^2-m_\pi^2}{2m_{a_1}}\right)^2 - m_\rho^2}$.

[33] C_ω and C_ϕ can be fit to the decay branch of ω and ϕ mesons, respectively. It turns out that they are ~ 10 smaller compared to C_ρ. So the photon emission processes that involve these particles are subdominant and hence being ignored here.

Using Eq. (16.41) to Eq. (16.44), we can get the vaules of m_0, ξ, γ, and $\tilde{g}$,

$$\tilde{g} = 6.4483, \gamma = -0.2913, \xi = 0.0585, m_0 = 0.875. \tag{16.45}$$

The parameter C_ρ can be fixed using the ρ meson decay branch, $\rho \to e^+e^-$,

$$\Gamma_{\rho\to e^+e^-} = \frac{\alpha_{\rm EM} C_\rho^2 m_\rho}{3} \tag{16.46}$$

from which one can get $C_\rho = 0.059$.

Now, all the parameters in the model have been fixed. We can use this theory to calculate the matrix elements for various $2 \to 2$ scattering processes involved in photon production. There are in total 8 important reaction channels in the hadronic phase that will produce photons. They are listed here:

- $\pi + \rho \to \pi + \gamma$,
- $\pi + \rho \to \omega \to \pi + \gamma$,
- $\pi + \pi \to \rho + \gamma$,
- $\pi + \rho \to \pi + \gamma$,
- $\rho \to \pi + \pi + \gamma$,
- $\pi + K^* \to K + \gamma$,
- $\pi + K \to \bar{K}^* + \gamma$,
- $\rho + K \to \bar{K} + \gamma$,
- $K + K^* \to \pi + \gamma$.

16.2 Kinematics: $2 \to 2$ scattering processes

According to relativistic kinetic theory, the real photon emission rates from $1 + 2 \to 3 + \gamma$ processes can be calculated from the following phase space integrals:

$$\begin{aligned} E_q \frac{dR}{d^3q} &= \int \frac{d^3p_1}{2E_1(2\pi)^3} \frac{d^3p_2}{2E_2(2\pi)^3} \frac{d^3p_3}{2E_3(2\pi)^3} \frac{2\pi}{2} |\mathcal{M}|^2 \delta^{(4)}(p_1 + p_2 - p_3 - q) \\ &\times f(p_1) f(p_2)(1 \pm f(p_3)). \end{aligned} \tag{16.47}$$

In the local rest frame, following the same procedure as our derivations in the QGP phase from the last chapter, we assume for the particle distribution functions the following form:

$$f(p) = f_0(E) + \delta f = f_0(E) + f_0(E)(1 \pm f_0(E))\frac{\hat{p}^\mu \hat{p}^\nu \pi_{\mu\nu}}{2(e+P)}\chi\left(\frac{p}{T}\right), \tag{16.48}$$

Here $\chi(p)$ is only a function of the magnitude of p, $\chi(p/T) \propto (p/T)^\alpha$ and $1 \leq \alpha \leq 2$. Different from the derivation in the last chapter, the distribution functions for mesons we considered here contain non-zero rest masses in their equilibrium distribution functions. We include $(1 - f_0(E))$ factor in the derivations for the bayronic case for future extension.

In Appendix F.1, we work out the phase space limits in detail. Eq. (16.47) gives

$$\begin{aligned} E_q\frac{dR}{d^3q} &= \frac{1}{32(2\pi)^8 q}\int_{s_{\min}}^{\infty} ds \int_{t_{\min}}^{t_{\max}} dt \int_{E_{1\min}}^{\infty} dE_1 \int_{E_{2\min}}^{E_{2\max}} dE_2 \int_0^{2\pi} d\phi_1 \sum_{\phi_2 = \phi_{2\pm}} \\ &\quad \times |M|^2 \frac{1}{\sqrt{aE_2^2 + 2bE_2 + c}} f(p_1^\mu) f(p_2^\mu)(1 \pm f(p_3^\mu)), \end{aligned} \tag{16.49}$$

where the coefficients a, b, and c are specified in Appendix F.1. We now expand the particle distribution functions in Eq. (16.48):

$$\begin{aligned} f(p_1^\mu)f(p_2^\mu)(1 \pm f(p_3^\mu)) &= \left(f_0(E_1) + f_0(E_1)(1 \pm f_0(E_1))\frac{\hat{p}_{1\mu}\hat{p}_{1\nu}\pi^{\mu\nu}}{2(e+p)}\chi\left(\frac{p_1}{T}\right)\right) \\ &\times \left(f_0(E_2) + f_0(E_2)(1 \pm f_0(E_2))\frac{\hat{p}_{2\mu}\hat{p}_{2\nu}\pi^{\mu\nu}}{2(e+p)}\chi\left(\frac{p_2}{T}\right)\right) \\ &\times \left(1 \pm f_0(E_3) \pm f_0(E_3)(1 \pm f_0(E_3))\frac{\hat{p}_{3\mu}\hat{p}_{3\nu}\pi^{\mu\nu}}{2(e+p)}\chi\left(\frac{p_3}{T}\right)\right) \\ &= f_0(E_1)f_0(E_2)(1 \pm f_0(E_3)) + \frac{\pi^{\mu\nu}}{2(e+p)} \times \\ &\quad \Bigg[f_0(E_1)(1 \pm f_0(E_1))f_0(E_2)(1 \pm f_0(E_3))\hat{p}_{1\mu}\hat{p}_{1\nu}\chi\left(\frac{p_1}{T}\right) \\ &+ f_0(E_1)f_0(E_2)(1 \pm f_0(E_2))(1 \pm f_0(E_3))\hat{p}_{2\mu}\hat{p}_{2\nu}\chi\left(\frac{p_2}{T}\right) \\ &\pm f_0(E_1)f_0(E_2)f_0(E_3)(1 \pm f_0(E_3))\hat{p}_{3\mu}\hat{p}_{3\nu}\chi\left(\frac{p_3}{T}\right)\Bigg] \\ &+ O((\delta f)^2). \end{aligned} \tag{16.50}$$

Using the tensor projection operator Eq. (15.6), the photon production rate can be decomposed into a dominant equilibrium part and its corresponding first order viscous correction,

$$q\frac{dR}{d^3q} = \Gamma_0(q,T) + \frac{\pi^{\mu\nu}\hat{q}_\mu\hat{q}_\nu}{2(e+P)}a_{\alpha\beta}\Gamma^{\alpha\beta}(q,T), \tag{16.51}$$

where

$$\begin{aligned} \Gamma_0 &= \frac{1}{16(2\pi)^7 q}\int_{s_{\min}}^{\infty} ds \int_{t_{\min}}^{t_{\max}} dt \int_{E_{1\min}}^{\infty} dE_1 \int_{E_{2\min}}^{E_{2\max}} dE_2 \\ &\quad |M|^2 \frac{1}{\sqrt{aE_2^2 + 2bE_2 + c}} f_0(E_1)f_0(E_2)(1 \mp f_0(E_3)). \end{aligned} \tag{16.52}$$

and the off-equilibrium contribution is

$$\begin{aligned}
\Gamma_1(q,T) &= a_{\mu\nu}\Gamma^{\mu\nu}(q,T) \\
&= \frac{1}{16(2\pi)^7 q}\int_{s_{\min}}^{\infty} ds \int_{t_{\min}}^{t_{\max}} dt \int_{E_{1\min}}^{\infty} dE_1 \int_{E_{2\min}}^{E_{2\max}} dE_2 \\
&\times \; |M|^2 \frac{1}{\sqrt{aE_2^2+2bE_2+c}} f_0(E_1) f_0(E_2)(1 \pm f_0(E_3)) \\
&\times \; \Bigg[(1 \pm f_0(E_1))\chi\left(\frac{p_1}{T}\right)\left(-\frac{1}{2}+\frac{3}{2}\cos^2\theta_1\right) \\
&\quad +(1 \pm f_0(E_2))\chi\left(\frac{p_2}{T}\right)\left(-\frac{1}{2}+\frac{3}{2}\cos^2\theta_2\right) \\
&\quad \pm f_0(E_3)\chi\left(\frac{p_3}{T}\right)\left(-\frac{1}{2}+\frac{3}{2}\frac{(p_1\cos\theta_1+p_2\cos\theta_2-E_q)^2}{p_3^2}\right)\Bigg]. \qquad (16.53)
\end{aligned}$$

The remaining 4 integrals in Eq. (16.52) and Eq. (16.53) have to be calculated numerically. For given s, t, E_1, E_2, we have

$$p_{1(2,3)} = \sqrt{E_{1(2,3)}^2 - m_{1(2,3)}^2} \qquad (16.54)$$

$$E_3 = E_1 + E_2 - E_q \qquad (16.55)$$

$$\cos\theta_1 = \frac{-s-t+m_2^2+m_3^2+2E_1E_q}{2p_1E_q} \qquad (16.56)$$

$$\cos\theta_2 = \frac{t-m_2^2+2E_2E_q}{2p_2E_q} \qquad (16.57)$$

16.3 Kinematics: $1 \to 3$ decay processes

During the evolution of the hot dense hadronic phase, ρ mesons can be regenerated through $\pi + \pi$ scattering and then they decay back to $\pi + \pi$ in the medium. The ρ meson has a small branching ratio to decay into the $\pi+\pi+\gamma$ final state, generating a photon. This contribution can not be subtracted experimentally from the total photon yield. So in the calculation of the direct photons, one must include the contributions from these ρ in-medium decays. For the process $\rho \to \pi + \pi + \gamma$, although its matrix elements can be easily obtained from $\pi + \rho \to \pi + \gamma$ using crossing symmetry , the structure of the kinematic integration limits is rather different from that of the $2 \to 2$ scattering processes. So we here deal with it differently.

The differential decay rate of an unstable particle A to a given final state is [216],

$$d\Gamma = \frac{1}{2m_A}\left(\prod_f \frac{d^3p_f}{(2\pi)^3 2E_f}\right)|\mathcal{M}(m_A \to p_f)|^2(2\pi)^4\delta^{(4)}(p_A - \sum_f p_f). \qquad (16.58)$$

So the total decay rate of the process $1 \to 2+3+\gamma$ can be calculated by,

$$\Gamma = \frac{1}{2E_1}\int \frac{d^3p_2}{(2\pi)^3 2E_2}\frac{d^3p_3}{(2\pi)^3 2E_3}\frac{d^3q}{(2\pi)^3 2E_q}|\mathcal{M}|^2(2\pi)^4\delta^{(4)}(p_1-p_2-p_3-q). \qquad (16.59)$$

The decay rate is formally defined by

$$\Gamma = \frac{\text{number of decays per unit time}}{\text{number of particles present}}. \tag{16.60}$$

We can get the photon emission rate per unit volume as

$$R = \frac{1}{V}\sum_{E_1} dE_1 g(E_1) f(E_1)\Gamma, \tag{16.61}$$

where $g(E)$ is the density of the states and $f(E)$ is the thermal distribution function. In the thermodynamic limit, $V \to \infty$, we have,

$$\sum_{E_1} dE_1 g(E_1) \to \int d^3x \frac{d^3p_1}{(2\pi)^3} = V\int \frac{d^3p_1}{(2\pi)^3}. \tag{16.62}$$

Thus, the differential photon emission rate can be calculated as,

$$\begin{aligned} E_q\frac{d^3R}{d^3q} &= \int \frac{d^3p_1}{(2\pi)^3 2E_1}\frac{d^3p_2}{(2\pi)^3 2E_2}\frac{d^3p_3}{(2\pi)^3 2E_3}\frac{2\pi}{2}\delta^{(4)}(p_1 - p_2 - p_3 - q)|\mathcal{M}|^2 \\ &\times f(E_1)(1 \pm f(E_2))(1 \pm f(E_3)). \end{aligned} \tag{16.63}$$

After some simplifications shown in Appendix F.2, we obtain,

$$\begin{aligned} E_q\frac{dR}{d^3q} &= \frac{1}{32(2\pi)^8 E_q}\int_{s'_{\min}}^{s'_{\max}} ds' \int_{t'_{\min}}^{t'_{\max}} dt' \int_{E_{1\min}}^{\infty} dE_1 \int_{E_{2\min}}^{E_{2\max}} dE_2 \int_0^{2\pi} d\phi_1 \sum_{\phi_2 = \phi_{2\pm}} \\ &|\mathcal{M}|^2 f(E_1)(1 \pm f(E_2))(1 \pm f(E_1 + E_2 - E_q))\frac{1}{\sqrt{a'E_2^2 + 2b'E_2 + c'}}, \end{aligned} \tag{16.64}$$

where the definitions of s', t' and the coefficients a', b', and c' are specified in Appendix F.2. The product of distribution functions can be expanded to linear order in $\pi^{\mu\nu}$ as follows:

$$\begin{aligned} &f(p_1)(1 \pm f(p_2))(1 \pm f(p_3)) = \\ &\quad\left[f_0(E_1) + f_0(E_1)(1 \pm f_0(E_1))\frac{\hat{p}_1^\mu \hat{p}_1^\nu \pi_{\mu\nu}}{2(e+P)}\chi\left(\frac{p_1}{T}\right)\right] \\ &\quad\times\left[1 \pm f_0(E_2) \pm f_0(E_2)(1 \pm f_0(E_2))\frac{\hat{p}_2^\mu \hat{p}_2^\nu \pi_{\mu\nu}}{2(e+P)}\chi\left(\frac{p_2}{T}\right)\right] \\ &\quad\times\left[1 \pm f_0(E_3) \pm f_0(E_3)(1 \pm f_0(E_3))\frac{\hat{p}_3^\mu \hat{p}_3^\nu \pi_{\mu\nu}}{2(e+P)}\chi\left(\frac{p_3}{T}\right)\right] \\ &\quad= f_0(E_1)(1 \pm f_0(E_2))(1 \pm f_0(E_3))\Bigg[1 + \\ &\qquad+\frac{\pi_{\mu\nu}}{2(e+P)}\Bigg((1 \pm f_0(E_1))\hat{p}_1^\mu \hat{p}_1^\nu \chi\left(\frac{p_1}{T}\right) \pm f_0(E_2)\hat{p}_2^\mu \hat{p}_2^\nu \chi\left(\frac{p_2}{T}\right) \\ &\qquad\pm f_0(E_3)\hat{p}_3^\mu \hat{p}_3^\nu \chi\left(\frac{p_3}{T}\right)\Bigg)\Bigg] \end{aligned} \tag{16.65}$$

The photon production rate can now be written in the form of Eq. (16.51), with

$$\begin{aligned}\Gamma_0 &= \frac{1}{16(2\pi)^7 q}\int_{s'_{\rm min}}^{s'_{\rm max}} ds' \int_{t'_{\rm min}}^{t'_{\rm max}} dt' \int_{E_{1\rm min}}^{\infty} dE_1 \int_{E_{2\rm min}}^{E_{2\rm max}} dE_2 \\ &\quad |\mathcal{M}|^2 \frac{1}{\sqrt{a'E_2^2+2b'E_2+c'}} f_0(E_1)(1\pm f_0(E_2))(1\pm f_0(E_3)) \end{aligned} \tag{16.66}$$

and

$$\begin{aligned}\Gamma_1(q,T) &= a_{\mu\nu}\Gamma^{\mu\nu}(q,T) \\ &= \frac{1}{16(2\pi)^7 q}\int_{s'_{\rm min}}^{s'_{\rm max}} ds' \int_{t'_{\rm min}}^{t'_{\rm max}} dt' \int_{E_{1\rm min}}^{\infty} dE_1 \int_{E_{2\rm min}}^{E_{2\rm max}} dE_2 \\ &\times |\mathcal{M}|^2 \frac{1}{\sqrt{a'E_2^2+2b'E_2+c'}} f_0(E_1)(1\pm f_0(E_2))(1\pm f_0(E_3)) \\ &\times \left[(1\pm f_0(E_1))\chi\left(\frac{p_1}{T}\right)\left(-\frac{1}{2}+\frac{3}{2}\cos^2\theta_1\right)\right. \\ &\quad \pm f_0(E_2)\chi\left(\frac{p_2}{T}\right)\left(-\frac{1}{2}+\frac{3}{2}\cos^2\theta_2\right) \\ &\quad \left.\pm f_0(E_3)\chi\left(\frac{p_3}{T}\right)\left(-\frac{1}{2}+\frac{3}{2}\frac{(p_1\cos\theta_1-p_2\cos\theta_2-E_q)^2}{p_3^2}\right)\right]. \end{aligned} \tag{16.67}$$

The remaining four integrals in Eqs. (16.66) and (16.67) have to be calculated numerically. For given s', t', E_1, E_2, we have

$$p_{1(2,3)} = \sqrt{E_{1(2,3)}^2 - m_{1(2,3)}^2} \tag{16.68}$$

$$E_3 = E_1 - E_2 - E_q \tag{16.69}$$

$$\cos\theta_1 = \frac{-s'-t'+m_2^2+m_3^2+2E_1E_q}{2p_1E_q} \tag{16.70}$$

$$\cos\theta_2 = \frac{-t'+m_2^2+2E_2E_q}{2p_2E_q} \tag{16.71}$$

16.4 Numerical Results

In this section we perform the remaining four integrals in Eqs. (16.52, 16.53, 16.66, 16.67) numerically, using gaussian quadratures to achieve good accuracy, and graph the results.

16.4.1 Thermal equilibrium rates

At the end of Sec. 16.1, we listed the eight dominant photon production channels in the hadronic phase. We will here compare them channel by channel, as well as the total equilibrium emission rates against parameterizations given in [182]. Each reaction channel involves 4 to 5 Feynman diagrams which need to be summed up coherently. So the squared matrix elements

usually contain 16 to 25 terms for each channel, and each term is quite lengthy. In order to reduce coding typos, we use `Mathematica` with the `Feyncalc` package to perform the contractions for all the terms in the matrix elements squared. The Ward identities are checked for each channel.

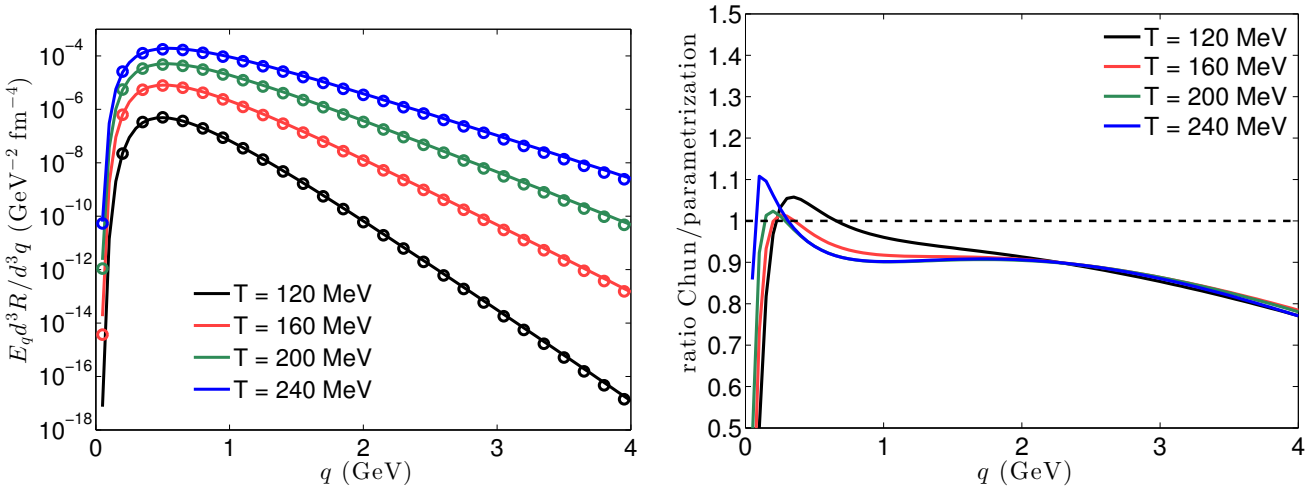

Figure 16.1: Check our thermal photon emission rate (open dots) $\Gamma_0(q,T)$ for channel $\pi+\rho\to(a_1,\rho,\pi)\to\pi+\gamma$ against the parameterization (solid curve) from [182] at four different temperatures ranging from 120 MeV to 240 MeV.

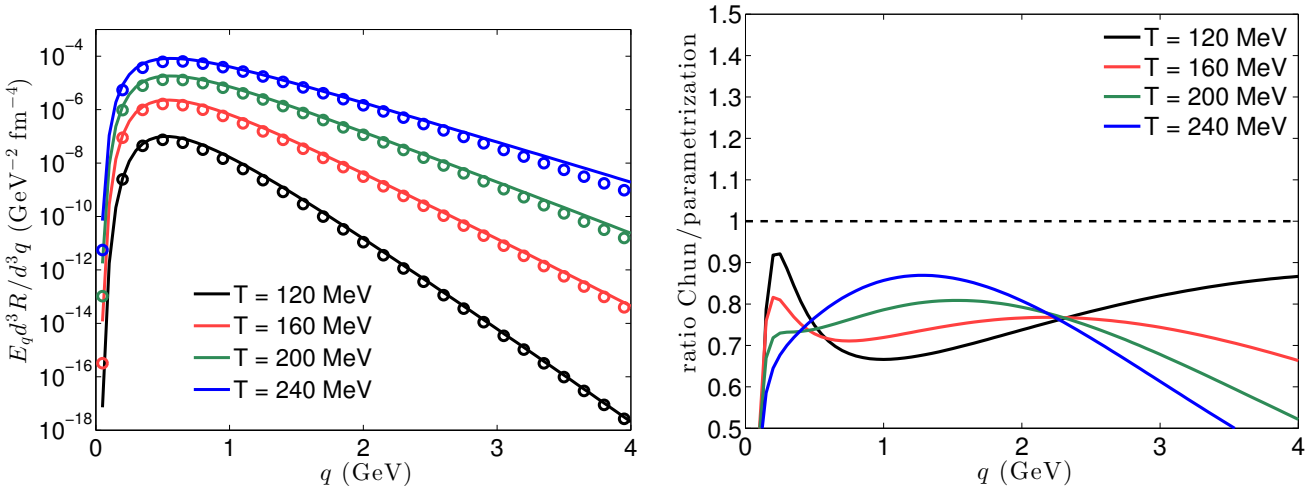

Figure 16.2: Similar as Fig. 16.1 but for channel $\pi+\rho\to\omega\to\pi+\gamma$ (t-channel only)

In Fig. 16.1, we show the photon emission rate for the reaction channel $\pi+\rho\to\pi+\gamma$ at four different temperatures. In the left panel, we compare our numerical results (open dots) with the parameterization [182] (solid line). For this comparison, no non-equilibrium chemical potentials are included in either calculation. On a logarithmic scale, we get a fair agreement. In order to better quantify the difference, the ratio between the two sets of calculations is shown in the right panel. In the very low q region, $q<0.1$, the ratio varies rapidly due to the steep threshold suppression which is not well captured by the parameterization [182]. For $0.5\leq q\leq 4$ GeV, the ratio stays around 0.9 and is basically flat as a function of q through the temperature region that

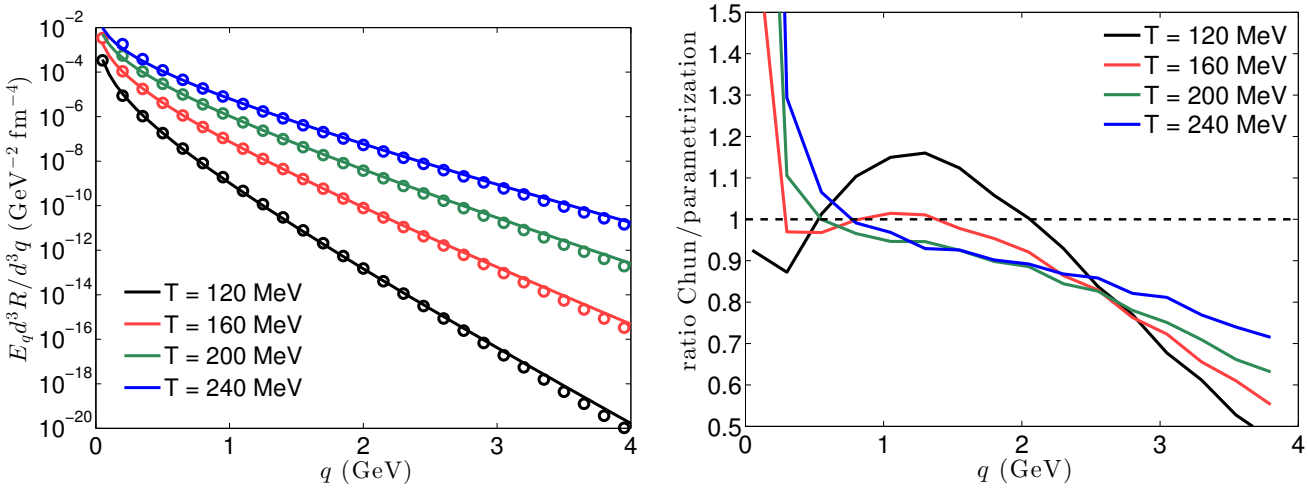

Figure 16.3: Similar as Fig. 16.1 but for channel $\pi + \pi \to \rho + \gamma$

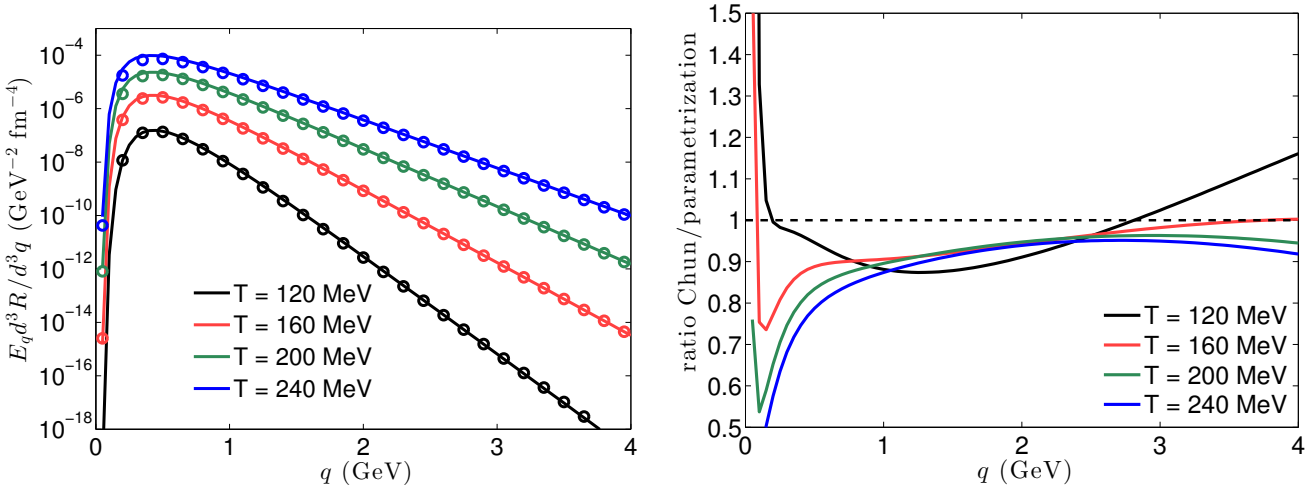

Figure 16.4: Similar as Fig. 16.1 but for channel $\pi + K^* \to K + \gamma$

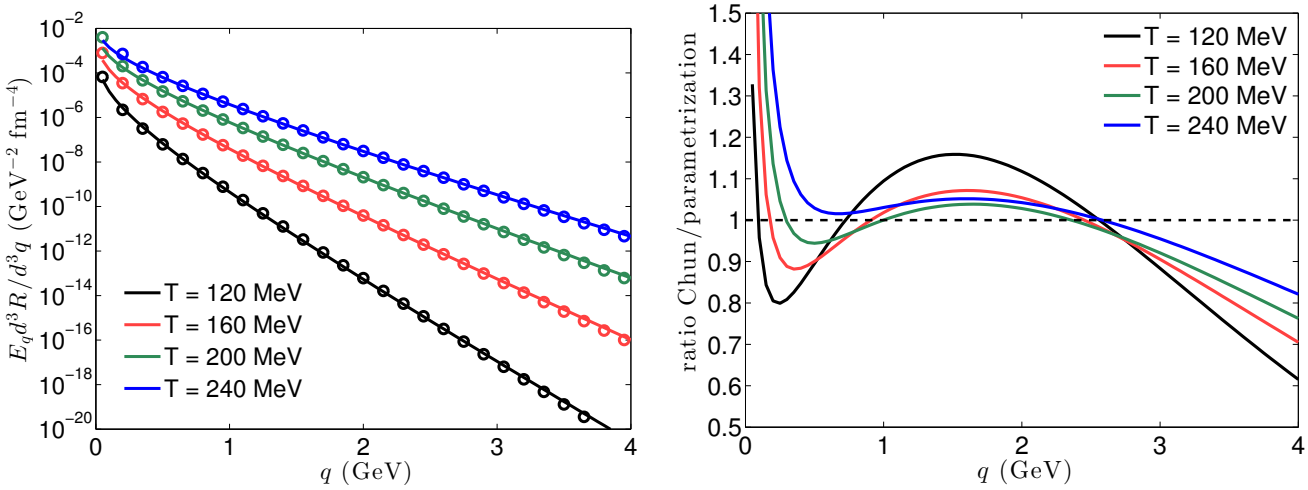

Figure 16.5: Similar as Fig. 16.1 but for channel $\pi + K \to K^* + \gamma$

we are interested in. Overall, the parameterization given in [182] is accurate within 15-20% in this q region.

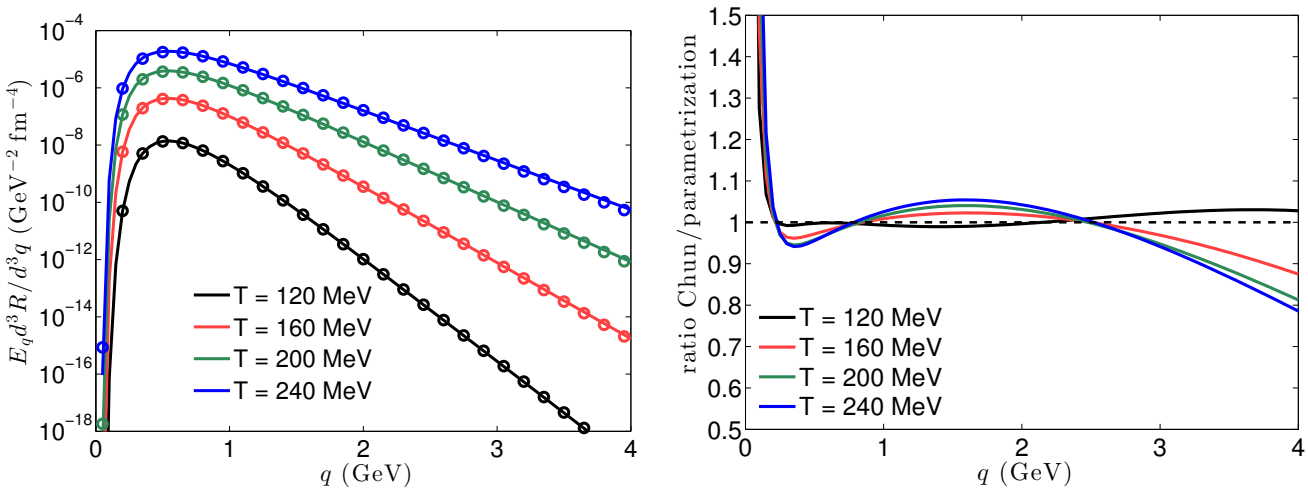

Figure 16.6: Similar as Fig. 16.1 but for channel $\rho + K \to K + \gamma$

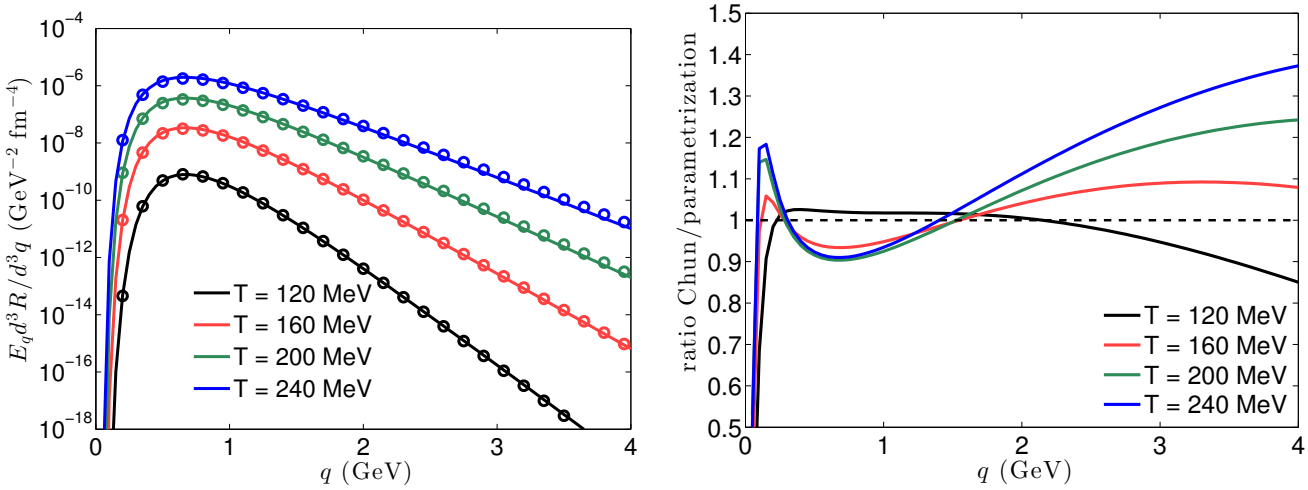

Figure 16.7: Similar as Fig. 16.1 but for channel $K + K^* \to \pi + \gamma$

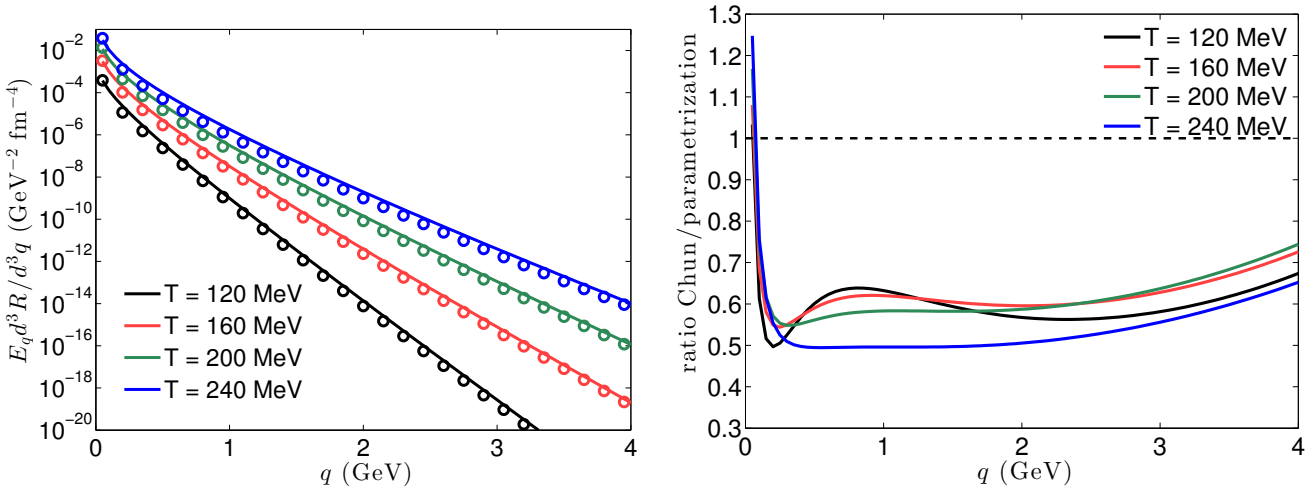

Figure 16.8: Photon emission rate check. $\rho \to \pi + \pi + \gamma$

For the channel $\pi + \rho \to \omega \to \pi + \gamma$, only the t-channel diagram is included in the final results of [182] because the contribution from the s-channel diagram is calculated in the in-medium

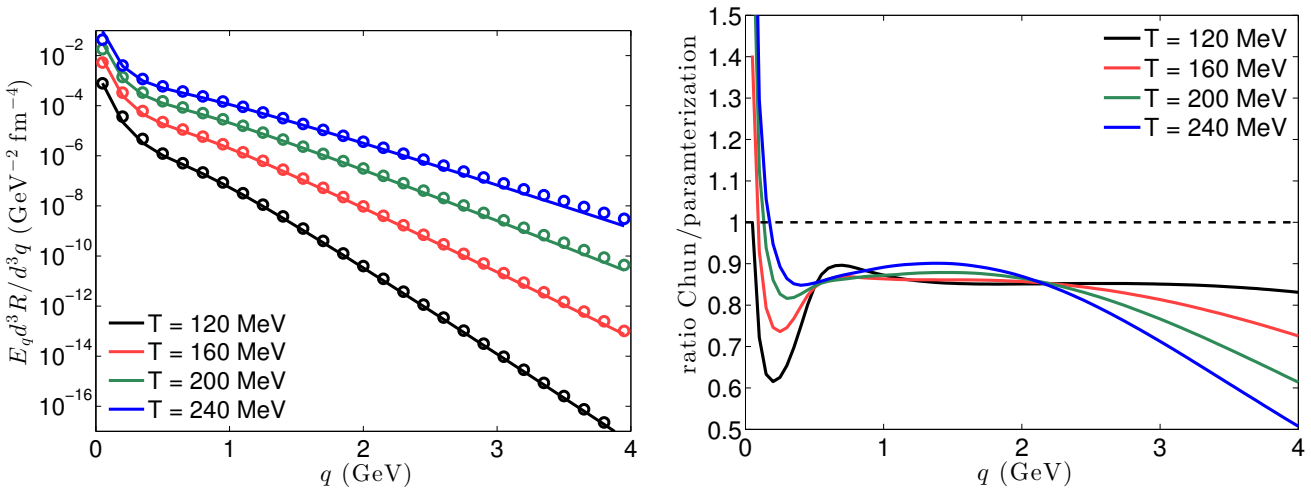

Figure 16.9: Similar as Fig. 16.1 but for total thermal photon emission rate from hadronic phase.

ρ calculations in [182, 211]. And the cross term between s and t-channels is relatively small [211]. The comparisons are shown in Fig. 16.2. Our rates are about 30% smaller than the parametrization. Fig. 16.3 shows the analogous results for the $\pi + \pi \to \rho + \gamma$ channel. Here our numerical calculations are significantly below the parameterization for large q. Figs. 16.4 to 16.7 shows analogous comparisons for the $2 \to 2$ reaction channels involving strange sector mesons. Our numerical results agree with the parameterizations very well. However, in Fig. 16.8, these numerical results is almost a factor of 2 smaller than the parameterization. I have been unable to tract the origin for this discrepancy, which must be sorted out in the future.

Finally, Fig. 16.9 shows the total thermal photon emission rate (sum over all eight channels). We find that our numerical results agree fairly well with the parameterization.

16.4.2 Viscous corrections

Now, we proceed to discuss the numerical results for the viscous correction to the photon emission rates as defined in Eq. (16.53). The first order viscous correction to the photon emission rates comes in the combination, $\frac{\pi^{\mu\nu}\hat{q}_\mu\hat{q}_\nu}{2(e+P)}\Gamma_1(q,T)$. The prefactor $\frac{\pi^{\mu\nu}\hat{q}_\mu\hat{q}_\nu}{2(e+P)}$ is controlled by the local thermodynamic and dissipative properties of the medium obtained from the hydrodynamic evolution. Its size depends on the details of the collision system. In order to get some feeling for the size of the viscous correction, we will compare the relative size of $\Gamma_1(q,T)$ to its equilibrium partner, $\Gamma_0(q,T)$. For this we can construct the ratio

$$r_{\rm vis}(q,T) = \frac{\Gamma_1}{\Gamma_0}\frac{1}{\chi\left(\frac{q}{T}\right)}. \tag{16.72}$$

For charged hadrons, we can define an analogous ratio with distribution functions, as in Eq. (16.48),

$$r_{\rm vis}^{\rm had}(q,T) = \frac{\delta f}{f_0}\frac{1}{\chi(\frac{q}{T})} \tag{16.73}$$

this ratio simply becomes $r_{\rm vis}^{\rm had}(E,T) = 1 \pm f_0(E)$, "+" for bosons and "−" for fermions. With finite rest masses, we expect $r_{\rm vis}^{\rm had}$ to be close to 1 for hadrons, except for π at low energy. So any deviation of this ratio from 1 for photons will expose the detailed non-trivial structure of its viscous corrections.

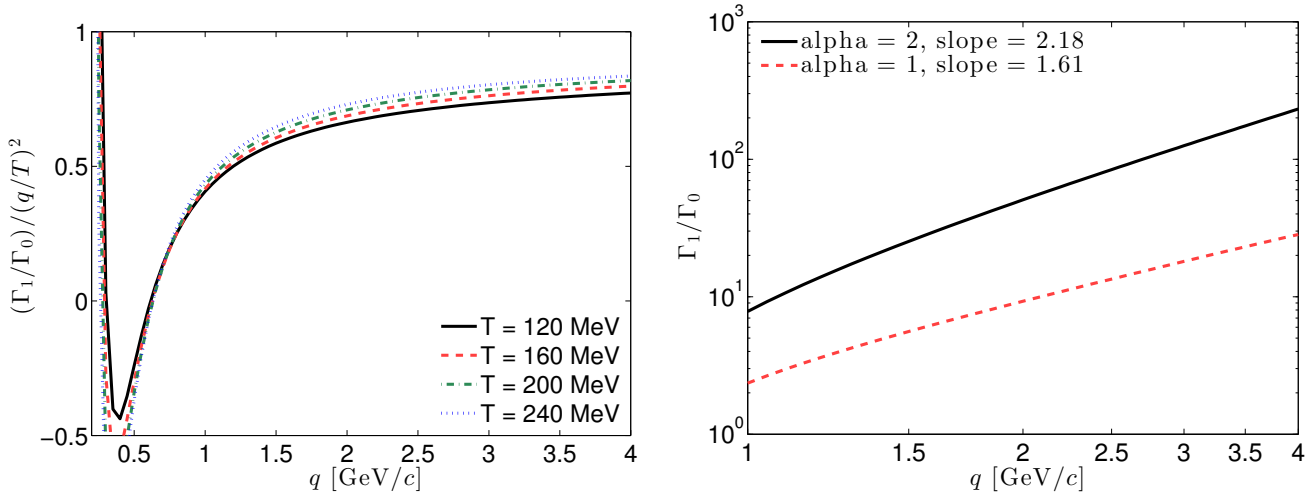

Figure 16.10: Left panel: The ratio between the viscous correction to its equilibrium rate for the channel $\pi + \rho \to (a_1, \rho, \pi) \to \pi + \gamma$ divided by $(q/T)^2$. (We take $\alpha = 2$ in $\chi\left(\frac{p}{T}\right)$ in the δf corrections for the hadrons.) Right panel: log-log plot for the ratio of Γ_1/Γ_0 with different α-dependence in $\chi\left(\frac{p}{T}\right) \propto \left(\frac{p}{T}\right)^\alpha$ in Eq. (16.53).

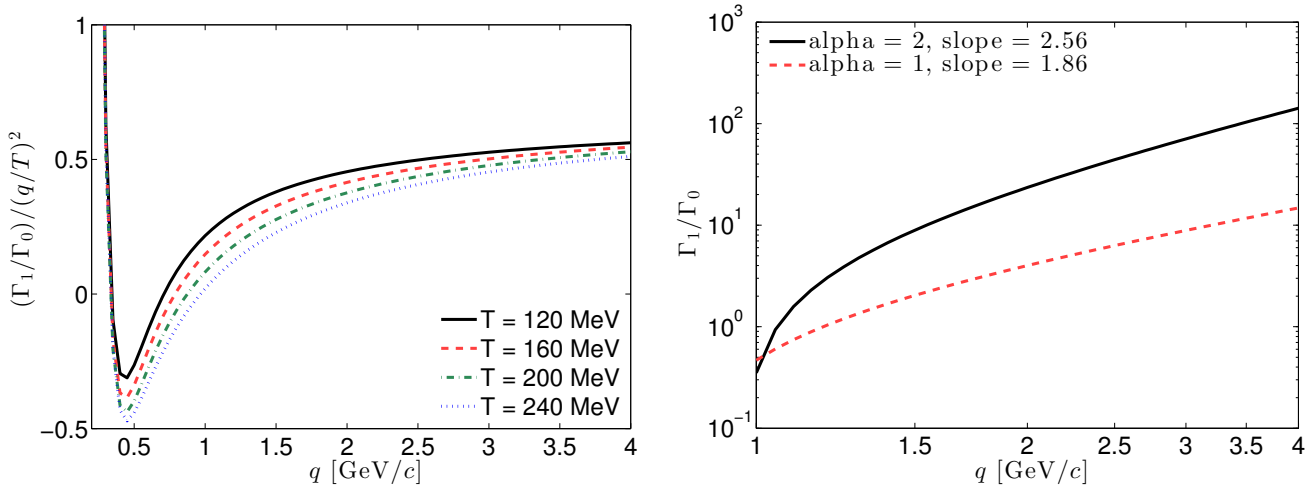

Figure 16.11: Similar as Fig. 16.10, but for $\pi + \rho \to \omega \to \pi + \gamma$.

In the left panel of Fig. 16.10, we show the ratio $r_{\rm vis}$ from Eq. (16.72) for channel $\pi + \rho \to (a_1, \rho, \pi) \to \pi + \gamma$ at four different temperatures. We find that for photons $r_{\rm vis}$ shows interesting structures as a function of photon momentum. Even though we start with a quadratic form of δf as in Eq. (16.48) for the particles involved in the underlying reaction, after all phase-space integrations are done the viscous correction to photon emission is formed not to be quadratic in photon momentum for small q. For $q > 2$ GeV, $r_{\rm vis}$ becomes flat, which indicates that the viscous

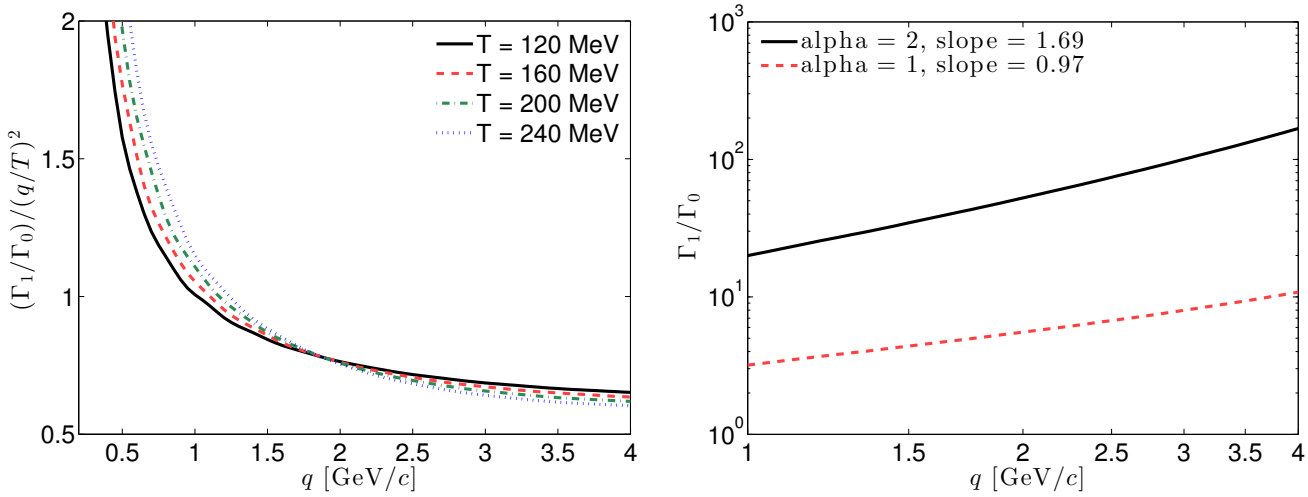

Figure 16.12: Similar as Fig. 16.10, but for $\pi + \pi \to \rho + \gamma$.

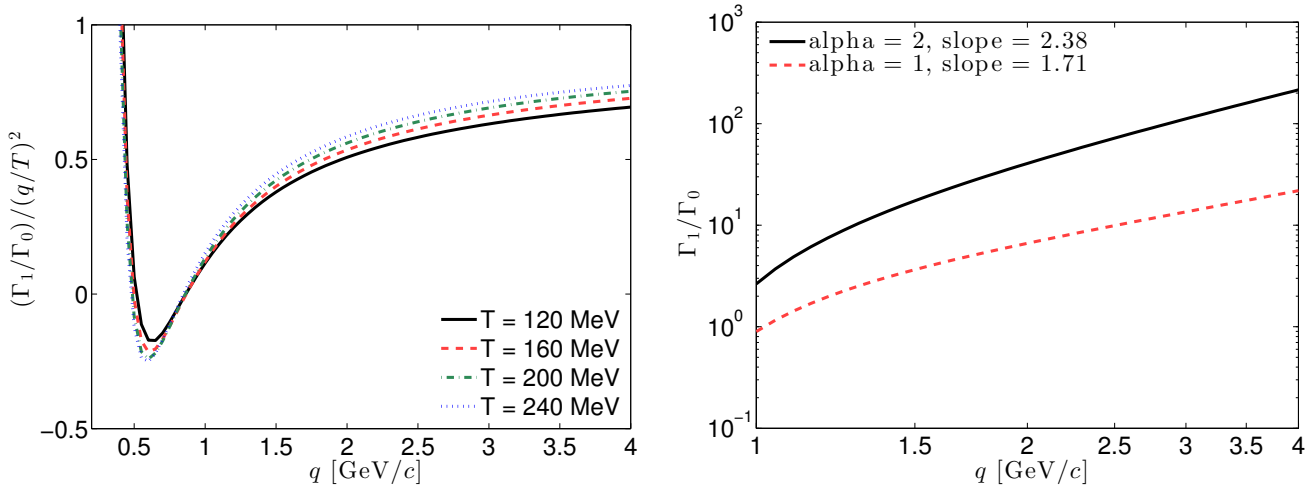

Figure 16.13: Similar as Fig. 16.10, but for $\pi + K^* \to K + \gamma$

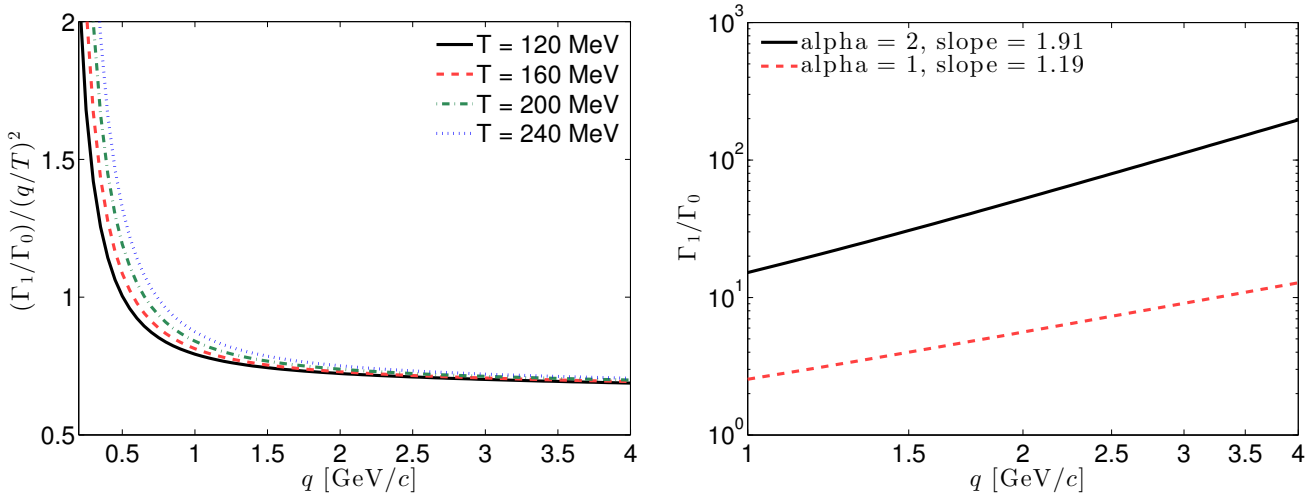

Figure 16.14: Similar as Fig. 16.10, but for $\pi + K \to K^* + \gamma$

correction becomes roughly quadratic in photon momentum at asymptotically large q. The size of $r_{\rm vis}$ varies from -0.5 to 0.7 for $0.3 < q < 4$ GeV. Since the absolute value of $r_{\rm vis}$ is smaller than 1,

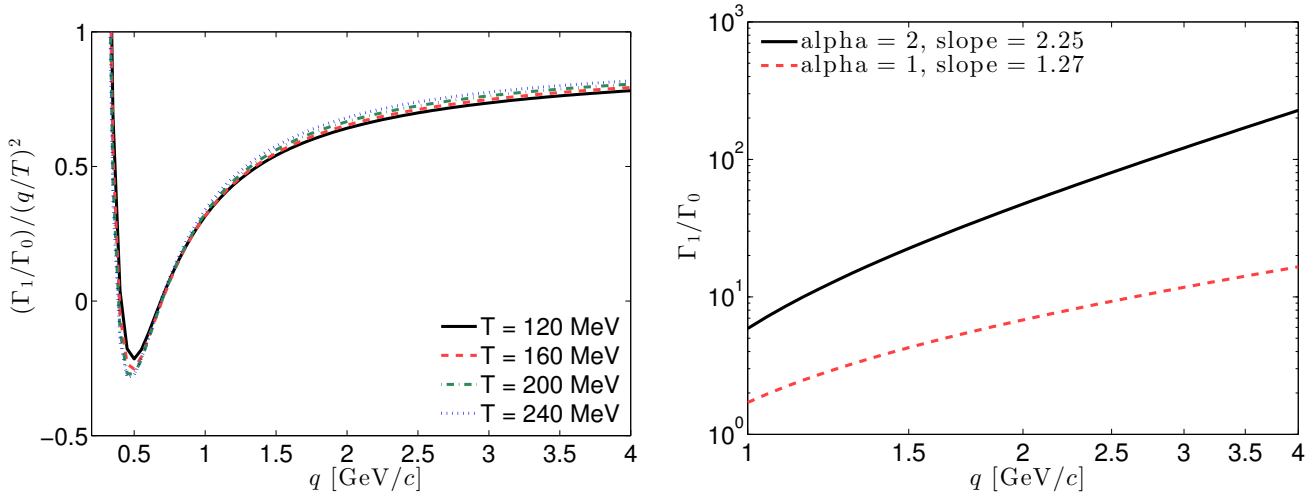

Figure 16.15: Similar as Fig. 16.10, but for $\rho + K \to K + \gamma$

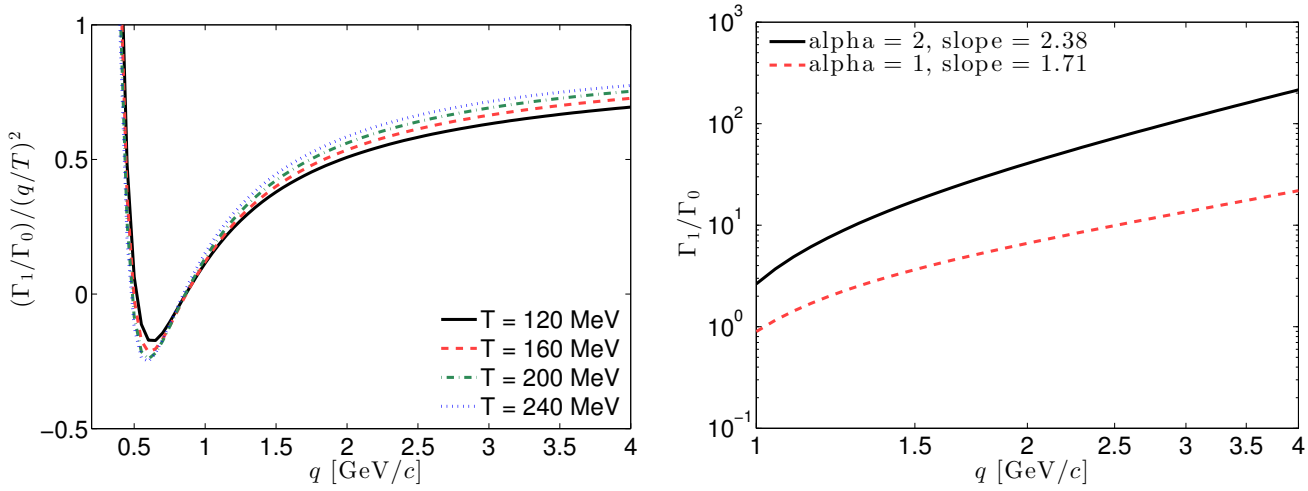

Figure 16.16: Similar as Fig. 16.10, but for $K + K^* \to \pi + \gamma$

this means that for a given fluid cell the viscous correction to the photon emission rate from this channel is smaller than the δf corrections for the hadrons. Finally, we observe that $r_{\rm vis}$ shows only weak sensitivity to the temperature, which means that most of the temperature dependence in the ratio $\frac{\Gamma_1}{\Gamma_0}$ has been taken out by dividing by $\chi\left(\frac{q}{T}\right)$. In the right panel of Fig. 16.10, we further explore the power law dependence of Γ_1/Γ_0 as a function of photon momentum on log-log scale . For $q > 2\,\mathrm{GeV}/c$, both choices of α in $\chi\left(\frac{p}{T}\right)$ in Eq. (16.48) result in linear curves, which means that the ratio follows a power law in the photon momentum. For $\alpha = 1$, the slope is $k = 1.61$ while for $\alpha = 2$ it is $k = 2.18$. Similar analysis are shown for other hadronic photon production channels in Figs. 16.11 to 16.16. They then do look qualitatively similar to the $\pi + \rho \to \pi + \gamma$ channel, except for the $\pi + \pi \to \rho + \gamma$ and $\pi + K \to K^* + \gamma$ channels which, due to the heavy vector meson in the outgoing channel, have different kinematics.

Chapter 17: Thermal photon emission rates: Transition between QGP and HG rates

In the preceding two chapters, the photon emission rates were derived for the QGP and hadron resonance gas phases. However, the leading order QGP photon emission rates are only reliable for a small strong coupling constant, $g_s \ll 1$, which implies the limit $T \to \infty$. The effective Massive Yang-Mills theory in the hadronic phase requires for its validity well-defined spectral functions for the interacting mesons. This is the case only for temperature $T < 150$ MeV. In the phase transition region (a rapid cross-over) from QGP to hadron resonance gas, neither effective theory is expected to be reliable, because neither of them can provide a satisfactory description of the equation of state as calculated from lattice QCD. A robust theoretical description of the transition region and the photon production from it does not exist and is an interesting but difficult subject for future research.

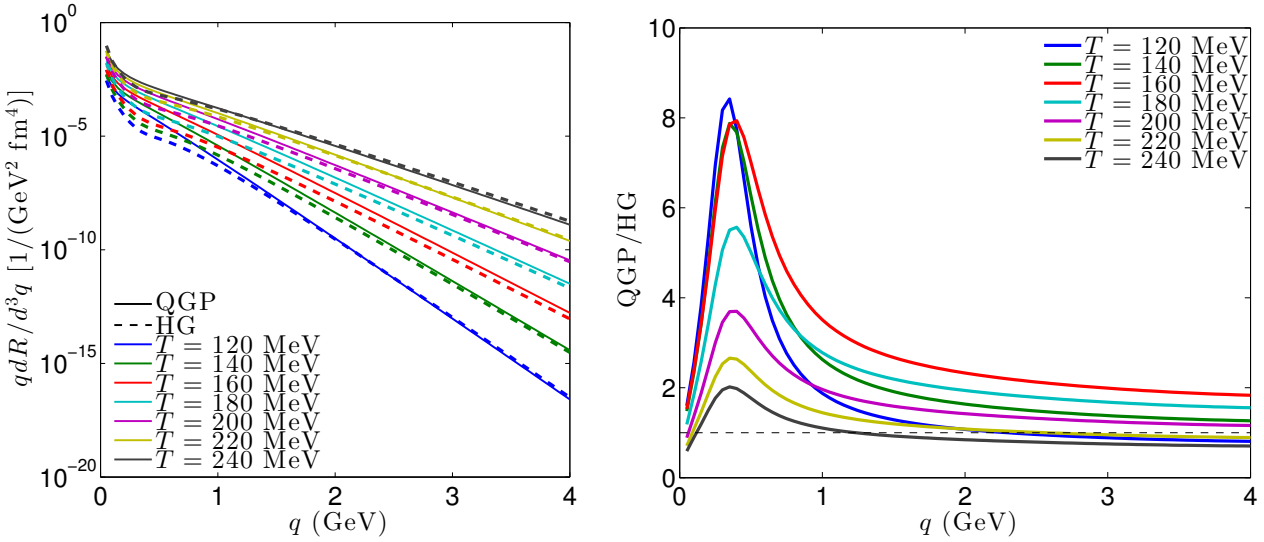

Figure 17.1: The comparison of photon production rates between QGP and HG phase in the transition temperature regions.

For the following phenomenological studies, we extrapolate the photon emission rates computed from the low-temperature and extreme high temperature approaches of the preceding chapters and smoothly interpolate them in the phase transition region. In Fig. 17.1, we show a comparison of

the QGP and HG photon emission rates from $T = 120$ to 240 MeV. In the right panel of Fig. 17.1 which shows the ratio between the QGP and HG rates for different T as a function of photon energy q, we see that the photon rates from the QGP phase (solid lines in the left panel) exhibit a quite a different q dependence than the HG rates (dashed lines in the left panel). Overall, the QGP rates are larger than the HG rates in the transition region, especially for $q < 1$ GeV where the excess can reach almost an order of magnitude.[34]. The relative difference increases as the temperature drops. Due to the partial chemical equilibrium below 165 MeV, the non-zero chemical potentials increase the photon production rates in the hadronic phase. We introduced an artificial QGP rate fraction parameter, $\alpha_{\rm QGP}$, which linearly decreases from 1 to 0 as the local temperature crosses in the rate transition region. The photon emission rates in the transition region are parameterized as

$$E\frac{d^3R}{d^3q} = \alpha_{\rm QGP}(T)\left(E\frac{d^3R}{d^3q}\right)_{\rm QGP} + (1-\alpha_{\rm QGP}(T))\left(E\frac{d^3R}{d^3q}\right)_{\rm HG} \tag{17.1}$$

with

$$\alpha_{\rm QGP}(T) = \frac{T - T_{\rm sw,low}}{T_{\rm sw,high} - T_{\rm sw,low}}, \tag{17.2}$$

where $T_{\rm sw,low}$ and $T_{\rm sw,high}$ are the boundaries of the rate switching interval.

Please note that such a smooth cross over rate transition procedure in Eq. (17.1) is only introduced to avoid a discontinuity in the photon emission rate when we switch from the QGP to the HG phase. It does not imply the assumption of a first order transition for the equation of state. The parameter $\alpha_{\rm QGP}$ should not be mis-interpreted as the QGP volume fraction in the transition region.

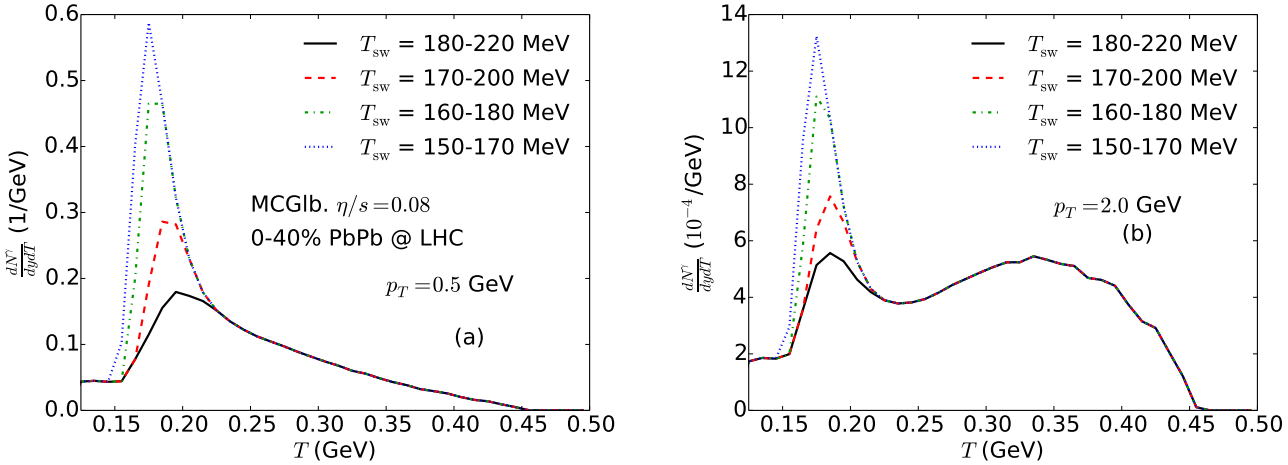

Figure 17.2: Thermal photon yield as a function of local temperature from hydrodynamic simulations with different transition temperature regions.

[34]Please note the our HG rates do not include the contributions from the in-medium broadening of ρ-meson spectral function which will increase the HG photon rates below 1.5 GeV and thus alleviate some of the discrepancy.

In Fig. 17.2, we examine the sensitivity of to the emitted thermal photon yield to $T_{\rm sw,low(high)}$. For low momentum photons, $p_T \sim 0.5$ GeV, the thermal photon production features a peak near the phase transition region due to the large corresponding hydrodynamic space-time volume (see Fig. 20.7). For thermal photons carrying $p_T \sim 2$ GeV, shown in Fig. 17.2b, a two-wave emission structure is observed. The production peak around the transition region is preserved, while another broader bump appears at higher temperature above 300 MeV. This broader bump is caused by the relativly larger photon emission rates at high temperature.[35] From Fig. 17.2, with the currently available thermal photon emission rates, we find that the thermal photon production is very sensitive to the choice of the rate transition region. If we switch from QGP to HG rates at lower temperatures, thermal photon production around the phase transition region is enhanced. This is expected from the rate comparisons in Fig. 17.1. Because the thermal photon emission rates in the QGP phase are larger than in the HG phase and their relative ratio increases as the temperature drops, more thermal photons will be emitted if we switch between the rates at lower temperatures.

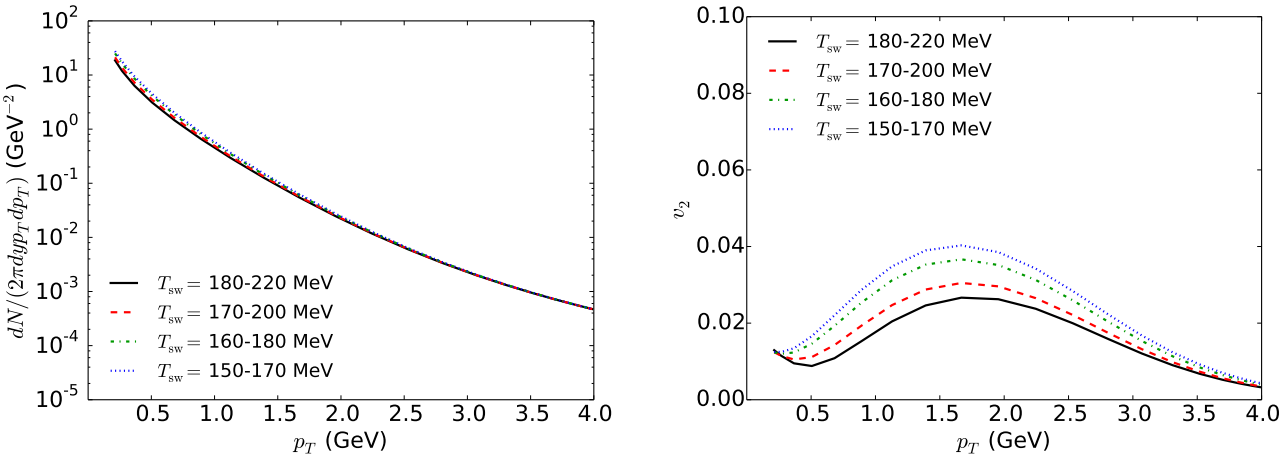

Figure 17.3: Direct photon spectra and v_2 from hydrodynamic simulation with different transition temperature regions.

In Fig. 17.3, we show the effect of the choice of the photon rate transition region on the final direct photon observables. In the left panel of Fig. 17.3, we show the direct photon spectra (thermal + pQCD prompt (described in Eqs. 14.4 to 14.6 in Chapter 14)) for different switching temperature regions. With a lower transition temperature, the direct photon spectra are enhanced at $p_T < 2$ GeV. The p_T-integrated yield of thermal photons is increased by about 30% for $T_{\rm sw} = 150 - 170$ MeV compared to switching at $T_{\rm sw} = 180 - 220$ MeV. In the right panel of Fig. 17.3, we find that the direct photon v_2 changes by an almost factor of 2 between these two rate switching windows, even after the dilution of the signal by the prompt pQCD photons, which are assumed

[35]Note that the photon emission rate decreases as $\exp(-p/T)$ as T decreases.

to carry zero v_2. With a lower switching temperature, more photons are emitted in the transition region as shown in Fig. 17.2. Since the medium anisotropic flow has been almost fully developed in the transition region, the photons emitted from this region carry large anisotropy, which contribute significantly to the final direct photon v_2.

Chapter 18: Phenomenological study: Direct photon spectra

18.1 Chapter introduction

Recently the PHENIX and ALICE experiments measured an excess of direct photon production over prompt photons, attributed to thermal radiation, in 200 A GeV Au+Au collisions at RHIC [217] and in 2.76 A TeV Pb+Pb collisions at the LHC [218]. In the low-p_T region the direct photon spectra are approximately exponential and can be well characterized by their inverse logarithmic slope $T_{\rm eff}$: $\frac{dN}{dy\,p_T dp_T} \propto e^{-p_T/T_{\rm eff}}$. The PHENIX Collaboration reported $T_{\rm eff} = 221 \pm 19 \pm 19\,{\rm MeV}$ for Au+Au collisions with 0−20% centrality at top RHIC energy [217] while the ALICE Collaboration found $T_{\rm eff} = 304 \pm 51^{\rm sys.+stat.}\,{\rm MeV}$ for 0−40% centrality Pb+Pb collisions at the LHC [218]. Both values are significantly larger than the critical temperature for chiral restoration and color deconfinement, $T_{\rm c} \simeq 155 - 170\,{\rm MeV}$ [219, 220]. Since photons are emitted from all stages of the collision, their momentum distributions integrate over the temperature and flow history of the expanding fireball, weighting it with emission rates that depend on the collision stage and the corresponding radiating degrees of freedom [221]. The interpretation of the shape of experimentally measured photon spectra is therefore complex and requires theoretical modeling based on cross-checks with other experimental observables.

In this Chapter which is based on Ref. [222], we use a realistic hydrodynamic simulation of the fireball evolution to explore the effects of hydrodynamic flow on the effective temperature (inverse slope) of the emitted thermal photon spectrum quantitatively. Both our evolution and photon emission rates incorporate viscous effects, which are discussed in details in previous chapters. We also study schematically the consequences of a hypothetical scenario where the fireball medium initially consists entirely of gluons (which do not radiate electromagnetically) and quark-antiquark creation (chemical equilibration) is delayed by several fm/c [223, 224]. How much will theoretical and experimental precision have to improve to allow to distinguish empirically between an initially "dim" gluon plasma and a QGP that reaches chemical equilibrium very quickly? In an attempt to start answering questions such as these, and to exploit the penetrating nature of the electromagnetic radiation, the space-time history of photon emission is explored. We show that

strategic cuts on the photon transverse momentum have the potential to make their thermometric nature even more explicit.

18.2 Hydrodynamic modeling and photon production

The dynamical evolution of the radiating fireball is modeled with the boost-invariant hydrodynamic code `VISH2+1` [39], using parameters extracted from previous phenomenologically successful studies of hadron production in 200 A GeV Au+Au collisions at RHIC [17, 40] and in 2.76 A TeV Pb+Pb collisions at the LHC [48, 118]. We here use ensemble-averaged Monte-Carlo Glauber (MCGlb) initial conditions which we propagate with $\eta/s = 0.08$ [17, 40, 48, 118] and the lattice-based equation of state (EoS) `s95p-PCE-v0` [16] which implements chemical freeze-out at $T_{\rm chem} = 165\,{\rm MeV}$. We start the hydrodynamic evolution at $\tau_0 = 0.6\,{\rm fm}/c$, corresponding to a peak initial temperature (energy density) in the fireball center of $T_0 = 452\,{\rm MeV}$ ($e_0 = 62\,{\rm GeV/fm}^3$) at the LHC (Pb+Pb at 0−40% centrality), and of $T_0 = 370\,{\rm MeV}$ ($e_0 = 35\,{\rm GeV/fm}^3$) at RHIC (Au+Au at 0−20% centrality). We end it on an isothermal hadronic freeze-out surface of temperature $T_{\rm dec} = 120\,{\rm MeV}$.

Photons are emitted from the fireball using photon emission rates that are corrected for deviations from local thermal equilibrium caused by the non-zero shear viscosity of the medium as described in Chapters 15 and 16. In the QGP phase, we only consider viscous corrections to $2 \to 2$ scattering processes. We focus on photons with $p_T < 4\,{\rm GeV}$ and ignore the contributions from hard pre-equilibrium processes which do not significantly affect the extraction of the inverse photon slope in this p_T-region [225]. The hadronic phase (HG) is modeled as an interacting meson gas within the SU(3) × SU(3) massive Yang-Mills approach (see Refs. [213, 182, 226] and Chapter 16 for details), with non-equilibrium chemical potentials to account for chemical decoupling at $T_{\rm chem} = 165\,{\rm MeV}$. Both approaches to computing the emission rates are expected to break down in the phase transition region. As described in Chapter 17, to avoid discontinuities, the QGP and HG emission rates are linearly interpolated in the temperature window $184\,{\rm MeV} < T < 220\,{\rm MeV}$ where our employed EoS [16] interpolates continuously between the lattice QCD data and the hadron resonance gas model in such a way that the smooth crossover character of the phase transition seen on the lattice is preserved. For comparisons, we will also show results with rate transition region between $150\,{\rm MeV} < T < 170\,{\rm MeV}$, which covers the physical chiral restoration and deconfinement region.

18.3 Direct photon spectra

As a prelude, it is useful to compare the results of our calculations with the photon spectra measurements performed at RHIC and at the LHC by the PHENIX and ALICE collaboration,

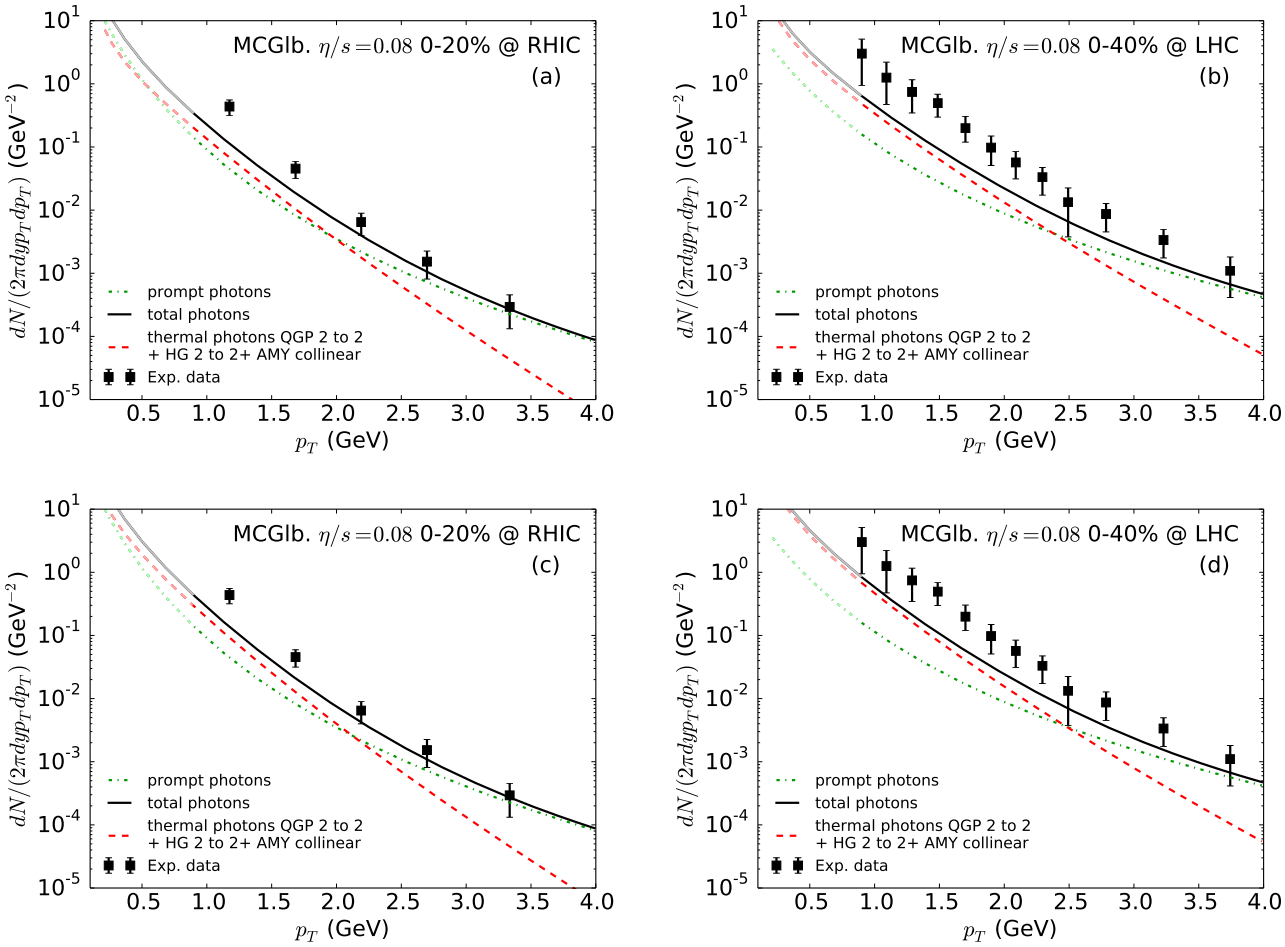

Figure 18.1: Measured and calculated photon spectra in 0−20% centrality Au+Au collisions at RHIC (a) and 0−40% centrality Pb+Pb collisions at the LHC (b) with rate transition region chosen between 184 MeV and 220 MeV. Panels (c) and (d) are similar plots but with $150\,\mathrm{MeV} < T_{\rm sw} < 170\,\mathrm{MeV}$. Photons from thermal sources and from pQCD are shown separately, as well as their sum. The Au+Au collisions data at RHIC (a) are from the PHENIX Collaboration [217], those for Pb+Pb collisions at the LHC (b) from the ALICE Collaboration [218]. The shaded curves below 1 GeV are to remind of the uncertainties in extrapolating pQCD to low values of the photon transverse momentum.

respectively. The calculated spectra shown in Figure 18.1 include the thermal rates corrected for shear viscosity effects integrated over the viscous hydrodynamical space-time evolution, and also the prompt photons resulting from the very early interactions of the partons distributed inside the nucleus. For the QGP contribution shown in Fig. 18.1, the full leading order *ideal* rate for collinear emission is added to the viscous-corrected $2 \to 2$ rate. On the hadron gas side, we use the rates derived in Chapter 16 considering meson reactions. Please note that our HG rates do not include the contribution of baryons to the production of real photons. The prompt photon calculation is performed at next-to-leading-order (NLO) in the strong coupling constant [227], and the nuclear parton distribution functions are corrected for isospin and shadowing effects [228]. The calculation

is extrapolated to low transverse momentum using a fit of the form $A/(1+p_T/p_0)^n$, a form that we checked describes very well the available low p_T photon data from proton-proton collisions [217]. For RHIC and LHC conditions, the agreement between the calculated results and measured data shown here is not untypical of that obtained with other contemporary hydrodynamic simulations [221, 229, 230]. Our results with lower transition temperature for the photon emission rates give $\sim 30\%$ larger photon yield. We note that the data allow room for additional photon sources in addition to the ones considered here. Among the possible candidates are photons from jet-plasma interactions [229]; one should also keep in mind the role played by fluctuating initial states [231, 189].

18.4 Inverse Slope of the direct photon spectra

The equilibrium emission rates as well as the non-equilibrium photon spectra emitted during the hydrodynamic evolution are approximately exponential in p_T between 1 and 4 GeV, and we can characterize them by their inverse logarithmic slopes $T_{\rm eff}$ just as the experiments did for the measured direct photon spectra. The green lines in Fig. 18.2 show $T_{\rm eff}$ as a function of the true temperature T for the equilibrium photon emission rates. One sees that, due to phase-space factors associated with the radiation process, the effective temperature of the emission rate is somewhat larger than the true temperature: At high T, the QGP photon emission rate goes roughly as $\exp(-E_\gamma/T)\log(E_\gamma/T)$ [207], and the logarithmic factor is responsible for the somewhat harder emission spectrum. The double kink in the green line at $T=184$ and 220 MeV reflects the interpolation between the QGP and HG rates. The effect of that interpolation on the slope of the spectrum is weak, one mainly interpolates between rates with different normalization.

The circles in Fig. 18.2 show the effective temperatures of photons emitted with equilibrium rates (open black circles) and with viscously corrected rates (filled red circles) from cells of a given temperature within the hydrodynamically evolving viscous medium. The area of the circles is proportional to the total photon yield emitted from all cells at that temperature. One sees here and also in Fig. 18.3 below that viscous corrections to the photon emission rates are large at early times (high T), due to the initially very large longitudinal expansion rate, but become negligible at later times (lower T). Viscous effects on the emission rates harden the photon spectrum (i.e. they increase $T_{\rm eff}$) but do not affect the photon yields. The hydrodynamic photon spectra using ideal rates (open black circles) have lower effective temperatures than the local emission rates themselves (green solid lines): This is due to the integration of the Boltzmann factor $e^{-E_\gamma/T}=e^{-p_T\cosh(y-\eta)/T}$ over space-time rapidity η which, for fixed T, sums over contributions[36] with different effective temperatures $T_{\rm eff}(\eta)=\frac{T}{\cosh(y-\eta)}<T$ (we here consider photons at midrapidity, $y=0$). Surprisingly,

[36]Recall that we assume a boost-invariant (i.e. η-independent) distribution of thermal sources.

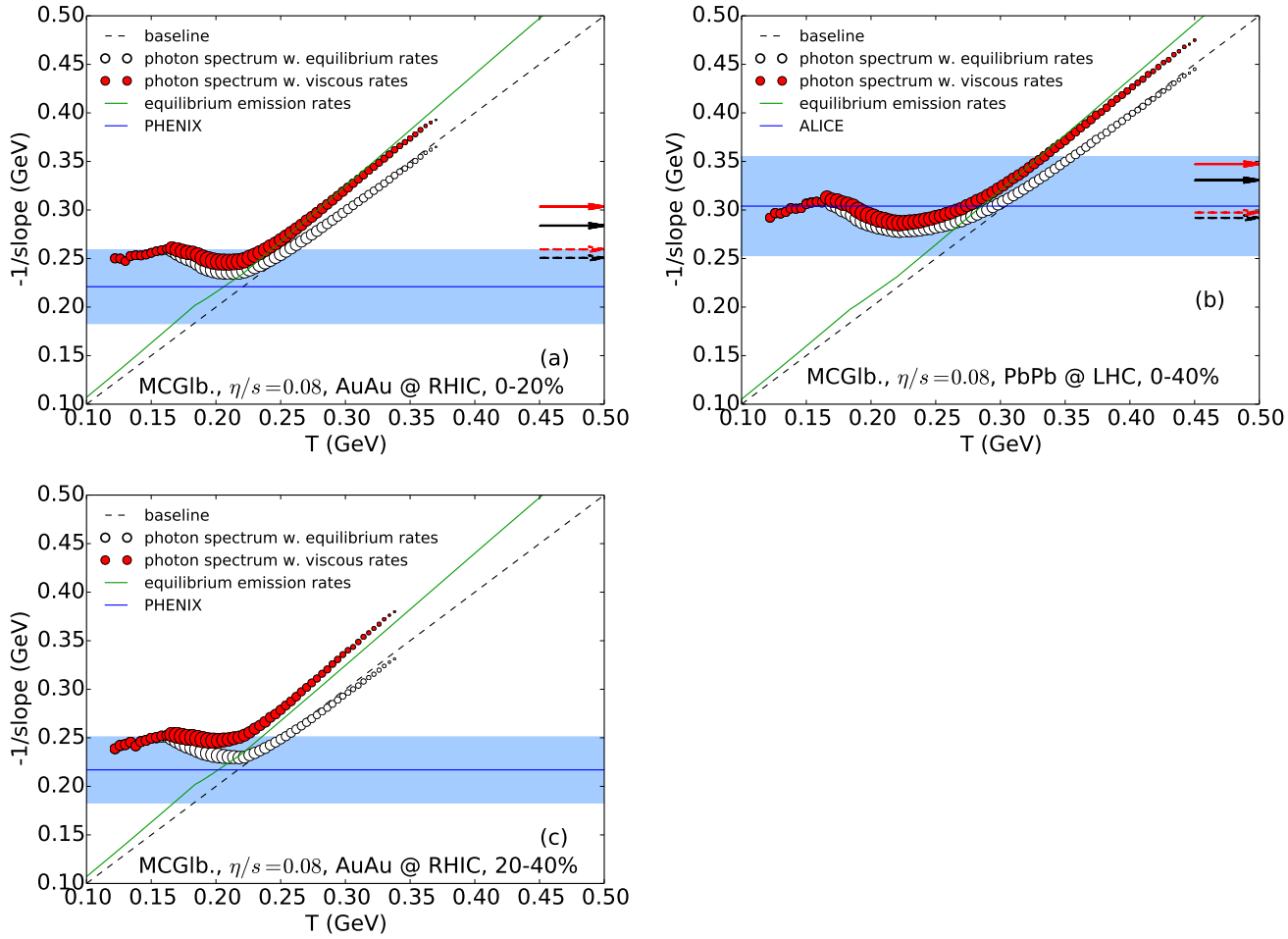

Figure 18.2: The inverse photon slope parameter $T_{\rm eff} = -1/\text{slope}$ as a function of the local fluid cell temperature, from the equilibrium thermal emission rates (solid green lines) and from hydrodynamic simulations (open and filled circles), compared with the experimental values (horizontal lines and error bands), for (a) 0-20% Au+Au collisions at RHIC, (b) 0-40% Pb+Pb collisions at the LHC and (c) for 20-40% Au+Au collsions at RHIC. The experimental values and error bands are from the PHENIX Collaboration [217] in (a,c) and from the ALICE Collaboration [218] in (b).

this rapidity-smearing effect leads, for ideal emission rates, to photon spectra whose inverse slope reflects at early times almost exactly the temperature of the emitting fluid cells in their rest frame. Including viscous corrections in the emission rates increases the effective photon temperatures by about 10% at early times.

As the system cools, Fig. 18.2 shows that the effective photon temperature begins to deviate upward from the true temperature. Below $T \sim 220\,\text{MeV}$ the effective photon temperature actually begins to increase again while the true temperature continues to decrease. This is caused by the strengthening radial flow; below $T \sim 220\,\text{MeV}$, the radial boost effect on $T_{\rm eff}$ overcompensates for the fireball cooling. Once the system reaches chemical freeze-out at $T_{\rm chem} = 165\,\text{MeV}$, the character of the equation of state changes, leading to faster cooling [77] without developing additional radial

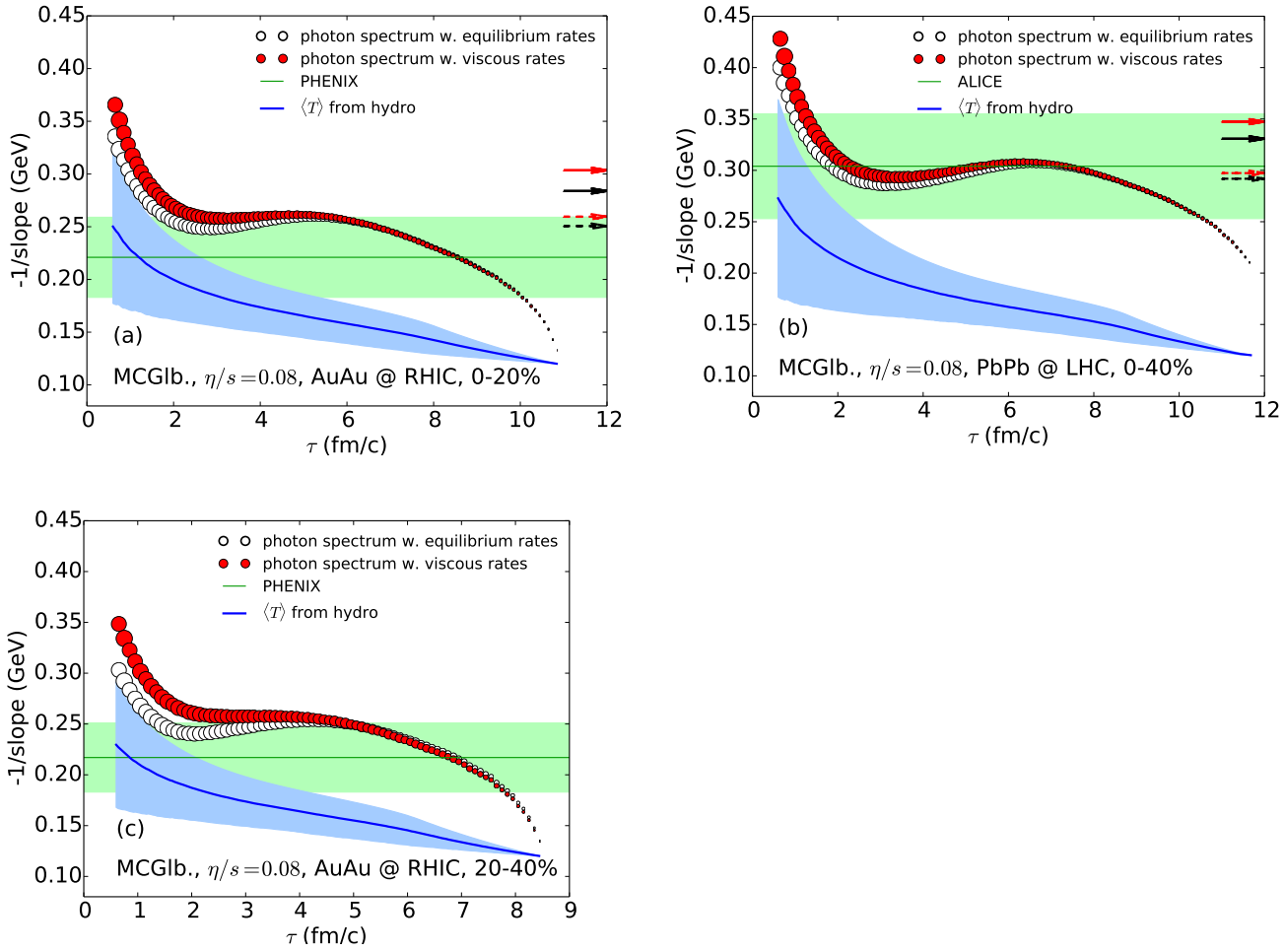

Figure 18.3: The inverse photon slope parameter $T_{\rm eff} = -1/\text{slope}$ as a function of emission time from hydrodynamic simulations, compared with the experimental (time-integrated) values (horizontal lines and error bands), for (a) 0-20% Au+Au collisions at RHIC, (b) 0-40% Pb+Pb collisions at the LHC and (c) 20-40% Au+Au collisions at RHIC. The blue solid lines and surrounding shaded areas show for comparison the time evolution of the average fireball temperature and its standard deviation.

flow at a sufficient rate to keep compensating for the drop in effective temperature due to this cooling. The faster expansion below $T_{\rm chem}$ is also seen in the solid blue lines in Fig. 18.3, and it is reflected in the shrinking size of the circles (integrated photon yields) in Fig. 18.2 below $T_{\rm chem}$, reflecting the smaller space-time volumes occupied by cells with temperatures $T < T_{\rm chem}$.

Fig. 18.3 shows the effective slopes of photons emitted at different times from the expanding fireball, again compared with the time-integrated experimental values (horizontal bands). (A similar graph, based on a parametrized fireball evolution model with thermal equilibrium rates and a first-order phase transition, can be found in Fig. 7 in Ref. [232]). As before, the open black circles use equilibrium emission rates while the filled red circles account for viscous corrections to the photon emission rates. (The hydrodynamic expansion is viscous in both cases.) For comparison, the blue lines show the evolution of the average fireball temperature (averaged over all cells with

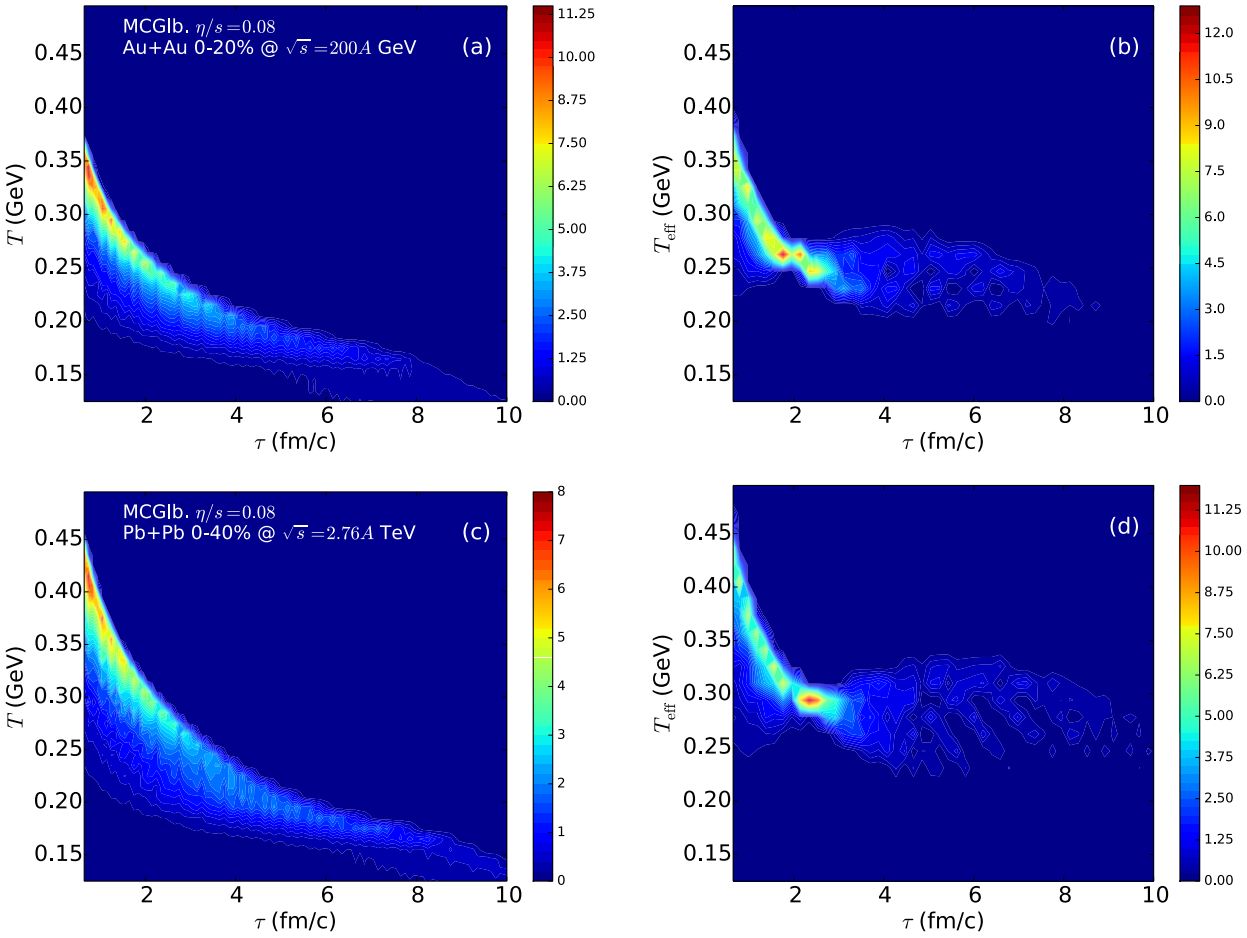

Figure 18.4: Contour plots of the normalized differential photon yield $\frac{dN^\gamma(T,\tau)/(dy\,dT\,d\tau)}{dN^\gamma/dy}$ (panels (a) and (c)) and $\frac{dN^\gamma(T_{\rm eff},\tau)/(dy\,dT_{\rm eff}\,d\tau)}{dN^\gamma/dy}$ (panels (b) and (d)) for Au+Au collisions at RHIC at 0-20% centrality (panels (a) and (b)) and for Pb+Pb collisions at the LHC at 0-40% centrality (panels (c) and (d)). The photon rate transition region is between 184 MeV and 220 MeV. The color bars translate the colors into absolute values (in $c/(\mathrm{GeV\,fm})$) for the quantities plotted.

$T > 120\,\mathrm{MeV}$ at time τ), with shaded regions indicating its standard deviation. After about $2\,\mathrm{fm}/c$, the effective photon temperature begins to get significantly blue-shifted by radial flow. This radial boost is clearly stronger at the LHC than at RHIC. Radial flow effects decrease again at very late times when only a small region near the fireball center survives where the radial flow goes to zero. The difference between open and filled circles shows that viscous effects on the photon emission rates are concentrated at early times.

While Fig. 18.3 demonstrates that the early photons are associated with a high yield (as is commonly understood), Fig. 18.2 shows that most photons are emitted from a relatively narrow temperature band between 165 and 220 MeV. Relatively few of the photons thus come from the hot core of the fireball; a much larger fraction comes from the cooler periphery and is emitted with temperatures close to the quark-hadron transition. Averaged over time, these photons from

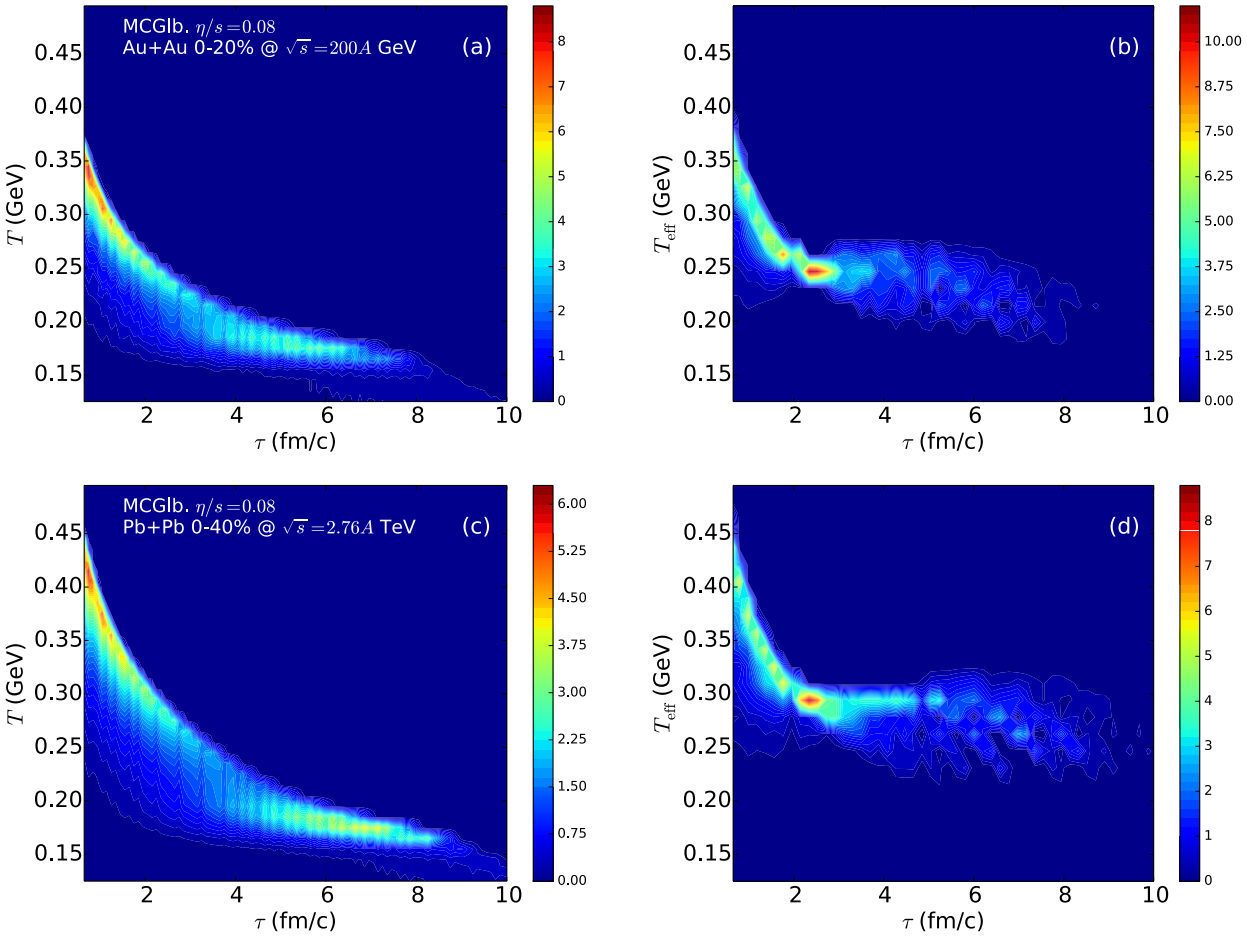

Figure 18.5: Similar to Fig. 18.4, but rate transition temperature region is chosen for $150\,\mathrm{MeV} < T_{\rm sw} < 170\,\mathrm{MeV}$

the transition region are strongly affected by radial flow, resulting in inverse slopes ("effective temperatures") that are much larger than their true emission temperatures. These findings can even be put on a firmer quantitative basis, by considering the following: At each value of proper time, τ, photons are emitted with a distribution of thermodynamic temperatures. This distribution is shown in Figs. 18.4a (for Au+Au at RHIC) and 18.4c (for Pb+Pb at the LHC), where the color-coding of the contour plots reflects the differential photon yield (normalized to the total yield dN^γ/dy) per time and temperature (in $c/(\mathrm{GeV\,fm})$) in the $T-\tau$ plane. The corresponding distribution of flow-blue-shifted effective temperatures $T_{\rm eff}$ (inverse slopes) is shown in Figs. 18.4b (for RHIC) and 18.4d (for the LHC). Comparing the left and right panels one observes, after a proper time $\tau \sim 2\,\mathrm{fm}/c$, a clear shift to higher effective temperatures, owing to the development of radial hydrodynamic flow. Furthermore, the dependence of the effective temperature on the flow velocity (which depends on radial position) leads to an additional broadening of the distribution of $T_{\rm eff}$ at any given time.

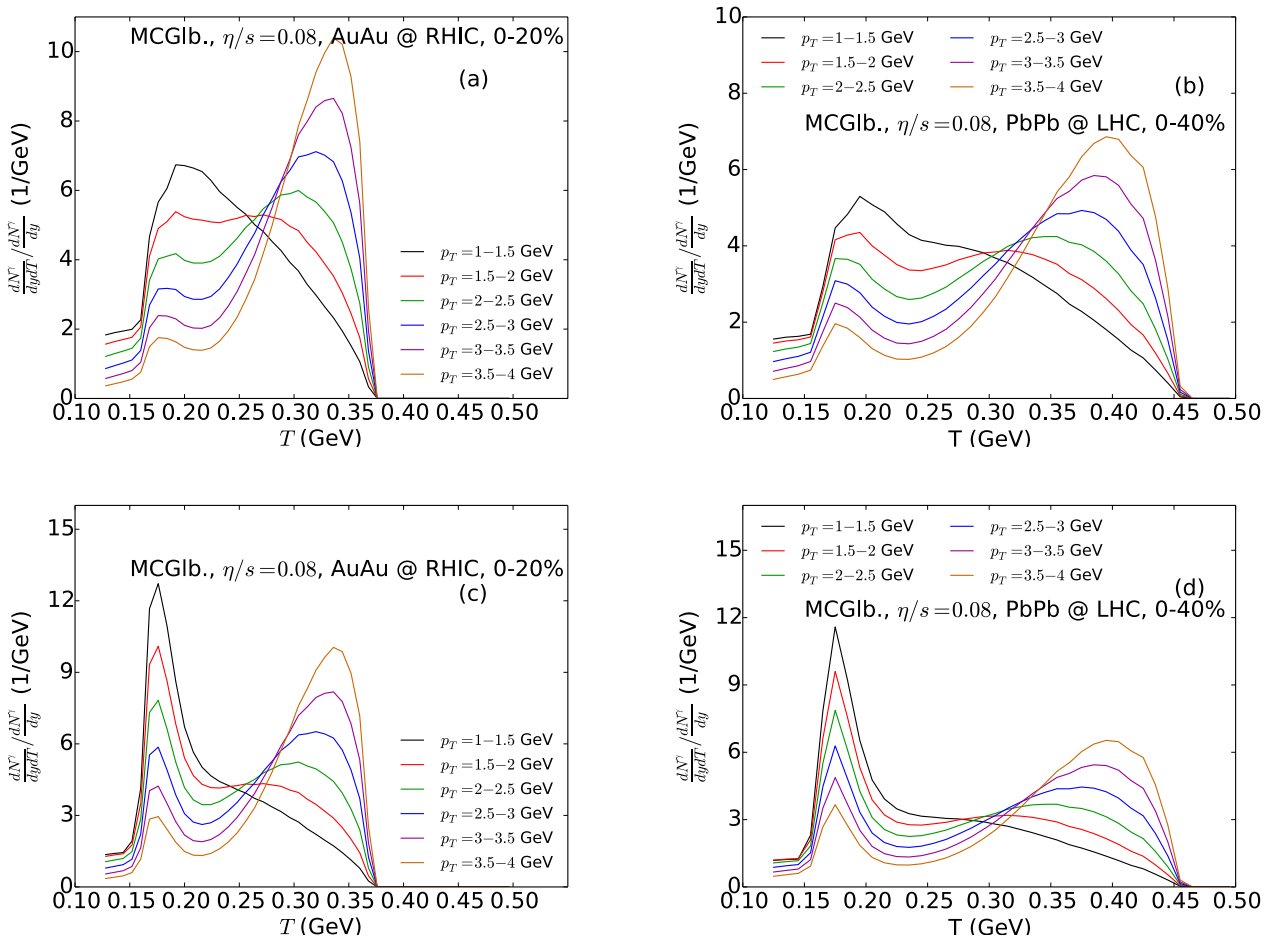

Figure 18.6: The differential photon yield, as a function of the temperature T, for different windows in photon transverse momentum, for 0-20% Au+Au collisions at RHIC (a,c) and 0-40% Pb+Pb collisions at the LHC (b,d). We tranisite the photon emission rates in $184\,\mathrm{MeV} < T_{\mathrm{sw}} < 220\,\mathrm{MeV}$ for (a) and (b), and $150\,\mathrm{MeV} < T_{\mathrm{sw}} < 170\,\mathrm{MeV}$ for (c) and (d).

In order to further quantify the connection between the photon spectrum and the emission temperature, a model calculation allows to dissect the photon contribution in terms of transverse momentum. Figure 18.6 shows the relative photon yield in different transverse momentum regions, as a function of the temperature at which those photons were radiated. The photon yield is obtained by integrating the flow-boosted photon emission rate over the space-time volume. The rate is large at high temperatures, but the corresponding space-time volume is small. As the system cools and the rate drops, the decrease in the rate is (partially) offset by the increasing fireball volume, and the shift to lower photon energies resulting from the cooling is counteracted by the increasing radial flow. The combination of these effects can create a bi-modal distribution of the thermodynamic temperatures that contribute to photon production in a given p_T window. The relative size of the two peaks corresponding to emission from very hot cells with little flow and rather cool cells with strong radial flow depends on the photon momentum, as is shown in

Fig. 18.6. The curves in Fig. 18.6 can be viewed as thermal photons probability distribution function, with the local temperature as the independent variable. At RHIC, one observes that for $p_T = 1{-}1.5\,\mathrm{GeV}$, photons are mostly coming from the transition region $T = 150{-}220\,\mathrm{MeV}$. For harder thermal photons with $p_T = 3.5{-}4\,\mathrm{GeV}$, on the other hand, the emission probability is peaked at temperatures above 300 MeV, followed by a second wave of emission from a much larger space-time volume at temperatures around $T = 150{-}220\,\mathrm{GeV}$, blue-shifted by large radial flow. Interestingly, this bimodal structure does not require a first order phase transition but, as can be seen here, is also observed for a smooth cross-over. The right panel in Fig. 18.6 shows the situation for conditions specific to the LHC. This figure illustrates well the power and advantages related to the use of a quantitative space-time modeling of the nuclear collisions: the momentum cuts shown here can be used to guide experimental analyses and simulations that seek to extract precise temperature information from high-energy nuclear collisions[37].

18.5 Centrality dependence of the thermal photon yield and spectra

Our hydrodynamical treatment allows us to study the centrality dependence of the thermal photon yields, reported by the PHENIX Collaboration recently [233]. Thermal photons should exhibit a stronger centrality dependence than hadrons and photons from hadronic decays[234, 235]. Fig. 18.7 illustrates this for RHIC conditions with two different choices of the temperature transition regions for smooth matching the photon emission rates from two phases.

We integrate the thermal photon spectra from a variable lower p_T cutoff to a fixed upper limit of $p_T = 4\,\mathrm{GeV}$ and plot the result in Fig. 18.7 as function of centrality, measured either through N_{part} in panels (a, c) or through the charged multiplicity $dN_{\mathrm{ch}}/d\eta$ in panels (b, d). The latter plot permits a direct comparison with experimental measurements. The four points in each curve, from right to left, represent 0-20%, 20-40%, 40-60%, and 60-95% centrality bins. The dashed lines are power-law fits to the points. One observes a thermal photon yield that grows like a power of N_{part} and as a (different) power of the multiplicity, with exponents stronger than linear. The powers depend on the lower p_T cutoff with which the yield is evaluated. For the region $p_T > 0.6$ GeV, the slopes in the logarithmic plots of Fig. 18.7a,c are within the range 1.65$\sim$1.8, larger than the experimentally measured value of $1.48 \pm 0.08 \pm 0.04$ [233]. In order to further explore the possible implications of this difference in slopes between theory and data, we compute, for the case shown in Fig. 18.7, the centrality dependences of the total QGP and HG photon yields above $p_T = 0.4\,\mathrm{GeV}$ in Fig. 18.8. The QGP photon yield is defined as all photons from cells with $T > 220\,\mathrm{MeV}$ plus the QGP fraction of photons from cells with temperatures between 184 and 220 MeV where we linearly interpolate between the QGP and HG emission rates. The HG photon

[37]Note however, that the high-momentum bins will receive pQCD contributions.

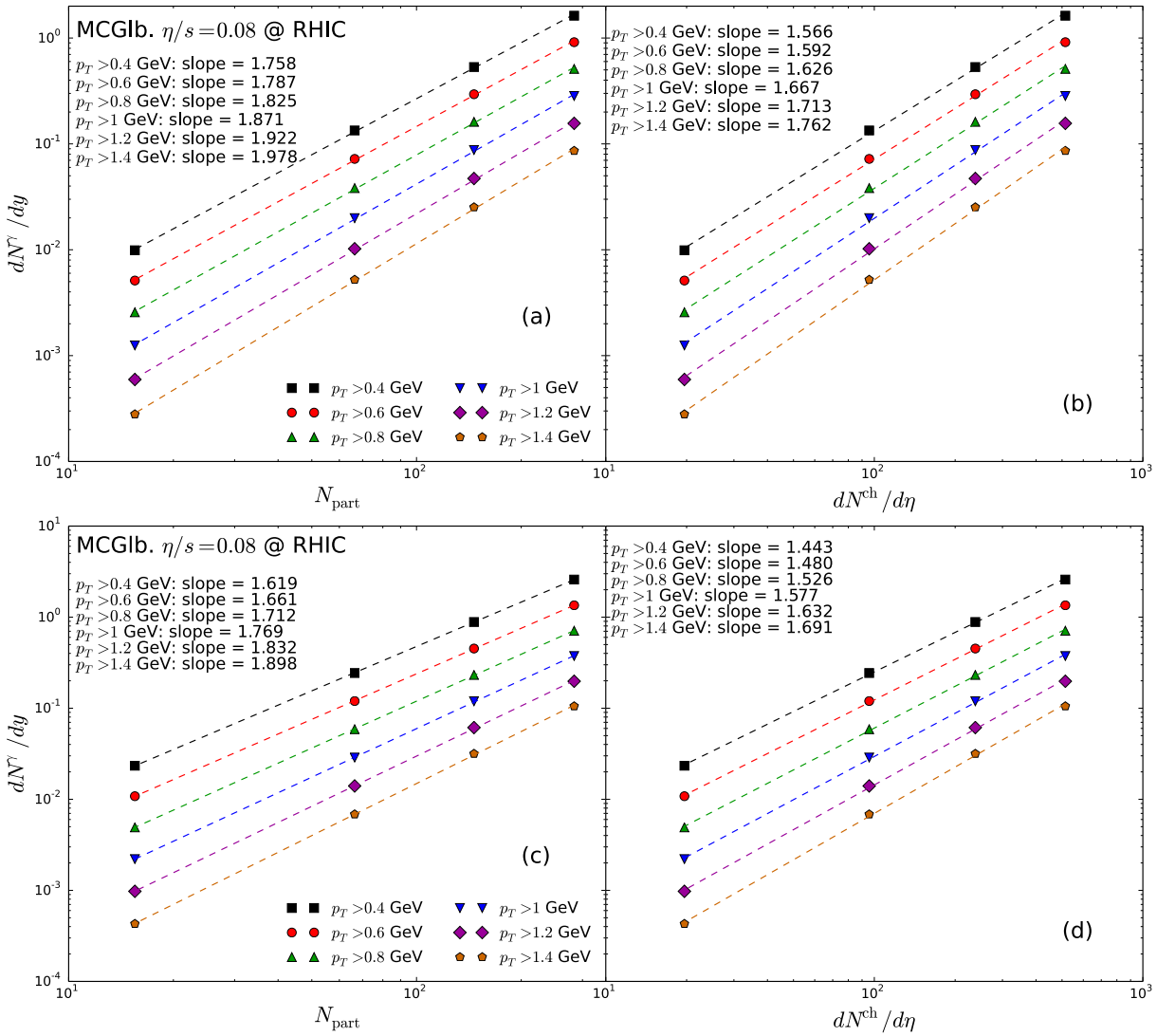

Figure 18.7: The centrality dependence of the photon yield, for Au+Au collisions at RHIC. The centrality may be expressed in terms of (a,c) $N_{\rm part}$ or of (b,d) $dN^{\rm ch}/d\eta$ for the MC-Glauber initial conditions with $\eta/s = 0.08$. Panels (a, b) are results with the transition region of photon rates $T_{\rm sw} = 184 - 220$ MeV and (c, d) for $T_{\rm sw} = 150 - 170$ MeV.

yield is the complement of the total photon yield with respect to the QGP photon yield. We find the HG photon yield above $p_T = 0.4\,\text{GeV}$ to scale as function of $N_{\rm part}$ with power 1.46 and as function of $dN_{\rm ch}/d\eta$ with power 1.30; the corresponding scaling powers for the QGP photons are larger, 2.07 and 1.84, respectively. QGP photons thus have a significantly stronger centrality dependence than HG photons. The experimentally measured centrality dependence of all thermal photons is closer to the power predicted in our calculations for HG photons than for QGP photons. Together with our observation that our calculations significantly under-predict the measured total thermal photon yields at all centrality bins, this may indicate that our hydrodynamic calculations underestimate the photon production rate in the HG phase and/or near the quark-hadron phase

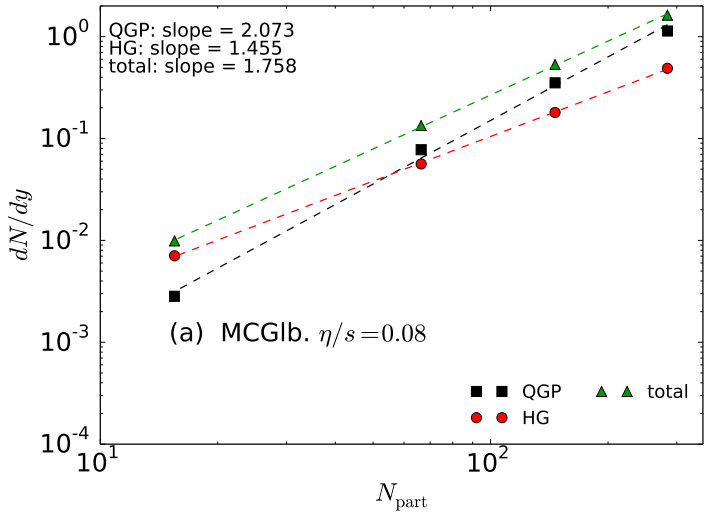

Figure 18.8: The centrality dependence of the themal photon yield from QGP and HG phases for MCGlb initial conditions with $\eta/s = 0.08$. The rate transition region is between 184 MeV and 220 MeV.

transition. This observation invites further scrutiny in terms of its sensitivity to variations in the initial conditions and the transport coefficients the expanding hydrodynamic fluid.

In Figs 18.9 and 18.10, we show the p_T spectra of thermal photons compared to the preliminary PHENIX measurement for the direct photon excess. Our calculation systematically underestimates the data at all p_T but the slope of the photon spectra is close to the measurements. We investigated the centrality dependence of the inverse slope of the thermal photon spectra in Au+Au collisions at RHIC. Our results show a very weak centrality dependence, with $T_{\rm eff}$ being slightly smaller in peripheral than in central collisions.

18.6 Reduced radiation from a dim gluon plasma: a schematic study

Returning to Figs. 18.2 and 18.3, we see that the large measured values for the inverse photon slope reflect, on average, true emission temperatures that lie *well below* the observed effective temperature. This raises an interesting question: Could it be that in the experiments we don't see any photons *at all* from temperatures well above $T_{\rm c}$, and that all measured photons stem from regions close to $T_{\rm c}$ and below, blue-shifted by radial flow to effective temperature values above $T_{\rm c}$? To get an idea what the answer to this question might be we performed a schematic study where in Fig. 18.2 we turned off by hand all contributions to the photon spectrum from cells with true temperatures above 220 MeV at RHIC and above 250 MeV at the LHC (corresponding to about 1/3 of the total photon yield in both cases), and in Fig. 18.3 all contributions from $\tau < 2\,{\rm fm}/c$ (corresponding to 26% and 28.5% of the total photon yield for RHIC and LHC collisions, respectively,

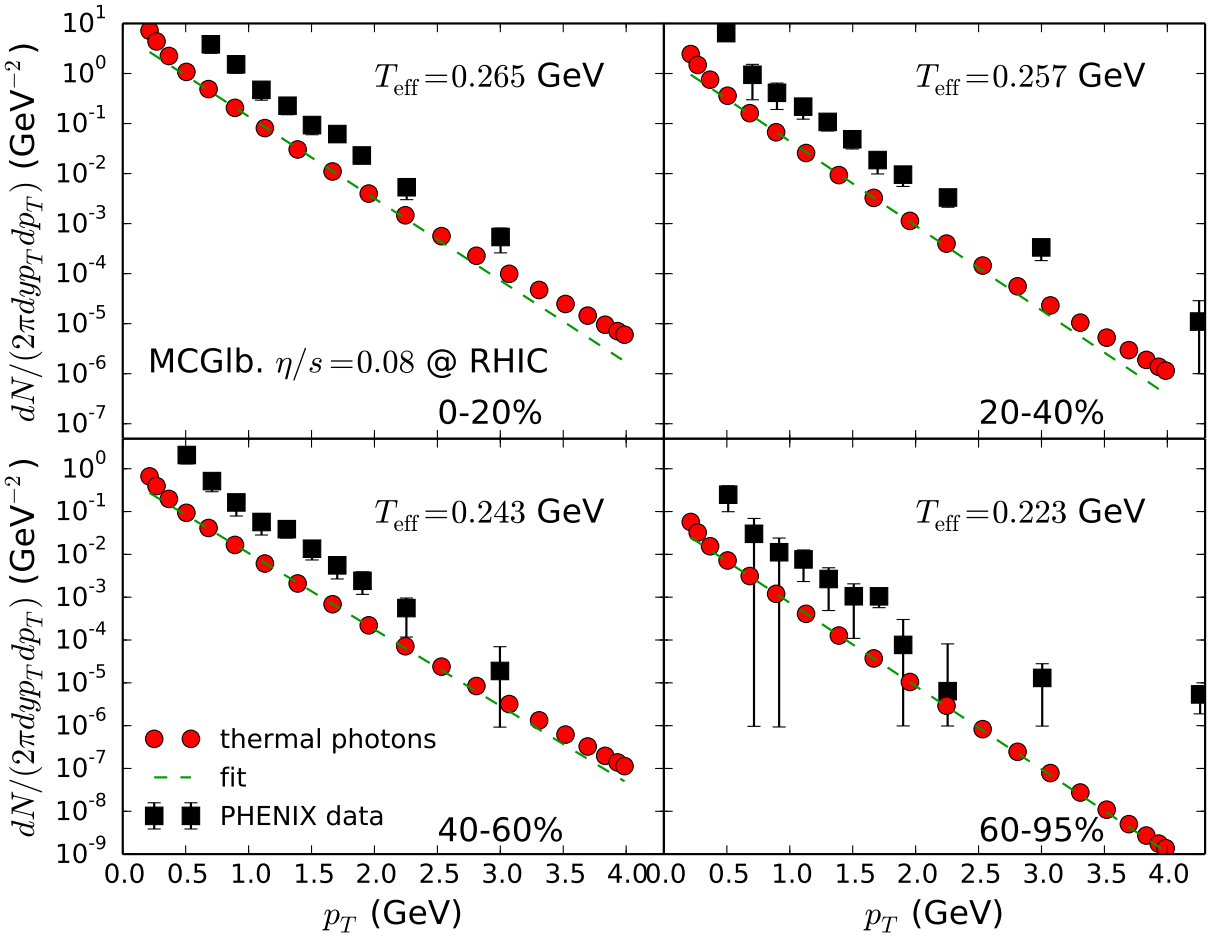

Figure 18.9: Centrality dependence of thermal photon spectra compared with the preliminary results of the direct excess photon spectra for 200 A GeV Au+Au collisions obtained by the PHENIX Collaboration [233] (pQCD prompt photons are substracted in the data). The inverse slope parameters of the thermal photon spectra are extracted for the 4 centrality bins. The fit range is chosen to be the same interval in [233] $0.6 < p_T < 2.0$ GeV .

see Table 18.1).[38] We show as arrows pointing to the right vertical axes in Figs. 18.2 and 18.3 the inverse slopes of the final space-time integrated hydrodynamic photon spectra: Solid black and red lines correspond to calculations assuming full chemical equilibrium from the beginning and using thermal equilibrium and viscously corrected photon emission rates, respectively. The dashed black and red arrows show the same for calculations with delayed chemical equilibration, as described above. The (overestimated) effects of our schematic handling of delayed chemical

[38]This implements, in a very rough way, the idea that the initial fireball state might be purely gluonic, and that chemical equilibration of quarks can be characterized by a time constant taken to be about 2 fm/c. It ignores, however, that an initial suppression of quarks must be compensated by an increase in the gluon temperature [223, 224], in order to maintain the same total entropy and final multiplicity. As quarks are being produced from gluons, these quarks thus radiate more strongly than in chemical equilibrium, leading to a cancellation that leaves the total photon spectrum almost unchanged [224]. Our simplified treatment ignores this increase in temperature and thus overestimates the effect of early-time quark suppression on the photon spectrum. In this sense, our conclusion from this study is conservative.

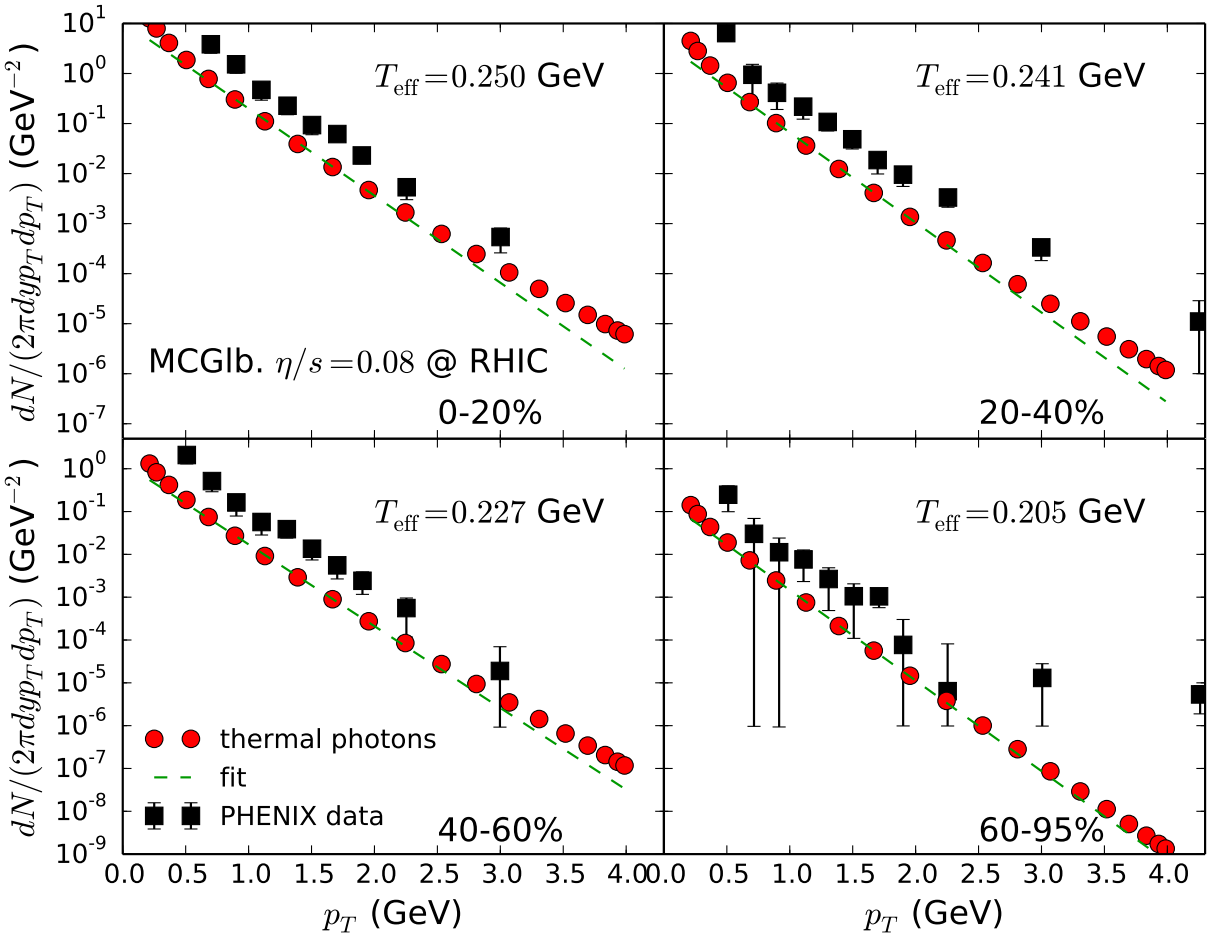

Figure 18.10: Similar as Fig. 18.9, but photon rate transition region is chosen between 150 MeV and 170 MeV.

equilibration on the final inverse photon slope are seen to be roughly of the same order of magnitude as those from viscous corrections to the photon emission rates ($\sim 10\%$ for $T_{\rm eff}$), and thus too small to be experimentally resolved with the present experimental accuracy of $T_{\rm eff}$. We note that, for both RHIC and LHC energies, the calculated inverse slopes are consistent (within errors) with the experimentally measured values, although near the high end of the observationally allowed band for RHIC.

18.7 Chapter summary

We conclude that thermal photons can indeed be used as a thermometer in relativistic nuclear collisions, but that their interpretation requires a dynamical model which has the sophistication demanded by the wealth of hadronic data that currently exist at RHIC and at the LHC. We observe that the large observed effective temperatures of thermal photons emitted from heavy-ion collisions, and their significant increase from RHIC to LHC energies, reflect mostly the strong radial flow generated in these collisions and do not *directly* prove the emission of electromagnetic

range of photon emission	fraction of total photon yield		
	AuAu@RHIC 0-20% centr.	AuAu@RHIC 20-40% centr.	PbPb@LHC 0-40% centr.
$T = 120$-$165\,\mathrm{MeV}$	11%	18%	9%
$T = 165$-$250\,\mathrm{MeV}$	59%	66%	48%
$T > 250\,\mathrm{MeV}$	30%	16%	43%
$\tau = 0.6 - 2.0\,\mathrm{fm/c}$	38%	35%	34%
$\tau > 2.0\,\mathrm{fm/c}$	62%	65%	66%

Table 18.1: Fractions of the total photon yield emitted from the expanding viscous hydrodynamic fireball from various space-time regions as indicated, for the two classes of collisions considered in this work.

radiation from quark-gluon plasma with temperatures well above T_c. In particular, they are not representative of the initial temperature of the QGP generated in the collision. We hasten to say, however, that a hot and dense early stage of the expanding medium is necessary to generate (either hydrodynamically or by pre-equilibrium evolution) the large radial flow causing the high effective photon temperatures (inverse slopes). The dense early stage thus plays a crucial role, even if it does not dominate the electromagnetic radiation.

Our conclusion that the measured thermal photons are mostly emitted at a relatively late, strongly flowing stage of the fireball is consistent with the unexpectedly [236, 232, 237, 189, 230, 238] large photon elliptic flow measured by both PHENIX [239] and ALICE [240]. In fact, these data appear to require an even stronger weighting of photon emission towards the end of the expansion stage where flow is strong [232, 240]. Our finding that the experimentally measured centrality dependence of thermal photon yields appears to be closer to what our model predicts for hadronic radiation than for QGP radiation lends further support to this line of thought. Making a compelling argument for photon radiation from the earliest and hottest stages of the fireball requires combining the photon inverse slope measurements with other electromagnetic observables and a detailed and quantitative comparison with theory. To be convincing, the argument must be based on measurements and theories that determine T_{eff} for thermal photons with about 5% precision. While it is unlikely that future improvements in the theoretical rates change their effective temperatures by a large margin (see the small difference between QGP and HG inverse slopes (green line) in Fig. 18.2), it is possible that the currently used T-dependent rates receive corrections that increase photon yields in the critical quark-hadron transition region, and that further improvements in the dynamical modeling, in particular towards the end of the collision where hydrodynamics begins to break down, will change the weighting of the emission rates by altering the space-time volumes corresponding to each temperature slice.

Chapter 19: Phenomenological study: Direct photon v_n

19.1 Chapter introduction

In chapter 18, we have shown that, thermal photon yields and their (azimuthally averaged) spectral slopes provide experimental information that is heavily weighted in a temperature region of $\pm\,50\,\mathrm{MeV}$ around the quark-hadron phase transition. Anisotropies in the photon spectra [236], in particular the dependence of their magnitudes v_n on the harmonic order n, are most sensitive to the large shear viscous effects prevailing during the earliest, most rapidly expanding stage of the collision fireball. A measurement of anisotropic photon flow thus provides a window into fireball stages that precede those accessible through hadronic observables. Higher-order thermal photon flow anisotropies thus offer the chance to experimentally constrain the QGP specific shear viscosity with a larger weight on higher emission temperatures than provided by complementary measurements of hadronic spectra and their anisotropies.

Measurements by the PHENIX collaboration of direct photons in $200\,A\,\mathrm{GeV}$ Au + Au collisions established a strong excess over the known pQCD sources that has been attributed to thermal radiation [217]. The measured azimuthal anisotropy of this radiation [239] implies an unexpectedly large photon elliptic flow, comparable to that of pions. Recent direct photon measurements by the ALICE collaboration in $2.76\,A\,\mathrm{TeV}$ Pb+Pb collisions at the LHC [218, 240] confirmed these findings which challenge our current theoretical understanding of microscopic rates and/or bulk dynamics [236, 189, 232]. This *direct photon flow puzzle* further motivates us to develop more advanced theoretical tools to resolve it and gain a better understanding of the medium evolution as well as photon production mechanism in relativistic heavy-ion collisions. The work reported in this chapter was published in [238, 241, 242]

19.2 Photon flow anisotropies from event-by-event hydrodynamics

The dynamical evolution of the radiating fireball is again modeled with the boost-invariant hydrodynamic code `VISH2+1` [39], using parameters extracted from earlier phenomenologically successful studies of hadron production in $200\,A\,\mathrm{GeV}$ Au+Au collisions at RHIC [17, 40] and in

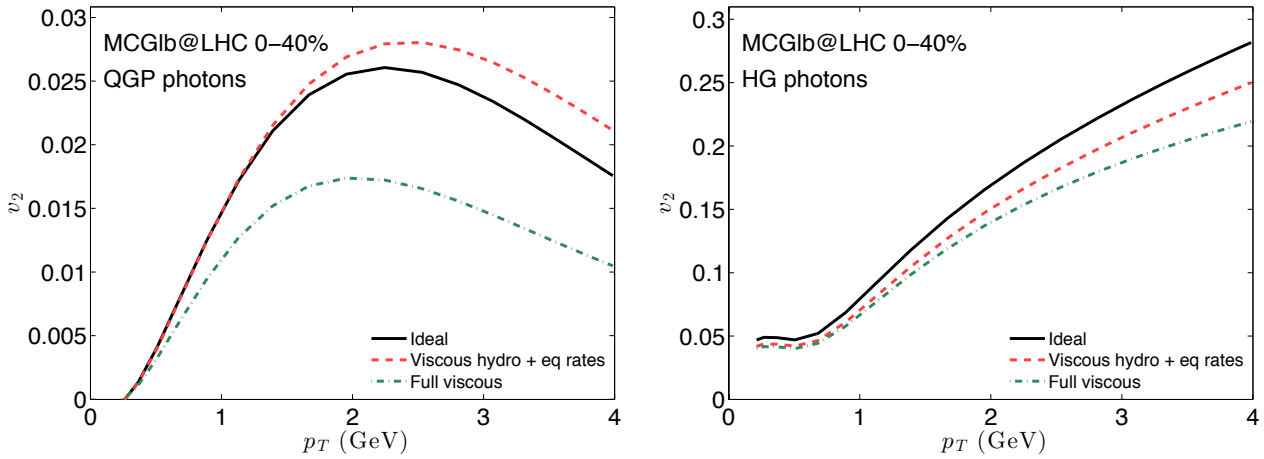

Figure 19.1: Thermal photon elliptic flow from QGP (left panel) and hadron gas phase (right) as a function of p_T at 0-40% centrality Pb+Pb collisions at $\sqrt{s} = 2.76\ A$ TeV. Comparisons between thermal photons emitted from ideal and viscous hydrodynamic medium.

2.76 A TeV Pb+Pb collisions at the LHC [48, 118] as reported in Chapters 5, 6, and 7. Once again we explore both Monte-Carlo Glauber (MCGlb) and Monte-Carlo KLN (MCKLN) initial conditions which we propagate with $\eta/s = 0.08$ and $\eta/s = 0.2$, respectively [17, 40, 48, 118], using the lattice-based equation of state (EoS) `s95p-PCE-v0` [16]. We start the hydrodynamic evolution at $\tau_0 = 0.6\,\mathrm{fm}/c$ and end it on an isothermal hadronic freeze-out surface of temperature $T_{\mathrm{dec}} = 120\,\mathrm{MeV}$. We include prompt photons but ignore contributions from other pre-equilibrium processes which tend to carry small momentum anisotropy.

19.2.1 Shear viscous effect on photon v_n

In Fig. 19.1 and 19.2, we study the shear viscous correction to the thermal photon elliptic flow. In the left panel of Fig. 19.1, , we find that the viscous hydrodynamic evolution alone results in slightly larger QGP photon v_2 at high p_T compared to results from an ideal hydrodynamic medium. This is because the initial peak temperature of the viscous hydrodynamic medium (with $\eta/s = 0.08$) needs to be tuned $\sim 5\%$ lower than in the ideal case to compensate for the extra viscous entropy production during the evolution. This reduces the proportion of high momentum photons coming from the early hot region of the fireball which carries negligible anisotropic flow. However, this increases in the elliptic flow of the QGP photons is overwhelmed by a much larger suppression arising from the viscous correction to the thermal photon emission rate.

Hadronic photons are coming from late stage of the hydrodynamic evolution. In the right panel of Fig. 19.2, we find their elliptic flow receives similar shear viscous effect as the charged hadron v_2, where $\sim 50\%$ of the suppression coming from the reduction of the fireball flow anisotropy. Fig. 19.2 shows the comparisons for the total thermal photons. Since for $p_T > 1$ GeV, a large proportion of the thermal photons are coming from the QGP phase, the viscous correction to thermal photon

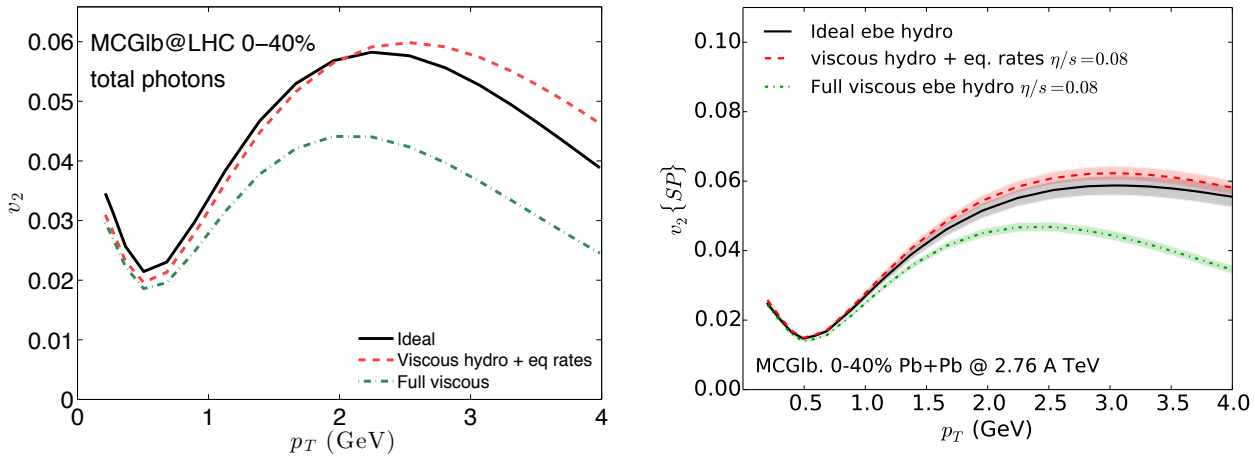

Figure 19.2: Thermal photon elliptic flow as a function of p_T at 0-40% centrality Pb+Pb collisions at $\sqrt{s} = 2.76\ A$ TeV. Comparisons between thermal photons emitted from ideal and viscous hydrodynamic medium. Left panel shows the results from single-shot hydrodynamic simulation with event-average initial condition. Right panel shows the comparison from event-by-event calculations, where $v_n\{\mathrm{SP}\}$ is defined in Eq. (19.1).

v_2 shows similar characteristics as the correction to the QGP photons. In contrast to the elliptic flow of hadrons, the viscous correction to the photon emission rates dominates the suppression for photons. More realistic event-by-event simulation give qualitative the same conclusion as shown in the right panel of Fig. 19.2.

19.2.2 Initial state fluctuation

With event-by-event simulations, we first study the influence of initial state fluctuation to the final photon observables. We use the scalar-product method to compute the thermal photon elliptic flow coefficient from our event-by-event simulations,

$$v_n^\gamma\{\mathrm{SP}\}(p_T) = \frac{\left\langle \frac{dN^\gamma}{dy p_T dp_T}(p_T) v_n^\gamma(p_T) v_n^{\mathrm{ch}} \cos(n(\Psi_n^\gamma(p_T) - \Psi_n^{\mathrm{ch}})) \right\rangle}{\left\langle \frac{dN^\gamma}{dy p_T dp_T}(p_T) \right\rangle v_n^{\mathrm{ch}}\{2\}}. \tag{19.1}$$

Please note that Eq. (19.1) differs from the usual definition of the scalar-product v_n (as in Eq. 10.8) by the additional photon multiplicity factors in both numerator and denominator. This photon multiplicity weight is essential in order to have a consistent definition with the experimental measurement (see chapter 21 for details).

In Fig. 19.3, we compare the difference between thermal photon v_2 from smooth event-averaged and event-by-event hydrodynamic calculations. For both ideal and viscous cases, the photon $v_2\{\mathrm{SP}\}$ from event-by-event simulations is about 10-20% smaller than the mean v_2 from the smooth event-averaged hydrodynamic medium. In more detail, we find the initial state fluctuation increases the final flow anisotropy, however the photon multiplicity weight factor in Eq. (19.1)

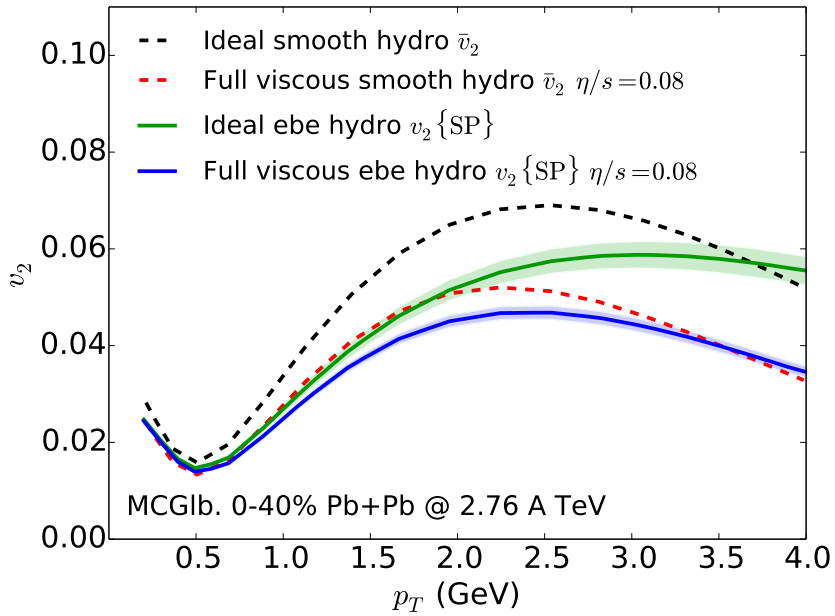

Figure 19.3: Thermal photon elliptic flow as a function of p_T at 0-40% centrality Pb+Pb collisions at $\sqrt{s} = 2.76$ A TeV. Comparisons between thermal photons elliptic flow from smooth event averaged and event-by-event hydrodynamic medium.

biases the final results towards central collisions with smaller elliptic flow, especially for bumpy profiles with temperature hot spots.

19.2.3 p_T-integrated photon v_n

The centrality dependence of the p_T-integrated thermal photon $v_n\{\mathrm{SP}\}$ is shown in the left panel of Fig. 19.4 for $n = 2, 3$. Thermal photon $v_n\{\mathrm{SP}\}$ shows similar centrality dependence as charged hadrons. The elliptic flow of thermal photons increases with centrality due to the increasing geometric eccentricity of the nuclear overlap area. The triangular flow has little centrality dependence because it is purely driven by event-by-event fluctuations. The ratio between thermal photon elliptic and triangular flow is shown in the right panel of Fig. 19.4. Since prompt photons carry a small anisotropy their contribution is expected to be negligible in this ratio:

$$\frac{v_2^\gamma\{\mathrm{SP}\}(p_T)}{v_3^\gamma\{\mathrm{SP}\}(p_T)} \simeq \frac{\left\langle \frac{dN^{\gamma,\mathrm{thermal}}}{dy p_T \mathrm{d}p_T}(p_T) v_2^{\gamma,\mathrm{thermal}}(p_T) v_2^{\mathrm{ch}} \cos(2(\Psi_2^{\gamma,\mathrm{thermal}}(p_T) - \Psi_2^{\mathrm{ch}})) \right\rangle}{\left\langle \frac{dN^{\gamma,\mathrm{thermal}}}{dy p_T \mathrm{d}p_T}(p_T) v_3^{\gamma,\mathrm{thermal}}(p_T) v_3^{\mathrm{ch}} \cos(3(\Psi_3^{\gamma,\mathrm{thermal}}(p_T) - \Psi_3^{\mathrm{ch}})) \right\rangle} \frac{v_3^{\mathrm{ch}}\{2\}}{v_2^{\mathrm{ch}}\{2\}}. \tag{19.2}$$

The ratio $v_2^\gamma\{\mathrm{SP}\}/v_3^\gamma\{\mathrm{SP}\}$ is generically larger than the ratio of charged hadrons, reflecting the fact that thermal photons are more sensitive to the viscous effects in the hot dense region of the fireball during the early time of the evolution. The ratio increases with the specific shear viscosity η/s of the medium because the higher order harmonic flows are suppressed more strongly by the shear viscous effects. For a fixed $\eta/s = 0.20$, the centrality dependence of this ratio is stronger for MCKLN than for MCGlb initial conditions. This is due to the stronger centrality dependence

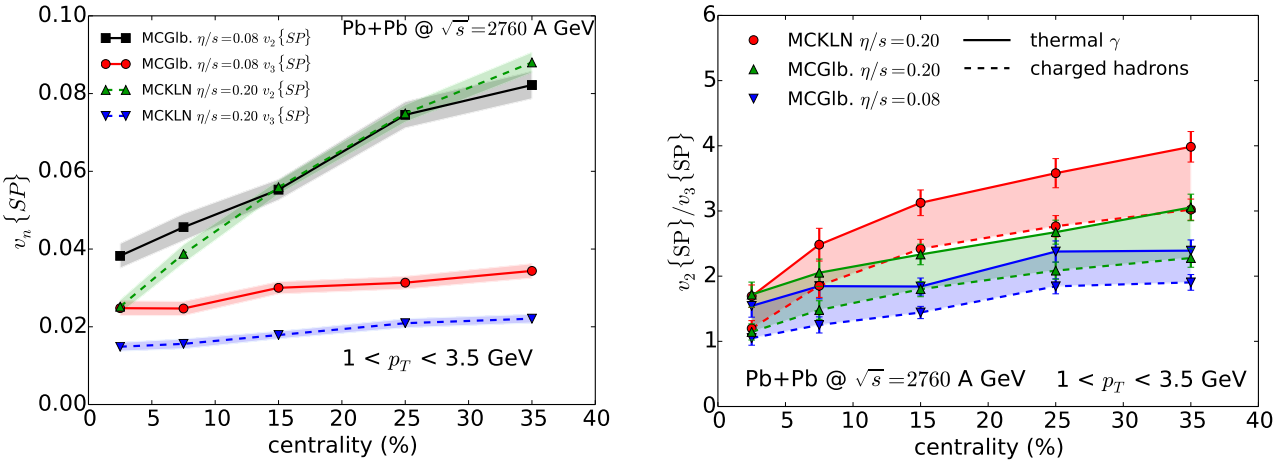

Figure 19.4: Left panel: Centrality dependence of the p_T-integrated $v_n\{\mathrm{SP}\}$ of thermal photons from MCGlb. and MCKLN initial conditions for 2.76 A TeV Pb+Pb collisions. p_T is integrated from 1 to 3.5 GeV. Right panel: The ratio of $v_2\{\mathrm{SP}\}/v_3\{\mathrm{SP}\}$ as a function of collision centrality. Solid and dashed lines show the ratio for thermal photons and for charged hadrons, respectively. The ratio is shown for three pairings of initial conditions (MCGlb and MCKLN) and specific shear viscosities (η/s), as detailed in the legend. Note that both MCGlb initial conditions with $\eta/s = 0.08$ and MCKLN initial conditions with $\eta/s = 0.2$ correctly reproduce the measured hadron spectra and elliptic flows while MCGlb initial conditions with $\eta/s = 0.2$ do not [40, 48]. The shaded regions between corresponding solid and dashed lines emphasize the increase of this ratio for thermal photons, due to their higher sensitivity to shear viscous effects at early times.

of $v_2^\gamma\{\mathrm{SP}\}$ in the MCKLN model, shown in the left panel of Fig. 19.4. Eq. (19.2) shows that the $v_2^\gamma\{\mathrm{SP}\}/v_3^\gamma\{\mathrm{SP}\}$ ratio in Fig. 19.4 and later Fig. 19.7 (for p_T-differential case) is insensitive to the yields from direct photon sources that carry zero anisotropic flow (prompt photons). A measurement of this ratio thus allows to focus attention on those photons that reflect and probe the space-time history of the evolving near-thermal medium. Pre-equilibrium photons generated by the strong magnetic field of the passing nuclei through the QCD anomaly [243] are predicted to carry sizable v_2 but are expected to have small triangular flow v_3; they would generate much larger v_2/v_3 than thermal photons. Measuring this ratio will allow us to disentangle these two mechanisms for the already observed (large) direct photon elliptic flow.

In the left panel of Fig. 19.5, we further show higher order anisotropic flow coefficients up to $n = 5$ for thermal photons. The right panel of Fig. 19.5 tests whether the v_n/ε_n of thermal photons falls off exponentially as a function of n^2 as suggested in [178]. We find that v_n/ε_n falls faster than $c_1 e^{-c_2 n^2}$ for $n > 3$ for both MCGlb and MCKLN initial conditions.

19.2.4 p_T-differential photon v_n

Results for $v_{2,3,4,5}(p_T)$ for thermal photons from central and semi-peripheral Au+Au and Pb+Pb collisions at RHIC and LHC are shown in Fig. 19.6. For each centrality bin and initialization model we run 1000 fluctuating events. We emphasize that such an event-by-event approach is

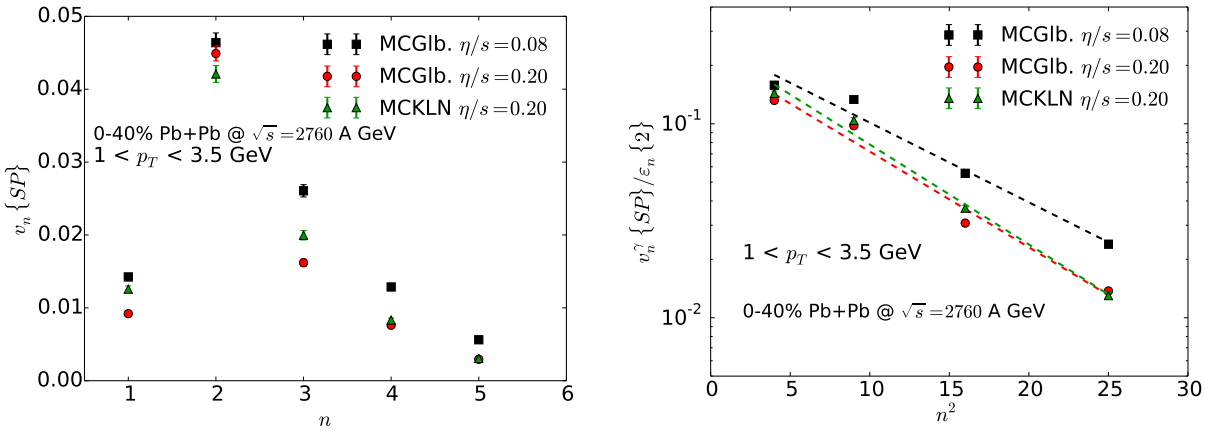

Figure 19.5: p_T integrated photon anisotropic flow as a function of its harmonic order,n for 0-40% Pb + Pb collisions at $\sqrt{s} = 2.76$ A TeV. Right panel: $v_n^\gamma\{\mathrm{SP}\}/\varepsilon_n\{2\}$ vs n^2. Dashed lines indicate fits according to the functional form $c_1 e^{-c_2 n^2}$.

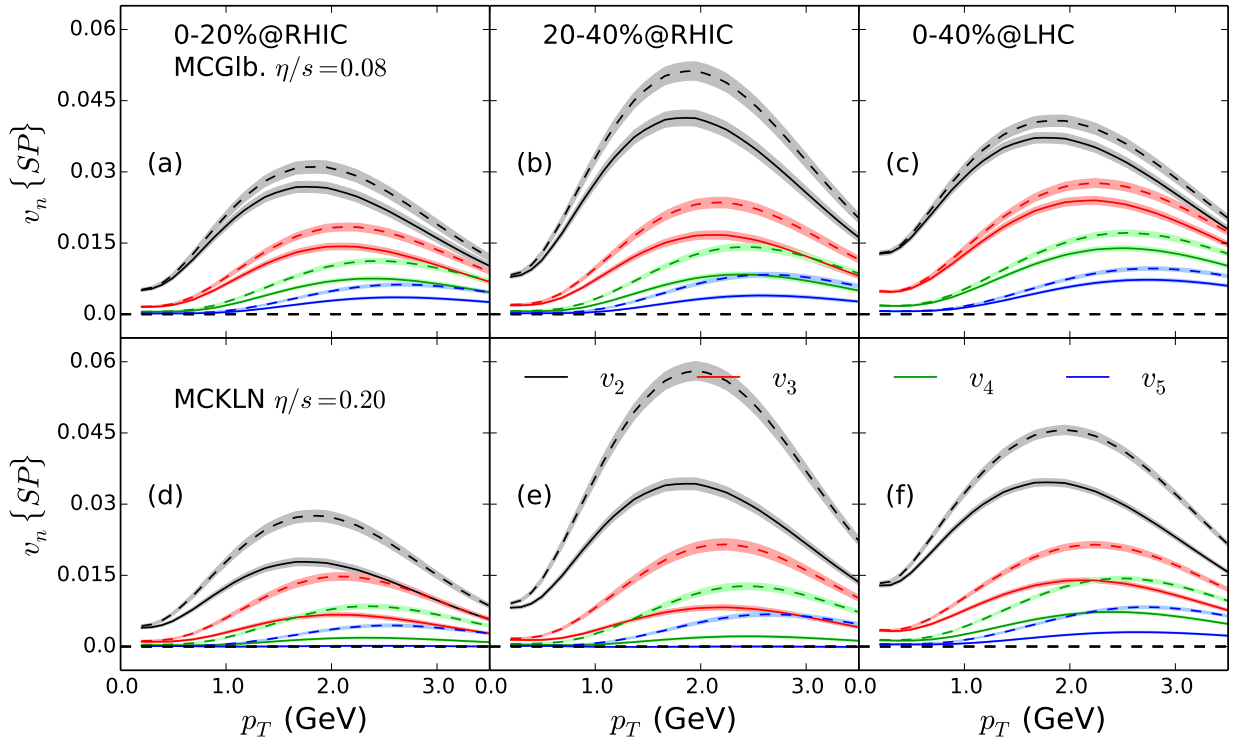

Figure 19.6: Direct photon (prompt+ thermal(QGP + HG)) anisotropic flow coefficients v_2-v_5 for 200 A GeV Au+Au collisions at 0−20% and 20−40% centrality (left four panels) and for 2.76 A TeV Pb+Pb collisions at 0−40% centrality (right two panels). The upper (lower) row of panels shows results using MCGlb (MCKLN) initial conditions with $\eta/s = 0.08$ (0.2). Solid (dashed) lines depict results that include (neglect) viscous corrections to the photon emission rates. The shaded bands indicate statistical uncertainties.

indispensable for the higher-order flow harmonics $n \geq 3$, and does influence the flow magnitude as shown in Sec. 19.2.2. Different harmonics are plotted in different colors. The difference between solid and dashed lines illustrates the importance of including viscous corrections in the emission rates; both line styles include viscous effects on the evolution of the hydrodynamic flow in the

medium. Note that for MCKLN initial conditions with $\eta/s = 0.20$, the off-equilibrium correction in the photon spectrum from the term $\sim \pi^{\mu\nu}$ remains smaller than the equilibrium contribution up to $p_T \sim 3.5\,\mathrm{GeV}$ in 0-40% Pb+Pb at the LHC, and up to $p_T \sim 2.5\,\mathrm{GeV}$ in 20-40% Au+Au at RHIC, indicating validity of our results up to these momenta.

Since the MCKLN-initialized fireballs are evolved with 2.5 times larger shear viscosity than the MCGlb fireballs, the viscous corrections to the emission rates are larger in the bottom panels of Fig. 19.6. After inclusion of viscous effects, all higher order photon $v_n (n > 3)$ are smaller for MCKLN initial conditions than for MCGlb ones due to the larger associated shear viscosity. In the 20%-40% centrality at RHIC energy, the v_4 and v_5 are almost completely damped away in the MCKLN case by the large viscous corrections to the photon emission rates.

Note that, before including viscous effects on the emission rates (dashed lines), the higher-order anisotropic flows generated from MCKLN initial conditions are larger than those from the MCGlb model, in spite of the larger η/s used in the MCKLN runs. This is due to lower initial temperatures in hydrodynamic simulations with larger shear viscosity, in order to compensate for larger entropy production. This reduces the space-time volume for photon emission from the QGP phase and increases the ratio of photons from the hadronic phase to those from the QGP phase. Since hadronic photons carry about 10 times larger flow anisotropies, the v_n of the final total photons increase.

The rise and fall of all v_n with increasing p_T reflects the dominance of hadronic photon sources (which exhibit strong flow) at low p_T and the increasing weight of QGP photons from earlier and hotter stages (where flow is weak) and of prompt photons (whose anisotropic flow is assumed to vanish) at higher p_T [236].

Comparing central ($0-20\%$) to semi-peripheral ($20-40\%$) RHIC collisions we see that only v_2 increases in the more peripheral collisions, due to the increasing geometric elliptic deformation ε_2 of the reaction zone. The higher-order v_n show little centrality dependence, reflecting a cancellation between increasing hydrodynamic flow anisotropies (dashed lines) and increasing shear viscous suppression of the photon emission rate anisotropies, probably due to the smaller fireball size in peripheral collisions.

Comparing RHIC with LHC collisions we find an increase of thermal photon v_n with collision energy, mainly due to the $\sim 15\%$ longer fireball lifetime at the LHC which affects mostly the QGP phase. It allows QGP photons to develop larger flow anisotropies at LHC compared to RHIC energies. The longer fireball lifetime also helps the system to evolve closer to local thermal equilibrium. The smaller ratio $\pi^{\mu\nu}/(e+P)$, when averaged over the fireball history, explains the smaller difference between dashed and solid lines (reflecting the photon emission rate anisotropy) at LHC energies compared to RHIC.

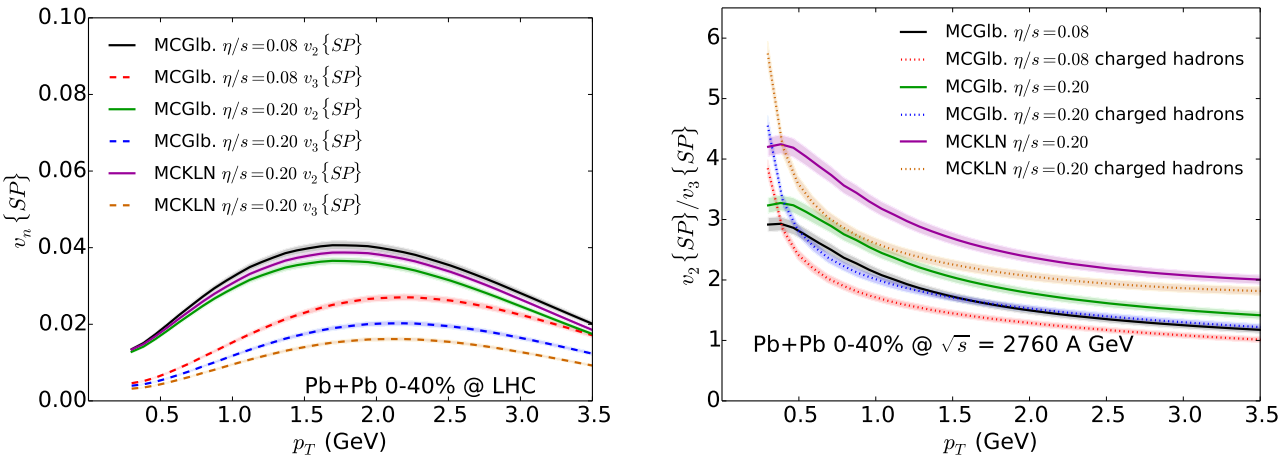

Figure 19.7: Left panel: Comparison of p_T-differential $v_2\{\mathrm{SP}\}$ (solid lines) and $v_3\{\mathrm{SP}\}$ (dashed curves) of thermal photons for different η/s and initial conditions at 0-40% centrality in Pb + Pb collisions at $\sqrt{s} = 2.76\ A$ TeV. Right panel: The corresponding ratio $v_2\{\mathrm{SP}\}/v_3\{\mathrm{SP}\}$ as a function of p_T, compared with the same ratio for charged hadrons (dotted lines).

Proceeding to Fig. 19.7, in order to separate the effects from initial conditions and shear viscosity to thermal photon anisotropic flow, we show comparisons of p_T-differential elliptic and triangular flows of thermal photons additionally with the results using MCGlb initial conditions with $\eta/s = 0.20$. Similar to v_n of charged hadrons, with the same MCGlb initial conditions, a larger η/s results smaller photon $v_n(p_T)$. Thermal photon v_3 receives a strong suppression from the shear viscosity compared to v_2. On the other hand, with the same η/s, MCKLN initial conditions result in a larger v_2 but a smaller v_3 compared to MCGlb runs. This is different from hadrons where, for the same η/s, MC-Glauber and MCKLN initial conditions produced similar v_3 value [117]. In the right panel, we plot the p_T-differential ratio of $v_2\{\mathrm{SP}\}/v_3\{\mathrm{SP}\}$. Compared to charged hadrons, the thermal photon $v_2^\gamma\{\mathrm{SP}\}/v_3^\gamma\{\mathrm{SP}\}$ ratio is larger. For $0.7 < p_T < 2.0$ GeV, the difference between thermal photons and charged hadrons is the biggest.

19.3 Comparison with experimental measurements

In Fig. 19.8 we compare the differential elliptic flow $v_2^\gamma\{\mathrm{SP}\}(p_T)$ of direct photons (i.e. the sum of prompt and thermal photons) from our event-by-event hydrodynamic simulations with experimental data from the PHENIX and ALICE Collaborations. One sees that the elliptic photon flow predicted by the theoretical model falls severely short of the measured elliptic flow. Our calculations do not include pre-equilibrium photons emitted before the start of our hydrodynamic evolution at $\tau_0 = 0.6\,\mathrm{fm}/c$ which presumably carry little flow anisotropy and would thus further dilute the predicted v_2. On the other hand, our calculation also does not include hadronic emission processes that involve collisions between mesons and (anti-)baryons and baryon-induced modifications of the vector meson spectral functions [182], as well as meson-meson and meson-baryon

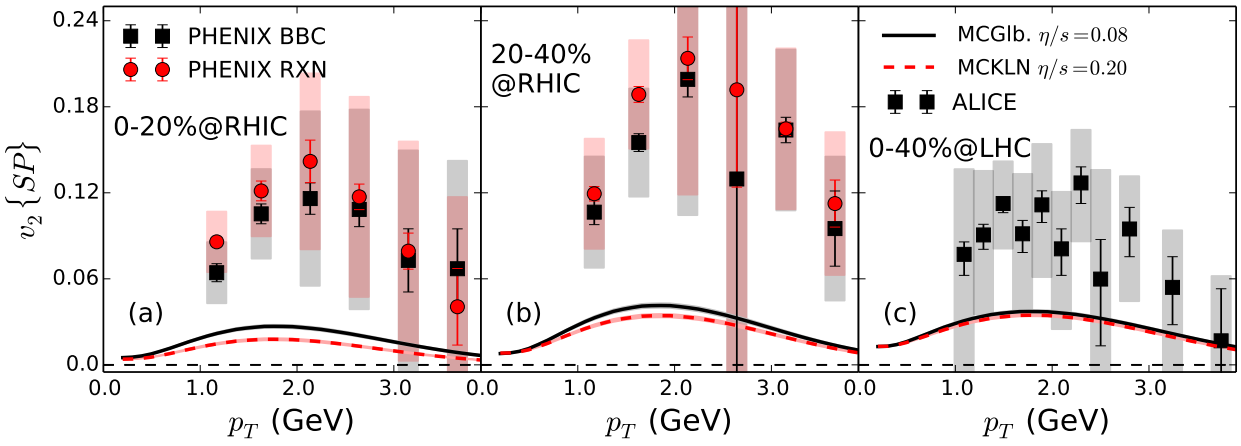

Figure 19.8: Comparison of direct photon (prompt + thermal (QGP+HG)) elliptic flow from event-by-event viscous hydrodynamics with recent experimental data from (a) 0-20% and (b) 20-40% central 200 A GeV Au+Au collisions at RHIC [239] and (c) from 0-40% central 2.76 A TeV Pb+Pb collisions at the LHC [240]. Solid black (dashed red) lines correspond to MCGlb (MCKLN) initial conditions evolved with a shear viscosity $\eta/s = 0.08$ (0.2), respectively.

bremsstrahlung processes [244, 245]. Since all these additional hadronic photon emission processes occur during a stage where the hydrodynamic flow anisotropies have reached (most of) their final strength, their inclusion would increase the direct photon elliptic flow. Whether doing so will succeed in reproducing the experimental data remains to be seen. Finally, the calculations shown in Fig. 19.8 do not include any pre-equilibrium transverse flow, nor any photons from the decays of short-lived resonances after kinetic freeze-out. These two machanism will be explored in the following subsection.

19.3.1 Efforts towards solving direct photon flow puzzle

Our hydrodynamic simulations seriously underpredict the measured photon elliptic flow. We also find in Chapter 18 that they also significantly underpredict the photon yield at low $p_T < 2$ GeV. In chapter 18, our study of photon slope as well as the centrality dependence of the direct photon yield suggests missing strength in the photon emission at late times. The large elliptic flow that must be carried by these missing photons, the centrality dependence of their yield, and the fact that we lack thermal photons in the spectrum mostly at low p_T [222, 230], all indicate that most of the missing photons must come from either the phase transition region or the hadronic rescattering phase.

Some of the many hadronic resonances emitted from the decoupling hadron resonance gas have photon-producing decay channels that were not included in hydrodynamic simulations before. These resonances decouple with large anisotropic flows and pass them on to their decay-photon daughters. Even though the corresponding branching ratio for each resonance is small, after adding up photons from all such short-lived resonance decays, the direct photon elliptic and triangular

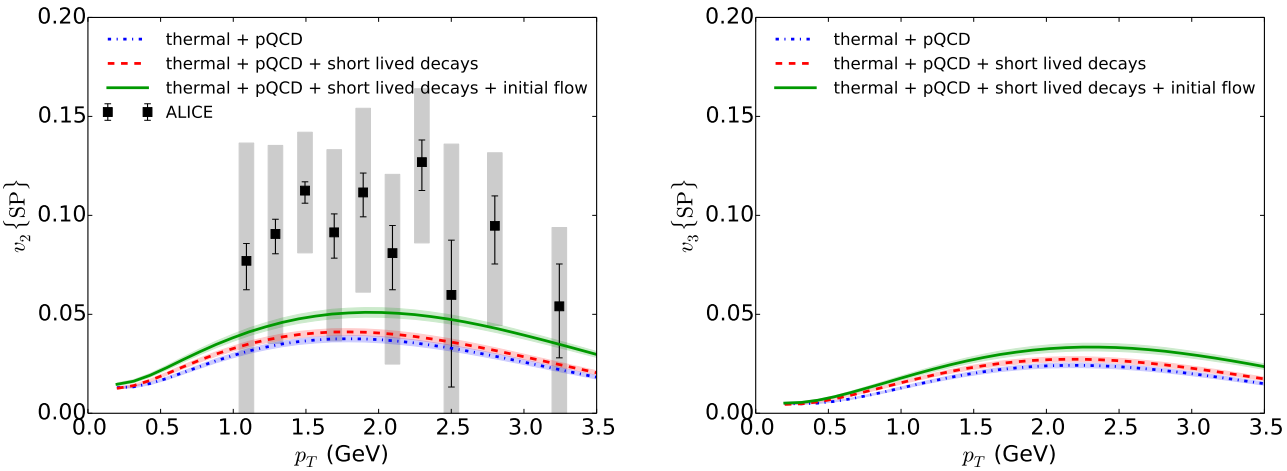

Figure 19.9: Effect of pre-equilibrium flow and photons from the decay of short-lived hadronic resonances after hadronic decoupling on the direct (thermal + prompt) photon elliptic and triangular flow.

flows are found to increase by up to 25%. This is shown by the difference between the red dashed and blue dash-dotted curves in Fig. 19.9.

Pre-equilibrium dynamics has, however, also the potential to increase the photon elliptic flow after thermalization. In contrast to hadrons, which are only sensitive to the final elliptic flow at hadronic freeze-out, even a small increase of the flow anisotropy at each time will affect the elliptic flow of photons *emitted during all stages* of the collision; given the small flow predicted so far, this could turn out to be a significant improvement. Comparing the green and red curves in Fig. 19.9 illustrates the possible effect of pre-equilibrium flow: while the red curves assume zero transverse flow at the beginning of the hydrodynamic stage at $\tau_0 = 0.6\,\mathrm{fm}/c$, the green solid curves allow the massless partons created at $\tau = 0$ with a bumpy initial density profile to free-stream until $\tau_0 = 0.6\,\mathrm{fm}/c$, where the resulting energy momentum tensor is Landau-matched to viscous hydrodynamic form, yielding an non-zero anisotropic initial flow profile (together with a non-zero initial viscous pressure tensor). Since massless partons move with light speed, free-streaming likely overestimates the initial flow at the matching time somewhat. Still, its effect on the photon anisotropic flow is not negligible, and any effect that helps to increase the elliptic flow signal is welcome. Adding both the pre-equilibrium flow and post-freeze-out resonance decay contributions thus enhances the photon elliptic and triangular flows by 40-50%.

19.4 Correlations and event distributions of photon v_n

In Fig. 19.10, we investigate the correlation between the direct photon v_n and the initial eccentricity ε_n. We find that the thermal photon v_n can be parametrized as $v_n = a(\{\varepsilon_m\}) + b\varepsilon_n, (m \neq n)$, where b represents the relative strength of the linear correlation between v_n and ε_n and the intercept $a(\{\varepsilon_m\})$ captures the residual non-linear coupling with the other orders

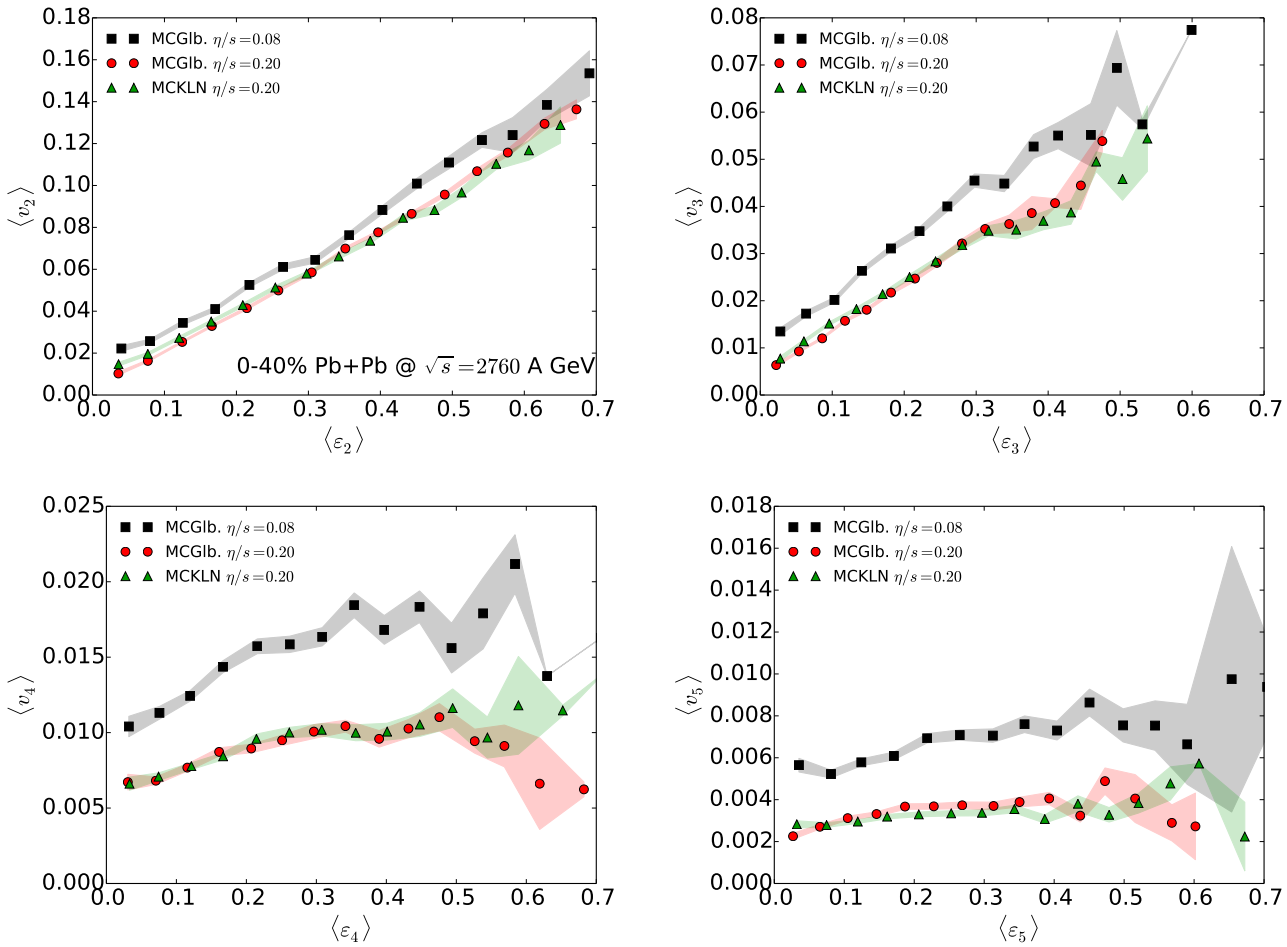

Figure 19.10: Direct photon anisotropic flow v_n as a function of the initial eccentricity ε_n for $n = 2 - 5$ at 0-40% Pb+Pb collisions at $\sqrt{s} = 2.76$ A TeV.

of harmonic flows. For $n = 2, 3$, the intercept a is much smaller compared to the typical size of v_n, which indicates a strong dominance of the linear correlation between direct photon v_n and the initial ε_n, while non-linear couplings to higher order ϵ_m's are suppressed. This linear correlation becomes weaker as n increases. For $n = 5$, v_5 shows almost no sensitivity to ε_5, which means v_5 of direct photons is mostly generated from other harmonics by non-linear mode-coupling. Furthermore, for all orders of n, the intercepts a are smaller from hydrodynamic simulations with $\eta/s = 0.20$. This means that shear viscosity damps the non-linear mode coupling between different orders of harmonic flows. Interestingly, we find that the two sets of simulations with $\eta/s = 0.20$ give almost identical correlations between direct photon v_n and initial ε_n independent of the difference in the used initial condition models. This reflects the fact that the conversion efficiency from the initial eccentricity to final flow anisotropy is almost entirely controlled by the shear viscosity of the medium.

Due to the limited number of photons emitted in each collision event, the anisotropic flow of direct photons is usually measured through the correlation with all charged hadrons from the

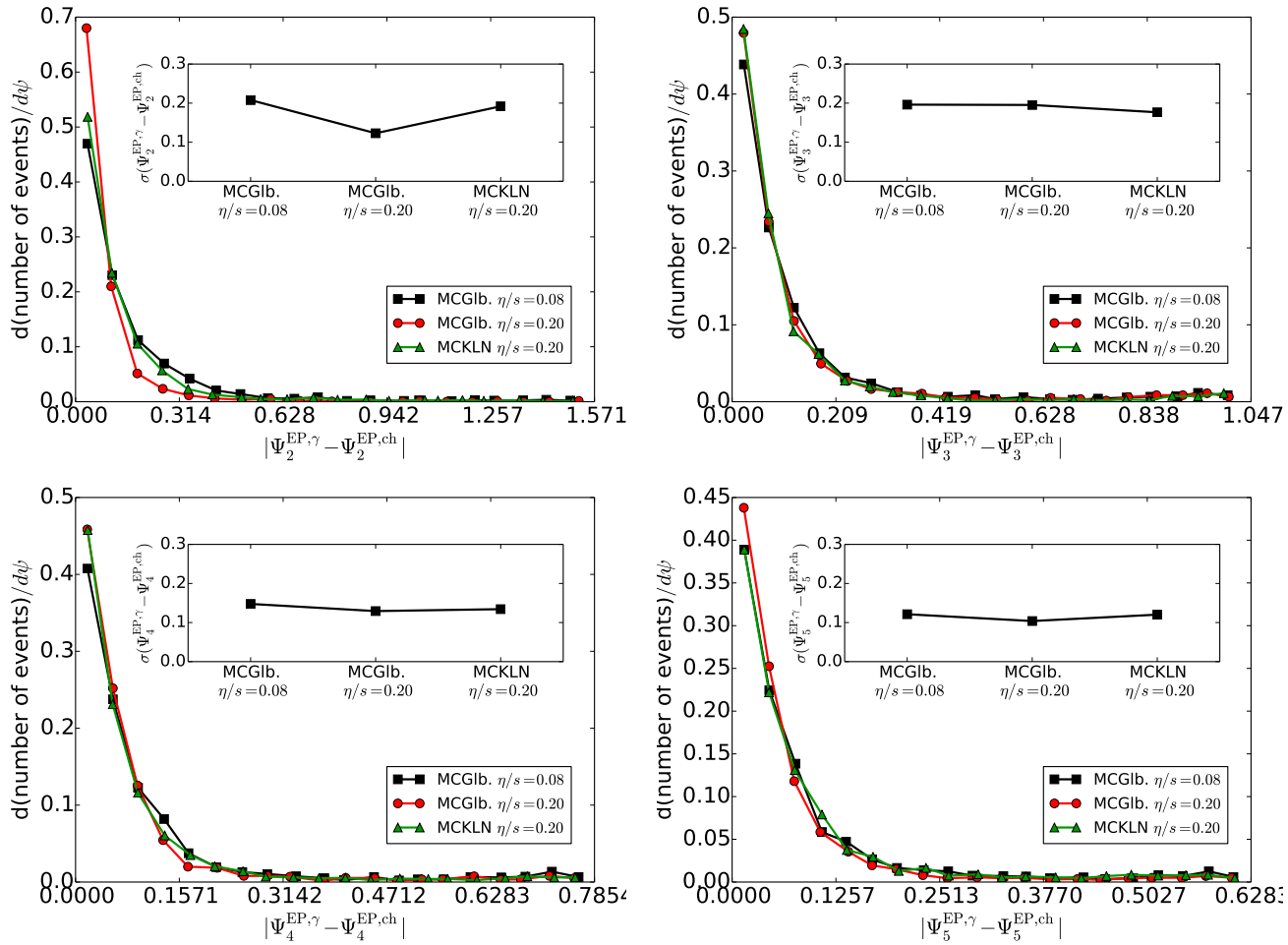

Figure 19.11: Correlation between n-th order flow plane angle of direct photon vs charged hadrons for n = 2-5 at 0-40% Pb + Pb collision at $\sqrt{s} = 2.76$ A TeV.

same event. Thus the difference between the underlying flow angles of direct photons and charged hadrons and how it fluctuates from event to event influences the final photon anisotropic flow. In Fig. 19.11, we study the correlation between the n-th order flow plane angles of direct photons and charged hadrons. For $n = 2 - 5$, the direct photon flow angles $\Psi_n^{EP,\gamma}$ are tightly correlated with the charged hadron flow angles $\Psi_n^{\mathrm{EP,ch}}$. For $n = 2$, a larger shear viscosity results in a stronger correlation between $\Psi_2^{EP,\gamma}$ and $\Psi_2^{\mathrm{EP,ch}}$.

19.5 Chapter summary

In this chapter, we presented a phenomenological study of the anisotropic photon flow coefficients from event-by-event viscous hydrodynamic simulations. We find that the shear viscosity suppresses the photon v_n. The dominant suppression comes from the viscous correction to the photon emission rates. Event-by-event simulations show sizable triangular flow v_3 as well as higher order $v_n (n = 4, 5)$ of direct photons at both RHIC and LHC energies. A comparison of p_T-integrated v_2/v_3 of direct photons and charged hadrons as a function of collision centrality

shows strong sensitivity to medium viscosity as well as to the initial conditions. Compared to experimentally measured elliptic flow data, the non-equilibrium corrections from shear viscosity do not help to solve the "direct photon flow puzzle" (i.e. the fact that our hydrodynamic simulations severely underpredict the elliptic flow of direct photons). We find that pre-equilibrium flow as well as photons coming from short lived resonance decays increase the final direct photon v_n by significant amounts and thus need to be included in the theoretical calculations. Finally, we find that photon v_n shows a similar correlation with the initial ε_n as charged hadron v_n. Also, the photon flow plane angles are strongly correlated with the corresponding hadronic ones.

Chapter 20: Phenomenological study: Effects from partial chemical equilibrium in the hadronic phase

20.1 Chapter introduction

Relativistic heavy-ion collisions feature a sequential freeze-out in the hadronic phase. Based on the thermal model fit to final measured particle yields, the chemical freeze-out happens around $T_{\rm chem} = 165$ MeV. Below $T_{\rm chem}$, hadrons can still exchange momenta through elastic scatterings and decays. A later kinetic freeze out happens around $T_{\rm kin} = 100 - 120$ MeV which can be extracted from blast wave model fits to the identified particle p_T spectra [107]. Between the chemical and kinetic freeze-out, the system develops non-vanishing chemical potentials for the stable hadron species, which fix the relative yields between different species of particles, after resonance decays, at their values established at $T_{\rm chem}$ [77]. These chemical potentials will increase the photon emission rates by corresponding fugacity factors. On the other hand, as the system evolves out of chemical equilibrium, the thermal cooling rate also accelerates, which results in a smaller space-time volume for electromagnetic radiation. These two effects act against each other. In this chapter, we perform hydrodynamic simulations to study the competition between these two effects and more generally, explore the sensitivity of photon observables to the EOS of our fireball.

20.2 Model setup

20.2.1 Equation of State

We use the lattice QCD based equation of state, `s95p`, for our simulations. There are three sub-versions of `s95p`, namely `s95p-v0-PCE`, `s95p-v1`, and `s95p-v1-PCE`. "v0" and "v1" represent two different parameterizations of the trace anomaly at high temperature measured by Lattice QCD. The detail parameterizations of "v0" and "v1" are described in Ref. [16]. The equations of state `xxx-PCE` implement partial chemical equilibrium below $T_{\rm chem}$ as discussed below.

In Fig. 20.1, the relation between pressure and energy density is plotted in the left panel and the square of speed of sound c_s^2 is plotted in the right panel. The three lattice QCD based EOS

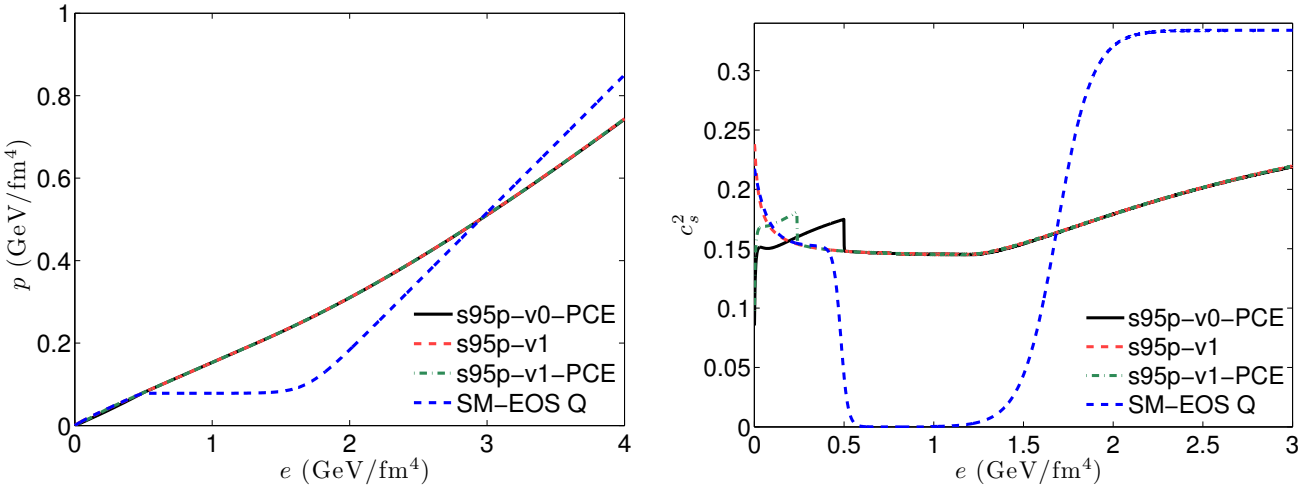

Figure 20.1: Pressure (left panel) and square of speed of sound (right panel) as a function of energy density for three different subversions of `s95p` equation of state are compared with first order phase transition EOS.

are compared with `SM-EOS Q` which assumes a (slightly smoothed) first order phase transition. As seen from the plot of c_s^2 vs. e (right panel), `s95p` does not have any soft point within the transition region. Since the acceleration in the local rest frame is controlled by the pressure gradients as

$$D_t u^\mu = \frac{\nabla^\mu P}{e+P} \simeq \frac{c_s^2}{c_s^2+1}\frac{\nabla^\mu e}{e}, \tag{20.1}$$

a larger speed of sound in the transition region leads to faster hydrodynamic expansion. In the high temperature region, the speed of sound is smaller than that of an ideal gas. So with the `s95p` EOS, the fireball will expand more slowly in the QGP phase but faster in the phase transition region than for `SM-EOS Q`. This affects the space-time volume of the fireball in these two stages, and this is crucial for thermal photon emission.

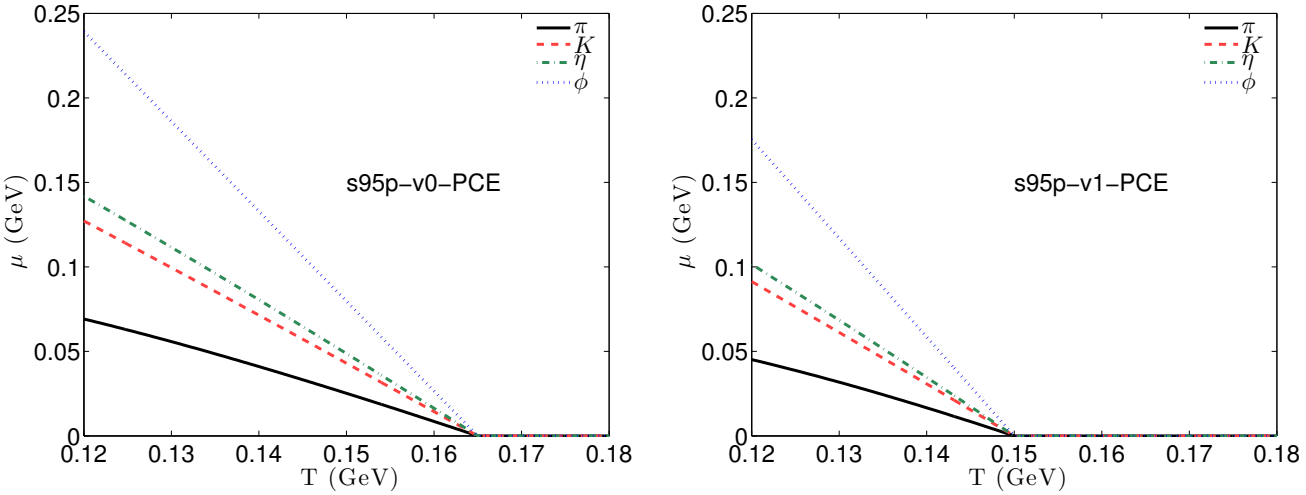

Figure 20.2: The chemical potential of stable mesons as a function of temperature for the partial chemical equilibrium EOS, s95p-v0-PCE (left) and s95p-v1-PCE (right).

The label "PCE" means that the equation of state implements partial chemical equilibrium in the hadronic phase. In order to fixed the relative ratios between the yields of different particles species, temperature dependent chemical potentials are assigned to each stable hadron species below the chemical freeze out temperature. The chemical potentials of short lived unstable resonances are the sums of the chemical potentials of their stable decay daughters. `s95p-v0-PCE` implements chemical freeze out at $T_{\rm chem} = 165\,{\rm MeV}$. `s95p-v1-PCE` implements PCE below $T_{\rm chem} = 150\,{\rm MeV}$. `s95p-v1` assumes that the system always stays in chemical equilibrium. The chemical freeze out temperature is chosen to fit the measured particle ratios. $T_{\rm chem} = 165$ MeV is chosen to fit the proton to π ratio that is measured by the STAR collaboration at RHIC, while $T_{\rm chem} = 150$ MeV is chosen to fit the PHENIX measurements which have a lower proton yield than STAR (see the upper right panel of Fig. 20.3 below). Above $T_{\rm chem}$, the three versions of `s95p` have the same thermodynamic relation among energy density, pressure, entropy density, and temperature (see left panel of Fig. 20.1). In the right panel of Fig. 20.1, we find there are little kinks in c_s^2 in the low energy density region for the two PCE EOS. They correspond to a discontinuity caused by turning on the non-equilibrium chemical potentials. In Fig. 20.2, we show the chemical potentials of several stable mesons as functions of temperature for `s95p-v0-PCE` and `s95p-v1-PCE`. The temperature dependence of the chemical potential is almost linear. Chemical potentials for heavy particles are seen to increase faster than those for light particles. At a fixed temperature, the chemical potentials in `s95p-v0-PCE` are larger than those for `s95p-v1-PCE`.

20.2.2 Hadron spectra and flow anisotropies

For this study, we use event-averaged initial conditions generated with the Monte-Carlo Glauber model which are evolved with ideal hydrodynamics. For different equations of state, the other hydrodynamic input parameters (freeze out temperature and thermalization time) are tuned to reproduce as well as possible the hadronic spectra and elliptic flow data for charged hadrons, pions, and protons. For `s95p-v0-PCE`, we set $\tau_0 = 0.6\,{\rm fm}/c$, and $T_{\rm dec} = 120\,{\rm MeV}$. For `s95p-v1`, we choose $\tau_0 = 1.0\,{\rm fm}/c$, and $T_{\rm dec} = 150\,{\rm MeV}$. For `s95p-v1-PCE`, we take $\tau_0 = 0.6\,{\rm fm}/c$ and $T_{\rm dec} = 120\,{\rm MeV}$. The comparison with experimental data is shown in Fig. 20.3.

In the upper panels of Fig. 20.3, charged hadron, π^+ and proton spectra are compared with both the STAR and the PHENIX data in the 0-5% most central collisions. The overall normalization factors of initial conditions are tuned to reproduce the total yield of the charged particles. With the chosen sets of hydrodynamic parameters, all three equations of state give fairly good descriptions to the charged hadron and π^+ spectra, but not for the proton spectra. For `s95p-v0-PCE`, since the chemical potentials are tuned to match the p/π ratio measured by STAR, the total yield of the proton matches with the STAR data but is about a factor of two higher than the PHENIX

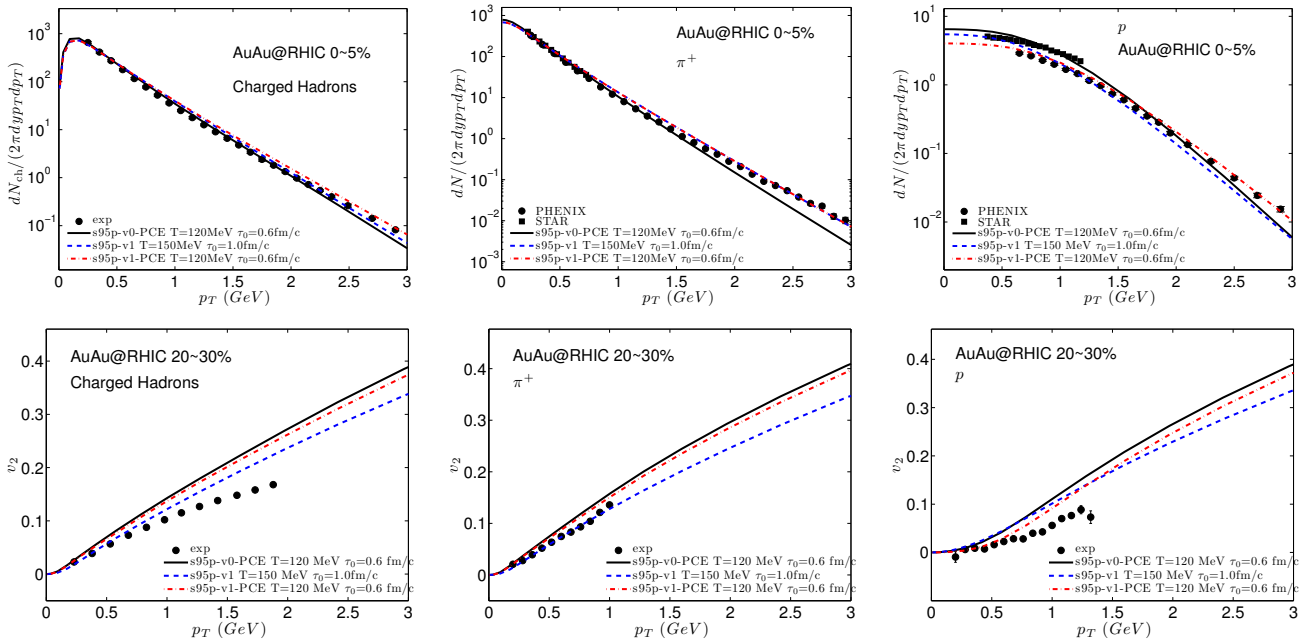

Figure 20.3: Upper panels: Charged hadrons, pion and proton spectra at 0-5% most central collisions at RHIC. Lower panels: Charged hadrons, π^+, and proton differential elliptic flow coefficients at 20-30% centrality.

measurements. The slope of the proton spectra from `s95p-v0-PCE` is too steep compared to the STAR data, which indicates that more radial flow is needed. `s95p-v1` assumes chemical equilibrium all the way to kinetic freeze out. So the p/π ratio changes with the kinetic freeze out temperature. Once we fixed $T_{\rm kin}$ by matching the slope of the π^+ spectra, the p/π ratio is also determined. In our case with $T_{\rm dec} = 150$ MeV, the proton yield is close to the value measured by PHENIX. But since we freeze out the fireball at 150 MeV, the system does not have enough time to fully develop hydrodynamic radial flow, the slope of the proton spectra is too steep compared to the data. For `s95p-v1-PCE`, the p/π ratio is matched to the PHENIX measurements. It also reproduces the shape of the PHENIX proton spectra fairly well. In the lower panels of Fig. 20.3, we compare the elliptic flow coefficients v_2 with experimental data at 20-30% centrality. All three equations of state result in larger v_2 for $p_T > 1\,\text{GeV}$ than measured experimentally. This leaves room for a small but non-zero specific shear viscosity.

20.3 Thermal photon emission

The above exercise dose not aim at a precise description of the hadron spectra but at a hadronically constrained space-time evolution of the fireball medium that we can now use for photon studies. We focus on ideal fluid dynamics because we want to emphasize the effect from the EOS without conflagration from non-ideal fluid effects. The following study is thus schematic only, without pretense of quantitative precision. Using our constrained hydrodynamic medium

from the preceding section, we now couple the thermal photon emission rates to its space-time evolution.

20.3.1 Hadronic photon spectra and anisotropy

Since the PCE is differently implemented in the late hadronic phase for the three versions of `s95p`, we first study the photon emission in the hadronic phase.

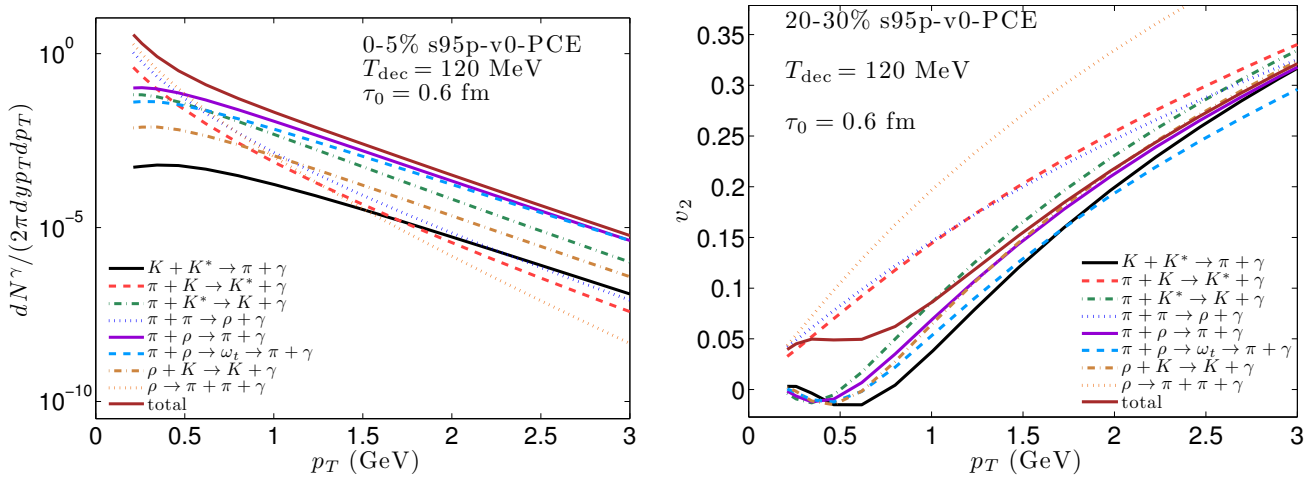

Figure 20.4: Thermal photon spectra in 0-5% and v_2 in 20-30% are plotted from different reaction channels with `s95p-v0-PCE`.

In Fig. 20.4, we show hadronic contribution to the thermal photon spectra for Au+Au collisions at 200 A GeV in 0-5% centrality and the photon elliptic flow v_2 in 20-30% centrality from different reaction channels in the hadronic phase. In the left panel, the thermal photon spectra fall into two main categories. The first class has a steep Bose-enhancement behavior at low $p_T < 0.5\,\mathrm{GeV}$. Processes like $\pi + K \to K^* + \gamma$, $\pi + \pi \to \rho + \gamma$ and $\rho \to \pi + \pi + \gamma$ are in this class. These processes dominate the hadronic photon spectra for $p_T < 0.5\,\mathrm{GeV}$. The other category contains a threshold cut-off in the low p_T region and involve heavy vector mesons with strong radial flow in the initial state. The remaining five reaction channels are in this category. The processes from this second category dominate photon production at $p_T > 0.7\,\mathrm{GeV}$. In the right panel, we show the hadronic photon differential elliptic flow at 20-30% centrality. The first category processes have positive differential v_2 at all p_T values. For the processes, $\pi + K \to K^* + \gamma$, $\pi + \pi \to \rho + \gamma$, the shape of the photon v_2 follows the v_2 of the pions in the initial state [236]. The decay channel $\rho \to \pi + \pi + \gamma$ produces the largest differential photon v_2 in the hadronic phase. The processes in the second category result in a small negative $v_2(p_T)$ at low p_T. This is because the photon spectra from these processes have a shoulder-like structure at low p_T originating from the reaction threshold and radial flow effects. Since the first category processes dominate photon spectra at low p_T, the total differential photon v_2 follows that of the first category of processes for $p_T < 0.5\,\mathrm{GeV}$ and

then transits to the second category for $p_T > 0.7\,\mathrm{GeV}$. This transition causes the structure of the total hadronic photon v_2 (red solid line in the right panel of Fig. 20.4) around $p_T \sim 0.5$ GeV [236].

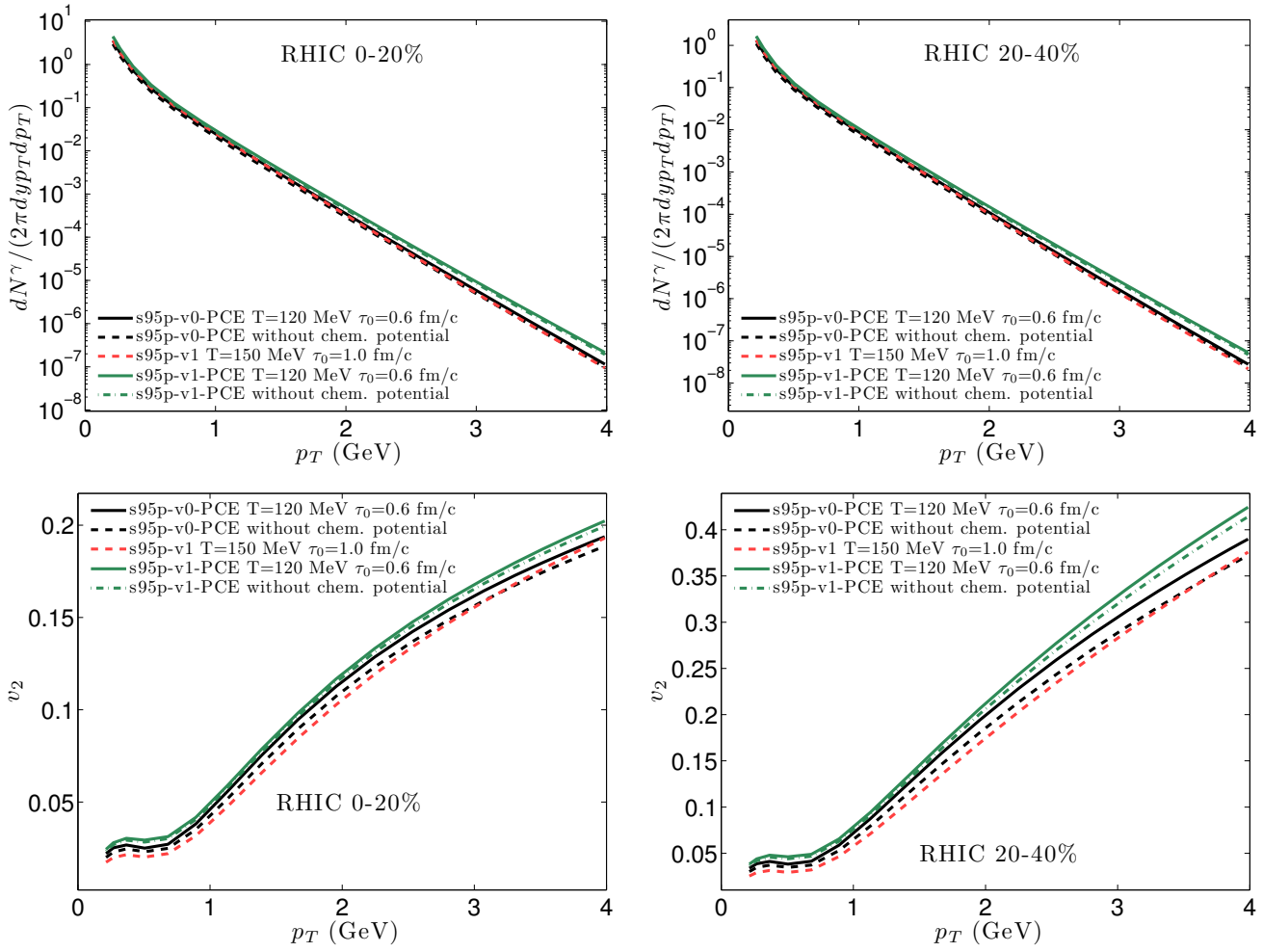

Figure 20.5: Hadronic photon spectra and their anisotropies from chemical equilibrium and partial chemical equilibrium EOS are compared at 0-20% and 0-40% centrality at the top RHIC energy.

In Fig. 20.5, photon spectra and elliptic flow are shown for different equations of state. Overall, there is little differences between the results using CE and PCE EOS. In the upper panels, `s95p-v1-PCE` results in slightly flatter photon spectra compared to the other two EOS. This is because `s95p-v1-PCE` generates stronger radial flow during the hydrodynamic evolution as we have seen from the proton spectra in Fig. 20.3. The difference between the dashed and solid lines illustrates the enhancement from non-zero chemical potentials caused by the breaking of chemical equilibrium. Although it is barely visible on the logarithmic scale, quantitatively, the non-zero chemical potentials in the PCE EOS enhance the photon spectra by about 30%. Since the chemical freeze out temperature of 165 or 150 MeV, respectively, is below the temperature of transition region between the QGP and HG photon emission rates, used in this study ($T_{\mathrm{sw}} = 184 - 220$ MeV), the fraction of the space-time volume where the hdronic rates are modified by the large chemical potentials is small. In the lower panels of Fig. 20.5, we find that the non-zero chemical

potentials result in larger differential v_2 especially at high p_T. This is because the chemical potentials increase the photon yields at low temperature, where the flow anisotropy is larger, resulting in a larger total v_2 compared to the CE case.

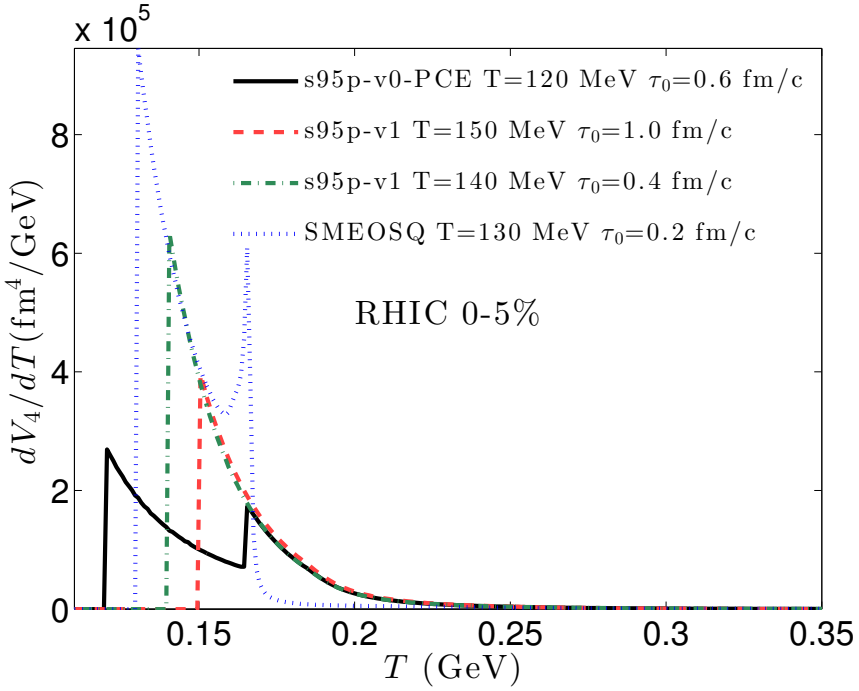

Figure 20.6: The space-time volume per temperature, dV_4/dT, is plotted as a function of temperature.

In order to illustrate the cancellation between the fugacity enhancement and faster cooling rate caused by non-equilibrium chemical potentials in the hadronic phase, we further plot the space-time volume per unit temperature interval as a function of temperature in Fig. 20.6. For reference, we also include the case of an EOS with a first order phase transition. The area below the curves indicates the total space-time volume of the hydrodynamic expansion. At the chemical freeze-out temperature, dV_4/dT exhibits discontinuities for the PCE EOS. This is consequence of the sudden increase in the cooling rate below the chemical freeze-out temperature. Although the results with PCE EOS have a lower kinetic freeze-out temperature, the net enhancement of the photon spectra is small since the photon emission rate decreases very fast with decreasing temperature, even including fugacity enhancement.

20.3.2 Comparison with experimental data

Direct photon observables contain multiple components. In Fig. 20.7, we illustrate the individual contribution from each component to the total direct photon spectrum and elliptic flow. In the left panel, we find that the pQCD prompt component becomes important for $p_T > 1.5$ GeV. In the thermal photon signal, QGP radiation dominates over that from the HG phase. In order

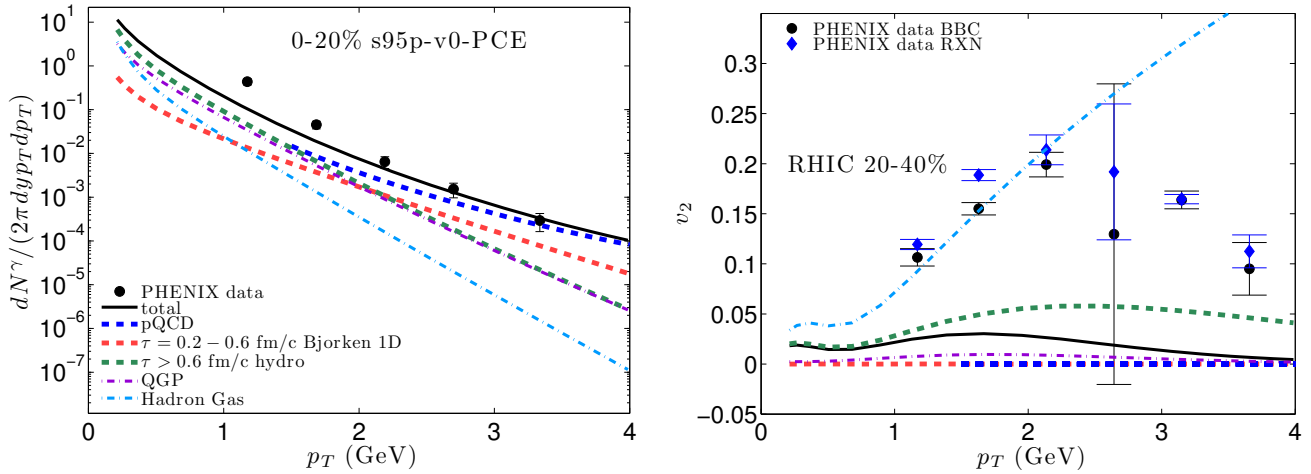

Figure 20.7: Contributions from individual component to direct photon spectra and elliptic flow compared with experimental data.

to estimate the contribution from the pre-equilibrium stage, we extrapolate the local temperature evolution to early time, between $\tau = 0.2$ fm/c and $\tau_0 = 0.6$ fm/c, according to 1D Bjorken longitudinal expansion. In the right panel of Fig. 20.7, photons from hadronic phase carry large v_2 as large as the experimental measurements. However, The QGP photons, who emit during the early stages of the evolution carry negligible elliptic flow (purple dash-dotted line). The total thermal photon (QGP + HG) elliptic flow is a weighted average between the photons from the two phases. Since QGP photons have a larger yield compared to HG photons, the total thermal photon v_2 (green dashed line) is small. The pre-equilibrium photons from 1-D Bjorken expansion carry zero anisotropic flow. They further dilute the total direct photon v_2 to the black solid line, which significant underestimates the PHENIX data.

We compare our full direct photon spectra (thermal + pQCD) with the experimental data in Fig. 20.8. In the upper panels, we show the thermal photon spectra (QGP + HG) and pQCD photon spectra separately. The full thermal photon spectra show little sensitivity to different PCE implementations of the EOS in the hadronic phase. In the lower panels, we compare the full thermal + pQCD photon spectra with the PHENIX data. (The extrapolated pQCD components is only shown for reference.) We underestimate the experimental data by about factor of 5 for $p_T < 2$ GeV. In Fig. 20.9, we further compare the p_T differential elliptic coefficient against the experimental data. For all choices of the EOS, we severely underestimate the PHENIX measurement. In the `s95p-v1` case, since we start our hydrodynamic evolution at $\tau_0 = 1$ fm/c, the contribution of the pre-equilibrium photons from 1D Bjorken expansion (which carries no transverse flow) is larger than for the two PCE cases for which the hydrodynamic simulations start at $\tau_0 = 0.6$ fm/c. Since these estimated pre-equilibrium photons come from 1D longitudinal expansion, they do not carry any elliptic flow, and therefore dilute the final direct photon v_2 signal.

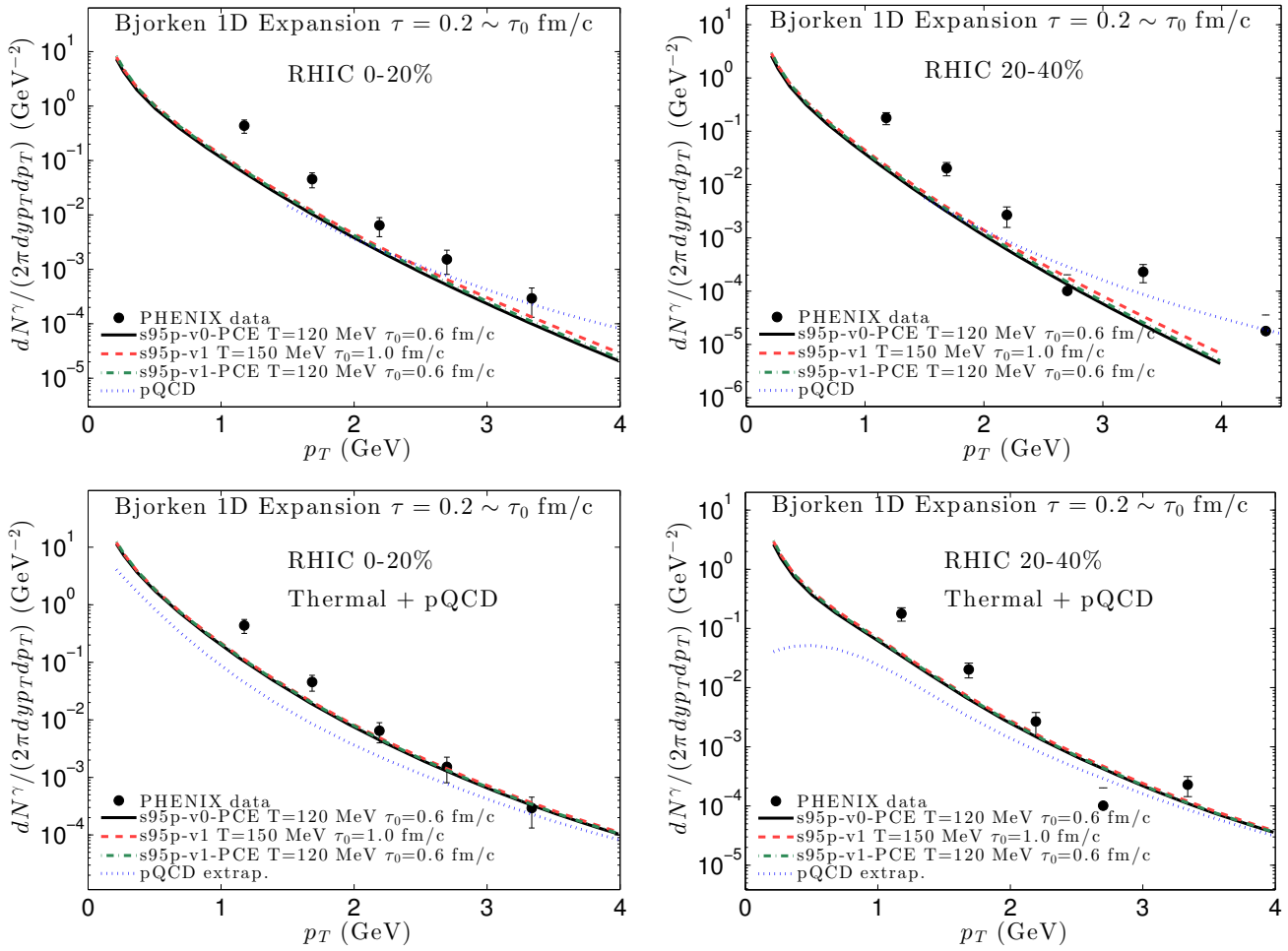

Figure 20.8: Comparisons of our thermal + pQCD photon results with measured direct photon spectra at 0-20% and 20-40% centrality at the top RHIC energy. All thermal contributions include thermal radiation from a "pre-equilibrium" stage between $\tau = 0.2$ fm/c and τ_0, assuming 1-D Bjorken expansion (i.e. zero transverse flow).

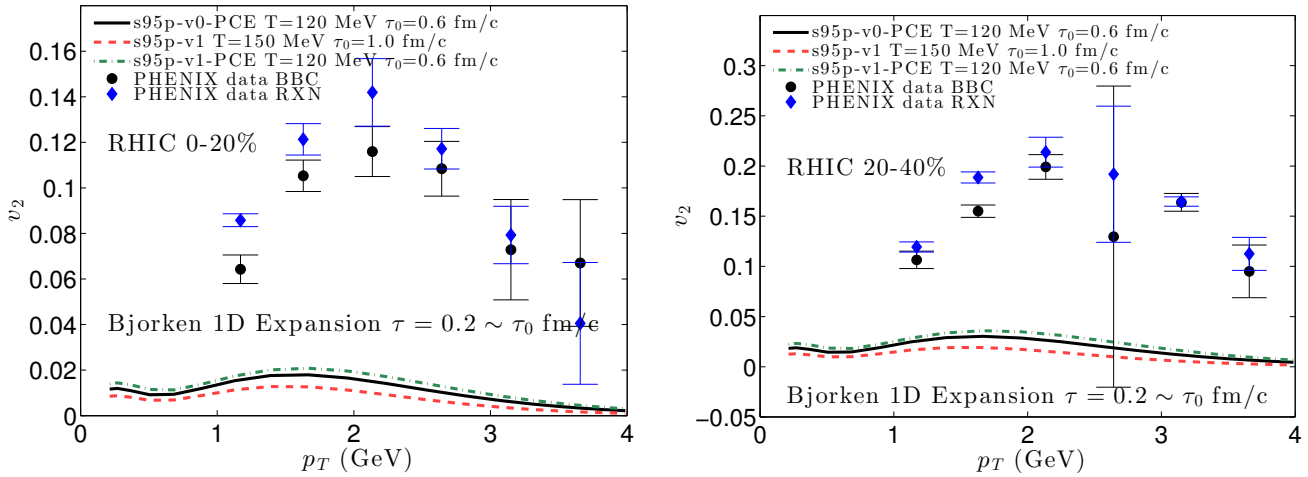

Figure 20.9: Comparisons of direct photon elliptic flow results with experimental data at 0-20% and 20-40% centrality at the top RHIC energy.

20.4 Chapter summary

In this chapter, we studied the effects of partial chemical equilibrium in the EOS below $T_{\rm chem}$ on the direct photon observables. We find that the fugacity enhancement in the photon emission rates is compensated by the reduction of the space-time volume caused by the accompanying more rapid cooling of the hydrodynamic evolution. The final photon spectra and v_2 show little sensitivity to the detailed implementation of the PCE in the EOS. The PCE in the late hadronic phase does not help much in solving the missing yield in the direct photon spectra and direct photon flow puzzle.

Chapter 21: Phenomenological study: Inclusive and decay photons

In this chapter, we calculate the inclusive and decay photons from event-by-event viscous hydrodynamic simulations. We apply the experimental extraction procedure for the determination of the direct photon anisotropic flow to our event ensemble and find that only after including a photon multiplicity weighting factor in the definition of the direct photon v_n the theoretical calculations correspond to what is being measured experimentally.

21.1 Definition of direct photon anisotropic flow

Experimentally, one can only measure the inclusive photon yield and its anisotropy. In order to extract the direct photon signal from an overwhelming background, one first computes the background of decay photons based on measured or extrapolated π^0, η, and ω spectra. (As we will see below, other contributions from electromagnetic decays of long-lived but unstable hadrons are small and can be neglected.) π^0 spectra can be measured directly in the p_T-range needed to compute their contribution to the measured photon signal while other heavier particle spectra can only be measured at higher p_T, and their contribution to the measured photon signal at lower p_T must be estimated. This is usually done [239, 240] by assuming m_T-scaling for the hadron spectra. Once this "decay cocktail" of decay photons and their anisotropies is computed, the direct photon anisotropic flow can be calculated as

$$v_n^{\rm dir}(p_T) = \frac{R^\gamma(p_T) v_n^{\rm incl}(p_T) - v_n^{\rm bg}(p_T)}{R^\gamma(p_T) - 1}, \tag{21.1}$$

where $R^\gamma = \frac{N^{\gamma incl}}{N^{\gamma bg}}$is the ratio of the measured inclusive photon signal and the computed decay photon background. However, Eq. (21.1) is only exact for one single event. Due to finite statistics, the v_n measurement can only be done on an ensemble averaged basis. Experimentally, Eq. (21.1) is therefore used with ensemble average values in all entries. The goal of this section is to establish the correct relation between this experimental definition of $v_n^{\rm dir}$ and quantities we can extract theoretically from our fluctuating event sample, where we compute the direct photon signal directly, i.e. without first adding and later dividing our the background from long-lived electromagnetic hadron decays.

In the following, we will use the scalar-product method as an example. Similar algebra can be applied to the event plane method. [39] For each event, we define the underlying anisotropic flow vector in the complex plane

$$V_n(p_T) = v_n(p_T)e^{in\Psi_n(p_T)} = \frac{\int d\phi \frac{dN}{dyp_T dp_T d\phi} e^{in\phi}}{\int d\phi \frac{dN}{dyp_T dp_T d\phi}}, \tag{21.2}$$

together with the ratio $R^\gamma(p_T)$ between the inclusive and decay photons at a a given p_T in the event. Both quantities fluctuate from event to event. Experimentally, one can only extract the ensemble averaged ratio, $\bar{R}^\gamma(p_T) = \frac{\langle dN^{\gamma,\mathrm{incl}}/(dyp_T dp_T)\rangle}{\langle dN^{\gamma,\mathrm{bg}}/(dyp_T dp_T)\rangle}$.

21.1.1 Flow coefficients without photon multiplicity weight

The direct photon $v_n^{\mathrm{dir}}\{\mathrm{SP}\}$ is defined by

$$\begin{aligned}
v_n^{\gamma,\mathrm{dir}}\{\mathrm{SP}\}(p_T) &= \frac{\langle V_n^{\gamma,\mathrm{dir}}(p_T)\cdot(V_n^{\mathrm{ch}})^\star\rangle}{v_n^{\mathrm{ch}}\{2\}} \qquad (21.3)\\
&= \frac{\left\langle \frac{R^\gamma(p_T)V_n^{\gamma,\mathrm{incl}}(p_T)-V_n^{\gamma,\mathrm{bg}}(p_T)}{R^\gamma(p_T)-1}\cdot(V_n^{\mathrm{ch}})^\star\right\rangle}{v_n^{\mathrm{ch}}\{2\}}\\
&= \frac{\left\langle \frac{R^\gamma(p_T)}{R^\gamma(p_T)-1}V_n^{\gamma,\mathrm{incl}}(p_T)\cdot(V_n^{\mathrm{ch}})^\star\right\rangle - \left\langle \frac{1}{R^\gamma(p_T)-1}V_n^{\gamma,\mathrm{bg}}(p_T)\cdot(V_n^{\mathrm{ch}})^\star\right\rangle}{v_n^{\mathrm{ch}}\{2\}}\\
&\neq \frac{\bar{R}^\gamma(p_T)v_n^{\gamma,\mathrm{incl}}\{\mathrm{SP}\}(p_T) - v_n^{\gamma,\mathrm{bg}}\{\mathrm{SP}\}(p_T)}{\bar{R}^\gamma(p_T)-1}. \qquad (21.4)
\end{aligned}$$

This inequality in the last line shows that the standard scalar-product v_n for direct photons is in general not equal to the experimentally measured quantity Eq. (21.1).

[39] The event place method is presently being used in the experiment but since the theoretical interpretation of its results is affected by the experimental event-plane resolution [22], which is impossible to simulate theoretically, it is theoretically inconvenient. The scalar product method avoids these interpretational ambiguities without additional effort on the experimental side [22]. It is therefore much preferred for a comparison with theoretical predictions.

21.1.2 Flow coefficients with photon multiplicity weight

Now, let us consider the multiplicity weighted scalar-product anisotropic flows:

$$
\begin{aligned}
v_n^{\gamma,\mathrm{dir}}\{\mathrm{SP},\mathrm{mult}\}(p_T) &= \frac{\left\langle \frac{dN^{\gamma,\mathrm{dir}}}{dyp_T\mathrm{d}p_T} V_n^{\gamma,\mathrm{dir}}(p_T)\cdot(V_n^{\mathrm{ch}})^\star \right\rangle}{\left\langle \frac{dN^{\gamma,\mathrm{dir}}}{dyp_T\mathrm{d}p_T} \right\rangle v_n^{\mathrm{ch}}\{2\}} \qquad (21.5)\\
&= \frac{\left\langle \left(\frac{dN^{\gamma,\mathrm{incl}}}{dyp_T\mathrm{d}p_T} - \frac{dN^{\gamma,\mathrm{bg}}}{dyp_T\mathrm{d}p_T} \right) \frac{R^\gamma(p_T)V_n^{\gamma,\mathrm{incl}}(p_T) - V_n^{\gamma,\mathrm{bg}}(p_T)}{R^\gamma(p_T)-1}\cdot(V_n^{\mathrm{ch}})^\star \right\rangle}{\left\langle \frac{dN^{\gamma,\mathrm{incl}}}{dyp_T\mathrm{d}p_T} - \frac{dN^{\gamma,\mathrm{bg}}}{dyp_T\mathrm{d}p_T} \right\rangle v_n^{\mathrm{ch}}\{2\}}\\
&= \frac{\left\langle \left(\frac{dN^{\gamma,\mathrm{incl}}}{dyp_T\mathrm{d}p_T} V_n^{\gamma,\mathrm{incl}}(p_T) - \frac{dN^{\gamma,\mathrm{bg}}}{dyp_T\mathrm{d}p_T} V_n^{\gamma,\mathrm{bg}}(p_T) \right)\cdot(V_n^{\mathrm{ch}})^\star \right\rangle}{\left(\left\langle \frac{dN^{\gamma,\mathrm{incl}}}{dyp_T\mathrm{d}p_T} \right\rangle - \left\langle \frac{dN^{\gamma,\mathrm{bg}}}{dyp_T\mathrm{d}p_T} \right\rangle \right) v_n^{\mathrm{ch}}\{2\}}\\
&= \frac{\bar{R}^\gamma(p_T)v_n^{\gamma,\mathrm{incl}}\{\mathrm{SP},\mathrm{mult}\}(p_T) - v_n^{\gamma,\mathrm{bg}}\{\mathrm{SP},\mathrm{mult}\}(p_T)}{\bar{R}^\gamma(p_T)-1}. \qquad (21.6)
\end{aligned}
$$

One sees that with the extra photon multiplicity weight in both numerator and denominator of the definition of the scalar-product flow coefficients, the new quantity $v_n\{\mathrm{SP},\mathrm{mult}\}$ defined in the first line agrees exactly with what is extracted experimentally from the measured inclusive and computed decay photons. Since the photon multiplicity weight factor implements a strong bias towards more central collisions which produce more photons pre event but less elliptic flow, it is crucial to include the photon multiplicity weight in the v_n definition for direct photons, in order to have an apples-to-apples comparison between theoretical calculations and the experimental measurements, especially when the latter are averaged over a wide range of collision centralities.

21.2 Photon emission sources in heavy-ion collisions

21.2.1 Decay photons

In relativistic heavy-ion collisions, 80-90% of the measured photons are generated as decay products from unstable hadrons. The most abundant decay source is $\pi^0 \to \gamma + \gamma$. It contributes about 85% of the total decay photons in a heavy-ion collision. The decay photon yield is much larger than the direct photon yield. Since hadrons are much more abundant than directly emitted photons in heavy-ion collisions, the direct photon excess is only a 10-20% fraction of the inclusive photon yield at RHIC and LHC energies. In table 21.1, we list the primary decay channels included in the experimental "decay cocktail" calculations of electromagnetic decays from long-lived unstable hadrons. (Note that photons from electromagnetic decays of short-lived resonances are not included in the cocktail since such resonances can not be reconstructed experimentally and their abundance and p_T distributions can not be easily estimated.) In Fig. 21.1, we show the decay photon spectra as a function of p_T for individual cocktail hadron species, computed from

Meson	Mass (GeV)	Decay mode	branching ratio(%)
π^0	0.13498	$\gamma + \gamma$	98.823 ± 0.034
		$\gamma + e^+ + e^-$	1.174 ± 0.035
η	0.54775	$\gamma + \gamma$	39.31 ± 0.20
		$\pi^+\pi^- + \gamma$	4.6 ± 0.16
ω	0.78259	$\pi^0 + \gamma$	8.28 ± 0.28
η'	0.95778	$\rho + \gamma$	29.3 ± 0.6
		$\omega + \gamma$	2.75 ± 0.22
		$\gamma + \gamma$	2.18 ± 0.08
ϕ	1.01946	$\eta + \gamma$	1.309 ± 0.024
Σ^0	1.19264	$\Lambda + \gamma$	1.00

Table 21.1: Cocktail hadrons, their electromagnetic decay modes and the corresponding relative branch ratio.

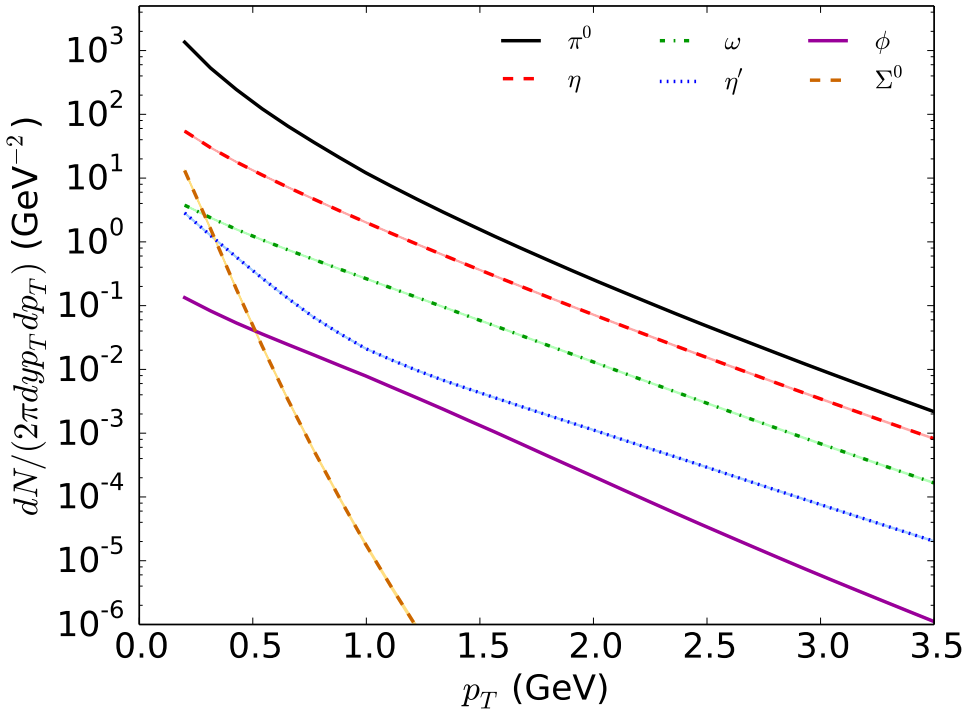

Figure 21.1: Decay photon spectra from individual hadron species,computed from viscous hydrodynamics for 2760 A GeV Pb+Pb collisions at 0-40% centrality with MC-Glauber initial conditions and $\eta/s = 0.08$.

hydrodynamics. Most of the decay photons are coming from π^0, followed by η, and ω decays. Experimentally, one defines the photons from π^0, η, ω, η', ϕ, and Σ^0 decays as decay photons, and they form the "decay cocktail" used in the measurements [239, 240]. The decay photons imprint the flow pattern of their parent particles, hence they carry large anisotropic flow compared to direct photons, many of which are emitted at earlier stages of the evolution. [40]

[40]Note that the computation of the "decay cocktail" requires knowledge of the spectra (shape and normalization) of the parent hadrons. Ideally, these parent hadrons are directly measured in the same experiment, in the p_T range needed for their decay photons. In practice, this often involves extrapolation of experimental measurements of the

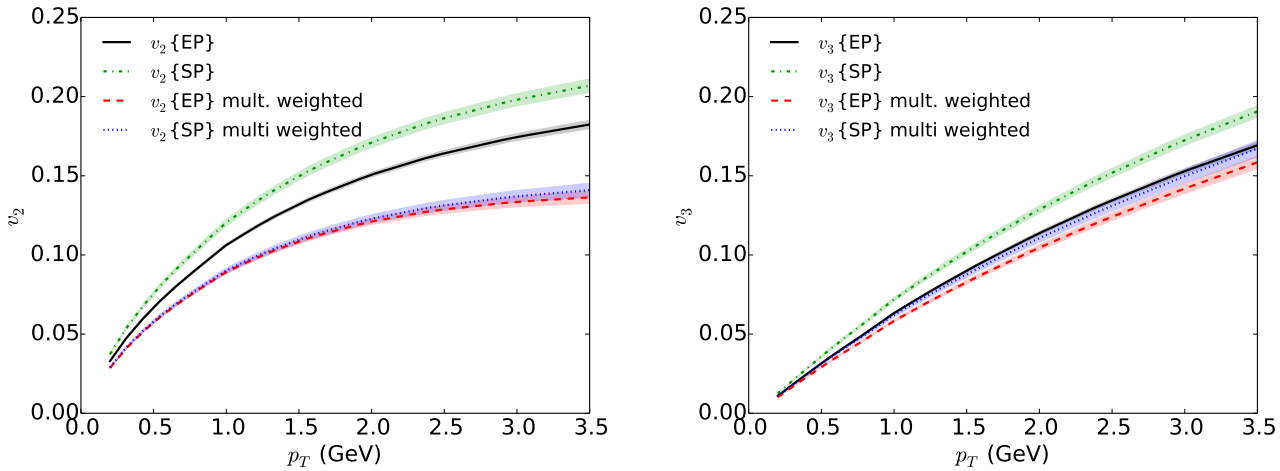

Figure 21.2: Elliptic and triangular flow of decay cocktail photons, for 0-40% Pb+Pb collision at $\sqrt{s} = 2.76\ A$ TeV.

In Fig. 21.2, we plot the p_T differential elliptic and triangular flow coefficients of the decay photons using different methods for the flow measurement. Both elliptic and triangular flow of the decay photons are about as large as those typical of hadrons. Elliptic flow measurements that include a photon multiplicity weight are smaller than the unweighted ones. This is because the multiplicity weight biases the measurement towards central collisions in which the geometric contribution to v_2 is smaller. Please note that for v_2 the difference between flow measures with and without multiplicity weight is quite large due to the strong centrality dependence of elliptic flow arising from collision geometry. Since triangular flow is purely driven by fluctuations and has no contribution from overlap geometry, the bias towards more central collisions caused by the photon multiplicity weight has a smaller effect on the final result and the difference between multiplicity weighted and unweighted methods is smaller. We also notice that the difference between $v_n\{\text{SP}\}$ and $v_n\{\text{EP}\}$ becomes smaller when we weight with the photon multiplicity.

21.2.2 Direct photons

In the experiments, the direct photons are extracted from the difference between the measured inclusive photons and simulated decay photons. The extracted signal contains thermal photons (believed to be the most dominant source at low photon momentum), prompt photons, decay photons from short lived resonances, pre-equilibrium photons, fragmentation photons, jet-plasma conversion photons, etc. In our current theoretical calculations, we only consider the contribution from the first three listed sources.

Thermal photon emission is the major source in the direct photon signal in the low p_T region. We consider emission from quark gluon plasma (QGP) and hadron gas (HG) phases. In the QGP

parent hadrons in one p_T-range to a different p_T-range that matters for the decay photons included in the photon measurement.

phase, we include both 2 to 2 scattering processes and the AMY rate for collinear emissions [185]. In the HG phase, we include all 2 to 2 scattering processes between pseudo-scalar, vector, and axial vector mesons. We account for first order in the QGP corrections in all the 2 to 2 scattering processes, leaving the collinear emission contribution uncorrected. In the high-p_T region, prompt photons from hard scatterings become the dominant source. In our calculations, we use the NLO pQCD parameterization [225]. For 0-40% centrality at the LHC, the prompt photons component can be parameterized as follows:

$$\frac{dN}{2\pi dy p_T dp_T} = 12.8 \frac{1.21}{(1+p_T/0.692)^{-5.5}} \left(\frac{1}{\mathrm{GeV}^2}\right). \tag{21.7}$$

Decay photons from short-lived resonances decaying after kinetic freeze-out have various components. We summarize the contributions decay channels in table 21.2, 21.3, and 21.4, including all decay channels for resonances with masses below 2 GeV [246]. In Fig. 21.3, we show the

reaction	branching ratio
$\rho^0 \to \pi^+ + \pi^- + \gamma$	1%
$b_1(1235) \to \pi^\pm + \gamma$	$1.6 * 10^{-3}$
$h_1(1170) \to \pi^0 + \gamma$	$1.7 * 10^{-3}$
$a_1(1260) \to \pi^0 + \gamma$	$1.7 * 10^{-3}$
$f_1(1285) \to \rho_0 + \gamma$	5.5%
$a_2(1320) \to \pi^\pm + \gamma$	$2.68 * 10^{-3}$
$K^\star(892) \to K^0 + \gamma$	$2.4 * 10^{-3}$
$K^\star(892) \to K^\pm + \gamma$	$1 * 10^{-3}$
$K_1(1270) \to K^0 + \gamma$	$8.4 * 10^{-4}$
$K_1(1400) \to K^0 + \gamma$	$1.6 * 10^{-3}$
$K_2^\star(1430) \to K^+ + \gamma$	$2.4 * 10^{-3}$
$K_2^\star(1430) \to K^0 + \gamma$	$9 * 10^{-4}$

Table 21.2: Mesonic decay channels to photons from the short lived resonances

individual contributions to the direct photon spectrum from the three sources for $p_T < 3.5$ GeV. We see that over the entire p_T-range the short-lived resonance decays contribute to the direct photon spectrum at a level of about 5 to 10% the thermal emission. Their contribution is larger at low p_T, and peaks around $p_T \sim 0.5$ GeV. The net contribution of these photons to the total direct photon spectrum is rather small. Prompt photons from pQCD are smaller than thermal radiation at low p_T and gradually take over at higher p_T, dominating the spectrum for $p_T > 3.0$ GeV. In Fig. 21.4, we study the individual contributions to the total decay photon spectra from short-lived resonances. The biggest contribution is from radiative ρ decays, $\rho^0 \to \pi + \pi + \gamma$. We listed only the resonances contributing the top 80% of the yield from short-lived decays. As we can see, their sum (yellow dotted line in Fig. 21.4 exhausts the total decay photon spectrum at low $p_T < 1$ GeV. At the higher p_T, there still a significant contribution coming from the rest of

reaction	branching ratio
$N(1440) \to p + \gamma$	$4.15 * 10^{-4}$
$N(1440) \to n + \gamma$	$3 * 10^{-4}$
$N(1520) \to p + \gamma$	$4.15 * 10^{-3}$
$N(1520) \to n + \gamma$	$4.15 * 10^{-3}$
$N(1530) \to p + \gamma$	$2.25 * 10^{-3}$
$N(1530) \to n + \gamma$	$2.25 * 10^{-3}$
$N(1650) \to p + \gamma$	$1.2 * 10^{-3}$
$N(1650) \to n + \gamma$	$8.5 * 10^{-4}$
$N(1675) \to p + \gamma$	$1 * 10^{-4}$
$N(1675) \to n + \gamma$	$7.5 * 10^{-4}$
$N(1680) \to p + \gamma$	$2.65 * 10^{-3}$
$N(1680) \to n + \gamma$	$3.35 * 10^{-4}$
$N(1700) \to p + \gamma$	$3 * 10^{-4}$
$N(1700) \to n + \gamma$	$1.2 * 10^{-3}$
$N(1710) \to p + \gamma$	$4.1 * 10^{-4}$
$N(1710) \to n + \gamma$	$1 * 10^{-4}$
$N(1720) \to p + \gamma$	$1.5 * 10^{-3}$
$N(1720) \to n + \gamma$	$8 * 10^{-5}$
$\Delta(1232) \to N + \gamma$	0.6%
$\Delta(1600) \to N + \gamma$	$1.8 * 10^{-4}$
$\Delta(1620) \to N + \gamma$	$6.5 * 10^{-4}$
$\Delta(1700) \to N + \gamma$	$4.1 * 10^{-3}$
$\Delta(1905) \to N + \gamma$	$2.4 * 10^{-4}$
$\Delta(1910) \to N + \gamma$	$1 * 10^{-4}$
$\Delta(1920) \to N + \gamma$	$2 * 10^{-3}$
$\Delta(1950) \to N + \gamma$	$1.05 * 10^{-3}$

Table 21.3: Baryonic decay channels to photons from the short lived resonances

reaction	branching ratio
$\Lambda(1405) \to \Lambda + \gamma$	$5.4 * 10^{-4}$
$\Lambda(1405) \to \Sigma^0 + \gamma$	$2 * 10^{-4}$
$\Lambda(1520) \to \Lambda + \gamma$	$8.5 * 10^{-3}$
$\Lambda(1520) \to \Sigma^0 + \gamma$	2%
$\Sigma^0(1385) \to \Lambda + \gamma$	1.25%
$\Xi(1530) \to \Xi + \gamma$	4%

Table 21.4: Baryonic decay channels to photons from the short lived resonances continued.

the short-lived resonances although each individual of them contributes less than 1% to the total short-lived decay yield.

In Fig. 21.5, we compute the direct photon elliptic and triangular flow with and without the contributions from short-lived resonances. Although the yields of the decay photons from short-lived resonances are only 5 to 10% of the thermal photons, they increase the total direct elliptic and triangular flows by about 20% and 25%, respectively. This is because they carry large

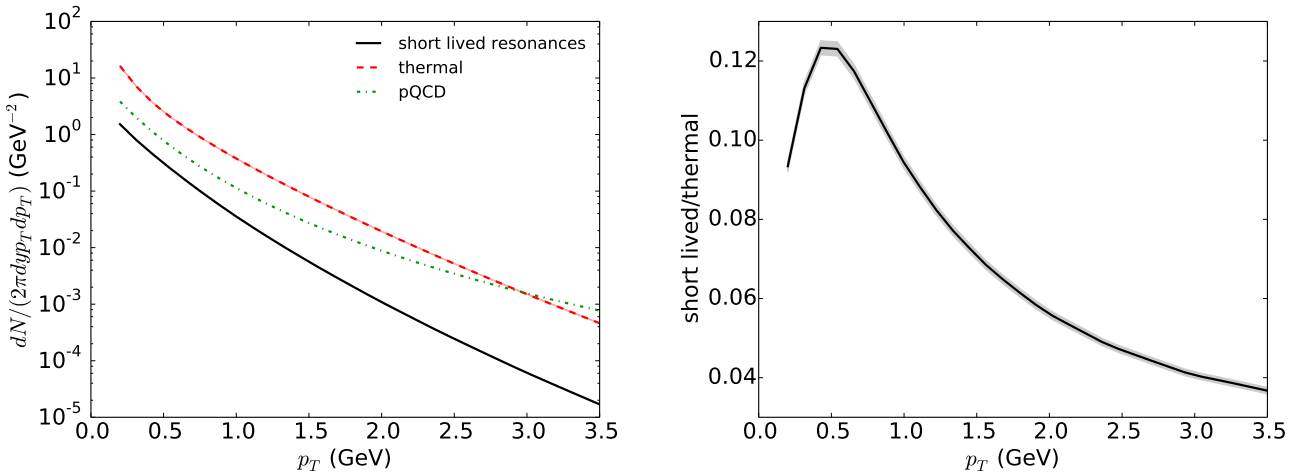

Figure 21.3: Left panel: direct photon spectra from the individual components. Right panel: the ratio between the photons coming from short lived resonances decay and the thermal photons.

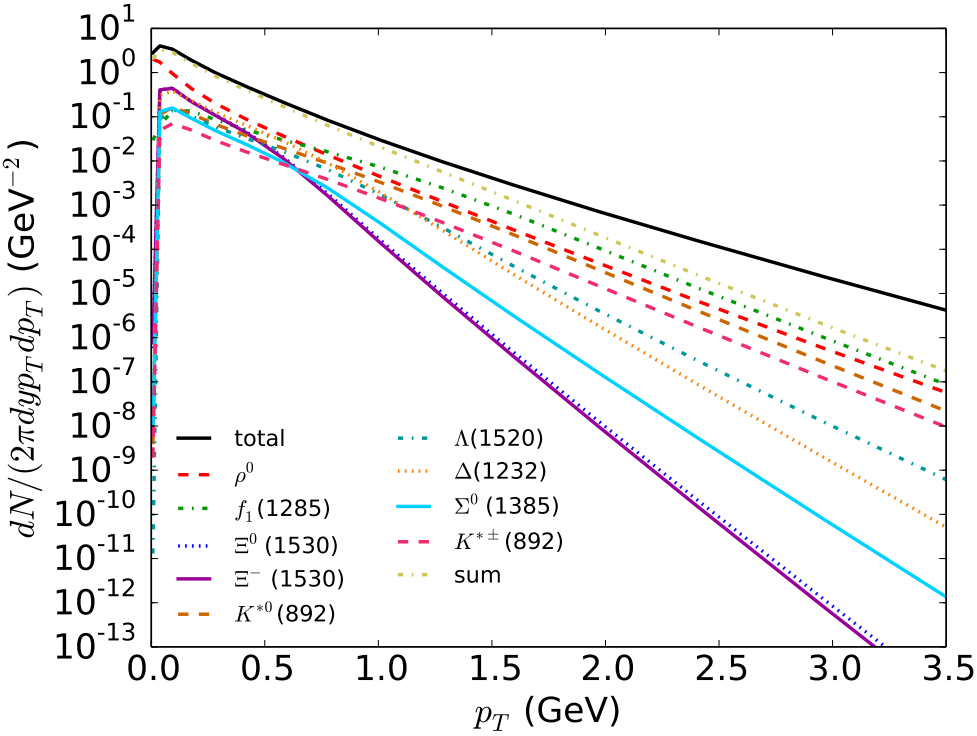

Figure 21.4: Individual contributions to the decay photon spectra from short lived resonances for 2760 A GeV Pb+Pb collisions at 0-40% centrality.

anisotropic flow which is inherited from their parent hadrons which are only emitted at kinetic freeze-out when the hydrodynamic flow anisotropy is fully developed. From Figs. 21.3 and 21.5, we conclude that the decay photons from short-lived heavy resonances make small contributions to the direct photon spectra but increase the direct photon anisotropic flow by appreciable amounts. Their contributions thus need to be included in realistic comparisons with experimental data.

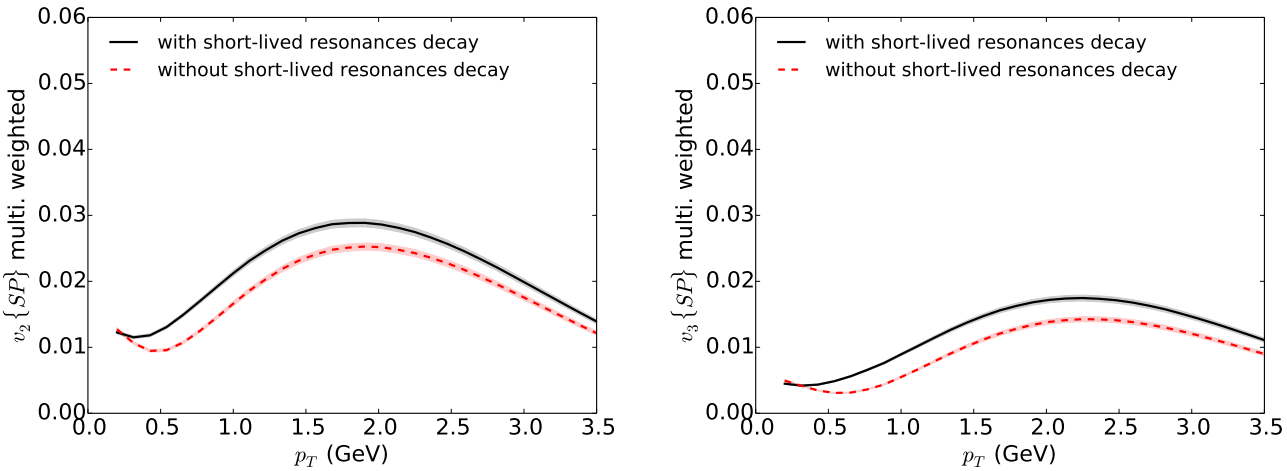

Figure 21.5: Elliptic and triangular flow for direct photons with and without contributions from short-lived resonance decays.

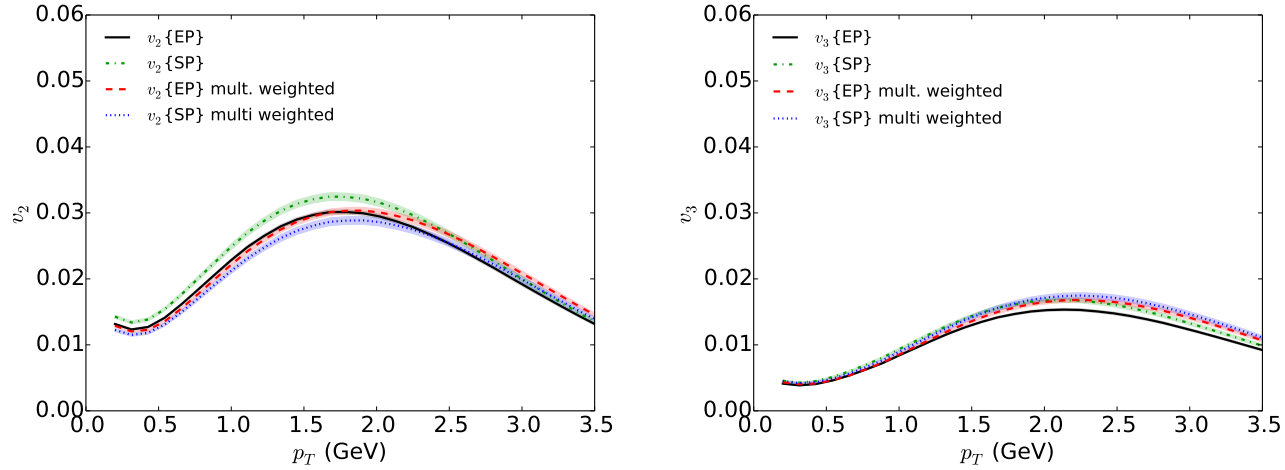

Figure 21.6: Elliptic and triangular flow for direct photons for 2760 A GeV Pb+Pb collisions at 0-40% centrality.

In Fig. 21.6, we show the direct photon elliptic and triangular flow from different measurement methods. Unlike the long-lived decay photon v_n shown in Fig. 21.2, all four different flow definitions give rather similar direct photon v_n.

21.2.3 Inclusive photons and comparison with experimental data

By calculating both direct and decay photons, we can get the inclusive photon yield and its anisotropies and compare them with experimental data.

In Fig. 21.7, in the left panel, we show our inclusive photon spectra as well as the individual components and their comparison with the inclusive photon spectra measured by ALICE in 2760 A GeV Pb+Pb collisions at 0-40% centrality. Our calculations show a fairly good agreement with the measured inclusive photon spectra for $p_T < 1.5$ GeV, although the slope of the calculated photon spectra is a little bit steeper than the experimental data. In the right panel, we show the

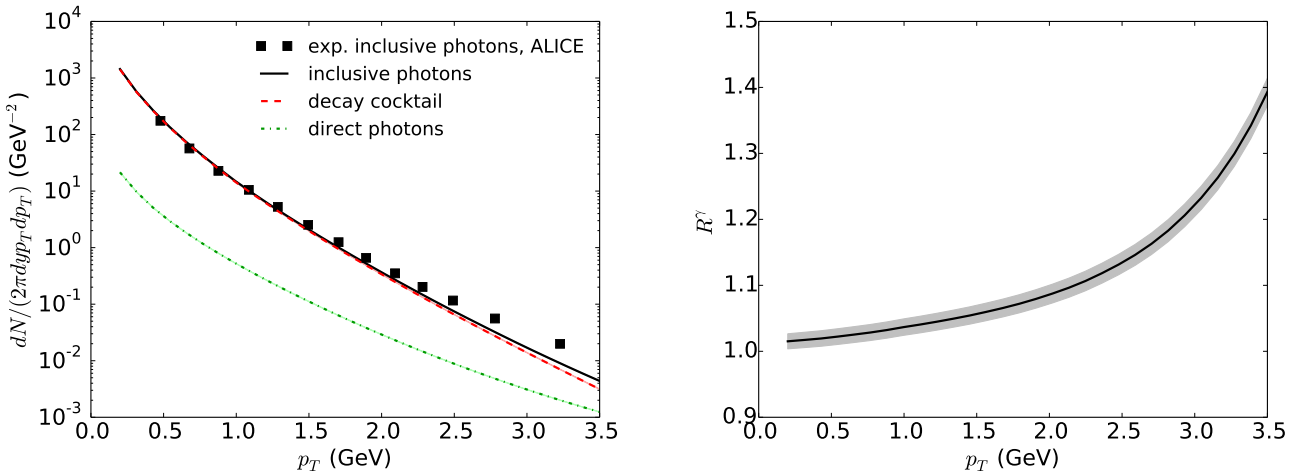

Figure 21.7: Left panel: Inclusive photon spectra with individual decay and direct photon contribution. Right panel: R^γ as a function of p_T. The experimental data are extracted from Daniel Lohner's Ph.D thesis.

theoretical ratio between the inclusive and decay photon yield, R^γ. Our model is seem to produce R^γ values around 1.02 - 1.1 for $p_T < 2.0$ GeV; this significantly underestimates the R^γ values reported by the experiment which are around 1.2 at low p_T. Theoretical R^γ curve also shows a stronger p_T-dependence than the experimentally measured results.

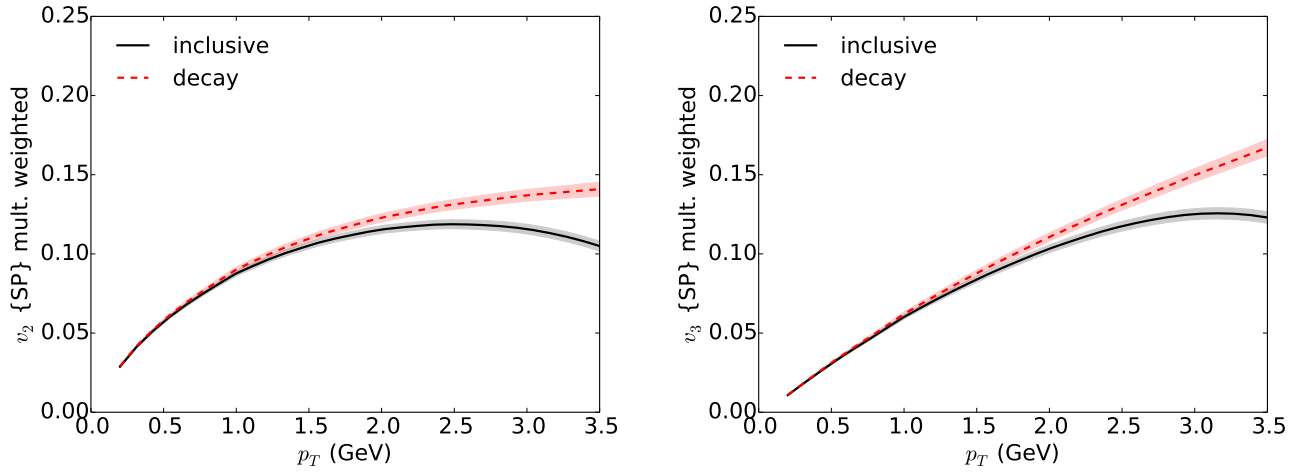

Figure 21.8: Comparison between inclusive and decay photon elliptic and triangular flow.

In Fig. 21.8, we show a comparison between the anisotropic flow coefficients for inclusive and decay photons. At low p_T, decay and inclusive photons are seem to have very similar v_n. The v_n of the inclusive photons fall below those of the decay photons at $p_T > 3.0$ GeV where pQCD photons, who carry zero v_n, become important.

In Fig. 21.9, we compare the elliptic and triangular flows of inclusive photons, computed according to different flow definitions, and compare them to the experimental data. Our calculations roughly agree with the experimental measurements. Since the experimental measurements include a photon multiplicity weight, they should be compared with the red dashed or blue dashed curves.

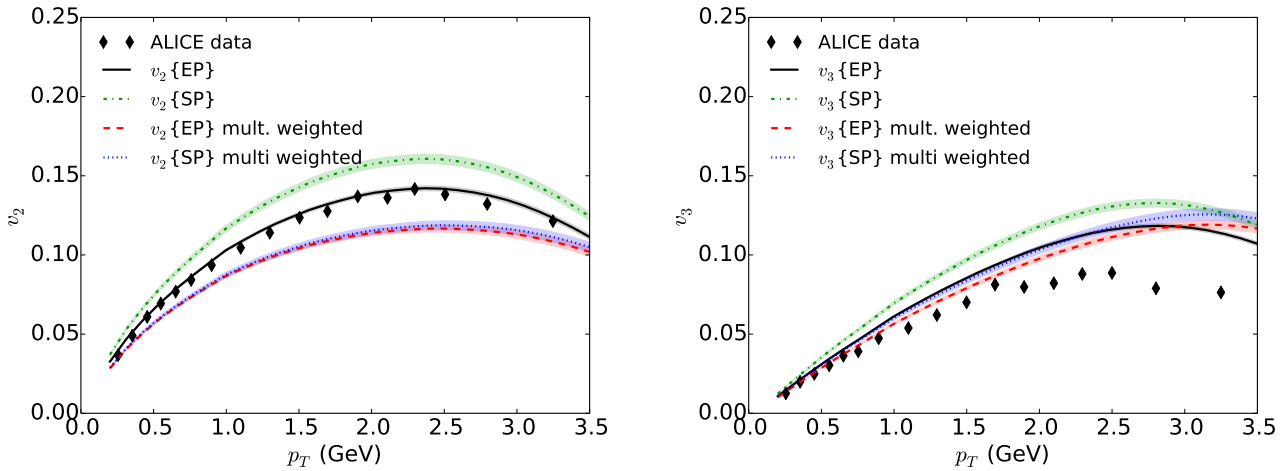

Figure 21.9: Inclusive photon v_2 and v_3 compared to experimental data. The experimental data are extracted from Daniel Lohner's Ph. D thesis.

One sees that we underestimate the elliptic flow while slightly overestimating the triangular flow of the inclusive photons.

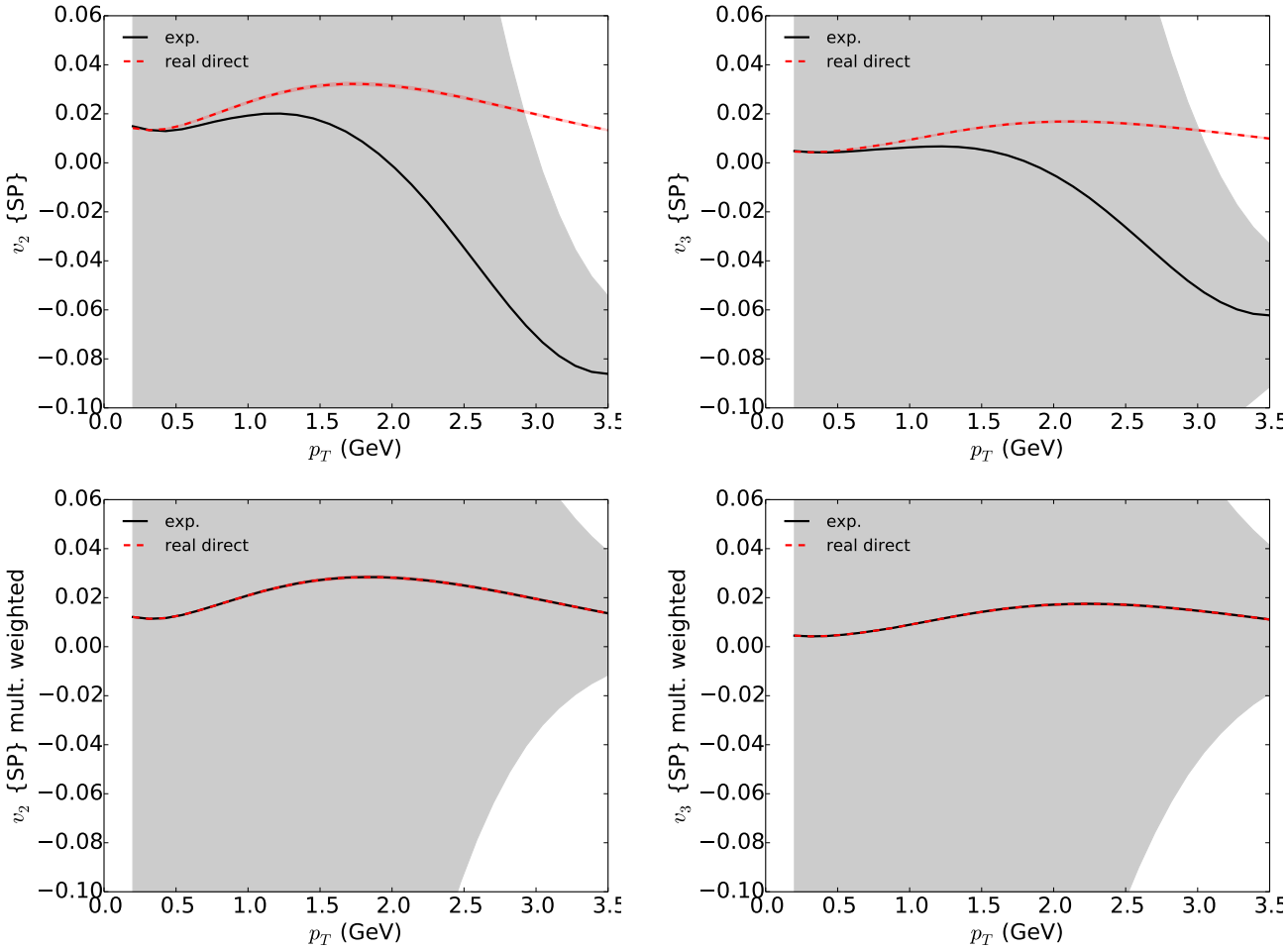

Figure 21.10: Comparison between direct photon v_n and experimental extracted v_n from Eq. (21.1). Calculations are for 2760 A GeV Pb+Pb collisions at 0-40% centrality.

Finally, in Fig. 21.10, we investigate whether we can use Eq. (21.1) as the experimentalists did to reproduce the true underlying direct photon v_n. In the upper panels, we checked the scalar-product anisotropic flow $v_n^{\gamma,\mathrm{dir}}\{SP\}$ without multiplicity weighting, as given in Eq. (21.4). As expected, the result obtained by using the experimental extraction method Eq. (21.1) does not agree with the directly computed direct photon scalar-product anisotropic flow. In the lower panels, we show the same comparison for the multiplicity-weighted scalar-product v_n. Despite the huge statistical errors, the central values of the two curves from the two approaches (directly computed and extracted from Eq. (21.1)) agree perfectly with each other. This verifies the correctness of our derivation in Eq. (21.6). Fig. 21.10 illustrates the indispensable role of including the photon multiplicity weights in the theoretical v_n.

Chapter 22: Conclusions and Outlook

The field of relativistic heavy-ion physics is evolving rapidly. Starting from the year 2000, ideal hydrodynamic simulations first achieved a great success in predicting the elliptic flow measurements at RHIC, which led to the discovery of the strongly-coupled QGP, the most perfect fluid currently known in nature. In order to further quantify the transport properties of the QGP, viscous hydrodynamic models (with and without the assumption of longitudinal boost invariance) were developed and applied to phenomenological studies at RHIC and LHC. The realization of the importance of event-by-event initial state fluctuations together with event-by-event viscous hydrodynamic simulations open new opportunities to constrain the initial state quantum fluctuation spectrum and the specific shear viscosity of the QGP medium with unprecedented precision.

In our current modeling of relativistic heavy-ion collisions, hydrodynamics is not fighting alone but equipped with the state-of-the-art EOS, event-by-event initial state fluctuations and a microscopic hadronic afterburner. In this thesis, we have focused on developing and applying such an advanced integrated model framework, the `iEBE` code package (Chapter 2), for large scale precise phenomenological studies of relativistic heavy-ion collisions in the near future.

The main part (chapters 3 to 13) of my thesis contains a collection of phenomenological studies of the bulk dynamics of relativistic heavy-ion collisions using the viscous hydrodynamic model. Extraction of the QGP specific shear viscosity from phenomenological studies requires tight constraints on all the model parameters used in the simulations. We studied the effect of the hydrodynamic model parameters on the final experimental observables (particle spectra and their elliptic flow coefficients) in Chapter 4. Based on a well-constrained fit to RHIC data, we extrapolated our calculations to LHC energy in Chapter 5 which accurately predicted the measured identified particle elliptic flow data. A follow-up analysis of both elliptic and triangular flow (v_2 and v_3) measurements at Pb + Pb collisions at $\sqrt{s} = 2.76\ A$ TeV (Chapter 6) at the LHC helped us to discriminate for the first time between the MC-Glauber and MCKLN initial condition models, simultaneously constraining the value of the QGP specific shear viscosity η/s to be close to $\frac{1}{4\pi}$. We further extended our calculations at LHC energies to event-by-event mode in Chapter 7 which confirmed the rubustness of our previous conclusions once event-by-event fluctuations on the nucleonic scale are included. In order to explore the possibility of accessing the temperature

dependence of η/s in the QGP phase, we perform model studies in Chapter 8. We found that the charge hadron elliptic flow is sensitive to $(\eta/s)(T)$, the relaxation time for the shear stress tensor τ_π, and the initialization of the $\pi^{\mu\nu}$ tensor, all at the level of $\mathcal{O}(10\%)$. An ambitious extraction of $(\eta/s)(T)$ requires a quantitatively precise model description of experimental flow observables over the wide range of collision energies probed at RHIC and LHC. Chapter 9 was devoted to such a systematic study of the collision energy dependence of hadron elliptic flow data.

The initial state fluctuations in heavy-ion collisions also imprint themselves in the measurable flow correlations between anisotropic flow coefficients of different harmonic order. These non-trivial correlations in the flow observables provide us with additional constraints on our theoretical modeling of the collisions. In Chapter 10, we discussed the measurable consequences of fluctuations in the flow angles at different p_T, together with comparisons with recent preliminary experimental data. These comparisons provided additional strong support for the success of hydrodynamic paradigm. We also studied ultra-central Pb+Pb collisions at the LHC in Chapter 11, where initial state fluctuations dominate over geometric contributions to the final flow observables. This analysis showed that the measured hierarchy of the flow spectrum $\{v_n\{2\}\}$ in these collisions challenges the current theoretical models, in particular our modeling of the initial-state quantum fluctuations.

In the last part of this thesis I studied viscous and fluctuation effects to electromagnetic probes of relativistic heavy-ion collisions. In Chapters 15 and 16, we derived thermal photon emission rates and their first order viscous corrections for the QGP and Hadron gas phases, respectively. These rates were then coupled with event-by-event viscous hydrodynamic evolution to study the direct photon spectra and their anisotropies in relativistic heavy-ion collisions. In Chapter 18, we studied the direct photon spectrum, especially the physical interpretation of its inverse slope parameter. We found that the direct photon spectrum is strongly affected by the hydrodynamic radial flow, which blue-shifts the photons coming from the low temperature region of the fireball during its late stage of the evolution. The anisotropic flows of direct photons were studied in Chapter 19. Similar to hadrons, the shear viscosity suppresses thermal photon v_n. However, the suppression is larger in the thermal photon case, because most of them come from inside the fireball where the shear stress tensor is large. This makes direct photon anisotropic flow a more sensitive viscometer for the QGP than hadronic observables. In Chapters 18 and 19 we also showed that current theory calculations underestimate the measured direct photon spectrum and its anisotropic flow by at least a factor of 5, which poses a big challenge to our current theoretical modeling. We investigated effects from pre-equilibrium flow and from contributions from short-lived resonance decays on the direct photon spectrum and v_n in Chapters 18 and 19. Both give small but significant contributions and improve the theoretical description. Effects from partial chemical equilibrium in the hadronic state EOS on photon spectra and anisotropic flows were studied in Chapter 20.

The fugacity enhancement in the photon emission rates was found to be largely compensated by the reduction in hydrodynamic space-time volume due to faster cooling, leaving only a small net effect. Finally, in order to have a thorough comparison of theoretically computed photon observables with experimental data, the inclusive and decay photons were studied in Chapter 21, focussing on a precise understanding of the experimental measurements and the resulting demands on their accurate theoretical simulation.

Appendix A: Subtracting self-correlation in multi-particle correlations

The flow correlation function, especially the multi-plane correlation, involves multiple Q_n vectors. One can avoid to deal with self-correlation by simply introducing rapidity gap between different sub-events. But this will lose statistics very quickly if the correlation function involves more and more Q_n vectors. Here, we derive a general formula to subtract the self-correlations for any number of Q_n vectors by induction method. Suppose we had known the expression for m-particle correlation function with self-correlation subtracted, $C(\{Q_{n_i}\}_m)$. We denote

$$P(m, \{\tilde{Q}_{n_i}\}_m) = \frac{N!}{(N-m)!} C(\{Q_{n_i}\}_m), \tag{A.1}$$

with $\tilde{Q}_n = \sum_{i=1}^{N} e^{in\phi_i} = NQ_n$ and N is the number of particles in the event. Then the correlation for $m+1$ particles can be calculated as

$$P(m+1, \{\tilde{Q}_{n_i}\}_{m+1}) = \tilde{Q}_{n_{m+1}} P(m, \{\tilde{Q}_{n_i}\}_m) - \sum_{j=1}^{m} P(m, \{\tilde{Q}_{n_j+n_{m+1}}\}_m), \tag{A.2}$$

where the second term subtracts the self-correlations from the $m+1$-th particle being the same as any of the previous m particles. The normalized correlation function can be evaluated as,

$$C(\{Q_{n_i}\}_{m+1}) = \frac{1}{N-m} \left(NQ_{n_{m+1}} C(\{Q_{n_i}\}_m) - \sum_{j=1}^{m} C(\{Q_{n_j+n_{m+1}}\}_m) \right). \tag{A.3}$$

The initial starting point is the trivial case $P(1, \tilde{Q}_n) = \tilde{Q}_n$ for $m = 1$. Then for $m = 2$,

$$P(2, \{\tilde{Q}_{n_1}, \tilde{Q}_{n_2}\}) = \tilde{Q}_{n_2} \cdot \tilde{Q}_{n_1} - \tilde{Q}_{n_1+n_2}. \tag{A.4}$$

For the ensemble average of $P(2, \{Q_{n_1}, Q_{n_2}\})$ not to vanish due to random orientation of the reaction plane, we must have $n_1 + n_2 = 0$, and then $\tilde{Q}_{n_1+n_2} = N$. The normalized correlation function is then,

$$C(\{Q_{n_1}, Q^*_{n_1}\}) = \frac{N}{N-1} Q_{n_1} \cdot Q^*_{n_1} - \frac{1}{N-1}. \tag{A.5}$$

For $m = 3$,

$$\begin{aligned} P(3, \{\tilde{Q}_{n_1}, \tilde{Q}_{n_2}, \tilde{Q}_{n_3}\}) \;=\; & \tilde{Q}_{n_3}(\tilde{Q}_{n_2} \cdot \tilde{Q}_{n_1} - \tilde{Q}_{n_1+n_2}) \\ & -(\tilde{Q}_{n_2} \cdot \tilde{Q}_{n_1+n_3} - \tilde{Q}_{n_1+n_2+n_3}) \\ & -(\tilde{Q}_{n_1} \cdot \tilde{Q}_{n_2+n_3} - \tilde{Q}_{n_1+n_2+n_3}) \end{aligned} \tag{A.6}$$

and

$$\begin{aligned} C(\{Q_{n_1}, Q_{n_2}, Q_{n_3}\}) &= \frac{N^2}{(N-1)(N-2)} Q_{n_3} Q_{n_2} Q_{n_1} \\ &\quad - \frac{N}{(N-1)(N-2)} (Q_{n_3} Q_{n_1+n_2} + Q_{n_2} Q_{n_1+n_3} + Q_{n_1} Q_{n_2+n_3}) \\ &\quad + \frac{2}{(N-1)(N-2)}. \end{aligned} \tag{A.7}$$

The four-particle cumulant method involves $m = 4$ case,

$$\begin{aligned} P(4, \{\tilde{Q}_{n_1}, \tilde{Q}_{n_2}, \tilde{Q}_{n_3}, \tilde{Q}_{n_4}\}) &= Q_{n_4} P(3, \{\tilde{Q}_{n_1}, \tilde{Q}_{n_2}, \tilde{Q}_{n_3}\}) \\ &\quad - P(3, \{\tilde{Q}_{n_1+n_4}, \tilde{Q}_{n_2}, \tilde{Q}_{n_3}\}) - P(3, \{\tilde{Q}_{n_1}, \tilde{Q}_{n_2+n_4}, \tilde{Q}_{n_3}\}) \\ &\quad - P(3, \{\tilde{Q}_{n_1}, \tilde{Q}_{n_2}, \tilde{Q}_{n_3+n_4}\}). \end{aligned} \tag{A.8}$$

and

$$\begin{aligned} C(\{Q_{n_1}, Q_{n_2}, Q_{n_3}, Q_{n_4}\}) &= \frac{1}{N-3} [N Q_{n_4} C(\{Q_{n_1}, Q_{n_2}, Q_{n_3}\}) \\ &\quad - C(\{Q_{n_1+n_4}, Q_{n_2}, Q_{n_3}\}) - C(\{Q_{n_1}, Q_{n_2+n_4}, Q_{n_3}\}) \\ &\quad - C(\{Q_{n_1}, Q_{n_2}, Q_{n_3+n_4}\}]. \end{aligned} \tag{A.9}$$

Appendix B: On the form of δf corrections [131]

In thermal equilibrium, the momentum distribution function for particle species i can be written as,

$$f^i_{\rm eq}(x,p) = \frac{1}{e^{p\cdot u(x)/T(x) - \mu(x)} \pm 1}. \tag{B.1}$$

For a system near thermal equilibrium, the evolution of the particle distribution function can be described by linear Boltzmann equation. In the relaxation time approximation,

$$\delta f^i = -\tau^i_R p^\mu \partial_\mu f^i_{\rm eq}. \tag{B.2}$$

The spatial derivative will act on $u^\mu(x)$, $T(x)$, and $\mu(x)$ in Eq. B.1. We can write down a general tensor form of δf,

$$\delta f^i = -f^i_{\rm eq}(1 \mp f^i_{\rm eq})(p^\alpha \epsilon_\alpha + p^\alpha p^\beta \epsilon_{\alpha\beta}). \tag{B.3}$$

In Eq. (B.3), ϵ_α and $\epsilon_{\alpha\beta}$ are tensors contains the gradients of $u^\mu(x)$, $T(x)$, and $\mu(x)$. Since $p^\alpha p^\beta$ is symmetric in α and β, $\epsilon_{\alpha\beta}$ is also symmetric. Thus it only has 10 independent components. Together with the 4 independent components in ϵ_α, there are 14 unknowns in Eq. (B.3). The expansion in Eq. (B.3) is called the 14-moment approximation [247]. The system's baryon and energy momentum tensor can be written as

$$N^\mu = N^\mu_{\rm eq} + V^\mu \tag{B.4}$$

and

$$T^{\mu\nu} = eu^\mu u^\nu - (P + \Pi)\Delta^{\mu\nu} + \pi^{\mu\nu}. \tag{B.5}$$

By using the Landau matching condition, we can relate the macroscopic quantities in Eq. (B.4) and (B.5) with δf as follows,

$$T^{\mu\nu}u_\nu = T^{\mu\nu}_{\rm eq}u_\nu = eu^\mu, \tag{B.6}$$

$$u_\mu N^\mu = u_\mu N^\mu_{\rm eq} = n, \tag{B.7}$$

$$V^\mu = \Delta^{\mu\nu}N_\nu, \tag{B.8}$$

$$\Pi = -\frac{1}{3}\Delta_{\mu\nu}\delta T^{\mu\nu}, \tag{B.9}$$

$$\pi^{\mu\nu} = \Delta^{\mu\nu}_{\alpha\beta}\delta T^{\alpha\beta}, \tag{B.10}$$

where $\delta T^{\mu\nu} = T^{\mu\nu} - eu^\mu u^\nu + P\Delta^{\mu\nu}$. Here, V^μ can be related to heat current q^μ as,

$$q^\mu = -\frac{e+P}{n}V^\mu. \tag{B.11}$$

There are 14 equations in total from Eq. (B.6) to Eq. (B.10), which can help us to map the macroscopic hydrodynamic quantities in Eq. (B.4) and (B.5) onto ϵ_α and $\epsilon_{\alpha\beta}$.

In order to simplify the notation, we define the following thermodynamic integrals,

$$\begin{aligned} J^{\mu_1\mu_2\cdots\mu_m} &= \sum_i \int \frac{g_i}{(2\pi)^3}\frac{d^3p}{E_i} f^i_{\rm eq}(p)(1 \pm f^i_{\rm eq}(p))p^{\mu_1}p^{\mu_2}\cdots p^{\mu_m} \\ &= \sum_n [\Delta^{\mu_1\mu_2}\cdots\Delta^{\mu_{2n-1}\mu_{2n}}u^{\mu_{2n+1}}\cdots u^{\mu_m} + \text{permutations}]J_{mn} \end{aligned} \tag{B.12}$$

and

$$\begin{aligned} \tilde{J}^{\mu_1\mu_2\cdots\mu_m} &= \sum_i \int \frac{b_i g_i}{(2\pi)^3}\frac{d^3p}{E_i} f^i_{\rm eq}(p)(1 \pm f^i_{\rm eq}(p))p^{\mu_1}p^{\mu_2}\cdots p^{\mu_m} \\ &= \sum_n [\Delta^{\mu_1\mu_2}\cdots\Delta^{\mu_{2n-1}\mu_{2n}}u^{\mu_{2n+1}}\cdots u^{\mu_m} + \text{permutations}]\tilde{J}_{mn} \end{aligned} \tag{B.13}$$

where i runs over all particle species. Then Eq. (B.6) to Eq. (B.10) can be evaluated as,

$$\begin{aligned} u_\mu\delta T^{\mu\nu} = 0 \;&\Rightarrow\; -u_\mu J^{\mu\nu\alpha}\epsilon_\alpha - u_\mu J^{\mu\nu\alpha\beta}\epsilon_{\alpha\beta} = 0 \\ &\Rightarrow\; J_{30}\epsilon_\star u^\nu + J_{31}\Delta^{\nu\alpha}\epsilon_\alpha + J_{40}u^\nu\epsilon_{\star\star} + J_{41}u^\nu\Delta^{\alpha\beta}\epsilon_{\alpha\beta} + 2J_{41}\Delta^{\nu\alpha}\epsilon_{\alpha\star} = 0 \\ &\Rightarrow\; (J_{30}\epsilon_\star + J_{40}\epsilon_{\star\star} + J_{41}\Delta^{\alpha\beta}\epsilon_{\alpha\beta})u^\nu + (J_{31}\epsilon_\alpha + 2J_{41}\epsilon_{\alpha\star})\Delta^{\nu\alpha} = 0 \\ &\Rightarrow\; \begin{cases} J_{30}\epsilon_\star + J_{40}\epsilon_{\star\star} + J_{41}\Delta^{\alpha\beta}\epsilon_{\alpha\beta} = 0 \\ (J_{31}\epsilon_\alpha + 2J_{41}\epsilon_{\alpha\star})\Delta^{\nu\alpha} = 0 \end{cases} \\ &\Rightarrow\; \begin{cases} J_{30}\epsilon_\star + (J_{40} - J_{41})\epsilon_{\star\star} + J_{41}\mathrm{Tr}\{\epsilon\} = 0 \\ J_{31}\Delta^{\nu\alpha}\epsilon_\alpha + 2J_{41}\Delta^{\nu\alpha}\epsilon_{\alpha\star} = 0 \end{cases}, \end{aligned} \tag{B.14}$$

where $\epsilon_\star = \epsilon_\mu u^\mu$, $\epsilon_{\star\star} = \epsilon_{\mu\nu}u^\mu u^\nu$, and $\mathrm{Tr}\{\epsilon\} = g^{\mu\nu}\epsilon_{\mu\nu}$.

$$\begin{aligned} u_\mu\delta N^\mu = 0 \;&\Rightarrow\; -u_\mu\tilde{J}^{\mu\alpha}\epsilon_\alpha - u_\mu\tilde{J}^{\mu\alpha\beta}\epsilon_{\alpha\beta} = 0 \\ &\Rightarrow\; -\tilde{J}_{20}\epsilon_\star - \tilde{J}_{30}\epsilon_{\star\star} - \tilde{J}_{31}\Delta^{\alpha\beta}\epsilon_{\alpha\beta} = 0 \\ &\Rightarrow\; -\tilde{J}_{20}\epsilon_\star - (\tilde{J}_{30} - \tilde{J}_{31})\epsilon_{\star\star} - \tilde{J}_{31}\mathrm{Tr}\{\epsilon\} = 0. \end{aligned} \tag{B.15}$$

$$\begin{aligned} \Pi = -\frac{1}{3}\Delta_{\mu\nu}\delta T^{\mu\nu} \;&\Rightarrow\; \Pi = -\frac{1}{3}(-\Delta_{\mu\nu}J^{\mu\nu\alpha}\epsilon_\alpha - \Delta_{\mu\nu}J^{\mu\nu\alpha\beta}\epsilon_{\alpha\beta}) \\ &\Rightarrow\; \Pi = J_{31}\epsilon_\star + J_{41}\epsilon_{\star\star} + \frac{5}{3}J_{42}\Delta^{\alpha\beta}\epsilon_{\alpha\beta} \\ &\Rightarrow\; \Pi = J_{31}\epsilon_\star + \left(J_{41} - \frac{5}{3}J_{42}\right)\epsilon_{\star\star} + \frac{5}{3}J_{42}\mathrm{Tr}\{\epsilon\}. \end{aligned} \tag{B.16}$$

$$V^\mu = \Delta^{\mu\nu} N_\nu \;\Rightarrow\; V_\mu = \frac{1}{3}(-\Delta_{\mu\nu} J^{\nu\alpha}\epsilon_\alpha - \Delta_{\mu\nu} J^{\nu\alpha\beta}\epsilon_{\alpha\beta})$$
$$\Rightarrow\; V^\mu = -\tilde{J}_{21}\Delta^{\mu\nu}\epsilon_\nu - 2\tilde{J}_{31}\Delta^{\mu\nu}\epsilon_{\nu\star}. \tag{B.17}$$

$$\pi^{\mu\nu} = \Delta^{\mu\nu}_{\alpha\beta}\delta T^{\alpha\beta} \;\Rightarrow\; \pi^{\mu\nu} = -\Delta^{\mu\nu}_{\alpha\beta} J^{\alpha\beta\rho}\epsilon_\rho - \Delta^{\mu\nu}_{\alpha\beta} J^{\alpha\beta\rho\sigma}\epsilon_{\rho\sigma}$$
$$\Rightarrow\; \pi^{\mu\nu} = -2J_{42}\Delta^{\mu\nu}_{\alpha\beta}\epsilon^{\alpha\beta}. \tag{B.18}$$

Now, we can solve for ϵ^μ and $\epsilon^{\mu\nu}$,

$$\epsilon_\star = D_0\Pi, \tag{B.19}$$
$$\epsilon_{\star\star} = \widetilde{B_0}\Pi, \tag{B.20}$$
$$\mathrm{Tr}\{\epsilon\} = B_0\Pi, \tag{B.21}$$
$$\Delta^{\mu\nu}\epsilon_\nu = \widetilde{D_1}V^\mu, \tag{B.22}$$
$$\Delta^{\mu\nu}\epsilon_{\nu\star} = \widetilde{B_1}V^\mu, \tag{B.23}$$
$$\Delta^{\mu\nu}_{\alpha\beta}\epsilon^{\alpha\beta} = B_2\pi^{\mu\nu}, \tag{B.24}$$

where B_i, $\widetilde{B_i}$, D_i, and $\widetilde{D_i}$ are functions of the themodynamic integrals, J_{mn} and $\tilde{J}_{mn}$,

$$D_0 = 3(J_{40}\tilde{J}_{31} - J_{41}\tilde{J}_{30})\mathcal{J}_3^{-1}, \tag{B.25}$$
$$\widetilde{B_0} = 3(J_{41}\tilde{J}_{20} - J_{30}\tilde{J}_{31})\mathcal{J}_3^{-1}, \tag{B.26}$$
$$B_0 = (J_{30}\tilde{J}_{30} - J_{40}\tilde{J}_{20})\mathcal{J}_3^{-1}, \tag{B.27}$$
$$\widetilde{D_1} = 2J_{41}\mathcal{J}_2^{-1}, \tag{B.28}$$
$$\widetilde{B_1} = -J_{31}\mathcal{J}_2^{-1}, \tag{B.29}$$
$$B_2 = \mathcal{J}_1^{-1}, \tag{B.30}$$

and,

$$\mathcal{J}_3 = 5J_{30}J_{42}\tilde{J}_{30} + 3J_{31}J_{40}\tilde{J}_{31} + 3J_{41}J_{41}\tilde{J}_{20}$$
$$-3J_{31}J_{41}\tilde{J}_{30} - 3J_{30}J_{41}\tilde{J}_{31} - 5J_{40}J_{42}\tilde{J}_{20}, \tag{B.31}$$
$$\mathcal{J}_2 = 2J_{31}\tilde{J}_{31} - 2J_{41}\tilde{J}_{21,} \tag{B.32}$$
$$\mathcal{J}_1 = -2J_{42}, \tag{B.33}$$

Thus,

$$\epsilon^\mu = \epsilon_\star u^\mu + \Delta^{\mu\nu}\epsilon_\nu = D_0\Pi u^\mu + \widetilde{D_1}V^\mu. \tag{B.34}$$
$$\epsilon^{\mu\nu} = (B_0\Delta^{\mu\nu} + \widetilde{B_0}u^\mu u^\nu)\Pi + 2\widetilde{B_1}u^{(\mu}V^{\nu)} + B_2\pi^{\mu\nu}. \tag{B.35}$$

We can put Eqs. (B.34) and (B.35) back into Eq. (B.3) and obtain,

$$\begin{aligned}
\delta f^i &= -f_0^i(1 \pm f_0^i)(p^\mu \epsilon_\mu + p^\mu p^\nu \epsilon_{\mu\nu}) \\
&= -f_0^i(1 \pm f_0^i)(p^\mu(D_0 \Pi u_\mu + \widetilde{D_1} V_\mu) + p^\mu p^\nu[((B_0 \Delta_{\mu\nu} + \widetilde{B_0} u_\mu u_\nu)\Pi \\
&\quad + 2\widetilde{B_1} u_{(\mu} V_{\nu)} + B_2 \pi_{\mu\nu})]) \\
&= -f_0^i(1 \pm f_0^i)[\Pi(D_0(p \cdot u) - B_0 m_i^2 + (B_0 + \widetilde{B_0})(p \cdot u)^2) \\
&\quad + (p \cdot V)(\widetilde{D_1} + 2\widetilde{B_1}(p \cdot u)) \\
&\quad + B_2 p^\mu p^\nu \pi_{\mu\nu}]
\end{aligned} \tag{B.36}$$

So, we can see that the δf^i for bulk viscosity is,

$$\delta f^i_{\rm bulk} = f_0^i(1 \pm f_0^i)\Pi[B_0 m_i^2 - D_0(p \cdot u) - (B_0 + \widetilde{B_0})(p \cdot u)^2]. \tag{B.37}$$

And the δf^i for heat current is,

$$\delta f^i_{\rm heat} = f_0^i(1 \pm f_0^i)(p \cdot V)(-\widetilde{D_1} - 2\widetilde{B_1}(p \cdot u)) \tag{B.38}$$

or

$$\delta f^i_{\rm heat} = f_0^i(1 \pm f_0^i)\frac{e + P}{n}(p \cdot q)(\widetilde{D_1} + 2\widetilde{B_1}(p \cdot u)). \tag{B.39}$$

Finally the δf^i for shear viscosity is,

$$\delta f^i_{\rm shear} = f_0^i(1 \pm f_0^i)(-B_2 p^\mu p^\nu \pi_{\mu\nu}). \tag{B.40}$$

Appendix C: Small transverse momentum limit of v_n [248]

C.1 Massive case

Here we perform the calculation for the boson case. The fermion case is exactly the same, but with the fermi distribution functions. The anisotropic flows can be calculated using the Cooper-Frye formula,

$$v_n(k_\perp) = \frac{N_n}{N_0}, \tag{C.1}$$

where

$$N_n = \frac{g_i}{(2\pi)^2} \int d^2x_\perp \tau_f \int d\eta N_n^\phi, \tag{C.2}$$

with

$$N_n^\phi = \int_{-\pi}^{\pi} \frac{d\phi}{2\pi} \cos(n\phi) \frac{m_\perp \cosh\eta - \vec{k}_\perp \cdot \vec{\nabla}_\perp \tau_f}{e^{\gamma_\perp (m_\perp \cosh\eta - k_\perp \cdot v_\perp)/T} - 1}, \tag{C.3}$$

For non-zero rest mass, $m \neq 0$, we can expand in both cases the ϕ integrand for small $k_\perp$ and keep only terms up to first order in $k_\perp$,

$$\begin{aligned} N_n^\phi &= \frac{m\cosh\eta}{e^{\gamma_\perp m\cosh\eta/T} - 1} \int_{-\pi}^{\pi} \frac{d\phi}{2\pi} \cos(n\phi) \left(1 - \frac{\vec{k}_\perp \cdot \vec{\nabla}_\perp \tau_f}{m\cosh\eta}\right) \\ &\quad \times \left(1 + \frac{\gamma_\perp}{T} \vec{k}_\perp \cdot \vec{v}_\perp \frac{1}{1 - e^{-\gamma_\perp m\cosh\eta/T}} + \ldots\right) \\ &\simeq \frac{m\cosh\eta}{e^{\gamma_\perp m\cosh\eta/T} - 1} \int_{-\pi}^{\pi} \frac{d\phi}{2\pi} \cos(n\phi) \left(1 - \frac{\vec{k}_\perp \cdot \vec{\nabla}_\perp \tau_f}{m\cosh\eta} + \frac{\gamma_\perp}{T} \frac{\vec{k}_\perp \cdot \vec{v}_\perp}{1 - e^{-\gamma_\perp m\cosh\eta/T}}\right). \end{aligned} \tag{C.4}$$

We write

$$\vec{k}_\perp \cdot \vec{v}_\perp = k_\perp v_\perp \cos(\phi - \phi_v) = k_\perp v_\perp \cos\theta. \tag{C.5}$$

and change the integration variable from ϕ to θ,

$$\hat{k}_\perp \cdot \nabla_\perp \tau_f = (\partial_r \tau_f)\cos\theta + \left(\frac{1}{r}\partial_\phi \tau_f\right)\sin\theta, \tag{C.6}$$

where $\partial_r \tau_f = \widehat{v_\perp} \cdot \nabla_\perp \tau_f$ and $\frac{1}{r}\partial_\phi \tau_f = \hat{z} \cdot (\widehat{v_\perp} \times \nabla_\perp \tau_f)$. $\hat{v}_\perp = (\cos\phi_v, \sin\phi_v)$. We also need,

$$\cos(n\phi) = \cos n(\theta + \phi_v) \quad = \quad \cos(n\phi_v)\cos(n\theta) - \sin(n\phi_v)\sin(n\theta),$$

Then,

$$\begin{aligned}
N_n^\phi &= \frac{m\cosh\eta}{e^{\gamma_\perp m\cosh\eta/T}-1}\int_{-\pi}^{\pi}\frac{d\theta}{2\pi}(\cos(n\phi_v)\cos(n\theta)-\sin(n\phi_v)\sin(n\theta)) \\
&\quad \times\left(1-\frac{k_\perp}{m\cosh\eta}\left((\partial_r\tau_f)\cos\theta+\left(\frac{1}{r}\partial_\phi\tau_f\right)\sin\theta\right)+\frac{\gamma_\perp}{T}\frac{k_\perp v_\perp\cos\theta}{1-e^{-\gamma_\perp m\cosh\eta/T}}\right) \\
I_n^1 &= \frac{m\cosh\eta}{e^{\gamma_\perp m\cosh\eta/T}-1}\int_{-\pi}^{\pi}\frac{d\theta}{2\pi}(\cos(n\phi_s)\cos(n\theta)-\sin(n\phi_s)\sin(n\theta)) \qquad \text{(C.7)} \\
I_n^2 &= \frac{m\cosh\eta}{e^{\gamma_\perp m\cosh\eta/T}-1}\int_{-\pi}^{\pi}\frac{d\theta}{2\pi}\frac{k_\perp}{m\cosh\eta}(\cos(n\phi_v)\cos(n\theta)-\sin(n\phi_v)\sin(n\theta) \\
&\quad \times\left((\partial_r\tau_f)\cos\theta+\left(\frac{1}{r}\partial_\phi\tau_f\right)\sin\theta\right) \qquad \text{(C.8)} \\
I_n^3 &= \frac{m\cosh\eta}{e^{\gamma_\perp m\cosh\eta/T}-1}\int_{-\pi}^{\pi}\frac{d\theta}{2\pi}(\cos(n\phi_v)\cos(n\theta)-\sin(n\phi_v)\sin(n\theta)) \\
&\quad \times\frac{\gamma_\perp}{T}\frac{k_\perp v_\perp\cos\theta}{1-e^{-\gamma_\perp m\cosh\eta/T}} \qquad \text{(C.9)}
\end{aligned}$$

So,

$$I_n^1 \quad = \quad \frac{m\cosh\eta}{e^{\gamma_\perp m\cosh\eta/T}-1}\frac{1}{2\pi}\left(\cos(n\phi_v)\frac{2\sin(n\pi)}{n}\right), \qquad \text{(C.10)}$$

$$\begin{aligned}
I_n^2 &= \frac{m\cosh\eta}{e^{\gamma_\perp m\cosh\eta/T}-1}\frac{k_\perp}{m\cosh\eta}\frac{1}{2\pi} \\
&\quad \times\left(\cos(n\phi_v)(\partial_r\tau_f)\frac{2n\sin(n\pi)}{n^2-1}+\sin(n\phi_v)\left(\frac{1}{r}\partial_\phi\tau_f\right)\frac{2\sin(n\pi)}{n^2-1}\right), \qquad \text{(C.11)}
\end{aligned}$$

$$I_n^3 \quad = \quad \frac{m\cosh\eta}{e^{\gamma_\perp m\cosh\eta/T}-1}\frac{1}{2\pi}\frac{\gamma_\perp}{T}\frac{k_\perp v_\perp}{1-e^{-\gamma_\perp m\cosh\eta/T}}\cos(n\phi_v)\frac{2n\sin(n\pi)}{n^2-1}, \qquad \text{(C.12)}$$

and

$$N_n^\phi \quad = \quad I_n^1 - I_n^2 + I_n^3. \qquad \text{(C.13)}$$

For $n = 2$, I_n^1, I_n^2, I_n^3, are zero. So, $N_2 = O(k_\perp^2)$. And for $n = 0$, I_0^1, I_0^2, I_0^3, are non-zero, so $N_0 = a + bk_\perp + O(k_\perp^2)$. For higher order n, since we want to prove $N_n = O(k_\perp^n)$, we need to expand N_n^ϕ to higher order in $k_\perp$.

At $O(k_\perp^2)$, $m_\perp \cosh\eta$ will contribute,

$$m_\perp\cosh\eta = m\cosh\eta\left(1+\frac{1}{2}\frac{k_\perp^2}{m^2}+\ldots\right) \qquad \text{(C.14)}$$

But this term will not affect the angular integration. The new term at $O(k_\perp^2)$ that matters is

$$\begin{aligned} I_n^4 &= \frac{m\cosh\eta}{e^{\gamma_\perp m\cosh\eta/T}-1}\int_{-\pi}^{\pi}\frac{d\theta}{2\pi}(\cos(n\phi_v)\cos(n\theta)-\sin(n\phi_v)\sin(n\theta)) \\ &\quad\times\frac{\vec{k}_\perp\cdot\vec{\nabla}_\perp\tau_f}{m\cosh\eta}\frac{\gamma_\perp}{T}\frac{\vec{k}_\perp\cdot\vec{v}_\perp}{1-e^{-\gamma_\perp m\cosh\eta/T}} \end{aligned} \tag{C.15}$$

$$\begin{aligned} I_n^4 &= \frac{\gamma_\perp}{T}\frac{e^{\gamma_\perp m\cosh\eta/T}}{(e^{\gamma_\perp m\cosh\eta/T}-1)^2}\int_{-\pi}^{\pi}\frac{d\theta}{2\pi}(\cos(n\phi_v)\cos(n\theta)-\sin(n\phi_v)\sin(n\theta)) \\ &\quad\times(\vec{k}_\perp\cdot\vec{\nabla}_\perp\tau_f)(\vec{k}_\perp\cdot\vec{v}_\perp) \\ &= \frac{\gamma_\perp}{T}\frac{e^{\gamma_\perp m\cosh\eta/T}}{(e^{\gamma_\perp m\cosh\eta/T}-1)^2}\int_{-\pi}^{\pi}\frac{d\theta}{2\pi}(\cos(n\phi_v)\cos(n\theta)-\sin(n\phi_v)\sin(n\theta)) \\ &\quad\times((\partial_r\tau_f)\cos\theta+(\partial_\phi\tau_f)\sin\theta)k_\perp v_\perp\cos\theta \\ &= \frac{\gamma_\perp}{T}\frac{e^{\gamma_\perp m\cosh\eta/T}}{(e^{\gamma_\perp m\cosh\eta/T}-1)^2}\frac{k_\perp v_\perp}{2\pi} \\ &\quad\times\left(\cos(n\phi_v)(\partial_r\tau_f)\frac{2(-2+n^2)\sin(n\pi)}{n(-4+n^2)}-\sin(n\phi_v)\left(\frac{1}{r}\partial_\phi\tau_f\right)\frac{2\sin(n\pi)}{-4+n^2}\right). \end{aligned}$$

$I_2^4\neq 0$, but $I_3^4=0$. So for v_2, it goes like $k_\perp^2$ in the small transverse momentum limit. But for v_3, it still vanishes at $O(k_\perp^2)$. The momentum dependence needs to be higher order than $O(k_\perp^2)$.

At $O(k_\perp^3)$ order, the new angular integral is

$$\begin{aligned} I_n^5 &= \#\int_{-\pi}^{\pi}\frac{d\theta}{2\pi}(\cos(n\phi_v)\cos(n\theta)-\sin(n\phi_v)\sin(n\theta)) \\ &\quad\times((\partial_r\tau_f)\cos\theta+(\partial_\phi\tau_f)\sin\theta)(k_\perp v_\perp\cos\theta)^2 \\ &= \#\frac{1}{2\pi}\left(\cos(n\phi_v)(\partial_r\tau_f)\frac{-2n(-7+n^2)\sin(n\pi)}{9-10n^2+n^4}\right. \\ &\quad\left.-\sin(n\phi_v)\left(\frac{1}{r}\partial_\phi\tau_f\right)\frac{-2(-3+n^2)\sin(n\pi)}{9-10n^2+n^4}\right). \end{aligned} \tag{C.16}$$

I_n^5 vanishes for $n\neq 3$. So for v_3, it would go like $O(k_\perp^3)$.

Now, we know that when we want to compute higher order terms in this expansion, the new angular integrals that will enter has the following structure. For $O(k_\perp^m)$,

$$J_n^m=\int_{-\pi}^{\pi}\frac{d\theta}{2\pi}\cos(n\theta)\cos^m\theta \tag{C.17}$$

and

$$\tilde{J}_n^m=\int_{-\pi}^{\pi}\frac{d\theta}{2\pi}\sin(n\theta)\sin\theta\cos^{m-1}\theta \tag{C.18}$$

For general m, the analytic expression for J_n^m and $\tilde{J}_n^m$ can be found in `Mathematica`, which are complicated functions. But we are interested in whether J_m^m and $\tilde{J}_m^m$ equal zero or not. We find $J_n^m=0$, if $m\neq n$. So this proves that $v_n\propto k_\perp^n$ in the small $k_\perp$ limit.

C.2 Massless case

For massless bosons, v_n has different small $k_\perp$ limit compared to the massive case. The expansion parameter becomes $\gamma_\perp k_\perp(\cosh\eta - \hat{\vec{k}}_\perp \cdot \vec{v}_\perp)/T$. So in every order there will be an additional $\cosh\eta$. Unfortunately, the η integral of the expansion coefficient diverges. So we need to perform the η integral before the $k_\perp$ expansion. We write the m-th order anisotropic flow coefficient as,

$$v_m(k_\perp) = \frac{N_n}{N_0}, \tag{C.19}$$

where,

$$N_n = \frac{g_i}{(2\pi)^2}\int d^2x_\perp \tau_f \int d\eta N_n^\phi, \tag{C.20}$$

with

$$N_n^\phi = \frac{T}{\gamma_\perp}\int_{-\pi}^{\pi}\frac{d\phi}{2\pi}\cos(m\phi)\frac{\gamma_\perp k_\perp(\cosh\eta - \widehat{\vec{k}_\perp}\cdot\vec{\nabla}_\perp\tau_f)}{Te^{\gamma_\perp k_\perp(\cosh\eta - \widehat{\vec{k}_\perp}\cdot\vec{v}_\perp)/T}-1}, \tag{C.21}$$

Define, $\xi = \frac{\gamma_\perp k_\perp}{T}$, then

$$N_n^\phi = \frac{T}{\gamma_\perp}\int_{-\pi}^{\pi}\frac{d\phi}{2\pi}\cos(m\phi)\frac{\xi(\cosh\eta - \widehat{\vec{k}_\perp}\cdot\vec{\nabla}_\perp\tau_f)}{e^{\xi(\cosh\eta - \widehat{\vec{k}_\perp}\cdot\vec{v}_\perp)}-1}. \tag{C.22}$$

Now, we expand the denominator in terms of $\xi(\cosh\eta - v_\perp\cos\theta)$, where θ is the angle between $\widehat{\vec{k}_\perp}$ and $\vec{v}_\perp$. We define the integral,

$$\begin{aligned} I_\eta &= \xi\sum_{n=1}^{\infty}e^{nv_\perp\xi\cos\theta}\int_{-\infty}^{\infty}d\eta e^{-n\xi\cosh\eta}\left(\cosh\eta - (\partial_r\tau_f)\cos\theta - \left(\frac{1}{r}\partial_\phi\tau_f\right)\sin\theta\right) \\ &= 2\xi\sum_{n=1}^{\infty}e^{nv_\perp\xi\cos\theta}\left[K_1(n\xi) - \left((\partial_r\tau_f)\cos\theta + \left(\frac{1}{r}\partial_\phi\tau_f\right)\sin\theta\right)K_0(n\xi)\right] \end{aligned} \tag{C.23}$$

Thus, the numerator of v_m can be written as,

$$\int d\eta N_\phi = \frac{T}{\gamma_\perp}\int_{-\pi}^{\pi}\frac{d\phi}{2\pi}\cos(m\phi)I_\eta(\xi). \tag{C.24}$$

For the ϕ integral, similar to the massive case, $\phi = \phi_v + \theta$ and

$$\cos(m\phi) = \cos(m\phi_v)\cos(m\theta) - \sin(m\phi_v)\sin(m\theta). \tag{C.25}$$

We will use the following integral,

$$I_\theta = \int\frac{d\theta}{2\pi}\cos(\nu\theta)e^{z\cos\theta} = I_\nu(z). \tag{C.26}$$

$$
\begin{aligned}
\int d\eta N_\phi &= \frac{T}{\gamma_\perp}\int_{-\pi}^{\pi}\frac{d\theta}{2\pi}(\cos(m\phi_v)\cos(m\theta)-\sin(m\phi_v)\sin(m\theta))\times\sum_{n=1}^{\infty}e^{nv_\perp\xi\cos\theta}\\
&\quad\times 2\xi\left[K_1(n\xi)-\left((\partial_r\tau_f)\cos\theta+\left(\frac{1}{r}\partial_\phi\tau_f\right)\sin\theta\right)K_0(n\xi)\right]\\
&= \frac{T}{\gamma_\perp}2\xi\sum_{n=1}^{\infty}\Bigg[\\
&\quad K_1(n\xi)\left(\int_{-\pi}^{\pi}\frac{d\theta}{2\pi}(\cos(m\phi_v)\cos(m\theta)-\sin(m\phi_v)\sin(m\theta))\right)e^{nv_\perp\xi\cos\theta}\Bigg]\\
&\quad -K_0(n\xi)\int_{-\pi}^{\pi}\frac{d\theta}{2\pi}\left((\partial_r\tau_f)\cos\theta+\left(\frac{\partial_\phi\tau_f}{r}\right)\sin\theta\right)\\
&\quad\times(\cos(m\phi_v)\cos(m\theta)-\sin(m\phi_v)\sin(m\theta))e^{nv_\perp\xi\cos\theta}\\
&= \frac{T}{\gamma_\perp}2\xi\sum_{n=1}^{\infty}\cos(m\phi_v)\Bigg[K_1(n\xi)I_m(nv_\perp\xi)\\
&\quad -K_0(n\xi)\frac{(\partial_r\tau_f)}{2}(I_{m+1}(nv_\perp\xi)+I_{m-1}(nv_\perp\xi))\Bigg]\\
&\quad +\sin(m\phi_v)\frac{\left(\frac{1}{r}\partial_\phi\tau_f\right)}{2}(I_{m+1}(nv_\perp\xi)+I_{m-1}(nv_\perp\xi))K_0(n\xi),
\end{aligned}
$$

$$
\begin{aligned}
\int d\eta N_0^\phi &= \frac{T}{\gamma_\perp}\int_{-\pi}^{\pi}\frac{d\theta}{2\pi}\sum_{n=1}^{\infty}e^{nv_\perp\xi\cos\theta}2\xi\\
&\quad\left[K_1(n\xi)-\left((\partial_r\tau_f)\cos\theta+\left(\frac{1}{r}\partial_\phi\tau_f\right)\sin\theta\right)K_0(n\xi)\right]\\
&= \frac{T}{\gamma_\perp}2\xi\sum_{n=1}^{\infty}K_1(n\xi)I_0(nv_\perp\xi). \qquad \text{(C.27)}
\end{aligned}
$$

As $k_\perp\to 0$, $\xi\to 0$. And we define,

$$
f_{v_\perp}(\zeta)=I_\nu(v_\perp\zeta)K_\mu(\zeta), \qquad \text{(C.28)}
$$

we have

$$
\xi\sum_{n=1}^{\infty}I_\nu(nv_\perp\xi)K_\mu(n\xi)=\sum_{n=1}^{\infty}\xi f_{v_\perp}(n\xi)=\sum_{n=1}^{\infty}\Delta\zeta f_{v_\perp}(\zeta)\to\int_{\xi/2}^{\infty}f_{v_\perp}(\zeta)d\zeta \qquad \text{(C.29)}
$$

I think the reason to choose the lower bound as $\xi/2$ is considering ξ as the middle point of the first interval for $n=1$. Then since $\Delta\zeta=\xi$, the starting point of the integral will be $\zeta/2$. To extract the small $k_\perp$-dependence, we do the following trick,

$$
\int_{\xi/2}^{\infty}f_{v_\perp}(\zeta)d\zeta=\int_{\xi/2}^{\lambda}f_{v_\perp}(\zeta)d\zeta+\int_{\lambda}^{\infty}f_{v_\perp}(\zeta)d\zeta=\int_{\xi/2}^{\lambda}f_{v_\perp}(\zeta)d\zeta+F(\lambda,v_\perp), \qquad \text{(C.30)}
$$

where $F(\lambda,v_\perp)$ is a finite number. By taking $\xi/2<\lambda\ll 1$, we can evaluate the first integral analytically by making use of the expansion of the Bessel functions for small arguments, keeping

only the leading terms. In the limit $\xi \to 0$ we find,

$$\int_{\xi/2}^{\lambda} I_2(v_\perp \zeta) K_1(\zeta) d\zeta \to \frac{\lambda^2 v_\perp^2}{16}, \tag{C.31}$$

$$\int_{\xi/2}^{\lambda} I_1(v_\perp \zeta) K_0(\zeta) d\zeta \to \frac{v_\perp}{16} \xi^2 \ln(a\xi) + C(\lambda), \tag{C.32}$$

$$\int_{\xi/2}^{\lambda} I_3(v_\perp \zeta) K_0(\zeta) d\zeta \to 0, \tag{C.33}$$

$$\int_{\xi/2}^{\lambda} I_0(v_\perp \zeta) K_1(\zeta) d\zeta \to \ln \frac{2\lambda}{\xi} + C'(\lambda), \tag{C.34}$$

So, we finally obtain,

$$\lim_{k_\perp \to 0} v_2(k_\perp) = \frac{\text{const.}}{\ln \frac{T}{k_\perp}} \propto -\frac{1}{\ln k_\perp}. \tag{C.35}$$

For v_3,

$$\int_{\xi/2}^{\lambda} I_3(v_\perp \zeta) K_1(\zeta) d\zeta \to \frac{\lambda^3 v_\perp^3}{144}, \tag{C.36}$$

$$\int_{\xi/2}^{\lambda} I_2(v_\perp \zeta) K_0(\zeta) d\zeta \to \frac{v_\perp^2}{24} \xi^3 \ln(a\xi) + C(\lambda), \tag{C.37}$$

$$\int_{\xi/2}^{\lambda} I_4(v_\perp \zeta) K_0(\zeta) d\zeta \to 0, \tag{C.38}$$

So, we finally obtain,

$$\lim_{k_\perp \to 0} v_3(k_\perp) = \frac{\text{const.}}{\ln \frac{T}{k_\perp}} \propto -\frac{1}{\ln k_\perp}. \tag{C.39}$$

Similar $k_\perp$ dependence can be found for higher order v_n.

Appendix D: Hadron Resonance Gas

The thermodynamic quantities in a hadronic system can be described by a non-interacting hadron gas with resonances states. The interaction between hadrons are replaced by regarding the intermediate resonance state as long-lived well-defined quasi-particles.

D.1 Bulk Thermodynamic Variables

Here we work in the Grand Canonical Ensemble. The partition function can be written as,

$$Z(T,\mu,V) = e^{-V\Omega(T,\mu)/T}, \tag{D.1}$$

with the Grand Canonical thermodynamic potential,

$$\Phi(T,\mu,V) = V\Omega(T,\mu). \tag{D.2}$$

The system pressure can be calculated by

$$P = -\frac{\partial\Phi}{\partial V}\bigg|_{T,\mu} = -\Omega(T,\mu). \tag{D.3}$$

For a thermalized system, the pressure can be calculated from the energy momentum tensor at local rest frame,

$$P = -\frac{1}{3}\sum_i \frac{g_i}{(2\pi)^3}\int \frac{d^3p}{E} p^\mu p^\nu \Delta_{\mu\nu} f_0(x,p), \tag{D.4}$$

where $f_0 = \frac{1}{\exp(\beta(E-\mu))\pm 1}$. Since f_0 is isotropic, the angular integral of the above expression can be done easily.

$$P = -\Omega(T,\mu) = \sum_i (\mp)\frac{g_i T}{2\pi^2}\int_0^{+\infty} p^2 dp \ln(1 \pm e^{-\beta(E-\mu_i)}). \tag{D.5}$$

For number density of particle species j,

$$\begin{aligned} n_j = \frac{N_j}{V} &= -\frac{\partial\Omega}{\partial\mu_j}\bigg|_{T,\mu_i(i\neq j)} \\ &= \frac{g_j}{2\pi^2}\int_0^{+\infty} p^2 dp \frac{1}{e^{\beta(E-\mu_j)}\pm 1}. \end{aligned} \tag{D.6}$$

For particle species j, its chemical potential $\mu_j = \mu_B B_j + \mu_S S_j$, where B_j and S_j correspond to baryon and strangeness quantum of hadron species j, respectively. Thus, the net baryon density can be calculated as,

$$\rho_B = \sum_j n_j B_j, \tag{D.7}$$

and similarly, the net strangeness density,

$$\rho_S = \sum_j n_j S_j. \tag{D.8}$$

For entropy density of the system,

$$s = \frac{S}{V} = -\left.\frac{\partial \Omega}{\partial T}\right|_{\mu_i} = \frac{P}{T} - \sum_i \mu_i n_i + \frac{e}{T}. \tag{D.9}$$

From this equation, we can get the energy density,

$$e = \sum_i \frac{g_i}{2\pi^2} \int_0^{+\infty} p^2 dp \frac{E}{e^{\beta(E-\mu_j)} \pm 1}. \tag{D.10}$$

Due to the complication of the quantum statistics, the integrals for pressure, energy density, and particle number density are hard to solve analytically. But it is possible to write them as a series of infinite sum of Bessel functions. For massive mesons and baryons with small chemical potentials, we can truncate the sum at some finite order (usually up to $n = 10$ is good enough for all species of particles).

$$n_i = \frac{g_i}{2\pi^2} m_i T \sum_{k=1}^{\infty} (\mp)^{k+1} \frac{\lambda^k}{k} K_2\left(k\frac{m_i}{T}\right). \tag{D.11}$$

$$e = \sum_i \frac{g_i}{2\pi^2} m_i^4 \sum_{k=1}^{\infty} (\mp)^{k+1} \lambda^k \left(\frac{3}{\left(k\frac{m_i}{T}\right)^2} K_2\left(k\frac{m_i}{T}\right) + \frac{1}{k\frac{m_i}{T}} K_1\left(k\frac{m_i}{T}\right) \right). \tag{D.12}$$

$$P = \sum_i \frac{g_i}{2\pi^2} m_i^2 T^2 \sum_{k=1}^{\infty} (\mp)^{k+1} \frac{\lambda^k}{k^2} K_2\left(k\frac{m_i}{T}\right). \tag{D.13}$$

The entropy density of the system can be calculated by the first law of thermodynamic.

D.2 Thermal Fluctuations [249]

For thermal fluctuation in the Grand Canonical Ensemble, we can calculate the number fluctuation as,

$$\langle (\Delta N)^2 \rangle = -T \left.\frac{\partial^2 \Omega}{\partial^2 \mu}\right|_{T,V} \tag{D.14}$$

So the fluctuation per volume is,

$$\langle (\Delta n)^2 \rangle = \frac{\langle (\Delta N)^2 \rangle}{V} = \frac{g_i}{2\pi^2} \int_0^{+\infty} p^2 dp \frac{e^{\beta(E-\mu_i)}}{(e^{\beta(E-\mu_i)} \pm 1)^2}. \tag{D.15}$$

It is easy to see that at a given energy, the number fluctuation for bosons is,

$$\langle(\Delta N)^2\rangle = \langle N\rangle^2 + \langle N\rangle, \tag{D.16}$$

and its probability distribution satisfies the Geometric distribution.

Similarly, fermions at given energy has,

$$\langle(\Delta N)^2\rangle = \langle N\rangle - \langle N\rangle^2, \tag{D.17}$$

and its probability distribution satisfies Bernoulli distribution.

For classical Boltzmann particles at given energy, the number fluctuation becomes,

$$\langle(\Delta N)^2\rangle = \langle N\rangle \tag{D.18}$$

its probability distribution satisfy Poison distribution. This is why most of people use Poisson distribution for particle number fluctuation on the top of Cooper-Frye formula.

From central limit theorem, the number fluctuation will be an approximate Gaussian distribution when the deviation $N - \bar{N}$ is small compared with the averaged number $\bar{N}$. If the selected volume becomes smaller, the number of particles inside the volume decreases. So $N - \bar{N}$ will become comparable to $\bar{N}$. Then the number fluctuation becomes Poisson distribution for Boltzmann particles.

D.3 Partial chemical equilibrium (PCE) [77, 16]

To implement partial chemical equilibrium in the EOS, we can evaluate the thermodynamic quantities along the isentropic curve, $\frac{\bar{n}_i}{s} = \text{const}$. At chemical freeze out, we have our initial condition $n_i(T_{\rm chem}, \mu_B, \mu_S)$ and $s(T_{\rm chem}, \mu_B, \mu_S)$, where we set $\{\tilde{\mu}_i\} = 0$ at $T = T_{\rm chem}$. Next, we want to solve for the chemical potentials $\{\tilde{\mu}_i\}$ at $T = T_{\rm chem} - \Delta T$. We will apply a multidimensional generalization of Newton's method to look for the root of the equation,

$$\frac{\bar{n}_i(T_{\rm chem} - \Delta T, \{\tilde{\mu}_i(T_{\rm chem} - \Delta T)\})}{s(T_{\rm chem} - \Delta T, \{\tilde{\mu}_i(T_{\rm chem} - \Delta T)\})} = \frac{\bar{n}_i(T_{\rm chem}, \{\tilde{\mu}_i = 0\})}{s(T_{\rm chem}, \{\tilde{\mu}_i = 0\})}, \tag{D.19}$$

where $\bar{n}_i$ is the number density for stable particles,

$$\bar{n}_i(T, \mu_B, \mu_S; \{\tilde{\mu}_i\}) = n_i(T, \mu_B, \mu_S; \{\tilde{\mu}_i\}) + \sum_{j=1}^{N_{\rm reso}} d_{j\to i} n_j(T, \mu_B, \mu_S; \{\tilde{\mu}_i\}), \tag{D.20}$$

where j runs over all resonance states that can decay into particle species i. The parameter $d_{j\to i}$ is the effective probability for resonance state j decays into i. It can be calculated as,

$$d_{j\to i} = \sum_{k=1}^{N_{\rm ch}} {\rm Br}^k_{j\to i} N^k_{j\to i}, \tag{D.21}$$

where k runs through all the decay channels, $N_{\rm ch}$. In Eq. (D.21), $\mathrm{Br}^k_{j\to i}$ is the branching ratio of decay channel k for $j \to i$ and $N^k_{j\to i}$ represents the number of daughter i particles through the decay channel k.

In the PCE model, $\{\tilde{\mu}_i\}$ are independent variables only for the stable particle species. For heavy resonance states j, its chemical potential can be constructed through its decay chains to stable particles,

$$\tilde{\mu}_j = \sum_{i=1}^{N_{\rm stable}} d_{j\to i}\mu_i, \tag{D.22}$$

where i runs over all stable particle species, $N_{\rm stable}$.

According to Newton, we can solve the chemical evolution equation, Eq. (D.19) iteratively,

$$\begin{pmatrix} \frac{\partial}{\partial\mu_1}\frac{\bar{n}_1}{s} & \frac{\partial}{\partial\mu_2}\frac{\bar{n}_1}{s} & \cdots & \frac{\partial}{\partial\mu_{N_{\rm stable}}}\frac{\bar{n}_1}{s} \\ \frac{\partial}{\partial\mu_1}\frac{\bar{n}_2}{s} & \frac{\partial}{\partial\mu_2}\frac{\bar{n}_2}{s} & \cdots & \frac{\partial}{\partial\mu_{N_{\rm stable}}}\frac{\bar{n}_2}{s} \\ \vdots & \vdots & \ddots & \vdots \\ \frac{\partial}{\partial\mu_1}\frac{\bar{n}_{N_{\rm stable}}}{s} & \frac{\partial}{\partial\mu_2}\frac{\bar{n}_{N_{\rm stable}}}{s} & \cdots & \frac{\partial}{\partial\mu_{N_{\rm stable}}}\frac{\bar{n}_{N_{\rm stable}}}{s} \end{pmatrix} \begin{pmatrix} \Delta\mu_1 \\ \Delta\mu_2 \\ \vdots \\ \Delta\mu_{N_{\rm stable}} \end{pmatrix} = \begin{pmatrix} \bar{A}_1 - \frac{\bar{n}_1}{s} \\ \bar{A}_2 - \frac{\bar{n}_2}{s} \\ \vdots \\ \bar{A}_{N_{\rm stable}} - \frac{\bar{n}_{N_{\rm stable}}}{s} \end{pmatrix}. \tag{D.23}$$

The iteration can be truncated when the largest variation of $\frac{\bar{n}_i}{s}$ is less than 10^{-9}.

The derivatives in Eq. (D.23) can be evaluated as follows,

$$\begin{aligned} \frac{\partial}{\partial\tilde{\mu}_i}\frac{\bar{n}_j(T,\mu_B,\mu_S;\{\tilde{\mu}_j\})}{s(T,\mu_B,\mu_S;\{\tilde{\mu}_j\})} &= \frac{\frac{\partial}{\partial\tilde{\mu}_i}\bar{n}_j(T,\mu_B,\mu_S;\{\tilde{\mu}_j\})}{s(T,\mu_B,\mu_S;\{\tilde{\mu}_j\})} \\ &\quad - \frac{\bar{n}_j(T,\mu_B,\mu_S;\{\tilde{\mu}_j\})}{s^2(T,\mu_B,\mu_S;\{\tilde{\mu}_j\})}\frac{\partial}{\partial\tilde{\mu}_i}s(T,\mu_B,\mu_S;\{\tilde{\mu}_j\}), \end{aligned} \tag{D.24}$$

where

$$\frac{\partial}{\partial\tilde{\mu}_i}\bar{n}_j(T,\mu_B,\mu_S;\{\tilde{\mu}_j\}) = \frac{\partial}{\partial\tilde{\mu}_i}n_j(T,\mu_B,\mu_S;\tilde{\mu}_j) + \sum_{k=1}^{N_{\rm reso}} d_{k\to j}\frac{\partial}{\partial\tilde{\mu}_i}n_k(T,\mu_B,\mu_S;\tilde{\mu}_k). \tag{D.25}$$

In Eq. (D.24),

$$\frac{\partial}{\partial\tilde{\mu}_i}n_j(T,\mu_B,\mu_S;\tilde{\mu}_j) = \frac{\partial\tilde{\mu}_j}{\partial\tilde{\mu}_i}\frac{\partial}{\partial\tilde{\mu}_j}n_j(T,\mu_B,\mu_S;\tilde{\mu}_j).$$

If particle j is a stable particle,

$$\frac{\partial\tilde{\mu}_j}{\partial\tilde{\mu}_i} = \delta_{ij}.$$

If particle j is a heavy unstable resonance state,

$$\frac{\partial\tilde{\mu}_j}{\partial\tilde{\mu}_i} = d_{j\to i}.$$

So,

$$\frac{\partial}{\partial\tilde{\mu}_i}\bar{n}_j(T,\mu_B,\mu_S;\{\tilde{\mu}_j\}) = \delta_{ij}\frac{\partial}{\partial\tilde{\mu}_j}n_j(T,\mu_B,\mu_S;\tilde{\mu}_j) + \sum_{k=1}^{N_{\rm reso}} d_{k\to j}d_{k\to i}\frac{\partial}{\partial\tilde{\mu}_k}n_k(T,\mu_B,\mu_S;\tilde{\mu}_k). \quad \text{(D.26)}$$

Similarly,

$$\frac{\partial}{\partial\tilde{\mu}_i}s(T,\mu_B,\mu_S;\{\tilde{\mu}_j\}) = \sum_{j=1}^{N_{\rm stable}}\delta_{ij}\frac{\partial}{\partial\tilde{\mu}_j}s_j(T,\mu_B,\mu_S;\tilde{\mu}_j) + \sum_{j=1}^{N_{\rm reso}} d_{j\to i}\frac{\partial}{\partial\tilde{\mu}_j}s_j(T,\mu_B,\mu_S;\tilde{\mu}_j). \quad \text{(D.27)}$$

To compute Eqs. (D.26) and (D.27), we need to evaluate $\frac{\partial}{\partial\tilde{\mu}_j}n_j(T,\mu_B,\mu_S;\tilde{\mu}_j)$ and $\frac{\partial}{\partial\tilde{\mu}_j}s_j(T,\mu_B,\mu_S;\tilde{\mu}_j)$. The derivative for particle number density can be easily computed from Eqs. (D.9),

$$\frac{\partial}{\partial\tilde{\mu}_i}n_i(T,\mu_B,\mu_S;\tilde{\mu}_i) = \frac{g_i}{2\pi^2}m_i\sum_{k=1}^{\infty}(\mp)^{k+1}\lambda^k K_2\left(k\frac{m_i}{T}\right). \quad \text{(D.28)}$$

and for entropy density from particle species i,

$$s_i = \frac{P_i}{T} - \mu_i n_i + \frac{e_i}{T}. \quad \text{(D.29)}$$

So

$$\frac{\partial}{\partial\tilde{\mu}_i}s_i(T,\mu_B,\mu_S;\tilde{\mu}_i) = \frac{\partial}{\partial\tilde{\mu}_i}\left(\frac{P_i}{T} - \mu_i n_i + \frac{e_i}{T}\right). \quad \text{(D.30)}$$

We have,

$$\frac{\partial}{\partial\tilde{\mu}_i}\left(\frac{P_i}{T}\right) = \frac{g_i}{2\pi^2}m_i^2\sum_{k=1}^{\infty}(\mp)^{k+1}\frac{\lambda^k}{k}K_2\left(k\frac{m_i}{T}\right), \quad \text{(D.31)}$$

$$\frac{\partial}{\partial\tilde{\mu}_i}(\mu_i n_i) = n_i + \mu_i\frac{\partial}{\partial\tilde{\mu}_i}n_i(T,\mu_B,\mu_S;\tilde{\mu}_i), \quad \text{(D.32)}$$

and

$$\frac{\partial}{\partial\tilde{\mu}_i}\left(\frac{e_i}{T}\right) = \frac{g_i}{2\pi^2}m_i^4\sum_{k=1}^{\infty}(\mp)^{k+1}k\lambda^k\left(3\frac{K_2\left(k\frac{m_i}{T}\right)}{\left(k\frac{m_i}{T}\right)^2} + \frac{K_1\left(k\frac{m_i}{T}\right)}{\left(k\frac{m_i}{T}\right)}\right). \quad \text{(D.33)}$$

D.4 Some Remark for Coding

The tricky part of this approach is to calculate $d_{j\to i}$ for every species of particles. My approach is to build an array of $d_{j\to i}[i]$ for every species of particles. The array will have length $N_{\rm stable}$.

For stable particle species i, only $d_{i\to i} = 1$ and all other elements are zero. For unstable resonances, $d_{j\to i} = \sum_{k=1}^{N_{\rm ch}} {\rm Br}^k_{j\to i}N^k_{j\to i}$, where k runs over all decay channels of the particle species j, ${\rm Br}^k_{j\to i}$ is the branching ratio for channel k, and $N^k_{j\to i}$ is the number of produced daughter particles who is species i in channel k. In the actual implementation, we go over every decay particle and add the corresponding ${\rm Br}^k_{j\to i}$ together.

Once $d_{j\to i}[i]$ is constructed, we can perform numerical test for particle chemical potentials,

$$\tilde{\mu}_j = \sum_{i=1}^{N_{\rm stable}} d_{j\to i}\mu_i \tag{D.34}$$

and for the particle decay yields,

$$\bar{N}_i = N_i + \sum_{j=1}^{N_{\rm reso}} d_{j\to i}N_j. \tag{D.35}$$

Please note that $d_{j\to i}$ includes both direct and indirect contributions. One easy way to take account for all indirect contributions is to start the calculations from the lightest particles. For heavy resonances, who have indirect decays to final stable particles, (e.g., $k \to j \to i$),

$$d_{k\to i} = \bar{d}_{k\to i} + \sum_j \bar{d}_{k\to j} d_{j\to i}, \tag{D.36}$$

where j runs over all possible intermediate states and $\bar{d}_{k\to i}$ stands for the direct decay.

Appendix E: On multiplicity fluctuations

E.1 Multiplicity in pp collisions

In every p-p collisions, the produced number of charged particles fluctuates. The probability distribution of the charged particle number agree well with negative binomial distribution (NBD) [250], which is defined as,

$$\Pr(n = N) = \left(\begin{array}{c} N + r - 1 \\ N \end{array} \right) (1-p)^r p^N, \tag{E.1}$$

where p and r are parameters to determine the mean and shape of the distribution. The mean of NBD is $\frac{pr}{1-p}$, and the variance is $\frac{pr}{(1-p)^2}$. The continuous generalization of this distribution can be defined as,

$$\Pr(X = x) = \frac{\Gamma(x+r)}{\Gamma(x+1)\Gamma(r)} (1-p)^r p^x. \tag{E.2}$$

In nucleus-nucleus collisions, we can assume that each binary collision as a p-p collision. The actual mount of energy density or entropy density dumped into the medium fluctuates from collision to collision. In the MC Glauber model, one can determine the spatial positions of every binary collisions and the wounded nucleons in each event. One usually assigns a gaussian profile for the dumped energy (or entropy) density in the transverse plane. We here assume that the probability distribution of the net mount of energy (or entropy) density dumped into the medium is the same for binary collision and wounded nucleon.

In the nucleus-nucleus collisions, the number of emitted particles from the kinetic freeze-out surface can be calculated according to the hadron resonance gas model (see Appendix D) in the grand canonical ensemble. The fluctuation of the emitted particles satisfies Poisson distributions for classical Boltzmann particles. So the final measured particle number distribution is a folded result of the initial state fluctuation with the number fluctuation at kinetic freeze-out.

Experimentally, the particle fluctuations in nucleus-nucleus collisions also agree well with the negative binomial distribution. In general, the measured particle distribution is a convoluted result

of the initial and final state fluctuations,

$$\Pr(n=N)=\sum_{k=0}^{\infty} f_{\rm initial}(n=k) f_{\rm fo}(n=N;k), \tag{E.3}$$

The fluctuation at the freeze-out is taken as Poisson distribution with mean equals k.

$$f_{\rm fo}(n=N;k)=\frac{k^N}{N!}e^{-k}. \tag{E.4}$$

if we consider the initial state fluctuation is a continuous distribution in k, then

$$\Pr(n=N)=\int_0^{\infty} dk f_{\rm initial}(X=k) f_{\rm fo}(n=N;k). \tag{E.5}$$

For the initial state fluctuations, since there are more than one collision happening in each nucleus-nucleus collisions, the fluctuation of total produced entropy dS/dy is the sum of multiple individual dS_i/dy in the transverse plane. Negative binomial distribution in Eq. (E.1) has a nice property that the sum of any independent NBD with same value of p is still a NBD with $r=r_1+r_2+\ldots+r_n$. But this property only valid for the discrete version of NBD not the continuous extension in Eq. (E.2). So the continuous the NBD distribution in Eq. (E.2) can not be used for individual entropy density fluctuations in the MC-Glauber model.

Furthermore, we can fold the discrete NBD distribution with Poisson to calculate the final fluctuation of particles and check whether it is a NBD. The left panle Fig.E.1 shows such a simple numerical test, in which the final folded results deviate from a NBD in the tail of the distribution.

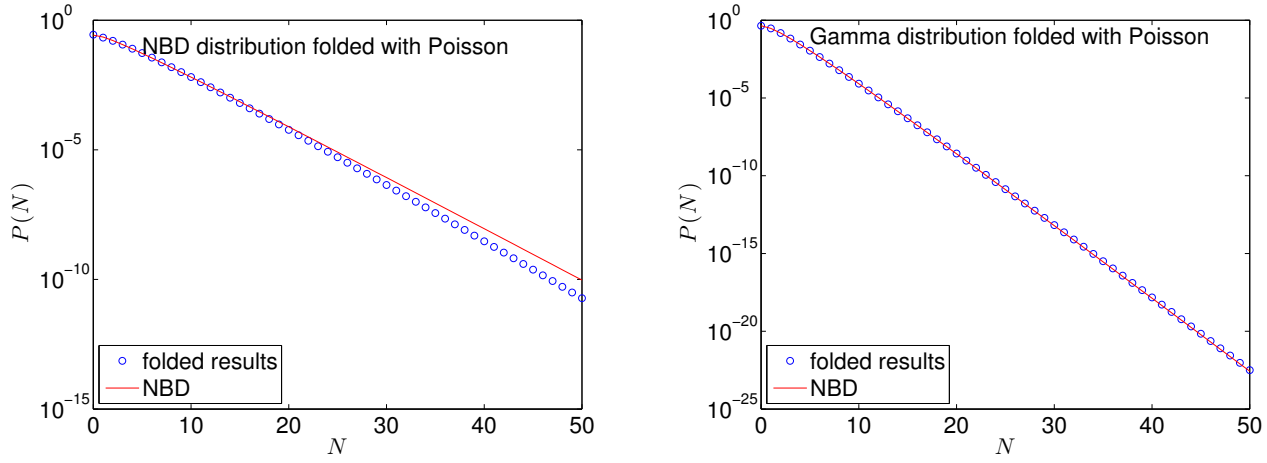

Figure E.1: Left panel: numerical test for a NBD convoluted with a Poisson distribution. Right panel: numerical test for a Gamma distribution convoluted with a Poisson distribution.

In order to reproduce an exact NBD in the final convoluted results, one can choose Gamma distribution for the initial conditions, instead [251].

$$\Pr(X=x)=\frac{\beta^{\alpha}}{\Gamma(\alpha)}x^{\alpha-1}e^{-\beta x}. \tag{E.6}$$

Gamma distribution has two parameters, $\alpha > 0$ is called shape parameter and $\beta > 0$ is called the rate parameter. The mean of Gamma distribution is α/β and variance is α/β^2. Gamma distribution has additive property, namely the sum of any independent Gamma distribution with same β is a Gamma distribution with $\alpha = \alpha_1 + \ldots + \alpha_n$. Since Gamma distribution is defined in a continuous space, it has its advantage for the initial multiplicity fluctuations. In the right panel of Fig. E.1, we show a numerical test of folding a Gamma distribution with a Poisson distribution. It agrees with the NBD fit perfectly.

Above all, we argue that we can use Gamma distribution for each binary collision and wounded nucleon in the initial conditions and Poisson distribution at kinetic freeze out. Such combination can provide us a desired NBD fluctuation for charged particle number in the final state.

We think the Gamma distribution yields a good candidate to implement multiplicity fluctuation in the MC-Glauber model. However, please note that all the arguments made here considered the fluctuations only in the initial states and final kinetic freeze-out. There are other sources of the fluctuations during the fireball evolution. For example, due to different shape of the initial profile, the viscous entropy production during hydrodynamic evolution also fluctuates event-by-event. And there are additional hydrodynamic fluctuation due to the fluctuation-dissipation theorem.

Appendix F: Kinematics for photon production rate phase space integrals

In the appendix, we work out the phase space integrals for evaluating photon production rates from kinetic approach in details.

F.1 $2 \to 2$ scattering processes

In the local rest frame, the production rate of $2 \to 2$ scattering processes are given by,

$$\begin{aligned} E_q \frac{dR}{d^3q} &= \int \frac{d^3p_1}{2E_1(2\pi)^3}\frac{d^3p_2}{2E_2(2\pi)^3}\frac{d^3p_3}{2E_3(2\pi)^3}\frac{2\pi}{2}|\mathcal{M}|^2\delta^{(4)}(p_1+p_2-p_3-q) \\ &\times \; f(E_1)f(E_2)(1\pm f(E_3)) \\ &= \int \frac{d^3p_1}{2E_1(2\pi)^3}\frac{d^3p_2}{2E_2(2\pi)^3}\frac{d^4p_3}{(2\pi)^4}(2\pi)\delta(p_3^2-m_3^2)\frac{2\pi}{2}|\mathcal{M}|^2 \\ &\times \; \delta^{(4)}(p_1+p_2-p_3-q)f(E_1)f(E_2)(1\pm f(E_3)) \\ &= \int \frac{d^3p_1 d^3p_2}{8E_1E_2(2\pi)^8}\delta((p_1+p_2-q)^2-m_3^2)|\mathcal{M}|^2 f(E_1)f(E_2)(1\pm f(E_1+E_2-E_q)) \\ &\times \; \int ds\delta(s-(p_1+p_2)^2)\int dt\delta(t-(p_2-p)^2), \end{aligned}$$

where we use the energy-momentum conservation δ-function to kill the $\int d^4p_3$ and insert the Mandelstam variables, s, t. For $\int d^3p_1$ and $\int d^3p_2$, we have

$$\frac{d^3p}{E} = \frac{p^2}{E}dpd\cos\theta d\phi = pdEd\cos\theta d\phi \tag{F.1}$$

So

$$\begin{aligned} E_q \frac{dR}{d^3p} &= \int \frac{1}{8(2\pi)^8}p_1dE_1d\cos\theta d\phi_1 p_2dE_2d\cos\theta_2 d\phi_2\delta((p_1+p_2-q)^2-m_3^2)|\mathcal{M}|^2 \\ &\times \; \int ds\delta(s-(p_1+p_2)^2)\int dt\delta(t-(p_2-p)^2) \\ &\times \; f(E_1)f(E_2)(1\pm f(E_1+E_2-E_q)) \end{aligned} \tag{F.2}$$

We define the angles of p_1 and p_2 with respect to photon momentum. We have,

$$(p_2-q)^2 = m_2^2 - 2E_2E_q + 2p_2E_q\cos\theta_2 \tag{F.3}$$

$$(p_1+p_2)^2 = m_1^2 + m_2^2 + 2E_1E_2 - 2p_1p_2\cos\theta_{12}, \tag{F.4}$$

where

$$\cos\theta_{12} = \cos\theta_1\cos\theta_2 + \sin\theta_1\sin\theta_2\cos(\phi_2-\phi_1). \tag{F.5}$$

For the remaining three δ functions can be written as,

$$\begin{aligned}\delta((p_1+p_2-q)^2 - m_3^2) &= \delta(s+t-m_2^2-m_3^2-2E_1E_q+2p_1q\cos\theta_1)\\ &= \frac{1}{2p_1E_q}\delta\left(\cos\theta_1 - \frac{-s-t+m_2^2+m_3^2+2E_1E_q}{2p_1E_q}\right)\end{aligned} \tag{F.6}$$

$$\begin{aligned}\delta(t-(p_2-q)^2) &= \delta(t-m_2^2+2E_2E_q-2p_2q\cos\theta_2)\\ &= \frac{1}{2p_2E_q}\delta\left(\cos\theta_2 - \frac{t-m_2^2+2E_2E_q}{2p_2E_q}\right)\end{aligned} \tag{F.7}$$

$$\delta(s-(p_1+p_2)^2) = \delta(s-m_1^2-m_2^2-2E_1E_2+2p_1p_2\cos\theta_{12}) \tag{F.8}$$

We can use Eq. (F.6) and Eq. (F.7) to kill the two θ integrals. Then the rate becomes,

$$\begin{aligned}E_q\frac{dR}{d^3q} &= \frac{1}{32(2\pi)^8E^2}\int ds\,dt\,dE_1\,dE_2\,d\phi_2\,d\phi_2|\mathcal{M}|^2\\ &\times\ f(E_1)f(E_2)(1\mp f(E_1+E_2-E_q))\\ &\times\ \delta(s-m_1^2-m_2^2-2E_1E_2+2p_1p_2\cos\theta_{12})\end{aligned} \tag{F.9}$$

With the last δ function, we kill the $\int d\phi_2$. The δ function has roots for ϕ_2,

$$\phi_{2\pm} = \phi_1 \pm \arccos\left(\frac{-s+m_1^2+m_2^2+2E_1E_2-2p_1p_2\cos\theta_1\cos\theta_2}{2p_1p_2\sin\theta_1\sin\theta_2}\right) \tag{F.10}$$

and the final expression for photon emission rate is,

$$\begin{aligned}E_q\frac{dR}{d^3p} &= \frac{1}{32(2\pi)^8E_q}\int_{s_{\min}}^{\infty}ds\int_{t_{\min}}^{t_{\max}}dt\int_{E_{1\min}}^{\infty}dE_1\int_{E_{2\min}}^{E_{2\max}}dE_2\int_0^{2\pi}d\phi_1\sum_{\phi_2=\phi_{2\pm}}\\ &|\mathcal{M}|^2f(E_1)f(E_2)(1\mp f(E_1+E_2-E_q))\frac{1}{\sqrt{aE_2^2+2bE_2+c}}\end{aligned} \tag{F.11}$$

where

$$a = -(s+t-m_2^2-m_3^2)^2, \tag{F.12}$$

$$\begin{aligned}b &= E_q\left[(s+t-m_2^2-m_3^2)(s-m_1^2-m_2^2)-2m_1^2(m_2^2-t)\right]\\ &+E_1(m_2^2-t)(s+t-m_2^2-m_3^2),\end{aligned} \tag{F.13}$$

$$\begin{aligned}c &= -(t-m_2^2)^2E_1^2\\ &-2E_q\left(2m_2^2(s+t-m_2^2-m_3^2)-(m_2^2-t)(s-m_1^2-m_2^2)\right)E_1\\ &+4E_q^2m_1^2m_2^2+m_2^2(s+t-m_2^2-m_3^2)^2+m_1^2(m_2^2-t)^2\\ &-E_q^2(s-m_1^2-m_2^2)^2+(s-m_1^2-m_2^2)(t-m_2^2)(s+t-m_2^2-m_3^2).\end{aligned} \tag{F.14}$$

For the boundaries of the integrals, $s_{\min} = \mathrm{Max}\{(m_1+m_2)^2, m_3^2\}$. Since $t = (p_2-q)^2 = (p_1-p_3)^2$ is Lorentz invariant, we can find its boundary in the center of mass frame of the reaction $1+2 \to 3+\gamma$,

$$\begin{aligned} t_{\min(\max)} &= m_1^2 + m_3^2 - 2E_1^{\rm CM}E_3^{\rm CM} - (+)2|\vec{p_1}^{\rm CM}||\vec{p_3}^{\rm CM}| \\ &= m_1^2 + m_3^2 - 2\left(\frac{s+m_1^2-m_2^2}{2\sqrt{s}}\right)\left(\frac{s+m_3^2}{2\sqrt{s}}\right) \\ &\quad -(+)2\frac{\sqrt{(s+m_1^2-m_2^2)^2-4sm_1^2}}{2\sqrt{s}}\frac{s-m_3^2}{2\sqrt{s}}. \end{aligned} \tag{F.15}$$

The lower bound for E_1 can be found from,

$$\begin{aligned} u &= (p_1-q)^2 = m_1^2 - 2E_qE_1 + 2|\vec{p_1}|E_q\cos\theta_1 \\ &\to 2E_1E_q \geq m_1^2 - u - 2E_q|\vec{p_1}| \end{aligned} \tag{F.16}$$

which gives

$$E_{1\min} = \frac{E_qm_1^2}{m_1^2-u} + \frac{m_1^2-u}{4E_q}. \tag{F.17}$$

We can derive a similar boundary for E_2 from t,

$$E_2 \geq \frac{E_qm_2^2}{m_2^2-t} + \frac{m_2^2-t}{4E_q} \tag{F.18}$$

Furthermore, the function under the square root in Eq. (F.11) has to be positive, giving ($a<0$)

$$\frac{-b+\sqrt{b^2-ac}}{a} < E_2 < \frac{-b-\sqrt{b^2-ac}}{a} \tag{F.19}$$

F.2 $1 \to 3$ decay processes

The production rate of $1 \to 3$ decay processes can be calculated as follows,

$$\begin{aligned} E_q\frac{dR}{d^3q} &= \int \frac{d^3p_1}{2E_1(2\pi)^3}\frac{d^3p_2}{2E_2(2\pi)^3}\frac{d^3p_3}{2E_3(2\pi)^3}\frac{2\pi}{2}|\mathcal{M}|^2\delta^{(4)}(p_1-p_2-p_3-q) \\ &\quad \times f(E_1)(1\pm f(E_2))(1\pm f(E_3)) \\ &= \int \frac{d^3p_1}{2E_1(2\pi)^3}\frac{d^3p_2}{2E_2(2\pi)^3}\frac{d^4p_3}{(2\pi)^4}(2\pi)\delta(p_3^2-m_3^2)\frac{2\pi}{2}|\mathcal{M}|^2 \\ &\quad \times\delta^{(4)}(p_1-p_2-p_3-q)f(E_1)(1\pm f(E_2))(1\pm f(E_3)) \\ &= \int \frac{d^3p_1d^3p_2}{8E_1E_2(2\pi)^8}\delta((p_1-p_2-q)^2-m_3^2)|\mathcal{M}|^2 \\ &\quad \times f(E_1)(1\pm f(E_2))(1\pm f(E_1-E_2-E_q)) \\ &\quad \times \int ds'\delta(s'-(p_1-p_2)^2)\int dt'\delta(t'-(p_2+p)^2), \end{aligned} \tag{F.20}$$

where s and t are the analgous variables as standard Manderstan variables defined in 2 to 2 scattering processes. For the remaining three δ functions can be written as,

$$\begin{aligned}\delta((p_1-p_2-q)^2-m_3^2) &= \delta(s'+t'-m_2^2-m_3^2-2E_1E_q+2p_1q\cos\theta_1)\\ &= \frac{1}{2p_1E_q}\delta\left(\cos\theta_1-\frac{-s'-t'+m_2^2+m_3^2+2E_1E_q}{2p_1E_q}\right)\end{aligned} \tag{F.21}$$

$$\begin{aligned}\delta(t'-(p_2+q)^2) &= \delta(t'-m_2^2-2E_2E_q+2p_2q\cos\theta_2)\\ &= \frac{1}{2p_2E_q}\delta\left(\cos\theta_2+\frac{t'-m_2^2-2E_2E_q}{2p_2E_q}\right)\end{aligned} \tag{F.22}$$

$$\delta(s'-(p_1-p_2)^2)=\delta(s'-m_1^2-m_2^2+2E_1E_2-2p_1p_2\cos\theta_{12}) \tag{F.23}$$

With the last δ function, we kill the $\int d\phi_2$. The δ function has roots for ϕ_2,

$$\phi_{2\pm}=\phi_1\pm\arccos\left(\frac{s'-m_1^2-m_2^2+2E_1E_2-2p_1p_2\cos\theta_1\cos\theta_2}{2p_1p_2\sin\theta_1\sin\theta_2}\right) \tag{F.24}$$

$$\begin{aligned}E_q\frac{dR}{d^3p} &= \frac{1}{32(2\pi)^8E_q}\int_{s'_{\min}}^{s'_{\max}}ds'\int_{t'_{\min}}^{t'_{\max}}dt'\int_{E_{1\min}}^{\infty}dE_1\int_{E_{2\min}}^{E_{2\max}}dE_2\int_0^{2\pi}d\phi_1\sum_{\phi_2=\phi_{2\pm}}\\ &\quad |\mathcal{M}|^2f(E_1)f(E_2)(1\pm f(E_1+E_2-E_q))\frac{1}{\sqrt{a'E_2^2+2b'E_2+c'}}\end{aligned} \tag{F.25}$$

where

$$a' = -(s'+t'-m_2^2-m_3^2)^2, \tag{F.26}$$

$$\begin{aligned}b' &= -E_q\left[(s'+t'-m_2^2-m_3^2)(s'-m_1^2-m_2^2)-2m_1^2(m_2^2-t')\right]\\ &\quad -E_1(m_2^2-t')(s'+t'-m_2^2-m_3^2),\end{aligned} \tag{F.27}$$

$$\begin{aligned}c' &= -(t'-m_2^2)^2E_1^2\\ &\quad -2E_q\left(2m_2^2(s'+t'-m_2^2-m_3^2)-(m_2^2-t')(s'-m_1^2-m_2^2)\right)E_1\\ &\quad +4E_q^2m_1^2m_2^2+m_2^2(s'+t'-m_2^2-m_3^2)^2+m_1^2(m_2^2-t')^2\\ &\quad -E_q^2(s'-m_1^2-m_2^2)^2+(s'-m_1^2-m_2^2)(t'-m_2^2)(s'+t'-m_2^2-m_3^2).\end{aligned} \tag{F.28}$$

For the boundaries of the integrals, $s'_{\min}=m_3^2$ and $s'_{\max}=(m_1-m_2)^2$. For t, in order to perform the same trick as we did in $2\to2$ process, we go to a frame that $\vec{p_1}=\vec{p_2}$ and $\vec{p}_3=-\vec{q}$,

$$\begin{aligned}t'_{\min(\max)} &= m_1^2+m_3^2-2E_1E_3-(+)2|\vec{p_1}||\vec{p_3}|\cos(\theta_{13})\\ &= m_1^2+m_3^2-2\left(\frac{s'+m_1^2-m_2^2}{2\sqrt{s'}}\right)\left(\frac{s'+m_3^2}{2\sqrt{s'}}\right)\\ &\quad -(+)2\frac{\sqrt{(s'+m_1^2-m_2^2)^2-4s'm_1^2}}{2\sqrt{s'}}\frac{s'-m_3^2}{2\sqrt{s'}}.\end{aligned} \tag{F.29}$$

The lower bound for E_1 can be found from,

$$\begin{aligned} u' &= (p_1 - q)^2 = m_1^2 - 2E_q E_1 + 2|\vec{p_1}|E_q \cos\theta_1 \\ &\rightarrow 2E_1 E_q \geq m_1^2 - u' - 2E_q|\vec{p_1}| \end{aligned} \tag{F.30}$$

which gives

$$E_{1\min} = \frac{E_q m_1^2}{m_1^2 - u'} + \frac{m_1^2 - u'}{4E_q}. \tag{F.31}$$

We can derive a similar boundary for E_2 from t,

$$E_2 \geq \frac{E_q m_2^2}{t' - m_2^2} + \frac{t' - m_2^2}{4E_q} \tag{F.32}$$

Furthermore, the function under the square root in Eq. (F.25) has to be positive, giving ($a' < 0$)

$$\frac{-b' + \sqrt{b'^2 - a'c'}}{a'} < E_2 < \frac{-b' - \sqrt{b'^2 - a'c'}}{a'} \tag{F.33}$$

Appendix G: Centrality cuts in relativistic heavy-ion collisions

In relativistic heavy-ion collisions, centrality is introduced to categorize the geometric structure of the collisions. Experimentally, since it is impossible to accurately measure the impact parameter for each collision, the centrality of a single collision event is defined by its relative position in the entire event array sorted according to the measured charged multiplicity. In the theoretical simulations, we would like to determine the centrality of the simulating event as close as possible to the experimental procedure. In order to save numerical cost, we choose to cut centrality according to the initial total entropy density at the mid-rapidity, $dS/dy|_{y=0}$, i.e. we assume that the initial entropy density is monotonically related with the final charged multiplicity. The additional viscous entropy production during the hydrodynamic evolution has minor effect on changing the ordering of the collision events as a function of the final charged multiplicity (see Fig. 2.7).

In the following tables (ordered descending in collision energy), we list the centrality cut parameters used in `superMC` for simulating relativistic heavy-ion collisions at different the collision energies from RHIC to LHC with the MC-Glauber and the MCKLN models. We also listed the averaged collision parameters for each centrality.

For both initial condition models, we use Gaussian shape nucleon with width determined by the inelastic nucleon-nucleon cross section at the given colliding energy. The minimum distance between two individual nucleons inside one nucleus is $r_{\min} = 0.9$ fm which gives a good approximation for the hard core repulsion effect from a realistic nucleon-nucleon potential [252]. The actual values of dS/dy in the tables represent for the uncorrected transverse entropy per unit of rapidity, $\kappa = 1$ in Eq. (2.10).

centrality (%)	N_{min}	N_{max}	dS/dy_{min}	dS/dy_{max}	b_{min} (fm)	b_{max} (fm)
0-0.2	373	416	434.66	491.89	0.05	3.17
0-1	339	416	408.07	491.89	0.02	3.91
0-5	296	416	346.22	491.89	0.01	4.99
5-10	249	409	285.45	346.22	0.76	6.22
10-20	174	365	194.05	285.45	3.24	8.05
20-30	119	285	129.39	194.04	5.58	9.61
30-40	74	206	83.01	129.38	6.91	11.11
40-50	43	152	50.33	83.01	8.33	12.65
50-60	19	107	28.35	50.33	9.35	13.80
60-70	3	73	14.45	28.35	10.41	15.49
70-80	2	53	6.36	14.45	10.98	17.87

Table G.1: Centrality cut table for Pb + Pb collisions at $\sqrt{s} = 5.5$ A TeV with the MC-Glauber model.

centrality (%)	$\langle N_{\mathrm{part}} \rangle$	$\langle b \rangle$ (fm)	$\langle dS/dy \rangle$	$\langle N_{\mathrm{coll}} \rangle$
0-0.2	406.17 ± 0.14	1.13 ± 0.01	445.96 ± 0.23	2004.42 ± 1.83
0-1	402.63 ± 0.09	1.41 ± 0.01	424.50 ± 0.13	1948.96 ± 0.95
0-5	384.71 ± 0.09	2.34 ± 0.00	384.92 ± 0.12	1784.27 ± 0.69
5-10	333.61 ± 0.10	4.14 ± 0.00	314.68 ± 0.08	1418.69 ± 0.60
10-20	265.60 ± 0.09	5.87 ± 0.00	237.04 ± 0.08	1016.84 ± 0.49
20-30	192.81 ± 0.07	7.61 ± 0.00	159.96 ± 0.06	636.35 ± 0.35
30-40	136.33 ± 0.06	9.01 ± 0.00	104.90 ± 0.04	381.16 ± 0.24
40-50	92.47 ± 0.05	10.23 ± 0.00	65.70 ± 0.03	213.45 ± 0.16
50-60	58.92 ± 0.04	11.33 ± 0.00	38.58 ± 0.02	108.72 ± 0.10
60-70	34.57 ± 0.03	12.33 ± 0.00	20.85 ± 0.01	49.74 ± 0.06
70-80	17.89 ± 0.02	13.27 ± 0.00	10.01 ± 0.01	19.84 ± 0.03

Table G.2: The averaged collision parameters for each centrality in Pb + Pb collisions at $\sqrt{s} = 5.5$ A TeV with the MC-Glauber model.

centrality (%)	$N_{\rm min}$	$N_{\rm max}$	$dS/dy_{\rm min}$	$dS/dy_{\rm max}$	$b_{\rm min}$ (fm)	$b_{\rm max}$ (fm)
0-0.2	402	416	2265.50	2386.12	0.02	1.41
0-1	390	416	2172.28	2386.12	0.02	1.98
0-5	334	416	1815.15	2386.12	0.02	3.73
5-10	288	381	1478.88	1815.13	2.95	5.16
10-20	201	340	999.19	1478.88	4.24	7.35
20-30	138	260	666.11	999.18	6.28	9.03
30-40	95	192	426.42	666.10	7.59	10.63
40-50	60	136	257.44	426.42	8.65	11.90
50-60	32	96	142.70	257.43	9.74	13.06
60-70	17	60	70.53	142.70	10.33	14.39
70-80	7	35	29.54	70.53	11.18	16.00

Table G.3: Centrality cut table for Pb + Pb collisions at $\sqrt{s} = 5.5$ A TeV with the MCKLN model.

centrality (%)	$\langle N_{\rm part} \rangle$	$\langle b \rangle$ (fm)	$\langle dS/dy \rangle$	$\langle N_{\rm coll} \rangle$
0-0.2	411.38 ± 0.05	0.60 ± 0.01	2286.40 ± 0.36	2044.31 ± 1.39
0-1	407.74 ± 0.04	1.04 ± 0.00	2230.47 ± 0.37	1980.79 ± 0.69
0-5	387.07 ± 0.07	2.27 ± 0.00	2033.77 ± 0.61	1796.78 ± 0.62
5-10	333.92 ± 0.07	4.15 ± 0.00	1639.18 ± 0.43	1419.71 ± 0.47
10-20	265.52 ± 0.08	5.87 ± 0.00	1223.73 ± 0.43	1015.95 ± 0.44
20-30	192.52 ± 0.06	7.61 ± 0.00	822.99 ± 0.30	634.66 ± 0.30
30-40	136.08 ± 0.05	9.02 ± 0.00	539.26 ± 0.22	379.64 ± 0.20
40-50	92.40 ± 0.04	10.23 ± 0.00	336.89 ± 0.15	212.46 ± 0.13
50-60	59.08 ± 0.03	11.31 ± 0.00	196.13 ± 0.10	108.38 ± 0.08
60-70	34.63 ± 0.02	12.31 ± 0.00	103.53 ± 0.07	49.08 ± 0.04
70-80	17.88 ± 0.01	13.25 ± 0.00	47.78 ± 0.04	19.28 ± 0.02

Table G.4: The averaged collision parameters for each centrality in Pb+Pb collisions at $\sqrt{s} = 5.5$ A TeV with the MCKLN model.

centrality (%)	$N_{\rm min}$	$N_{\rm max}$	$dS/dy_{\rm min}$	$dS/dy_{\rm max}$	$b_{\rm min}$ (fm)	$b_{\rm max}$ (fm)
0-0.2	360	416	411.31	473.64	0.06	3.01
0-1	351	416	386.06	473.64	0.01	3.46
0-5	301	416	327.03	473.64	0.01	4.79
5-10	249	406	269.65	327.03	1.22	6.23
10-20	167	369	183.93	269.65	3.20	8.47
20-30	118	278	123.15	183.93	5.43	9.76
30-40	74	214	79.55	123.15	6.81	11.24
40-50	41	153	48.73	79.55	8.22	12.54
50-60	21	114	27.67	48.73	9.40	13.56
60-70	6	77	14.14	27.67	9.96	15.27
70-80	2	50	6.26	14.14	10.90	17.27

Table G.5: Centrality cut table for Pb + Pb collisions at $\sqrt{s} = 2.76$ A TeV with the MC-Glauber model.

centrality (%)	$\langle N_{\rm part} \rangle$	$\langle b \rangle$ (fm)	$\langle dS/dy \rangle$	$\langle N_{\rm coll} \rangle$
0-0.2	404.60 ± 0.16	1.14 ± 0.01	422.24 ± 0.22	1806.24 ± 1.73
0-1	400.87 ± 0.10	1.41 ± 0.01	401.62 ± 0.13	1762.10 ± 0.87
0-5	382.24 ± 0.09	2.33 ± 0.00	363.87 ± 0.11	1615.13 ± 0.63
5-10	329.88 ± 0.10	4.13 ± 0.00	297.27 ± 0.07	1285.77 ± 0.55
10-20	261.57 ± 0.09	5.85 ± 0.00	224.12 ± 0.08	921.63 ± 0.45
20-30	189.32 ± 0.07	7.58 ± 0.00	151.72 ± 0.06	578.95 ± 0.31
30-40	133.85 ± 0.06	8.97 ± 0.00	100.11 ± 0.04	349.92 ± 0.22
40-50	90.85 ± 0.05	10.17 ± 0.00	63.21 ± 0.03	197.88 ± 0.15
50-60	58.10 ± 0.04	11.25 ± 0.00	37.49 ± 0.02	102.56 ± 0.10
60-70	34.04 ± 0.03	12.25 ± 0.00	20.36 ± 0.01	47.37 ± 0.06
70-80	17.65 ± 0.02	13.19 ± 0.00	9.81 ± 0.01	19.12 ± 0.03

Table G.6: The averaged collision parameters for each centrality in Pb + Pb collisions at $\sqrt{s} = 2.76$ A TeV with the MC-Glauber model.

centrality (%)	$N_{\rm min}$	$N_{\rm max}$	$dS/dy_{\rm min}$	$dS/dy_{\rm max}$	$b_{\rm min}$ (fm)	$b_{\rm max}$ (fm)
0-0.2	400	416	2005.56	2095.40	0.01	1.37
0-1	388	416	1922.31	2095.40	0.01	1.99
0-5	336	416	1608.28	2095.40	0.01	3.70
5-10	284	383	1311.87	1608.26	2.89	5.21
10-20	200	333	889.53	1311.87	4.36	7.26
20-30	138	256	593.51	889.53	6.24	9.05
30-40	94	185	381.45	593.50	7.60	10.49
40-50	60	135	231.38	381.45	8.71	11.90
50-60	34	95	128.55	231.38	9.60	13.11
60-70	18	60	63.73	128.55	10.38	14.21
70-80	7	37	26.88	63.73	11.08	15.67

Table G.7: Centrality cut table for Pb + Pb collisions at $\sqrt{s} = 2.76$ A TeV with the MCKLN model.

centrality (%)	$\langle N_{\rm part} \rangle$	$\langle b \rangle$ (fm)	$\langle dS/dy \rangle$	$\langle N_{\rm coll} \rangle$
0-0.2	410.29 ± 0.06	0.60 ± 0.01	2025.29 ± 0.34	1852.21 ± 1.22
0-1	406.37 ± 0.04	1.04 ± 0.00	1974.49 ± 0.34	1795.07 ± 0.63
0-5	384.73 ± 0.07	2.25 ± 0.00	1800.59 ± 0.53	1627.77 ± 0.56
5-10	330.71 ± 0.07	4.12 ± 0.00	1453.52 ± 0.38	1289.99 ± 0.43
10-20	262.55 ± 0.08	5.83 ± 0.00	1087.14 ± 0.38	926.32 ± 0.40
20-30	190.11 ± 0.06	7.56 ± 0.00	733.51 ± 0.27	582.65 ± 0.27
30-40	134.19 ± 0.05	8.96 ± 0.00	481.73 ± 0.19	350.77 ± 0.18
40-50	90.94 ± 0.04	10.17 ± 0.00	301.84 ± 0.14	197.79 ± 0.12
50-60	58.16 ± 0.03	11.24 ± 0.00	176.47 ± 0.09	101.90 ± 0.07
60-70	34.05 ± 0.02	12.24 ± 0.00	93.42 ± 0.06	46.61 ± 0.04
70-80	17.62 ± 0.01	13.17 ± 0.00	43.42 ± 0.03	18.56 ± 0.02

Table G.8: The averaged collision parameters for each centrality in Pb+Pb collisions at $\sqrt{s} = 2.76$ A TeV with the MCKLN model.

centrality (%)	N_{min}	N_{max}	dS/dy_{min}	dS/dy_{max}	b_{min} (fm)	b_{max} (fm)
0-0.2	337	394	347.31	408.78	0.03	2.97
0-1	314	394	324.42	408.78	0.03	3.66
0-5	266	394	274.00	408.78	0.03	4.73
5-10	221	380	226.48	274.00	1.15	6.09
10-20	149	343	155.01	226.48	2.77	7.79
20-30	103	250	104.67	155.00	5.23	9.52
30-40	57	191	68.13	104.67	6.64	10.63
40-50	37	137	42.15	68.13	7.77	11.84
50-60	18	102	24.13	42.15	8.81	13.48
60-70	3	67	12.48	24.13	9.71	15.04
70-80	2	44	5.59	12.48	10.29	16.85

Table G.9: Centrality cut table for Au + Au collisions at $\sqrt{s} = 200$ A GeV with the MC-Glauber model.

centrality (%)	$\langle N_{\mathrm{part}} \rangle$	$\langle b \rangle$ (fm)	$\langle dS/dy \rangle$	$\langle N_{\mathrm{coll}} \rangle$
0-0.2	376.76 ± 0.18	1.12 ± 0.01	357.05 ± 0.20	1188.72 ± 1.18
0-1	372.45 ± 0.11	1.38 ± 0.01	338.52 ± 0.12	1158.62 ± 0.60
0-5	352.91 ± 0.09	2.24 ± 0.00	305.46 ± 0.10	1064.18 ± 0.42
5-10	301.87 ± 0.10	3.93 ± 0.00	249.36 ± 0.06	852.85 ± 0.37
10-20	237.63 ± 0.09	5.58 ± 0.00	188.52 ± 0.06	616.88 ± 0.30
20-30	171.04 ± 0.07	7.22 ± 0.00	128.51 ± 0.05	393.57 ± 0.21
30-40	120.30 ± 0.05	8.54 ± 0.00	85.42 ± 0.03	242.21 ± 0.15
40-50	81.36 ± 0.04	9.69 ± 0.00	54.41 ± 0.02	140.49 ± 0.11
50-60	51.81 ± 0.03	10.72 ± 0.00	32.55 ± 0.02	75.06 ± 0.07
60-70	30.31 ± 0.03	11.67 ± 0.00	17.82 ± 0.01	36.04 ± 0.04
70-80	15.79 ± 0.02	12.58 ± 0.00	8.69 ± 0.01	15.30 ± 0.02

Table G.10: The averaged collision parameters for each centrality in Au + Au collisions at $\sqrt{s} =$ 200 A GeV with the MC-Glauber model.

centrality (%)	N_{min}	N_{max}	dS/dy_{min}	dS/dy_{max}	b_{min} (fm)	b_{max} (fm)
0-0.2	373	394	1069.02	1123.70	0.02	1.41
0-1	362	394	1024.34	1123.70	0.01	2.02
0-5	309	394	859.67	1123.70	0.01	3.64
5-10	261	348	705.69	859.67	2.62	5.00
10-20	182	305	483.84	705.68	4.13	7.08
20-30	127	231	327.26	483.83	5.86	8.63
30-40	87	165	213.66	327.26	7.21	10.13
40-50	54	119	132.21	213.65	8.09	11.22
50-60	31	82	75.31	132.21	9.07	12.60
60-70	16	56	38.36	75.31	9.89	13.79
70-80	7	30	16.81	38.36	10.60	15.20

Table G.11: Centrality cut table for Au + Au collisions at $\sqrt{s} = 200$ A GeV with the MCKLN model.

centrality (%)	$\langle N_{\rm part} \rangle$	$\langle b \rangle$ (fm)	$\langle dS/dy \rangle$	$\langle N_{\rm coll} \rangle$
0-0.2	383.95 ± 0.07	0.61 ± 0.01	1080.30 ± 0.20	1218.38 ± 0.91
0-1	378.84 ± 0.05	1.00 ± 0.00	1052.19 ± 0.18	1181.54 ± 0.44
0-5	355.63 ± 0.08	2.15 ± 0.00	960.52 ± 0.28	1072.96 ± 0.37
5-10	302.26 ± 0.07	3.93 ± 0.00	778.92 ± 0.20	854.41 ± 0.28
10-20	238.53 ± 0.07	5.56 ± 0.00	587.71 ± 0.20	620.13 ± 0.26
20-30	171.72 ± 0.06	7.20 ± 0.00	401.23 ± 0.14	395.72 ± 0.18
30-40	120.62 ± 0.04	8.53 ± 0.00	267.29 ± 0.10	242.74 ± 0.12
40-50	81.45 ± 0.03	9.68 ± 0.00	170.53 ± 0.07	140.36 ± 0.08
50-60	51.86 ± 0.03	10.71 ± 0.00	101.90 ± 0.05	74.66 ± 0.05
60-70	30.27 ± 0.02	11.66 ± 0.00	55.35 ± 0.03	35.52 ± 0.03
70-80	15.71 ± 0.01	12.55 ± 0.00	26.53 ± 0.02	14.86 ± 0.01

Table G.12: The averaged collision parameters for each centrality in Au+Au collisions at $\sqrt{s} = 200$ A GeV with the MCKLN model.

centrality (%)	$N_{\rm min}$	$N_{\rm max}$	$dS/dy_{\rm min}$	$dS/dy_{\rm max}$	$b_{\rm min}$ (fm)	$b_{\rm max}$ (fm)
0-0.2	93	126	95.11	124.28	0.01	3.06
0-1	81	126	85.87	124.28	0.01	3.80
0-5	65	126	71.19	124.28	0.01	4.39
5-10	52	124	59.82	71.19	0.03	5.33
10-20	35	121	42.27	59.82	0.12	7.11
20-30	22	107	29.44	42.27	2.17	8.26
30-40	11	78	19.96	29.44	3.68	9.34
40-50	6	66	13.05	19.96	4.55	10.15
50-60	2	45	8.13	13.05	5.23	12.38
60-70	2	39	4.79	8.13	5.67	12.63
70-80	2	25	2.58	4.79	6.10	13.51

Table G.13: Centrality cut table for Cu + Cu collisions at $\sqrt{s} = 200$ A GeV with the MC-Glauber model.

centrality (%)	$\langle N_{\rm part} \rangle$	$\langle b \rangle$ (fm)	$\langle dS/dy \rangle$	$\langle N_{\rm coll} \rangle$
0-0.2	114.47 ± 0.11	1.11 ± 0.01	99.52 ± 0.09	233.81 ± 0.48
0-1	112.66 ± 0.06	1.28 ± 0.01	91.56 ± 0.05	225.15 ± 0.22
0-5	107.32 ± 0.04	1.75 ± 0.00	80.23 ± 0.03	207.55 ± 0.12
5-10	94.86 ± 0.05	2.71 ± 0.00	65.29 ± 0.01	172.52 ± 0.12
10-20	76.26 ± 0.04	3.87 ± 0.00	50.59 ± 0.02	127.67 ± 0.09
20-30	55.79 ± 0.03	5.03 ± 0.00	35.52 ± 0.01	83.17 ± 0.06
30-40	40.06 ± 0.03	5.97 ± 0.00	24.46 ± 0.01	52.93 ± 0.05
40-50	27.88 ± 0.02	6.78 ± 0.00	16.32 ± 0.01	32.51 ± 0.04
50-60	18.56 ± 0.02	7.53 ± 0.00	10.45 ± 0.00	19.03 ± 0.02
60-70	11.81 ± 0.01	8.21 ± 0.00	6.35 ± 0.00	10.66 ± 0.02
70-80	7.19 ± 0.01	8.85 ± 0.00	3.61 ± 0.00	5.73 ± 0.01

Table G.14: The averaged collision parameters for each centrality in Cu + Cu collisions at $\sqrt{s} =$ 200 A GeV with the MC-Glauber model.

centrality (%)	$N_{\rm min}$	$N_{\rm max}$	$dS/dy_{\rm min}$	$dS/dy_{\rm max}$	$b_{\rm min}$ (fm)	$b_{\rm max}$ (fm)
0-0.2	112	126	300.75	328.59	0.02	1.48
0-1	108	126	285.50	328.59	0.00	1.92
0-5	94	126	243.82	328.59	0.00	3.00
5-10	78	115	202.91	243.82	0.50	3.78
10-20	57	103	141.84	202.91	2.30	5.34
20-30	39	77	98.18	141.84	3.66	6.72
30-40	26	59	65.99	98.18	4.39	7.74
40-50	17	43	42.81	65.99	5.20	8.89
50-60	11	31	26.35	42.81	5.76	9.67
60-70	6	24	15.25	26.35	6.02	10.80
70-80	4	14	8.17	15.25	6.45	12.30

Table G.15: Centrality cut table for Cu + Cu collisions at $\sqrt{s} = 200$ A GeV with the MCKLN model.

centrality (%)	$\langle N_{\rm part} \rangle$	$\langle b \rangle$ (fm)	$\langle dS/dy \rangle$	$\langle N_{\rm coll} \rangle$
0-0.2	119.59 ± 0.05	0.60 ± 0.01	306.20 ± 0.10	248.97 ± 0.36
0-1	117.07 ± 0.03	0.82 ± 0.00	294.82 ± 0.07	237.42 ± 0.17
0-5	110.21 ± 0.02	1.52 ± 0.00	269.83 ± 0.07	214.32 ± 0.09
5-10	95.09 ± 0.02	2.74 ± 0.00	222.65 ± 0.05	172.78 ± 0.07
10-20	76.14 ± 0.02	3.88 ± 0.00	170.59 ± 0.06	127.13 ± 0.06
20-30	55.85 ± 0.02	5.03 ± 0.00	118.92 ± 0.04	83.06 ± 0.04
30-40	40.06 ± 0.02	5.96 ± 0.00	81.25 ± 0.03	52.57 ± 0.03
40-50	27.81 ± 0.01	6.77 ± 0.00	53.77 ± 0.02	32.05 ± 0.02
50-60	18.54 ± 0.01	7.50 ± 0.00	34.07 ± 0.02	18.64 ± 0.01
60-70	11.74 ± 0.01	8.17 ± 0.00	20.43 ± 0.01	10.29 ± 0.01
70-80	6.95 ± 0.00	8.81 ± 0.00	11.42 ± 0.01	5.32 ± 0.00

Table G.16: The averaged collision parameters for each centrality in Cu+Cu collisions at $\sqrt{s} = 200$ A GeV with the MCKLN model.

centrality (%)	$N_{\rm min}$	$N_{\rm max}$	$dS/dy_{\rm min}$	$dS/dy_{\rm max}$	$b_{\rm min}$ (fm)	$b_{\rm max}$ (fm)
0-0.2	383	476	426.95	510.22	0.03	3.39
0-1	381	476	397.10	510.22	0.03	3.74
0-5	306	476	335.57	510.22	0.03	5.25
5-10	258	448	278.08	335.57	0.50	6.44
10-20	186	402	191.53	278.08	2.96	8.84
20-30	126	302	129.53	191.53	5.31	10.85
30-40	81	225	84.72	129.53	6.92	12.26
40-50	47	173	52.39	84.72	7.99	13.85
50-60	21	122	29.93	52.39	8.90	15.42
60-70	6	77	15.32	29.93	9.90	16.54
70-80	2	54	6.72	15.32	10.76	18.70

Table G.17: Centrality cut table for U + U collisions at $\sqrt{s} = 193$ A GeV with the MC-Glauber model .

centrality (%)	$\langle N_{\rm part} \rangle$	$\langle b \rangle$ (fm)	$\langle dS/dy \rangle$	$\langle N_{\rm coll} \rangle$
0-0.2	452.79 ± 0.23	1.21 ± 0.01	439.83 ± 0.26	1567.38 ± 2.20
0-1	445.51 ± 0.14	1.51 ± 0.01	415.36 ± 0.15	1487.49 ± 0.99
0-5	421.58 ± 0.11	2.40 ± 0.00	373.94 ± 0.12	1341.55 ± 0.57
5-10	361.24 ± 0.11	4.20 ± 0.00	305.80 ± 0.07	1074.10 ± 0.45
10-20	285.30 ± 0.10	5.97 ± 0.00	232.33 ± 0.08	783.60 ± 0.36
20-30	205.74 ± 0.08	7.74 ± 0.00	158.86 ± 0.06	504.06 ± 0.26
30-40	145.09 ± 0.06	9.16 ± 0.00	105.93 ± 0.04	312.75 ± 0.19
40-50	98.32 ± 0.05	10.39 ± 0.00	67.62 ± 0.03	182.85 ± 0.13
50-60	62.63 ± 0.04	11.51 ± 0.00	40.41 ± 0.02	97.93 ± 0.09
60-70	36.66 ± 0.03	12.51 ± 0.00	22.05 ± 0.01	46.98 ± 0.05
70-80	18.94 ± 0.02	13.45 ± 0.00	10.60 ± 0.01	19.49 ± 0.03

Table G.18: The averaged collision parameters for each centrality in U + U collisions at $\sqrt{s} = 193$ A GeV with the MC-Glauber model.

centrality (%)	$N_{\rm min}$	$N_{\rm max}$	$dS/dy_{\rm min}$	$dS/dy_{\rm max}$	$b_{\rm min}$ (fm)	$b_{\rm max}$ (fm)
0-0.2	447	476	1272.33	1372.28	0.03	1.72
0-1	429	476	1212.92	1372.28	0.02	2.47
0-5	372	476	1022.73	1372.28	0.02	4.30
5-10	308	419	842.39	1022.72	2.58	5.83
10-20	222	361	580.33	842.39	4.11	8.24
20-30	153	276	394.42	580.33	5.95	10.18
30-40	103	199	259.03	394.42	7.27	11.95
40-50	64	141	160.63	259.02	8.29	13.50
50-60	38	98	92.16	160.63	9.15	14.77
60-70	20	62	46.84	92.16	9.88	16.04
70-80	8	37	20.04	46.84	10.58	17.40

Table G.19: Centrality cut table for U + U collisions at $\sqrt{s} = 193$ A GeV with the MCKLN model .

centrality (%)	$\langle N_{\rm part} \rangle$	$\langle b \rangle$ (fm)	$\langle dS/dy \rangle$	$\langle N_{\rm coll} \rangle$
0-0.2	461.28 ± 0.10	0.77 ± 0.01	1291.55 ± 0.35	1583.56 ± 1.98
0-1	453.08 ± 0.07	1.14 ± 0.00	1249.70 ± 0.27	1497.41 ± 0.89
0-5	424.39 ± 0.09	2.32 ± 0.00	1140.10 ± 0.33	1345.88 ± 0.54
5-10	361.09 ± 0.08	4.22 ± 0.00	928.99 ± 0.23	1075.08 ± 0.39
10-20	285.13 ± 0.09	5.97 ± 0.00	703.00 ± 0.24	783.81 ± 0.34
20-30	205.80 ± 0.07	7.74 ± 0.00	482.52 ± 0.17	504.55 ± 0.23
30-40	144.97 ± 0.05	9.16 ± 0.00	323.34 ± 0.12	312.55 ± 0.16
40-50	98.04 ± 0.04	10.40 ± 0.00	207.05 ± 0.09	181.94 ± 0.11
50-60	62.53 ± 0.03	11.50 ± 0.00	124.10 ± 0.06	97.34 ± 0.07
60-70	36.70 ± 0.02	12.49 ± 0.00	67.80 ± 0.04	46.55 ± 0.04
70-80	18.87 ± 0.01	13.43 ± 0.00	32.04 ± 0.02	19.02 ± 0.02

Table G.20: The averaged collision parameters for each centrality in U + U collisions at $\sqrt{s} = 193$ A GeV with the MCKLN model.

centrality (%)	N_{min}	N_{max}	dS/dy_{min}	dS/dy_{max}	b_{min} (fm)	b_{max} (fm)
0-0.2	322	394	322.23	373.87	0.04	3.49
0-1	299	394	300.41	373.87	0.01	3.82
0-5	245	394	253.60	373.87	0.00	5.05
5-10	209	380	210.30	253.60	0.44	6.05
10-20	145	339	145.11	210.30	2.62	7.92
20-30	96	250	98.23	145.10	5.02	9.35
30-40	61	192	64.38	98.23	6.47	10.55
40-50	32	140	39.80	64.38	7.64	11.92
50-60	9	102	22.93	39.80	8.54	13.45
60-70	2	66	11.95	22.93	9.50	14.64
70-80	2	44	5.39	11.95	10.19	17.09

Table G.21: Centrality cut table for Au + Au collisions at $\sqrt{s} = 62.4$ A GeV with the MC-Glauber model.

centrality (%)	$\langle N_{\mathrm{part}} \rangle$	$\langle b \rangle$ (fm)	$\langle dS/dy \rangle$	$\langle N_{\mathrm{coll}} \rangle$
0-0.2	373.60 ± 0.20	1.10 ± 0.01	331.76 ± 0.19	1021.23 ± 1.03
0-1	368.59 ± 0.12	1.37 ± 0.01	313.79 ± 0.11	995.22 ± 0.53
0-5	348.55 ± 0.10	2.23 ± 0.00	282.80 ± 0.09	915.52 ± 0.36
5-10	297.02 ± 0.10	3.90 ± 0.00	231.16 ± 0.06	736.96 ± 0.33
10-20	233.75 ± 0.09	5.51 ± 0.00	175.70 ± 0.06	537.29 ± 0.26
20-30	168.06 ± 0.07	7.14 ± 0.00	120.46 ± 0.04	345.93 ± 0.19
30-40	117.87 ± 0.05	8.47 ± 0.00	80.43 ± 0.03	214.40 ± 0.14
40-50	79.37 ± 0.04	9.61 ± 0.00	51.39 ± 0.02	125.28 ± 0.10
50-60	50.31 ± 0.03	10.64 ± 0.00	30.83 ± 0.02	67.53 ± 0.06
60-70	29.37 ± 0.03	11.59 ± 0.00	17.00 ± 0.01	32.93 ± 0.04
70-80	15.35 ± 0.02	12.48 ± 0.00	8.36 ± 0.01	14.25 ± 0.02

Table G.22: The averaged collision parameters for each centrality in Au + Au collisions at $\sqrt{s} = 62.4$ A GeV with the MC-Glauber model.

centrality (%)	N_{min}	N_{max}	dS/dy_{min}	dS/dy_{max}	b_{min} (fm)	b_{max} (fm)
0-0.2	370	394	605.31	633.79	0.01	1.44
0-1	357	394	580.14	633.79	0.01	2.04
0-5	306	394	488.00	633.79	0.01	3.64
5-10	256	345	402.28	487.99	2.55	4.98
10-20	180	295	278.63	402.28	4.02	6.97
20-30	126	219	190.82	278.63	5.70	8.60
30-40	85	163	126.29	190.81	7.13	10.05
40-50	53	119	79.17	126.29	8.18	11.27
50-60	31	76	45.97	79.17	8.91	12.46
60-70	16	50	23.91	45.97	9.77	13.46
70-80	7	29	10.76	23.91	10.58	14.95

Table G.23: Centrality cut table for Au + Au collisions at $\sqrt{s} = 62.4$ A GeV with the MCKLN model.

centrality (%)	$\langle N_{\rm part} \rangle$	$\langle b \rangle$ (fm)	$\langle dS/dy \rangle$	$\langle N_{\rm coll} \rangle$
0-0.2	381.58 ± 0.07	0.61 ± 0.01	611.84 ± 0.12	1043.53 ± 0.80
0-1	375.68 ± 0.05	1.00 ± 0.00	595.88 ± 0.10	1014.82 ± 0.40
0-5	351.27 ± 0.08	2.15 ± 0.00	544.41 ± 0.16	922.70 ± 0.32
5-10	297.01 ± 0.07	3.91 ± 0.00	443.11 ± 0.11	736.64 ± 0.25
10-20	233.65 ± 0.07	5.52 ± 0.00	336.64 ± 0.11	536.93 ± 0.23
20-30	167.79 ± 0.05	7.15 ± 0.00	232.28 ± 0.08	344.99 ± 0.16
30-40	117.72 ± 0.04	8.47 ± 0.00	156.90 ± 0.06	213.80 ± 0.11
40-50	79.24 ± 0.03	9.61 ± 0.00	101.46 ± 0.04	124.68 ± 0.07
50-60	50.21 ± 0.02	10.63 ± 0.00	61.51 ± 0.03	66.98 ± 0.05
60-70	29.28 ± 0.02	11.58 ± 0.00	34.12 ± 0.02	32.43 ± 0.03
70-80	15.18 ± 0.01	12.46 ± 0.00	16.70 ± 0.01	13.78 ± 0.01

Table G.24: The averaged collision parameters for each centrality in Au+Au collisions at $\sqrt{s} = 62.4$ A GeV with the MCKLN model.

centrality (%)	$N_{\rm min}$	$N_{\rm max}$	$dS/dy_{\rm min}$	$dS/dy_{\rm max}$	$b_{\rm min}$ (fm)	$b_{\rm max}$ (fm)
0-0.2	331	394	314.58	365.84	0.02	3.13
0-1	299	394	292.93	365.84	0.02	3.78
0-5	259	394	247.21	365.84	0.01	4.81
5-10	210	380	204.88	247.21	0.15	6.06
10-20	138	345	141.40	204.88	2.71	7.88
20-30	93	253	95.76	141.39	4.79	9.60
30-40	56	189	62.76	95.76	6.46	10.48
40-50	33	136	39.04	62.76	7.61	11.85
50-60	15	99	22.51	39.04	8.68	13.56
60-70	3	67	11.74	22.51	9.40	14.66
70-80	2	43	5.32	11.74	10.19	17.12

Table G.25: Centrality cut table for Au + Au collisions at $\sqrt{s} = 39$ A GeV with the MC-Glauber model.

centrality (%)	$\langle N_{\rm part} \rangle$	$\langle b \rangle$ (fm)	$\langle dS/dy \rangle$	$\langle N_{\rm coll} \rangle$
0-0.2	372.30 ± 0.20	1.10 ± 0.01	323.80 ± 0.18	969.26 ± 1.00
0-1	367.54 ± 0.12	1.36 ± 0.01	306.17 ± 0.11	945.34 ± 0.50
0-5	347.06 ± 0.10	2.21 ± 0.00	275.77 ± 0.09	869.31 ± 0.35
5-10	295.34 ± 0.10	3.88 ± 0.00	225.23 ± 0.05	700.46 ± 0.31
10-20	231.99 ± 0.09	5.50 ± 0.00	171.28 ± 0.06	511.12 ± 0.25
20-30	166.30 ± 0.07	7.14 ± 0.00	117.32 ± 0.04	328.84 ± 0.18
30-40	116.45 ± 0.05	8.46 ± 0.00	78.41 ± 0.03	204.17 ± 0.13
40-50	78.34 ± 0.04	9.59 ± 0.00	50.21 ± 0.02	119.68 ± 0.09
50-60	49.72 ± 0.03	10.62 ± 0.00	30.21 ± 0.02	64.92 ± 0.06
60-70	29.07 ± 0.03	11.56 ± 0.00	16.71 ± 0.01	31.90 ± 0.04
70-80	15.17 ± 0.02	12.46 ± 0.00	8.22 ± 0.01	13.87 ± 0.02

Table G.26: The averaged collision parameters for each centrality in Au + Au collisions at $\sqrt{s} = 39$ A GeV with the MC-Glauber model.

centrality (%)	$N_{\rm min}$	$N_{\rm max}$	$dS/dy_{\rm min}$	$dS/dy_{\rm max}$	$b_{\rm min}$ (fm)	$b_{\rm max}$ (fm)
0-0.2	370	394	459.02	484.16	0.01	1.48
0-1	357	394	439.98	484.16	0.01	2.13
0-5	308	394	370.90	484.16	0.01	3.68
5-10	256	338	305.65	370.90	2.52	5.07
10-20	177	291	212.40	305.64	4.00	7.00
20-30	127	216	146.14	212.39	5.68	8.53
30-40	84	157	97.26	146.14	7.05	10.01
40-50	52	112	61.40	97.26	8.13	11.35
50-60	31	76	36.03	61.40	8.85	12.43
60-70	16	50	18.88	36.03	9.72	13.54
70-80	7	29	8.55	18.88	10.59	15.28

Table G.27: Centrality cut table for Au + Au collisions at $\sqrt{s} = 39$ A GeV with the MCKLN model.

centrality (%)	$\langle N_{\rm part} \rangle$	$\langle b \rangle$ (fm)	$\langle dS/dy \rangle$	$\langle N_{\rm coll} \rangle$
0-0.2	380.76 ± 0.07	0.61 ± 0.01	463.87 ± 0.09	989.92 ± 0.79
0-1	374.69 ± 0.05	0.99 ± 0.00	451.83 ± 0.08	962.33 ± 0.39
0-5	350.08 ± 0.08	2.13 ± 0.00	413.25 ± 0.12	876.75 ± 0.30
5-10	295.35 ± 0.07	3.89 ± 0.00	336.67 ± 0.08	700.49 ± 0.24
10-20	231.75 ± 0.07	5.51 ± 0.00	256.07 ± 0.09	510.19 ± 0.22
20-30	166.24 ± 0.05	7.13 ± 0.00	177.50 ± 0.06	328.53 ± 0.15
30-40	116.42 ± 0.04	8.45 ± 0.00	120.41 ± 0.04	203.89 ± 0.11
40-50	78.33 ± 0.03	9.59 ± 0.00	78.38 ± 0.03	119.37 ± 0.07
50-60	49.67 ± 0.02	10.61 ± 0.00	47.95 ± 0.02	64.54 ± 0.04
60-70	28.96 ± 0.02	11.54 ± 0.00	26.83 ± 0.02	31.45 ± 0.03
70-80	15.01 ± 0.01	12.43 ± 0.00	13.23 ± 0.01	13.45 ± 0.01

Table G.28: The averaged collision parameters for each centrality in Au+Au collisions at $\sqrt{s} = 39$ A GeV with the MCKLN model.

centrality (%)	$N_{\rm min}$	$N_{\rm max}$	$dS/dy_{\rm min}$	$dS/dy_{\rm max}$	$b_{\rm min}$ (fm)	$b_{\rm max}$ (fm)
0-0.2	326	394	309.50	360.13	0.00	3.09
0-1	312	394	287.96	360.13	0.00	3.40
0-5	250	394	243.02	360.13	0.00	5.15
5-10	211	381	201.55	243.02	0.48	6.01
10-20	145	333	139.26	201.55	2.92	7.76
20-30	97	251	94.50	139.25	4.96	9.22
30-40	48	190	62.07	94.49	6.35	10.59
40-50	33	137	38.76	62.07	7.62	11.85
50-60	13	96	22.35	38.76	8.61	13.19
60-70	4	69	11.68	22.35	9.22	14.54
70-80	2	45	5.31	11.68	10.12	16.40

Table G.29: Centrality cut table for Au + Au collisions at $\sqrt{s} = 27$ A GeV with the MC-Glauber model.

centrality (%)	$\langle N_{\rm part} \rangle$	$\langle b \rangle$ (fm)	$\langle dS/dy \rangle$	$\langle N_{\rm coll} \rangle$
0-0.2	371.47 ± 0.21	1.10 ± 0.01	318.50 ± 0.18	936.55 ± 0.94
0-1	366.30 ± 0.12	1.37 ± 0.01	301.06 ± 0.11	912.44 ± 0.48
0-5	345.73 ± 0.10	2.22 ± 0.00	270.95 ± 0.09	839.09 ± 0.33
5-10	294.18 ± 0.10	3.87 ± 0.00	221.53 ± 0.05	677.16 ± 0.31
10-20	230.98 ± 0.09	5.49 ± 0.00	168.52 ± 0.06	494.51 ± 0.24
20-30	165.66 ± 0.07	7.12 ± 0.00	115.77 ± 0.04	319.25 ± 0.17
30-40	115.93 ± 0.05	8.44 ± 0.00	77.41 ± 0.03	198.55 ± 0.13
40-50	78.10 ± 0.04	9.57 ± 0.00	49.71 ± 0.02	117.00 ± 0.09
50-60	49.69 ± 0.03	10.59 ± 0.00	30.04 ± 0.02	63.91 ± 0.06
60-70	29.02 ± 0.03	11.53 ± 0.00	16.60 ± 0.01	31.43 ± 0.04
70-80	15.13 ± 0.02	12.42 ± 0.00	8.19 ± 0.01	13.71 ± 0.02

Table G.30: The averaged collision parameters for each centrality in Au + Au collisions at $\sqrt{s} = 27$ A GeV with the MC-Glauber model.

centrality (%)	$N_{\rm min}$	$N_{\rm max}$	$dS/dy_{\rm min}$	$dS/dy_{\rm max}$	$b_{\rm min}$ (fm)	$b_{\rm max}$ (fm)
0-0.2	369	394	357.12	376.31	0.03	1.49
0-1	357	394	342.57	376.31	0.02	2.05
0-5	307	394	288.67	376.31	0.02	3.76
5-10	256	336	238.57	288.67	2.52	5.02
10-20	181	290	166.51	238.57	3.88	6.99
20-30	124	214	114.88	166.51	5.78	8.54
30-40	84	158	76.93	114.88	7.10	10.03
40-50	53	113	48.93	76.93	8.02	11.32
50-60	32	75	28.87	48.93	9.03	12.46
60-70	16	48	15.38	28.87	9.84	13.61
70-80	7	28	7.00	15.38	10.23	14.99

Table G.31: Centrality cut table for Au + Au collisions at $\sqrt{s} = 27$ A GeV with the MCKLN model.

centrality (%)	$\langle N_{\rm part} \rangle$	$\langle b \rangle$ (fm)	$\langle dS/dy \rangle$	$\langle N_{\rm coll} \rangle$
0-0.2	380.19 ± 0.07	0.62 ± 0.01	360.99 ± 0.07	952.38 ± 0.80
0-1	373.94 ± 0.05	0.99 ± 0.00	351.69 ± 0.06	928.81 ± 0.38
0-5	348.92 ± 0.08	2.13 ± 0.00	321.61 ± 0.09	846.29 ± 0.30
5-10	294.16 ± 0.07	3.89 ± 0.00	262.50 ± 0.06	676.70 ± 0.23
10-20	230.75 ± 0.07	5.50 ± 0.00	200.33 ± 0.07	494.03 ± 0.21
20-30	165.30 ± 0.05	7.12 ± 0.00	139.37 ± 0.05	318.24 ± 0.15
30-40	115.55 ± 0.04	8.44 ± 0.00	94.92 ± 0.03	197.52 ± 0.10
40-50	77.73 ± 0.03	9.58 ± 0.00	62.19 ± 0.03	116.05 ± 0.07
50-60	49.27 ± 0.02	10.59 ± 0.00	38.31 ± 0.02	62.92 ± 0.04
60-70	28.82 ± 0.02	11.52 ± 0.00	21.67 ± 0.01	30.86 ± 0.03
70-80	14.95 ± 0.01	12.40 ± 0.00	10.80 ± 0.01	13.28 ± 0.01

Table G.32: The averaged collision parameters for each centrality in Au+Au collisions at $\sqrt{s} = 27$ A GeV with the MCKLN model.

centrality (%)	N_{min}	N_{max}	dS/dy_{min}	dS/dy_{max}	b_{min} (fm)	b_{max} (fm)
0-0.2	320	394	305.25	372.94	0.01	3.01
0-1	309	394	284.59	372.94	0.01	3.65
0-5	250	394	239.89	372.94	0.01	4.78
5-10	207	377	198.84	239.89	0.50	6.11
10-20	142	331	137.22	198.84	2.90	7.86
20-30	89	248	93.40	137.22	4.94	9.41
30-40	60	189	61.30	93.40	6.00	10.91
40-50	28	144	38.24	61.30	7.48	12.15
50-60	14	95	22.12	38.24	8.59	13.18
60-70	4	67	11.59	22.12	9.51	14.48
70-80	2	47	5.27	11.59	10.30	16.69

Table G.33: Centrality cut table for Au + Au collisions at $\sqrt{s} = 19.6$ A GeV with the MC-Glauber model.

centrality (%)	$\langle N_{\mathrm{part}} \rangle$	$\langle b \rangle$ (fm)	$\langle dS/dy \rangle$	$\langle N_{\mathrm{coll}} \rangle$
0-0.2	370.85 ± 0.21	1.10 ± 0.01	314.11 ± 0.18	912.74 ± 0.96
0-1	365.50 ± 0.12	1.38 ± 0.01	297.32 ± 0.10	889.86 ± 0.48
0-5	344.93 ± 0.10	2.22 ± 0.00	267.80 ± 0.09	819.50 ± 0.33
5-10	292.92 ± 0.10	3.88 ± 0.00	218.64 ± 0.05	660.32 ± 0.30
10-20	229.70 ± 0.09	5.50 ± 0.00	166.20 ± 0.06	482.08 ± 0.23
20-30	164.56 ± 0.07	7.12 ± 0.00	114.21 ± 0.04	311.36 ± 0.17
30-40	115.24 ± 0.05	8.43 ± 0.00	76.49 ± 0.03	193.99 ± 0.12
40-50	77.59 ± 0.04	9.57 ± 0.00	49.13 ± 0.02	114.47 ± 0.09
50-60	49.27 ± 0.03	10.58 ± 0.00	29.65 ± 0.01	62.51 ± 0.06
60-70	28.76 ± 0.03	11.52 ± 0.00	16.44 ± 0.01	30.85 ± 0.04
70-80	15.05 ± 0.02	12.41 ± 0.00	8.12 ± 0.01	13.54 ± 0.02

Table G.34: The averaged collision parameters for each centrality in Au + Au collisions at $\sqrt{s} =$ 19.6 A GeV with the MC-Glauber model.

centrality (%)	N_{min}	N_{max}	dS/dy_{min}	dS/dy_{max}	b_{min} (fm)	b_{max} (fm)
0-0.2	370	394	278.14	291.36	0.01	1.49
0-1	356	394	266.71	291.36	0.01	2.05
0-5	307	394	225.23	291.36	0.01	3.69
5-10	253	334	186.58	225.23	2.56	5.04
10-20	179	285	130.65	186.58	3.91	6.96
20-30	127	213	90.60	130.65	5.78	8.57
30-40	85	155	61.21	90.60	6.98	10.00
40-50	54	108	39.16	61.21	8.11	11.22
50-60	30	74	23.36	39.16	8.88	12.55
60-70	16	48	12.53	23.36	9.79	13.64
70-80	7	29	5.77	12.53	10.39	15.21

Table G.35: Centrality cut table for Au + Au collisions at $\sqrt{s} = 19.6$ A GeV with the MCKLN model.

centrality (%)	$\langle N_{\rm part} \rangle$	$\langle b \rangle$ (fm)	$\langle dS/dy \rangle$	$\langle N_{\rm coll} \rangle$
0-0.2	379.59 ± 0.07	0.62 ± 0.01	281.19 ± 0.05	926.72 ± 0.79
0-1	373.16 ± 0.05	1.00 ± 0.00	273.86 ± 0.05	904.89 ± 0.38
0-5	348.07 ± 0.08	2.13 ± 0.00	250.61 ± 0.07	825.65 ± 0.29
5-10	293.48 ± 0.07	3.88 ± 0.00	205.04 ± 0.05	661.59 ± 0.23
10-20	229.94 ± 0.07	5.49 ± 0.00	156.79 ± 0.05	482.65 ± 0.21
20-30	164.72 ± 0.05	7.11 ± 0.00	109.62 ± 0.04	311.53 ± 0.15
30-40	115.26 ± 0.04	8.42 ± 0.00	75.19 ± 0.03	194.10 ± 0.10
40-50	77.58 ± 0.03	9.56 ± 0.00	49.61 ± 0.02	114.28 ± 0.07
50-60	49.17 ± 0.02	10.57 ± 0.00	30.79 ± 0.01	62.13 ± 0.04
60-70	28.73 ± 0.02	11.51 ± 0.00	17.56 ± 0.01	30.54 ± 0.03
70-80	14.96 ± 0.01	12.38 ± 0.00	8.85 ± 0.01	13.23 ± 0.01

Table G.36: The averaged collision parameters for each centrality in Au+Au collisions at $\sqrt{s} = 19.6$ A GeV with the MCKLN model.

centrality (%)	N_{min}	N_{max}	dS/dy_{min}	dS/dy_{max}	b_{min} (fm)	b_{max} (fm)
0-0.2	325	394	302.67	351.84	0.05	3.05
0-1	303	394	281.65	351.84	0.01	3.45
0-5	247	394	237.65	351.84	0.01	5.03
5-10	206	377	196.92	237.64	0.79	6.07
10-20	139	333	136.04	196.92	2.83	7.82
20-30	88	257	92.54	136.04	4.99	9.44
30-40	54	186	60.82	92.54	6.31	10.65
40-50	33	149	37.92	60.81	7.49	11.63
50-60	14	98	21.95	37.92	8.56	13.04
60-70	4	65	11.49	21.95	9.54	14.94
70-80	2	42	5.22	11.49	10.06	17.16

Table G.37: Centrality cut table for Au + Au collisions at $\sqrt{s} = 11.5$ A GeV with the MC-Glauber model.

centrality (%)	$\langle N_{\mathrm{part}} \rangle$	$\langle b \rangle$ (fm)	$\langle dS/dy \rangle$	$\langle N_{\mathrm{coll}} \rangle$
0-0.2	370.01 ± 0.22	1.11 ± 0.01	311.22 ± 0.17	893.18 ± 0.94
0-1	365.07 ± 0.12	1.37 ± 0.01	294.45 ± 0.10	871.57 ± 0.47
0-5	344.07 ± 0.10	2.23 ± 0.00	265.03 ± 0.08	801.90 ± 0.32
5-10	292.21 ± 0.10	3.87 ± 0.00	216.50 ± 0.05	647.09 ± 0.29
10-20	229.10 ± 0.09	5.49 ± 0.00	164.65 ± 0.06	472.87 ± 0.23
20-30	164.03 ± 0.07	7.11 ± 0.00	113.14 ± 0.04	305.39 ± 0.17
30-40	114.87 ± 0.05	8.42 ± 0.00	75.86 ± 0.03	190.59 ± 0.12
40-50	77.28 ± 0.04	9.56 ± 0.00	48.73 ± 0.02	112.58 ± 0.09
50-60	49.03 ± 0.03	10.58 ± 0.00	29.43 ± 0.01	61.51 ± 0.06
60-70	28.67 ± 0.03	11.51 ± 0.00	16.33 ± 0.01	30.52 ± 0.04
70-80	14.93 ± 0.02	12.40 ± 0.00	8.05 ± 0.01	13.35 ± 0.02

Table G.38: The averaged collision parameters for each centrality in Au + Au collisions at $\sqrt{s} = 11.5$ A GeV with the MC-Glauber model.

centrality (%)	N_{min}	N_{max}	dS/dy_{min}	dS/dy_{max}	b_{min} (fm)	b_{max} (fm)
0-0.2	368	394	169.63	178.49	0.01	1.48
0-1	358	394	162.46	178.49	0.01	2.09
0-5	304	394	137.52	178.49	0.01	3.73
5-10	258	333	114.45	137.52	2.58	5.04
10-20	180	285	80.77	114.45	3.81	6.98
20-30	127	213	56.72	80.77	5.70	8.78
30-40	84	156	38.67	56.72	7.02	10.19
40-50	53	108	25.15	38.66	8.09	11.30
50-60	31	75	15.24	25.15	8.69	12.42
60-70	16	49	8.29	15.24	9.73	13.56
70-80	7	28	3.89	8.29	10.43	15.00

Table G.39: Centrality cut table for Au + Au collisions at $\sqrt{s} = 11.5$ A GeV with the MCKLN model.

centrality (%)	$\langle N_{\mathrm{part}} \rangle$	$\langle b \rangle$ (fm)	$\langle dS/dy \rangle$	$\langle N_{\mathrm{coll}} \rangle$
0-0.2	379.39 ± 0.07	0.62 ± 0.01	171.45 ± 0.03	902.50 ± 0.81
0-1	372.75 ± 0.05	0.99 ± 0.00	166.91 ± 0.03	884.93 ± 0.39
0-5	347.48 ± 0.08	2.12 ± 0.00	152.79 ± 0.04	808.51 ± 0.29
5-10	292.95 ± 0.07	3.87 ± 0.00	125.44 ± 0.03	648.51 ± 0.24
10-20	229.69 ± 0.07	5.48 ± 0.00	96.58 ± 0.03	474.12 ± 0.21
20-30	164.34 ± 0.05	7.10 ± 0.00	68.11 ± 0.02	306.12 ± 0.14
30-40	115.07 ± 0.04	8.41 ± 0.00	47.27 ± 0.02	191.15 ± 0.10
40-50	77.38 ± 0.03	9.55 ± 0.00	31.58 ± 0.01	112.77 ± 0.07
50-60	49.10 ± 0.02	10.56 ± 0.00	19.92 ± 0.01	61.47 ± 0.04
60-70	28.63 ± 0.02	11.49 ± 0.00	11.53 ± 0.01	30.26 ± 0.03
70-80	14.87 ± 0.01	12.37 ± 0.00	5.89 ± 0.00	13.10 ± 0.01

Table G.40: The averaged collision parameters for each centrality in Au+Au collisions at $\sqrt{s} = 11.5$ A GeV with the MCKLN model.

centrality (%)	N_{min}	N_{max}	dS/dy_{min}	dS/dy_{max}	b_{min} (fm)	b_{max} (fm)
0-0.2	322	394	303.07	358.50	0.01	3.31
0-1	301	394	282.43	358.50	0.01	3.67
0-5	252	394	238.20	358.50	0.01	4.99
5-10	212	381	197.41	238.19	0.64	5.89
10-20	139	343	136.52	197.41	2.42	7.79
20-30	94	245	92.66	136.52	4.92	9.39
30-40	60	200	60.84	92.66	6.40	10.75
40-50	30	131	37.92	60.84	7.57	11.83
50-60	11	95	22.02	37.92	8.74	13.12
60-70	2	68	11.54	22.02	9.47	15.30
70-80	2	47	5.26	11.54	10.18	16.37

Table G.41: Centrality cut table for Au + Au collisions at $\sqrt{s} = 7.7$ A GeV with the MC-Glauber model.

centrality (%)	$\langle N_{\rm part} \rangle$	$\langle b \rangle$ (fm)	$\langle dS/dy \rangle$	$\langle N_{\rm coll} \rangle$
0-0.2	370.60 ± 0.21	1.10 ± 0.01	311.74 ± 0.17	899.93 ± 0.95
0-1	365.05 ± 0.12	1.38 ± 0.01	295.12 ± 0.10	875.77 ± 0.48
0-5	344.41 ± 0.10	2.22 ± 0.00	265.73 ± 0.08	806.53 ± 0.32
5-10	292.37 ± 0.10	3.88 ± 0.00	216.99 ± 0.05	650.31 ± 0.29
10-20	229.37 ± 0.09	5.49 ± 0.00	165.15 ± 0.06	475.47 ± 0.23
20-30	164.20 ± 0.07	7.11 ± 0.00	113.38 ± 0.04	306.98 ± 0.17
30-40	114.86 ± 0.05	8.43 ± 0.00	75.99 ± 0.03	191.33 ± 0.12
40-50	77.25 ± 0.04	9.56 ± 0.00	48.73 ± 0.02	112.84 ± 0.09
50-60	48.98 ± 0.03	10.58 ± 0.00	29.45 ± 0.01	61.60 ± 0.06
60-70	28.72 ± 0.03	11.51 ± 0.00	16.39 ± 0.01	30.65 ± 0.04
70-80	15.02 ± 0.02	12.40 ± 0.00	8.10 ± 0.01	13.46 ± 0.02

Table G.42: The averaged collision parameters for each centrality in Au + Au collisions at $\sqrt{s} = 7.7$ A GeV with the MC-Glauber model.

centrality (%)	$N_{\rm min}$	$N_{\rm max}$	$dS/dy_{\rm min}$	$dS/dy_{\rm max}$	$b_{\rm min}$ (fm)	$b_{\rm max}$ (fm)
0-0.2	369	394	107.73	113.91	0.02	1.69
0-1	357	394	103.24	113.91	0.00	2.27
0-5	304	394	87.34	113.91	0.00	3.86
5-10	254	332	72.94	87.34	2.53	5.19
10-20	180	285	51.89	72.94	3.73	7.06
20-30	126	209	36.73	51.89	5.63	8.64
30-40	85	153	25.34	36.73	6.89	10.10
40-50	53	107	16.69	25.34	7.94	11.08
50-60	31	74	10.28	16.69	9.03	12.54
60-70	16	47	5.69	10.28	9.77	13.68
70-80	7	30	2.72	5.69	10.38	14.94

Table G.43: Centrality cut table for Au + Au collisions at $\sqrt{s} = 7.7$ A GeV with the MCKLN model.

centrality (%)	$\langle N_{\rm part} \rangle$	$\langle b \rangle$ (fm)	$\langle dS/dy \rangle$	$\langle N_{\rm coll} \rangle$
0-0.2	379.28 ± 0.07	0.65 ± 0.01	108.90 ± 0.02	900.54 ± 0.82
0-1	372.83 ± 0.05	1.01 ± 0.00	106.03 ± 0.02	887.34 ± 0.40
0-5	347.42 ± 0.08	2.13 ± 0.00	97.05 ± 0.03	811.63 ± 0.30
5-10	292.71 ± 0.07	3.88 ± 0.00	79.80 ± 0.02	650.72 ± 0.24
10-20	229.51 ± 0.07	5.49 ± 0.00	61.76 ± 0.02	475.72 ± 0.21
20-30	164.23 ± 0.05	7.11 ± 0.00	43.94 ± 0.01	307.24 ± 0.15
30-40	114.88 ± 0.04	8.42 ± 0.00	30.78 ± 0.01	191.39 ± 0.11
40-50	77.32 ± 0.03	9.55 ± 0.00	20.82 ± 0.01	112.98 ± 0.07
50-60	49.07 ± 0.02	10.56 ± 0.00	13.32 ± 0.01	61.70 ± 0.05
60-70	28.66 ± 0.02	11.50 ± 0.00	7.84 ± 0.00	30.42 ± 0.03
70-80	14.90 ± 0.01	12.37 ± 0.00	4.08 ± 0.00	13.17 ± 0.01

Table G.44: The averaged collision parameters for each centrality in Au+Au collisions at $\sqrt{s} = 7.7$ A GeV with the MCKLN model.

Bibliography

[1] U. W. Heinz, *Towards the Little Bang Standard Model*, *J.Phys.Conf.Ser.* **455** (2013) 012044, [arXiv:1304.3634].

[2] G. Steigman, *Big bang nucleosynthesis: Probing the first 20 minutes*, astro-ph/0307244.

[3] U. A. Wiedemann and U. W. Heinz, *Particle interferometry for relativistic heavy ion collisions*, *Phys.Rept.* **319** (1999) 145–230, [nucl-th/9901094].

[4] Y. V. Kovchegov and E. Levin, *Quantum chromodynamics at high energy*. Cambridge monographs on particle physics, nuclear physics and cosmology. Cambridge Univ. Press, Cambridge, 2012.

[5] T. Epelbaum and F. Gelis, *Pressure isotropization in high energy heavy ion collisions*, *Phys.Rev.Lett.* **111** (2013) 232301, [arXiv:1307.2214].

[6] K. Dusling, T. Epelbaum, F. Gelis, and R. Venugopalan, *Role of quantum fluctuations in a system with strong fields: Onset of hydrodynamical flow*, *Nucl.Phys.* **A850** (2011) 69–109, [arXiv:1009.4363].

[7] U. Heinz and J. S. Moreland, *Energy dependent growth of the nucleon and hydrodynamic initial conditions*, *Phys.Rev.* **C84** (2011) 054905, [arXiv:1108.5379].

[8] D. Kharzeev, E. Levin, and M. Nardi, *The Onset of classical QCD dynamics in relativistic heavy ion collisions*, *Phys.Rev.* **C71** (2005) 054903, [hep-ph/0111315].

[9] D. Kharzeev, E. Levin, and M. Nardi, *Color glass condensate at the LHC: Hadron multiplicities in pp, pA and AA collisions*, *Nucl.Phys.* **A747** (2005) 609–629, [hep-ph/0408050].

[10] T. Hirano and Y. Nara, *Hydrodynamic afterburner for the color glass condensate and the parton energy loss*, *Nucl.Phys.* **A743** (2004) 305–328, [nucl-th/0404039].

[11] T. Hirano and Y. Nara, *Eccentricity fluctuation effects on elliptic flow in relativistic heavy ion collisions*, *Phys. Rev. C* **79** (2009) 064904, [arXiv:0904.4080].

[12] **CMS Collaboration** Collaboration, V. Khachatryan et al., *Charged particle multiplicities in pp interactions at $\sqrt{s} = 0.9$, 2.36, and 7 TeV*, *JHEP* **1101** (2011) 079, [arXiv:1011.5531].

[13] **UA5 Collaboration** Collaboration, R. Ansorge et al., *Charged Particle Multiplicity Distributions at 200-GeV and 900-GeV Center-Of-Mass Energy*, *Z.Phys.* **C43** (1989) 357.

[14] **CMS Collaboration** Collaboration, S. Chatrchyan et al., *Multiplicity and transverse momentum dependence of two- and four-particle correlations in pPb and PbPb collisions*, *Phys.Lett.* **B724** (2013) 213–240, [arXiv:1305.0609].

[15] U. W. Heinz and H. Song, *Causal relativistic hydrodynamics for viscous fluids*, *J.Phys.* **G35** (2008) 104126, [arXiv:0806.0352].

[16] P. Huovinen and P. Petreczky, *QCD Equation of State and Hadron Resonance Gas*, *Nucl. Phys.* **A837** (2010) 26–53, [arXiv:0912.2541].

[17] C. Shen, U. Heinz, P. Huovinen, and H. Song, *Systematic parameter study of hadron spectra and elliptic flow from viscous hydrodynamic simulations of Au+Au collisions at $\sqrt{s_{\rm NN}}$ = 200 GeV*, *Phys. Rev. C* **82** (2010) 054904, [arXiv:1010.1856].

[18] S. S. Gubser, *Symmetry constraints on generalizations of Bjorken flow*, *Phys.Rev.* **D82** (2010) 085027, [arXiv:1006.0006].

[19] S. S. Gubser and A. Yarom, *Conformal hydrodynamics in Minkowski and de Sitter spacetimes*, *Nucl.Phys.* **B846** (2011) 469–511, [arXiv:1012.1314].

[20] H. Marrochio, J. Noronha, G. S. Denicol, M. Luzum, S. Jeon, et al., *Solutions of Conformal Israel-Stewart Relativistic Viscous Fluid Dynamics*, arXiv:1307.6130.

[21] P. F. Kolb and U. W. Heinz, *Hydrodynamic description of ultrarelativistic heavy ion collisions*, nucl-th/0305084.

[22] M. Luzum and J.-Y. Ollitrault, *Eliminating experimental bias in anisotropic-flow measurements of high-energy nuclear collisions*, *Phys.Rev.* **C87** (2013), no. 4 044907, [arXiv:1209.2323].

[23] A. M. Poskanzer and S. Voloshin, *Methods for analyzing anisotropic flow in relativistic nuclear collisions*, *Phys.Rev.* **C58** (1998) 1671–1678, [nucl-ex/9805001].

[24] F. G. Gardim, F. Grassi, M. Luzum, and J.-Y. Ollitrault, *Breaking of factorization of two-particle correlations in hydrodynamics*, *Phys.Rev.* **C87** (2013), no. 3 031901, [arXiv:1211.0989].

[25] U. Heinz, Z. Qiu, and C. Shen, *Fluctuating flow angles and anisotropic flow measurements*, *Phys.Rev.* **C87** (2013), no. 3 034913, [arXiv:1302.3535].

[26] A. Bilandzic, C. H. Christensen, K. Gulbrandsen, A. Hansen, and Y. Zhou, *Generic framework for anisotropic flow analyses with multi-particle azimuthal correlations*, arXiv:1312.3572.

[27] **ATLAS Collaboration** Collaboration, J. Jia, *Measurement of Event Plane Correlations in Pb-Pb Collisions at $\sqrt{s_{\rm NN}}$=2.76 TeV with the ATLAS Detector*, *Nucl.Phys.* **A910-911** (2013) 276–280, [arXiv:1208.1427].

[28] **ATLAS Collaboration** Collaboration, G. Aad et al., *Measurement of event-plane correlations in $\sqrt{s_{NN}}$=2.76 TeV lead-lead collisions with the ATLAS detector*, arXiv:1403.0489.

[29] R. S. Bhalerao, J.-Y. Ollitrault, and S. Pal, *Event-plane correlators*, *Phys.Rev.* **C88** (2013) 024909, [arXiv:1307.0980].

[30] P. F. Kolb, J. Sollfrank, and U. Heinz, *Anisotropic transverse flow and the quark-hadron phase transition*, *Phys. Rev. C* **62** (2000) 054909, [hep-ph/0006129].

[31] D. Teaney, J. Lauret, and E. V. Shuryak, *Flow at the SPS and RHIC as a quark gluon plasma signature*, *Phys.Rev.Lett.* **86** (2001) 4783–4786, [nucl-th/0011058].

[32] P. Huovinen, P. Kolb, U. Heinz, P. Ruuskanen, and S. Voloshin, *Radial and elliptic flow at RHIC: Further predictions*, *Phys. Lett.* **B503** (2001) 58–64, [hep-ph/0101136].

[33] R. A. Lacey and A. Taranenko, *What do elliptic flow measurements tell us about the matter created in the little bang at RHIC?*, *PoS* **CFRNC2006** (2006) 021, [nucl-ex/0610029].

[34] T. Hirano, U. Heinz, D. Kharzeev, R. Lacey, and Y. Nara, *Hadronic dissipative effects on elliptic flow in ultrarelativistic heavy-ion collisions*, *Phys. Lett.* **B636** (2006) 299–304, [nucl-th/0511046].

[35] P. Romatschke and U. Romatschke, *Viscosity Information from Relativistic Nuclear Collisions: How Perfect is the Fluid Observed at RHIC?*, *Phys. Rev. Lett.* **99** (2007) 172301, [arXiv:0706.1522].

[36] M. Luzum and P. Romatschke, *Conformal Relativistic Viscous Hydrodynamics: Applications to RHIC results at $\sqrt{s_{\rm NN}}$ = 200 GeV*, *Phys. Rev.* **C78** (2008) 034915, [arXiv:0804.4015]. [Erratum: Phys. Rev. C79, 039903 (2009)].

[37] M. Luzum and P. Romatschke, *Viscous Hydrodynamic Predictions for Nuclear Collisions at the LHC*, *Phys.Rev.Lett.* **103** (2009) 262302, [arXiv:0901.4588].

[38] H. Song and U. Heinz, *Causal viscous hydrodynamics in 2+1 dimensions for relativistic heavy-ion collisions*, *Phys. Rev. C* **77** (2008) 064901, [arXiv:0712.3715].

[39] H. Song and U. Heinz, *Suppression of elliptic flow in a minimally viscous quark- gluon plasma*, *Phys. Lett. B* **658** (2008) 279–283, [arXiv:0709.0742].

[40] H. Song, S. A. Bass, U. Heinz, T. Hirano, and C. Shen, *200 A GeV Au+Au collisions serve a nearly perfect quark-gluon liquid*, *Phys.Rev.Lett.* **106** (2011) 192301, [arXiv:1011.2783].

[41] M. Luzum, *Elliptic flow at energies available at the CERN Large Hadron Collider: Comparing heavy-ion data to viscous hydrodynamic predictions*, *Phys.Rev.* **C83** (2011) 044911, [arXiv:1011.5173].

[42] R. A. Lacey, A. Taranenko, N. Ajitanand, and J. Alexander, *Initial indications for the production of a strongly coupled plasma in Pb+Pb collisions at $\sqrt{s_{NN}} = 2.76$ TeV*, *Phys.Rev.* **C83** (2011) 031901, [arXiv:1011.6328].

[43] P. Bozek, M. Chojnacki, W. Florkowski, and B. Tomasik, *Hydrodynamic predictions for Pb+Pb collisions at $\sqrt{s_{NN}}$ = 2.76 TeV*, *Phys.Lett.* **B694** (2010) 238–241, [arXiv:1007.2294].

[44] T. Hirano, P. Huovinen, and Y. Nara, *Elliptic flow in U+U collisions at $\sqrt{s_{NN}} = 200$ GeV and in Pb+Pb collisions at $\sqrt{s_{NN}} = 2.76$ TeV: Prediction from a hybrid approach*, *Phys.Rev.* **C83** (2011) 021902, [arXiv:1010.6222].

[45] B. Schenke, S. Jeon, and C. Gale, *Elliptic and triangular flow in event-by-event (3+1)D viscous hydrodynamics*, *Phys.Rev.Lett.* **106** (2011) 042301, [arXiv:1009.3244].

[46] B. Schenke, S. Jeon, and C. Gale, *Anisotropic flow in $\sqrt{s} = 2.76$ TeV Pb+Pb collisions at the LHC*, *Phys.Lett.* **B702** (2011) 59–63, [arXiv:1102.0575].

[47] H. Song, S. A. Bass, and U. Heinz, *Elliptic flow in 200 A GeV Au+Au collisions and 2.76 A TeV Pb+Pb collisions: insights from viscous hydrodynamics + hadron cascade hybrid model*, *Phys.Rev.* **C83** (2011) 054912, [arXiv:1103.2380].

[48] C. Shen, U. Heinz, P. Huovinen, and H. Song, *Radial and elliptic flow in Pb+Pb collisions at the Large Hadron Collider from viscous hydrodynamic*, *Phys.Rev.* **C84** (2011) 044903, [arXiv:1105.3226].

[49] U. Heinz, C. Shen, and H. Song, *The viscosity of quark-gluon plasma at RHIC and the LHC*, *AIP Conf.Proc.* **1441** (2012) 766–770, [arXiv:1108.5323].

[50] C. Shen and U. Heinz, *Collision Energy Dependence of Viscous Hydrodynamic Flow in Relativistic Heavy-Ion Collisions*, *Phys.Rev.* **C85** (2012) 054902, [arXiv:1202.6620].

[51] D. Teaney, *Effect of shear viscosity on spectra, elliptic flow, and Hanbury Brown-Twiss radii*, *Phys. Rev. C* **68** (2003) 034913, [nucl-th/0301099].

[52] **ALICE Collaboration** Collaboration, K. Aamodt et al., *Elliptic flow of charged particles in Pb-Pb collisions at 2.76 TeV*, *Phys.Rev.Lett.* **105** (2010) 252302, [arXiv:1011.3914].

[53] P. B. Arnold, G. D. Moore, and L. G. Yaffe, *Transport coefficients in high temperature gauge theories. 1. Leading log results*, *JHEP* **0011** (2000) 001, [hep-ph/0010177].

[54] P. B. Arnold, G. D. Moore, and L. G. Yaffe, *Transport coefficients in high temperature gauge theories. 2. Beyond leading log*, *JHEP* **0305** (2003) 051, [hep-ph/0302165].

[55] H. Song and U. Heinz, *Extracting the QGP viscosity from RHIC data – a status report from viscous hydrodynamics*, *J. Phys. G: Part. Nucl. Phys.* **36** (2009) 064033, [arXiv:0812.4274].

[56] H. Song, *Causal Viscous Hydrodynamics for Relativistic Heavy Ion Collisions*, arXiv:0908.3656. Ph. D. Thesis, The Ohio State University (August 2009) [arXiv:0908.3656 [nucl-th]].

[57] P. F. Kolb, J. Sollfrank, and U. Heinz, *Anisotropic flow from ags to lhc energies*, *Phys. Lett.* **B459** (1999), no. 4 667 – 673.

[58] P. F. Kolb, U. Heinz, P. Huovinen, K. J. Eskola, and K. Tuominen, *Centrality dependence of multiplicity, transverse energy, and elliptic flow from hydrodynamics*, *Nucl. Phys.* **A696** (2001) 197–215, [hep-ph/0103234].

[59] D. Kharzeev and M. Nardi, *Hadron production in nuclear collisions at rhic and high-density qcd*, *Phys. Lett. B* **507** (2001), no. 1-4 121 – 128.

[60] D. Kharzeev, E. Levin, and M. Nardi, *Qcd saturation and deuteron-nucleus collisions*, *Nucl. Phys.* **A730** (2004), no. 3-4 448 – 459.

[61] A. Adil, H.-J. Drescher, A. Dumitru, A. Hayashigaki, and Y. Nara, *The eccentricity in heavy-ion collisions from color glass condensate initial conditions*, *Phys. Rev. C* **74** (2006) 044905, [nucl-th/0605012].

[62] H. J. Drescher and Y. Nara, *Effects of fluctuations on the initial eccentricity from the color glass condensate in heavy ion collisions*, *Phys. Rev. C* **75** (2007) 034905, [nucl-th/0611017].

[63] H. Holopainen, H. Niemi, and K. J. Eskola, *Event-by-event hydrodynamics and elliptic flow from fluctuating initial state*, 1007.0368.

[64] H. Petersen and M. Bleicher, *Eccentricity fluctuations in an integrated hybrid approach: Influence on elliptic flow*, *Phys. Rev. C* **81** (2010) 044906, [arXiv:1002.1003].

[65] R. P. G. Andrade, F. Grassi, Y. Hama, T. Kodama, and W. L. Qian, *Importance of Granular Structure in the Initial Conditions for the Elliptic Flow*, *Phys. Rev. Lett.* **101** (2008) 112301, [arXiv:0805.0018].

[66] H.-J. Drescher, "fKLN code." available at URL http://th.physik.uni-frankfurt.de/~drescher/CGC/.

[67] H. Song and U. Heinz, *Multiplicity scaling in ideal and viscous hydrodynamics*, *Phys. Rev. C* **78** (2008) 024902, [arXiv:0805.1756].

[68] U. Heinz, J. S. Moreland, and H. Song, *Viscosity from elliptic flow: the path to precision*, *Phys. Rev. C* **80** (2009) 061901, [arXiv:0908.2617].

[69] F. Cooper and G. Frye, *Comment on the Single Particle Distribution in the Hydrodynamic and Statistical Thermodynamic Models of Multiparticle Production*, *Phys. Rev. D* **10** (1974) 186.

[70] J. Sollfrank, P. Koch, and U. Heinz, *The Influence of resonance decays on the P(t) spectra from heavy ion collisions*, *Phys. Lett.* **B252** (1990) 256–264.

[71] J. Sollfrank, P. Koch, and U. Heinz, *Is there a low p(T) 'anomaly' in the pion momentum spectra from relativistic nuclear collisions?*, *Z. Phys.* **C52** (1991) 593–610.

[72] Y. Aoki, Z. Fodor, S. D. Katz, and K. K. Szabo, *The equation of state in lattice QCD: With physical quark masses towards the continuum limit*, *JHEP* **01** (2006) 089, [hep-lat/0510084].

[73] M. Cheng et al., *The QCD Equation of State with almost Physical Quark Masses*, *Phys. Rev. D* **77** (2008) 014511, [arXiv:0710.0354].

[74] A. Bazavov et al., *Equation of state and QCD transition at finite temperature*, *Phys. Rev. D* **80** (2009) 014504, [arXiv:0903.4379].

[75] **Particle Data Group** Collaboration, S. Eidelman et al., *Review of particle physics*, *Phys. Lett.* **B592** (2004) 1.

[76] H. Bebie, P. Gerber, J. L. Goity, and H. Leutwyler, *The Role of the entropy in an expanding hadronic gas*, *Nucl. Phys.* **B378** (1992) 95–130.

[77] T. Hirano and K. Tsuda, *Collective flow and two pion correlations from a relativistic hydrodynamic model with early chemical freeze out*, *Phys. Rev. C* **66** (2002) 054905, [nucl-th/0205043].

[78] P. F. Kolb and R. Rapp, *Transverse flow and hadro-chemistry in Au + Au collisions at $\sqrt{s_{\rm NN}}$ = 200-GeV*, *Phys. Rev. C* **67** (2003) 044903, [hep-ph/0210222].

[79] D. Teaney, *Chemical freezeout in heavy ion collisions*, nucl-th/0.

[80] P. Huovinen, *Chemical freeze-out temperature in hydrodynamical description of Au+Au collisions at $\sqrt{s_{\rm NN}} = 200$ GeV*, *Eur. Phys. J.* **A37** (2008) 121–128, [arXiv:0710.4379].

[81] D. Zschiesche, S. Schramm, H. Stoecker, and W. Greiner, *Space-time evolution and HBT analysis of relativistic heavy ion collisions in a chiral SU(3) x SU(3) model*, *Phys. Rev. C* **65** (2002) 064902, [nucl-th/0107037].

[82] C. M. Hung and E. V. Shuryak, *Hydrodynamics near the QCD phase transition: Looking for the longest lived fireball*, *Phys. Rev. Lett.* **75** (1995) 4003–4006, [hep-ph/9412360].

[83] **PHENIX Collaboration** Collaboration, A. Adare et al., *Elliptic and hexadecapole flow of charged hadrons in Au+Au collisions at $\sqrt{s_{NN}} = 200$ GeV*, *Phys.Rev.Lett.* **105** (2010) 062301, [arXiv:1003.5586].

[84] **PHENIX Collaboration** Collaboration, S. S. Adler et al., *Identified charged particle spectra and yields in au + au collisions at $\sqrt{s_{NN}} = 200gev$*, *Phys. Rev. C* **69** (Mar, 2004) 034909.

[85] U. Heinz, *Thermalization at RHIC*, *AIP Conf. Proc.* **739** (2005) 163–180, [nucl-th/0407067].

[86] D. A. Teaney, *Viscosity and thermalization*, *J. Phys.* **G30** (2004) S1247–S1250, [nucl-th/0403053].

[87] A. K. Chaudhuri and U. Heinz, *Hydrodynamical evolution of dissipative QGP fluid*, *J. Phys. Conf. Ser.* **50** (2006) 251–258, [nucl-th/0504022].

[88] U. Heinz, H. Song, and A. K. Chaudhuri, *Dissipative hydrodynamics for viscous relativistic fluids*, *Phys. Rev. C* **73** (2006) 034904, [nucl-th/0510014].

[89] K. Dusling and D. Teaney, *Simulating elliptic flow with viscous hydrodynamics*, *Phys. Rev. C* **77** (2008) 034905, [arXiv:0710.5932].

[90] T. Hirano and M. Gyulassy, *Perfect Fluidity of the Quark Gluon Plasma Core as Seen through its Dissipative Hadronic Corona*, *Nucl. Phys.* **A769** (2006) 71–94, [nucl-th/0506049].

[91] E. Schnedermann, J. Sollfrank, and U. Heinz, *Fireball spectra*, *NATO Adv. Study Inst. Ser. B Phys.* **303** (1993) 175–206.

[92] E. Schnedermann, J. Sollfrank, and U. Heinz, *Thermal phenomenology of hadrons from 200-A/GeV S+S collisions*, *Phys. Rev. C* **48** (1993) 2462–2475, [nucl-th/9307020].

[93] **PHOBOS Collaboration** Collaboration, B. Back et al., *Collision geometry scaling of Au+Au pseudorapidity density from s(NN)**(1/2) = 19.6-GeV to 200-GeV*, *Phys.Rev.* **C70** (2004) 021902, [nucl-ex/0405027].

[94] **ALICE Collaboration** Collaboration, K. Aamodt et al., *Centrality dependence of the charged-particle multiplicity density at mid-rapidity in Pb-Pb collisions at* $\sqrt{s_{NN}} = 2.76$ *TeV*, *Phys.Rev.Lett.* **106** (2011) 032301, [arXiv:1012.1657].

[95] J. L. ALbacete and A. Dumitru, *A model for gluon production in heavy-ion collisions at the LHC with rcBK unintegrated gluon densities*, arXiv:1011.5161.

[96] I. Balitsky, *Quark contribution to the small-x evolution of color dipole*, *Phys.Rev.* **D75** (2007) 014001, [hep-ph/0609105].

[97] J. L. Albacete, *Particle multiplicities in Lead-Lead collisions at the LHC from non-linear evolution with running coupling*, *Phys.Rev.Lett.* **99** (2007) 262301, [arXiv:0707.2545].

[98] Y. V. Kovchegov and H. Weigert, *Triumvirate of Running Couplings in Small-x Evolution*, *Nucl.Phys.* **A784** (2007) 188–226, [hep-ph/0609090].

[99] **ALICE Collaboration** Collaboration, K. Aamodt et al., *Charged-particle multiplicity density at mid-rapidity in central Pb-Pb collisions at* $\sqrt{s_{NN}} = 2.76$ *TeV*, *Phys.Rev.Lett.* **105** (2010) 252301, [arXiv:1011.3916].

[100] **STAR Collaboration** Collaboration, J. Adams et al., *Transverse momentum and collision energy dependence of high p(T) hadron suppression in Au+Au collisions at ultrarelativistic energies*, *Phys.Rev.Lett.* **91** (2003) 172302, [nucl-ex/0305015].

[101] **STAR Collaboration** Collaboration, J. Adams et al., *Identified particle distributions in pp and Au+Au collisions at s(NN)**(1/2) = 200 GeV*, *Phys.Rev.Lett.* **92** (2004) 112301, [nucl-ex/0310004].

[102] **STAR Collaboration** Collaboration, B. Abelev et al., *Systematic Measurements of Identified Particle Spectra in* $pp, d+$ *Au and Au+Au Collisions from STAR*, *Phys.Rev.* **C79** (2009) 034909, [arXiv:0808.2041].

[103] **PHENIX Collaboration** Collaboration, S. Adler et al., *High p_T charged hadron suppression in Au + Au collisions at $\sqrt{s_{NN}} = 200$ GeV*, *Phys.Rev.* **C69** (2004) 034910, [nucl-ex/0308006].

[104] H. Song, S. Bass, and U. W. Heinz, *Spectra and elliptic flow for identified hadrons in 2.76 A TeV Pb+Pb collisions*, *Phys.Rev.* **C89** (2014) 034919, [arXiv:1311.0157].

[105] **STAR Collaboration** Collaboration, B. Abelev et al., *Centrality dependence of charged hadron and strange hadron elliptic flow from s(NN)**(1/2) = 200-GeV Au + Au collisions*, *Phys.Rev.* **C77** (2008) 054901, [arXiv:0801.3466].

[106] **ALICE Collaboration** Collaboration, K. Aamodt et al., *Suppression of Charged Particle Production at Large Transverse Momentum in Central Pb–Pb Collisions at $\sqrt{s_{NN}} = 2.76$ TeV*, *Phys.Lett.* **B696** (2011) 30–39, [arXiv:1012.1004].

[107] **ALICE Collaboration** Collaboration, B. Abelev et al., *Centrality dependence of π, K, p production in Pb-Pb collisions at $\sqrt{s_{NN}} = 2.76$ TeV*, *Phys.Rev.* **C88** (2013), no. 4 044910, [arXiv:1303.0737].

[108] **ALICE Collaboration** Collaboration, M. Krzewicki, *Elliptic and triangular flow of identified particles at ALICE*, *J.Phys.* **G38** (2011) 124047, [arXiv:1107.0080].

[109] J.-Y. Ollitrault, A. M. Poskanzer, and S. A. Voloshin, *Effect of flow fluctuations and nonflow on elliptic flow methods*, *Phys.Rev.* **C80** (2009) 014904, [arXiv:0904.2315].

[110] T. Hirano, U. W. Heinz, D. Kharzeev, R. Lacey, and Y. Nara, *Elliptic Flow from a Hybrid CGC, Full 3D Hydro and Hadronic Cascade Model*, *J.Phys.* **G34** (2007) S879–882, [nucl-th/0701075].

[111] **STAR Collaboration** Collaboration, J. Adams et al., *Azimuthal anisotropy in Au+Au collisions at s(NN)**(1/2) = 200-GeV*, *Phys.Rev.* **C72** (2005) 014904, [nucl-ex/0409033].

[112] Z. Qiu and U. W. Heinz, *Event-by-event shape and flow fluctuations of relativistic heavy-ion collision fireballs*, *Phys.Rev.* **C84** (2011) 024911, [arXiv:1104.0650].

[113] Z. Qiu and U. Heinz, *Event-by-event hydrodynamics for heavy-ion collisions*, *AIP Conf.Proc.* **1441** (2012) 774–776, [arXiv:1108.1714].

[114] G.-Y. Qin, H. Petersen, S. A. Bass, and B. Muller, *Translation of collision geometry fluctuations into momentum anisotropies in relativistic heavy-ion collisions*, *Phys.Rev.* **C82** (2010) 064903, [arXiv:1009.1847].

[115] D. Teaney and L. Yan, *Triangularity and Dipole Asymmetry in Heavy Ion Collisions*, *Phys.Rev.* **C83** (2011) 064904, [arXiv:1010.1876].

[116] E. Shuryak, *The Cone, the Ridge and the Fate of the Initial State Fluctuations in Heavy Ion Collisions*, *Phys.Rev.* **C80** (2009) 054908, [arXiv:0903.3734].

[117] C. Shen, S. A. Bass, T. Hirano, P. Huovinen, Z. Qiu, et al., *The QGP shear viscosity: Elusive goal or just around the corner?*, *J.Phys.* **G38** (2011) 124045, [arXiv:1106.6350].

[118] Z. Qiu, C. Shen, and U. Heinz, *Hydrodynamic elliptic and triangular flow in Pb-Pb collisions at* $\sqrt{s} = 2.76 ATeV$, *Phys.Lett.* **B707** (2012) 151–155, [arXiv:1110.3033].

[119] **ALICE Collaboration** Collaboration, K. Aamodt et al., *Higher harmonic anisotropic flow measurements of charged particles in Pb-Pb collisions at* $\sqrt{s_{NN}}$*=2.76 TeV*, *Phys.Rev.Lett.* **107** (2011) 032301, [arXiv:1105.3865].

[120] H. Holopainen, H. Niemi, and K. J. Eskola, *Event-by-event hydrodynamics and elliptic flow from fluctuating initial state*, *Phys.Rev.* **C83** (2011) 034901, [arXiv:1007.0368].

[121] M. Miller and R. Snellings, *Eccentricity fluctuations and its possible effect on elliptic flow measurements*, nucl-ex/0312008.

[122] S. A. Voloshin, A. M. Poskanzer, A. Tang, and G. Wang, *Elliptic flow in the Gaussian model of eccentricity fluctuations*, *Phys.Lett.* **B659** (2008) 537–541, [arXiv:0708.0800].

[123] R. S. Bhalerao and J.-Y. Ollitrault, *Eccentricity fluctuations and elliptic flow at RHIC*, *Phys.Lett.* **B641** (2006) 260–264, [nucl-th/0607009].

[124] H. Song, S. A. Bass, and U. Heinz, *Viscous QCD matter in a hybrid hydrodynamic+Boltzmann approach*, *Phys.Rev.* **C83** (2011) 024912, [arXiv:1012.0555].

[125] **PHENIX Collaboration** Collaboration, A. Adare et al., *Measurements of Higher-Order Flow Harmonics in Au+Au Collisions at* $\sqrt{s_{NN}} = 200$ *GeV*, *Phys.Rev.Lett.* **107** (2011) 252301, [arXiv:1105.3928].

[126] C. Gale, S. Jeon, B. Schenke, P. Tribedy, and R. Venugopalan, *Event-by-event anisotropic flow in heavy-ion collisions from combined Yang-Mills and viscous fluid dynamics*, *Phys.Rev.Lett.* **110** (2013) 012302, [arXiv:1209.6330].

[127] C. Shen and U. Heinz, *Hydrodynamic flow in heavy-ion collisions with large hadronic viscosity*, *Phys.Rev.* **C83** (2011) 044909, [arXiv:1101.3703].

[128] H. Niemi, G. S. Denicol, P. Huovinen, E. Molnar, and D. H. Rischke, *Influence of the shear viscosity of the quark-gluon plasma on elliptic flow in ultrarelativistic heavy-ion collisions*, *Phys.Rev.Lett.* **106** (2011) 212302, [arXiv:1101.2442].

[129] R. Baier and P. Romatschke, *Causal viscous hydrodynamics for central heavy-ion collisions*, *Eur. Phys. J.* **C51** (2007) 677–687, [nucl-th/0610108].

[130] P. Romatschke, *Causal viscous hydrodynamics for central heavy-ion collisions. II. Meson spectra and HBT radii*, *Eur. Phys. J.* **C52** (2007) 203–209, [nucl-th/0701032].

[131] A. Monnai and T. Hirano, *Effects of Bulk Viscosity at Freezeout*, *Phys. Rev. C* **80** (2009) 054906, [arXiv:0903.4436].

[132] K. Dusling, G. D. Moore, and D. Teaney, *Radiative energy loss and v2 spectra for viscous hydrodynamics*, *Phys. Rev. C* **81** (2010) 034907, [arXiv:0909.0754].

[133] T. Koide, E. Nakano, and T. Kodama, *Shear viscosity coefficient and relaxation time of causal dissipative hydrodynamics in QCD*, *Phys.Rev.Lett.* **103** (2009) 052301, [arXiv:0901.3707].

[134] H. B. Meyer, *A Calculation of the shear viscosity in SU(3) gluodynamics*, *Phys.Rev.* **D76** (2007) 101701, [arXiv:0704.1801].

[135] **STAR Collaboration** Collaboration, H. Caines, *The RHIC Beam Energy Scan: STAR'S Perspective*, arXiv:0906.0305.

[136] **STAR** Collaboration, L. Kumar, *Results from the STAR Beam Energy Scan Program*, *Nucl.Phys.* **A862-863** (2011) 125–131, [arXiv:1101.4310].

[137] **STAR Collaboration** Collaboration, Y. Pandit, *Beam Energy Dependence of Directed and Elliptic Flow Measurement from the STAR Experiment*, *J.Phys.Conf.Ser.* **316** (2011) 012001, [arXiv:1109.2799].

[138] **STAR collaboration** Collaboration, S. Shi, *The Elliptic flow in Au+Au collisions at $\sqrt{s_{NN}}$ = 7.7, 11.5 and 39 GeV at STAR*, *Acta Phys.Polon.Supp.* **5** (2012) 311–316, [arXiv:1111.5385].

[139] **STAR Collaboration** Collaboration, L. Kumar, *Identified Hadron Production from the RHIC Beam Energy Scan*, *J.Phys.* **G38** (2011) 124145, [arXiv:1106.6071].

[140] **STAR Collaboration** Collaboration, A. Schmah, *Event anisotropy v(2) of identified hadrons and light nuclei in Au + Au collisions at s(NN)**(1/2) = 7.7-GeV, 11.5-GeV and 39-GeV with STAR*, *J.Phys.* **G38** (2011) 124049.

[141] M. G. Alford, A. Schmitt, K. Rajagopal, and T. Schfer, *Color superconductivity in dense quark matter*, *Rev.Mod.Phys.* **80** (2008) 1455–1515, [arXiv:0709.4635].

[142] Z. Fodor and S. Katz, *Lattice determination of the critical point of QCD at finite T and μ*, *JHEP* **0203** (2002) 014, [hep-lat/0106002].

[143] S. Ejiri, C. R. Allton, S. J. Hands, O. Kaczmarek, F. Karsch, et al., *Study of QCD thermodynamics at finite density by Taylor expansion*, *Prog.Theor.Phys.Suppl.* **153** (2004) 118–126, [hep-lat/0312006].

[144] R. Gavai and S. Gupta, *The Critical end point of QCD*, *Phys.Rev.* **D71** (2005) 114014, [hep-lat/0412035].

[145] G. Kestin and U. W. Heinz, *Hydrodynamic radial and elliptic flow in heavy-ion collisions from AGS to LHC energies*, *Eur.Phys.J.* **C61** (2009) 545–552, [arXiv:0806.4539].

[146] K. Morita, S. Muroya, C. Nonaka, and T. Hirano, *Comparison of space-time evolutions of hot / dense matter in S(NN)**1/2 = 17-GeV and 130-GeV relativistic heavy ion collisions based on a hydrodynamical model*, *Phys.Rev.* **C66** (2002) 054904, [nucl-th/0205040].

[147] J. Vredevoogd and S. Pratt, *Viscous Hydrodynamics and Relativistic Heavy Ion Collisions*, *Phys.Rev.* **C85** (2012) 044908, [arXiv:1202.1509].

[148] S. Bass, M. Belkacem, M. Bleicher, M. Brandstetter, L. Bravina, et al., *Microscopic models for ultrarelativistic heavy ion collisions*, *Prog.Part.Nucl.Phys.* **41** (1998) 255–369, [nucl-th/9803035].

[149] **PHOBOS Collaboration** Collaboration, B. Alver et al., *Scaling properties in bulk and p(T)-dependent particle production near midrapidity in relativistic heavy ion collisions*, *Phys.Rev.* **C80** (2009) 011901, [arXiv:0808.1895].

[150] **PHOBOS Collaboration** Collaboration, B. Back et al., *Centrality dependence of the charged particle multiplicity near mid-rapidity in Au + Au collisions at $\sqrt{s_{\rm NN}}$ = 130-GeV and 200-GeV*, *Phys.Rev.* **C65** (2002) 061901, [nucl-ex/0201005].

[151] **PHENIX Collaboration** Collaboration, S. Adler et al., *Systematic studies of the centrality and s(NN)**(1/2) dependence of the $dE(T)/d\eta$ and $dN^{\rm ch}/d\eta$ in heavy ion collisions at mid-rapidity*, *Phys.Rev.* **C71** (2005) 034908, [nucl-ex/0409015].

[152] **NA49 Collaboration** Collaboration, C. Alt et al., *Directed and elliptic flow of charged pions and protons in Pb + Pb collisions at 40-A-GeV and 158-A-GeV*, *Phys.Rev.* **C68** (2003) 034903, [nucl-ex/0303001].

[153] U. W. Heinz, *Can the energy dependence of elliptic flow reveal the QGP phase transition?*, *Nucl.Phys.* **A830** (2009) 287C–290C, [arXiv:0907.4256].

[154] U. W. Heinz, *Concepts of heavy ion physics*, hep-ph/0407360.

[155] M. A. Lisa, U. W. Heinz, and U. A. Wiedemann, *Tilted pion sources from azimuthally sensitive HBT interferometry*, *Phys.Lett.* **B489** (2000) 287–292, [nucl-th/0003022].

[156] F. Retiere and M. A. Lisa, *Observable implications of geometrical and dynamical aspects of freeze out in heavy ion collisions*, *Phys.Rev.* **C70** (2004) 044907, [nucl-th/0312024].

[157] **E877 Collaboration** Collaboration, J. Barrette et al., *Two pion correlations in Au + Au collisions at 10.8-GeV/c per nucleon*, *Phys.Rev.Lett.* **78** (1997) 2916–2919, [physics/9702008].

[158] **E895 Collaboration** Collaboration, M. Lisa et al., *Bombarding energy dependence of pi-minus interferometry at the Brookhaven AGS*, *Phys.Rev.Lett.* **84** (2000) 2798–2802.

[159] **STAR Collaboration** Collaboration, J. Adams et al., *Pion interferometry in Au+Au collisions at S(NN)**(1/2) = 200-GeV*, *Phys.Rev.* **C71** (2005) 044906, [nucl-ex/0411036].

[160] **STAR Collaboration** Collaboration, B. Abelev et al., *Pion Interferometry in Au+Au and Cu+Cu Collisions at RHIC*, *Phys.Rev.* **C80** (2009) 024905, [arXiv:0903.1296].

[161] **STAR Collaboration** Collaboration, C. Anson, *Energy dependence of the freeze out eccentricity from the azimuthal dependence of HBT at STAR*, *J.Phys.* **G38** (2011) 124148, [arXiv:1107.1527].

[162] U. W. Heinz and P. F. Kolb, *Emission angle dependent pion interferometry at RHIC and beyond*, *Phys.Lett.* **B542** (2002) 216–222, [hep-ph/0206278].

[163] E. Frodermann, R. Chatterjee, and U. Heinz, *Evolution of pion HBT radii from RHIC to LHC: Predictions from ideal hydrodynamics*, *J.Phys.* **G34** (2007) 2249–2254, [arXiv:0707.1898].

[164] B. Alver, B. Back, M. Baker, M. Ballintijn, D. Barton, et al., *Importance of correlations and fluctuations on the initial source eccentricity in high-energy nucleus-nucleus collisions*, *Phys.Rev.* **C77** (2008) 014906, [arXiv:0711.3724].

[165] S. A. Voloshin, A. M. Poskanzer, and R. Snellings, *Collective phenomena in non-central nuclear collisions*, arXiv:0809.2949.

[166] N. Borghini, P. M. Dinh, and J.-Y. Ollitrault, *A New method for measuring azimuthal distributions in nucleus-nucleus collisions*, *Phys.Rev.* **C63** (2001) 054906, [nucl-th/0007063].

[167] N. Borghini, P. M. Dinh, and J.-Y. Ollitrault, *Flow analysis from multiparticle azimuthal correlations*, *Phys.Rev.* **C64** (2001) 054901, [nucl-th/0105040].

[168] A. Bilandzic, R. Snellings, and S. Voloshin, *Flow analysis with cumulants: Direct calculations*, *Phys.Rev.* **C83** (2011) 044913, [arXiv:1010.0233].

[169] M. Luzum, *Flow fluctuations and long-range correlations: elliptic flow and beyond*, *J.Phys.* **G38** (2011) 124026, [arXiv:1107.0592].

[170] **PHOBOS Collaboration** Collaboration, B. Alver et al., *Non-flow correlations and elliptic flow fluctuations in gold-gold collisions at* $\sqrt{s_{NN}} = 200$ *GeV*, *Phys.Rev.* **C81** (2010) 034915, [arXiv:1002.0534].

[171] **ALICE Collaboration** Collaboration, K. Aamodt et al., *Harmonic decomposition of two-particle angular correlations in Pb-Pb collisions at* $\sqrt{s_{NN}} = 2.76$ *TeV*, *Phys.Lett.* **B708** (2012) 249–264, [arXiv:1109.2501].

[172] **CMS Collaboration** Collaboration, S. Chatrchyan et al., *Centrality dependence of dihadron correlations and azimuthal anisotropy harmonics in PbPb collisions at* $\sqrt{s_{NN}} = 2.76$ *TeV*, *Eur.Phys.J.* **C72** (2012) 2012, [arXiv:1201.3158].

[173] **ATLAS Collaboration** Collaboration, G. Aad et al., *Measurement of the azimuthal anisotropy for charged particle production in* $\sqrt{s_{NN}} = 2.76$ *TeV lead-lead collisions with the ATLAS detector*, *Phys.Rev.* **C86** (2012) 014907, [arXiv:1203.3087].

[174] Z. Qiu and U. Heinz, *Hydrodynamic event-plane correlations in Pb+Pb collisions at* $\sqrt{s} = 2.76ATeV$, *Phys.Lett.* **B717** (2012) 261–265, [arXiv:1208.1200].

[175] **CMS** Collaboration, S. Chatrchyan et al., *Studies of azimuthal dihadron correlations in ultra-central PbPb collisions at* $\sqrt{s_{NN}} = 2.76$ *TeV*, *JHEP* **1402** (2014) 088, [arXiv:1312.1845].

[176] M. Luzum and J.-Y. Ollitrault, *Extracting the shear viscosity of the quark-gluon plasma from flow in ultra-central heavy-ion collisions*, *Nucl.Phys.* **A904-905** (2013) 377c–380c, [arXiv:1210.6010].

[177] F. G. Gardim, F. Grassi, M. Luzum, and J.-Y. Ollitrault, *Mapping the hydrodynamic response to the initial geometry in heavy-ion collisions*, *Phys.Rev.* **C85** (2012) 024908, [arXiv:1111.6538].

[178] R. A. Lacey, A. Taranenko, J. Jia, D. Reynolds, N. Ajitanand, et al., *Beam energy dependence of the viscous damping of anisotropic flow in relativistic heavy ion collisions*, *Phys.Rev.Lett.* **112** (2014) 082302, [arXiv:1305.3341].

[179] G. Basar and D. Teaney, *A scaling relation between pA and AA collisions*, arXiv:1312.6770.

[180] J. Serreau, *Out-of-equilibrium electromagnetic radiation*, *JHEP* **0405** (2004) 078, [hep-ph/0310051].

[181] P. B. Arnold, G. D. Moore, and L. G. Yaffe, *Photon emission from ultrarelativistic plasmas*, *JHEP* **0111** (2001) 057, [hep-ph/0109064].

[182] S. Turbide, R. Rapp, and C. Gale, *Hadronic production of thermal photons*, *Phys.Rev.* **C69** (2004) 014903, [hep-ph/0308085].

[183] U. Heinz and R. Snellings, *Collective flow and viscosity in relativistic heavy-ion collisions*, *Ann.Rev.Nucl.Part.Sci.* **63** (2013) 123–151, [arXiv:1301.2826].

[184] C. Gale, S. Jeon, and B. Schenke, *Hydrodynamic Modeling of Heavy-Ion Collisions*, *Int.J.Mod.Phys.* **A28** (2013) 1340011, [arXiv:1301.5893].

[185] P. B. Arnold, G. D. Moore, and L. G. Yaffe, *Photon emission from quark gluon plasma: Complete leading order results*, *JHEP* **0112** (2001) 009, [hep-ph/0111107].

[186] J. Ghiglieri, J. Hong, A. Kurkela, E. Lu, G. D. Moore, et al., *Next-to-leading order thermal photon production in a weakly coupled quark-gluon plasma*, *JHEP* **1305** (2013) 010, [arXiv:1302.5970].

[187] K. Dusling and S. Lin, *Dilepton production from a viscous QGP*, *Nucl.Phys.* **A809** (2008) 246–258, [arXiv:0803.1262].

[188] K. Dusling, *Photons as a viscometer of heavy ion collisions*, *Nucl.Phys.* **A839** (2010) 70–77, [arXiv:0903.1764].

[189] M. Dion, J.-F. Paquet, B. Schenke, C. Young, S. Jeon, et al., *Viscous photons in relativistic heavy ion collisions*, *Phys.Rev.* **C84** (2011) 064901, [arXiv:1109.4405].

[190] R. Baier, M. Dirks, K. Redlich, and D. Schiff, *Thermal photon production rate from nonequilibrium quantum field theory*, *Phys.Rev.* **D56** (1997) 2548–2554, [hep-ph/9704262].

[191] B. Schenke and M. Strickland, *Fermionic Collective Modes of an Anisotropic Quark-Gluon Plasma*, *Phys.Rev.* **D74** (2006) 065004, [hep-ph/0606160].

[192] B. Schenke and M. Strickland, *Photon production from an anisotropic quark-gluon plasma*, *Phys.Rev.* **D76** (2007) 025023, [hep-ph/0611332].

[193] P. Romatschke, *New Developments in Relativistic Viscous Hydrodynamics*, *Int. J. Mod. Phys.* **E19** (2010) 1–53, [arXiv:0902.3663].

[194] R. Baier, P. Romatschke, and U. A. Wiedemann, *Dissipative hydrodynamics and heavy ion collisions*, *Phys. Rev. C* **73** (2006) 064903, [hep-ph/0602249].

[195] J. Rammer, *Quantum field theory of non-equilibrium states*, .

[196] H. A. Weldon, *Simple Rules for Discontinuities in Finite Temperature Field Theory*, *Phys.Rev.* **D28** (1983) 2007.

[197] F. Gelis, *Cutting rules in the real time formalisms at finite temperature*, *Nucl.Phys.* **B508** (1997) 483–505, [hep-ph/9701410].

[198] A. Majumder and C. Gale, *On the imaginary parts and infrared divergences of two loop vector boson selfenergies in thermal QCD*, *Phys.Rev.* **C65** (2002) 055203, [hep-ph/0111181].

[199] M. Le Bellac, *Thermal field theory*. Cambridge monographs on mathematical physics. Cambridge Univ. Press, Cambridge, 1996.

[200] C. Greiner and S. Leupold, *Stochastic interpretation of Kadanoff-Baym equations and their relation to Langevin processes*, *Annals Phys.* **270** (1998) 328–390, [hep-ph/9802312].

[201] A. Das, *Finite Temperature Field Theory*. World scientific lecture notes in physics. World Scientific Publishing Company, Incorporated, 1997.

[202] C. Greiner and S. Leupold, *Interpretation and resolution of pinch singularities in nonequilibrium quantum field theory*, *Eur.Phys.J.* **C8** (1999) 517–522, [hep-ph/9804239].

[203] S. Mrowczynski and M. H. Thoma, *Hard loop approach to anisotropic systems*, *Phys.Rev.* **D62** (2000) 036011, [hep-ph/0001164].

[204] J.-P. Blaizot and E. Iancu, *The Quark gluon plasma: Collective dynamics and hard thermal loops*, *Phys.Rept.* **359** (2002) 355–528, [hep-ph/0101103].

[205] E. Braaten and R. D. Pisarski, *Soft Amplitudes in Hot Gauge Theories: A General Analysis*, *Nucl.Phys.* **B337** (1990) 569.

[206] E. Braaten, R. D. Pisarski, and T.-C. Yuan, *Production of Soft Dileptons in the Quark - Gluon Plasma*, *Phys.Rev.Lett.* **64** (1990) 2242.

[207] J. I. Kapusta, P. Lichard, and D. Seibert, *High-energy photons from quark - gluon plasma versus hot hadronic gas*, *Phys.Rev.* **D44** (1991) 2774–2788.

[208] R. Baier, H. Nakkagawa, A. Niegawa, and K. Redlich, *Production rate of hard thermal photons and screening of quark mass singularity*, *Z.Phys.* **C53** (1992) 433–438.

[209] P. B. Arnold, G. D. Moore, and L. G. Yaffe, *Effective kinetic theory for high temperature gauge theories*, *JHEP* **0301** (2003) 030, [hep-ph/0209353].

[210] V. Koch, *Aspects of chiral symmetry*, *Int.J.Mod.Phys.* **E6** (1997) 203–250, [nucl-th/9706075].

[211] S. Turbide, *Electromagnetic radiation from matter under extreme conditions*. PhD thesis, McGill University, 2006.

[212] H. Gomm, O. Kaymakcalan, and J. Schechter, *Anomalous Spin 1 Meson Decays From the Gauged Wess-Zumino Term*, *Phys.Rev.* **D30** (1984) 2345.

[213] C. Song, *Photon emission from hot hadronic matter described by an effective chiral Lagrangian*, *Phys.Rev.* **C47** (1993) 2861–2874.

[214] J. Schechter, *Electromagnetism in a Gauged Chiral Model*, *Phys.Rev.* **D34** (1986) 868.

[215] C. Gale and J. I. Kapusta, *Vector dominance model at finite temperature*, *Nucl.Phys.* **B357** (1991) 65–89.

[216] M. Peskin and D. Schroeder, *An Introduction to Quantum Field Theory*. Advanced book classics. Addison-Wesley Publishing Company, 1995.

[217] **PHENIX Collaboration** Collaboration, A. Adare et al., *Enhanced production of direct photons in Au+Au collisions at $\sqrt{s_{NN}} = 200$ GeV and implications for the initial temperature*, *Phys.Rev.Lett.* **104** (2010) 132301, [arXiv:0804.4168].

[218] **ALICE Collaboration** Collaboration, M. Wilde, *Measurement of Direct Photons in pp and Pb-Pb Collisions with ALICE*, *Nucl.Phys.* **A904-905** (2013) 573c–576c, [arXiv:1210.5958].

[219] Y. Aoki, Z. Fodor, S. Katz, and K. Szabo, *The QCD transition temperature: Results with physical masses in the continuum limit*, *Phys.Lett.* **B643** (2006) 46–54, [hep-lat/0609068].

[220] A. Bazavov, T. Bhattacharya, M. Cheng, C. DeTar, H. Ding, et al., *The chiral and deconfinement aspects of the QCD transition*, *Phys.Rev.* **D85** (2012) 054503, [arXiv:1111.1710].

[221] S. Turbide, C. Gale, E. Frodermann, and U. Heinz, *Electromagnetic radiation from nuclear collisions at RHIC energies*, *Phys.Rev.* **C77** (2008) 024909, [arXiv:0712.0732].

[222] C. Shen, U. W. Heinz, J.-F. Paquet, and C. Gale, *Thermal photons as a quark-gluon plasma thermometer revisited*, *Phys.Rev.* **C89** (2014) 044910, [arXiv:1308.2440].

[223] T. Biro, E. van Doorn, B. Muller, M. Thoma, and X. Wang, *Parton equilibration in relativistic heavy ion collisions*, *Phys.Rev.* **C48** (1993) 1275–1284, [nucl-th/9303004].

[224] F. Gelis, H. Niemi, P. Ruuskanen, and S. Rasanen, *Photon production from nonequilibrium QGP in heavy ion collisions*, *J.Phys.* **G30** (2004) S1031–S1036, [nucl-th/0403040].

[225] M. Klasen, C. Klein-Bsing, F. Knig, and J. Wessels, *How robust is a thermal photon interpretation of the ALICE low-p_T data?*, *JHEP* **1310** (2013) 119, [arXiv:1307.7034].

[226] S. Turbide, *Electromagnetic radiation from matter under extreme conditions*, .

[227] P. Aurenche, M. Fontannaz, J.-P. Guillet, E. Pilon, and M. Werlen, *A New critical study of photon production in hadronic collisions*, *Phys.Rev.* **D73** (2006) 094007, [hep-ph/0602133].

[228] K. Eskola, H. Paukkunen, and C. Salgado, *EPS09: A New Generation of NLO and LO Nuclear Parton Distribution Functions*, *JHEP* **0904** (2009) 065, [arXiv:0902.4154].

[229] G.-Y. Qin, J. Ruppert, C. Gale, S. Jeon, and G. D. Moore, *Jet energy loss, photon production, and photon-hadron correlations at RHIC*, *Phys.Rev.* **C80** (2009) 054909, [arXiv:0906.3280].

[230] R. Chatterjee, H. Holopainen, I. Helenius, T. Renk, and K. J. Eskola, *Elliptic flow of thermal photons from event-by-event hydrodynamic model*, *Phys.Rev.* **C88** (2013) 034901, [arXiv:1305.6443].

[231] R. Chatterjee, H. Holopainen, T. Renk, and K. J. Eskola, *Enhancement of thermal photon production in event-by-event hydrodynamics*, *Phys.Rev.* **C83** (2011) 054908, [arXiv:1102.4706].

[232] H. van Hees, C. Gale, and R. Rapp, *Thermal Photons and Collective Flow at the Relativistic Heavy-Ion Collider*, *Phys.Rev.* **C84** (2011) 054906, [arXiv:1108.2131].

[233] **PHENIX** Collaboration, B. Bannier, *Measurements of direct photons in Au+Au collisions with PHENIX*, arXiv:1404.3024.

[234] E. Feinberg, *Direct Production of Photons and Dileptons in Thermodynamical Models of Multiple Hadron Production*, *Nuovo Cim.* **A34** (1976) 391.

[235] R. Hwa and K. Kajantie, *Diagnosing Quark Matter by Measuring the Total Entropy and the Photon Or Dilepton Emission Rates*, *Phys.Rev.* **D32** (1985) 1109.

[236] R. Chatterjee, E. S. Frodermann, U. W. Heinz, and D. K. Srivastava, *Elliptic flow of thermal photons in relativistic nuclear collisions*, *Phys.Rev.Lett.* **96** (2006) 202302, [nucl-th/0511079].

[237] R. Rapp, *Theory of Soft Electromagnetic Emission in Heavy-Ion Collisions*, *Acta Phys.Polon.* **B42** (2011) 2823–2852, [arXiv:1110.4345].

[238] C. Shen, U. W. Heinz, J.-F. Paquet, I. Kozlov, and C. Gale, *Anisotropic flow of thermal photons as a quark-gluon plasma viscometer*, arXiv:1308.2111.

[239] **PHENIX Collaboration** Collaboration, A. Adare et al., *Observation of direct-photon collective flow in $\sqrt{s_{NN}} = 200$ GeV Au+Au collisions*, *Phys.Rev.Lett.* **109** (2012) 122302, [arXiv:1105.4126].

[240] **ALICE** Collaboration, D. Lohner, *Measurement of Direct-Photon Elliptic Flow in Pb-Pb Collisions at $\sqrt{s_{NN}} = 2.76$ TeV*, *J.Phys.Conf.Ser.* **446** (2013) 012028, [arXiv:1212.3995].

[241] C. Shen, U. Heinz, J.-F. Paquet, and C. Gale, *Thermal photon anisotropic flow serves as a quark-gluon plasma viscometer*, arXiv:1403.7558.

[242] U. W. Heinz, J. Liu, and C. Shen, *Electromagnetic fingerprints of the Little Bang*, arXiv:1403.8101.

[243] G. Basar, D. Kharzeev, D. Kharzeev, and V. Skokov, *Conformal anomaly as a source of soft photons in heavy ion collisions*, *Phys.Rev.Lett.* **109** (2012) 202303, [arXiv:1206.1334].

[244] W. Liu and R. Rapp, *Low-energy thermal photons from meson-meson bremsstrahlung*, *Nucl.Phys.* **A796** (2007) 101–121, [nucl-th/0604031].

[245] O. Linnyk, W. Cassing, and E. Bratkovskaya, *Centrality dependence of the direct photon yield and elliptic flow in heavy-ion collisions at sqrt(s)=200 GeV*, *Phys.Rev.* **C89** (2014) 034908, [arXiv:1311.0279].

[246] **Particle Data Group** Collaboration, J. Beringer et al., *Review of Particle Physics (RPP)*, *Phys.Rev.* **D86** (2012) 010001.

[247] H. Grad, *On the kinetic theory of rarefied gases*, *Communications on Pure and Applied Mathematics* **2** (1949), no. 4 331–407.

[248] U. W. Heinz and S. Wong, *Elliptic flow from a transversally thermalized fireball*, *Phys.Rev.* **C66** (2002) 014907, [hep-ph/0205058].

[249] L. Landau and E. Lifshitz, *Statistical Physics*. No. v. 5. Elsevier Science, 1996.

[250] **ALICE Collaboration** Collaboration, K. Aamodt et al., *Charged-particle multiplicity measurement in proton-proton collisions at $\sqrt{s} = 0.9$ and 2.36 TeV with ALICE at LHC*, *Eur.Phys.J.* **C68** (2010) 89–108, [arXiv:1004.3034].

[251] W. Broniowski, P. Bozek, and M. Rybczynski, *Fluctuating initial conditions in heavy-ion collisions from the Glauber approach*, *Phys.Rev.* **C76** (2007) 054905, [arXiv:0706.4266].

[252] M. Alvioli, H. Holopainen, K. Eskola, and M. Strikman, *Initial state anisotropies and their uncertainties in ultrarelativistic heavy-ion collisions from the Monte Carlo Glauber model*, *Phys.Rev.* **C85** (2012) 034902, [arXiv:1112.5306].